AGU Reference Shelf 1

Global Earth Physics

A Handbook of Physical Constants

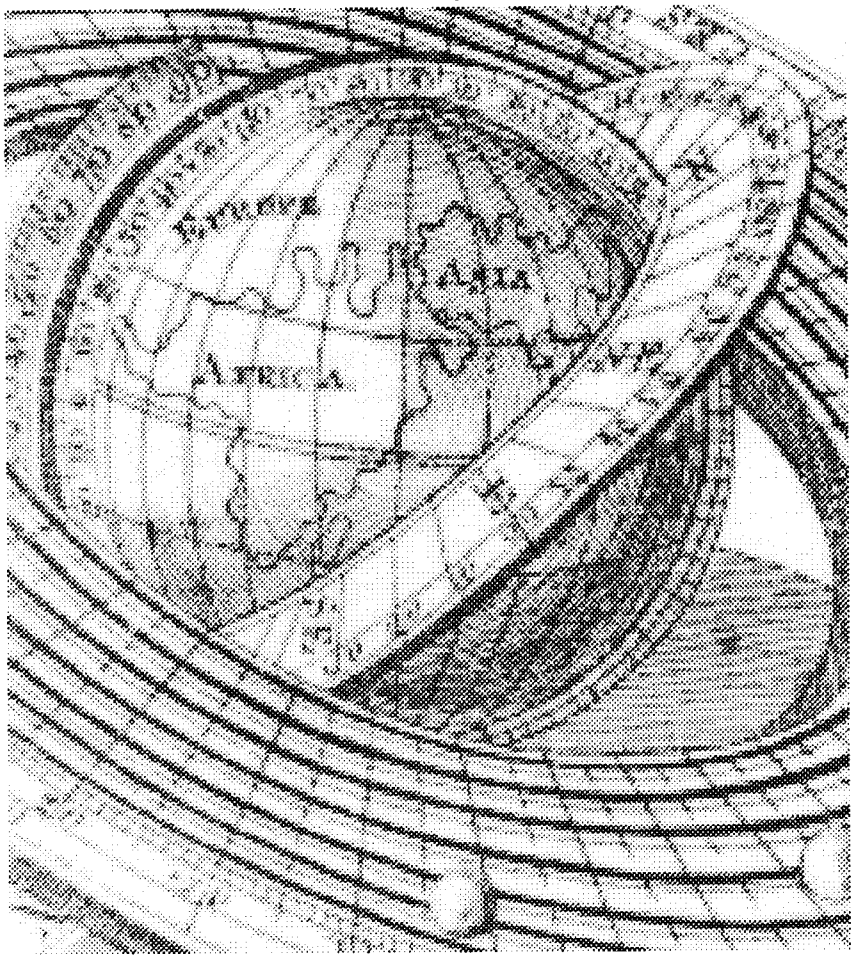

Thomas J. Ahrens, Editor

Published under the aegis of the AGU Books Board

Library of Congress Cataloging-in-Publication Data

Global earth physics : a handbook of physical constants / Thomas J. Ahrens, editor.
p. cm. — (AGU reference shelf ; 1)
Includes bibliographical references and index.
ISBN 0-87590-851-9
1. Geophysics—Handbooks, manuals, etc. 2. Physical constants—
—Handbooks, manuals, etc. I. Ahrens, Thomas J., 1936– .
II. Series.
QC808.8.G56 1995
550—dc20 94-44745
CIP

ISBN 0-87590-851-9
ISSN 1080-305X

Published by
American Geophysical Union

Printed in the United States of America.

This document is navigable.
Click on a Chapter heading below to view that document

CONTENTS

CONTENTS

PREFACE

The purpose of this Handbook is to provide, in highly accessible form, selected critical data for professional and student solid Earth and planetary geophysicists. Coverage of topics and authors were carefully chosen to fulfill these objectives.

These volumes represent the third version of the "Handbook of Physical Constants." Several generations of solid Earth scientists have found these handbooks to be the most frequently used item in their personal library. The first version of this Handbook was edited by F. Birch, J. F. Schairer, and H. Cecil Spicer and published in 1942 by the Geological Society of America (GSA) as Special Paper 36. The second edition, edited by Sydney P. Clark, Jr., was also published by GSA as Memoir 92 in 1966. Since 1966, our scientific knowledge of the Earth and planets has grown enormously, spurred by the discovery and verification of plate tectonics and the systematic exploration of the solar system.

The present revision was initiated, in part, by a 1989 chance remark by Alexandra Navrotsky asking what the Mineral Physics (now Mineral and Rock Physics) Committee of the American Geophysical Union could produce that would be a tangible useful product. At the time I responded, "update the Handbook of Physical Constants." As soon as these words were uttered, I realized that I could edit such a revised Handbook. I thank Raymond Jeanloz for his help with initial suggestions of topics, the AGU's Books Board, especially Ian McGregor, for encouragement and enthusiastic support. Ms. Susan Yamada, my assistant, deserves special thanks for her meticulous stewardship of these volumes. I thank the technical reviewers listed below whose efforts, in all cases, improved the manuscripts.

Thomas J. Ahrens, Editor
California Institute of Technology
Pasadena

Carl Agee
Thomas J. Ahrens
Orson Anderson
Don Anderson
George H. Brimhall
John Brodholt
J. Michael Brown
Bruce Buffett
Robert Butler
Clement Chase
Robert Creaser
Veronique Dehant
Alfred G. Duba
Larry Finger
Michael Gaffey
Carey Gazis
Michael Gurnis
William W. Hay
Thomas Heaton
Thomas Herring
Joel Ita
Andreas K. Kronenberg
Robert A. Langel
John Longhi
Guenter W. Lugmair
Stephen Mackwell
Gerald M. Mavko
Walter D. Mooney
Herbert Palme
Dean Presnall
Richard H. Rapp
Justin Revenaugh
Rich Reynolds
Robert Reynolds
Yanick Ricard
Frank Richter
William I. Rose, Jr.
George Rossman
John Sass
Surendra K. Saxena
Ulrich Schmucker
Ricardo Schwarz
Doug E. Smylie
Carol Stein
Maureen Steiner
Lars Stixrude
Edward Stolper
Stuart Ross Taylor
Jeannot Trampert
Marius Vassiliou
Richard P. Von Herzen
John M. Wahr
Yuk Yung

Astrometric and Geodetic Properties of Earth and the Solar System

Charles F. Yoder

1. BACKGROUND

The mass, size and shape of planets and their satellites and are essential information from which one can consider the balance of gravity and tensile strength, chemical makeup and such factors as internal temperature or porosity. Orbits and planetary rotation are also useful clues concerning origin, internal structure and tidal history. The tables compiled here include some of the latest results such as detection of densities of Pluto-Charon from analysis of HST images and the latest results for Venus' shape, gravity field and pole orientation based on Magellan spacecraft data. Data concerning prominent asteroids, comets and Sun are also included.

Most of the material here is presented as tables. They are preceded by brief explanations of the relevant geophysical and orbit parameters. More complete explanations can be found in any of several reference texts on geodesy [109, 74], geophysics [56, 58, 110] and celestial mechanics [13, 88, 98].

2. GRAVITY FIELD SHAPE AND INTERNAL STRUCTURE

External Gravity Field: The potential external of a non-spherical body [109, 57] at latitude ϕ and longitude λ and distance $r(\phi,\lambda) > R_e$ can be represented as a series with associated Legendre polynomials, $P_{nj}(\sin\phi)$,

$$U = \frac{GM}{r}\sum_{n,j=0}^{n=\infty}\left(\frac{R_e}{r}\right)^n (C_{nj}\cos\lambda + S_{nj}\sin\lambda)\,P_{nj}, \quad (1)$$

and $j \le n$. The zonal Legendre polynomials $P_{n0}(x)$ for $n < 7$ are

$$\begin{aligned} P_{00} &= 1 \\ P_{10} &= x \\ P_{20} &= \left(3x^2 - 1\right)/2 \\ P_{30} &= \left(5x^3 - 3x\right)/2 \\ P_{40} &= \left(35x^4 - 30x^2 + 3\right)/8 \\ P_{50} &= \left(63x^5 - 70x^3 + 15x\right)/8 \\ P_{60} &= \left(231x^6 - 315x^4 + 105x^2 - 5\right)/16. \end{aligned} \quad (2)$$

Higher order zonal functions can be derived from

$$P_{n0} = \frac{1}{2^n n!}\frac{d^n}{dx^n}(x^2-1)^n. \quad (3)$$

or from the recursion relation

$$(n+1)P_{n+1,0} = (2n+1)xP_{n,0} - nP_{n-1,0}\,. \quad (4)$$

The tesseral ($j < n$) and sectorial ($j = n$) functions can be deduced from

$$P_{nj} = \cos^j\phi\,\frac{d^j}{dx^j}P_{n0}\,. \quad (5)$$

Thus $P_{11} = \cos\phi$, $P_{21} = 3\sin\phi\cos\phi$, $P_{22} = 3\cos^2\phi$, etc.

Surface topography can be expanded in similar fashion with $R_e C^T_{nm}$ and $R_e S^T_{nm}$ as coefficients of the respective Legendre functions.

Gravity Field Expansion Coefficients: The dimensionless gravity field coefficients C_{nj} : S_{nj} of harmonic degree n and tesseral order j are related to the following volume integral.

C. Yoder, Jet Propulsion Laboratory, 183-501, 4800 Oak Grove Drive, Pasadena, CA 91109

Global Earth Physics
A Handbook of Physical Constants
AGU Reference Shelf 1

$$(C_{nj} : S_{nj}) = \frac{(2-\delta_{j0})}{M R_e^n} \frac{(n-j)!}{(n+j)!} \times \int dV \rho(\mathbf{r}) r^n P_{nj}(\sin\phi') (\cos j\lambda' : \sin j\lambda') \quad (6)$$

where ϕ^* and λ' are the latitude and longitude at internal position $\mathbf{r}(\phi', \lambda')$.

Both surface undulations and internal density variations contribute to the effective field. For an equivalent representation in terms of just density variations, then

$$\rho(\mathbf{r}) = \sum_{C,S,n,j} (\rho_{nj}^C(r) : \rho_{nj}^S(r)) \times P_{nj}(\sin\phi) (\cos j\theta : \sin j\theta), \quad (7)$$

and

$$(C_{nj} : S_{nj}) = \frac{4\pi}{M R_e^n (2n+1)} \int_0^{R_e} dr\, r^{n+2} \rho_{nj}^{C:S}(r). \quad (8)$$

A first order estimate of the contribution of *uncompensated* topography with radial harmonic coefficient C_{nj}^{T} to gravity is given by [12]

$$(C_{nj} : S_{nj}) = \frac{3}{(2n+1)} \frac{\rho_s}{\overline{\rho}} (C_{nj}^{\mathrm{T}} : S_{nj}^{\mathrm{T}}), \quad (9)$$

where ρ_s and $\overline{\rho}$ are the crustal and mean densities, respectively.

Airy compensation, where surface topography of a uniform density crust with average thickness H is compensated by bottom crustal topography, has external gravity which is smaller by a factor of $(1 - ((R_e - H)/R_e)^{n+2})$.

$\mathbf{J}_n$: The usual convention for representation of the zonal coefficients is as J_n,

$$J_n = -C_{n0}\,. \quad (10)$$

The *normalized* $\overline{C}_{nj} : \overline{S}_{nj}$ coefficients are

$$(\overline{C}_{nj} : \overline{S}_{nj}) = N_{nj} (C_{nj} : S_{nj})\,. \quad (11)$$

The normalization factor N_{nj} is

$$N_{nj}^2 = \frac{1+\delta_{j0}}{2} \int_{-\frac{\pi}{2}}^{\frac{\pi}{2}} \cos\phi d\phi P_{nj}^2 = \frac{(1+\delta_{j0})}{2(2n+1)} \frac{(n+j)!}{(n-j)!} \quad (12)$$

Kaula's Rule: The gravity field power spectra function σ_{g} for many solid planetary bodies tend to follow *Kaula's rule,*

$$\sigma_{\mathrm{g}} = \sum_{n=0}^{\infty} \sum_{j=0}^{j=n} \left(\overline{C}_{nj}^2 + \overline{S}_{nj}^2\right) \simeq (2n+1) \frac{u^2}{n^q}, \quad (13)$$

where u is constant and q is $\simeq 4$. A similar scaling is found for topography with

$$\sigma_{\mathrm{t}} \simeq \frac{t^2}{n(n+1)}. \quad (14)$$

and t a constant.

Moments of Inertia: The 2nd harmonic coefficients are related to the moments of inertia tensor I_{ij} where i and $j = 1, 2, 3$ correspond to the $\{x, y, z\}$ axes, respectively.

$$M R_e^2 C_{20} = -\left(C - \frac{1}{2}(B+A)\right), \quad (15)$$

$$M R_e^2 C_{21} = -I_{13}, \qquad M R_e^2 S_{21} = -I_{23}, \quad (16)$$

$$M R_e^2 C_{22} = \frac{1}{4}(B-A), \quad (17)$$

where C, B and A are the principal moments about the z, y and x axes, respectively (that is, $C = I_{33}, B = I_{22}$ and $A = I_{11}$). The coordinate frame can be chosen such that the off-diagonal I_{ij} vanish and $C > B > A$ and is significant as it represents a minimum energy state for a rotating body. The choice for R_e is somewhat arbitrary, although the convention is to choose the equatorial radius. The moment for a uniform sphere is $\frac{2}{5} M R^2$, and if we wish to preserve the 2/5 coefficient for the mean moment $I = (A+B+C)/3$ for a triaxial ellipsoid, then $R_o = (a^2 + b^2 + c^2)/3$ is the appropriate choice. The volumetric mean radius $R_{\mathrm{V}} = \sqrt[3]{abc}$ and differs from $\mathrm{R_o}$ in the second order.

The potential contributions from surface topography can be appreciated from a consideration of a uniform triaxial ellipsoid with surface defined by

$$\left(\frac{x}{a}\right)^2 + \left(\frac{y}{b}\right)^2 + \left(\frac{z}{c}\right)^2 = 1\,. \quad (18)$$

The harmonic coefficients and maximum principal moment for a triaxial ellipsoid with body axes $a > b > c$ and with *uniform density* are (to 4th degree)

$$C_{20} = \frac{1}{5R_o^2}\left(c^2 - \frac{1}{2}(a^2+b^2)\right), \quad (19)$$

$$C_{22} = \frac{1}{20R_o^2}\left(b^2 - a^2\right), \quad (20)$$

$$C_{40} = \frac{15}{7} C_{20}^2, \quad (21)$$

$$C_{42} = \frac{15}{14} C_{20} C_{22}, \quad (22)$$

$$C_{44} = \frac{15}{49} C_{20} C_{22}\,, \tag{23}$$

$$C = \frac{1}{5}\left(a^2 + b^2\right) M = I - \frac{2}{3} M R_o^2 C_{20}\,. \tag{24}$$

while from symmetry the coefficients with either odd degree n or order j vanish.

Hydrostatic Shape: The hydrostatic shape [24, 18, 124] of a uniformly rotating body with rotation rate ω_s and radial density structure is controlled by the rotation parameter m and flattening f,

$$m \equiv \frac{\omega_s^2 a^3}{GM}\,, \qquad f = \frac{a-b}{a}\,. \tag{25}$$

Other choices for the spin factor which appear in the literature are $m_v = \omega_s^2 b a^2/GM = m(1-f)$, $m_o = \omega_s^2 R_0^3/GM \simeq m_v(1-\frac{2}{3}f^2)$ and $m_g = \omega_s^2 a/g_e$. The *ellipticity* $\widehat{e} = \sqrt{1-(b/a)^2}$ is sometimes used instead of f.

The relationship between J_2, J_4 and f ($\widetilde{f} = f(1-\frac{1}{2}f)$ and $\widetilde{m}_v = m_v(1-\frac{2}{7}f)$) is [24]

$$J_2 \simeq \frac{1}{3}\left(2\widetilde{f} - \widetilde{m}_v + \frac{11}{49} m f^2\right), \tag{26}$$

$$J_4 \simeq -\frac{15}{7} J_2^2 + \frac{5}{21}\left(\frac{4}{5}\widetilde{f} - \widetilde{m}_v\right)^2. \tag{27}$$

An expression for the hydrostatic flattening, accurate to second order, is [50]

$$f = \frac{1}{2}\left(m_v + 3J_2\right)\left(1 + \frac{3}{2}J_2\right) + \frac{5}{8}J_4. \tag{28}$$

The mean moment of inertia for a fluid planet is also related to f and m through an approximate solution to Clairaut's equation.

$$x\frac{d\eta}{dx} - \eta^2 + \left(\frac{\rho}{\rho_o} - 5\right)\eta = 6\left(\frac{\rho}{\rho_o} - 1\right) \tag{29}$$

where $\eta = d\ln f(x)/d\ln x$ is the logarithmic derivative of the flattening, and $\rho_o(x) = 3g(x)/4\pi x$ is the mean density inside radius x, and is proportional to gravity $g(x)$. The solution of (29) results in a relationship between f, m and the mean moment of inertia I which is only weakly dependent on the actual density profile for solid bodies.

$$I \simeq \frac{2}{3} M R_o^2\left[1 - \frac{2}{5}\left(\frac{1}{1+\delta_1}\right)\sqrt{\frac{5m_v}{2f} - 1 + \delta_2}\right], \tag{30}$$

$$\delta_2 \simeq \frac{3}{7}f + \left(\frac{5m_v}{2f} - 2\right)\left(\frac{8m_v - 3f}{42}\right), \tag{31}$$

$$\delta_1 = \frac{\int_0^{R_o} x^3 g(x)\overline{\psi}(\eta)dx}{\int_0^{R_o} x^3 g(x)dx}, \tag{32}$$

$$\overline{\psi}(\eta) = \frac{1 + \frac{1}{2}\eta - \frac{1}{10}\eta^2 - \sqrt{1+\eta}}{\sqrt{1+\eta}}. \tag{33}$$

Both δ_1 and δ_2 are small for terrestrial planets (e.g. $-0.0005 \leq \delta_1 \leq 0.0008$ and $0.48m \leq \delta_2 \leq 0.8m$). For Earth, $\delta_1 = -0.00040$ and $\delta_2 = 0.49m$. The above relationships connecting f, m_v, and J_2 appear to be self-consistent for the giant planets though significant surface zonal winds are observed. However, the factor δ_1 can be relatively large ($0.05 < \delta_1 < 0.08$) for a variety of plausible giant planet interior models [51], such that (30) provides an upper bound on I/MR^2 for $\delta_1 = 0$.

A satellite's shape is also influenced by secular tides raised by the planet. The spin factor is augmented by the factor $\left[1 + \frac{3}{2}\left(n/\omega_s\right)^2\left(1 - \frac{3}{2}\sin^2\epsilon\right)\right]$ for non-synchronous rotation. Here n is orbital mean motion, ω_s is satellite spin rate and ϵ is satellite inclination of its equator to the orbit. Most satellites have synchronous rotation for which the hydrostatic shape is triaxial. The expected value for the ratio $(b-c)/(a-c)$ is $1/4$ for small m [20, 30]. A first order solution relating the flattening $f_1 = (a-c)/a$, gravity factor $J^1 = J_2 + 2C_{22}$ and spin $m_1 = 4m$ is obtained by replacing these factors (i.e. $f \rightarrow f_1$, $J_2 \rightarrow J^1$ and $m \rightarrow m_1$) in (26).

Surface Gravity: The radial component of surface gravity $g(r,\phi)$ for a uniformly rotating fluid body is

$$g = \frac{GM}{r^2}\left(1 + \frac{3}{2}J_2\left(\frac{a}{r}\right)^2\left(1 - 3\sin^2\phi\right)\right. \tag{34}$$

$$\left. -m\left(\frac{r}{a}\right)^3\cos^2\phi\right). \tag{35}$$

The equatorial gravity is

$$g_e = g(a,0) = \frac{GM}{a^2}\left(1 + \frac{3}{2}J_2 - m\right), \tag{36}$$

while the polar gravity is

$$g_p = \frac{GM}{b^2}\left(1 - 3\left(\frac{a}{b}\right)^2 J_2\right). \tag{37}$$

Geodetic Latitude: The geodetic (or geographic) latitude ϕ' measures the angle formed by the surface normal vector on the plane of the equator and is related to the geocentric latitude ϕ by (see Figure 1)

$$\tan\phi' = \left(\frac{b}{a}\right)^2 \tan\phi = (1-f)^2\tan\phi\,. \tag{38}$$

An expansion for the difference angle is

$$\phi - \phi' \simeq \widehat{f}\sin 2\phi'(1 - 2\widehat{f}\sin^2\phi'), \tag{39}$$

where

$$\widehat{f} = f(1 - \frac{1}{2}f)/(1-f)^2. \tag{40}$$

Normal gravity to the ellipsoid is [74]

$$g = \frac{ag_e \cos^2\phi' + bg_p \sin^2\phi'}{\sqrt{a^2\cos^2\phi' + b^2\sin^2\phi'}}. \tag{41}$$

3. ORBITS AND THEIR ORIENTATIONS

Orbits of all planets and satellites are slightly elliptical in shape where the orbit focus lies at the primary center of mass and is displaced from the ellipse center of figure by ea, where e is the orbit *eccentricity* and a is the *semimajor axis.* The ratio of minor to major axes of the orbit ellipse is $\sqrt{1-e^2}$. The rate that area is swept out relative to the focus is governed by the Keplerian condition $r^2 \frac{d}{dt} f \simeq$constant where the angle f (true anomaly) is measured relative to the minimum separation or pericenter. The mean motion $n = \frac{d}{dt}(\ell + \omega + \Omega)$ and the orbital period is $2\pi/n$. The radial position is governed by the following two relations which connect the radial separation r, semimajor axis a, eccentricity e, true anomaly f and mean anomaly ℓ (which varies linearly with time for the strictly two body case),

$$r = \frac{a(1-e^2)}{1+e\cos f} \;\; ; \;\; \sin(\ell + \frac{er\sin f}{a\sqrt{1-e^2}}) = \frac{r\sin f}{a\sqrt{1-e^2}}. \tag{42}$$

If f is known, then r and ℓ are found directly. On the other hand, if ℓ (or the time relative to perihelion passage) is known, then f and r can be obtained by iteration. An alternative is to employ the eccentric anomaly E which is directly connected to f and ℓ.

$$\tan\frac{1}{2}f = \sqrt{\frac{1+e}{1-e}}\tan\frac{1}{2}E, \tag{43}$$

$$\ell = E - e\sin E, \tag{44}$$

$$r = a(1 - e\cos E). \tag{45}$$

The eccentric anomaly E measures the angular position relative to the ellipse center.

For small e, the equation of center is [88]

$$f - \ell \simeq e(2 - \frac{1}{4}e^2)\sin\ell + \frac{5}{4}e^2\sin 2\ell + \frac{13}{12}e^3\sin 3\ell. \tag{46}$$

Similar expansions of a/r and r/a in terms of the mean anomaly are

$$\frac{a}{r} = 1 + e(1 - \frac{1}{8}e^2)\cos\ell + e^2\cos 2\ell + \frac{9}{8}e^3\cos 3\ell, \tag{47}$$

$$\frac{r}{a} = 1 + \frac{1}{2}e^2 - e(1 - \frac{3}{8}e^2)\cos\ell - \frac{1}{2}e^2\cos 2\ell - \frac{3}{8}e^3\cos 3\ell \tag{48}$$

The natural $\{x, y, z\}$ coordinates of the orbit which lie in the $\{x, y\}$ plane are

$$\mathbf{r} = \begin{bmatrix} r\cos(f+\omega) \\ r\sin(f+\omega) \\ 0 \end{bmatrix} \tag{49}$$

The spatial orientation of an orbit relative to the ecliptic and equinox is specified by three Euler angles: longitude of the ascending node Ω describing the position of the intersection line relative to a fixed point on the ecliptic, argument of perihelion ω measured from the node to the pericenter and orbit inclination I. The $\{x, y, z\}$ coordinates in this frame are

$$\frac{\mathbf{r}_e}{r} = \begin{bmatrix} \cos(f+\omega)\cos\Omega - \cos I\sin(f+\omega)\sin\Omega \\ \cos(f+\omega)\sin\Omega + \cos I\sin(f+\omega)\cos\Omega \\ \sin I\sin(f+\omega) \end{bmatrix} \tag{50}$$

The ecliptic spherical coordinates (longitude ψ and latitude β) of the position vector r_e are defined by

$$\begin{bmatrix} x_e \\ y_e \\ z_e \end{bmatrix} = \begin{bmatrix} \cos\psi\cos\beta \\ r\sin\psi\cos\beta \\ r\sin\beta \end{bmatrix} \tag{51}$$

The $\{x, y, z\}$ planetary, orbital coordinates relative to an angular, *equatorial* coordinate frame centered in the sun depend on earth's obliquity ϵ and are

$$\mathbf{r_g} = \mathbf{R}\mathbf{r}. \tag{52}$$

The rotation matrix $\mathbf{R}$, by column, is

$$\mathbf{R_1} = \begin{bmatrix} \cos\Omega \\ \cos\epsilon\sin\Omega \\ \sin\epsilon\sin\Omega \end{bmatrix}, \tag{53}$$

$$\mathbf{R_2} = \begin{bmatrix} -\cos I\sin\Omega \\ \cos\epsilon\cos I\cos\Omega - \sin\epsilon\sin I \\ \sin\epsilon\cos I\cos\Omega + \cos\epsilon\sin I \end{bmatrix}, \tag{54}$$

$$\mathbf{R_3} = \begin{bmatrix} \sin I\sin\Omega \\ -\cos\epsilon\sin I\cos\Omega - \sin\epsilon\cos I \\ -\sin\epsilon\sin I\cos\Omega + \cos\epsilon\cos I \end{bmatrix} \tag{55}$$

The geocentric position $\mathbf{r}'_g$ of a planet (still in equatorial coordinates) is given by

$$\mathbf{r}'_g = \mathbf{r_g} + \mathbf{r}_\odot \tag{56}$$

where $\mathbf{r}_\odot$ points from earth towards sun and $\mathbf{r_g}$ points from sun towards planet.

R.A. and Dec.: The *right ascension* α and *decli-*

nation δ of an object relative to earth's equator and equinox (see Figure 2) are related to the components of $\mathbf{r}'_{\rm g}$ by

$$\begin{aligned} x'_{\rm g} &= r\cos\alpha\cos\delta \\ y'_{\rm g} &= r\sin\alpha\cos\delta \\ z'_{\rm g} &= r\sin\delta \end{aligned} \tag{57}$$

If a translation is unnecessary, as with planetary poles of rotation or distant objects , then (57) can be used to relate the orbital elements to α and δ. The equatorial and ecliptic coordinates are related by

$$\mathbf{r}_{\rm e} = \begin{bmatrix} 1 & 0 & 0 \\ 0 & \cos\epsilon & \sin\epsilon \\ 0 & -\sin\epsilon & \cos\epsilon \end{bmatrix} \mathbf{r}_{\rm g} \tag{58}$$

Kepler's Third Law: $GM_{\rm t} = n^2a^3$ ($M_{\rm t} = M_{\rm planet} + M_{\rm satellite}$) for satellite orbits is modified by zonal planetary gravity, other satellites and Sun. The lowest order expression is [82, 79]

$$N^2A^3 = GM_{\rm t}\left(1 + \frac{3}{2}J_2\left(\frac{R_e}{a}\right)^2 - \frac{15}{8}J_4\left(\frac{R_e}{a}\right)^2 - \frac{1}{2}\left(\frac{n_\odot}{N}\right)^2(1 - \frac{3}{2}\sin^2\epsilon) + P\right), \tag{59}$$

$$P = \frac{1}{2}\sum_j S_j\frac{M_j}{M_{\rm p}}\frac{a}{a_>}\frac{1}{(1-\alpha_j^2)}\times \left(\left[(1+S_j)(1-\alpha_j^2) + 2\alpha_j^2\right]b^0_{1/2}(\alpha_j) - 2\alpha_j b^1_{1/2}(\alpha_j)\right). \tag{60}$$

where N and A are the *observed* mean motion and semimajor axis, respectively and ϵ is the planetary obliquity to its orbit. The orbital period is $2\pi/N$. The sum P gives the contributions from all other satellites of mass M_j and depends on *Laplace coefficients* $b^0_{1/2}(\alpha)$ and $b^1_{1/2}(\alpha)$ which in turn can be expressed as a series [88, 13] in $\alpha = a_</a_>$. For a given pair, $a_<$ and $a_>$ are the semimajor axes of the interior and exterior satellites, respectively. The factor $S_j = 1$ if $a < a_j$ and $S_j = -1$ if $a > a_j$.

Laplace Coefficients: The expansion of the function $\Delta^{-s} = \left(1 + \alpha^2 - 2\alpha\cos x\right)^{-s}$ is

$$\Delta^{-s} = \frac{1}{2}b^0_s + \sum_{j=1}^{\infty} b^j_s\cos jx. \tag{61}$$

The general coefficient $b^j_s(\alpha)$ is

$$\begin{aligned} b^j_s(\alpha) &= \frac{2}{\pi}\int_0^\pi dx\cos jx\left(1+\alpha^2-2\alpha\cos x\right)^{-s} \\ &= 2\alpha^j\frac{\Gamma(s+j)}{\Gamma(s)\Gamma(j+1)}\sum_q C_{jsq}\alpha^{2q}, \end{aligned} \tag{62}$$

$$C_{jsq} = \left(\frac{\Gamma(s+q)\Gamma(s+j+q)\Gamma(j+1)}{\Gamma(s)\Gamma(s+j)\Gamma(I+1+q)\Gamma(q+1)}\right) \tag{63}$$

$\Gamma(x) = (x-1)\Gamma(x-1)$ is the Gamma function. Also, $\Gamma(1) = 1$ and $\Gamma(1/2) = \sqrt{\pi}$.

Apsidal and Nodal Precession: The satellite node and argument of periapse also precess and the lowest order expressions are [82] ($\tilde{\omega} = \omega + \Omega$)

$$\frac{d}{dt}\tilde{\omega} \simeq \tfrac{3}{2}N\left(\tfrac{R_e}{A}\right)^2\left(J_2 - \tfrac{5}{2}J_4\left(\tfrac{R_e}{A}\right)^2 - \tfrac{3}{4}J_2^2\right) + \tfrac{3}{4}\left(\tfrac{n_\odot}{N}\right)^2(2 - \cos\epsilon - \tfrac{5}{2}\sin^2\epsilon) + N\overline{P}) \tag{64}$$

$$\frac{d}{dt}\Omega \simeq -\tfrac{3}{2}N\left(\tfrac{R_e}{A}\right)^2\left(J_2 - \tfrac{5}{2}J_4\left(\tfrac{R_e}{A}\right)^2 - \tfrac{9}{4}J_2^2\right) - \tfrac{3}{4}\left(\tfrac{n_\odot}{N}\right)^2(1 - \tfrac{3}{2}\sin^2\epsilon) - N\overline{P}). \tag{65}$$

Here $\overline{P}$ is the contribution from other satellites and is

$$\overline{P} = \frac{1}{4}\sum_j\frac{M_j}{M_p}\frac{a}{a_>}\alpha_j b^1_{3/2}(\alpha_j) \tag{66}$$

$$\simeq \frac{3}{4}\sum\frac{M_j}{M_p}\frac{a}{a_>}\alpha_j^2(1 + \frac{15}{8}\alpha_j^2). \tag{67}$$

Invariable Plane: The action of the sun causes satellites to precess about the normal to the invariable plane (also known as the Laplacian plane), which is inclined by i to the planetary equator, and defined to lowest order by

$$2J_2\sin(2i) = \left(\frac{n_\odot}{N}\right)^2(1-e^2)^{-1/2}\sin 2(\epsilon - i). \tag{68}$$

The invariable plane normal vector lies between the planetary spin vector and planetary orbit normal and the three normals are coplanar.

Planetary Precession: The precession of a planet's spin axis (if we ignore the variations induced by the motion of planetary orbit plane [64]) resulting from the sun and its own satellites is given by [98]

$$\frac{d}{dt}\phi = -\frac{3}{2}\frac{MR_{\rm e}^2}{C\omega_s}J_2n_\odot^2\times \left(\cos\epsilon + \sum_j\left(\frac{n_j}{n_\odot}\right)^2\frac{M_j}{M_j+M}\cos(\epsilon - i_j)\right), \tag{69}$$

where C is the polar moment of inertia and ω_s is the planet spin rate. Numerical modeling of the long term behavior of the obliquity of terrestrial planets [64, 112] indicate that their orientation (especially Mars) is at some time in their histories chaotic.

Cassini State: The mean orientation of a synchronously locked satellite is described by three laws:

The same side of the moon faces the planet. The satellite's rotation axis lies in the plane formed by the orbit normal and invariable plane normal. The lunar obliquity is constant.

The lunar obliquity relative to its orbit ϵ_s, depends of the satellite precession rate $\frac{d}{dt}\Omega$ in addition to the moments of inertia [87].

$$\frac{\frac{d}{dt}\Omega}{n}\sin(\epsilon_s - I) = -\frac{3}{2}\sin\epsilon_s\left(\frac{C-A}{C}\cos\epsilon_s + \frac{1}{4}\frac{B-A}{C}sin^2\frac{1}{2}\epsilon_s\right). \quad (70)$$

4. DYNAMICAL CONSTRAINTS

A few simple parameters are defined here which are useful in determining dynamical characteristics of planets and satellites.

Escape Velocity v_∞ and Minimum Orbit Velocity v_o : The minimum velocity to orbit just above the surface of an airless spherical body of mass M and radius R is v_o while the minimum velocity necessary for an object to just reach infinity is v_∞.

$$v_o = \sqrt{\frac{GM}{R}} = \sqrt{gR}, \quad (71)$$

$$v_\infty = \sqrt{2}v_o = 118.2\left(\frac{R}{100\text{km}}\right)\left(\frac{\overline{\rho}}{2.5\,\text{g cm}^{-3}}\right)^{1/2}\text{m s}^{-1}.$$

Hills' Sphere: A roughly spherical volume about a secondary body in which a particle *may* move in bounded motion, at least temporarily. The Hills' radius h is proportional to the cube root of the mass ratio M_s/M_p of satellite to planet.

$$h = \kappa a\left(\frac{M_s}{3M_p}\right)^{1/3} = \kappa R_s\frac{a}{R_p}\left(\frac{\rho_s}{3\rho_p}\right)^{1/3}. \quad (72)$$

where $\kappa \leq 1$. This factor also reduces the effective escape velocity by a factor of $\sim\sqrt{1 - R_s/h}$.

Roche Limit: A fluid satellite can be gravitationally disrupted by a planet if its Hills' radius is smaller than the satellite's mean radius of figure, R_s. That is, for $R_s \leq h$, a particle will move off the satellite at the sub- and anti-planet positions (orbit radius $A \leq 1.44R_p(\rho_p/\rho_s)^{1/3}$), and defines a minimum orbital radius inside which satellite accretion from ring material is impeded. The Darwin condition where a fluid body begins to fill its Roche lobe is less stringent and is [20]

$$A_{\text{Roche}} = 2.455R_p\left(\frac{\rho_p}{\rho_s}\right)^{1/3}. \quad (73)$$

5. TIDES AND TIDAL FRICTION

Love Numbers: The elastic deformation of a satellite due to either a tide raised by the planet or deformation caused a satellite's own rotation is set by the dimensionless Love number k_2. The corresponding changes in the moment of inertia tensor are

$$\delta I_{ij}(\text{tides}) = -\frac{k_2 M_p R_s^5}{r^3}\left(u_i u_j - \frac{1}{3}\delta_{ij}\right), \quad (74)$$

$$\delta I_{ij}(\text{spin}) = \frac{1}{3}\frac{R_s^5}{GM_s}\omega_i\omega_j\left(k_2 - (\frac{1}{3}k_2 - \frac{1}{2}n_o)\delta_{ij}\right). \quad (75)$$

Here u_i are the direction cosines of the tide-raising satellite as seen from the satellite's body-fixed reference system (i.e. $u_i = r_i/r$), while ω_i are the Cartesian components of the spin vector.

The Love number $k_2 \simeq 3/2/(1 + 19\mu/\rho gR)$ for small homogeneous satellites. An appropriate rigidity μ for rocky satellites is $\sim 5 \times 10^{11}$ dyne-cm^{-2} for rocky bodies and $\sim 4\times10^{10}$dyne-cm^{-2} for icy bodies. Fluid cores can substantially increase k_2. For fluid planets, the equivalent hydrostatic $k_2(\text{fluid}) = 3J_2/m$ is appropriate, where $m = \omega_s^2 R^3/GM$ is the rotation factor defined earlier in equation (25).

The term proportional to n_o arises from a purely radial distortion and depends on the bulk modulus, K. An expression for n_o has been derived for a uniform spherical body [120].

$$n_o = \frac{32}{105}\left(\frac{\rho gR}{K + \frac{4}{9}\mu}\right)\left(1 + \frac{14}{15}\frac{\mu}{K}\right). \quad (76)$$

Typically, $K \sim \frac{5}{3}\mu$ and thus $n_o \sim k_2$ for small satellites.

The surficial tidal deformation $\mathbf{d}(\mathbf{R}')$ of the satellite at a point $\mathbf{R}'$ depends on the interior angle θ subtending the surface $\mathbf{R}'$ and satellite $\mathbf{r}$ position vectors [62]. Its magnitude is set by two additional Love numbers h_2 and l_2. Also, $h_2 \simeq \frac{5}{3}k_2$ and $l_2 \simeq \frac{1}{2}k_2$ for small objects.

$$\mathbf{d} = \frac{GM_p R}{g_s r^3}\left(h_2\mathbf{R}'P_{20}(\cos\theta) - 3l_2\widehat{\theta}R'\sin\theta\cos\theta\right), \quad (77)$$

where g_s is satellite gravity and $\widehat{\theta}$ is a unit vector, normal to $\mathbf{R}'$ and pointing from $\mathbf{R}'$ toward $\mathbf{r}$.

Tidal Acceleration and Spin Down: The tidal acceleration of a satellite caused by the inelastic tide it raises on a planet with rotation rate ω_p is given by

$$\frac{d}{dt}n \simeq -\frac{9}{2}\frac{k_{2p}}{Q_p}\frac{M_s}{M_p}\left(\frac{R_p}{a}\right)^5 n^2 \mathrm{sgn}(\omega_p - n), \tag{78}$$

with a and n are semimajor axis and mean motion, respectively. The planetary dissipation factor $Q_p \propto 1/(\text{tidal phase lag})$ is defined by

$$Q^{-1} = \frac{1}{2\pi}\frac{\Delta E}{E_e}, \tag{79}$$

where E_e is the elastic distortion energy and ΔE is the energy dissipated during one flexing cycle. The rate that a satellite's own spin changes toward synchronous rate due to the inelastic tide that the planet raises on the satellite is

$$\frac{d}{dt}\omega_s \simeq -\frac{3}{2}\frac{k_{2s}}{Q_s}\frac{M_p R_s^2}{C_s}\left(\frac{R_s}{a}\right)^3 \frac{n^2}{\omega_s}\mathrm{sgn}(\omega_s - n), \tag{80}$$

where C_s is the satellite's principal moment of inertia. The contribution of a satellite to the despinning of a planet is

$$\frac{d}{dt}\omega_p \simeq -\frac{3}{2}\frac{k_{2p}}{Q_p}\frac{M_s R_p^2}{C_p}\left(\frac{R_p}{a}\right)^3 \frac{n^2}{\omega_p}\mathrm{sgn}(\omega_p - n), \tag{81}$$

Wobble Period and Damping Rate: The free eulerian nutation period T_W of a rigid triaxial body (which for earth is known as the Chandler wobble) is [62]

$$T_W = \frac{2\pi}{\omega_s}\sqrt{\frac{AB}{(C-A)(C-B)}} \tag{82}$$

if the object's spin is *not* locked in a spin-orbit resonance. The gravitational torque exerted by a planet a satellite's figure decreases the wobble period by the factor D^{-1}, where

$$D^2 = D_1 D_2 \tag{83}$$

and

$$D_1 = 1 + \tfrac{3}{2}(1 - \delta_{n,\omega_s})\left(\frac{n}{\omega_s}\right)^2, \tag{84}$$

$$D_2 = 1 + \tfrac{3}{2}(1 + \delta_{n,\omega_s})\left(\frac{n}{\omega_s}\right)^2. \tag{85}$$

The function $\delta_{n,\omega_s} = 1$ if satellite rotation is synchronous (i.e. $\omega_s = n$) and zero otherwise [12, 118]. For a body with a fluid core, the moments of inertia $C > B > A$ are of the mantle only. Finally, the elasticity of a body increases the period by a factor of $\simeq J_2/(J_2 - \frac{1}{3}k_2 m)$.

The wobble damping time scale τ_W is

$$\tau_W^{-1} \simeq \frac{1}{3}\omega_s m \frac{k_2}{Q_W}\frac{M_s R_s^2}{C_s}F(\alpha,\beta). \tag{86}$$

The function F is of order unity and depends on the moment differences, $\alpha = (C-B)/B$ and $\beta = (C-A)/B$. For non-synchronous rotation, the explicit expression is [118]

$$F = \left(1 + \frac{3}{2}\left(\frac{n}{\omega_s}\right)^2\right)^2 \frac{1 + \sqrt{\frac{\alpha}{\beta}}}{\sqrt{\frac{\beta}{\alpha}} + \sqrt{\frac{\alpha}{\beta}}} \tag{87}$$

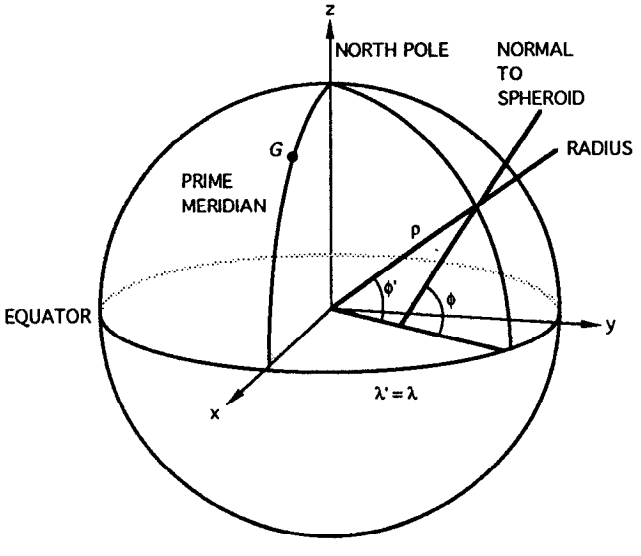

Fig. 1. Spheroidal coordinate system.

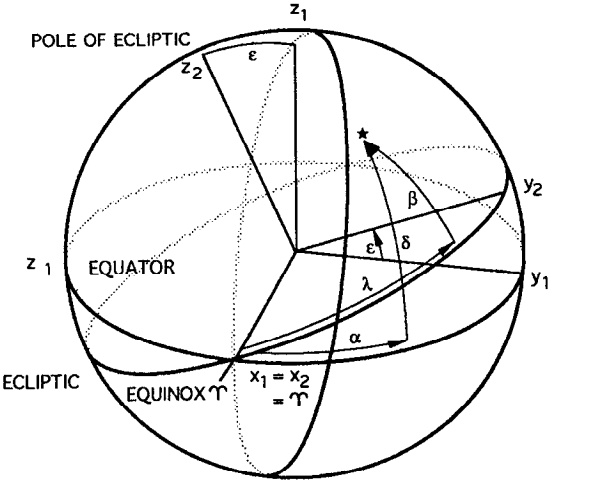

Fig. 2. Angular location of distant object relative to equatorial (α, δ) and ecliptic (ψ, β) reference planes. Equinox origin is known as the first point of Aries.

Table 1. Basic Astronomical Constants

Time units	
Julian day	d = 86400 s
Julian year	yr = 365.25 d
Julian Century	Cy = 36525 d
Tropical year (equinox to equinox)	365.2421897 d
Sidereal (quasar reference frame)	365.25636 d
Anomalistic year (apse to apse)	365.25964 d
Mean sidereal day	$23^h56^m04^s.09054$ 86164.09054 s
Defining constants	
Speed of light	$c \equiv 299792458$ m s^{-1}
Gaussian constant	$k \equiv 0.01720209895$
Derived constants	
Light time for 1 AU: τ_A	499.00478370 s
Astronomical unit distance **AU** $= c\tau_A$	$1.495978706(6 \pm 5) \times 10^{11}$ m
Gravitational constant: **G**	$6.672(59 \pm 84) \times 10^{-11}$ kg^{-1} m^3 s^{-2}
Solar $GM_\odot = k^2 AU^3 d^{-2}$	$1.327124399(4 \pm 3) \times 10^{20}$ m^3 s^{-2}
Solar parallax $\pi_0 = \sin^{-1}(a_e/AU)$	8″.794144
Constant of aberration (J2000)	$\kappa = 20''.49552$
Earth-Moon mass ratio	$81.3005(87 \pm 49)$
Obliquity of ecliptic (J2000)	$\epsilon = 23°26'21''.4119$
General precession in longitude	5029″.0966 Cy^{-1}
IAU(1976) values	
Light time for 1 AU: τ_A	499.004782 s
Astronomical unit distance **AU**	$1.49597870 \times 10^{11}$ m

Table 1: Notes: Modern planetary ephemerides such as DE 200 [103] determine the primary distance scale factor, the astronomical unit (AU). This unit is the most accurate astrometric parameter, with an estimated uncertainty of ±50m (Standish, priv. comm.). Lunar laser ranging and lunar orbiter Doppler data determine the earth-moon mass ratio [38][32]. The (IAU,1976) system [95].

Table 2. Earth: Geodetic and Geophysical Data

Mass	5.9736×10^{24} kg
Mean radius R_V [1]	6371.01 ± 0.02 km
Density	5.515 g cm^{-3}
Equatorial radius	
(IAU,1976)	$a = 6378140$ m
(Geod. ref. sys., 1980) [2]	$a = 6378137$ m
(Merit,1983)	$a = 6378136$ m
Flattening $f = (a-b)/a$	
(IAU,1976; Merit)	1/298.257
(G.R.S.,1980)	1/298.257222
Polar axis: $b = a(1-f)$ [2]	6356.752 km
Gravity J_2 coeff.	
(IAU,1976)	0.00108263
(GEM T2,1990) [3]	0.0010826265
$C_{22}(\times 10^{-6})$	1.5744
$S_{22}(\times 10^{-6})$	−0.9038
$(B-A)/Ma^2$ $(\times 10^{-6})$	7.2615
Longitude of axis a	14.9285° E
Surface gravity [2]	
g_p (m s^{-2})	9.8321863685
g_e	9.7803267715
$g_o = GM/R_V^2$	9.82022
Precession constant [7]	$H = J_2 Ma^2/C$ 3.2737634×10^{-3}
C (Polar moment)	$0.3307007 Ma^2$
B	$0.3296181 Ma^2$
A	$0.3296108 Ma^2$
Mean moment I	$0.3299765 Ma^2$ $0.3307144 MR_o^2$
Mean rotation rate: ω	7.292115×10^{-5} rad s^{-1}
$m_V = \omega^2 R_V^3/GM_\oplus$	1/289.872
$m = \omega^2 a^3/GM_\oplus$	1/288.901
Hydrostatic J_{2h}	0.0010722
Hydrostatic f_h	1/299.66
Fluid core radius(PREM)	3480 km
Inner core radius	1215 km
Mass of layers	
atmosphere	5.1×10^{18} kg
oceans	1.4×10^{21} kg
crust	2.6×10^{22} kg
mantle	4.043×10^{24} kg
outer core	1.835×10^{24} kg
inner core	9.675×10^{22} kg
Moments of inertia	
Mantle $I_m/M_\oplus a^2$	0.29215
Fluid core: $I_f/M_\oplus a^2$	0.03757

Table 2(cont). Geodetic and Geophysical data

Fluid core: $I_{f+ic}/M_{f+ic}a_f^2$	0.392
inner core: $I_{ic}/M_{\oplus}a^2$	2.35×10^{-4}
Hydrostatic $(C_f - A_f)/C_f$	1/393.10
Observed $(C_f - A_f)/C_f$	1/373.81
Hydrostatic $(C_{ic} - A_{ic})/C_{ic}$	1/416
Free core nutation period [4]	429.8 d
Chandler wobble period [5]	434.3 d
Surface area [6]	
land	1.48×10^8 km^2
sea	3.62×10^8 km^2
total	5.10×10^8 km^2

Table 2: References: 1) Rapp [90]; 2) Geodetic Reference system [74]; 3) Souchay and Kinoshita [100] and Kinoshita (priv. comm.). 4) Herring *et al.* [49]. 5) Clark and Vicente [23] also find that the Chandler wobble Q is 179(74, 790). 6) Stacey [101]. 7) Williams [116]. Moments of inertia of each internal unit are based on the PREM model and were provided by E. Ivins.

Table 3a. Moon: Physical Data

GM [a]	4902.798 ± 0.005
$M_{\oplus}/M$ [b]	81.300587 ± 0.000049
Mass	7.349×10^{22} kg
Radius R_V [c]	1737.53 ± 0.03 km
Density	3.3437
	± 0.0016 gm cm^{-3}
Surface gravity	1.62 m s^{-2}
$\beta = (C - A)/B$ [b]	$6.31(72 \pm 15) \times 10^{-4}$
$\gamma = B - A/C$	$2.278(8 \pm 2) \times 10^{-4}$
Moment of inertia: C/MR^2	
[a]	0.3935 ± 0.0011
[b,d]	0.3940 ± 0.0019
Heat flow [e]	
Apollo 15	3.1 ± 0.6 mW m^{-2}
Apollo 17	2.2 ± 0.5 mW m^{-2}
Crustal thickness	
nearside [f]	58 ± 8 km
farside [c,g]	$\sim 80 - 90$ km
Mean crustal density [g]	2.97 ± 0.07 gm cm^{-3}
k_2	0.0302 ± 0.0012
Tidal Q (see note h)	26.5 ± 1.0
Induced magnetic moment [j]	4.23×10^{22} G cm^3
Core radius constraints	
Source	Radius (km)

TABLE 3a. (continued).

Magnetometer moment [j]	435 ± 15
Seismic [f]	< 500
$I = 0.3933$	~ 350
LLR [h]	~ 400
Semimajor axis	384400km
	$60.27R_{\oplus}$
Orbit eccentricity	0.05490
Inclination	5.145°
Mean motion n	2.6616995
	$\times 10^{-6}$ rad s^{-1}
Orbit period	27.321582 d
Nodal period	6798.38 d
Apsidal period	3231.50 d
Obliquity to orbit	6.67°
Mean Angular Diameter	31′05″.2

Table 3b. Seismic velocity profiles

Depth km	Q_S km s^{-1}	Q_P km s^{-1}
Nakamura [f]		
$0 - 1$	0.29	0.51
$1 - 15$	2.82	4.90
$15 - 30$	3.59	6.25
$30 - 58$	3.84	6.68
$58 - 270$	4.49 ± 0.03	7.74 ± 0.12
$270 - 500$	4.25 ± 0.10	7.46 ± 0.25
$500 - 1000$	4.65 ± 0.16	8.26 ± 0.40
Goins *et al.* [k]		
$0 - 20$	2.96	5.10
$20 - 60$	3.90	6.80
60	4.57 ± 0.05	7.75 ± 0.15
400	4.37 ± 0.05	7.65 ± 0.15
480	4.20 ± 0.10	7.60 ± 0.60
1100	4.20 ± 0.10	7.60 ± 0.60

Seismic Q [f]

Depth km	Q_S km s^{-1}	Q_P km s^{-1}
0-60	~ 6000	~ 6000
60-270	4000+	$4000 - 7000+$
270-500	~ 1500	
$500 - 1000$	$< 100(?)$	

Table 3c. Lunar gravity field [a,b]

nm	$C_{nm} \times 10^9$	$S_{nm} \times 10^9$
20	-203805 ± 570	
22	22372 ± 110	
30	-8252 ± 600	
	$[-8610 \pm 230]$	
31	28618 ± 190	5871 ± 200
32	4891 ± 100	1646 ± 90
	$[4827 \pm 30]$	$[1682 \pm 11]$
33	1727 ± 35	-211 ± 34
	$[1710 \pm 100]$	$[-270 \pm 30]$
40	9235 ± 72	
41	-4032 ± 14	97 ± 15
42	1691 ± 73	1478 ± 61
43	94 ± 21	798 ± 22
44	127 ± 8	74 ± 6
50	-2552 ± 800	
60	15152 ± 1500	

Bracketed [ ] terms are from a 1994 LLR solution.

Table 3d. Low order topography [c]

nm	$C_{nm} \times 10^6$	$S_{nm} \times 10^6$
10	-367.7 ± 44.6	
11	-1049.3 ± 30.3	-255.4 ± 23.6
20	-303.9 ± 49.5	
21	-193.4 ± 34.2	30.4 ± 24.9
22	7.4 ± 7.4	107.8 ± 9.4

Table 3e. Retroreflector coordinates [b]

Station	Radius meters	Longitude degrees	Latitude degrees
Apollo 11	1735474.22	23.472922	0.673390
Apollo 14	1736338.34	−17.478790	−3.644200
Apollo 15	1735477.76	3.628351	26.133285
Lunakhod 2	1734638.78	30.921980	25.832195

Table 3: Notes and references: a) New solution for lunar GM and gravity field ($R_e = 1738$ km) obtained by Konopliv *et al.* [61] using lunar orbiter and Apollo spacecraft Doppler data for which the realistic error is estimated to be 10 times formal σ (except for GM which is 4σ).

b) Lunar laser ranging (LLR) solution from Williams *et al.* [114] and Dickey *et al.* [32].

c) Bills and Ferrari [9].

d) Ferrari *et al.* [38] and Dickey *et al.* [32].

e) Heiken [48].

f) Crustal thickness beneath Apollo 12 and 14 sites from Nakamura [76, 77].

g) Farside thickness estimated from 2 km center of figure - center of mass offset [9].

h) Based on 1994 LLR solution [32]. The LLR Q signature is a $0.26'' \cos F$ amplitude figure libration which is 90° out of phase with the primary term. This effect could just as easily be due to lunar fluid core mantle friction with core radius $\sim 300 - 400$ km [38, 119, 32].

j) Russell *et al.* [92].

k) Goins *et al.* [44]. Sellers [96] obtains a siesmic upper bound for R_c of 450 km.

Table 4a. Lunar orbit: Angle Arguments

$$
\begin{aligned}
D &= 297°51'00.735'' + 1602961601.4603T - 6.93659T^2 + 0.006559T^3 - 0.00003184T^4 \\
\ell &= 134°57'48.184'' + 1717915922.8022T + 31.2344T^2 + 0.051612T^3 - 0.00024470T^4 \\
\ell' &= 357°31'44.793'' + 129596581.0474T - 0.5529T^2 + 0.000147T^3 \\
F &= 93°16'19.558'' + 1739527263.0983T - 13.3498T^2 - 0.001057T^3 + 0.00000417T^4 \\
\Omega &= 125°02'40.39816'' - 6962890.2656T + 6.9366T^2 + 0.007702T^3 - 0.00005939T^4 \\
L &= 218°18'59.956'' + 1732564372.8326T - 5.84479T^2 + 0.006568T^3 - 0.0000317T^4
\end{aligned}
$$

Table 4: Major periodic orbit perturbations due to the Sun are from Chapront-Touze *et al.* [21] model. Lunar arguments: L is the lunar mean longitude, ℓ is the mean anomaly, $F = L - \Omega$ (ascending node) and $D = L - L'$. Solar angles are mean longitude L' and mean anomaly ℓ'. The time T has units of Julian centuries from J2000(JD2451545.0). Factors of T^q have units of arc seconds Cy^{-q}, except for the constant term.

Changing the lunar acceleration from the adopted value of $-25.900''\mathrm{Cy}^{-2}$ by $+1.00''\mathrm{Cy}^{-2}$, changes the T^2 coefficient of D and L by $+0.55042''T^2$, ℓ by $+0.55853''T^2$ and F by $+0.54828''T^2$.

Table 4b. Truncated Lunar Orbit Model

radius (km)	=	$385000 - 20905\cos\ell - 3699\cos(2D-\ell) - 2956\cos 2D - 570\cos 2\ell$
		$+246\cos(2D-2\ell) - 205\cos(2D-\ell') - 171\cos(2D+\ell)$
longitude ($''$)	=	$L + 22640\sin\ell + 4586\sin(2D-\ell) + 2370\sin 2D + 769\sin 2\ell$
		$-666\sin\ell' - 412\sin 2F + 212\sin(2D-2\ell) + 205\sin(2D-\ell-\ell')$
		$+192\sin(2D+\ell) + 165\sin(2D-\ell) + 147\sin(\ell-\ell') - 125\sin D$
latitude ($''$)	=	$18461\sin F + 1010\sin(F+l) + 1000\sin(\ell-F) + 624\sin(2D-F)$
		$+200\sin(2D-\ell+F) + 167\sin(2D-\ell-F) + 117\sin(4D+\ell)$

Table 5. Planetary Gravity Field

	Mercury	Venus	Earth	Mars
GM (km^3 s^{-2})	22032.09	324858.63	398600.440	42828.3
σ_{GM}	±0.91	±0.04		±0.1
GM_t			403503.235	
$M_\odot/M_t$	6023600	408523.61	328900.56	3098708
	±250	±0.15	±0.02	±9
R_e (km)	2440	6051.893	6378.137	3394.0
J_2 ($\times 10^{-6}$)	60	4.458	1082.626523	1960.454
	±20	±0.026		±0.18
C_{22}	10	0.539	1.5744	−54.73
	±5	±0.008	±0.0004	±0.02
S_{22}		−0.057	−0.9038	31.340
		±0.010	±0.0004	±0.02
J_3		1.928	−2.112	31.45
		±0.018	±0.0020	±0.51
J_4		2.381	−2.156	−18.89
		±0.021	±0.0030	±0.72

	Jupiter	Saturn	Uranus	Neptune
GM (km^3 s^{-2})	126,686,537	37,931,187	5,793,947	6,835,107
σ_{GM}	±100	±100	±23	±15
GM_t	126,712,767	37,940,554	5,794,560	6,836,534
	±100	±100	±10	±15
$M_\odot/M_t$	1047.3486	3497.898	22902.94	19412.240
	±0.0008	±0.018	±0.04	±0.057
R_e (km)	71398	60330	26200	25,225
J_2 ($\times 10^{-6}$)	14736	16298	3343.43	3411
	±1	±10	±0.32	±10
J_4	−587	−915	−28.85	−35
	±5	±40	±0.45	±10
J_6	31	103		
	±20	±50		

Table 5: Planetary system GM_t, inverse system mass, planet GM, and selected gravity field coefficients and their corresponding reference radius R_e for Mercury [3], Venus [73, 60] (the quoted, realistic errors are 4× formal) , Earth (GEM T2) [71], Mars [5, 37], Jupiter [16], Saturn [17, 79], Uranus [40, 55] and Neptune [111].

$GM_\odot = 1.3271243994 \times 10^{11}$ km^3 s^{-2}.

Table 6. Terrestial Planets: Geophysical Data

	Mercury	Venus	Earth	Mars
Mean radius R_V (km)	2440 ± 1	$6051.8(4 \pm 1)$	$6371.0(1 \pm 2)$	$3389.9(2 \pm 4)$
Mass ($\times 10^{23}$ kg)	3.302	48.685	59.736	6.4185
Volume ($\times 10^{10}$ km^3)	6.085	92.843	108.321	16.318
Density (g cm^{-3})	5.427	5.204	5.515	$3.933(5 \pm 4)$
Flattening f			1/298.257	1/154.409
Semimajor axis			6378.136	3397 ± 4
Siderial rotation period	58.6462d	−243.0185d	23.93419hr	24.622962hr
Rotation rate ω ($\times 10^5$s)	0.124001	−0.029924	7.292115	7.088218
Mean solar day (in days)	175.9421	116.7490	1.002738	1.0274907d
$m_V = \omega^2 {R_V}^3/GM$	10×10^{-7}	61×10^{-9}	0.0034498	0.0045699
Polar gravity (m s^{-2})			9.832186	3.758
Equatorial gravity (m s^{-2})	3.701	8.870	9.780327	3.690
Moment of inertia: I/MR_o^2	0.33	0.33	0.3308	0.366
Core radius (km)	~ 1600	~ 3200	3485	~ 1700
Potential Love no. k_2		~ 0.25	0.299	~ 0.14
Grav. spectral factor: u ($\times 10^5$)		1.5	1.0	14
Topo. spectral factor: t ($\times 10^5$)		23	32	96
Figure offset($R_{CF} - R_{CM}$) (km)		0.19 ± 01	0.80	2.50 ± 0.07
Offset (lat./long.)		11°/102°	46°/35°	62°/88°
Planetary Solar constant (W m^2)	9936.9	2613.9	1367.6	589.0
Mean Temperature (K)		735	270	210
Atmospheric Pressure (bar)		90	1.0	0.0056
Maximum angular diameter	11″.0	60″.2		17″.9″
Visual magnitude V(1,0)	−0.42	−4.40	−3.86	−1.52
Geometric albedo	0.106	0.65	0.367	0.150
Obliquity to orbit (deg)	~ 0.1	177.3	23.45	25.19
Sidereal orbit period (yr)	0.2408445	0.6151826	0.9999786	1.88071105
Sidereal orbit period (day)	87.968435	224.695434	365.242190	686.92971
Mean daily motion: n (° d^{-1})	4.0923771	1.6021687	0.9856474	0.5240711
Orbit velocity (km s^{-1})	47.8725	35.0214	29.7859	24.1309
Escape velocity v_∞ (km s^{-1})	4.435	10.361	11.186	5.027
Hill's sphere radius (R_p)	94.4	167.1	234.9	319.8
Magnetic moment (gauss ${R_p}^3$)			0.61	$< 1 \times 10^{-4}$

Table 6: Geodetic data for Mercury [46], Venus [73], Earth and Mars [10, 37]. Except for Venus [73], gravity and topographic field strength coefficients are from [11].

Venus topography: The topographic second harmonic (normalized) coefficients of Venus [73] are:
$\overline{C}_{20}^T = -25 \times 10^{-6}$; $\overline{C}_{21}^T = 14 \times 10^{-6}$; $\overline{S}_{21}^T = -8 \times 10^{-6}$; $\overline{C}_{22}^T = -20 \times 10^{-6}$; $\overline{S}_{22}^T = -5 \times 10^{-6}$.

Of Mars [10] are:
$\overline{C}_{20}^T = -1824 \pm 12 \times 10^{-6}$; $\overline{C}_{21}^T = 72 \pm 12 \times 10^{-6}$; $\overline{S}_{21}^T = 103 \pm 12 \times 10^{-6}$; $\overline{C}_{22}^T = -288 \pm 10 \times 10^{-6}$; $\overline{S}_{22}^T = -0.5 \times 10^{-6}$

The derivation of Mars' mean moment of inertia assumes that Tharsis is the primary non-hydrostatic source and that the hydrostatic

$J_{2h} = J_2 - (B - A)/2MR_e^2 = 0.001832$.

Except for Earth, the values for mean moment I, potential Love number k_2, core radius and mass are model calculations based on plausible structure [7].

Table 7. Giant Planets: Physical Data

	Jupiter	Saturn	Uranus	Neptune
Mass (10^{24} kg)	1898.6	568.46	86.832	102.43
Density (g cm^{-3})	1.326	0.6873	1.318	1.638
Equatorial radius (1bar) a (km)	71492 ± 4	60268 ± 4	25559 ± 4	24766 ± 15
Polar radius b (km)	66854 ± 10	54364 ± 10	24973 ± 20	24342 ± 30
Volumetric mean radius: R_V (km)	69911 ± 6	58232 ± 6	25362 ± 12	24624 ± 21
flattening $f = (a-b)/a$	0.06487	0.09796	[A]0.02293	0.0171
	± 0.00015	± 0.00018	± 0.0008	± 0.0014
Rotation period: T_{mag}	$9^h55^m27^s3$	$10^h39^m22^s4$	17.24 ± 0.01 h	16.11 ± 0.01 h
Rotation rate ω_{mag} (10^{-4} rad s^{-1})	1.75853	1.63785	1.012	1.083
$m = \omega^2 a^3/GM$	0.089195	0.15481	0.02954	0.02609
Hydrostatic flattening f_h [B]	0.06509	0.09829	0.01987	0.01804
Inferred rotation period T_h (hr)	9.894 ± 0.02	10.61 ± 0.02	17.14 ± 0.9	16.7 ± 1.4
$k_s = 3J_2/m$	0.494	0.317	0.357	0.407
Moment of inertia: I/MR_o^2 [C]	0.254	0.210	0.225	
$I/MR^2{}_o$ (upper bound) [D]	0.267	0.231	0.232	0.239
Rocky core mass (M_c/M) [C]	0.0261	0.1027	0.0012	
Y factor (He/H ratio)	0.18 ± 0.04	0.06 ± 06	0.262 ± 0.048	0.235 ± 0.040
Equatorial gravity g_e (m s^{-2})	23.12 ± 0.01	8.96 ± 0.01	8.69 ± 0.01	11.00 ± 0.05
Polar gravity g_p (m s^{-2})	27.01 ± 0.01	12.14 ± 0.01	9.19 ± 0.02	11.41 ± 0.03
Geometric albedo	0.52	0.47	0.51	0.41
Visual magnitude $V(1,0)$	-9.40	-8.88	-7.19	-6.87
Visual magnitude (opposition)	-2.70	$+0.67$	$+5.52$	$+7.84$
Obliquity to orbit (deg)	3.12	26.73	97.86	29.56
Sidereal orbit period (yr)	11.856523	29.423519	83.747407	163.72321
Sidereal orbit period (day)	4330.595	10746.940	30588.740	59799.900
Mean daily motion n (° d^{-1})	0.0831294	0.0334979	0.0117690	0.0060200
Mean orbit velocity (km s^{-1})	13.0697	9.6624	5.4778	4.7490
Atmospheric temperature (1 bar) (K)	165 ± 5	134 ± 4	76 ± 2	72 ± 2
Heat flow/Mass ($\times 10^7$erg g^{-1}s^{-1})	15	15	0.6 ± 0.6	2
Planetary solar constant (W m^{-2})	50.5	15.04	3.71	1.47
Mag. dipole moment (gauss-$R_p{}^3$)	4.2	0.21	0.23	0.133
Dipole tilt/offset (deg/R_p)	9.6/0.1	0.0/0.0	58.6/0.3	47/0.55
Escape velocity v (km s^{-1})	59.5	35.5	21.3	23.5
A_{Roche}(ice)/R_p	2.76	2.71	2.20	2.98
Hill's sphere radius h (in R_p)	740	1100	2700	4700

Table 7: Geodetic and temperature data (1 bar pressure level) for the giant planets obtained from Voyager radio occultation experiments for Jupiter [66], Saturn [67], Uranus [68] and Neptune [111, 69]. The magnetic field rotation periods (system III) and dipole moment for Jupiter, Saturn [25], Uranus and Neptune [78].

Notes:

A) The Uranian flattening determined from stellar occultations [6] is significantly smaller $f = 0.0019(7 \pm 1)$ at 1μbar than at the 1 bar level. The heat flow and Y factor are from Podolak *et al.* [89]. Geometric albedos and visual magnitudes are from Seidelmann[95].

B) The hydrostatic flattening is derived from (28), using the observed J_2 and the magnetic field rotation rate. The inferred mean rotation rate uses J_2 and the observed flattening (for Uranus, I adopt $f = 0.0019(7 \pm 1)$).

C) Upper bounds to the mean moment of inertia using (30) with $\delta_1 = 0$. D) Hubbard and Marley [52] solution.

Table 8. Planetary Mean Orbits

Planet	A	e	I	Ω	$\tilde{\omega}$	L
	AU		deg	deg	deg	deg
	$AU\ Cy^{-1}$	Cy^{-1}	$''Cy^{-1}$	$''Cy^{-1}$	$''Cy^{-1}$	$''Cy^{-1}$
Mercury	0.38709893	0.20563069	7.00487	48.33167	77.45645	252.25084
	0.00000066	0.00002527	−23.51	−446.30	573.57	538101628.29
mean	0.38709880	0.20563175	7.00499	48.33089	77.45612	252.25091
orbit		0.00002041	−21.43	−451.52	571.91	538101628.89
Venus	0.72333199	0.00677323	3.39471	76.68069	131.53298	181.97973
	0.00000092	−0.00004938	−2.86	−996.89	−108.80	210664136.06
	0.72333201	0.00677177	3.39447	76.67992	131.56371	181.97980
		−0.00004777	−3.08	−1000.85	17.55	21066136.43
Earth	1.00000011	0.01671022	0.00005	−11.26064	102.94719	100.46435
	−0.00000005	−0.00003804	−46.94	−18228.25	1198.28	129597740.63
	1.00000083	0.016708617	0.0	0.0	102.93735	100.46645
		−0.00004204	−46.60	−867.93	1161.12	129597742.28
Mars	1.52366231	0.09341233	1.85061	49.57854	336.04084	355.45332
	−0.00007221	0.00011902	−25.47	−1020.19	1560.78	68905103.78
	1.52368946	0.09340062	1.84973	49.55809	336.60234	355.43327
		0.00009048	−29.33	−1062.90	1598.05	68905077.49
Jupiter	5.20336301	0.04839266	1.30530	100.55615	14.75385	34.40438
	0.00060737	−0.00012880	−4.15	1217.17	839.93	10925078.35
	5.20275842	0.04849485	1.30327	100.46444	14.33131	34.35148
		0.00016322	−7.16	636.20	777.88	10925660.38
Saturn	9.53707032	0.05415060	2.48446	113.71504	92.43194	49.94432
	−0.00301530	−0.00036762	6.11	−1591.05	−1948.89	4401052.95
	9.54282442	0.05550862	2.48888	113.66552	93.05678	50.07747
		−0.00034664	9.18	−924.02	2039.55	4399609.86
Uranus	19.19126393	0.04716771	0.76986	74.22988	170.96424	313.23218
	0.00152025	−0.00019150	6.11	−1591.05	−1948.89	1513052.95
	19.19205970	0.04629590	0.77320	74.00595	173.00516	314.05501
		−0.00002729	−6.07	266.91	321.56	1542481.19
Neptune	30.06896348	0.00858587	1.76917	131.72169	44.97135	304.88003
	−0.00125196	0.00002514	−3.64	−151.25	−844.43	786449.21
	30.06893043	0.00898809	1.76995	131.78406	48.12369	304.34867
		0.00000603	8.12	−22.19	105.07	786550.32
Pluto	39.48168677	0.24880766	17.14175	110.30347	224.06676	238.92881
	−0.00076912	0.00006465	11.07	−37.33	−132.25	522747.90

Table 8: This table contains two distinct mean orbit solutions referenced to the J2000 epoch. First, a 250 yr. least squares fit (first two rows for each planet) of the *DE 200* planetary ephemeris [103] to a Keplerian orbit where each element is allowed to vary linearly with time. This solution fits the terrestrial planet orbits to ∼25″ or better, but achieves only ∼600″ for Saturn. The second solution (the third and fourth rows for each planet) is a mean element solution (from table 15.6 in [95]), except that the semimajor axis is the average value defined by eq(37). The fit for this case over the same 250 yr. is worse (M. Standish, priv. comm.) for the giant planets because of pairwise near commensurabilities in the mean motions of Jupiter-Saturn ($S_1 = (2L_5 - 5L_6)$ with 883 yr. period) and Uranus-Neptune ($S_2 = (L_7 - 2L_8)$ with 4233 yr. period). However, the mean orbit should be more stable over longer periods.

Table 9. North Pole of Rotation (α_0, δ_0 and Prime Meridian) of Planets and Sun

	α_0 deg	δ_0 deg	W (prime meridian) deg	reference feature
Sun	286.13	63.87	$84.10 + 14.1844000d$	
Mercury	$281.01 - 0.003T$	$61.45 - 0.005T$	$329.71 + 6.1385025d$	Hun Kai(20.00° W)
Venus [A]	272.76	67.16	$160.20 - 1.481545d$	Ariadne(central peak)
Earth	$0.00 - 0.641T$	$90.00 - 0.557T$	$190.16 + 306.9856235d$	Greenwich,England
Mars	$317.681 - 0.108T$	$52.886 - 0.061T$	$176.868 + 350.8919830d$	crater Airy-0
Jupiter	$268.05 - 0.009T$	$64.49 + 0.003T$	$284.95 + 870.53600000d$	magnetic field
Saturn [B]	$40.5954 - 0.0577T$	$83.5380 - 0.0066T$	$38.90 + 810.7939024d$	magnetic field
Uranus [C]	257.43	-15.10	$203.81 - 501.1600928d$	magnetic field
Neptune [D]	$299.36 + 0.70 \sin N$	$43.46 - 0.51 \cos N$	$253.18 + 536.3128492d - 0.48 \sin N$	
Pluto	313.02	9.09	$236.77 - 56.3623195d$	sub-Charon [E]

Table 9: Reference date is 2000 Jan 1.5 (JD 2451545.0). The time interval T (in Julian centuries) and d (days) from the standard epoch. The prime meridian W is measured from the ascending node of the planet equator on the J2000 earth equator to a reference point on the surface. Venus, Uranus and Pluto rotate in a retrograde sense.

A) The Magellan values [28] for α_0, δ_0 and W for Venus are:
$\alpha_0 = 272.^\circ 76 \pm 0.02$; $\delta_0 = 67.^\circ 16 \pm 0.01$;
$W = 160.^\circ 20 - 19.^\circ 4813688$d.

B) Saturn's pole is based on French *et al.* [42] which include the 1989 occultation of 28 Sgr. They claim detection of Saturn's pole precession rate.

C) Improved Uranian pole (B1950 epoch) position is [40]:
$\alpha_0 = 256.^\circ 5969 \pm 0.0034$,
$\delta_0 = -15.^\circ 1117 \pm 0.0033$.

D) Neptune angle $N = 359.^\circ 28 + 549.^\circ 308T$.

E) The sub-Charon meridian on Pluto is fixed since Pluto rotates synchronously with Charon's orbit.

Invariable plane: The invariable plane coordinates are (J2000) [85]:
$\alpha_0 = 273.^\circ 8657$; $\delta_0 = 66.^\circ 9723$.

This table is an updated version of the 1991 IAU [29] recommended values and also appears in [95].

Table 10. Pluto Charon System

GM_{sys} [1]	947 ± 13 km^3 s^{-2}
M_{sys}	$1.42 \pm 0.02 \times 10^{22}$ kg
Mass ratio (M_C/M_P) [1]	0.12
[2]	0.1543 ± 0.0028
Mass of Pluto [1]	$1.27 \pm 0.02 \times 10^{22}$ kg
[2]	$1.231 \pm 0.01 \times 10^{22}$ kg
Mass of Charon [1]	1.5×10^{21} kg
[2]	$1.90 \pm 0.04 \times 10^{21}$ kg
Semi-major axis a [1]	19405 ± 86 km
a [2]	19481 ± 49 km
Eccentricity [3] e	$0.000(20 \pm 21)$
Inclination to mean equator & equinox [1]	$96.56 \pm 0.26°$
Radius R_P [1,3]	1137 ± 8 km
[4]	1206 ± 11 km
Radius R_C	586 ± 13 km
Density of Pluto	
$(R = 1137 \pm 8$ km) [1]	2.06 g cm^{-3}
$(R = 1206 \pm 11$ km) [1]	1.73 g cm^{-3}
$(R = 1137 \pm 8$ km) [2]	2.00 g /cm^{-3}
$(R = 1206 \pm 11$ km) [2]	1.67 g cm^{-3}
Density of Charon [1]	1.8 g cm^{-3}
Density of Charon [2]	2.24 g cm^{-3}
Orbital Period	$6.3872(30 \pm 21)$ d
Pluto's Albedo (blue & var.)	$0.43 - 0.60$
Charon's albedo	0.375 ± 0.08
Surface gravity	
Pluto (R=1137 km) [1]	65.5 cm s^{-2}
Charon [1]	21.3 cm s^{-2}
Hill's Sphere (Charon) [1]	5800 km
Escape velocity (Charon) [1]	0.58 km s^{-1}
Planetary orbit period	248.0208 yr
Planetary orbit velocity	4.749 km s^{-1}

Table 10: 1) The discovery of a coordinate distortion in the HST camera reduces the mass ratio q from 0.0873 ± 0.0147 [83] to 0.12 [Null, priv. comm.], which is still low relative to q from low ground-based imaging [122]. Solution for semimajor axis and q determined from HST observations of the barycentric wobble of Pluto relative to a background star observed for 3.2 d [83].

2) Solution based on 6 nights of CCD imaging at Mauna Kea [].

3) The radii and period derive from mutual event data [15].

4) The presence of an atmosphere on Pluto introduces uncertainty into its radius. Models indicate that R_P is either 1206 ± 6 km (thermal gradient model) or ≤ 1187 km (haze model) [34]. 5) Young and Binzel [123].

Table 11. Satellite Tidal Acceleration

Satellite	dn/dt	Notes
Moon		
Orbit		
(Optical [1]	-26.0 ± 2.0 ″Cy^{-2}	total
astronomy)		
(LLR)[2]	-22.24 ± 0.6 ″Cy^{-2}	1/2 d & l.p.
	-4.04 ± 0.4 ″Cy^{-2}	1 d
	$+0.40$ ″Cy^{-2}	lunar tide
	-25.88 ± 0.5 ″Cy^{-2}	total
Tidal gravity field		
(SLR) [3]	-22.10 ± 0.4 ″Cy^{-2}	1/2 d
	-3.95 ″Cy^{-2}	1 d
	$+0.18$ ″Cy^{-2}	l.p.
	-25.8 ± 0.4″Cy^{-2}	total
Ocean tide height		
(GEOSAT) [4]	-25.0 ± 1.8 ″Cy^{-2}	total
Phobos [5]	24.74 ± 0.35 ° Cy^{-2}	1/2 d
Io [6]	-29 ± 14 ″ Cy^{-2}	1/2 d

Table 11: 1) Morrison and Ward [75].

2) Lunar laser ranging (LLR) result [115] [32]. Separation of diurnal and semidiurnal bands is obtained from 18.6 yr modulation [113];

3) Result from satellite laser ranging to LAGEOS, STARLETTE, etc [22] inferred from the observed tidal gravity field.

4) Altimeter result [22] [19] of the ocean tide, with estimated 7% uncertainty. Both the SLR and Geosat results have been augmented by a factor of $(1 + M/M_\oplus)(1 + 2(n_\oplus/n)^2)$ due to a difficient dynamical model which ignored a barycentric correction [113] and the solar contribution to mean motion (see eq(36)). The inferred solid body Q for earth is $\sim 340(100(\text{min}), \infty(\text{max}))$.

5) Sinclair's solution [97] is typical of several independent analyses of both ground-based and spacecraft data. The tidal acceleration due to solid tides is $dn/dt = k_2/Q \times (15260 \pm 150)°Cy^{-2}$ [120], from which we can deduce Mars' $Q = 86 \pm 2$ for $k_2 = 0.14$. If Mars' k_2 is larger, Q is also larger.

6) Io's acceleration is from analysis of 3 Cy of Galilean satellite observations [65] and the above LLR value for earth moon's dn/dt. An equivalent form is:
$dn_{Io}/dt = n_{Io} \times (-1.09 \pm 0.50) \times 10^{-11}\text{yr}^{-1}$.
Lieske [65] also finds
$d/dt(n_{Io} - n_{Europa}) = n_{Io} \times (+0.08 \pm 0.42) \times 10^{-11}\text{yr}^{-1}$.

Table 12. Planetary Satellites: Physical Properties

Satellite	Radius (km)	Mass 10^{20} kg	Density gm cm^{-3}	Geom. albedo	V(1,0)
Earth	6378	59742	5.515	0.367	−3.86
Moon	1737.53 ± 0.03	734.9	3.34	0.12	+0.21
Mars	3394	641.9	3.933	0.150	−1.52
M1 Phobos [1,2]	$13.1 \times 11.1 \times 9.3(\pm 0.1)$	$1.08(\pm 0.01) \times 10^{-4}$	1.90 ± 0.08	0.06	+11.8
M2 Deimos [2]	$(7.8 \times 6.0 \times 5.1)(\pm 0.2)$	$1.80(\pm 0.15) \times 10^{-5}$	1.76 ± 0.30	0.07	+12.89
Jupiter	71492	1.8988×10^{7}	1.326	0.52	−9.40
JXVI Metis	20 ± 10			0.05	+10.8
JXV Adrastea	10 ± 10			0.05	+12.4
JV Almethea	$(131 \times 73 \times 67)(\pm 3)$			0.05	+7.4
JXIV Thebe	50 ± 10			0.05	+9.0
JI Io [3]	1821.3 ± 0.2	893.3 ± 1.5	3.530 ± 0.006	0.61	
JII Europa	1565 ± 8	479.7 ± 1.5	2.99 ± 0.05	0.64	
JIII Ganymede	2634 ± 10	1482 ± 1	1.94 ± 0.02	0.42	
JIV Callisto	2403 ± 5	1076 ± 1	1.851 ± 0.004	0.20	
JXIII Leda	5				+13.5
JVI Himalia	85 ± 10				+8.14
JX Lysithea	12				+11.7
JXVI Elara	40 ± 10				+10.07
JXII Ananke	10				+12.2
JXI Carme	15				+11.3
JVIII Pasiphae	18				+10.33
JIX Sinope	14				+11.6
Saturn	60268	$5.6850E6$	0.687	0.47	−8.88
XVIII Pan	10			0.5	
SXV Atlas	$(18.5 \times 17.2 \times 13.5)(\pm 4)$			0.9	+8.4
XVI Prometheus [4]	$74 \times 50 \times 34(\pm 3)$	$0.001(4(^{+8}_{-7}))$	0.27 ± 0.16	0.6	+6.4
SXVII Pandora	$(55 \times 44 \times 31)(\pm 2)$	$0.001(3(^{+8}_{-7}))$	0.42 ± 0.28	0.9	+6.4
SX Janus [5]	$(99.3 \times 95.6 \times 75.6)(\pm 3)$	0.0198 ± 0.0012	0.65 ± 0.08	0.8	+4.4
SXI Epimetheus	$(69 \times 55 \times 55)(\pm 3)$	0.0055 ± 0.0003	0.63 ± 0.11	0.8	+5.4
SI Mimas [6]	198.8 ± 0.6	0.375 ± 0.009	1.14 ± 0.02	0.5	+3.3
SII Enceladus [7]	249.1 ± 0.3	0.73 ± 0.36	1.12 ± 0.55	1.0	+2.1
SIII Tethys [8]	529.9 ± 1.5	6.22 ± 0.13	1.00 ± 0.02	0.9	+0.6
SXIV Calypso(T−)	$15 \times 8 \times 8(\pm 4)$			0.6	+9.1
SXIII Telesto(T+)	$15(2.5) \times 12.5(5) \times 7.5(2.5)$			0.5	+8.9
SIV Dione [8]	560 ± 5	10.52 ± 0.33	1.44 ± 0.06	0.7	+0.8
SXII Helene(T+)	16 ± 5			0.7	+8.4
Saturn	60268	$5.6850E6$	0.687	0.47	−8.88
SV Rhea	764 ± 4	23.1 ± 0.6	1.24 ± 0.04	0.7	+0.1
SVI Titan	2575 ± 2	1345.5 ± 0.2	1.881 ± 0.005	0.21	−1.28
SVII Hyperion [9]	$(185 \times 140 \times 113)(\pm 10)$			$0.19 - 0.25$	+4.6
SVIII Iapetus	718 ± 8	15.9 ± 1.5	1.02 ± 0.10	$0.05 - 0.5$	+1.5
SIX Phoebe	$(115 \times 110 \times 105)(\pm 10)$			0.06	+6.89

Table 12(cont). Planetary Satellites: Physical Properties

Satellite	Radius (km)	Mass 10^{20} kg	Density gm cm^{-3}	Geom. albedo	V(1,0)
Uranus [10]	25559	8.6625E5	1.318	0.51	−7.19
VI Cordelia	13 ± 2			0.07	+11.4
VII Ophelia	16 ± 2			0.07	+11.1
VIII Bianca	22 ± 3			0.07	+10.3
IX Cressida	33 ± 4			0.07	+9.5
X Desdemona	29 ± 3			0.07	+9.8
XI Juliet	42 ± 5			0.07	+8.8
XII Portia	55 ± 6			0.07	+8.3
XIII Rosalind	29 ± 4			0.07	+9.8
XIV Belinda	34 ± 4			0.07	+9.4
XV Puck	77 ± 3			0.07	+7.5
UV Miranda	$240(0.6) \times 234.2(0.9) \times 232.9(1.2)$	0.659 ± 0.075	1.20 ± 0.14	0.27	+3.6
UI Ariel	$581.1(0.9) \times 577.9(0.6) \times 577.7(1.0)$	13.53 ± 1.20	1.67 ± 0.15	0.34	+1.45
UII Umbriel	584.7 ± 2.8	11.72 ± 1.35	1.40 ± 0.16	0.18	+2.10
UIII Titania	788.9 ± 1.8	35.27 ± 0.90	1.71 ± 0.05	0.27	+1.02
UIV Oberon	761.4 ± 2.6	30.14 ± 0.75	1.63 ± 0.05	0.24	+1.23
Neptune	24764	1.0278E6	1.638	0.41	−6.87
NIII Naiad	29			0.06	+10.0
NIV Thalassa	40			0.06	+9.1
NV Despina	74 ± 10			0.06	+7.9
NVI Galatea	79 ± 12			0.06	+7.6
NVII Larissa	$104 \times 89(\pm 7)$			0.06	+7.3
NVIII Proteus	$218 \times 208 \times 201$			0.06	+5.6
NI Triton	1352.6 ± 2.4	214.7 ± 0.7	2.054 ± 0.032	0.7	−1.24
NII Nereid	170 ± 2.5			0.2	+4.0

Table 12: Satellite radii are primarily from Davies *et al.* [29]. For synchronously locked rotation, the satellite figure's long axis points toward the planet while the short axis is normal to the orbit. Geometric and visual magnitude $V(1,0)$ (equivalent magnitude at 1 AU and zero phase angle) are from [95]; $V_\odot(1,0) = -26.8$. Satellite masses are from a variety of sources: Galilean satellites [16]; Saturnian large satellites [17]; Uranian large satellites [55]; Triton: mass [111] and radius [27].

Notes:

1) Duxbury [33, 8] has obtained an $n = j = 8$ harmonic expansion of Phobos' topography and obtains a mean radius of 11.04 ± 0.16 and mean volume of 5680 ± 250km^3 based on a model derived from over 300 normal points. The Phobos mission resulted in a much improved mass for Phobos [4].

2) Thomas (priv. comm.).

3) Gaskell *et al.* [43] find from analysis of 328 surface normal points that the figure axes are (1830.0 km×1818.7 km×1815.3 km)(±0.2 km). The observed $(b-c)/(a-c) = 0.23 \pm 0.02$, close to the hydrostatic value of 1/4, while $f_1 = 0.00803 \pm 0.00011$ is consistent with $I/MR^2 = 0.382 \pm 0.003$.

4). The masses of Prometheus and Pandora [91] should be viewed with caution since they are estimated from amplitudes of Lindblad resonances they excite in Saturn's rings.

5) Janus' radii are from [121]. Thomas [107] independently finds radii $97 \times 95 \times 77(\pm 4)$ for Janus. The coorbital satellite masses include new IR observations [81] and are firm. Rosen *et al.* [91] find $1.31(^{+1.7}_{-0.3}) \times 10^{18}$ kg for Janus and $0.33(^{+0.11}_{-0.06}) \times 10^{18}$ kg for Epimetheus from density wave models.

6)Dermott and Thomas find that the observed $(b-c)/(a-c) = 0.27 \pm 0.04$ for Mimas [30] and $(b-c)/(a-c) = 0.24 \pm 0.15$ for Tethys [108], and deduce that Mimas $I/MR^2 = 0.35 \pm 0.01$, based on a second order hydrostatic model.

7) Dermott and Thomas (priv. comm.) estimate Enceladus' mass $= 0.66 \pm 0.01 \times 10^{23}$ gm and density $= 1.01 \pm 0.02$ gm cm^{-3} from its shape.

8) Harper and Taylor [47].

9) Klavetter [59] has verified that Hyperion rotates chaotically from analysis of 10 weeks of photometer data. Furthermore, he finds that the moment ratios are $A/C = 0.54 \pm 0.05$ and $B/C = 0.86 \pm 0.16$ from a fit of the light curve to a dynamic model of the tumbling.

10) The radii of the small Uranian satellites are from Thomas, Weitz and Veverka [106]. Masses of major satellites are from Jacobson *et al.* [55].

Table 13. Planetary Satellites: Orbital Data

Planet		Satellite	a (10^3 km)	Orbital period days	Rot. period days	e	I deg
Earth		Moon	384.40	27.321661	S	0.054900	5.15
Mars	I	Phobos	9.3772	0.318910	S	0.0151	1.082
	II	Deimos	23.4632	1.262441	S	0.00033	1.791
Jupiter	XVI	Metis [1]	127.96	0.294780	S	< 0.004	~ 0
	XV	Adrastea [1]	128.98	0.29826	S	~ 0	~ 0
	V	Almathea [1]	181.3	0.498179	S	0.003	0.40
	XIV	Thebe	221.90	0.6745		0.015	0.8
	I	Io	421.6	1.769138	S	0.041	0.040
	II	Europa	670.9	3.551810	S	0.0101	0.470
	III	Ganymede	1,070	7.154553	S	0.0015	0.195
	IV	Callisto	1,883	16.689018	S	0.007	0.281
	XIII	Leda	11,094	238.72		0.148	*27
	VI	Himalia	11,480	250.5662	0.4	0.163	*175.3
	X	Lysithea	11,720	259.22		0.107	*29
	VII	Elara	11,737	259.6528	0.5	0.207	*28
	XII	Ananka	21,200	631R		0.169	*147
	XI	Carme	22,600	692R		0.207	*163
	VIII	Pasiphae	23,500	735R		0.378	*148
	IX	Sinople	23,700	758R		0.275	*153
Saturn	XVIII	Pan	133.583	0.5750			
	XV	Atlas [2]	137.64	0.6019		~ 0	~ 0
	XVI	Prometheus [2]	139.35	0.612986		0.0024	0.0
	XVII	Pandora[2]	141.70	0.628804		0.0042	0.0
	XI	Epimetheus	151.422	0.694590	S	0.009	0.34
	X	Janus	151.472	0.694590	S	0.007	0.14
	I	Mimas	185.52	0.9424218	S	0.0202	1.53
	II	Enceladus	238.02	1.370218	S	0.0045	0.02
	III	Tethys	294.66	1.887802	S	0.0000	1.09
	XIV	Calypso(T−)	294.66	1.887802		~ 0	~ 0
	XIII	Telesto(T+)	294.66	1.887802		~ 0	~ 0
	IV	Dione	377.40	2.736915	S	0.0022	0.02
	XII	Helene(T+)	377.40	2.736915		0.005	0.2
	V	Rhea	527.04	4.517500	S	0.001	0.35
	VI	Titan	1221.85	15.945421		0.0292	0.33
	VII	Hyperion	1481.1	21.276609	C	0.1042	0.43
	VIII	Iapetus	3561.3	79.330183	S	0.0283	7.52
	IX	Phoebe	12952	550.48R	0.4	0.163	*175.3
Uranus [1]	VI	Cordelia	49.752	0.335033		0.000	0.1
	VII	Ophelia	53.764	0.376409		0.010	0.1
	VIII	Bianca	59.165	0.434577		0.001	0.2
	IX	Cressida	61.777	0.463570		0.000	0.0
	X	Desdemona	62.659	0.473651		0.000	0.2
	XI	Juliet	64.358	0.493066		0.001	0.1
	XII	Portia	66.097	0.513196		0.000	0.1

Table 13(cont). Planetary Satellites: Orbital Data

Planet		Satellite	a 10^3km	Orbital period days	Rot. period days	e	I deg
	XIII	Rosalind	69.927	0.558459		0.000	0.3
	XIV	Belinda	75.255	0.623525		0.000	0.0
	XV	Puck	86.004	0.761832		0.000	0.3
	V	Miranda	129.8	1.413	S	0.0027	4.22
	I	Ariel	191.2	2.520	S	0.0034	0.31
	II	Umbriel	266.0	4.144	S	0.0050	0.36
	III	Titania	435.8	8.706	S	0.0022	0.10
	IV	Oberon	582.6	13.463	S	0.0008	0.10
Neptune [2]	III	Naiad	48.227	0.294396		0.000	4.74
	IV	Thalassa	50.075	0.311485		0.000	0.21
	V	Despina	52.526	0.334655		0.000	0.07
	VI	Galatea	61.953	0.428745		0.000	0.05
	VII	Larissa	73.548	0.554654		0.000	0.20
	VIII	Proteus	117.647	1.122315		0.000	0.55
	I	Triton	354.76	$5.876854R$	S		156.834
	II	Nereid	5513.4	360.13619		0.7512	*7.23
Pluto	I	Charon	19.405	6.38723		0	0

Table 13: Abbreviations: R=retrograde orbit; T=: Trojan-like satellite which leads(+) or trails(−) by ∼60° in longitude the primary satellite with same semimajor axis; (*) The local invariable reference plane (see equation 68) of these distant satellites is controlled by Sun rather than planetary oblateness; S=synchronous rotation; C=chaotic rotation; References: From [95], with additional data for Saturn's F ring satellites [104], Jupiter's small satellites [105], the Uranian [84] and Neptune [86, 53] systems.

Table 14. Planetary Rings

Feature	Distance [b] km	r/R_e	Optical depth	Albedo	σ g cm^{-2}	e
Jupiter	71492	1.000				
Halo	> 100000	1.25 – 1.71	3×10^{-6}			
Main	> 122000	1.71 – 1.81	5×10^{-6}	[0.015]	$> 5 \times 10^{-6}$	
Gossamer	> 129000	1.8 – 3	1×10^{-7}			
Saturn	60268	1.000				
D ring	> 66900	> 1.11				
C inner edge	74658	1.239	0.05 – 0.35	0.12 – 0.30	0.4 → 5	
Titan ringlet	77871	1.292			17	0.00026
Maxwell ringlet	87491	1.452			17	0.00034
B inner edge	91975	1.526	0.4 – 2.5	0.4 – 0.6	20 – 100	
B outer edge [c]	117507	1.950				
Cassini division			0.05 – 0.15	0.2 – 0.4	5 – 20	
A inner edge	122340	2.030	0.4 – 1.0	0.4 → 0.6	30 – 40	
Encke gap [b]	133589	2.216				
A outer edge [d]	136775	2.269				
F-ring center	140374	2.329	0.1	0.6		0.0026

TABLE 14. (continued).

Feature	Distance [b] km	r/R_c	Optical depth	Albedo	σ g cm^{-2}	e
G-ring center	170000	2.82	1×10^{-6}			
E inner edge	$\sim$ 180000	3	1.5×10^{-5}			
E outer edge	$\sim$ 480000	8				
				Albedo $\times 10^{-3}$	**Width** km	e
Uranus [e]	25559	1.000				
6	41837	1.637	$\simeq 0.3$	~ 15	~ 1.5	0.0010
5	42235	1.652	~ 0.5	~ 15	~ 2	0.0019
4	42571	1.666	~ 0.3	~ 15	~ 2.5	0.0010
α	44718	1.750	~ 0.4	~ 15	$4 \rightarrow 10$	0.0008
β	45661	1.786	~ 0.3	~ 15	$5 \rightarrow 11$	0.0004
η	47176	1.834	≤ 0.4	~ 15	1.6	
γ	47626	1.863	≥ 1.5	~ 15	$1 \rightarrow 4$	0.0001
δ	48303	1.900	~ 0.5	~ 15	$3 \rightarrow 7$	
λ	50024	1.957	~ 0.1	~ 15	~ 2	
ϵ	51149	2.006	$0.5 \rightarrow 2.3$	18 ± 1	$20 \rightarrow 96$	0.0079
Neptune	24766	1.000				
Galle	$\sim$ 41900	1.692	$\sim 1 \times 10^{-4}$	[15]	~ 1700	
Leverrier	53200	2.148	0.01	[15]	~ 100	
1989N4R	$\sim$ 53200	2.148	$\sim 1 \times 10^{-4}$	[15]	~ 4000	
Adams(arcs)	62932	2.477	$0.01 - 0.1$	[15]	~ 15	

Table 14: See Nicholson and Dones [80] and for a review of ring properties. Bracketed [ ] albedos are adopted. Horn *et al.* [54] find from density wave analysis that the A ring mean surface desity is $\sigma = 45 \pm 11$ gm cm^{-2} for $a = 2.0 - 2.21R$, and $\sigma = 29 \pm 7$gm cm^{-2} for $a = 2.22 - 2.27R$, with mass(A-ring)$= 5.2 \times 10^{21}$gm.

a) See Esposito *et al.* [36] for a more complete list of Saturn's ring features.

b) Encke gap width=322 km.

c) Sharp B ring edge controlled by 2:1 Lindblad resonance with Janus.

d) Sharp A ring edge due to 7:6 Janus' resonance.

e) French *et al.* [41].

Table 15. Prominent Minor Planets or Asteroids

No.	Name	Dia. km	Tax	a AU	e	I deg	Ω deg	ω deg	M deg	Period year	rotation hrs
1	Ceres	933	G?	2.769	0.0780	10.61	80.0	71.2	287.3	4.607	9.075
2	Pallas	525		2.770	0.2347	34.81	172.6	309.8	273.8	4.611	7.811
4	Vesta	510	V	2.361	0.0906	7.14	103.4	150.1	43.3	3.629	5.342
10	Hygiea	429	C	3.138	0.1201	3.84	283.0	316.1	33.0	5.656	27.659
511	Davida	337	C	3.174	0.1784	15.94	107.3	339.0	244.5	5.656	5.130
704	Interamnia	333	F	3.064	0.1475	17.30	280.4	92.2	276.8	5.364	8.727
52	Europa	312	C	3.101	0.1002	7.44	128.6	337.0	92.6	5.460	5.631
15	Eunomia	272	S	2.644	0.1849	11.76	292.9	97.5	327.9	4.299	6.083
87	Sylvia	271	PC	3.490	0.0820	10.87	73.1	273.3	248.8	6.519	5.183
3	Juno	267	S	2.668	0.0258	13.00	169.9	246.7	115.4	4.359	7.210
16	Psyche	264	M	2.923	0.1335	3.09	149.9	227.5	318.7	4.999	4.196
31	Euphrosyne	248	C	3.146	0.2290	26.34	30.7	63.1	341.0	5.581	5.531

Table 15. (cont) Prominent Minor Planets or Asteroids

No.	Name	Dia. km	Tax	a AU	e	I deg	Ω deg	ω deg	M deg	Period year	Rotation hrs
65	Cybele	240	C	3.437	0.1044	3.55	155.4	109.8	20.1	6.372	4.041
107	Camilla	237	C	3.484	0.0842	9.93	173.5	296.0	139.7	6.503	4.840
624	Hektor	233	D	5.181	0.0246	18.23	342.1	178.0	2.9	11.794	6.921
88	Thisbe	232	C	2.767	0.1638	5.22	276.3	35.3	259.0	4.603	6.042
451	Patientia	230	C	3.062	0.0709	15.24	89.0	343.2	269.4	5.358	9.727
324	Bamberga	228	C	2.681	0.3409	11.14	327.8	43.4	189.6	4.390	29.43
48	Doris	225	C	3.110	0.0693	6.54	183.4	262.8	278.8	5.485	11.89
532	Herculina	225	S	2.771	0.1764	16.36	107.4	75.1	199.4	4.613	9.405
29	Amphitrite	219	S	2.555	0.0717	6.10	355.9	62.8	197.9	4.084	5.390
423	Diotima	217	C	3.067	0.0365	11.25	69.2	215.6	223.9	5.371	4.622
121	Hermione	217	C	3.438	0.1428	7.56	74.1	287.5	4.3	6.376	8.97
375	Ursula	216	C	3.126	0.1037	15.93	336.1	347.9	163.0	5.528	16.83
13	Egeria	215	G	2.576	0.0863	16.52	42.8	81.1	132.8	4.136	7.045
45	Eugenia	214	C	2.722	0.0821	6.60	147.4	86.0	188.9	4.490	5.699
94	Aurora	212	C	3.164	0.0814	8.01	2.5	51.8	223.8	5.628	7.22
7	Iris	203	S	2.386	0.2296	5.51	259.3	144.8	132.3	3.685	7.139
702	Alauda	202	C	3.195	0.0286	20.57	289.6	3.6	335.5	5.710	8.36
19	Fortuna	200	C	2.442	0.1580	1.57	210.9	182.0	287.9	3.817	7.445
24	Themis	200	C	3.126	0.1351	0.76	35.6	110.5	229.9	5.528	8.374
2060	Chiron			13.716	0.3816	6.93	208.6	339.0	315.0	50.801	5.918
130	Elektra	189	G	3.113	0.2182	22.88	145.3	234.7	177.2	5.492	5.225
22	Kalliope	187	M	2.912	0.0978	13.70	65.8	355.6	212.6	4.969	4.147
747	Winchester	178	C	2.995	0.3433	18.18	129.6	276.1	354.5	5.183	9.40
153	Hilda	175	C	3.975	0.1418	7.84	227.8	42.6	269.5	7.925	*8.11
334	Chicago	170	C	3.875	0.0407	4.66	130.1	136.5	300.6	7.627	9.19
51	Nemausa	153	G	2.366	0.0656	9.96	175.6	2.4	50.8	3.640	7.785
617	Patroclus	149	P	5.230	0.1396	22.04	43.8	306.8	32.1	11.961	* > 40.
420	Bertholda	146	P	3.416	0.0475	6.70	243.9	206.3	158.8	6.314	11.04
69	Hesperia	143	M	2.979	0.1673	8.55	185.2	285.8	34.6	5.142	5.655
8	Flora	141	S	2.201	0.1564	5.89	110.5	284.8	176.3	3.266	12.790
216	Kleopatra	140	M	2.795	0.2495	13.11	215.2	179.4	312.4	4.674	5.385
279	Thule	135	D	4.271	0.0119	2.34	73.2	76.7	17.8	8.825	7.44
419	Aurelia	133	F	2.595	0.2562	3.95	229.3	43.1	147.7	4.179	16.709
221	Eos	110	K	3.012	0.0973	10.87	141.6	191.9	20.9	5.229	10.436
233	Asterope	108	T	2.661	0.0996	7.68	221.8	125.3	72.1	4.342	19.70
181	Eucharis	107	K	3.137	0.2032	18.69	143.5	313.2	98.8	5.555	* > 7.
114	Kassandra	103	T	2.675	0.1398	4.95	163.8	352.0	151.4	4.376	10.758
773	Irmintraud	99	D	2.858	0.0805	16.68	322.1	331.6	21.3	4.831	
25	Phocaea	78	S	2.400	0.2557	21.58	213.7	90.5	189.5	3.719	9.945
44	Nysa	73	E	2.424	0.1497	3.71	131.0	342.0	142.7	3.773	6.422
64	Angelina	59	E	2.682	0.1251	1.31	309.0	179.7	133.8	4.393	8.752
170	Maria	46	S	2.552	0.0648	14.43	300.9	157.4	242.3	4.078	
446	Aeternitas	43	A	2.787	0.1267	10.62	41.8	279.6	167.7	4.652	
1036	Ganymed	41	S	2.665	0.5366	26.45	215.6	131.7	343.7	4.350	10.308
158	Koronis	39	S	2.870	0.0521	1.00	278.1	142.5	187.0	4.861	14.18
243	Ida	32	S	2.863	0.0421	1.14	323.9	110.6	203.5	4.843	4.65

Table 15. (cont) Prominent Minor Planets or Asteroids

No.	Name	Dia. km	Tax	a AU	e	I deg	Ω deg	ω deg	M deg	Period year	Rotation hrs
433	Eros	20	S	1.458	0.2229	10.83	303.7	178.6	122.1	1.761	5.270
951	Gaspra	14	S	2.210	0.1737	4.10	252.7	129.4	52.9	3.286	7.042
434	Hungaria	10	E	1.944	0.0740	22.51	174.8	123.8	258.3	2.711	26.51

Table 15: Size, Orbits and rotation periods [35] of prominent objects. This table is sorted by size which are largely determined from the visual and infrared (from IRAS) magnetudes, although a few are from stellar occultations and other sources. All objects with diameters larger than 200 km are included. A few smaller objects are included because of unusual characteristics or because they are Galileo fly-by targets (951 Gaspra and 243 Ida, a Koronis family member). 24 Themis, 221 Eos, 158 Koronis, 170 Maria and 8 Flora are prominent representatives of major asteroid families of collision fragments. The low perihelion distances (usually denoted $q = a(1-e)$) for 433 Eros ($q = 1.133$AU) and 1036 Ganymed ($q = 1.234$AU) indicate that they are Mars' crossers. 2060 Chiron is in a distant, comet-like orbit. Initially a point source, it was catalogued as an asteroid, but subsequently exhibited cometary activity as it approached perihelion. There is no secure diameter measurement, although its brightness indicates a large diameter of several hundred km. The three largest asteroids have rare or unusual taxonomies. The epoch for the orbit parameters is Oct. 1, 1989, although they are referenced to the 1950 equinox and ecliptic (table and notes from J. G. Williams).

*: Periods are uncertain or controversial.

Table 16. Near Earth Asteroids

No	**Name**	**Dia.** km	P_v	**Rot.** hrs	q AU	e	I	**Encounter** date(dist.in AU)
2062	**Aten**	0.9	0.20		0.790	0.183	18.9	1/12/95(0.127)
2100	Ra-Shalom	2.4	0.09	19.79	0.469	0.437	15.8	9/26/97(0.171)
2063	Bacchus				0.701	0.350	9.4	3/31/96(0.068)
2340	Hathor				0.464	0.450	5.9	10/25/00(0.197)
3362	Khufu	0.7	0.16		0.526	0.469	9.9	1/24/00(0.293)
3554	Amun	2.0	0.17		0.700	0.281	23.4	
1862	**Apollo**	1.5	0.21	3.065	0.647	0.560	6.35	
1566	Icarus	0.9	0.42	2.273	0.187	0.827	22.9	6/11/96(0.101)
1620	Geographos	2.0	0.19	5.227	0.827	0.336	13.3	8/25/94(0.033)
1685	Toro	5.2	0.14	10.196	0.771	0.436	9.4	8/02/96(0.221)
1863	Antinous	1.8	0.18	4.02	0.890	0.606	18.4	4/10/99(0.190)
1865	Cerberus	1.0	0.26	6.80	0.576	0.467	16.1	11/24/98(0.163)
1866	Sisyphus	8.2	0.18		0.873	0.539	41.2	
2102	Tantalus				0.905	0.299	64.0	12/21/97(0.138)
2201	Oljato	1.4	0.42	> 24.0	0.905	0.299	64.0	
3103	1982 BB				0.907	0.354	20.9	8/06/96(0.115)
3200	Phaethon	6.9	0.08		0.140	0.890	22.1	
4179	Toutatus				0.921	0.634	0.5	11/29/96(0.035)
4183	Cuno				0.718	0.637	6.8	12/22/00(0.143)
4197	1982 TA				0.522	0.773	12.2	10/25/96(0.085)
4486	1987 SB				0.743	0.663	3.0	8/14/00(0.047)
	1988 EG				0.636	0.499	3.9	2/28/98(0.032)
	1986 JK				0.896	0.680	2.1	7/11/00(0.122)
4034	1986 PA				0.589	0.444	11.2	8/28/97(0.206)

TABLE 16. (continued).

No	Name	Dia. km	P_v	Rot. hrs	q AU	e	I	Encounter date(dist.in AU)
4769	Castelia				0.550	0.483	8.9	4/08/93(0.132)
433	**Eros**	22	0.18	5.27	1.133	0.223	10.83	
887	Alinda	4.2	0.23	73.97	1.101	0.560	9.27	
1036	Ganymed	38.5	0.17	10.31	1.229	0.539	26.6	
1580	Betulia	7.4	0.03	6.13	1.119	0.490	52.1	
1627	Ivar	8.1	0.12	4.80	1.124	0.397	8.4	
1980	Tezcatlipoca	4.3	0.21		1.085	0.365	26.9	11/16/97(0.274)
3102	1981 QA			148	1.189	0.447	8.4	
3288	Seleucus	2.8	0.17	75.	1.103	0.457	5.9	
3361	Orpheus	0.8			0.819	0.323	2.7	2/12/98(0.167)
3552	Don Quixote	18.7	0.02		1.212	0.714	30.8	
3671	Dionysius				1.003	0.543	13.6	7/06/97(0.114)
3908	1982 PA				1.056	0.317	10.8	10/27/96(0.061)

Table 16: Prominent Aten, Apollo, and Amor class near earth asteroids. Orbit elements ($q \equiv a(1-e)$), e,inclination I, date (mm/dd/yr) of closest approach to earth and corresponding minimum separation (in AU) during the 1993-2000 time period are from D. Yeomans (priv. comm.). These are taken from a list of 85 objects with well determined orbits for which the estimated population is over 4000 ($V(1,0) < 18$). The size, visual albedo (P_v) and rotation period are given if known [72].

Table 17. Asteroid Mass Determinations

Object	Mass 10^{22} g	Diam. km	density g cm^{-3}	ref.
Ceres	117 ± 6	940	2.7	a
	104 ± 6		2.4	b
	99 ± 4		2.3	c
Pallas	22 ± 4	538	2.6	a
	28 ± 4		3.4	c
Vesta	28 ± 2	525	3.6	a
	30 ± 6		3.9	c
Hygeia	9 ± 4	427	2.3	c

Table 17: Masses and densities exist for only four large asteroids. These masses result from tracking their orbital perturbation of other asteroids (a,b,d) detected from ground-based astrometry: (a) Schubart [94], (b) Landgraf [63], (c) Scholl *et al.* [93] or radio tracking of Viking Mars' landers (d) Standish and Hellings [102], and from which these results were obtained.

Table 18. Prominent Short Period Comets: Epoch B1950

Comet	l	ω	Ω	I	e	a	T_p	M_1	M_2
	deg	deg	deg	deg		AU	JD		
Arend	359.75	47.06	355.49	19.929	0.53703	3.9961	2448402.5	9.5	15.0
Arend-Rigaux	358.31	329.06	121.45	17.888	0.60005	3.5950	2448532.2	10.0	15.5
Ashbrook-Jackson	2.36	348.69	1.97	12.494	0.39491	3.8279	2449182.5	1.0	11.5
Boethin	0.36	22.31	13.74	4.871	0.77436	5.1329	2450556.2	10.0	14.0
Borrelly	359.03	353.36	74.74	30.323	0.62390	3.6112	2452167.2	4.5	13.0
Brooks 2	0.56	197.99	176.25	5.548	0.49073	3.6196	2449596.5	9.0	13.5
Brorsen-Metcalf	0.27	129.62	310.88	19.331	0.99196	17.073	2447781.4	7.8	14.0
Churyumov-Gerasimenko	3.04	11.34	50.35	7.110	0.63021	3.5156	2450100.1	9.5	14.5
Comas Solá	359.50	45.74	60.20	12.914	0.56779	4.2719	2450244.9	8.0	12.5
Crommelin	359.36	195.99	249.93	28.959	0.91875	9.2046	2455778.5	12.0	16.0
d'Arrest	359.19	178.04	138.30	19.528	0.61404	3.4871	2449925.8	8.5	16.0
Denning-Fujikawa	0.43	337.56	35.72	9.130	0.81792	4.3372	2450236.5	15.0	19.0
du Toit-Hartley	3.48	251.57	308.56	2.938	0.60161	3.0050	2448862.1	14.0	18.0
Encke	1.00	186.49	333.89	11.750	0.84690	2.2177	2451797.1	9.8	14.5
Faye	357.83	203.95	198.88	9.091	0.57818	3.7774	2448576.6	8.0	14.0
Finlay	359.70	323.47	41.42	3.669	0.71030	3.5746	2449842.5	12.0	17.0
Forbes	2.88	310.72	333.65	7.16	0.56811	3.3481	2451302.5	10.5	15.5
Gehrels 2	1.77	192.80	209.90	6.263	0.46357	3.7289	2450667.6	5.5	13.0
Giacobini-Zinner	359.22	172.52	194.68	31.828	0.70649	3.5229	2448725.7	9.0	15.5
Grigg-Skjellerup	2.87	359.27	212.63	21.104	0.66433	2.9633	2448825.6	12.5	17.0
Gunn	358.78	196.79	67.86	10.378	0.31632	3.6010	2450288.9	5.0	10.0
Halley	0.12	111.85	58.14	162.239	0.96728	17.9415	2446470.9	5.5	13.0
Hartley 2	359.41	180.74	219.24	13.63	0.70037	3.4432	2450804.3	10.5	14.5
Honda-Mrkos-Padušáková	0.39	326.05	88.48	4.257	0.82512	3.0211	2451998.3	13.5	18.0
Kopff	2.11	162.76	120.28	4.724	0.54408	3.4645	2450266.6	3.0	13.5
Olbers	359.84	64.41	85.16	44.67	0.93031	16.8666	2460491.9	5.0	11.5
Pons-Winnecke	359.31	172.30	92.75	22.302	0.63443	3.4354	2450084.9	10.0	16.0
Schaumasse	358.79	57.45	80.39	11.846	0.70487	4.0734	2449050.6	9.0	15.5
Schwassmann-Wachmann 2	358.59	18.33	113.57	4.552	0.19529	4.2357	2452292.9	7.6	14.0
Tempel 2	1.91	195.00	117.54	11.980	0.52282	3.1051	2451429.9	4.0	15.0
Tempel-Tuttle	0.24	172.52	234.58	162.49	0.90551	10.335	2450872.5	9.0	13.0
Tuttle-Giacobini-Kresák	358.80	61.68	140.82	9.230	0.65642	3.1003	2449927.1	10.0	18.0
Wild 2	357.74	41.70	135.53	3.248	0.54023	3.4422	2450575.1	6.5	13.0
Wirtanen	0.06	356.15	81.61	11.683	65225	3.1152	2448520.1	9.0	15.5
Wolf	2.13	162.29	203.44	27.483	0.40560	4.0843	2448862.6	10.0	16.0

Table 18: This list of short period comets (period <200 yr) has been drawn from a much larger list compiled by D. Yeomans (priv. comm.) and are themselves primarily taken from Minor Planet Circulars (also see [117]). The material includes orbital data (epoch 1950): $a, e, I, \ell, \omega, \Omega$, the Julian date of perihelion passage and the absolute (M_1)and nuclear (M_2)magnitudes. All comets are affected by nongravitational forces related to sublimation of ices (H_2O, CO_2, N, NH_2, etc.) which can significantly change the orbit over time, especially the timings of perihelion passage. Some asteroids such as 944 Hildalgo may be extinct comets.

Table 19. Sun: Physical Properties

$GM_\odot$	$1.327124399(4 \pm 5) \times 10^{11}$ km^3 s^{-2}
Mass	1.9891×10^{30} kg
Radius [a] (photosphere)	6.960×10^5 km
Angular diameter at 1 AU	1919.″3
Mean density	1.408 g cm^{-3}
Surface gravity	274.0 m s^{-2}
Moment of inertia I/MR^2	0.059
Escape velocity $v_\infty = \sqrt{2GM/R}$	617.7 km s^{-1}
Adopted siderial period [b]	25.38d
Pole: (RA Dec)	$\alpha = 286.13°; \delta = 63.87°$
Obliquity to ecliptic	$7°15'$
Longitude of ascending node	$75°46' + 84'T$
Surface rotation rate[a] ν	$(\nu = 462 - 75\sin^2\phi - 50\sin^4\phi)$ nHz
as function of latitude ϕ	(462 nHz = 14.37° d^{-1})
Solar constant (1 AU) [f]	1367.6 W m^{-2}
Solar luminosity $L_\odot$	3.846×10^{33} ergs s^{-1}
Mass-energy conversion rate	4.3×10^{12} gm s^{-1}
Effective temperature $= (L_\odot/\sigma_{SB})^{1/4}$	5778°K
Surface Temperature (photosphere) [a]	$6600°K$(bottom); $4400°K$(top)
Motion relative to nearby stars [c]	apex: $\alpha = 271°$; $\delta = +30°$
	speed: 19.4 km s^{-}1 = 0.0112AU d^{-1}
Motion relative to $2.73°K$ BB	369 ± 11 km s^{-1}
deduced from thermal dipole [d]	apex: $l = 264°.7 \pm 0.8; b = 48°.2 \pm 0.5$
Sun spot cycle	11.4yr
Cycle 22 solar sunspot maximum	1991
Photospheric depth[a]	$\simeq 400$ km
Chromospheric depth	~ 2500 km

Table 19: See Cox *et al.* [26] for general summary of solar science. References: a) Alcock [2]; b) Davies *et al.* [29]; c) Allen [1]; d) Smoot *et al.* [99]; e) SMM/ACRIM result [70]. The solar constant varies by 0.04% during a solar cycle. During solar maximum, sunspots can change the solar constant by 1/4% during one rotation.

Table 20. Solar Interior Model

M_r/M_R	r/R)	Pressure dyne cm^{-2}	Temp. 10^6 K	Density g cm^{-3}	L_r/L_R L_R
0.0000	0.0000	2.477 + 17	15.710	162.2	0.0000
0.0103	0.0462	2.144 + 17	15.010	138.4	0.0819
0.0406	0.0766	1.716 + 17	14.000	110.6	0.2766
0.1026	0.1116	1.234 + 17	12.650	81.64	0.5514
0.2023	0.1520	7.889 + 16	11.100	56.62	0.7969
0.3036	0.1873	5.108 + 16	9.864	40.34	0.9150
0.4051	0.2216	3.248 + 16	8.803	28.42	0.9683
0.4981	0.2546	2.066 + 16	7.920	20.01	0.9896
0.5985	0.2943	1.182 + 16	7.012	12.93	0.9983
0.6979	0.3419	6.048 + 15	6.114	7.584	0.9999
0.7991	0.4073	2.460 + 15	5.138	3.679	1.0002
0.8989	0.5129	6.198 + 14	4.594	1.231	1.0002
0.9504	0.6177	1.731 + 14	3.082	0.4386	1.0001
0.9803	0.7363	4.203 + 13	2.031	0.1604	1.0001
0.9951	0.8489	7.059 + 12	1.000	0.0549	1.0001
0.9999	0.9634	9.941 + 10	0.190	0.0043	1.0001

Table 20: Standard model by Cox, Gudzik and Kidman [26] which constrains the metallicity factor $Z = 0.02$ and the helium mass fraction to $Y = 0.291$. Competing "standard" models [45] differ for internal radius $< 0.1 R_\odot$ and which have 10% lower central pressure and density.

a: Pressure column reads: $2.477 + 17 = 2.477 \times 10^{17}$.

Table 21. Solar Luminosity History

t Gyr	R(t)/R(4.6)	T_c 10^6 K	ρ_c g cm^{-3}	T_{eff} K	L(t)/L(4.6)
0.00	0.8755	13.69	81.44	5649	0.7044
0.50	0.8939	13.75	90.19	5678	0.7496
1.00	0.9050	13.92	95.55	5692	0.7745
1.50	0.9153	14.12	101.5	5704	0.8000
2.00	0.9268	14.32	108.3	5717	0.8262
2.50	0.9386	14.54	115.6	5729	0.8561
3.00	0.9516	14.78	124.3	5741	0.8872
3.50	0.9651	15.04	133.8	5750	0.9185
4.00	0.9801	15.32	145.2	5761	0.9539
4.64	1.0000	15.71	162.2	5770	1.0000

Table 21: Evolution of solar luminosity, radius, central temperature T_c, pressure P_c and density ρ_c, from solar ignition at zero age to the present at 4.6 Gy [26]. Note that the increase in luminosity is primarily due to a change in photospheric radius.

Acknowledgements. I wish to thank to a variety of individuals who contributed material or reviewed this paper, including J. Campbell, R. Gross, A. Harris, A. Konopliv, D. Nicholson, G. Null, W. Owen Jr., N. Rappaport, M. Standish, S. Synnott, P. Thomas, J. Wahr, J. G. Williams and D. Yeomans, but not excluding many others. This paper presents the results of one phase of research carried out at the Jet Propulsion Laboratory, California Institute of Technology, under NASA Contract NAS 7-100, supported by the National Aeronautics and Space Administration.

REFERENCES

1. Allen, C. W., *Astrophysical Quantities* (3rd ed.), Atholone Press, London, 310pp, 1985.
2. Altrock, R. C., H. L. DeMastus, J. W. Evans, S. L. Keil, D. F. Neidig, R. R. Radick, R. R. and G. W. Simon, The Sun, in *Handbook of Geophysics and the Space Environment*, edited by A. S. Jursa, Air Force Geophysics Laboratory, 1.1-1.25, 1985.
3. Anderson, J. D., G. Colombo, P. B. Esposito, E. L. Lau and G. B. Trager, The mass and gravity field of Mercury, *Icarus, 71*, 337-349, 1987.
4. Avensov, G. A. *et. al*, Television observations of Phobos, *Nature, 341*, 585-587, 1989.
5. Balmino, G., B. Moynot and N. Vales, Gravity Field of Mars in spherical harmonics up to degree and order 18, *J. Geophys. Res., 87*, 9735-9746, 1982.
6. Baron, R. L., R. G. French, and J. L. Elliot, The oblateness of Uranus at the 1-μbar level, *Icarus, 78*, 119-130, 1989.
7. Basaltic Volcanism Study Project, *Basaltic Volcanism on the Terrestrial Planets*, Pergamon Press, New York, 1286pp., 1981.
8. Batson, R. M., K. Edwards and T. C. Duxbury, Geodesy and Cartography of the Martian satellites, in *Mars*, edited by H. H. Kieffer, B. M. Jakosky, C.W. Snyder and M. S. Matthews, Univ. of Arizona Press, Tucson, 1992.
9. Bills, B. G. and A. J. Ferrari, A harmonic analysis of lunar topography, *Icarus, 31*, 244-259, 1977.
10. Bills, B. G. and A. J. Ferrari, Mars' topography harmonics and geophysical implications, *J. Geophys. Res., 83*, 3497-3508, 1978.
11. Bills, B. G. and M. Kobrick, Venus topography: a harmonic analysis,*J. Geophys. Res., 90*, 827-836, 1985.
12. Borderies, N. and C. F. Yoder, Phobos' gravity field and its influence on its orbit and physical librations, *Astron. Astrophys., 233*, 235-251, 1990.
13. Brouwer, D. and G. M. Clemence, *Methods of Celestial Mechanics*, Academic Press, New York, 598pp, 1961.
14. Burns, J. A., Some background about satellites, in *Satellites*, edited by J. A. Burns and M. S. Matthews, Univ. of Arizona Press, Tucson, 1-38, 1986.
15. Buie, M. W., D. J. Tholen and K. Horne, Albedo maps of Pluto and Charon: initial mutual event results, *Icarus, 97*, 211-227, 1992.
16. Campbell, J. K. and S. P. Synnott, Gravity field of the jovian system from pioneer and voyager tracking, *Astron. J., 90*,364-372, 1985.
17. Campbell, J. K. and J. D. Anderson, Gravity field of the Saturnian system from Pioneer and Voyager tracking data,*Astron. J., 97*, 1485-1495, 1989.
18. Caputo, M., The minimum strength of the earth, *J. Geophys. Res., 70*, 953-963, 1965.
19. Cartwright, D. E. and R. D. Ray, Oceanic tides from Geosat, *J. Geophys. Res., 95*, 3069-3090, 1990.
20. Chandrasekhar, S., *Ellipsoidal Figures of Equilibrium*, Yale Univ. Press, New Haven, CN, 1969.
21. Chapront-Touze, M., and J. Chapront, ELP2000-85: a semianalytic lunar ephemeris adequate for historical times, *Astron. Astrophys., 190*, 342-352, 1988.
22. Cheng, M. K., R. J. Eanes and B. D. Tapley, Tidal deceleration of the Moon's mean motion, *Geophys. J.*, , 401-409, 19912
23. Clark, C. R. and R. O. Vicente, Maximal likelihood estimates of polar motion parameters, in *Variations in earth rotation*, edited by D. D. McCarthy and W. E. Carter, American Geophysical Union monograph, 151-155, 1990.
24. Cook, A. H., The external gravity field of a rotating spheroid to the order of e^3, *Geophys. J. R. Astr. Soc., 2* ,199-214, 1959.
25. Connerney, J. E. P., L. Davis Jr. and D. L. Chenette, in *Saturn*, edited by T. Gehrels and M. S. Matthews , Univ. of Arizona Press, Tucson, 354-377, 1984.
26. Cox, A. N., W. C. Livingston and M. S. Matthews, *Solar Interior and Atmosphere*, Univ. of Arizona Press, Tucson, 1416pp, 1991.
27. Davies, M. E., P. G. Rogers and T. R. Colvin, A control network of Triton, *J. Geophys. Res., 96*, 15675-15681, 1991.
28. Davies, M. E., V. K. Abalkin, A. Brahic, M. Bursa, B. H. Chovitz, J. H. Lieske, P. K. Seidelmann, A. T. Sinclair and Y. S. Tjuflin, Report of the IUA/IAG/COSPAR working group on cartographic coordinates and rotational elements of the planets and satellites: 1991, *Icarus, 53*, 377-397, 1992.
29. Davies, M. E. and 8 authors, The rotation period, direction of the north pole, and geodetic control network of Venus, *J. Geophys. Res., 97*, 13141-13151, 1992.
30. Dermott, S. F. and P. C. Thomas, The shape and internal structure of Mimas, *Icarus, 73*, 25-65, 1988.
31. Dermott, S. F. and P. C. Thomas, Shapes, masses and interiors of satellites, *Adv. Space Res., 10*, 165-172, 1990.
32. Dickey, J. O., P. L. Bender, J. E. Faller, X X Newhall, R. L. Ricklets, J. G. Ries, P. J. Shelus, C. Veillet, A. L. Whipple, J. R. Wiant, J. G. Williams and C. F. Yoder, Lunar laser ranging: A continuing legacy of the Apollo Program, *Science, 265*, 482-490, 1994.
33. Duxbury, T. C., An analytic model for the Phobos surface, *Planet. Space Sci., 39*, 355-376, 1991.
34. Elliot, J.L. and L. A. Young, Analysis of stellar occultation data for planetary atmospheres. I: model fitting, with application to Pluto, *Astron. J.*, 103, 991-1015, 1992.
35. Ephemerides of the minor planets for 1993, Russian Academy of Sciences, Institute for Theoretical Astronomy, edited by Y. V. Batrakov, St. Petersberg, 511pp, 1992.
36. Esposito, L. W., C. C. Harris and K. E. Simmons, Features in Saturn's rings, *Astrophys. J. Supp., 63*, 749-

770, 1987.
37. Esposito, P. B., W. B. Banerdt, G. F. Lindal, W. L. Sjogren, M. A. Slade, B. G. Bills, D. E. Smith and G. Balmino, Gravity and Topography, in *Mars*, edited by H. H. Kieffer, B. M. Jabosky, C. W. Snyder and M. S. Matthews, Univ. of Arizona Press, Tucson, 209-248, 1992.
38. Ferrari, A. J., W. S. Sinclair, W. L. Sjogren, J. G. Williams and C. F. Yoder, Geophysical Parameters of the earth-moon system, *J. Geophys. Res., 85*, 3939- 3951, 1980.
39. French, F. G., J. L. Elliot, L. M. French, K. J. Meech, M. E. Ressler, M. W. Buie, J. A. Frogel, J. B. Holberg, J. J. Fuensalida and M. Joy, Uranian ring orbits from Earth-based and Voyager occultation data, *Icarus, 73*, 349-378, 1988.
40. French, R. G. *et al.*, Uranian ring orbits from Earth-based and Voyager occultation observations, *Icarus, 73*, 349-378, 1988.
41. French, R. G., P. D. Nicholson, C. C. Porco and E. A. Marouf, Dynamics of the Uranian rings, in *Uranus* edited by edited by J. T. Bergsthralh, E. D. Miner and M. S. Matthews, Univ. Arizona Press, Tucson, 327-409, 1991.
42. French, R. G. *et al.*, Geometry of the Saturn system from the 3 July 1989 occultation of 28 Sgr and Voyager observations, *Icarus, 103*, 1993.
43. Gaskell, R. W., S. P. Synnott, A. S. McEwen and G. G. Schaber, Large scale topography of Io: implications for internal structure and heat transfer, *Geophys. Res. Letters, 15*, 581-584, 1988.
44. Goins, N. , A. M. Dainty and M. N. Toksoz, Lunar Seismology: the internal structure of the moon, *J. Geophys. Res., 86*, 5061-5074, 1981.
45. Guzik, J. A. and Y. Lebreton, Solar interior models, in *Solar Interior and Atmosphere*, edited by A. N. Cox, W. C. Livingston snd M. S., Matthews, Univ. of Arizona Press, Tucson, 1235-1248, 1991.
46. Harmon, J. K., J. B. Campbell, D. L. Bindschadler, J. W. Head and I. I. Shapiro, Radar altimetry of Mercury: a preliminary analysis, *J. Geophys. Res., 91*, 385-401, 1986.
47. Harper D. and D. B. Taylor, The orbits of the major satellites of Saturn, *Astron. Astrophys.*, in press, 1993.
48. Heiken, G. H., D. V. Vaniman and B. M. French *Lunar Sourcebook*, Cambridge University Press and L.P.I., Houston Tx, 1993.
49. Herring, T. A., B. A. Buffett, P. M. Mathews and I. I. Shapiro, Forced nutations of the earth: influence of inner core dynamics 3. Very long interferometry data analysis, *J. Geophys. Res., 96*, 8259-8273, 1991.
50. Hubbard, W. M. and R. Smoluchowski, Structure of Jupiter and Saturn, *Space Sci. Rev., 14*, 599-662, 1973.
51. Hubbard, W. M. , Effects of differential rotation on the gravitational figures of Jupiter and Saturn, *Icarus, 52*, 509-515, 1982.
52. Hubbard, W. B. and M. S. Marley, Optimized Jupiter, Saturn and Uranus Interior models, *Icarus, 78*, 102-118, 1989.
53. Jacobson, R. A., J. E. Riedel and A. H. Taylor, The orbits of Triton and Nereid from spacescraft observations, *Astron. Astrophys., 247*, 565-575, 1991.
54. Horn, L. J., J. Hui, A. L. Lane, R. M. Nelson and C. T. Russell, Saturn A ring surface mass densities from spiral density wave dispersion behavior, *Icarus*, in press, 1993.
55. Jacobson, R. A., J. K. Campbell, A. H. Taylor and S. P. Synnott, The masses of Uranus and its major satellites from Voyager tracking data and earth-based Uranian satellite data, *Astron. J., 103*, 2068-2078, 1992.
56. Jefferies, H., *The Earth*, Cambridge University Press, Cambridge, 574pp, 1976.
57. Kaula, W. M., *Theory of satellite geodesy*, Blaisdell, Waltham, 124pp, 1966.
58. Kaula, W. M., *An Introduction to Planetary Physics, John Wiley & Sons, New York*, 490pp, 1968.
59. Klavetter, J. G., Rotation of Hyperion. II dynamics, *Astron. J., 98*, 1855-1874, 1989.
60. Konopliv, A. S., N. J. Borderies, P. W. Chodas, E. J. Christensen, W. L. Sjogren, G. Balmino and J. P. Barriot, Venus gravity and topography: 60th degree and order field, *Geophysical Res. Lett.*, in press, 1993.
61. Konopliv, A. S., W. L. Sjogren, R. N. Wimberly, R. A. Cook and A. Vijayaraghaven, A high resolution lunar gravity field and predicted orbit behavior, *AAS/AIAA Astrodynamics Conf.*, AIAA/AAS, 93-622, Victoria BC, 1993.
62. Lambeck, K., *The earth's variable rotation*, Cambridge university press, Cambridge, 449pp, 1980.
63. Landgraf, W., The mass of Ceres, *Astron. Astrophys., 191*, 161-166, 1988.
64. Laskar, J. and P. Robutel, The chaotic obliquity of the planets, *Nature,361*, 608-612, 1993.
65. Lieske, J. H., Galilean satellite evolution: observational evidence for secular changes in mean motion, *Astron. Astrophys., 176*, 146-158, 1988.
66. Lindal, G. F., The atmosphere of Jupiter: an analysis of the radio occultation measurements, *J. Geophys. Res., 86*, 8721-8727, 1981.
67. Lindal, G. F., D. N. Sweetnam and V. R. Eshelman, The atmosphere of Saturn: an analysis of the Voyager radio occultation measurements, *Astron. J., 90*, 1136-1146, 1985.
68. Lindal, G. F., J. R. Lyons, D. N. Sweetham, V. R. Eshleman, D. P. Hinson and G. L. Tylor, The atmosphere of Uranus: results of radio occultation measurements with Voyager 2, *J. Geophys. Res., 92*, 14,987-15,001, 1987.
69. Lindal, G. F., An analysis of radio occulation data aquired with Voyager 2, *Astron. J., 103*, 967-982, 1992.
70. Livingston, W., R. F. Donnelly, V. Grioryev, M. L. Demidov, J. Lean, M. Steffan, O. R. White and R. L. Willson, Sun as a star spectrum variability, in *Solar interior and Atmosphere*, edited by A, N, Cox, W. C. Livingston and M. S. Matthews, Univ. of Arizona Press, Tucson, 1109-1160, 1991.
71. Marsh, J. G., F. J. Lerch, B. H. Putney, T. L. Felsentreger, B. V. Sanchez, S. M. Klosko, G. B. Patel,

J.W. Robbins, R. G. Williamson, T. L. Englis, W. F. Eddy, N. L. Chandler, D. S. Chinn, S. Kapoor, K. E. Rachlin, L. E. Braatz and E. C. Pavlis, The GEM-T2 gravitational model, *J. Geophys. Res., 95*, 22043-22071, 1990.

72. McFadden, L. A. , D. J. Tholen and G. J. Vedder, Physical properties of Aten, Apollo and Amor Asteroids, in *Asteroids II*, edited by R. P. Binzel, T. Gehrels and M. S. Matthews, Univ. of Arizona Press, Tucson, 1258pp, 1992.
73. McNamee, J.B., N. J. Borderies, W. L. Sjogren, Global Gravity and Topography, *J. Geophys. Res., Planets, 98*, 9113-9128, 1993.
74. Moritz, H., Geodetic reference system 1980, in *The Geodesist's Handbook: 1984*, edited by C. C. Tscherning, 58, 1984.
75. Morrison, L. V. and C. G. Ward, *Mon. Not. Roy. astr. Soc., 173*, 183, 1975.
76. Nakamura, Y., G. V. Latham and H. J. Dorman, Apollo lunar seismic experiment - final summary, *J. Geophys. Res., 87*, a117-a123, 1981.
77. Nakamura, Y., Seismic velocity structure of the lunar mantle, *J. Geophys. Res., 88*, 677-686, 1983.
78. Ness, F.N., M. H. Acuna, L. F. Burlaga, J. E. P. Connerney, and F. M. Lepping, Magnetic Fields at Neptune, *Science, 246*, 1473-1477, 1989.
79. Nicholson, P.D. and C.L. Porco, A new constraint on Saturn's zonal gravity harmonics from Voyager observations of an eccentric ringlet, *J. Geophys Res., 93*, 10209-10224, 1988.
80. Nicholson, P. D. and L. Dones, Planetary Rings, *Rev. of Geophysics*, 313-327, 1991.
81. Nicholson, P. D., D. P. Hamilton, K. A. Matthews and C. F. Yoder, New observations of Saturn's coorbital satellites, *Icarus, 100*, 464-484, 1993.
82. Null, G. W., E. L. Lau, E. D. Biller and J. D. Anderson, Saturn Gravity results obtained from Pioneer 11 tracking data and Earth-based Saturn satellite data, *Astron. J., 86*, 456-468, 1981.
83. Null, G. W., W. M. Owen Jr., S. P. Synnott, Masses and densities of Pluto and Charon, *Astron. J., 105*, 2319, 1993.
84. Owen, W. M. Jr. and S. P. Synnott, Orbits of the ten small satellites of Uranus, *Astron. J., 93*, 1268-1271, 1987.
85. Owen, W. M. Jr., A theory of the earth's precession relative to the invariable plane, PhD Thesis, University of Florida, 1990.
86. Owen, W. M. Jr., R. M. Vaughan and S. J. Synnott, Orbits of the six new satellites of Neptune, *Astron. J., 101*, 1511-1515, 1991.
87. Peale, S. J., Generalized Cassini Laws, *Astron. J., 74*, 483-489, 1969.
88. Plummer, H. C., *An Introductory Treatise on Dynamical Astronomy*, Dover, New York, 343pp. 1960.
89. Podolak, M. B., W. M. Hubbard and D. J. Stevenson, Models of Uranus' interior and magnetic field, in *Uranus*, edited by J. T. Bergsthralh, E. D. Miner and M. S. Matthews, Univ. Arizona Press, Tucson, 29-61, 1991.
90. Rapp, R. H. , Current estimates of the mean earth ellipsoid parameters, *Geophys. Res. Lett., 1*, 35-38, 1974.
91. Rosen, P. A., G. L. Tyler, E. F. Marouf and J. J. Lissauer, Resonance structures in Saturn's rings probed by radio occultation, *Icarus, 32*, 25-44, 1991.
92. Russell, C. T., P. J. Coleman Jr. and B. E. Goldstein, Measurements of the lunar induced magnetic moment in the geomagnetic tail: evidence for a lunar core, *Proc. Lunar Planet. Sci., 12B*, 831-836, 1981.
93. Scholl, H., L. D. Schmadel and S. Roser, The mass of the asteroid(10) Hygeia derived from observations of (829) Academia, *Astron. Astrophys., 179*, 311-316, 1987.
94. Schubart, J., The mass of Pallas, *Astron. Astrophys., 39*, 147-148, 1975.
95. Seidelmann, P. K. (editor), *Explanatory supplement to the astronomical almanac*, University Science Books, Mill Valley, 752pp, 1992.
96. Sellers, P. C., Seismic Evidence for a low-velocity lunar core , *J. Geophys. Res., 97*, 11663-11672, 1992.
97. Sinclair, R. A., The orbits of the satellites of Mars from spacecraft and ground-based observations, *Astron. Astrophys., 220*, 321-328, 1989.
98. Smart, W. M., *Celestial Mechanics*, John Wiley, New York, 381pp, 1961.
99. Smoot, G. F. plus 27 authors, Structure in the COBE differential microwave Radiometer first year maps, *Astrophys. J., 396*, L1-L6, 1992.
100. Souchay, J. and H. Kinoshita, Comparison of new nutation series with numerical integration, *Cel. Mech. , 52*, 45-55, 1991.
101. Stacey, F.D., *Physics of the Earth*, John Wiley, New York, 414pp, 1977.
102. Standish, E. M. jr. and R. W. Hellings, A determination of the masses of Ceres, Pallas and Vesta from their perturbations upon the orbit of Mars, *Icarus, 80*, 326-333, 1989.
103. Standish, E. M., The observational basis for JPL's DE 200, the planetary ephemerides of the Astronomical Almanac, *Astron. Astrophys., 233*, 252-271, 1990.
104. Synnott, S. P., R. J. Terrile, R. A. Jacobson and B. A. Smith, Orbits of Saturn's F-Ring and its shepherding satellites, *Icarus, 53*, 156-258, 1983.
105. Synnott, S. P., Orbits of the small satellites of Jupiter, *Icarus, 58*, 178-181, 1984.
106. Thomas, P. C., C. Weitz and J. Veverka, Small satellites of Uranus: Disk-integrated photometry and estimated radii, *Icarus, 81*, 92-101, 1989.
107. Thomas, P. C., The shape of small satellites, *Icarus, 77*, 248-274,1989.
108. Thomas, P. C. and S. F. Dermott, The Shape of Tethys, *Icarus, 94*, 391-398, 1991.
109. Torge, W., *Geodesy*, Walter de Gruyter, New York, 254pp, 1980.
110. Turcotte, D. L. and G. Schubart, *Geodynamics*, John Wiley & Sons, New York, 450pp, 1982.
111. Tyler, G. L. and 17 authors, Radio Science observations of Neptune and Triton, *Science, 246*, 1466-1473, 1989.
112. Ward, W. R. and D. Jurdy, Resonant Obliquity of Mars?, *Icarus, 94*, 160-164, 1991.

113. Williams, J. G., W. S. Sinclair and C. F. Yoder, *Geophys. Res. Lett.*, 5, 943-946, 1978.
114. Williams, J. G., X X Newhall and J. O. Dickey, Lunar gravitational harmonics and the reflector coordinates, in *Proc. Int. Symp. Figure and Dynamics of the Earth, Moon and Planets, Prague, 1986*, Hotola, P. ed., 643-648 , 1987.
115. Williams, J. G. , X. X. Newhall and J. O. Dickey, Diurnal and semidiurnal contributions to lunar secular acceleration, *EOS, 73*, 126, 1992.
116. Williams, J. G., Contributions to the earth's obliquity rate, precession and nutation, *Astron. J., 108,* 711-724, 1994.
117. Yeomans, D. and R. N. Wimberly, Cometary apparitions: 1990-2011, in *Comets in the Post-Halley Era: Vol. II*, edited by R. L. Newburn, M. Neugebauer and J. Rahe, 1281-1308, 1991.
118. Yoder, C. F. and W. R. Ward, Does Venus wobble?, *Ap. J. Letters, 233,* L33-L37, 1979.
119. Yoder, C. F.,The free librations of a dissipative moon, *Philos. Trans. R. Soc. London Ser. A, 303*, 327-338, 1981.
120. Yoder, C. F., The tidal rigidity of Phobos, *Icarus, 49*, 327-345, 1982.
121. Yoder, C. F., S. P. Synnott and H. Salo, Orbits and masses of Saturn's coorbiting satellites, Janus and Epimetheus, *Astron. J., 98*, 1875-1889, 1989.
122. Young, L. A. , C. B. Olkin, J. L. Elliot, D. J. Tholen and M. W. Buie, The Charon-Pluto mass ratio from MKO astrometry, *Icarus, 108*, 186-199, 1994.
123. Young, L. A. and R. P. Binzel, A new determination of radii and limb parameters for Pluto and Charon from mutual event data, *Icarus, 108*, 219-224, 1994.
124. Zharkov, V. N. and V. P. Trubitsyn, *Physics of Planetary interiors*, Pachart Publishing, Tucson, 388pp, 1978.

Earth Tides

John Wahr

1. INTRODUCTION

The sun and moon exert gravitational forces on the earth, which cause the earth to orbit the earth-moon-sun center-of-mass. The gravitational acceleration (the force per unit mass) is not the same at every point in the earth, because different points are at different distances from the moon (or sun) and the gravitational force varies with distance. For example, Figure 1*a* shows the gravitational acceleration vectors due to the moon, at different points in the earth. The vectors are of unequal length and direction (the differences are greatly exaggerated in the figure).

This has two effects. One is to cause a gravitational torque on the earth tending to tip the earth's rotation axis. This tipping motion is the earth's precession and nutation. The other is to cause the solid earth (and oceans) to deform. This deformation is the earth (and ocean) tide [10].

Tidal deformation of the solid earth is modeled in two steps. First, the variability, in both time and space, of the luni-solar gravitational acceleration must be specified. A scalar quantity called the tidal potential is introduced to represent this variable acceleration. Finding the tidal potential requires detailed knowledge of the orbital motions of both the earth and moon. Second, the earth's response to the tidal potential must be modeled. This is a geophysical problem, and the results are usually represented in terms of dimensionless "Love numbers". The problem is complicated by the deformation of the earth caused by ocean tidal loading.

J. Wahr, University of Colorado, Department of Physics, Campus Box 390, Boulder, CO 80309

Global Earth Physics
A Handbook of Physical Constants
AGU Reference Shelf 1

2. THE TIDAL POTENTIAL

The tidal acceleration is defined as that part of the luni-solar gravitational acceleration that causes the precession, nutation, and earth tides. Its value at the point P = (r, θ, λ) (r is the radial coordinate, and θ and λ are co-latitude and eastward longitude, respectively) is defined as: [the total gravitational acceleration at P] minus [the acceleration of the earth's center-of-mass]. In this way, the tidal acceleration is defined so that it has no net effect on the earth's orbital motion. If the total gravitational acceleration were the same at every point in the earth, the tidal acceleration would vanish.

The tidal acceleration due to the moon is represented pictorially in Figure *b*. The acceleration of the earth's center-of-mass is approximately equal to the total gravitational acceleration at the center of the earth. Thus, to obtain Figure *b*, the acceleration vector at the center of the earth in Figure 1*a* has been subtracted from all the other vectors in Figure 1*a*. Note that the tidal acceleration vectors are directed radially outward on the sides nearest and furthest from the moon, and are directed radially inward elsewhere.

The tidal acceleration from the sun and moon is written as the gradient of a scalar function, V_T, called the tidal potential (V_T is the negative of the potential energy per unit mass). The tidal potential can be expanded as a sum of complex spherical harmonics, Y_n^m, in the form

$$V_T(r,\theta,\lambda,t) = Real\left[\sum_{n=2}^{\infty}\sum_{m=0}^{n} c_n^m(t) Y_n^m(\theta,\lambda)\left[\frac{r}{a}\right]^n\right] \qquad (1)$$

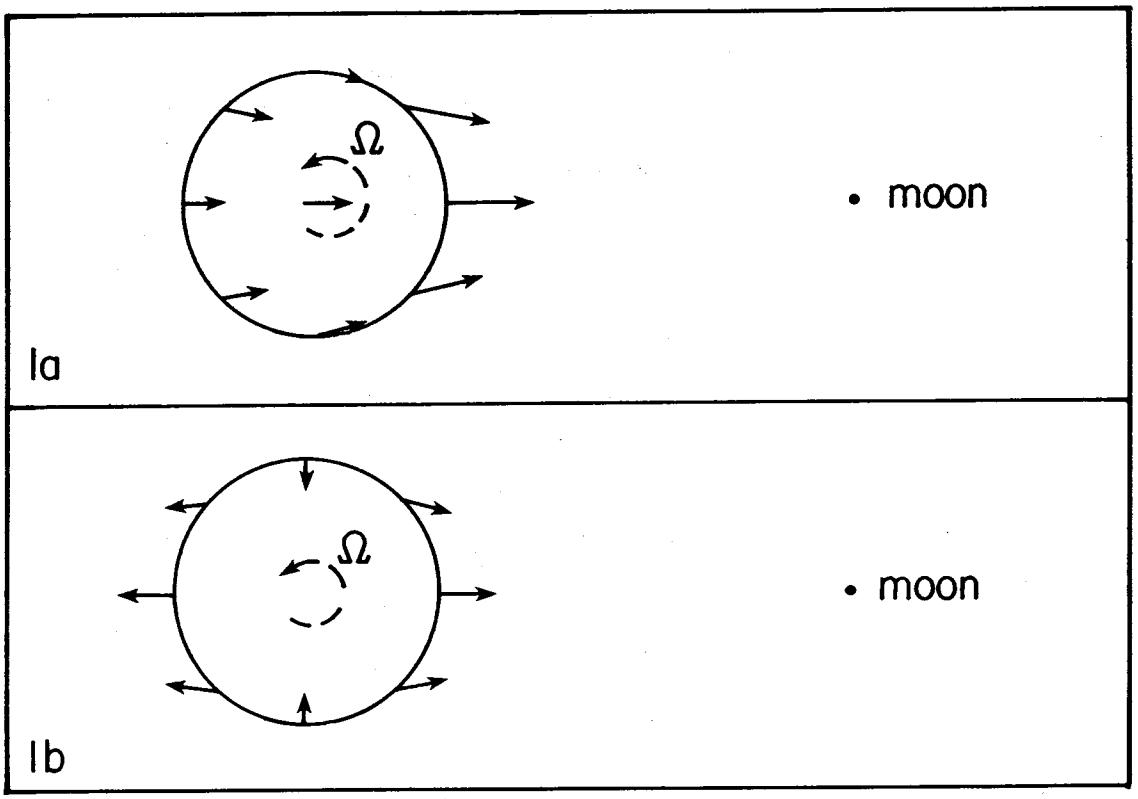

Fig. 1. Both panels show the earth as seen from above the North Pole. The earth's diurnal rotation is represented by Ω. The arrows in (*a*) illustrate the magnitude and direction of the gravitational acceleration toward the moon. The differences in length and direction are greatly exaggerated. The tidal acceleration, shown in (*b*), is obtained by subtracting the acceleration vector at the center of the earth from the other acceleration vectors. The tidal acceleration causes the earth to deform, and the deformation is the earth tide. Because the earth rotates with respect to these arrows (which are fixed relative to the moon), the tide at a fixed point on the earth varies both diurnally and semi-diurnally.

where a is the earth's radius and the $\{c_n^m(t)\}$ are complex, time-dependent coefficients. Note that the sum over n in (1) begins at $n=2$. In fact, V_T is the total gravitational potential per unit mass from the sun and moon, but without the $n=1$ spherical harmonic terms. The $n=1$ terms cause the earth's orbital motion. The $\{c_n^m(t)\}$ decrease quickly with n. For example, $c_n^m(t) \simeq (1/60)^n$ for the moon, and decreases with n even more quickly for the sun. For most applications only the $n=2$ terms are needed in (1), although occasionally $n=3$ terms are also used.

The time dependence of the $\{c_n^m(t)\}$ is determined by the earth's rotation rate, Ω, and by the orbital motions of the moon and earth. The dependence on the earth's rotation rate can be understood from Figure *b*. The pattern of arrows in that figure is fixed relative to the moon. Because the earth rotates within that pattern, the tidal acceleration at a given point on the earth's surface varies with time. That time dependence could be primarily diurnal, semi-diurnal, or infinite-period, depending on the declination of the moon above or below the equator. Since the moon's declination is continually changing as the moon orbits the earth, the time dependence of the $\{c_n^m(t)\}$ is a complicated combination of diurnal, semi-diurnal, and longer-period terms.

When computing V_T, there are two general methods for finding the $\{c_n^m(t)\}$. One is to use numerical ephemerides of the lunar and terrestrial orbital motion. The dependence of the $\{c_n^m(t)\}$ on the geocentric positions of the sun and moon is given, for example, in [1].

Alternatively, people have used ephemerides to find the $\{c_n^m(t)\}$, and have expanded the results as sums of frequency-dependent terms. For example, each $\{c_n^m(t)\}$ can be approximated as

TABLE 1. Selected Tidal Constituents

	Tidal Constituent	Period (solar hrs/dys/yrs)	amplitude (H_p/g in cm)	phase in degrees (ϕ_p relative to May 22.5, 1960)
long period (Y_2^0)	(lunar nodal tide)	18.613 years	2.79	188.82048
	S_a	365.26 days	0.49	137.86005
	S_{sa}	182.621 days	3.10	120.23846
	M_m	27.555 days	3.52	110.65598
	M_f	13.661 days	6.66	44.44202
diurnal (Y_2^1)	O_1	25.819 hours	26.22	105.67722
	P_1	24.066 hours	12.20	29.88078
	S_1	24 hours	0.29	12.25919
	K_1	23.934 hours	36.88	150.11923
	ψ_1	23.869 hours	0.29	287.97928
	ϕ_1	23.804 hours	0.52	270.35770
semi-diurnal (Y_2^2)	N_2	12.658 hours	12.10	325.14050
	M_2	12.421 hours	63.19	75.79645
	S_2	12 hours	29.40	0.00
	K_2	11.967 hours	8.00	120.23846

$$c_n^m(t) = \sum_p H_p e^{i(\omega_p t + \phi_p)} \qquad (2)$$

where ω_p and ϕ_p are the frequency and phase of the p'th frequency component, and H_p is the amplitude. It turns out that each ω_p is equal to $m\Omega$ modulated by one or more orbital frequencies of the moon or earth. Since the orbital frequencies are much smaller than Ω, $\omega_p \approx m\Omega$. In the usual case when only the $n=2$ terms are included in (1), m can take on the values $m = 0$, 1, or 2. The $m=2$ terms have frequencies $\approx 2\Omega$ and so are semi-diurnal tides. The $m=1$ terms have frequencies $\approx \Omega$ and so are diurnal tides. The $m=0$ terms are independent of the earth's rotation and so are determined entirely by the orbital motion of the moon and earth. These terms are the long-period tides.

The number of terms kept in (2) depends on the accuracy required. Tables of values for ω_p, ϕ_p, and H_p can be found in [2], [3], [14], and [18]. The tables of [14] and [18] are the most accurate and complete, and are in good agreement. Several thousand terms are included in these tables. Most of the terms have small amplitudes (H_p), and for many applications only a few of them are required. For example, many terms are close to one another in frequency. When fitting tidal amplitudes to a short data span, it is common to approximate each group of closely-spaced terms with a single large-amplitude term in the middle of that group.

Some of the more important tidal terms, with their periods, amplitudes, and phases relative to May 22.5, 1960 (Greenwich time), are shown in Table 1. The tides with the largest amplitudes are assigned standard alphanumeric representations, and those are also shown in Table 1. The amplitudes and phases are taken from [3]. The amplitudes (presented here as the absolute value of H_p/g in cm, where g is the gravitational acceleration at the earth's equator) correspond to spherical harmonics in (1) normalized according to:

$$Y_n^m(\theta,\lambda) = (-1)^m \left[\frac{2n+1}{4\pi}\frac{(n-m)!}{(n+m)!}\right]^{1/2} P_n^m(\cos\theta)\, e^{im\lambda}$$

where

$$P_n^m(\mu) = \frac{(1-\mu^2)^{m/2}}{2^n n!}\frac{d^{m+n}}{d\mu^{m+n}}(\mu^2-1)^n$$

Note that (1) involves taking

$$Real\left[e^{im\lambda}e^{i(\omega_p t+\phi_p)}\right] = \cos\left[m\lambda+\omega_p t+\phi_p\right].$$

The amplitudes shown in Table 1 give an indication of the importance of some of the major tidal lines. But, these amplitudes (and phases) should be used with caution. Each

of the lines shown here has side-bands that are not included in the table, and that may differ in frequency from the central line by as little as 1 cycle per 18.6 years. For some of the tidal lines included in Table 1, the sidebands have amplitudes of up to 10-20% (or more) of those shown. Thus, for a short span of data where it is impossible to separate the central line from its side-bands, the apparent amplitude and phase of that central line could differ by 10-20% (or more) from the values shown in Table 1. This problem is best resolved by using many more terms in the expansion, such as those included in the tables referred to above. Alternatively, if the objective is simply to remove the effects of tides from a geophysical record in order to study the residuals, it may be reasonable to include only the major tidal lines, but to fit an amplitude and phase to the data for each line, rather than to use the tabulated values.

3. THE EARTH'S TIDAL RESPONSE

The tidal potential (1) induces deformation in the solid earth and oceans. Solid earth effects can be observed using a variety of techniques. A gravimeter is sensitive to the vertical tidal displacement of the surface on which it sits and to the changes in gravity caused by tidal deformation inside the earth. Typical tidal perturbations of gravity are on the order of 100 μgals or more. A tiltmeter, which measures the angle between the gravitational acceleration vector and the geometric normal to the earth's surface, is affected by tidal tilting of the surface and by tidal changes in gravity. Tidal tilt amplitudes may be a few tenths of a μradian. A strainmeter measures the change in length between two points, and tidal changes in baseline length are roughly 10^{-7} times the unperturbed length. Tidal perturbations in the earth's gravitational potential can be determined from the orbits of artificial satellites. And, tidal displacements of the earth's surface, typically a few tens of centimeters, can be observed directly using space geodetic positioning techniques such as VLBI, GPS, and satellite laser ranging.

Solid earth deformation is conveniently described with three dimensionless "Love numbers", h_n, k_n, and l_n, defined as follows. Tidal deformation is small enough that its relation to the tidal forcing is essentially linear. Thus, the response to the tidal potential, V_T, is given by the sum of the responses to each individual term in the sum (1). Consider a term

$$V(r,\theta,\lambda,t) = H_p e^{i(\omega_p t+\phi_p)} Y_n^m(\theta,\lambda)(r/a)^n \qquad (3)$$

in the tidal potential (combine (2) with (1)). Because of the linearity of the earth's response, this term causes deformation which has the same $e^{i\omega_p t}$ time dependence. Furthermore, for a spherical, non-rotating earth, the induced deformation has an angular dependence which is described with the same spherical harmonic, Y_n^m, as is the forcing term (3). For example, let $s_r(\theta,\lambda,t)$, $s_\theta(\theta,\lambda,t)$, and $s_\lambda(\theta,\lambda,t)$, be the radial, southward, and eastward particle displacements at the surface of the earth ($r=a$), at the angular position (θ, λ) and at time t. Then, for a spherical, non-rotating earth, s_r, s_θ, and s_λ induced by (3) have the form:

$$s_r(\theta,\lambda,t) = \frac{h_n}{g} V(r=a,\theta,\lambda,t)$$

$$s_\theta(\theta,\lambda,t) = \frac{l_n}{g} \partial_\theta V(r=a,\theta,\lambda,t)$$

$$s_\lambda(\theta,\lambda,t) = \frac{l_n}{g\sin\theta} \partial_\lambda V(r=a,\theta,\lambda,t) \qquad (4)$$

Here, h_n and l_n are dimensionless scalars, called Love numbers, representing the response of the earth to unit forcing. The values of h_2 and l_2 are often written as simply h and l, since $n=2$ is by far the most important case. Note that

$$V(r=a,\theta,\lambda,t) = H_p e^{i(\omega_p t+\phi_p)} Y_n^m(\theta,\lambda)$$

Similarly, let $\Phi(\theta,\lambda,t)$ be the perturbation in the earth's gravitational potential at the outer surface caused by the tidally-deformed density distribution inside the earth. Then

$$\Phi(\theta,\lambda,t) = k_n V(r=a,\theta,\lambda,t) \qquad (5)$$

where k_n is another dimensionless Love number (again, k_2 is often abbreviated as k).

Values of the Love numbers h_n, l_n, and k_n depend on the angular order n. For a spherical, non-rotating, and elastic earth they are exactly independent of m, and, for all practical purposes, also independent of forcing frequency, ω_p. For a more realistic earth, there is some dependence on both m and ω_p, as described in the next section.

Tidal effects on surface gravity are proportional to a linear combination of the Love numbers. For example, the $n=2$ tidal gravity signal measured by a gravimeter on the earth's surface ($r=a$) is (for a spherical, non-rotating earth)

$$\Delta g = \delta \frac{2}{a} V(r=a,\theta,\lambda,t) \qquad (6)$$

where V is given by (3) and δ is the $n=2$ tidal "gravimetric

factor":

$$\delta = 1-\frac{3}{2}k+h \tag{7}$$

Equation (6) includes the effects of the direct gravitational attraction of the sun and moon (represented by the "1" in (7)), of the tidal perturbation in the earth's gravitational attraction (represented by the k term in (7)), and of the radial displacement of the gravimeter (represented by the h term in (7)). Similarly, southward tilt (Δ_S) and eastward tilt (Δ_E) of the gravity vector relative to the earth's outer surface are given by (for example, if $\Delta_S > 0$, the outward surface normal is displaced southward relative to the outward gravity normal):

$$\Delta_S = \frac{\eta}{ag}\,\partial_\theta V(r=a,\theta,\lambda,t)$$

$$\Delta_E = \frac{\eta}{ag\sin\theta}\,\partial_\lambda V(r=a,\theta,\lambda,t) \tag{8}$$

where η is the "tilt factor":

$$\eta = 1+k-h$$

For strain, let θ_s be the angle of the baseline as measured clockwise from north. Tidal strain is defined as $\delta L/L_0$, where δL is the total change in baseline length and L_0 is the unperturbed length. Then

$$\delta L/L_0 = \varepsilon_{NS}\cos^2\theta_s - \varepsilon_{NE}\cos\theta_s\sin\theta_s + \varepsilon_{EW}\sin^2\theta_s \tag{9}$$

where

$$\varepsilon_{NS} = \frac{1}{ag}\left[hV(r=a,\theta,\lambda,t) + l\,\partial_\theta^2 V(r=a,\theta,\lambda,t)\right]$$

$$\varepsilon_{EW} = \frac{1}{ga}\left[hV(r=a,\theta,\lambda,t) + l\left[\frac{\partial_\lambda^2}{\sin^2\theta}+\cot\theta\,\partial_\theta\right]V(r=a,\theta,\lambda,t)\right]$$

$$\varepsilon_{NE} = \frac{2l}{ag\sin\theta}\left[\partial_\theta-\cot\theta\right]\partial_\lambda V(r=a,\theta,\lambda,t) \tag{10}$$

As an example of how these results, (4)-(10), might be used to model the effects of tides on observations, consider gravity as measured by a gravimeter on the earth's surface. First, (1) is used to find the tidal potential V_T at the location of the gravimeter. Suppose the $\{c_n^m(t)\}$ in (1) are found using the expansion (2), together with tabulated values of H_p, ω_p, and ϕ_p. In that case, V_T reduces to a sum of terms of the form (3). To find the total tidal effect on gravity, each of those terms is evaluated at $r=a$, multiplied by $\delta\frac{2}{a}$ (see (6)), and the results are added together. Thus, assuming only $n=2$ terms are kept in (1), the total tidal contribution to gravity would be

$$\Delta g = Real\left[\sum_{m=0}^{2}\sum_{p}\delta\frac{2}{a}H_p e^{i(\omega_p t+\phi_p)}Y_2^m(\theta,\lambda)\right] \tag{11}$$

If the Love numbers are indeed independent of frequency and azimuthal number m, then the numerical value of $\delta\frac{2}{a}$ is the same for every term in the sum (11), and (11) reduces to

$$\Delta g = Real\left[\delta\frac{2}{a}V_T(r=a,\theta,\lambda,t)\right] \tag{12}$$

where V_T is the total ($n=2$) tidal potential. Thus, it is not necessary to expand V_T into the frequency domain, and the $\{c_n^m(t)\}$ could instead be found directly from the orbital ephemerides, if available.

For the real earth, the effective Love numbers are not completely independent of frequency or m. Thus, (11) does not reduce exactly to (12). In fact, for a realistic earth, the tidal response cannot even be fully represented using Love numbers. Instead, a single Y_n^m term in V_T causes deformation with other $Y_n^{m'}$ angular dependence, as well. These complications are due primarily to the oceans, and in most cases the oceanic effects can be included separately, as discussed below.

4. COMPLICATIONS

The earth is not spherically symmetric. Because of this, and because the earth is also rotating, its response to the tidal force is more complicated than that described above. The most important of these effects are from the oceans. Oceanic effects are most conveniently calculated by using oceanographic models to estimate ocean tide amplitudes, and then computing the deformation of the solid earth caused by those ocean tides. Ocean loading tidal effects are typically a few percent of the body tide effects for gravity, and can be as large as or larger than the body tide effects for tilt and strain observed near the coast.

Ocean loading deformation is usually computed using Green's functions, such as those tabulated by [7]. The Green's functions describe either the surface deformation or the change in gravity at a point on the earth's surface, caused by a point load an angular distance Θ away. Tabu-

lated values of the Green's functions, such as those presented by [7], are numerical values given at different Θ's. Those values can be convolved with results from ocean tide models to estimate the earth's deformation. Perhaps the most useful ocean tide models at present are those of [13], which are partly based on global tide gauge records. Ocean tide models should begin to improve even further as more high-accuracy satellite altimeter data become available from over the world's oceans.

Lateral inhomogeneities inside the earth can also be important. One effect of these inhomogeneities is that the diurnal tidal response exhibits a resonance due to the presence of the fluid outer core: the diurnal Love numbers are frequency dependent. The exact frequency of the resonance depends on the shape of the core, particularly on the ellipticity of the core/mantle boundary, and diurnal tidal observations have been been used to constrain that ellipticity [9; 11; 12; 5].

Theoretical numerical values for the $n=2$ Love numbers are given in Table 2 for a rotating, elliptical, elastic, and oceanless earth. These values are determined by solving a set of differential equations describing the dynamical behavior of the earth, and more complete results can be found in [15]. Numerical values for δ and η are also given. The resonant effects of the fluid core are evident in the diurnal Love numbers presented in Table 2. As the table also implies, there is no significant variation with frequency within the semi-diurnal band or within the long period band, although the semi-diurnal and long period Love numbers are slightly different from each other and from the diurnal Love numbers.

Another effect of the earth's non-sphericity, even without oceans, is that the effects of tides on observable quantities (surface displacement, gravity, tilt, etc.) can no longer be exactly represented using the simple Love number formalism described above. Instead, the Love numbers become, in effect, dependent on position. These position-dependent effects are important at slightly below the 1% level for an oceanless earth, and can be ignored for many applications. They are discussed more completely by [15].

Mantle anelasticity is also potentially important. It can affect the amplitudes of the Love numbers, and can introduce phase shifts into the tidal response. The phase shifts are usually represented mathematically by making the Love numbers complex. Because of dispersion associated with anelasticity, the real part of the Love numbers should increase with increasing tidal period. The exact effects of anelasticity are presently unknown (see [16] and [6]) because of uncertainties in the strength of mantle friction at tidal frequencies. It is likely, though, that anelastic effects are important at about the 1% level for semi-diurnal and diurnal tides, and may rise to a few percent for some of the longer-period ($n=2$, $m=0$) tides.

5. LOCAL AND INSTRUMENTAL EFFECTS

Tidal tilt and strain observations are sensitive to local geology and topography [e.g., [8]). Instruments in boreholes or in mines are sensitive to the shape of the cavity. These effects must usually be modeled numerically. Atmospheric effects can also pose problems. For example, there are important variations in atmospheric pressure at one cycle per solar day (the "atmospheric tide"; see [4]) and at seasonal periods that can affect all types of tidal observations (e.g., [17]).

Finally, many instruments, including relative gravimeters, are subject both to calibration errors and to long period drifts. These make it difficult to accurately determine absolute tidal amplitudes. It can also complicate the problem of removing tidal effects from the gravity record to study the residuals.

Acknowledgements. I thank Judah Levine for providing his program to compute tidal phases.

TABLE 2. Love Numbers

Tidal Constituent	k	h	l	δ	η
any long period tide	0.299	0.606	0.0840	1.155	0.689
O_1	0.298	0.603	0.0841	1.152	0.689
P_1	0.287	0.581	0.0849	1.147	0.700
S_1	0.280	0.568	0.0853	1.144	0.707
K_1	0.256	0.520	0.0868	1.132	0.730
ψ_1	0.466	0.937	0.0736	1.235	0.523
ϕ_1	0.328	0.662	0.0823	1.167	0.660
any semi-diurnal tide	0.302	0.609	0.0852	1.160	0.692

REFERENCES

1. Bartels, J., Tidal Forces. In *Earth Tides*, edited by J. C. Harrison, Van Nostrand Reinhold, pp.25-63, 1985.
2. Cartwright, D. E., and R. J. Tayler, New Computations of the Tide-generating Potential, *Geophys. J. R. Astron. Soc., 23*, 45-74, 1971.
3. Cartwright, D. E., and A. C. Edden, Corrected Tables of Tidal Harmonics, *Geophys. J.R. Astron. Soc., 33*, 253-264, 1973.
4. Chapman, S., and R. S. Lindzen, *Earth Tides*, Reidel, Dordrecht, 1970.
5. Cummins, P., and J.M. Wahr, A Study of the Earth's Free Core Nutation Using IDA Gravity Data *J. Geophys. Res.*, in press, 1992.
6. Dehant, V., Tidal parameters for an inelastic earth, *Phys. Earth and Planet. Interiors, 49*, 97-116, 1987.
7. Farrell, W. E., Deformation of the earth by surface loading, *Rev. Geophys., 10*, 761-797, 1972.
8. Harrison, J. C., Cavity and topographic effects in tile and strain measurement, *J. Geophys. Res., 81*, 319-328, 1976.
9. Levine, J., J. C. Harrison, and W. Dewhurst, Gravity tide measurements with a feedback gravity meter. *J. Geophys. Res., 91*, 12,835-12,841, 1986.
10. Melchior, P., *The Tides of the Planet Earth*, Pergamon Press, Oxford, 1983.
11. Neuberg, J., J. Hinderer, and W. Zurn, Stacking gravity tide observations in central Europe for the retrieval of the complex eigenfrequency of the nearly diurnal free-wobble. *Geophys. J. R. Astron. Soc., 91*, 853-868, 1987.
12. Sato, T., Fluid core resonances measured by quartz tube extensometers at the Esashi Earth Tides Station, *Proc. 11th Int. Sympos. on Earth Tides, Helsinki*, ed. J. Kakkuri, pp. 573-582, Schweizerbart'sche Verlangsbuchhandlung, Stuttgart, 1991.
13. Schwiderski, E. W., On charting global ocean tides, *Rev. Geophys. and Space Phys., 18*, 243-268, 1980.
14. Tamura, Y., A harmonic development of the tide-generating potential, *Marées Terrestres Bulletin d'Informations*, 99, 6813-6855, 1987.
15. Wahr, J. M., A normal mode expansion for the forced response of a rotating Earth, *Geophys. J. R. Astron. Soc., 64*, 651-676, 1981.
16. Wahr, J. M. and Z. Bergen, The effects of mantle anelasticity on nutations, earth tides, and tidal variations in rotation rate. *Geophys. J. Roy. Astron. Soc., 87*, 633-668, 1986.
17. Warburton, R. J., and J. M. Goodkind, Detailed gravity tide spectrum between one and four cycles per day, *Geophys. J. R. Astron. Soc.*, 52, 117-136,1978.
18. Xi Qin-Wen, A New Complete Development of the Tidal Generating Potential for the Epoch J 2000.0', *Marées Terrestres Bulletin d'Informations, 99*, 6786-6812, 1987.

Geoid, Topography and Distribution of Landforms

Anny Cazenave

1. GRAVITATION POTENTIAL

1.1. Spherical Harmonic Expansion of the Earth Gravitational Potential. Stokes Coefficients

The gravitational potential at point P outside the Earth due to the heterogeneous mass distribution inside the Earth volume is

$$U = G\int_M \frac{dM}{a} \tag{1}$$

where G is gravitational constant, M is Earth's mass and a is distance between a mass element dM and point P. The potential U is conveniently expressed through a spherical harmonic expansion in a terrestrial reference frame [1,2]

$$U = \frac{GM}{r} \sum_{n=0}^{\infty} \sum_{m=0}^{n} \left(\frac{R}{r}\right)^n$$

$$x \ (C_{nm}\cos m\lambda + S_{nm} \sin m\lambda \ ) P_{nm}(\sin \varphi) \tag{2}$$

where R is equatorial radius, r, φ, λ are spherical coordinates of point P. P_{nm} (sin φ) is Legendre polynomial of degree n and order m. C_{nm} and S_{nm} refer to the Stokes' coefficients which represent integral functions of the mass distribution inside the Earth [1, 2]

$$\left.\begin{matrix} C_{nm} \\ S_{nm} \end{matrix}\right\} = \frac{1}{MR^n}(2 - \delta_{on})\frac{(n-m)\ !}{(n+m)\ !}$$

$$x \int_M r'^n P_{nm}(\sin \varphi') \left\{\begin{matrix} \cos m\lambda' \\ \sin m\lambda' \end{matrix}\right\} dM \tag{3}$$

With definition (3), $C_{00} = 1$ and $S_{00} = 0$.
It is classical to choose the coordinate system located at the Earth center of mass, hence $C_{10}, C_{11}, S_{11} = 0$.

The second degree Stokes' coefficients are related to the moments and products of inertia I_{ij} with respect to the axes of the reference system

$$C_{20} = \frac{-1}{MR^2}\left[I_{33} - \frac{1}{2}(I_{11} + I_{22})\right] \tag{4}$$

$$C_{21} = \frac{I_{13}}{MR^2} \qquad S_{21} = \frac{I_{23}}{MR^2} \tag{5}$$

$$C_{22} = \frac{1}{4MR^2}(I_{22} - I_{11}) \qquad S_{22} = \frac{I_{12}}{2MR^2} \tag{6}$$

The choice of the coordinate system is usually made with the assumption that the z-axis lies close to the mean axis of rotation and mean axis of maximum inertia. Since the latter two are close together, C_{21} and S_{21} are small quantities. C_{20} is the largest of all Stokes' coefficients. It is called the dynamical flattening. It is on the order of 10^{-3}. All other coefficients are on the order of 10^{-6}.

Stokes' coefficients are classicaly derived from the analysis of orbital perturbations of Earth' satellites. Sets of C_{nm}, S_{nm} coefficients are improved regularly. Table 1 gives the first C_{nm}, S_{nm} coefficients (up to degree 6) of the GEM-T3 geopotential model [3]. The coefficients are

A. Cazenave, Groupe de Recherche de Géodésie Spatiale, Centre National d'Etudes Spatiales, 18 Av E. Belin, 31400 Toulouse, France

Global Earth Physics
A Handbook of Physical Constants
AGU Reference Shelf 1

normalized, i.e., are multiplied by a normalization factor equal to

$$\frac{1}{(2n+1)^{1/2}} \quad \text{for } n = 0 \tag{7}$$

and

$$\left[\frac{(n+m)!}{2\,(2n+1)(n-m)!}\right]^{1/2} \quad \text{for } n \neq 0 \tag{8}$$

The GEM-T3 model, complete to degree and order 50, is derived from tracking data of 31 satellites and combines satellite altimeter data over oceans and surface gravimetric data. Other combined geopotential models have been derived up to degree 360 [4].

The long-wavelength geoid surface (equipotential surface of the Earth gravity field coinciding with the mean sea level) is presented in Figure 1. It is based on the C_{nm}, S_{nm} coefficients of the GEM-T3 model up to degree 50.

During the past decade, shorter wavelength geoid undulations have been mapped directly by altimetric satellites over the whole oceanic domain. Figure 2 shows the medium and short-wavelength geoid undulations mapped by the Geosat satellite. Geoid undulations are due to density heterogeneities in the mantle. At the shortest wavelengths, geoid undulations result from topography and crustal density variations.

1.2. Power Spectrum of the Geopotential

The power spectrum or degree variance of the geopotential is given by

$$P_n = \sum_{m=0}^{n} \left(C_{nm}^2 + S_{nm}^2\right) \tag{9}$$

Figure 3 shows a Log plot of the power spectrum of a recent geopotential model as well as of the Kaula's empirical rule [5] stating that the dimensionless power spectrum of the geopotential follows as

$$P_n \approx (2n+1)\,(10^{-5} n^{-2})^2 \tag{10}$$

TABLE 1. Spherical Harmonic Normalized Coefficients of the GEM-T3 Geopotential Model (units of 10^{-6})

Index		Value	
n	m	C	S
1	0		
1	1		
2	0	–484.1651	
2	1		
2	2	2.439	-1.400
3	0	0.9572	
3	1	2.0277	0.2492
3	2	0.9045	-0.6194
3	3	0.7203	1.4139
4	0	0.5395	
4	1	–0.5361	-0.4734
4	2	0.3502	0.6630
4	3	0.9909	-0.2009
4	4	–0.1888	0.3094
5	0	0.0683	
5	1	–0.0582	-0.0960
5	2	0.6527	-0.3239
5	3	–0.4523	-0.2153
5	4	–0.2956	0.0497
5	5	0.1738	-0.6689
6	0	–0.1495	
6	1	–0.0769	0.0269
6	2	0.0487	-0.3740
6	3	0.0572	0.0094
6	4	–0.0868	-0.4713
6	5	–0.2673	-0.5367
6	6	0.0096	-0.2371
GM		$0.398600436 \times 10^{15}$ m^3 s^{-2}	
Equatorial Radius		0.6378137×10^{7} m	
Flattening		1/298.257	
Light Velocity		$0.299792458 \times 10^{9}$ m s^{-1}	

2. GEOID AND GRAVITY ANOMALIES

2.1. Geoid, Geoid Height, Gravity Anomalies and Deflection of the Vertical

The geoid is defined as the equipotential surface of the gravity potential W = U + Z and coincides with the mean sea level. Z is the kinetic potential due to the rotational motion of the Earth

$$Z = \frac{1}{2}\,\omega^2 r^2 \cos^2\varphi \tag{11}$$

ω is speed of rotation, r is geocentric distance and φ is latitude.

Geoid height is measured above a reference surface, a conventional ellipsoid of revolution approximating the real figure of the Earth. The reference ellipsoid is usually

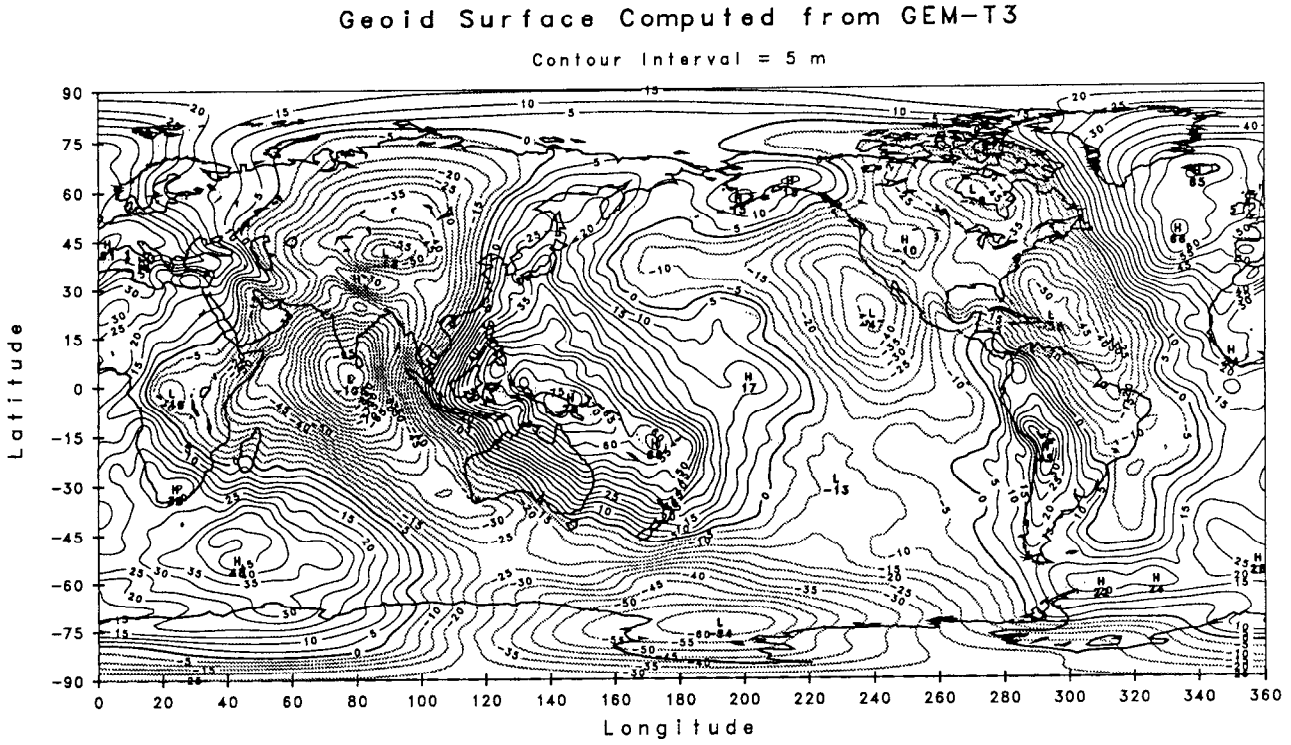

Fig. 1 : Long-wavelength geoid surface deduced from the C_{nm}, S_{nm} (up to n = 50) coefficients of the geopotential (GEM-T3 model, [3]). The C_{nm}, S_{nm} coefficients are derived from the analysis of orbital perturbations of a large number of geodetic satellites in different inclinations (Level curves at 5 m interval). Solid and dashed curves correspond respectively to positive and negative geoid anomalies.

defined as the equipotential surface V = constante with

$$V = \frac{GM}{r}\left[1 + \sum_{n=1}^{\infty} C_{2n0}\left(\frac{R}{r}\right)^{2n} P_{2n0}(\sin\varphi)\right] + Z \qquad (12)$$

The reference ellipsoid has same potential, same mass and center of mass, same angular velocity and same dynamical flattening as the real Earth. The geoid height measured above the reference ellipsoid (Figure 4) is related to the perturbing potential T, difference between true potential W and potential of the reference ellipsoid V (at the same point), through

$$N = \frac{T}{g} \qquad (13)$$

g is mean surface gravity
The actual gravity vector is

$$\mathbf{g} = \text{grad } W \qquad (14)$$

The gravity perturbation vector on the geoid is given by

$$\delta\mathbf{g}_p = \mathbf{g}_p - \gamma_p \qquad (15)$$

where γ = grad V is the normal gravity vector of the ellipsoid.
A more useful quantity is the gravity anomaly vector defined as

$$\Delta\mathbf{g}_p = \mathbf{g}_p - \gamma_q$$

where points p and q are on the geoid and ellipsoid respectively.
The magnitude and direction of the vector $\Delta\mathbf{g}$ are called respectively gravity anomaly and deflection of the vertical (i.e., angle between the normal to the geoid and the normal to the ellipsoid). Δg is related to the perturbing potential through

$$\Delta g = -\left(2\frac{T}{r} + \frac{\partial T}{\partial r}\right) \qquad (16)$$

The deflection of the vertical has two components (north-south ξ and east-west η). The relationships between components ξ and η of the deflection of the vertical, and

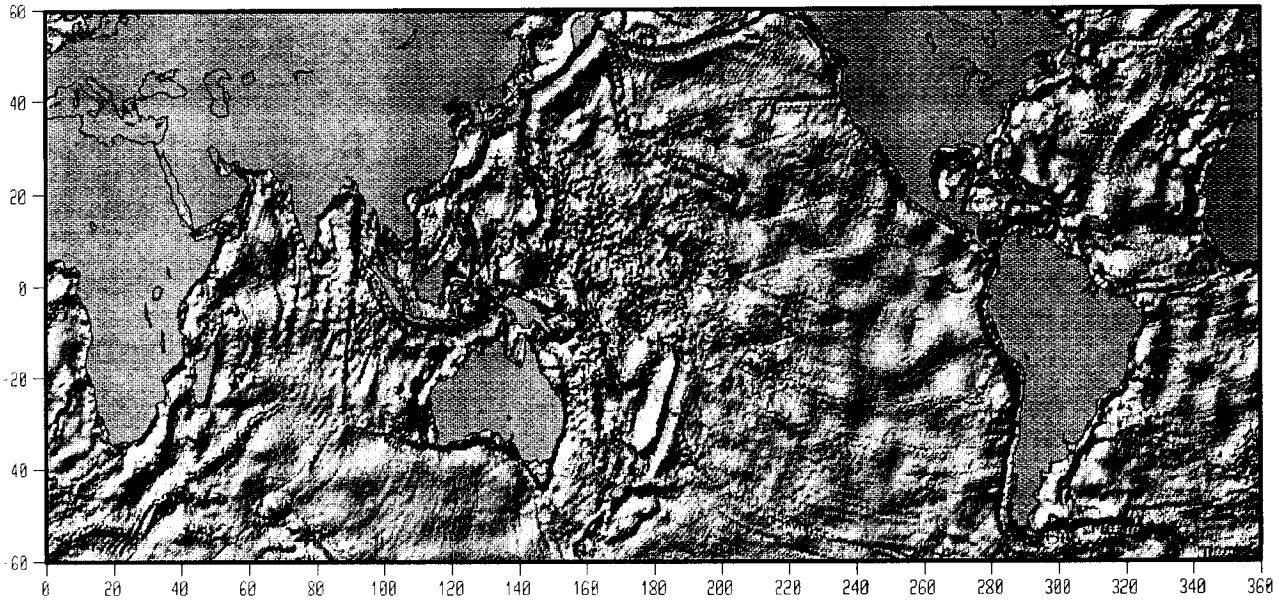

Fig. 2 : Marine geoid mapped by satellite altimetry.
Since 1975, several geodetic satellites carrying onboard altimeter instruments have performed a direct mapping of sea surface heights hence of geoid undulations. The geoid surface presented above is derived from altimetric measurements collected in 1987 and 1988 by the Geosat satellite from the US Defense Mapping Agency. Owing to the dense coverage of oceanic areas, satellite altimetry has revealed high resolution features in the geoid surface.

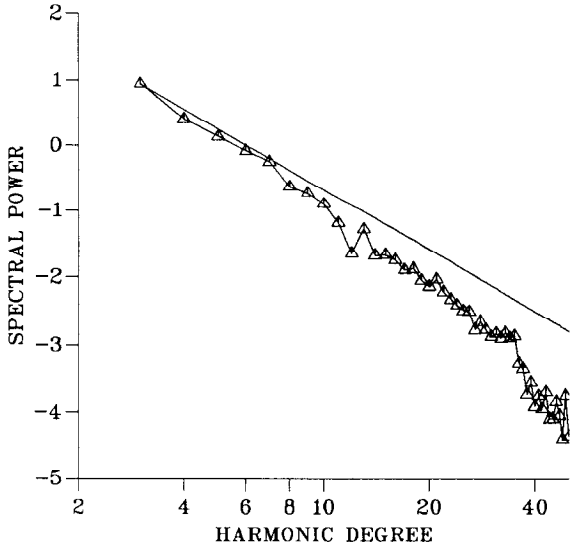

Fig. 3 : Log plot of the power spectrum of the GEM-T3 geopotential model (Δ) and of the Kaula's empirical rule (solid curve) versus harmonic degree.

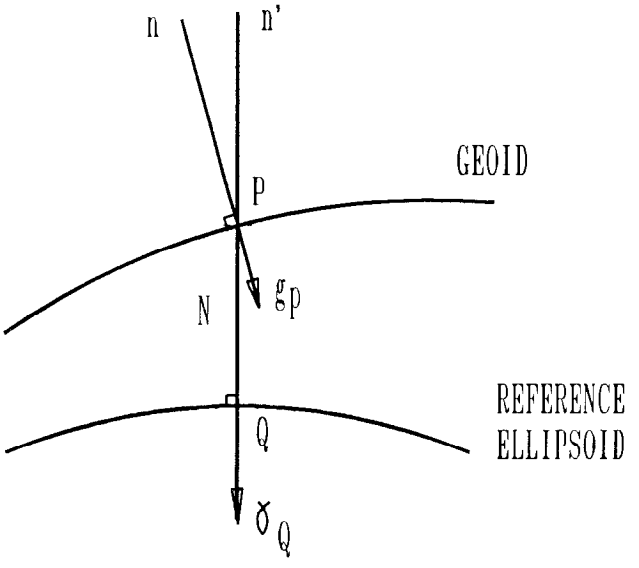

Fig. 4 : Schematic representation of the reference surfaces.

geoid height and gravity anomaly are

$$\xi = -\frac{1}{r}\frac{\partial N}{\partial \varphi} \tag{17}$$

$$\eta = -\frac{1}{r\cos\varphi}\frac{\partial N}{\partial \lambda} \tag{18}$$

$$-G\left[\frac{\partial \xi}{\partial x} + \frac{\partial \eta}{\partial y}\right] = \frac{\partial}{\partial r}\Delta g \tag{19}$$

x, y are local rectangular coordinates ($dx = Rd\varphi$, $dy = R\cos\varphi\, d\lambda$)

For geophysical purposes, it is sometimes convenient to refer geoid height with respect to the hydrostatic reference ellipsoid, i.e., the ellipsoid which has the hydrostatic flattening of a fluid rotating Earth.

Table 2 gives the numerical values of Earth geodetic parameters adopted by the International Earth Rotation Service (IERS) standards [6].

TABLE 2. Numerical Values of Earth's Geodetic Parameters According to the International Earth Rotation Service (IERS) Standards [6]

Name	Value in SI unit
Earth Mass (M)	5.973×10^{24} kg
Product of the Earth's mass by the gravitational constant (GM)	$3.986004418 \times 10^{14}$ $m^3\ s^{-2}$
Observed dynamical flattening	
Normalized value (C_{20})	-484.1651×10^{-6}
Non Normalized value (J_2)	1082.6362×10^{-6}
Equatorial radius (R_e)	6378136.3 m
Polar radius (R_p)	6356753.0 m
Angular velocity (ω)	7.292115×10^{-5} rad s^{-1}
Observed inverse flattening (f^{-1})	298.257
Hydrostatic inverse flattening (f_h^{-1})	299.638
Equatorial gravity (g_e)	9.780328 m s^{-2}
Polar gravity (g_p)	9.832186 m s^{-2}
Hydrostatic dynamical flattening ($C20_h$)	-480.2×10^{-6}
Equatorial moments of inertia (I_{11})	8.0094×10^{37} kg m^2
(I_{22})	8.0096×10^{37} kg m^2
Polar moment of inertia (I_{33})	8.0358×10^{37} kg m^2

2.2. Isostasy

The principle of isostasy states that topographic masses are balanced (or compensated) by underlying mass deficiency in such a way that at a given depth (the depth of compensation) the pressure is hydrostatic. To a good approximation, the Earth is in isostatic equilibrium. Isostatic compensation may be achieved through a variety of mechanisms. Most topographic loads of wavelengths < 50 km are supported by the strength of the lithosphere and are uncompensated. In the range 50-500 km, loads are supported by elastic flexure of the upper lithosphere. At wavelengths > 500 km, topography is in local isostatic equilibrium or dynamically supported [7, 8].

Classical models of local isostatic compensation are Airy and Pratt models (Figure 5). The Airy model assumes that the topography is balanced by a crust of constant density but variable thickness according to

$$t = \frac{\rho^* h}{(\rho_m - \rho_c)}, \tag{20}$$

with $\rho^* = \rho_c$ for topography above sea level and $\rho^* = \rho_c - \rho_w$ for topography below sea level.

t is crustal root, h is topographic height above or below sea level, ρ_w, ρ_c and ρ_m are seawater, crust and mantle densities.

In the Pratt model, the topography is compensated by lateral density variations in a layer of constant thickness above the depth of compensation. The variable density is

$$\rho = \frac{D^*}{H + h} \tag{21}$$

with $D^* = \rho_c H$ for topography above sea level and $D^* = \rho_c H + \rho_w h$ for topography below sea level. H is the compensation depth.

$\rho_w = 1.03 \times 10^3$ kg m^{-3}, $\rho_c = 2.8 \times 10^3$ kg m^{-3} and $\rho_m = 3.3 \times 10^3$ kg m^{-3},

For a two-dimensional locally compensated topography, the geoid height N is given by [7]

$$N = -\frac{2\pi G}{g}\int_0^H z\Delta\rho(x, z)\, dz \tag{22}$$

z is depth positive downward, $\Delta\rho$ (x, z) is 2-D density contrast occuring between z = 0 and z = H.

3. TOPOGRAPHY AND DISTRIBUTION OF LANDFORMS

3.1. Actual Earth Topography

The Earth topography presents a bimodal distribution with a peak near 0.5 km corresponding to the mean

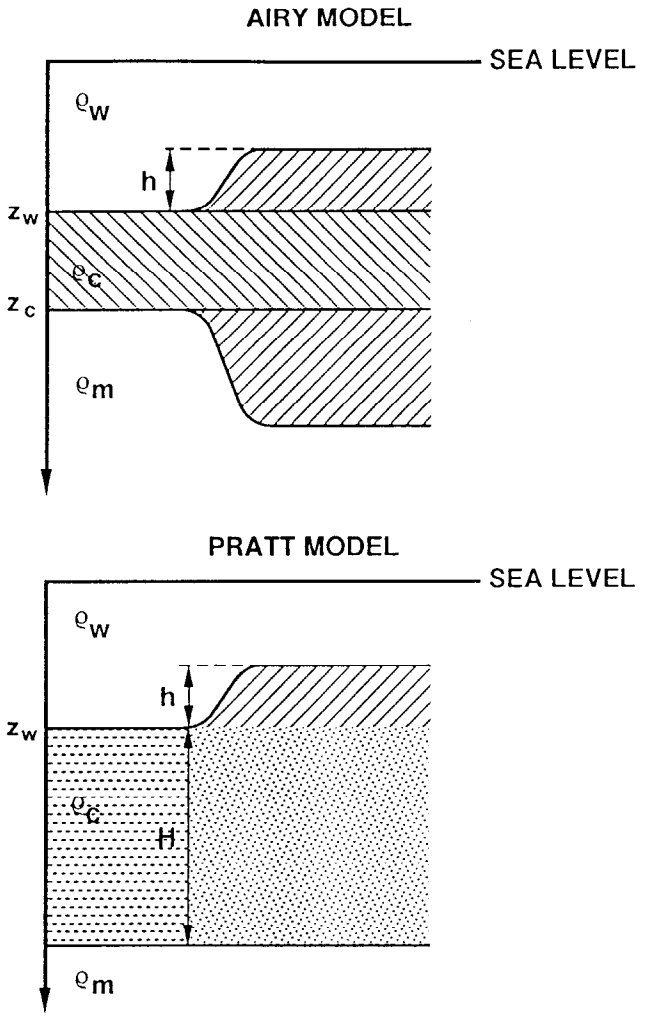

Fig. 5 : Classical models (Airy and Pratt) of local isostasy.

elevation of continental areas and a peak near 4.5 km corresponding to the mean ocean depth (Figure 6). Table 3 gives the coefficients t'_{nm}, t''_{nm} (up to degree 6) of the spherical harmonic expansion of the Earth topography T. Coefficient are defined according to

$$T(\varphi, \lambda) = \sum_{n=0}^{\infty} \sum_{m=0}^{n} (t'_{nm} \cos m\lambda + t''_{nm} \sin m\lambda) \times P_{nm}(\sin \varphi) \qquad (23)$$

The data set used to derive the t'_{nm}, t''_{nm} coefficients is the ETOPO 5 data base distributed by the National Geophysical Data Center in Boulder, Colorado. ETOPO 5 gives interpolated topography above and below sea level on a

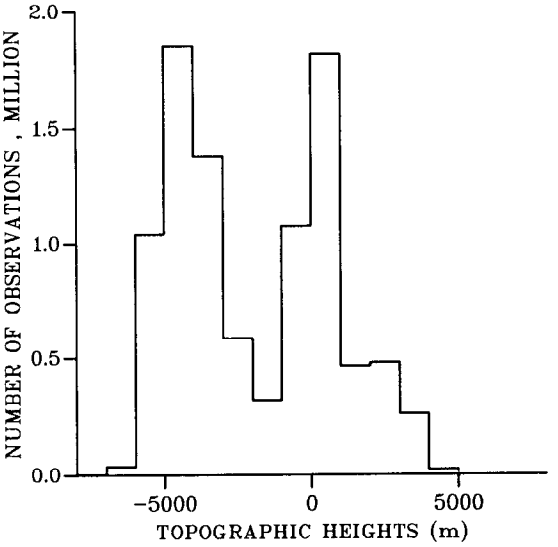

Fig. 6 : Histogram of the Earth topographic heights (above and below sea level) refered to sea level.

regular 5' x 5' grid. Other topographic data bases have also been developed (e.g., the OSUJAN89, [9]).
Figure 7 presents the power spectrum of T (defined as in relation (9)) showing a regular decrease with increasing degree. Peaks at n=1 and 3 relate to the preferential grouping of continents over a single hemispheric cap and in northern latitudes.

3.2. Oceanfloor Topography

The mean depth of ocean ridges is ≈ 2.5 km although regional variations of ± 1 km around the mean are observed. Depth of the oceanfloor increases regularly away from mid-ocean ridges as a result of thermal cooling and contraction of the oceanic lithosphere. Thermal subsidence of the seafloor is well approximated by an empirical relationship of the form [7]

$$d = d_0 + A\, t^{1/2} \qquad (24)$$

d is seafloor depth referred to sea-level and positive downward, d_0 is mean depth of mid-ocean ridges and t is crustal age.
The value of A is around 350 m/(my)$^{1/2}$ if d and d_0 are expressed in m and t in my.
Depth anomalies refer to oceanfloor topography corrected for thermal subsidence.

3.3. The Ocean-Continent Distribution

The uneven ocean-continent distribution is usually expressed through the ocean-continent function C, equal to 1 over oceanic areas and 0 over continents. It can be expressed through a spherical harmonic expansion

TABLE 3. Spherical Harmonic Normalized Coefficients of the Earth's Topography (in 10^3m)

Index		Value	
n	m	C	S
0	0	-2.3890	
1	0	0.6605	
1	1	0.6072	0.4062
2	0	0.5644	
2	1	0.3333	0.3173
2	2	0.4208	0.0839
3	0	-0.1683	
3	1	-0.1518	0.1244
3	2	0.4477	0.4589
3	3	0.1299	0.5733
4	0	0.3612	
4	1	-0.2241	-0.2563
4	2	-0.3928	0.0716
4	3	0.3761	-0.1291
4	4	-0.6387	0.4703
5	0	-0.5514	
5	1	-0.0406	-0.0770
5	2	-0.0216	-0.1577
5	3	0.1232	0.0386
5	4	0.5254	-0.0654
5	5	-0.0549	0.2276
6	0	0.2567	
6	1	0.0013	-0.0171
6	2	0.0247	-0.1323
6	3	0.0601	0.1865
6	4	0.1960	-0.1737
6	5	-0.1076	-0.2075
6	6	0.0354	0.0282

TABLE 4. Spherical Harmonic Normalized Coefficients of the Ocean-Continent Function (units of 10^{-1})

Index		Value	
n	m	C	S
0	0	–7.102	
1	0	–1.193	
1	1	–1.076	-0.5905
2	0	–0.5906	
2	1	–0.3954	-0.0061
2	2	0.3861	-0.0117
3	0	0.4747	
3	1	0.4709	-0.3871
3	2	0.6450	-0.8860
3	3	–0.1058	-0.8214
4	0	–0.2791	
4	1	0.3633	0.2661
4	2	0.8801	-0.2185
4	3	-0.4984	0.0526
4	4	0.1571	-1.0180
5	0	1.0320	
5	1	–0.0379	0.1281
5	2	0.4983	0.2619
5	3	–0.3027	-0.1275
5	4	–0.9289	0.3000
5	5	0.0058	-0.4907
6	0	–0.3264	
6	1	0.0612	0.1712
6	2	0.1454	-0.0220
6	3	0.0129	-0.2713
6	4	–0.2704	0.2420
6	5	0.1984	0.2467
6	6	–0.0623	-0.1399

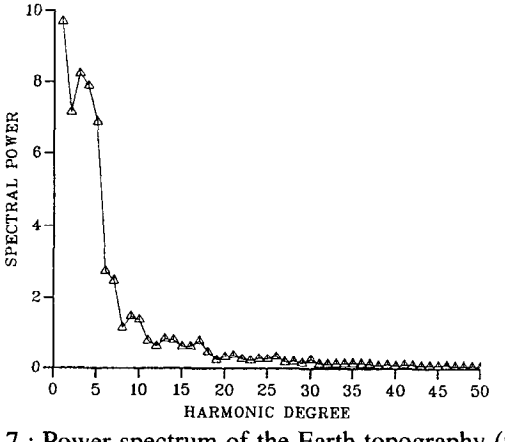

Fig. 7 : Power spectrum of the Earth topography (units : 10^5 m^2) versus harmonic degree.

$$C = \sum_{n=0}^{\infty} \sum_{m=0}^{n} \left(C_{onn} \cos m\lambda + S_{onn} \sin m\lambda\right) \times P_{nm}(\sin \varphi) \qquad (25)$$

Values of C_{onm}, S_{onm} are listed in Table 4 up to degree 6. The data set used to derive the ocean-continent function is the ETOPO 5 topography data base.

REFERENCES

1. Heiskanen, W. A., and H. Moritz, *Physical Geodesy,* W. H. Freeman Publ. Co., San Francisco, 1967.
2. Sanso, F., and R. Rummel, *Theory of satellite geodesy and gravity field determination*, Lecture Notes in Earth Sciences, Springer-Verlag, N. Y., 1989.
3. Lerch, F. J. et al., A geopotential model from satellite tracking, altimeter and surface gravity data: GEM-T3, J. Geophys. Res., 99, 2815-2839, 1994.
4. Rapp, R.H., and N.K. Pavlis, The development and analysis of geopotential coefficient models to spherical harmonic degree 360, *J. Geophys. Res.*, 95, 21885-21911, 1990.
5. Kaula, W. M., *Theory of Satellite Geodesy*, Blaisdell Publ. Co., N. Y., 1966.
6. IERS Standards, *Technical Report*, Central Bureau of IERS, Observatoire de Paris, 1992.
7. Turcotte, D. L., and G. Schubert, *Geodynamics*, John Wiley and Sons, N. Y., 1982.
8. Lambeck, K., *Geophysical Geodesy* ; The slow deformation of the Earth, Clarendon Press, Oxford, 1988.
9. Pavlis, N. K., The OSUJAN89 Global topographic data base. Origin, set-up and characteristics, *Internal Report*, Department of Geodetic Science and Surveying, Ohio State University, Columbus, Ohio, 1989.

Global Magnetic Field

Jeremy Bloxham

1.INTRODUCTION

The Earth's magnetic field changes on timescales from seconds to hundreds of millions of years. On the one hand, these changes in the field, which result from processes occuring both inside and outside the Earth, greatly complicate the process of providing reference models of the magnetic field; but on the other hand the temporal variations of the field, in particular those on periods of a few years and longer and predominantly of internal origin (the secular variation), provide us with one of the few available probes of the dynamics of the Earth's deep interior. Much of the effort that is currently invested in geomagnetic research is aimed at exploiting this potential, but this should not suggest that other applications are limited. The geomagnetic field is of great importance in fields as diverse as mineral exploration, long-range radio communications, cosmic ray physics, and, of course, navigation.

Largely because of its importance to navigation, observations of the magnetic field have been made for well over 500 years, and observations that are useful for mapping the global magnetic field date back almost 400 years. The very large number of observations that have accumulated over this period are reduced to form reference maps. These maps are important for a broad spectrum of practical and scientific endeavours, ranging from navigation of ships and aircraft to studies of the dynamo process in the core which is responsible for the generation of the Earth's magnetic field. We begin by summarizing the available data; then we review the various reference fields that are available; following this, we discuss the basic morphology of the field and its secular variation; and conclude by considering some of the inferences that may be drawn from maps of the field on the dynamical regime of the fluid core.

For a comprehensive recent review of geomagnetism we refer the reader to the first two volumes of Jacobs' *Geomagnetism*: of particular relevance are the chapters by Langel [18] and by Gubbins and Roberts [11].

2. MAGNETIC FIELD OBSERVATIONS

Over the last five hundred years, the technology of magnetic field measurement has progressed from the simplest magnetic compass to high resolution satellite measurements. In this section, we briefly discuss the various types of magnetic field measurements that are encompassed by this range of technology.

Rather than attempting a comprehensive review of geomagnetic observations (for which, see [19]), we aim instead to guide the reader towards the relevant literature and data archives. We do so by dividing our treatment into two parts: first we consider modern data, which we use to describe 20th Century data; and second histroical, or pre-1900 data.

The magnetic field is a vector quantity, so to describe it fully at a point in space three orthogonal components must be measured. For example, the three orthogonal components X, Y, and Z corresponding to the local north, east and vertically downward directions, could be measured as shown in Figure 1. Instead, other components are often measured, such as the magnetic declination (D), the magnetic inclination (I), the horizontal

J. Bloxham, Department of Earth and Planetary Science, Harvard University, 24 Oxford Street, Cambridge, MA 02138

Global Earth Physics
A Handbook of Physical Constants
AGU Reference Shelf 1

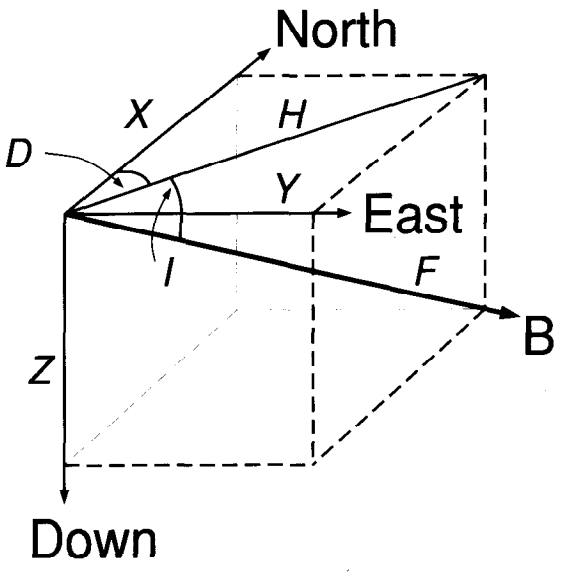

Fig. 1. Geomagnetic field elements.

field intensity (H), or the total field intensity (F). Observations of three oriented orthogonal components of the field at a point in space are commonly referred to as vector observations; other observations are referred to as scalar measurements.

2.1. Modern Data

The first magnetic observatory was established over 150 years ago. Since then, a large number of observatories have been founded, many of which have subsequently closed or re-located. The present network of permanent magnetic observatories represents an invaluable source of information on the secular variation.

For mapping the main field (the part of the geomagnetic field originating in the Earth's core) and the secular variation magnetic observatory data are normally reduced to an annual mean, generally the mean of all hourly means during a given year. This averaging removes much of the contamination due to external field variations, though contamination from solar cycle variations remains as a leading source of noise in the rate-of-change of field at some observatories. In addition a large quasi-stationary offset is present due to the local crustal field at the observatory site. This offset has been the subject of much attention, especially recently [16,23]. Generally the data are further reduced to yield the X (north), Y (east), and Z (vertically downward) components of the field in the local geodetic coordinate system.

Magnetic survey and repeat station data greatly expand the geographical coverage of magnetic observations, especially in the period prior to satellite observations. Repeat station data, observations made at intervals typically of a few years at the same site, lack the control of permanent magnetic observatory data (since the site is occupied at most for only a few days at a time) but are still of importance for tracking the secular variation. Repeat station data are reviewed by Barton [3].

Survey data on the other hand are observations made with no attempt to re-occupy sites at which observations were made previously. Although much of the motivation behind magnetic surveys is to map the crustal field, these data are of great use in mapping the global magnetic field. Land based survey data are reviewed by Barraclough and Macmillan [2]; marine survey data by Sharman and Metzger [24]; and aeromagnetic survey data for main field modelling by Coleman [10] and Hood [13].

The first satellite measurements of the field were made almost 25 years ago by Sputnik 3. Near global coverage was achieved with the POGO series of satellites from 1965 to 1971, which measured the total field intensity; Magsat in late 1979 and early 1980 achieved near global measurement of 3 orthogonal components of the field. Magsat remains unsurpassed in the quality of data provided, although several more recent satellite missions have provided useful data. These include the DE2 satellite in 1982, and the POGS satellite (part of the U.S. Defense Meteorological Satellite Program) launched in 1990. Satellite data are reviewed by Langel and Baldwin [21].

2.2. Historical Data

The last decade has seen a resurgence of interest in using historical measurements of the field to extend the timescale over which the field can be studied; a recent review is given by Jackson [17]. Adequate observations exist for mapping the global magnetic field back to the 17th century. These observations consist mostly of marine survey data early in the period, with an increasing number of land based survey measurements and some permanent magnetic observatory measurements later in the period. Many problems are encountered with these data, especially owing to the uncertainty in the geographical coordinates of the observation points, a problem that was especially great prior to the advent of reliable chronometers for the determination of longitude in 1768. Despite much work, the compilation of these data is incomplete, and it is likely that a substantial number of measurements remain to be included. The data available are summarised in Table 1. For more complete accounts of the problems associated with using histori-

TABLE 1. Compiled Historical Data

Time Period	Number of Data
1600 – 1699	3 135
1700 – 1799	10 042
1800 – 1899	45 494

cal data for global magnetic field mapping see [4,8,14].

In Table 1 we summarise the approximate number of data that are available prior to 1900. Generally, maps of the field for this period use all the available data, and would benefit from additional data.

3. THE GLOBAL MAGNETIC FIELD

Maps of the global magnetic field aim to describe the magnetic field originating in the Earth's core (the main field). Inevitably, these maps are contaminated by the crustal field at all wavelengths. These maps may be used either to study the core field, or to produce a reference field at the Earth's surface to be used, for example, as a baseline for crustal surveys, or for navigation.

3.1. Spherical Harmonic Expansion of the Magnetic Field

All models of the global magnetic field are based on a potential field representation of the magnetic field. The magnetic field $\mathbf{B}(r,\theta,\phi,t)$ where (r,θ,ϕ) are spherical polar coordinates, and t is time, can be written in the form

$$\mathbf{B}(r,\theta,\phi,t) = -\nabla V(r,\theta,\phi,t) \tag{1}$$

Most models use a spherical harmonic expansion of V

$$V(r,\theta,\phi,t) = a\sum_{l=1}^{L}\sum_{m=0}^{l}\left(\frac{a}{r}\right)^{l+1}\times \left(g_l^m(t)\cos m\phi + h_l^m(t)\sin m\phi\right) P_l^m(\cos\theta) \tag{2}$$

where a is the mean radius of the Earth (6371.2km), L is the truncation level of the expansion, and the $P_l^m(\cos\theta)$ are Schmidt quasi-normalized associated Legendre functions, where

$$\oint (P_l^m(\cos\theta))^2 d\Omega = \frac{4\pi}{2l+1} \tag{3}$$

The coefficients $g_l^m(t)$ and $h_l^m(t)$ are called the Gauss geomagnetic coefficients. Note that, given the Gauss geomagnetic coefficients, the expansion (2) can be used to determine the field at all points within the region in which the field is potential, thus, provided the weak electrical conductivity of the mantle is neglected, allowing determination of the field at the core-mantle boundary.

The components of the field in spherical polar coordinates are then given by

$$B_r = -\frac{\partial V}{\partial r} = \sum_{l=1}^{L}\sum_{m=0}^{l}(l+1)\left(\frac{a}{r}\right)^{l+2}\times \left(g_l^m(t)\cos m\phi + h_l^m(t)\sin m\phi\right) P_l^m(\cos\theta) \tag{4}$$

$$B_\theta = -\frac{1}{r}\frac{\partial V}{\partial \theta} = -\sum_{l=1}^{L}\sum_{m=0}^{l}\left(\frac{a}{r}\right)^{l+2}\times \left(g_l^m(t)\cos m\phi + h_l^m(t)\sin m\phi\right)\frac{dP_l^m(\cos\theta)}{d\theta} \tag{5}$$

$$B_\phi = -\frac{1}{r\sin\theta}\frac{\partial V}{\partial \phi} = \sum_{l=1}^{L}\sum_{m=0}^{l}\left(\frac{a}{r}\right)^{l+2}\times \left(g_l^m(t)\sin m\phi - h_l^m(t)\cos m\phi\right) P_l^m(\cos\theta) \tag{6}$$

Measurements are typically reported as one of the seven geomagnetic elements which, for a spherical reference Earth, are given by

X	$=$	$-B_\theta$	north component
Y	$=$	B_ϕ	east component
Z	$=$	$-B_r$	vertically downwards component
H	$=$	$\sqrt{X^2+Y^2}$	horizontal field intensity
F	$=$	$\sqrt{X^2+Y^2+Z^2}$	total field intensity
I	$=$	$\arctan(Z/H)$	inclination
D	$=$	$\arctan(Y/X)$	declination

Note that only the X, Y, and Z components are linearly related to the Gauss geomagnetic coefficients. The geometry of these seven field elements is illustrated in Figure 1.

A small complication is introduced by the slight asphericity of the Earth's surface. To a reasonable approximation, the Earth's surface can be described as an ellipsoid of revolution about the rotation axis. Observations on the Earth's surface are oriented with respect to the local geodetic frame, so that the X and Z components in the local geodetic frame must be transformed to give the $-B_\theta$ and $-B_r$ components in the geocentric frame; additionally, the coordinates of the observation site (altitude above the Earth's surface and geodetic latitude)

must also transformed to yield geocentric coordinates (radius and co-latitude, θ). Details are given in [18].

The time-dependency of the field can be handled in one of two ways. The first is to produce discrete models at particular points in time, using data from a window centered on the time point, usually with some correction for secular variation within the time window. The second approach is to solve for the time-dependency explicity by expanding the Gauss geomagnetic coefficients in time, using, for example, a Taylor expansion, an expansion in orthogonal polynomials, or an expansion in cubic B-splines. Using a Taylor expansion we then have

$$g_l^m(t) = g_l^m(t_0) + (t-t_0)\dot{g}_l^m(t_0) + \frac{(t-t_0)^2}{2}\ddot{g}_l^m(t_0) + \ldots \quad (7)$$

where t_0 is the reference epoch of the model. More generally, we can we can expand the field in basis functions, say, $M_n(t)$, giving

$$g_l^m(t) = \sum_n^N g_l^{mn} M_n(t) \quad (8)$$

The Taylor expansion is just a special case of this more general representation of the time dependency of the field.

One further aspect of field modelling is the choice of truncation level L in the spherical harmonic expansion (2) and N in the temporal expansion (8). The models discussed in this summary fall into two classes: truncated models where L and N are prescribed, and the remaining coefficients determined by a least squares procedure; and converged models where L and N are chosen large enough that the series (2) and (8) have converged, with some regularization imposed on the expansions to force convergence. Truncation can exacerbate some of the problems associated with uneven data distribution leading to models with spurious detail in areas of poor data coverage, and converged models require a rather subjective choice of regularization, so neither is without shortcomings.

How is the truncation level, or degree of regularization, chosen? In Figure 2 we plot the power spectrum of the magnetic field out to spherical harmonic degree 66, calculated from model M07AV6 [9]. A change in the slope of the spectrum is apparent around spherical harmonic degree 14 or 15. This break in the spectrum has been interpreted as representing the point where the crustal field overwhelms the main field at the Earth's surface: at longer wavelengths (lower degree) the main field dominates, and a shorter wavelengths (higher degree) the crustal field dominates. Accordingly, main field models are generally constructed so as to have negligible power above degree 14.

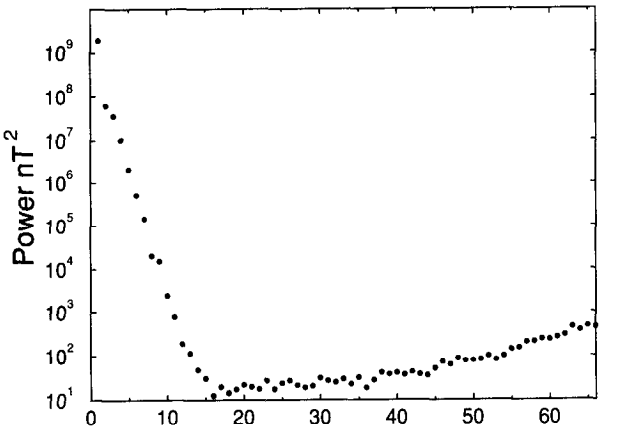

Fig. 2. Spectrum of the magnetic field at the Earth's surface in 1980, calculated from model M07AV6 [9]. The power is measured in nT^2.

3.2. Representative Field Models

The most widely used field model is the International Geomagnetic Reference Field (IGRF). The latest revision of the IGRF (1991 Revision) includes nine Definitive Geomagnetic Reference Field (DGRF) models (at five year intervals from 1945 to 1985) and a model for the period 1990-1995 (IGRF 1990), which consists of the main field and the first time derivative at 1990. The IGRF is tabulated in Table 2. However, the IGRF has several shortcomings. It is based on a truncation of the spherical harmonic expansion at degree 10 which unnecessarily excludes part of the main field resolved by recent data. Furthermore, by design the IGRF does not yield a model of the field at all points in time. Partly because of these shortcomings, a large number of other models of the field are used, especially in studies of the core which are particularly sensitive to these problems.

In Table 3 we list a number of models that have been produced recently. Our list is not comprehensive: more complete lists are given by [1] and [18]. Instead we have sought to give a representative list of field models that are in current use for a range of different purposes.

How different are these models of the field, and are these differences important to the user? In Table 4 we show the coefficients of model ufm1 evaluated at the epochs of the nine DGRF models, and model GSFC(9/80) evaluated at each DGRF from 1960.0 to 1980.0. Not surprisingly, the models do not agree precisely, with greater discrepancies at earlier times. In

TABLE 2. The International Geomagnetic Reference Field (1991 Revision)

	l	m	1945	1950	1955	1960	1965	1970	1975	1980	1985	1990
g	1	0	-30594	-30554	-30500	-30421	-30334	-30220	-30100	-29992	-29873	-29775
g	1	1	-2285	-2250	-2215	-2169	-2119	-2068	-2013	-1956	-1905	-1851
h	1	1	5810	5815	5820	5791	5776	5737	5675	5604	5500	5411
g	2	0	-1244	-1341	-1440	-1555	-1662	-1781	-1902	-1997	-2072	-2136
g	2	1	2990	2998	3003	3002	2997	3000	3010	3027	3044	3058
h	2	1	-1702	-1810	-1898	-1967	-2016	-2047	-2067	-2129	-2197	-2278
g	2	2	1578	1576	1581	1590	1594	1611	1632	1663	1687	1693
h	2	2	477	381	291	206	114	25	-68	-200	-306	-380
g	3	0	1282	1297	1302	1302	1297	1287	1276	1281	1296	1315
g	3	1	-1834	-1889	-1944	-1992	-2038	-2091	-2144	-2180	-2208	-2240
h	3	1	-499	-476	-462	-414	-404	-366	-333	-336	-310	-287
g	3	2	1255	1274	1288	1289	1292	1278	1260	1251	1247	1246
h	3	2	186	206	216	224	240	251	262	271	284	293
g	3	3	913	896	882	878	856	838	830	833	829	807
h	3	3	-11	-46	-83	-130	-165	-196	-223	-252	-297	-348
g	4	0	944	954	958	957	957	952	946	938	936	939
g	4	1	776	792	796	800	804	800	791	782	780	782
h	4	1	144	136	133	135	148	167	191	212	232	248
g	4	2	544	528	510	504	479	461	438	398	361	324
h	4	2	-276	-278	-274	-278	-269	-266	-265	-257	-249	-240
g	4	3	-421	-408	-397	-394	-390	-395	-405	-419	-424	-423
h	4	3	-55	-37	-23	3	13	26	39	53	69	87
g	4	4	304	303	290	269	252	234	216	199	170	142
h	4	4	-178	-210	-230	-255	-269	-279	-288	-297	-297	-299
g	5	0	-253	-240	-229	-222	-219	-216	-218	-218	-214	-211
g	5	1	346	349	360	362	358	359	356	357	355	353
h	5	1	-12	3	15	16	19	26	31	46	47	47
g	5	2	194	211	230	242	254	262	264	261	253	244
h	5	2	95	103	110	125	128	139	148	150	150	153
g	5	3	-20	-20	-23	-26	-31	-42	-59	-74	-93	-111
h	5	3	-67	-87	-98	-117	-126	-139	-152	-151	-154	-154
g	5	4	-142	-147	-152	-156	-157	-160	-159	-162	-164	-166
h	5	4	-119	-122	-121	-114	-97	-91	-83	-78	-75	-69
g	5	5	-82	-76	-69	-63	-62	-56	-49	-48	-46	-37
h	5	5	82	80	78	81	81	83	88	92	95	98
g	6	0	59	54	47	46	45	43	45	48	53	61
g	6	1	57	57	57	58	61	64	66	66	65	64
h	6	1	6	-1	-9	-10	-11	-12	-13	-15	-16	-16
g	6	2	6	4	3	1	8	15	28	42	51	60
h	6	2	100	99	96	99	100	100	99	93	88	83
g	6	3	-246	-247	-247	-237	-228	-212	-198	-192	-185	-178
h	6	3	16	33	48	60	68	72	75	71	69	68
g	6	4	-25	-16	-8	-1	4	2	1	4	4	2
h	6	4	-9	-12	-16	-20	-32	-37	-41	-43	-48	-52
g	6	5	21	12	7	-2	1	3	6	14	16	17
h	6	5	-16	-12	-12	-11	-8	-6	-4	-2	-1	2
g	6	6	-104	-105	-107	-113	-111	-112	-111	-108	-102	-96
h	6	6	-39	-30	-24	-17	-7	1	11	17	21	27
g	7	0	70	65	65	67	75	72	71	72	74	77
g	7	1	-40	-55	-56	-56	-57	-57	-56	-59	-62	-64
h	7	1	-45	-35	-50	-55	-61	-70	-77	-82	-83	-81
g	7	2	0	2	2	5	4	1	1	2	3	4
h	7	2	-18	-17	-24	-28	-27	-27	-26	-27	-27	-27
g	7	3	0	1	10	15	13	14	16	21	24	28

TABLE 2. (continued)

	l	m	1945	1950	1955	1960	1965	1970	1975	1980	1985	1990
h	7	3	2	0	-4	-6	-2	-4	-5	-5	-2	1
g	7	4	-29	-40	-32	-32	-26	-22	-14	-12	-6	1
h	7	4	6	10	8	7	6	8	10	16	20	20
g	7	5	-10	-7	-11	-7	-6	-2	0	1	4	6
h	7	5	28	36	28	23	26	23	22	18	17	16
g	7	6	15	5	9	17	13	13	12	11	10	10
h	7	6	-17	-18	-20	-18	-23	-23	-23	-23	-23	-23
g	7	7	29	19	18	8	1	-2	-5	-2	0	0
h	7	7	-22	-16	-18	-17	-12	-11	-12	-10	-7	-5
g	8	0	13	22	11	15	13	14	14	18	21	22
g	8	1	7	15	9	6	5	6	6	6	6	5
h	8	1	12	5	10	11	7	7	6	7	8	10
g	8	2	-8	-4	-6	-4	-4	-2	-1	0	0	-1
h	8	2	-21	-22	-15	-14	-12	-15	-16	-18	-19	-20
g	8	3	-5	-1	-14	-11	-14	-13	-12	-11	-11	-11
h	8	3	-12	0	5	7	9	6	4	4	5	7
g	8	4	9	11	6	2	0	-3	-8	-7	-9	-12
h	8	4	-7	-21	-23	-18	-16	-17	-19	-22	-23	-22
g	8	5	7	15	10	10	8	5	4	4	4	4
h	8	5	2	-8	3	4	4	6	6	9	11	12
g	8	6	-10	-13	-7	-5	-1	0	0	3	4	4
h	8	6	18	17	23	23	24	21	18	16	14	11
g	8	7	7	5	6	10	11	11	10	6	4	3
h	8	7	3	-4	-4	1	-3	-6	-10	-13	-15	-16
g	8	8	2	-1	9	8	4	3	1	-1	-4	-6
h	8	8	-11	-17	-13	-20	-17	-16	-17	-15	-11	-11
g	9	0	5	3	4	4	8	8	7	5	5	4
g	9	1	-21	-7	9	6	10	10	10	10	10	10
h	9	1	-27	-24	-11	-18	-22	-21	-21	-21	-21	-21
g	9	2	1	-1	-4	0	2	2	2	1	1	1
h	9	2	17	19	12	12	15	16	16	16	15	15
g	9	3	-11	-25	-5	-9	-13	-12	-12	-12	-12	-12
h	9	3	29	12	7	2	7	6	7	9	9	10
g	9	4	3	10	2	1	10	10	10	9	9	9
h	9	4	-9	2	6	0	-4	-4	-4	-5	-6	-6
g	9	5	16	5	4	4	-1	-1	-1	-3	-3	-4
h	9	5	4	2	-2	-3	-5	-5	-5	-6	-6	-6
g	9	6	-3	-5	1	-1	-1	0	-1	-1	-1	-1
h	9	6	9	8	10	9	10	10	10	9	9	9
g	9	7	-4	-2	2	-2	5	3	4	7	7	7
h	9	7	6	8	7	8	10	11	11	10	9	9
g	9	8	-3	3	2	3	1	1	1	2	1	2
h	9	8	1	-11	-6	0	-4	-2	-3	-6	-7	-7
g	9	9	-4	8	5	-1	-2	-1	-2	-5	-5	-6
h	9	9	8	-7	5	5	1	1	1	2	2	2
g	10	0	-3	-8	-3	1	-2	-3	-3	-4	-4	-4
g	10	1	11	4	-5	-3	-3	-3	-3	-4	-4	-4
h	10	1	5	13	-4	4	2	1	1	1	1	1
g	10	2	1	-1	-1	4	2	2	2	2	3	2
h	10	2	1	-2	0	1	1	1	1	0	0	0
g	10	3	2	13	2	0	-5	-5	-5	-5	-5	-5
h	10	3	-20	-10	-8	0	2	3	3	3	3	3

TABLE 2. (continued)

	l	m	1945	1950	1955	1960	1965	1970	1975	1980	1985	1990
g	10	4	-5	-4	-3	-1	-2	-1	-2	-2	-2	-2
h	10	4	-1	2	-2	2	6	4	4	6	6	6
g	10	5	-1	4	7	4	4	6	5	5	5	4
h	10	5	-6	-3	-4	-5	-4	-4	-4	-4	-4	-4
g	10	6	8	12	4	6	4	4	4	3	3	3
h	10	6	6	6	1	1	0	0	-1	0	0	0
g	10	7	-1	3	-2	1	0	1	1	1	1	1
h	10	7	-4	-3	-3	-1	-2	-1	-1	-1	-1	-1
g	10	8	-3	2	6	-1	2	0	0	2	2	2
h	10	8	-2	6	7	6	3	3	3	4	4	4
g	10	9	5	10	-2	2	2	3	3	3	3	3
h	10	9	0	11	-1	0	0	1	1	0	0	0
g	10	10	-2	3	0	0	0	-1	-1	0	0	0
h	10	10	-2	8	-3	-7	-6	-4	-5	-6	-6	-6

TABLE 3. Representative Models of the Main Magnetic Field

Epoch	Model Name	Spatial Expansion	Temporal Expansion	Reference
1945.0	DGRF 1945	Spherical Harmonics	None	15
1950.0	DGRF 1950	Spherical Harmonics	None	15
1955.0	DGRF 1955	Spherical Harmonics	None	15
1960.0	DGRF 1960	Spherical Harmonics	None	15
1965.0	DGRF 1965	Spherical Harmonics	None	15
1970.0	DGRF 1970	Spherical Harmonics	None	15
1975.0	DGRF 1975	Spherical Harmonics	None	15
1980.0	DGRF 1980	Spherical Harmonics	None	15
1985.0	DGRF 1985	Spherical Harmonics	None	15
1647.0		Spherical Harmonics	None	14
1715.0		Spherical Harmonics	None	4
1777.5		Spherical Harmonics	None	4
1842.5		Spherical Harmonics	None	4
1905.5		Spherical Harmonics	None	8
1915.5		Spherical Harmonics	None	8
1925.5		Spherical Harmonics	None	8
1935.5		Spherical Harmonics	None	8
1945.5		Spherical Harmonics	None	8
1955.5		Spherical Harmonics	None	8
1966.0		Spherical Harmonics	None	8
1969.5		Spherical Harmonics	None	12
1980.0		Spherical Harmonics	None	12
1980.0	phs80	Harmonic Splines	None	25
1978.0–1982.0	GSFC(12/83)	Spherical Harmonics	Taylor series (degree 1)	19
1960.0–1980.0	GSFC(9/80)	Spherical Harmonics	Taylor series (degree 3)	22
1990.0–1995.0	IGRF 1990	Spherical Harmonics	Taylor series (degree 1)	15
1690.0–1840.0	ufm2	Spherical Harmonics	cubic B-splines	7
1840.0–1990.0	ufm1	Spherical Harmonics	cubic B-splines	7

Table 5 we compare the models in Table 3 with the IGRF, listing for each model the RMS radial field at the Earth's surface and at the core-mantle boundary, and the RMS difference in the radial field between each model and the DGRF for that year, again at the surface and at the core-mantle boundary. Typical differences at the surface are less than 50nT (or less than 0.15%) for models at recent times and less than 200nT for models of the field at earlier periods. These differences should be compared with the typical crustal field contribution to the field (which is not accounted for by these models) of about 250nT, and the typical secular variation of about 50nT/year. Thus, at the Earth's surface the difference between different models is small compared to the uncertainties introduced by crustal fields and by the use of out of date field models. As a further example, in Figure 3 we show the difference in declination calculated from IGRF 1990 and ufm1 at 1990. The gradations in the greyscale are at intervals of 5′, so the difference between the models is typically very small compared to that required for safe navigation; local crustal anomalies, in particular, pose a far greater hazard to navigation than these small differences between field models.

These differences between models at the Earth's surface can be important, though, for crustal magnetic field models. Main field models are used to provide a baseline level for crustal surveys and small differences in baseline can have an important effect, especially for tying together adjacent surveys. However, all crustal surveys suffer from a more serious problem: the long wavelength part of the crustal signal is swamped by the main field, and is removed with the core field baseline. This problem is obviously most acute for largescale crustal surveys, especially attempts at mapping the global crustal field.

At the core-mantle boundary the situation is more complicated. The difference between different models amounts to around 15% of the field, even for recent models. This figure is perhaps somewhat biased by the fact that we are using as our reference the DGRF models, which as we have discussed are not well suited to modelling the field at the core-mantle boundary. However, the part of the core field that is masked by the crustal field is obviously not included in any of the models, so the true uncertainty may be very large. Certainly studies of the core field are very sensitive to the choice of field model. Indeed, the enterprise of using models of the magnetic field at the core-mantle boundary to study the kinematics and dynamics of the fluid outer core should not be separated from the enterprise of producing the field models in the first place.

The differences between different models are more apparent when we examine the instantaneous secular variation, the first temporal derivative of the field. In Table 6 we compare the secular variation of the radial field at the Earth's surface and at the core-mantle boundary computed from model ufm1 with the IGRF at 1990, and with GSFC(9/80) at 1980, 1970, and 1960.

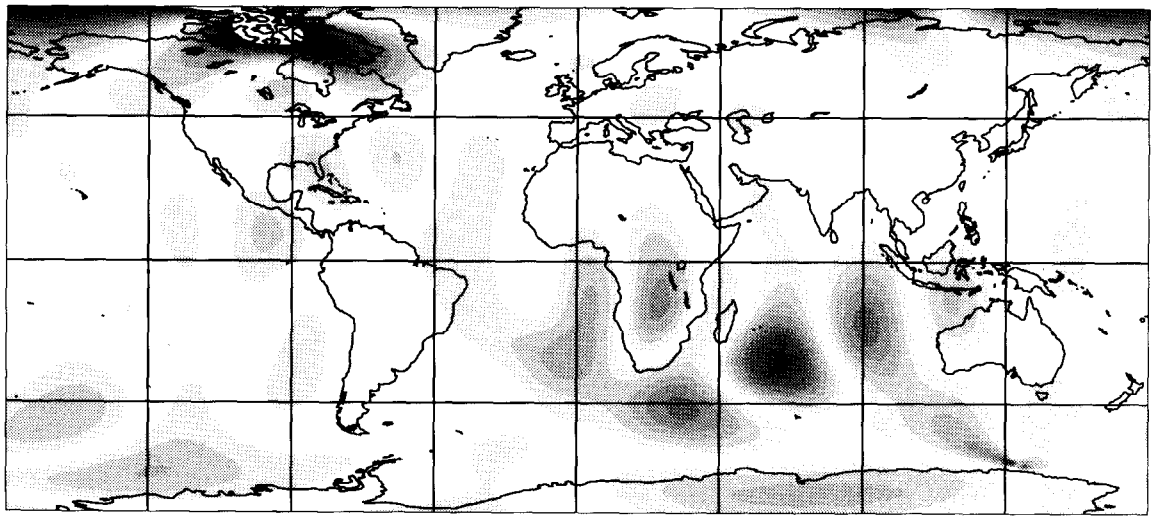

Fig. 3. Difference in declination at the Earth's surface in 1990 calculated from IGRF 1990 and ufm1. The greyscale gradations are at intervals of 5′.

TABLE 4a. Model ufm1 evaluated at the DGRF Epochs

	l	m	1945	1950	1955	1960	1965	1970	1975	1980	1985	1990
g	1	0	-30611	-30565	-30511	-30434	-30331	-30214	-30102	-29990	-29872	-29769
g	1	1	-2264	-2234	-2200	-2164	-2121	-2068	-2015	-1956	-1904	-1855
h	1	1	5815	5807	5801	5789	5778	5735	5678	5603	5496	5403
g	2	0	-1222	-1320	-1431	-1545	-1664	-1780	-1900	-1998	-2073	-2143
g	2	1	2974	2988	2998	2994	2997	3002	3014	3029	3043	3055
h	2	1	-1688	-1792	-1884	-1954	-2011	-2039	-2067	-2129	-2197	-2278
g	2	2	1580	1575	1578	1587	1597	1614	1634	1659	1683	1688
h	2	2	466	380	290	206	121	33	-71	-200	-306	-381
g	3	0	1265	1289	1298	1299	1290	1281	1273	1277	1294	1313
g	3	1	-1839	-1891	-1943	-1991	-2040	-2095	-2146	-2181	-2209	-2236
h	3	1	-513	-491	-464	-432	-402	-368	-345	-331	-305	-284
g	3	2	1251	1270	1288	1292	1291	1281	1265	1255	1250	1249
h	3	2	187	209	224	230	236	247	260	272	285	298
g	3	3	907	896	888	876	860	843	832	828	820	797
h	3	3	-15	-50	-86	-128	-166	-195	-223	-255	-300	-350
g	4	0	939	953	961	961	957	953	946	939	937	938
g	4	1	788	798	802	805	804	799	791	784	780	778
h	4	1	176	161	150	146	154	171	192	212	231	245
g	4	2	537	528	518	502	483	460	434	400	363	325
h	4	2	-277	-281	-280	-277	-273	-269	-265	-258	-250	-243
g	4	3	-409	-402	-395	-390	-389	-395	-406	-417	-422	-422
h	4	3	-49	-30	-12	3	17	29	41	57	72	87
g	4	4	295	295	285	270	253	236	222	200	172	142
h	4	4	-167	-200	-230	-252	-270	-282	-291	-298	-301	-305
g	5	0	-240	-236	-230	-225	-220	-218	-218	-219	-217	-215
g	5	1	345	350	355	358	360	361	360	358	354	351
h	5	1	-33	-15	-2	10	19	27	35	42	47	50
g	5	2	205	213	224	237	248	257	261	260	254	247
h	5	2	85	96	107	118	129	139	146	151	156	161
g	5	3	-25	-25	-25	-28	-33	-41	-53	-69	-87	-104
h	5	3	-77	-91	-104	-116	-128	-139	-149	-155	-158	-160
g	5	4	-147	-151	-154	-158	-160	-163	-164	-166	-169	-171
h	5	4	-118	-116	-112	-106	-99	-91	-83	-76	-69	-62
g	5	5	-75	-73	-69	-66	-61	-55	-48	-43	-38	-33
h	5	5	72	74	76	78	81	85	90	94	97	100
g	6	0	51	49	47	44	43	43	45	49	54	60
g	6	1	50	53	56	58	60	62	64	64	65	65
h	6	1	5	1	-3	-8	-11	-15	-17	-18	-19	-19
g	6	2	-8	-5	-1	4	11	19	29	39	49	60
h	6	2	106	106	106	105	103	100	97	92	87	82
g	6	3	-253	-250	-245	-237	-227	-216	-205	-195	-186	-178
h	6	3	34	44	53	62	68	71	71	71	71	70
g	6	4	-14	-8	-3	0	2	4	6	7	8	8
h	6	4	-15	-18	-22	-26	-31	-36	-41	-45	-49	-54
g	6	5	16	11	7	5	4	5	7	9	12	14
h	6	5	-8	-11	-13	-14	-13	-12	-9	-6	-3	0
g	6	6	-102	-105	-108	-110	-110	-110	-109	-106	-102	-98
h	6	6	-33	-25	-18	-10	-2	5	13	19	25	30
g	7	0	74	73	72	72	71	71	71	71	72	73
g	7	1	-52	-52	-52	-53	-54	-55	-56	-58	-60	-63
h	7	1	-50	-52	-54	-58	-63	-67	-72	-76	-79	-82
g	7	2	5	4	4	3	3	2	2	3	3	3
h	7	2	-20	-22	-24	-26	-27	-28	-29	-30	-31	-32
g	7	3	22	20	18	17	17	17	18	19	20	21

TABLE 4a. (continued)

	l	m	1945	1950	1955	1960	1965	1970	1975	1980	1985	1990
h	7	3	-12	-12	-11	-9	-8	-6	-4	-2	1	3
g	7	4	-31	-30	-29	-27	-25	-22	-19	-14	-10	-5
h	7	4	-1	1	3	6	8	10	12	14	17	19
g	7	5	-12	-10	-8	-6	-5	-3	-1	0	1	3
h	7	5	29	28	27	26	25	23	22	20	19	18
g	7	6	19	18	17	16	15	14	13	12	11	10
h	7	6	-17	-19	-20	-22	-23	-24	-25	-26	-26	-27
g	7	7	18	15	12	9	6	3	1	-1	-3	-5
h	7	7	-26	-24	-22	-20	-18	-16	-13	-11	-8	-5
g	8	0	9	9	10	10	11	12	14	15	17	18
g	8	1	5	6	6	6	6	6	6	6	6	6
h	8	1	6	7	7	8	9	9	10	11	11	12
g	8	2	-6	-5	-4	-4	-3	-2	-2	-1	-1	0
h	8	2	-15	-14	-14	-14	-14	-14	-14	-14	-15	-15
g	8	3	-11	-11	-12	-12	-12	-11	-11	-11	-11	-10
h	8	3	6	6	6	6	6	5	5	5	5	5
g	8	4	4	3	1	-1	-2	-4	-6	-7	-9	-10
h	8	4	-11	-12	-13	-14	-15	-16	-17	-18	-18	-19
g	8	5	7	7	7	6	6	6	6	5	5	5
h	8	5	4	4	4	4	4	5	6	7	8	9
g	8	6	-10	-9	-7	-6	-5	-3	-2	-1	0	2
h	8	6	17	18	18	19	19	19	18	17	17	16
g	8	7	9	9	10	10	10	10	10	9	8	8
h	8	7	-2	-2	-3	-4	-5	-7	-8	-10	-11	-13
g	8	8	7	7	6	5	4	3	2	1	0	-2
h	8	8	-14	-15	-16	-17	-18	-18	-19	-19	-19	-19
g	9	0	9	9	9	9	9	9	9	9	9	9
g	9	1	8	8	8	8	8	8	8	8	9	9
h	9	1	-18	-19	-20	-21	-22	-23	-23	-24	-25	-26
g	9	2	2	2	3	3	3	3	4	4	4	4
h	9	2	12	12	13	14	14	14	15	15	16	16
g	9	3	-10	-11	-11	-12	-12	-12	-13	-13	-13	-14
h	9	3	2	3	4	4	5	6	7	7	8	9
g	9	4	8	8	9	9	10	10	11	11	12	12
h	9	4	0	0	0	-1	-1	-1	-2	-2	-2	-3
g	9	5	5	5	4	3	2	1	0	-1	-2	-4
h	9	5	2	1	-1	-2	-3	-4	-4	-5	-6	-7
g	9	6	-1	-1	-1	-1	-1	-1	-1	-1	-1	-1
h	9	6	7	8	8	8	8	8	8	9	9	9
g	9	7	-3	-2	-1	0	1	2	3	4	5	6
h	9	7	9	9	10	10	10	10	10	10	10	10
g	9	8	-1	-1	0	0	1	1	2	2	2	3
h	9	8	-3	-3	-3	-3	-3	-3	-3	-3	-3	-3
g	9	9	1	1	1	1	0	0	0	-1	-1	-1
h	9	9	3	2	2	1	1	0	0	0	-1	-1
g	10	0	-2	-2	-1	-1	-1	-1	-1	-1	-1	-1
g	10	1	-1	-1	-1	-1	-1	-2	-2	-2	-2	-3
h	10	1	1	1	2	2	2	2	2	2	2	2
g	10	2	1	1	2	2	2	2	2	3	3	3
h	10	2	3	2	2	2	2	2	2	2	2	2
g	10	3	-1	-1	-1	-2	-2	-2	-2	-2	-2	-2
h	10	3	1	1	1	1	1	1	1	2	2	2
g	10	4	-1	-2	-2	-2	-2	-2	-2	-2	-2	-3
h	10	4	2	2	2	3	3	3	4	4	4	4

TABLE 4a. (continued)

	l	m	1945	1950	1955	1960	1965	1970	1975	1980	1985	1990
g	10	5	5	5	5	5	5	5	5	5	5	5
h	10	5	-1	-1	-2	-2	-2	-3	-3	-3	-4	-4
g	10	6	3	3	4	4	4	4	4	4	4	4
h	10	6	0	0	0	0	0	-1	-1	-1	-1	-1
g	10	7	0	0	0	0	0	0	0	1	1	1
h	10	7	-2	-2	-2	-2	-2	-2	-2	-2	-2	-3
g	10	8	-1	0	0	0	0	0	0	1	1	1
h	10	8	3	3	3	3	3	4	4	4	4	4
g	10	9	1	1	1	1	1	1	1	1	1	1
h	10	9	1	1	1	0	0	0	0	0	0	0
g	10	10	2	2	2	1	1	1	1	0	0	0
h	10	10	-2	-3	-3	-4	-4	-5	-5	-6	-6	-7

The differences at the surface range from about 10% to about 40% of the rms signal; at the core-mantle boundary the differences between the models are such as to render the secular variation effectively unresolved.

3.3. The Magnetic Field at the Earth's Surface

In Figure 4 we plot the seven geomagnetic elements for the IGRF 1990 model at the Earth's surface. The nearly dipolar nature of the field is apparent, with the geomagnetic equator deviating only slightly from the geographical equator. In addition, we plot three other quantities at the surface: the inclination anomaly (the departure of the inclination from that of an axial dipole), and the field intensity anomaly relative to both the axial dipole and the inclined centered dipole (the first three Gauss geomagnetic coefficients). Declination and inclination anomaly measure the angular departure of the field from an axial dipole. Apart from near the geomagnetic poles where the declination becomes large, typically both the declination and inclination anomalies are roughly 15°. The intensity anomaly relative to both the axial dipole and the inclined dipole reaches over 20 000nT, or roughly half the typical field intensity at the surface. The largest intensity anomaly is in the southern Atlantic Ocean, a large region of low field intensity. It is important to note that very substantial deviations from the dipole field exist at the Earth's surface, and that studies that assume some average percentage deviation from an axial dipole configuration may be in rather serious error in some regions. For example, the axial dipole accounts for over 90% of the power in the field at the Earth's surface, which gives a rather poor indication of the departure of the field from the axial dipole configuration in certain regions.

The secular variation of X, Y, and Z at the surface is shown in Figure 5 for IGRF 1990 and ufm1. The secular variation of the vertical field in the equatorial Atlantic Ocean reaches almost 200nT/year, so that in one year the change in the field can exceed the typical difference between the main field models. Thus, small inaccuracies in the secular variation models, combined with changes in the pattern of secular variation, constitute a significant error when models of the secular variation are used to extrapolate main field models to the present day. Indeed, the development of more reliable methods of extrapolating forward from the most recent global magnetic field model to calculate the present field is a pressing problem in geomagnetism of considerable practical importance.

3.4. The Magnetic Field at the Core-Mantle Boundary

In Figure 6, by contrast, we plot the radial component of the magnetic field at the core-mantle boundary for the interval 1690–1840 at 50 year intervals (calculated from model ufm2), and for the interval 1840–1990 at 25 year intervals (calculated from model ufm1). At the core-mantle boundary the field departs substantially from a dipole: several magnetic equators are evident, and the radial field has very low intensity near the geographical poles. The total intensity anomaly identified at the Earth's surface can be traced at the core-mantle boundary to the arrangement of patches of flux of opposite sign in the region beneath the southern Atlantic Ocean. Although the field intensity at the core-mantle boundary is not anomalously low in this region, the patches interfere destructively when the field is upwardly continued to the Earth's surface.

We do not plot the instantaneous secular variation at the core-mantle boundary. As we have argued, this is

TABLE 4b. Model GSFC(9/80) evaluated at the DGRF Epochs

	l	m	1960	1965	1970	1975	1980
g	1	0	-30440	-30336	-30219	-30099	-29988
g	1	1	-2166	-2118	-2063	-2007	-1957
h	1	1	5764	5765	5723	5662	5607
g	2	0	-1540	-1659	-1778	-1893	-1997
g	2	1	2996	2997	3000	3009	3028
h	2	1	-1947	-2010	-2037	-2065	-2129
g	2	2	1578	1582	1596	1622	1663
h	2	2	202	112	22	-78	-199
g	3	0	1299	1295	1281	1272	1280
g	3	1	-1994	-2041	-2097	-2149	-2181
h	3	1	-423	-398	-360	-332	-336
g	3	2	1294	1294	1282	1266	1251
h	3	2	229	238	249	261	271
g	3	3	873	857	838	826	833
h	3	3	-125	-168	-198	-223	-252
g	4	0	964	956	951	946	937
g	4	1	812	807	801	792	782
h	4	1	139	150	169	191	212
g	4	2	505	486	466	439	397
h	4	2	-277	-271	-266	-262	-257
g	4	3	-389	-389	-394	-404	-420
h	4	3	-7	14	22	30	52
g	4	4	267	251	237	221	198
h	4	4	-257	-268	-277	-286	-298
g	5	0	-228	-220	-215	-214	-217
g	5	1	355	359	361	360	357
h	5	1	14	15	21	31	45
g	5	2	237	250	259	263	262
h	5	2	113	127	138	146	150
g	5	3	-32	-33	-40	-54	-74
h	5	3	-113	-126	-137	-145	-151
g	5	4	-158	-160	-161	-162	-162
h	5	4	-107	-98	-90	-84	-78
g	5	5	-74	-68	-62	-55	-48
h	5	5	78	81	84	88	92
g	6	0	50	47	45	46	49
g	6	1	53	59	62	64	65
h	6	1	-6	-10	-13	-14	-15
g	6	2	3	7	15	27	42
h	6	2	103	103	102	98	93
g	6	3	-240	-227	-215	-203	-191
h	6	3	63	70	74	74	71
g	6	4	2	1	1	2	4
h	6	4	-26	-34	-39	-42	-43
g	6	5	-6	-4	0	6	14
h	6	5	-12	-10	-7	-5	-2
g	6	6	-103	-110	-113	-112	-107
h	6	6	-21	-14	-6	5	18
g	7	0	69	70	70	71	71
g	7	1	-51	-53	-55	-56	-58
h	7	1	-54	-62	-69	-76	-83
g	7	2	0	1	1	1	1
h	7	2	-27	-27	-27	-27	-27

TABLE 4b. (continued)

	l	m	1960	1965	1970	1975	1980
g	7	3	11	13	16	18	20
h	7	3	-9	-8	-7	-6	-6
g	7	4	-32	-27	-22	-18	-13
h	7	4	4	7	10	13	16
g	7	5	-3	-2	-1	0	1
h	7	5	25	23	22	20	18
g	7	6	15	14	13	12	11
h	7	6	-24	-24	-24	-24	-24
g	7	7	-4	-4	-4	-3	-3
h	7	7	-21	-18	-15	-13	-10
g	8	0	7	10	13	16	19
g	8	1	6	6	6	7	7
h	8	1	9	9	8	8	8
g	8	2	-4	-2	-1	0	1
h	8	2	-12	-13	-15	-16	-18
g	8	3	-12	-12	-11	-11	-10
h	8	3	5	5	4	4	3
g	8	4	-2	-4	-5	-6	-7
h	8	4	-16	-17	-19	-21	-22
g	8	5	11	9	8	6	4
h	8	5	3	5	6	8	9
g	8	6	-7	-4	-2	1	4
h	8	6	27	24	22	19	16
g	8	7	17	14	12	10	7
h	8	7	0	-3	-7	-10	-13
g	8	8	4	3	1	0	-1
h	8	8	-16	-16	-16	-15	-15
g	9	0	11	10	8	7	5
g	9	1	7	8	9	10	11
h	9	1	-23	-23	-23	-22	-22
g	9	2	2	2	1	1	1
h	9	2	14	15	15	16	16
g	9	3	-12	-12	-12	-12	-12
h	9	3	4	5	6	8	9
g	9	4	12	11	10	10	9
h	9	4	-1	-2	-3	-4	-5
g	9	5	2	0	-1	-3	-4
h	9	5	-2	-3	-5	-6	-8
g	9	6	0	-1	-1	-1	-1
h	9	6	10	10	10	10	10
g	9	7	2	3	4	6	7
h	9	7	12	12	11	11	11
g	9	8	2	2	2	2	2
h	9	8	0	-1	-3	-4	-5
g	9	9	4	2	-1	-3	-5
h	9	9	-1	0	1	1	2
g	10	0	-1	-2	-2	-3	-3
g	10	1	-2	-3	-3	-4	-4
h	10	1	2	2	2	1	1
g	10	2	2	2	2	2	3
h	10	2	1	1	1	0	0
g	10	3	-4	-4	-5	-5	-6
h	10	3	2	2	2	2	3

TABLE 4b. (continued)

	l	m	1960	1965	1970	1975	1980
g	10	4	-2	-2	-2	-2	-2
h	10	4	7	6	6	6	6
g	10	5	5	5	5	5	5
h	10	5	-4	-4	-4	-4	-4
g	10	6	6	5	5	4	3
h	10	6	1	1	0	-1	-1
g	10	7	-2	-1	0	0	1
h	10	7	-4	-3	-2	-2	-1
g	10	8	1	1	2	2	2
h	10	8	2	2	3	4	4
g	10	9	1	2	2	3	3
h	10	9	1	1	0	0	-1
g	10	10	-1	-1	-1	0	0
h	10	10	-5	-5	-6	-6	-6

extremely poorly determined, and any map would be essentially meaningless. Taking the lower estimates of the rms secular variation in Table 6, we derive a timescale for the secular variation at the core-mantle boundary of about 150 years. This is rather misleading since over the last three hundred years we observe that much of the pattern of the field at the core surface has changed little. In Figure 7 we show the average field at the core-mantle boundary over the period 1840–1990, which indeed shows substantial similarity to the individual maps in Figure 6. Note that the steady part of the field, which accounts for over 80% of the power in the radial field over this period, is nearly antisymmetric about the geographical equator.

How do we reconcile this sizeable steady component with the inference of such a short timescale for the secular variation? A clue is found from examining the timescale of the secular variation at the surface, for which we obtain an estimate about five times longer than the 150 years found above. The explanation of this is that long wavelength ingredients of the field are changing more slowly with time than short wavelength ingredients.

Much recent work has been devoted to explaining the origin of the secular variation, particularly to producing maps of the fluid flow at the core surface that generates the observed secular variation. A review of this work is given by [6]. In Figure 8 we show a typical flow map, representing the steady part of the fluid flow at the core surface over the last 150 years. This flow explains over 95% of the power in the time variations of the radial field during this period. Typical flow speeds of around 20km/yr are obtained, suggesting an advective timescale of order 10^2 years in the core. The pattern of fluid flow is nearly symmetric about the equator, and the flow is consistent with a nearly geostrophic balance.

TABLE 5. Comparison of Main Field Models

Model Name	RMS B_r		RMS ΔB_r	
	surface nT	cmb μT	surface nT	cmb μT
1990				
igrf 1990	35 967	299		
ufm1	35 958	299	73	66
1985				
dgrf 1985	36 073	300		
ufm1	36 071	304	65	63
1980				
dgrf 1980	36 205	300		
gsfc(9/80)	36 201	318	29	103
phs80	36 213	299	22	34
1980 (G&B)	36 206	304	20	49
ufm1	36 202	318	55	60
1975				
dgrf 1975	36 318	299		
gsfc(9/80)	36 312	314	57	94
ufm1	36 322	302	54	54
1970				
dgrf 1970	36 448	299		
gsfc(9/80)	36 442	315	57	97
ufm1	36 442	301	49	52
1965				
dgrf 1965	36 569	300		
gsfc(9/80)	36 568	300	64	113
ufm1	36 566	300	54	52
1960				
dgrf 1960	36 656	298		
gsfc(9/80)	36 668	330	114	144
ufm1	36 667	300	80	56
1955				
dgrf 1955	36 734	299		
ufm1	36 738	299	109	76
1950				
dgrf 1950	36 774	320		
ufm1	36 778	297	171	128
1945				
dgrf 1945	36 797	316		
ufm1	36 808	296	197	130

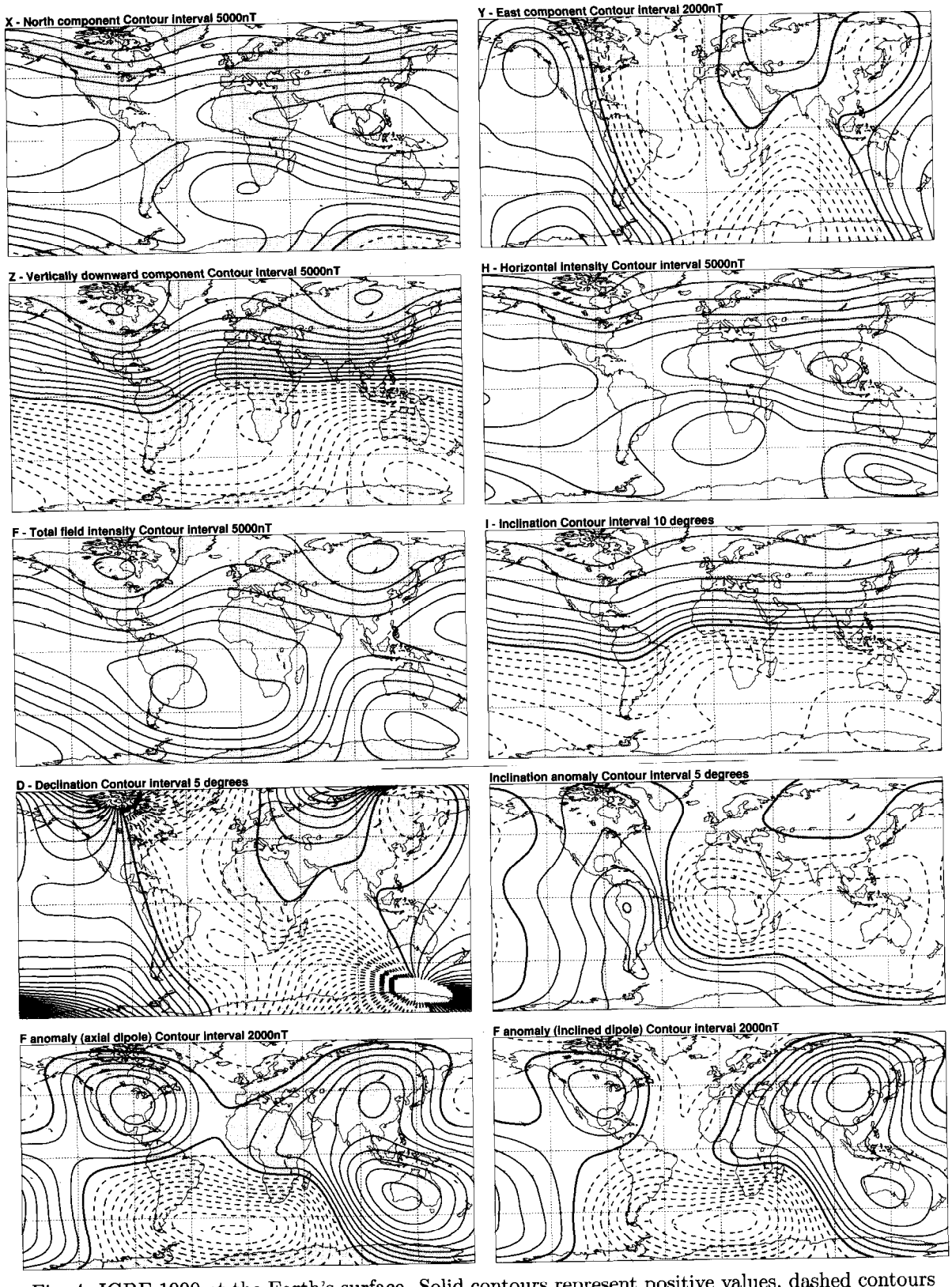

Fig. 4. IGRF 1990 at the Earth's surface. Solid contours represent positive values, dashed contours negative values, and bold contours zero.

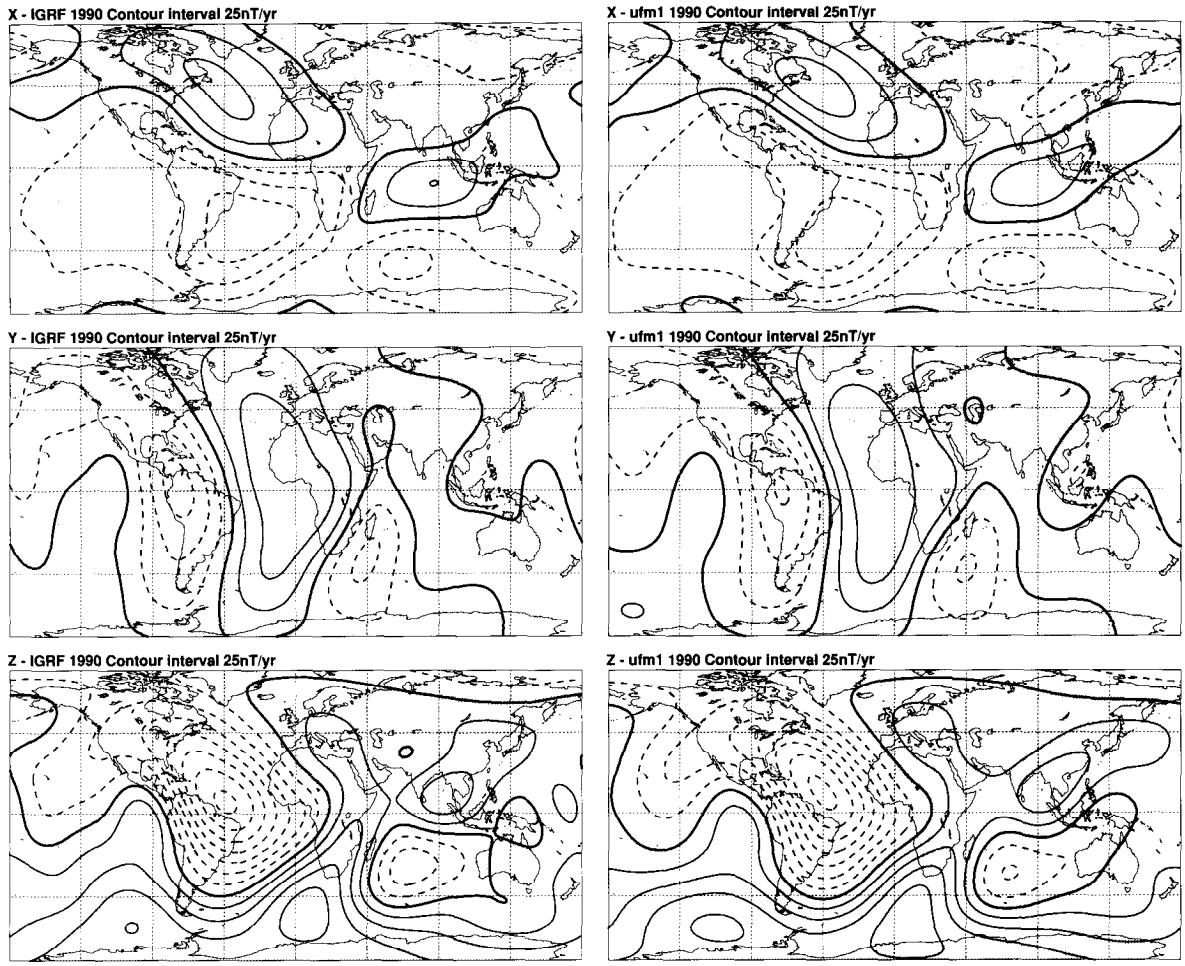

Fig. 5. Secular variation at the Earth's surface from IGRF 1990 and ufm1. Solid contours represent positive values, dashed contours negative values, and bold contours zero.

TABLE 6. Comparison of Secular Variation Models

Model Name	RMS $\partial B_r/\partial t$		RMS $\Delta\partial B_r/\partial t$	
	surface	cmb	surface	cmb
	nT/yr	nT/yr	nT/yr	nT/yr
1990				
ufm1	56	2053		
igrf 1990	55	2463	9	2105
1980				
ufm1	64	2066		
gsfc(9/80)	69	8016	26	7674
1970				
ufm1	61	2042		
gsfc(9/80)	61	7892	6	7633
1960				
ufm1	55	1983		
gsfc(9/80)	62	7938	19	7725

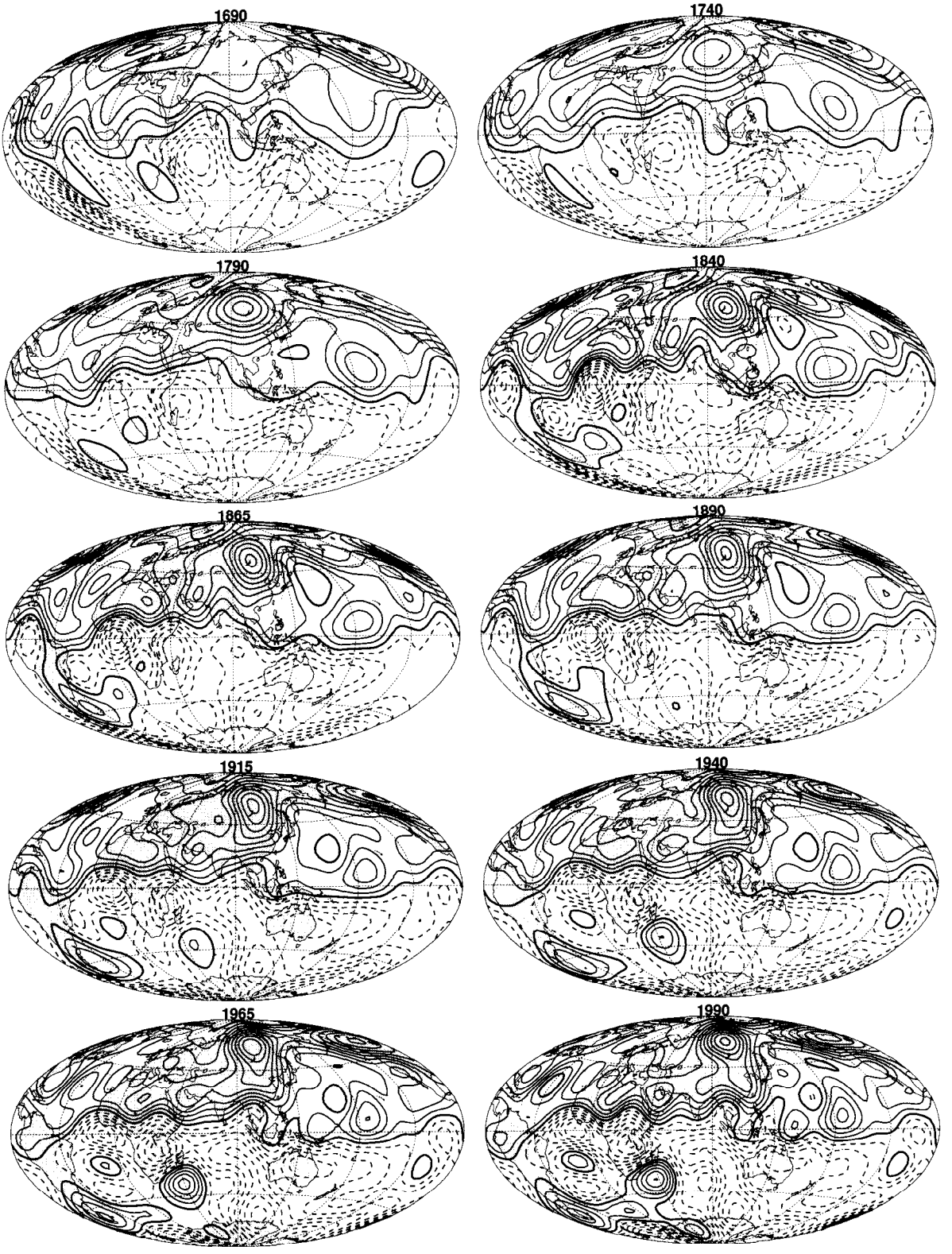

Fig. 6. The radial component of the magnetic field at the core-mantle boundary calculated from models ufm1 and ufm2. The contour interval is 100μT; solid contours represent flux into the core, dashed contours flux out of the core, and bold contours zero flux.

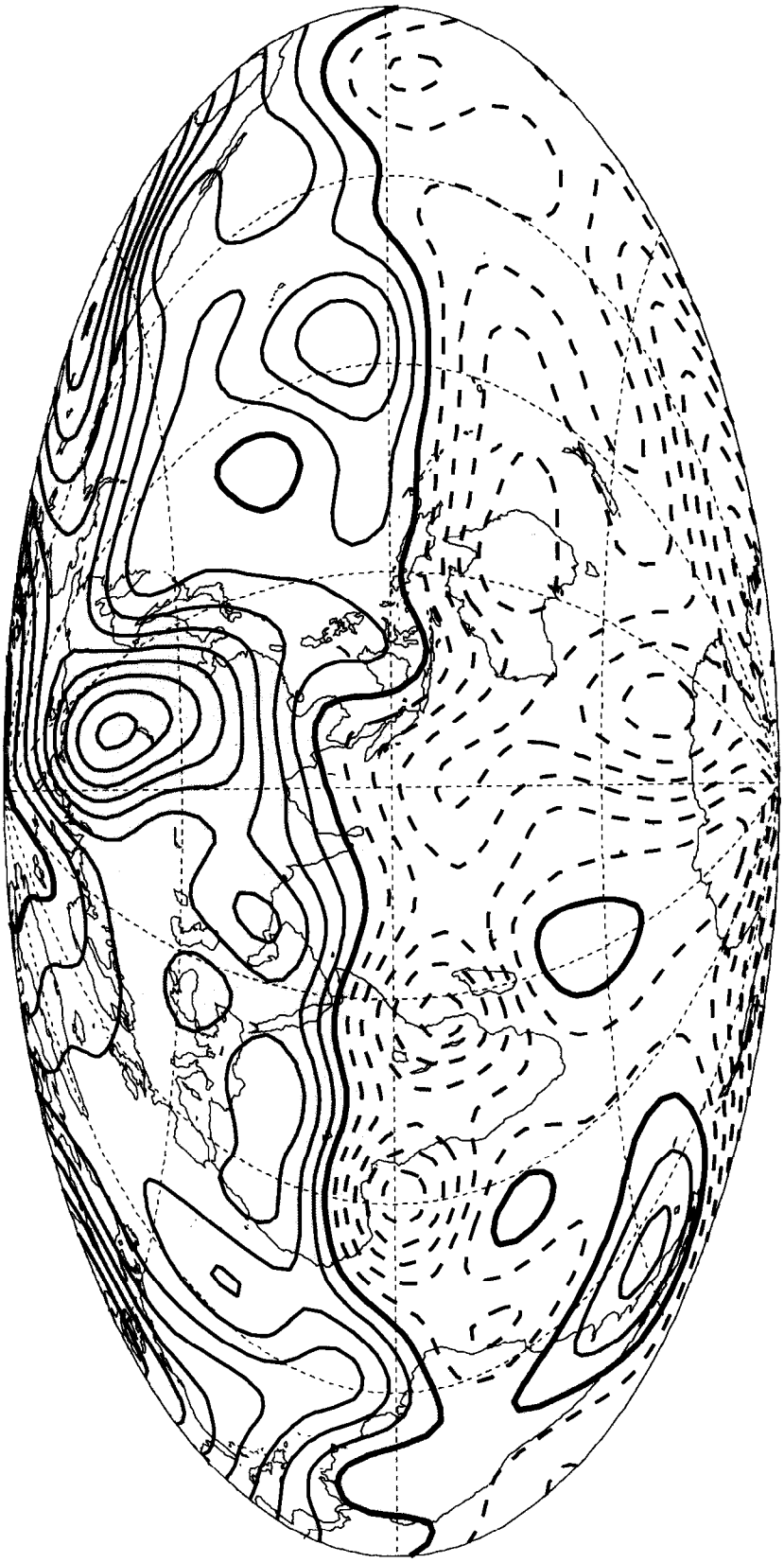

Fig. 7. The average radial field at the core-mantle boundary for the period 1840–1990.

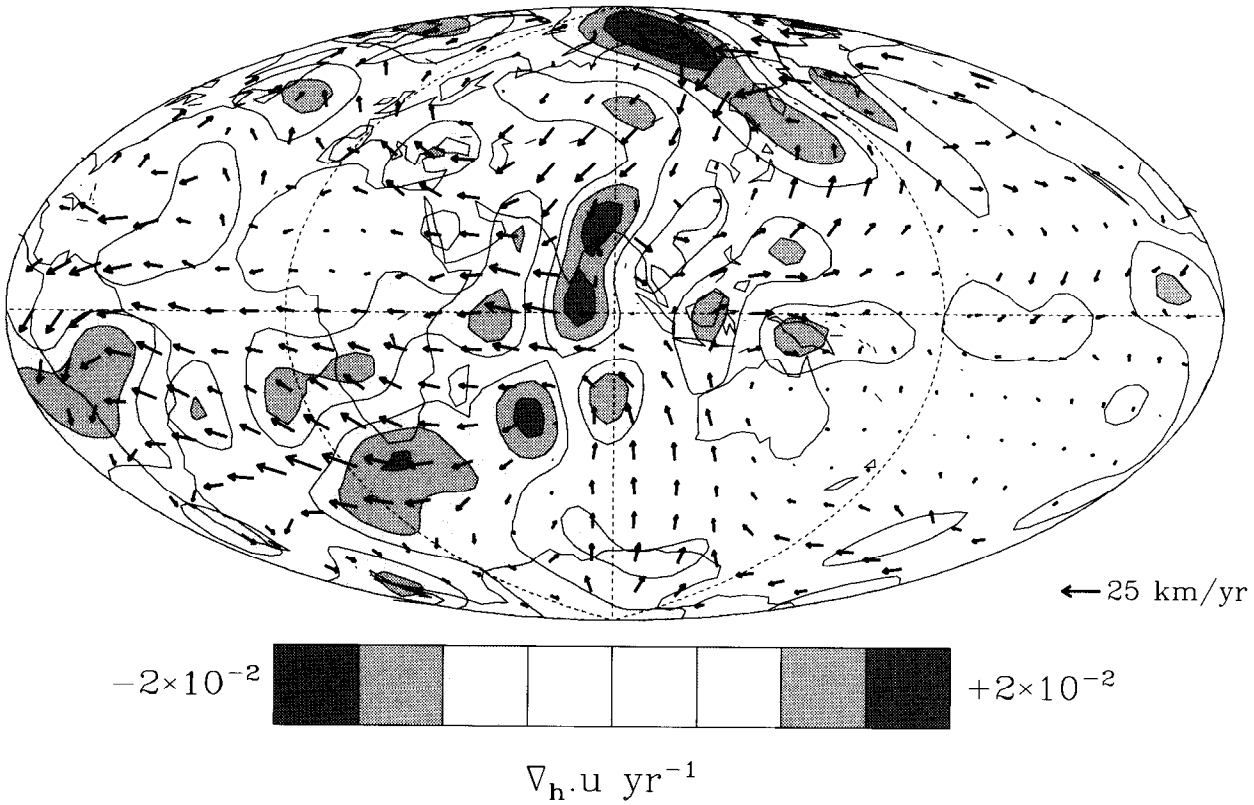

Fig. 8. The steady part of the fluid flow at the core surface for the period 1840–1990.

4. CONCLUDING REMARKS

It should be rather obvious to the reader from this article that the seemingly simple demand for accurate models of the magnetic field is not straightforwardly accommodated. Any map or model of the current magnetic field is necesarily based on data recorded some years previously, and so must be extrapolated forward using a model of the secular variation; maps of the magnetic field originating in the Earth's core are necessarily incomplete and are contaminated by crustal fields and external fields; and maps of the field, when continued downward to the core-mantle boundary, are very sensitive to the method of field modelling used. Any user of magnetic field maps or models must keep these shortcomings in mind, especially those who wish to map the magnetic field at the core-mantle boundary.

APPENDIX: DATA SOURCES

World Data Centers

World Data Center C1 for Geomagnetism
British Geological Survey
Murchison House
West Mains Road
Edinburgh
EH9 3LA
Scotland

World Data Center A for Marine Geology and Geophysics
National Geophysical Data Center
National Oceanic and Atmospheric Administration
325 Broadway
Boulder
CO 80303

World Data Center A for Rockets and Satellites
National Space Science Data Center
NASA Goddard Space Flight Center
Greenbelt
MD 20771

World Data Center A for Solid Earth Geophysics
National Geophysical Data Center
National Oceanic and Atmospheric Administration
325 Broadway
Boulder
CO 80303

Network Accessible Data Centers

Historical geomagnetic data are available over Internet by

1. anonymous ftp to geophysics.harvard.edu in directory ~ftp/geomag/data
2. anonymous ftp to earth.ox.ac.uk in directory ~ftp/geomag/data

REFERENCES

1. Barraclough, D.R., Spherical harmonic analysis of the geomagnetic field, *Geomagn. Bull. Inst. Geol. Sci., 8*, 1978.
2. Barraclough, D.R., and S. Macmillan, Survey data for geomagnetic field modelling, *Nasa Conf. Pub., 3153*, 41–74, 1992.
3. Barton, C.E., Magnetic repeat station data, *Nasa Conf. Pub., 3153*, 287–320, 1992.
4. Bloxham, J., Models of the magnetic field at the core-mantle boundary for 1715, 1777, and 1842, *J. Geophys. Res., 91*, 13,954–13,966, 1986.
5. Bloxham, J., and D. Gubbins, Geomagnetic field analysis - IV: Testing the frozen-flux hypothesis, *Geophys. J. R. Astron. Soc., 84*, 139–152, 1986.
6. Bloxham, J., and A. Jackson, Fluid flow near the surface of Earth's outer core, *Rev. Geophys., 29*, 97–120, 1991.
7. Bloxham, J., and A. Jackson, Time-dependent mapping of the magnetic field at the core-mantle boundary, *J. Geophys. Res., 97*, 19,537-19,563, 1992.
8. Bloxham, J., D. Gubbins, and A. Jackson, Geomagnetic secular variation, *Phil. Trans. R. Soc. Lond., A329*, 415–502, 1989.
9. Cain, J.C., Z. Wang, D.R. Schmitz, and J. Meyer, The geomagnetic spectrum for 1980 and core-crustal separation, *Geophys. J., 97*, 443–447, 1989.
10. Coleman, R.J., Project Magnet high-level vector survey data reduction, *Nasa Conf. Pub., 3153*, 215–248, 1992.
11. Gubbins, D., and P.H. Roberts, Magnetohydrodynamics of the Earth's core, in *Geomagnetism*, edited by J.A. Jacobs, vol. 2, pp. 1–183, Academic Press, London, 1987.
12. Gubbins, D., and J. Bloxham, Geomagnetic field analysis III: Magnetic fields on the core-mantle boundary, *Geophys. J. R. Astron. Soc., 80*, 695–713, 1985.
13. Hood, P., Survey parameters and availability of low-level aeromagnetic data for geomagnetic field modelling, *Nasa Conf. Pub., 3153*, 249–286, 1992.
14. Hutcheson, K.A., and D. Gubbins, Earth's magnetic field in the seventeenth century, *J. Geophys. Res., 95*, 10,769–10,781, 1990.
15. IAGA Division V, Working Group 8, IGRF, 1991 Revision, *Eos, Trans. Am. Geophys. Union, 73*, 182, 1992.
16. Jackson, A., Accounting for crustal magnetization in models of the core magnetic field, *Geophys. J. Int., 103*, 657–673, 1990.
17. Jackson, A., Historical data for geomagnetic field modelling, *Nasa Conf. Pub., 3153*, 1–30, 1992.
18. Langel, R.A., The main field, in *Geomagnetism*, edited by J.A. Jacobs, vol. 1, pp. 249–512, Academic Press, London, 1987.
19. Langel, R.A., and R.H. Estes, The near-earth magnetic field at 1980 determined from Magsat data, *J. Geophys. Res., 90*, 2487–2494, 1989.
20. Langel, R.A., and R.T. Baldwin, Types and characteristics of data for geomagnetic field modeling, *Nasa Conf. Pub., 3153*, 1992a.
21. Langel, R.A., and R.T. Baldwin, Satellite data for geomagnetic field modelling, *Nasa Conf. Pub., 3153*, 41–74, 1992b.
22. Langel, R A., R.H. Estes, and G.D. Mead, Some new methods in geomagnetic field modelling applied to the 1960–1980 epoch, *J. Geomagn. Geoelectr., 34*, 327–349, 1982.
23. Langel, R.A., R.H. Estes, and T.J. Sabaka, Uncertainty estimates in geomagnetic field modelling, *J. Geophys. Res., 94*, 12,281–12,299, 1989.
24. Sharman, G.F., and D. Metzger, Marine magnetic data holdings of World Data Center A for Marine Geology and Geophysics, *Nasa Conf. Pub., 3153*, 137–148, 1992.
25. Shure, L., R.L. Parker, and R.A. Langel, A preliminary harmonic spline model from Magsat data, *J. Geophys. Res., 90*, 11,505–11,512, 1985.

Present Plate Motions and Plate Boundaries

Richard G. Gordon

1. ABSTRACT

About 85% of Earth's surface is covered by (nearly) rigid tectonic plates and about 15% of Earth's surface is covered by deforming crust and lithosphere within plate boundary zones. Most plate boundaries within oceanic lithosphere are narrow (~1 to ~60 km wide), but some oceanic plate boundaries and nearly all continental boundaries are hundreds to thousands of kilometers wide. The geologically recent velocities between nearly all the plates are well described by global plate motion model NUVEL-1, which is determined from 3 types of data: spreading rates determined from the spacing of magnetic anomalies on profiles across mid-ocean ridges, the azimuths of submarine transform faults, and the azimuth of slip inferred from seismologically determined earthquake focal mechanisms. Plate motions relative to the deep mantle are known much less accurately and many questions still remain about the most appropriate approach, if any, for estimating such motions. Results over the past dozen years from space geodesy, which includes very long-baseline radio interferometry, satellite laser ranging, and the global positioning system, have been providing accurate long-distance measurements that can be used to estimate the present motion across and within wide plate boundary zones. In particular, space-geodetic data can be used to estimate motion between the Pacific, North American, and Eurasian plates, as well as the motion of the Sierra Nevada-Great Valley microplate relative to these plates; these results show that plate velocities averaged over years are remarkably similar to velocities averaged over millions of years.

R. G. Gordon, Department of Geological Sciences, Northwestern University, Evanston, IL 60208-2150

Global Earth Physics
A Handbook of Physical Constants
AGU Reference Shelf 1

2. INTRODUCTION

Plate motion, Earth's most important tectonic process, was first quantitatively described about 25 years ago [50, 61, 68, 98]. Earth's strong outer layer that comprises the plates is termed the lithosphere, which typically includes the crust and the uppermost mantle and is of variable thickness but may typically be ~100-km thick. The presumably much weaker layer immediately below the lithosphere is termed the asthenosphere. That geomagnetic reversals are recorded by the seafloor as it spreads away from mid-ocean ridges [90] made possible the confirmation of seafloor spreading and the estimation of seafloor spreading rates [71, 89], which vary from a low of 12 mm/yr across the Arctic Ridge to a high of 160 mm/yr across the East Pacific Rise between the Pacific and Nazca plates, with a median rate of ~40 mm/yr (Figure 1). Convergence rates between the stable interiors of plates meeting at deep sea trenches range from a low of ~20 mm/yr along the southern Chile trench, where the Antarctic plate underthrusts the South American plate, to ~110 mm/yr along the Australia-Pacific plate boundary with a median rate of ~70 mm/yr [23] (Figure 1).

Because tectonic plates move along the nearly spherical surface of Earth and because plates appear to an excellent approximation to be rigid, motion between plates can be represented simply as rigid body rotations. In the limiting case of geologically recent motion (that

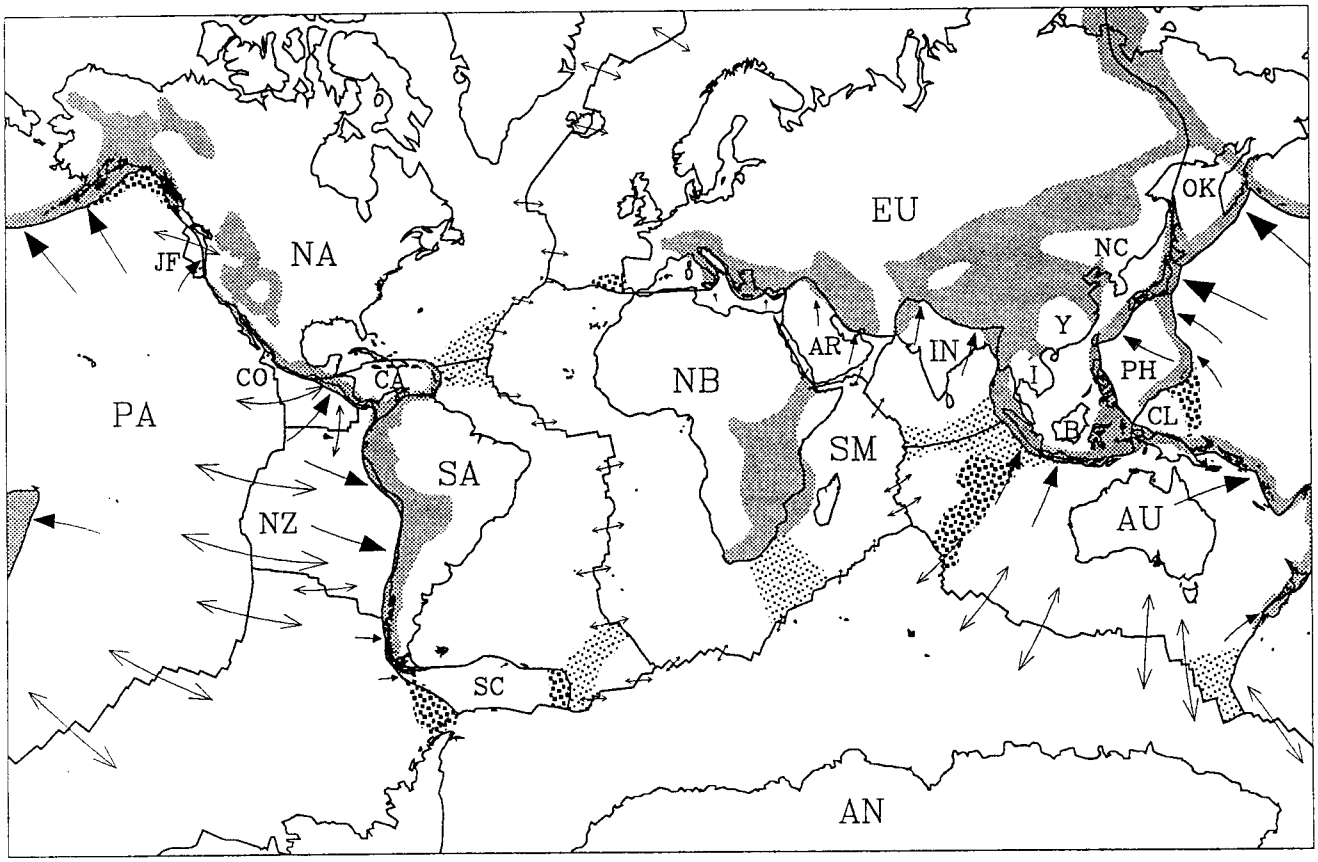

Fig. 1. Map showing idealized narrow plate boundaries, velocities between plates, and regions of deforming lithosphere. Plate velocities are shown by arrows. The length of the arrows shows what the displacement would be if the plates were to maintain their present relative angular velocity for 25 million years. The plate separation rate across mid-ocean ridges is shown by symmetrical diverging arrows with unclosed arrowheads at both ends. The plate convergence rate is shown by asymmetrical arrows with one solid arrowhead, which are shown on the underthrust plate where convergence is asymmetric and the polarity is known. Each convergence arrow points toward the overthrust plate. The outlines of deforming regions are approximate and the existence of some deforming zones is speculative. Separate small plates or blocks are labeled in southeast Asia, but their uncertainly located and possibly nonexistent boundaries are not shown in their entirety. Fine stipple shows mainly subaerial regions where the deformation has been inferred from seismicity, topography, other evidence of faulting, or some combination of these. Medium stipple shows mainly submarine regions where the nonclosure of plate circuits indicates measurable deformation; in most cases these zones are also marked by earthquakes. Coarse stipple shows mainly submarine regions where the deformation is inferred mainly from the presence of earthquakes. These deforming regions form wide plate boundary zones, which cover ~15% of Earth's surface. Future observations may demonstrate that deforming lithosphere covers an area larger or smaller than shown here. Idealized plate boundaries (solid curves) are after Argus and Gordon [4] with the addition of the Scotia plate and several other minor changes. Plate abbreviations: B, Borneo; AN, Antarctica; AR, Arabia; AU, Australia; CA, Caribbean; CL, Caroline; CO, Cocos; EU, Eurasia; I, Indo-China; IN, India; JF, Juan de Fuca; NA, North America; NB, Nubia; NC, North China; NZ, Nazca; OK, Okhotsk; PA, Pacific; SA, South America; SC, Scotia Sea; SM, Somalia; Y, Yangtze. Modified from Gordon and Stein [36].

is, the average over a few million years), the time derivative of rigid-body rotation can be described by an angular velocity, which is an axial vector. The assumption of plate rigidity allows geometrically precise and rigorously testable predictions to be made. The observed near rigidity of the plates also permits the treatment of plate kinematics separately from the dynamics. Abundant data describe the geologically recent motion across narrow boundaries linking nearly all the major plates, permitting many tests of plate tectonic predictions. An accurate description of geologically recent plate velocities is an essential constraint on the sum of deformation within mobile belts, which can be considered to be wide plate boundary zones.

In this chapter I first review current knowledge of geologically recent plate kinematics and the present plate configuration and boundaries. I then review available results and implications of space-geodetic data that describe the kinematics of the crust and lithosphere over approximately the past dozen years.

3. PLATE TECTONIC DATA

The ability to make and to test plate tectonic predictions grows with the accuracy of the available observations. Our knowledge of geologically recent plate motions depends mainly upon 3 types of data. The first data type is a spreading rate estimated from the observed spacing of magnetic anomalies across mid-ocean ridges. The spacing of the magnetic anomalies can be used to estimate rates of seafloor spreading, provided that the history of geomagnetic reversals is accurately known. The acquisition of marine magnetic anomaly data for determining seafloor spreading rates has not changed fundamentally in the past 25 years. However, the number and quality of data have improved through expanded geographical coverage, more accurate navigation, and the acquisition of closely spaced profiles and of profiles paralleling the direction of plate motion. The shortest interval over which spreading rates can be determined is the interval between geomagnetic reversals, which ranges from tens of thousands to tens of millions of years [18, 58]. The shortest possible averaging interval for geologically recent spreading rates is 780,000 years, the age of the most recent geomagnetic reversal [7], but rates are more typically averaged over the past few million years. These longer averaging intervals were probably adopted in early work to increase the accuracy of estimated rates (at the expense of less resolution in time), and have been carried through in later work for consistency and comparison with earlier work. With the data now available, however, spreading rates could be usefully estimated worldwide over the interval only since the most recent reversal.

The second data type is the azimuth of a submarine transform fault estimated from bathymetric observations. Although submarine transform-fault zones are narrow, they typically consist of several parallel fault strands. For the approximation to a single fault to be reasonable, the fault system should be long compared with its width. The overall azimuth of the fault zone, and not the azimuth of individual faults within it, is used to estimate the direction of relative plate motion. The accuracy with which the azimuth of transforms can be estimated depends on the type of bathymetric data used. Azimuths estimated from precision-depth-recorder surveys are less accurate (about ±10°) than azimuths from multi-beam or side-scan sonar bathymetry (about ±3°) [6, 23, 75]. The poorly known time interval over which the azimuth of a transform fault averages motion is probably less than millions of years, but more than centuries. Seismic sections across the active fault zone of the Vema transform fault show that faulting within the top 200–500 m of sediment is confined to a 500-m-wide zone, showing that the locus of faulting is stable over hundreds of thousands of years, at least at this one location [9, 27].

The third data type is the azimuth of slip calculated from a focal mechanism inferred from the radiation pattern of seismic waves from an earthquake along a transform fault or at a trench. The slip directions from large earthquakes along submarine transform faults surely give less accurate (about ±10° to ±15°) estimates of the direction of plate motion than are obtained from fault azimuths [6, 23], but the probable uncertainties and biases have never been thoroughly investigated as far as I know. The horizontal projection of the slip direction in shallow thrust-fault earthquakes at trenches provides the largest number of azimuths used to estimate plate motions. Because the slip in earthquakes releases the strain accumulated over decades, centuries, or millennia, earthquake slip directions probably average motion over a much shorter interval than is averaged by spreading rates or by transform fault azimuths. The number and the quality of estimates of earthquake slip directions have improved during the past decade. Before the 1980s, nearly all seismological data were in analog form. Most focal mechanisms were estimated only from the polarity of the first motion of body waves, with little or no use made from the information in the rest of the seismogram. Digitally recorded data,

which have become widely and rapidly available over the past decade through computer and telephone networks, facilitate the routine use of waveform modeling to estimate earthquake focal mechanisms. The increase in quality does not, however, imply that the slip directions have no systematic errors or even that the systematic errors in slip directions and mechanisms from digital data are any smaller than those from first motions from analog records.

4. GEOLOGICALLY RECENT PLATE MOTIONS

Global models of the geologically recent velocities between plates are determined by systematic inversion of all available plate motion data [13, 14, 62, 64]. Such a model is described by a set of angular velocities specifying the motion of each plate relative to one arbitrarily fixed plate. Table 1 specifies the motion of 11 plates relative to the Pacific plate for the most recently published global plate motion model, NUVEL-1, which gives a good fit to all available plate motion data [23]. The motion of 4 other plates relative to the Pacific plate are also given in Table 1. The angular velocity describing the motion between any pair of plates can then be determined by vector subtraction, as is given in Tables 2a and 2b. Angular velocities are often specified in spherical coordinates by their rotation rate (magnitude) and pole (latitude and longitude). The velocity of one plate relative to another at any point along their mutual narrow plate boundary is the cross product of the appropriate angular velocity and the point position vector.

The angular velocities given in Table 1 constitute a 16-plate model that represents the best estimates available from plate motion data. In this sense, the model is nearly complete, but with some shortcomings, including the following. The motion of China and southeast Asia, which may be composed of several plates (Figure 1), is incorrectly represented in this model because it is not possible to estimate its motion relative to other plates with plate motion data. Instead this region has been included with the Eurasian plate. Someday, it should be possible to resolve the motion of sites in this region using space-geodetic data, which would eventually resolve how much, if any, this region moves relative to the rest of the Eurasian plate and which portions of the region are part of a plate or plates and which are part of a deforming zone. Some small plates have also been omitted from Table 1, including the Caroline plate [92], the North Bismarck, South Bismarck, and Solomon Sea plates [49], the Adriatic microplate [1], which has been incorporated into the African plate, the Turkish, Central Iranian, and South Caspian Sea microplates [47], the South Sandwich plate [70], and the Sierra Nevada-Great Valley microplate [3, but see the section below on results from space geodesy]. Except possibly for the Caroline plate, all these plates are arguably part of plate boundary zones between much larger plates.

Another shortcoming of the model specified by Table 1 is the treatment of Nubia and Somalia as a single African plate. Extension across the East African Rift Valleys that separate Nubia from Somalia (Figure 1) is fast enough that Red Sea spreading rates are 2–4 mm/yr faster than predicted from the NUVEL-1 Arabia-Africa angular velocity [see figure 53 of DeMets et al., 23]. This observation, along with observations of the seismicity, geometry of African deformation, and lack of deformation in southernmost Africa and in the African seafloor northwest of the Southwest Indian Ridge suggest that extension of about 3 mm/yr occurs near the northernmost portion of the Nubian-Somalian plate boundary zone (in the Afar region) and decreases smoothly south- and southeastward toward the Nubia-Somalia pole, which might be located in the southern ocean southeast of South Africa but northwest of the Southwest Indian Ridge.

A final shortcoming of Table 1 and of any model that only incorporates the major plates is that predicted rates of subduction at converging plate boundaries are unlikely to be accurate because of the deformation of the leading edge of the overriding plate (discussed in part below). In particular, predicted rates of convergence will be too low where the overriding plate includes an actively spreading backarc basin [cf., 15].

5. PLATE BOUNDARY ZONES

A plate boundary zone is the zone of active deformation that takes up the motion between nearly rigid plates. Earth's surface would be covered completely by a mosaic of plates that interact only along their edges if plate boundaries were lines having no width (Figure 1), but real plate boundary zones vary in width from a few hundred meters [31, 75] for some oceanic transform plate boundaries to thousands of kilometers within the deforming zone taking up motion between India and Eurasia [67] (Figure 1). Herein I refer to plate boundary zones as narrow if they are up to ~60 km wide, the maximum width of the plate boundary zones of mid-ocean ridges [53, 54], and wide if they are hundreds to thousands of kilometers wide.

Plate boundaries can be classified into three types

Table 1. NUVEL-1 Angular Velocities (Pacific Plate Fixed)

Plate	Latitude °N	Longitude °E	ω (deg–Myr^{-1})	ω_x	ω_y (radians–Myr^{-1})	ω_z
Africa	59.160	–73.174	0.9695	0.002511	–0.008303	0.014529
Antarctica	64.315	–83.984	0.9093	0.000721	–0.006841	0.014302
Arabia	59.658	–33.193	1.1616	0.008570	–0.005607	0.017496
Australia	60.080	1.742	1.1236	0.009777	0.000297	0.016997
Caribbean	54.195	–80.802	0.8534	0.001393	–0.008602	0.012080
Cocos	36.823	–108.629	2.0890	–0.009323	–0.027657	0.021853
Eurasia	61.066	–85.819	0.8985	0.000553	–0.007567	0.013724
India	60.494	–30.403	1.1539	0.008555	–0.005020	0.017528
Nazca	55.578	–90.096	1.4222	–0.000023	–0.014032	0.020476
North America	48.709	–78.167	0.7829	0.001849	–0.008826	0.010267
South America	54.999	–85.752	0.6657	0.000494	–0.006646	0.009517
Additional Angular Velocities (Pacific Plate Fixed)						
Juan de Fuca	35.0	26.0	0.53	0.00681	0.00332	0.00531
Philippine	0.	–47.	1.0	0.0119	0.0128	0.000
Rivera	31.0	–102.4	2.562	–0.4716	–2.1448	1.3195
Scotia Sea	56.5	–79.1	0.63	0.0011	-0.0060	0.0092

Each angular velocity describes a right-handed rotation relative to the Pacific plate. NUVEL-1 angular velocities are from DeMets et al. [23]. The Juan de Fuca-Pacific angular velocity is from Wilson [96], the Philippine-Pacific angular velocity is from Seno et al. [76], the Rivera-Pacific angular velocity is from DeMets and Stein [21], and the Scotia Sea-Pacific angular velocity was calculated by adding the Scotia Sea-Antarctic angular velocity of Pelayo and Wiens [70] to the Antarctic-Pacific angular velocity given above. To revise these angular velocities for consistency with recent revisions to the geomagnetic reversal time scale [45], multiply the rates by 0.9562, as was done in constructing the NUVEL-1A global plate motion model [25].

depending on whether the motion between two plates (1) contains a component of divergence, (2) contains a component of convergence, or (3) is precisely parallel to the boundary with neither convergence nor divergence. The most common examples of the first are mid-ocean ridges where the divergence is distributed over a plate boundary zone 8 to 20 km wide at fast spreading centers to ~60 km wide at slow spreading centers [53, 54]. Most of the divergence, however, is likely concentrated in the neovolcanic zone (the area straddling the spreading axis in which most of the recent and ongoing surficial volcanism occurs), which is typically 1 to 3 km wide [53, 54]. The most common examples of the second are deep-sea trenches where oceanic lithosphere of one plate is subducted beneath another plate. A line of volcanoes atop the overriding plate marks the surface arc below which the subducting plate reaches a depth of ~100 km. Permanent deformation associated with trench plate boundaries is in many regions distributed within the overriding plate for hundreds of kilometers, but most of the motion is likely taken up along a single thrust fault zone, which may be only a few kilometers or less thick. The third type of plate boundary occurs in almost every case as a submarine transform fault, which with few exceptions offsets two mid-ocean ridge segments. Transform faults are vertical faults along which horizontal slip occurs parallel to the fault and parallel to the direction of relative plate motion. Continental transform faults are rarer and nearly everywhere are much further from a geometrically ideal transform fault than are submarine faults. Seafloor-imaging studies using multi-beam and side-scan sonar show that the active trace of submarine transform faults, which is termed the transform fault

Table 2a. NUVEL-1 Angular Velocities:
Pairs of Plates Sharing a Boundary

Plate Pair	Latitude °N	Longitude °E	ω (deg–Myr^{-1})	Error Ellipse σ_{max}	σ_{min}	ζ_{max}	σ_ω (deg–Myr^{-1})
			Pacific Ocean				
na-pa	48.7	–78.2	0.78	1.3	1.2	–61	0.01
co-pa	36.8	–108.6	2.09	1.0	0.6	–33	0.05
co-na	27.9	–120.7	1.42	1.8	0.7	–67	0.05
co-nz	4.8	–124.3	0.95	2.9	1.5	–88	0.05
nz-pa	55.6	–90.1	1.42	1.8	0.9	–1	0.02
nz-an	40.5	–95.9	0.54	4.5	1.9	–9	0.02
nz-sa	56.0	–94.0	0.76	3.6	1.5	–10	0.02
an-pa	64.3	–84.0	0.91	1.2	1.0	81	0.01
pa-au	–60.1	–178.3	1.12	1.0	0.9	–58	0.02
eu-pa	61.1	–85.8	0.90	1.3	1.1	90	0.02
co-ca	24.1	–119.4	1.37	2.5	1.2	–60	0.06
nz-ca	56.2	–104.6	0.58	6.5	2.2	–31	0.04
			Atlantic Ocean				
eu-na	62.4	135.8	0.22	4.1	1.3	–11	0.01
af-na	78.8	38.3	0.25	3.7	1.0	77	0.01
af-eu	21.0	–20.6	0.13	6.0	0.7	–4	0.02
na-sa	16.3	–58.1	0.15	5.9	3.7	–9	0.01
af-sa	62.5	–39.4	0.32	2.6	0.8	–11	0.01
an-sa	86.4	–40.7	0.27	3.0	1.2	–24	0.01
na-ca	–74.3	–26.1	0.11	25.5	2.6	–52	0.03
ca-sa	50.0	–65.3	0.19	15.1	4.3	–2	0.03
			Indian Ocean				
au-an	13.2	38.2	0.68	1.3	1.0	–63	0.00
af-an	5.6	–39.2	0.13	4.4	1.3	–42	0.01
au-af	12.4	49.8	0.66	1.2	0.9	–39	0.01
au-in	–5.6	77.1	0.31	7.4	3.1	–43	0.07
in-af	23.6	28.5	0.43	8.8	1.5	–74	0.06
ar-af	24.1	24.0	0.42	4.9	1.3	–65	0.05
in-eu	24.4	17.7	0.53	8.8	1.8	–79	0.06
ar-eu	24.6	13.7	0.52	5.2	1.7	–72	0.05
au-eu	15.1	40.5	0.72	2.1	1.1	–45	0.01
in-ar	3.0	91.5	0.03	26.1	2.4	–58	0.04

TABLE 2a. (continued).

Plate Pair	Latitude °N	Longitude °E	ω (deg–Myr^{-1})	Error Ellipse σ_{max}	σ_{min}	ζ_{max}	σ_ω (deg–Myr^{-1})
Additional (non-NUVEL-1) Angular Velocities for the Scotia Sea plate							
sc-sa	–18.7	-58.9	0.08	13.	2.	–4	
sc-an	–79.1	-64.4	0.30	2.	1.	10	

The first plate moves counterclockwise relative to the second plate. Plate abbreviations: af, Africa; an, Antarctica; ar, Arabia; au, Australia; ca, Caribbean; co, Cocos; eu, Eurasia; in, India; na, North America; nz, Nazca; pa, Pacific; sa, South America; sc, Scotia Sea. See Figure 1 for plate geometries. One sigma-error ellipses are specified by the angular lengths of the principal axes and by the azimuths (ζ_{max}, given in degrees clockwise from north) of the major axis. The rotation rate uncertainty is determined from a one-dimensional marginal distribution, whereas the lengths of the principal axes are determined from a two-dimensional marginal distribution. Rotation rate uncertainties are unavailable for the Scotia Sea plate. All angular velocities in Table 2 are from DeMets et al. [23], except for the two Scotia Sea angular velocities, which are from Pelayo and Wiens [70]. To revise these angular velocities for consistency with recent revisions to the geomagnetic reversal time scale [45], multiply the rates and the rate uncertainties by 0.9562, as was done in constructing the NUVEL-1A global plate motion model [25].

zone and constitutes the plate boundary zone, is typically 0.5- to 2-km wide [31, 75].

Wherever plate boundaries pass through continents, the boundaries are hundreds to thousands of kilometers wide (Figure 1). Examples include the Alpine-Himalayan deformation belt, the Pacific-North America boundary in the western conterminous U.S. and in southern Alaska, the East African Rift Valleys, and the Australia-Pacific boundary where it passes through New Zealand (Figure 1). Thus, as has been long recognized, plate tectonics poorly describes the kinematics and tectonics of continental plate boundary zones. Less obvious has been the failure of plate tectonics to describe the kinematics of all oceanic lithosphere. The distribution of earthquake epicenters in the oceans differs considerably from that on the continents. In contrast to the wide bands of earthquakes marking continental plate boundaries, narrow bands of earthquakes no wider than a few tens of kilometers mark many of the major oceanic plate boundaries (see, for example, figure 2 of Gordon and Stein [36]). Undoubtedly plate tectonics is more successful when applied to the oceans—mid-ocean ridges have narrow plate-boundary zones and submarine transform faults have very narrow plate-boundary zones.

Some oceanic deformation is nonetheless poorly described by a model of rigid plates separated by narrow boundaries. The outstanding example of a wide oceanic plate boundary is in the equatorial Indian Ocean east of the Central Indian Ridge and west of the Sumatra trench (Figure 1) [38, 73, 94]. Large earthquakes occur within this zone [40, 82, 86]. Reflection seismic profiles of the thick sediments in the Bengal Fan overlying equatorial Indian Ocean seafloor also show that this region has deformed [10, 11, 12, 19, 20, 26, 32, 93]. Instead of being flat-lying, as would be expected for deposition atop a rigid plate, the sediments are folded into wavelike undulations and are cut by high-angle reverse faults. The orientation of the folds and faults indicate that the oceanic crust is being shortened in a north-south direction. Undulations in the satellite-derived gravity field above the Indian Ocean also suggest north-south shortening [43, 56, 83]. Moreover, Indian Ocean plate motion data are poorly fit if a single, rigid Indo-Australian plate is assumed [23, 24, 38, 62, 81].

Wide plate boundary zones occur within oceanic lithosphere in several other regions. The Gorda deformation zone takes up part of the motion between the Juan de Fuca and Pacific plates [78, 84, 85, 95, 97] and can be interpreted as a wide plate boundary zone [33, 95]. Another region where it seems likely that the deformation of oceanic lithosphere has been distributed is in the Atlantic west of the Mid-Atlantic Ridge and east of the Lesser Antilles. Other examples of likely wide oceanic plate boundary zones are the lithosphere

Table 2b. NUVEL-1 Angular Velocities:
Pairs of Plates not Sharing a Boundary

Plate Pair	Latitude °N	Longitude °E	ω (deg–Myr^{-1})	Error Ellipse σ_{max}	σ_{min}	ζ_{max}	σ_ω (deg–Myr^{-1})
ca-af	–64.7	–165.0	0.16	19.5	9.8	–86	0.03
co-af	17.9	–121.4	1.37	1.7	0.8	–83	0.05
nz-af	43.5	–113.9	0.49	5.2	2.2	–26	0.02
ar-an	21.9	8.9	0.49	5.9	1.6	–80	0.04
ca-an	–49.7	–69.1	0.17	17.3	5.1	–06	0.03
co-an	18.1	–115.8	1.39	1.4	0.8	–78	0.05
eu-an	–37.8	–103.0	0.05	25.1	14.5	49	0.01
in-an	21.9	13.1	0.50	9.9	1.7	–84	0.05
ar-au	4.7	–101.6	0.35	7.5	2.4	61	0.05
ar-ca	34.9	22.7	0.54	7.0	4.6	–63	0.05
au-ca	21.9	46.7	0.76	3.9	3.2	–56	0.02
in-ca	34.2	26.6	0.55	9.4	4.4	–66	0.06
ar-co	–8.7	50.9	1.65	1.8	1.2	–72	0.07
au-co	–8.2	55.7	1.96	1.3	0.6	–79	0.05
in-co	–8.5	51.7	1.67	1.9	1.3	73	0.09
ca-eu	–51.0	–50.9	0.12	22.7	6.5	–25	0.03
co-eu	20.0	–116.2	1.36	1.6	1.0	–81	0.05
nz-eu	46.1	–95.1	0.54	4.8	2.5	–09	0.02
an-na	60.5	119.6	0.27	4.2	2.0	–22	0.01
ar-na	44.1	25.6	0.59	4.8	1.4	–39	0.04
au-na	29.1	49.0	0.79	1.6	1.0	–53	0.01
in-na	43.3	29.6	0.61	7.5	1.5	–52	0.06
nz-na	61.5	–109.8	0.67	4.0	1.8	–24	0.02
ar-nz	–13.9	44.4	0.71	4.2	2.2	31	0.05
au-nz	–11.3	55.6	1.01	2.2	1.3	43	0.02
in-nz	–13.3	46.4	0.73	5.3	1.9	42	0.07
af-pa	59.2	–73.2	0.97	1.1	1.0	86	0.01
ar-pa	59.7	–33.2	1.16	3.8	0.9	–88	0.02
ca-pa	54.2	–80.8	0.85	3.4	1.2	–11	0.03
in-pa	60.5	–30.4	1.15	5.5	1.1	82	0.02
sa-pa	55.0	–85.8	0.67	1.8	1.6	–64	0.01
ar-sa	44.4	7.3	0.65	5.2	1.5	–59	0.04
au-sa	32.8	36.8	0.79	1.3	1.2	18	0.01
co-sa	28.0	–115.0	1.51	1.5	0.8	–56	0.05
eu-sa	77.6	–86.3	0.25	4.8	1.4	–66	0.02
in-sa	44.2	11.4	0.66	8.1	1.7	–69	0.04

The conventions and notes are the same as in Table 2a.

immediately west of the Macquarie Ridge Complex [22, 55], lithosphere east of the South Sandwich trench [23], the boundary between the Caroline and Pacific plates [92], and the western boundary between the Scotia and Antarctic plates [70].

Another important, but lesser, exception to the assumption of narrow boundaries occurs in the leading edge of the overriding plate at obliquely converging trench plate boundaries. Many plates overriding trenches include strike-slip faults that are typically 100 to 300 km from—and parallel to—the trench [30, 48]. Examples include the Samangko fault (Sumatra), the Philippine fault, the Median Tectonic Line (southwest Japan), the Atacama fault (Chile), the Dolores-Guayaquil fault (Colombia and Ecuador), and the Liquina-Ofqui fault (south Chile). Where such strike-slip motion occurs, the azimuth of slip of the thrust earthquakes should not parallel the direction of motion between the underthrust plate and the interior of the overriding plate. If all the trench-parallel motion were taken up along the strike-slip fault or faults, then the azimuths of slip in the thrust earthquakes would be perpendicular to the trench. Observed slip azimuths lie between the direction of plate motion and the perpendicular to the trench [23, 48]. Moreover, the direction of motion estimated from earthquake slip azimuths along trench plate boundaries differs significantly in every case from independent estimates of the motion calculated from plate circuit closure [23]. Thus, the slip directions are biased indicators (up to ~30°) of the plate motion direction and the trench-parallel motion is only partly taken up by strike-slip faulting. Trench-parallel motion of the forearc relative to the main overriding plate varies along strike and therefore is not simply the motion of a rigid forearc plate relative to the main plate [57]. A probably small but very poorly known amount of this discrepancy between the plate motion direction and slip direction inferred from an earthquake may be due to as-of-yet poorly quantified biases due to lateral heterogeneities in the speed of propagation of seismic waves associated with the presence of subducting slabs. Nevertheless, the thrust-faulting slip directions lend further support to the conclusion that part of the plate motion is taken up within the overriding plate. The amount of convergence obliquity varies considerably along Earth's trenches, but there are few places where it is negligible; thus deforming belts hundreds of kilometers wide within the leading edge of the overriding plate are not the exception, but the rule.

6. PLATE RIGIDITY

Because no real materials are truly rigid, the assumption of plate rigidity is, of course, an idealization. The presence of small earthquakes in plate interiors, the vertical motions associated with mid-plate hotspot swells, and other evidence of minor deformation within plate interiors further show that the plates are only approximately rigid. Therefore, the fundamental question of interest is not the qualitative one of whether the plates are rigid—they are not. Instead the fundamental question is quantitative: how much do the plates deform, and what bounds can we place on this deformation from available or obtainable data?

Gordon et al. [37] formulated a test of plate circuit closure —and hence of plate rigidity— using plate motion data. This test was applied to carefully defined plate interiors, i.e., the most prominent wide plate boundary zones described above were excluded from plate interiors. Such tests using all available plate motion data show that most plate circuits are consistent with closure and therefore with plate rigidity [6, 22, 23, 24, 35]. None of the nonclosures found amounted to more than a ~3 mm/yr of inferred deformation. Many nonclosures seem explainable by deformation marked by earthquakes in small salients of plates, and the statistical significance of many nonclosures is marginal. The nonclosures are small enough that all might be due to systematic errors in the plate motion data. Very high accuracy, as might eventually be obtained from space-geodetic data, will be needed to obtain convincing estimates of any deformation in plate interiors. DeMets et al. [24] extended the test of Gordon et al. [37] to establish both the upper and lower bounds on plate rigidity imposed by the plate-circuit closure. They found that the data are consistent with closure of the Australia-Africa-Antarctic plate-motion circuit and place and upper bound of 7 mm/yr on the summed deformation around the Rodriguez triple junction if they accurately estimated the errors in the data. If instead systematic errors are negligible, in which case they overestimated the errors by about a factor or 2, and the errors are instead estimated from the dispersion of the data, then 95% confidence limits on intraplate deformation about a circuit traversed near the triple junction are 1 to 4 mm/yr.

Argus and Gordon [5] used geodetic data from very long baseline interferometry to place bounds on how much any individual site might be moving relative to

the plate on which it is believed to lie. They found that the data require only insignificant or marginally significant motion of any one site in stable North America relative to the rest of stable North America, if realistic errors are assumed. The data further provide useful upper bounds on possible deformation. The strongest bounds come from sites on the North American plate with 4 of 13 sites moving slower than 3 mm/yr and 8 of 13 sites moving slower than 4 mm/yr at the 95% confidence level. Future measurements should help shrink the distance between the lower and upper bounds so that we eventually will have a much clearer picture of the rate of deformation of true plate interiors.

7. "ABSOLUTE" PLATE MOTION

Global plate motion models such as NUVEL-1 completely specify the motion between the plates. As such, there is no need to specify the motion of the plates relative to an external frame of reference, i.e., a terrestrial frame of reference not assumed *a priori* to be stationary relative to any one plate. The specification of the motion of the plates relative to an external reference may be useful nonetheless. In particular, if the horizontal velocity between distant points in the presumably continuously deforming deep mantle is small compared with the typical velocity between plates. then the concept of plate motion relative to the deep mantle, which I refer to as the *mesosphere*, would be useful for both kinematic and dynamic applications.

Different geological and dynamical assumptions have been proposed for specifying the motion of the plates relative to the mesosphere. Motion relative to the mesosphere is often referred to as *absolute* plate motion. Methods for estimating absolute plate velocities are assumption dependent not only because the viscosity profile of the mantle is the subject of continuing research, but because so little is known about kinematics, dynamics, and other properties of processes within Earth. Differences between the resulting models may contain useful information about the driving and resisting forces of plate motion and mantle convection. Here I present models for plate motion relative to two particular plate motion reference frames: the hotspot reference frame and the no-net-rotation reference frame.

7.1 Plate motion relative to hotspots

Absolute plate motion can by estimated by assuming that various volcanic hotspots (e.g., the volcanic sources for the Hawaiian Island chain, the Society Islands including Tahiti, the Galapagos islands, or Yellowstone and the Snake River Plain) are stationary relative to one another and to the mesosphere, possibly because they are rooted in deep mantle plumes that originate in the comparatively non-deforming deep mantle [69, 99]. Given these assumptions, age progressions and trends of linear island chains reflect motion between the plates and the mesosphere.

Hotspot tracks are very wide (tens to hundreds of kilometers) and irregular in trend compared with submarine transform faults (as narrow as a few hundred meters and as wide as ~2 kilometers). Hotspot tracks also are very few in number compared with the hundreds of submarine transform faults. Hence the geologically recent direction of plate motion relative to the hotspots can be estimated much less accurately than can the geologically recent direction of motion between plates. Similarly, volcanic propagation rates can be estimated with much less accuracy than can spreading rates. Not only are the radiometric ages of the volcanic rocks subject to uncertainties, but a volcano may persist in one location for millions of years. In contrast, the duration of a geomagnetic reversal is believed to be only a few thousand years. Because of these considerable uncertainties in the trend and rate of volcanic propagation along hotspot tracks, it has not been possible to make a useful test of the stationariness of hotspots using data only from the portion of each hotspot track created in just the past few million years.

Table 3 gives angular velocities (and their uncertainties) describing present motion of the plates relative to the hotspots [39]. The angular velocity of any one plate relative to another has been constrained to consistency with NUVEL-1; the motion of this self-consistent network of plates relative to the hotspots was estimated from the set of hotspot trends, volcanic propagation rates, and subjectively estimated uncertainties of Minster and Jordan [62]. Velocities at representative points on the plates are shown in Figure 2. The velocities indicate several patterns that have long been recognized: plates attached to subducting slabs tend to move rapidly toward the trenches where the slabs are attached; plates without large continents tend to move faster than plates with large continents, although both the Indian and the Australian plates have significant continental area and move rapidly; equatorial lithosphere tends to move faster than polar lithosphere.

7.2 Plate motion relative to the no-net rotation reference frame

Another method for estimating absolute plate velocities follows from the requirement that no net torque is

Table 3. HS2-NUVEL1 Angular Velocities (Relative to the Hotspots)

Plate	Angular Velocity			Standard Error Ellipse			
	Latitude °N	Longitude °E	ω deg–Myr^{-1}	σ_{max}	σ_{min}	ζ_{max}	σ_ω deg–Myr^{-1}
Africa	-5.5	3.6	0.15	47.2°	40.5°	110°	0.05
Antarctica	-14.8	65.9	0.11	57.1°	34.2°	16°	0.09
Arabia	16.8	18.4	0.54	12.7°	10.6°	138°	0.05
Australia	9.6	41.8	0.76	8.4°	6.6°	172°	0.07
Caribbean	-62.4	-5.7	0.17	39.5°	20.7°	91°	0.08
Cocos	18.4	-115.9	1.29	4.6°	2.8°	162°	0.09
Eurasia	-44.8	58.1	0.09	72.0°	40.4°	28°	0.09
India	16.6	21.9	0.55	12.3°	10.3°	142°	0.05
Juan de Fuca	-34.8	60.0	0.95	6.3°	3.7°	25°	0.09
North America	-67.2	-11.1	0.28	24.7°	12.4°	95°	0.08
Nazca	45.7	-90.2	0.46	13.3°	8.1°	178°	0.09
Pacific	-60.2	90.0	0.98	6.5°	3.8°	176°	0.08
Philippine	-49.4	-19.9	1.11	6.3°	3.6°	107°	0.07
South America	-70.3	74.7	0.32	20.4°	10.9°	9°	0.08

Each angular velocity describes the right-handed rotation of a plate relative to the hotspots. The Juan de Fuca plate was incorporated using the Juan de Fuca-Pacific angular velocity of Wilson [96]. The Philippine plate was incorporated using the Pacific-Philippine angular velocity of Seno et al. [76]. Errors are only from plate-hotspot motion; relative plate motion errors are not included. In spherical coordinates ${}_{hs}\omega_{pa}$ is 60.192°N, 90.031°W 0.9753 deg/m.y and in Cartesian coordinates is $-0.000005\hat{\mathbf{x}} - 0.008462\hat{\mathbf{y}} + 0.014770\hat{\mathbf{z}}$ radians/Myr, where $\hat{\mathbf{x}}$ is a unit vector in the direction of 0°N, 0°E, $\hat{\mathbf{y}}$ is a unit vector in the direction of 0°N, 90°E, and $\hat{\mathbf{z}}$ is a unit vector in the direction of the north pole. The full, symmetric variance-covariance matrix is $\sigma^2_{xx} = 6404$, $\sigma^2_{xy} = 2794$, $\sigma^2_{xz} = -3243$, $\sigma^2_{yy} = 21470$, $\sigma^2_{yz} = -2426$, and $\sigma^2_{zz} = 17411$ in units of 10^{-10} radians^2/Myr^2

exerted on the lithosphere [80]. In this method, if (1) coupling between the lithosphere and asthenosphere is assumed to be laterally uniform and if (2) torques associated with plate boundaries are assumed to apply symmetrically to the two plates meeting at a boundary, then the no-net-rotation (or mean-lithosphere) reference frame specifies the velocity of the plates relative to the mesosphere. Condition (1) would be true if the lithosphere and asthenosphere had the same thickness everywhere and there were no lateral variations in viscosity structure. The flow of asthenosphere from trenches to ridges also affects the torques on individual plates and in some cases differs significantly in direction from the velocity of the plates [16, 41]. However, the global sum of these torques is zero, thus exerting no net torque on the lithosphere as a whole if these two conditions apply.

The integral of $\mathbf{v} \times \mathbf{r}$ over Earth's surface, where $\mathbf{v}$ is the plate velocity at position $\mathbf{r}$, vanishes if velocities are specified in the no-net-rotation reference frame. To evaluate the net rotation (or equivalently the torque assuming uniform drag) for each plate, it is convenient first to calculate the following tensor:

$$Q_{ij} = \int \left(\delta_{ij} - x_i x_j\right) dA = \int\int \left(\delta_{ij} - x_i x_j\right) \sin\theta \, d\phi \, d\theta \quad (1)$$

where δ_{ij} is the Kronecker delta, x_1, x_2, and x_3 are the Cartesian components of points along plate boundaries, dA is an area element, θ is colatitude, ϕ is longitude, and the integral is evaluated over a single plate on a

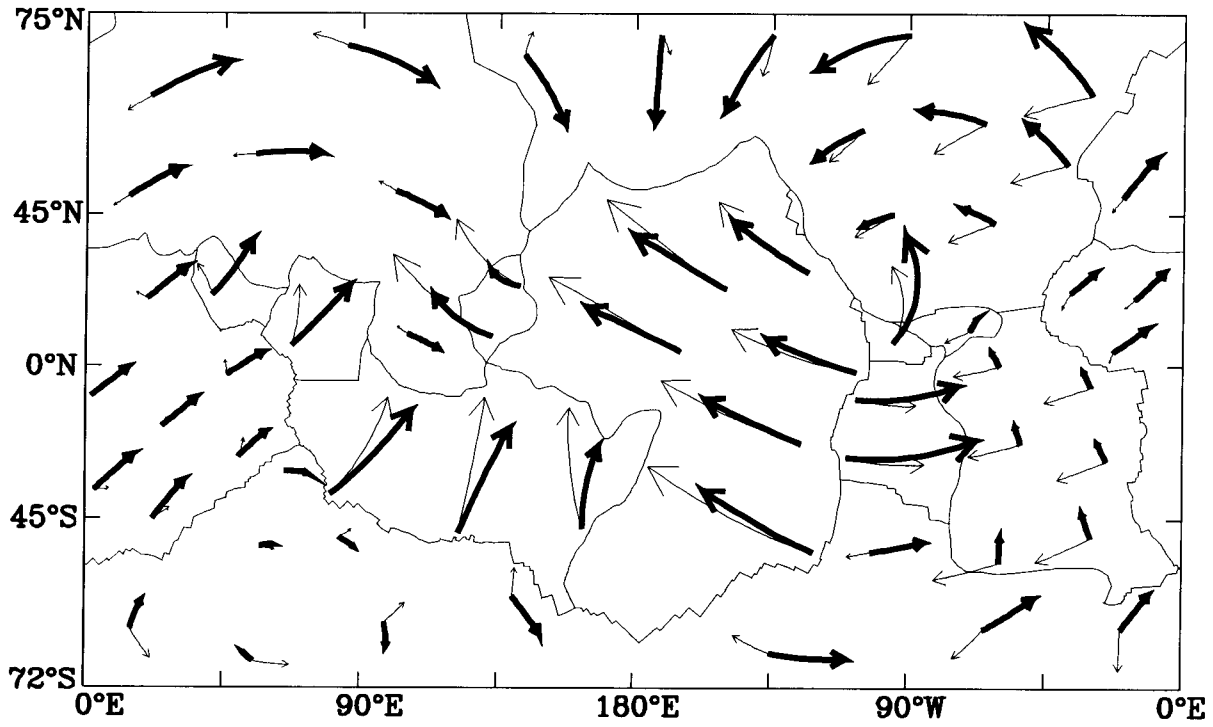

Fig. 2. Plate boundaries assumed to determine NNR-NUVEL1, plate velocities relative to the no-net-rotation reference frame in NNR-NUVEL1 (thick arrows) [4], and plate velocities relative to the hotspots in HS2-NUVEL1 (thin arrows) [39]. Arrows show the trajectory of the lithosphere if the current angular velocities remained unchanged over 50 Myr The map uses Mercator's projection, which distorts lengths of arrows so that the speed of plates near the geographic poles appears too fast. Several simplifications have been made relative to the plate geometries shown in Figure 1, including the following. All plate boundaries are assumed to be narrow. Nubia and Somalia were treated as a single African plate. The Rivera plate has been incorporated into the Cocos plate. The Scotia Sea plate has been incorporated into the Antarctic plate. Southeast Asia has been incorporated into the Eurasian plate. The Caroline plate has been incorporated into the Pacific plate. From Argus and Gordon [4].

unit sphere [80]. (Summation over i and j is not implied.) Integration over ϕ yields line integrals, which Argus and Gordon [4] evaluated numerically (Table 4). The angular velocity of the Pacific plate, for example, relative to the no-net-rotation reference frame can then be calculated from the following equation:

$$\omega_{PACIFIC} = (-3/8\pi) \sum_i Q_i \omega_i \qquad (2)$$

where ω_i is the NUVEL-1 angular velocity describing the motion of plate i relative to an arbitrarily fixed Pacific plate, Q_i is the tensor Q evaluated for plate i, and the sum is taken over all plates. The angular velocity of other plates relative to the no-net-rotation reference frame can then be found by vector addition, thus completely specifying global plate motion model NNR-NUVEL1 (Table 5, Figure 2).

7.3 Comparison of hotspot and no-net rotation reference frames

The NNR-NUVEL1 reference frame rotates relative to the HS2-NUVEL1 reference frame by a right-handed rotation of 0.33°/Myr about 49°S, 65°E. Differences between the two reference frames are completely specified by this rotation because NNR-NUVEL1 and HS2-NUVEL1 contain identical relative plate velocities. The velocity between the two reference frames is as large as 37 mm/yr. At Hawaii the HS2-NUVEL1 velocity of the Pacific plate relative to the hotspots equals 95 mm/yr toward N59°W, close to the observed volcanic propagation rate and azimuth along the Hawaiian chain, which the model was adjusted to fit (along with

Table 4. Elements of the symmetric tensor Q

Plate	Q_{11}	Q_{22}	Q_{33}	Q_{12}	Q_{13}	Q_{23}
Africa	0.6567	1.5366	1.6315	–0.2501	0.0553	0.1088
Antarctica	1.3638	1.2102	0.3772	–0.0466	0.0636	0.0715
Arabia	0.0777	0.0690	0.1037	–0.0501	–0.0308	–0.0326
Australia	0.8349	0.6325	0.9438	0.2193	–0.2252	0.2902
Caribbean	0.0844	0.0125	0.0863	0.0207	–0.0054	0.0198
Cocos	0.0747	0.0037	0.0738	–0.0064	0.0014	0.0112
Eurasia	1.3958	1.0749	0.8751	0.0961	–0.1620	–0.4086
India	0.2776	0.0424	0.2752	–0.0582	–0.0140	–0.0595
J. de Fuca	0.0057	0.0048	0.0035	–0.0017	0.0021	0.0028
Nazca	0.3941	0.0710	0.3471	–0.0134	–0.0036	–0.1164
N. Amer.	1.2717	0.9996	0.5749	0.0730	0.0241	0.3751
Pacific	1.1958	2.0171	2.0943	–0.3986	0.0719	–0.0556
Philippine	0.0799	0.0780	0.1253	0.0613	0.0293	–0.0292
S. Amer.	0.6647	0.6254	0.8659	0.3546	0.1935	–0.1773

The tensor Q is used to estimate the net rotation of the lithosphere, is defined in equation 1 in the body of this chapter, and equals the moment-of-inertia tensor of a hypothetical infinitesimally thick plate of unit density. These values were calculated for a sphere of unit radius and are given in steradians. Figure 2 shows the plate geometry used to evaluate these integrals. Its caption describes many of the simplifications made to obtain this plate geometry.

other data). However, the NNR-NUVEL1 velocity of the Pacific plate relative to the no-net-rotation reference frame is 70 mm/yr toward N61°W, along nearly the same direction but 25 mm/yr slower (Figure 2). The NNR-NUVEL1 Pacific angular velocity parallels that of HS2-NUVEL1, but with an angular speed that is 32% slower.

Every NNR-NUVEL1 angular velocity describing the motion of a plate relative to the no-net-rotation reference frame lies outside the three-dimensional 99% confidence ellipsoid of the corresponding HS2-NUVEL1 plate-hotspot angular velocity. It seems likely that the uncertainties of NNR-NUVEL1 are much smaller than those of HS2-NUVEL1 because motion between plates is known much better than motion of the hotspots relative to plates. Therefore the no-net-rotation reference frame almost surely differs significantly from the (HS2) hotspot reference frame.

The geodynamical and tectonic implications of this significant difference would be clear if we knew which reference frame gave the correct velocities relative to the deep mantle. An unambiguous interpretation cannot be made, however, because there are doubts about both reference frames. I think it likely that the hotspot reference frame is the more appropriate frame, mainly because the velocity between the no-net-rotation and hotspot reference frames seems large relative to what I think are the likely velocities between hotspots. However, much work remains before this can be conclusively established or refuted.

Argus and Gordon [4] discuss possible explanations and directions for future research that might resolve some of these ambiguities. In brief, either Pacific (and possibly other) hotspots move coherently relative to the mesosphere or the no-net-rotation reference frame is based on one or more dynamically incorrect premises. Argus and Gordon [4] suggest that the latter explanation is more likely, in particular (1) that greater torque is exerted on plates attached to downgoing slabs than to the plates overriding downgoing slabs and (2) that resistance to plate motion is greater beneath continental lithosphere than beneath oceanic lithosphere.

8. PLATE MOTION AND PLATE BOUNDARY ZONE DEFORMATION FROM SPACE-GEODETIC DATA

Space geodesy is a term applied to techniques for making precise position measurements between sites on Earth's surface, which may be separated by as much as

Table 5. NNR-NUVEL1 Angular Velocities

Plate	Latitude, °N	Longitude, °E	ω ° Myr^{-1}	RMS Velocity
Africa	50.6	–74.0	0.30	30
Antarctica	63.0	–115.9	0.25	16
Arabia	45.2	–4.4	0.57	46
Australia	33.8	33.2	0.68	66
Caribbean	25.0	–93.1	0.22	9
Cocos	24.5	–115.8	1.58	77
Eurasia	50.6	–112.4	0.24	25
India	45.5	0.4	0.57	59
Juan de Fuca	–27.4	58.1	0.64	20
Nazca	47.8	–100.2	0.78	79
North America	–2.5	–86.0	0.22	20
Pacific	–63.0	107.4	0.67	67
Philippine Sea	–39.0	–36.7	0.95	42
South America	–25.4	–124.6	0.12	12

All plates move with a right-handed sense of rotation relative to the no-net-rotation reference frame. The Pacific angular velocity equals 63.036°S, 107.359°E, 0.6705°/Myr in spherical coordinates. It equals $-0.001583\hat{\mathbf{x}} + 0.005064\hat{\mathbf{y}} - 0.010430\hat{\mathbf{z}}$ radians/Myr in Cartesian coordinates, where $\hat{\mathbf{x}}$ is a unit vector in the direction of 0°N, 0°E, $\hat{\mathbf{y}}$ is a unit vector in the direction of 0°N, 90°E, and $\hat{\mathbf{z}}$ is a unit vector in the direction of the geographic North pole. The global rms velocity of the lithosphere is 39 mm/yr. To revise these angular velocities for consistency with recent revisions to the geomagnetic reversal time scale [45], multiply the rates by 0.9562, as was done in constructing the NUVEL-1A global plate motion model [25].

~12,000 km. The three main techniques, very long-baseline radio interferometry (VLBI), satellite laser ranging (SLR), and the global positioning system (GPS), are based on technologies developed for space-related research, in particular radio astronomy and satellite tracking. Because only sparse results are yet available from GPS, herein I discuss only VLBI and SLR.

VLBI geodesy depends on the precise timing of radio noise from compact extragalactic sources observed at several radio telescopes. Analysis of the noise permits estimation of the location of a radio telescope site in the nearly inertial reference frame defined by the sources. In a typical geodetic VLBI experiment, two to seven radio telescopes simultaneously record noise from one source at a time and eventually record noise from 5 to 15 sources. The noise recorded at different sites is correlated to determine delays and delay rates between telescopes. These data are used to determine site locations, the orientation of Earth, and azimuths to radio sources. Uncertainty in tropospheric delay and Earth orientation are the main cause of site location errors. Repeat experiments allow site motion to be estimated (see, for example, Clark et al. [17] and Ryan et al. [74]).

SLR is based on the round-trip time of laser pulses reflected off a satellite, such as the Laser Geodynamics Satellite (LAGEOS), which orbits at an altitude of about 5900 km. The distance or range to the satellite is one-half of the product of the speed of light and the elapsed time between emission of a laser pulse and its reception at the same tracking site. Range estimates from many sites determine both the satellite trajectory and the three-dimensional coordinates of the tracking stations. Successive observations permit the position of the tracking station to be estimated as a function of time [79]. Because the satellite orbit moves with Earth's center of mass (the geocenter), site motions are referred to a dynamically defined nearly inertial reference frame that moves with the geocenter.

Space-geodetic data already have been used to test and verify within narrow confidence limits the hypothesis that plate motions are steady, that is, that the rates and directions of plate motion averaged over a few years (the shortest interval over which meaningful rates can be obtained) are very similar to rates and directions averaged over millions of years (the shortest interval

over which rates have been estimated systematically from marine magnetic anomalies) [2, 17, 42, 52, 74, 79, 91] (Figure 3; compare Table 6 with Tables 1 and 2). Of course, tests for the steadiness of plate motion have to be constructed using sites that lie outside the zone of elastic strain accumulation adjacent to faults.

Both VLBI plate motion models and global plate motion model NUVEL-1 give estimates of the Pacific-North America velocity that are very similar to one another but ~8 mm/yr slower than predicted by earlier models of geologically recent plate motion. Velocities estimated from space-geodetic data between other pairs of plates are also very similar to that predicted by NUVEL-1, but may differ by small but significant amounts. For example, space-geodetic estimates of velocities between North America and Europe are a few millimeters per year slower than predicted from NUVEL-1 (Table 6) [52, 79, D. F. Argus and R. G. Gordon, manuscript in preparation, 1994]. The small differences may be due to small systematic errors in plate velocities estimated from either geodetic or geologic data. In particular, recent recalibration of the geomagnetic reversal time scale using the correlation with and timing of Milankovitch cycles [45, 77], as partly confirmed by high-precision $^{40}Ar/^{39}Ar$ laser dating [7], would bring NUVEL-1 into better agreement with average plate velocities estimated from SLR and VLBI [34, 72, 79]. Nonetheless some small differences may be real, which would be unsurprising as changes in plate velocities of this size or larger are common over time scales of millions of years.

Conventional plate motion data cannot be used to estimate the motion of plates or microplates lacking narrow boundaries with adjacent plates, but space-geodetic data can [see, e.g., 3, 63]. Enough space-geodetic data are already available to estimate the motion of the Sierra Nevada-Great Valley microplate relative to the Pacific and North American plates (Table 6, Figure 4) [3]. Nearly three-fourths (~35 mm/yr; see, e.g., [51]) of the 48 mm/yr of motion between the Pacific and North American plates [23] is taken up by strike slip along the San Andreas fault in southern central California, which —along with the California Coast Ranges— separates the Pacific plate from the Sierra Nevada-Great Valley microplate. The angular velocity of the microplate relative to the North American plate (taken up by deformation in the Great Basin and calculated from VLBI data) predicts a velocity of the eastern edge of the Sierra Nevada relative to stable North America of 11 mm/yr toward N36°W, which accounts for nearly one-fourth of the 48 mm/yr velocity between the Pacific and North American plates [3] (Figure 4). The vector sum of strike slip along the San Andreas fault and motion of the Sierra Nevada-Great Valley microplate relative to stable North America differs insignificantly from the Pacific-North America plate velocity. The difference can be described at 36°N along the San Andreas fault by a residual velocity with components of 5 mm/yr parallel to the fault and 2 mm/yr perpendicular to the fault with 95% confidence intervals of 0 to 10 mm/yr and –1 to +5 mm/yr, respectively. Thus, this work leads to the important conclusion that motion taken up by western U.S. deformation other than strike slip along the San Andreas fault or deformation in the Great Basin is small [3].

9. VLBI PLATE MOTION MODEL

Enough radio telescope sites have been making geodetic VLBI observations long enough on three major plates (the Pacific, North American, and Eurasian plates), as well as the Sierra Nevada-Great Valley microplate, to estimate plate motion model IVEL-1, a four-plate plate motion model from only VLBI data (Table 6). The plate motion model depends not only on observed rates of change in baselines between the 21 sites on the four plates, but also on network closures from observed rates of change between 30 sites not constrained to lie on any tectonic plate (D. F. Argus and R. G. Gordon, manuscript in preparation, 1994). IVEL-1 agrees well with NUVEL-1. The IVEL-1 Pacific-North America and Pacific-Eurasia angular velocities differ insignificantly from the corresponding NUVEL-1 angular velocities, whereas the IVEL-1 Eurasia-North America angular velocity indicates marginally significantly slower motion than does the corresponding NUVEL-1 angular velocity. The differences correspond to differences in predicted spreading rate of ~1.5 to ~3.5 mm/yr. The revisions to the geomagnetic reversal time scale indicated by the calibration with Milankovitch cycles [i.e., 7, 25, 45, 77] would only reduce this difference by ~0.5 mm/yr.

10. DISCUSSION AND CONCLUSIONS

The geologically recent motions between the plates are now well established. The remaining questions about the motion of nearly all the major plates are probably matters of just a few millimeters per year (except for a very likely uniform fractional error associated with a systematic error in the geomagnetic reversal time scale). The largest errors likely occur on those boun-

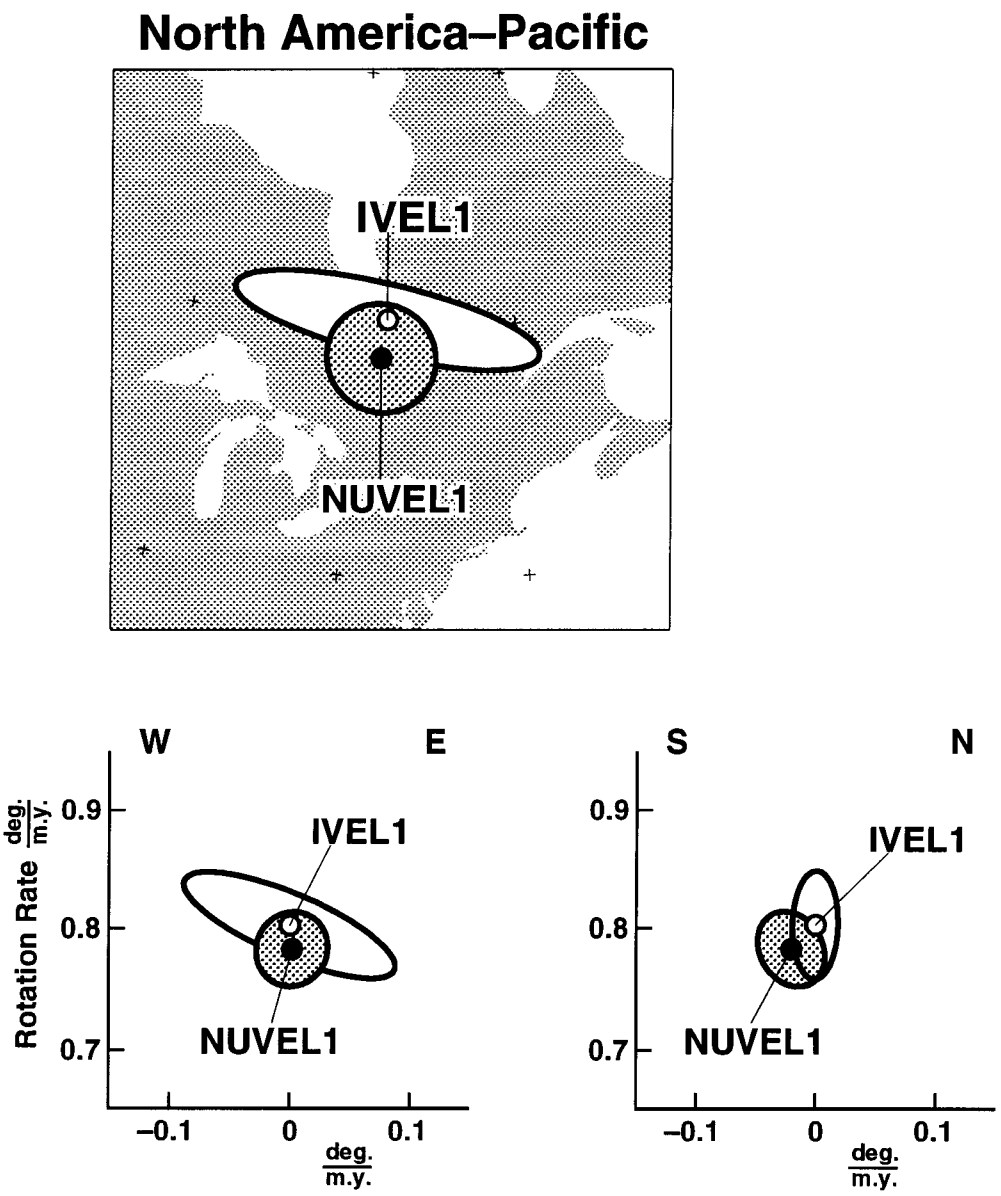

Fig. 3. Angular velocities and confidence limits describing motion between the North American and Pacific plates. The NUVEL-1 angular velocity is determined from a global set of transform fault slip azimuths from earthquake focal mechanisms, and spreading rates averaged over 3 Myr from marine magnetic anomalies. The IVEL-1 angular velocity is determined from VLBI geodetic observations from 1979 to 1990. Top panel shows the poles of rotation. The lower left panel shows the projection of the angular velocity and confidence limits onto the vertical plane through the IVEL-1 angular velocity and aligned with the major axis of its ellipse shown in the top panel. The lower right panel shows the projection of the angular velocities and confidence limits onto the perpendicular vertical plane through the IVEL-1 angular velocity. The two angular velocities differ insignificantly. From D. F. Argus and R. G. Gordon (manuscript in preparation, 1994).

Table 6. IVEL-1 Angular Velocities

Plate Pair	Angular Velocity			Error Ellipse			
	Lat. °N	Lon. °E	ω °/Myr	σ_{max}	σ_{min}	ζ_{max}	σ_ω deg–Myr^{-1}
North America-external	–9.7	–99.8	0.257	5.2	3.3	82	0.016
North America-Pacific	50.2	–77.9	0.803	3.6	0.8	–79	0.018
Eurasia-North America	67.4	119.1	0.219	11.5	4.3	–43	0.028
Eurasia-Pacific	62.0	–81.2	0.927	3.8	1.4	78	0.039
Sierra Nevada-North America	31.3	–128.0	0.623	3.3	0.7	43	0.142
Sierra Nevada-Pacific	44.8	–103.4	1.334	2.7	0.7	75	0.143

The angular velocity describes a right-handed rotation of the first plate relative to the second plate. One-sigma error ellipses are specified by the angular lengths (in degrees) of the principal semi-axes (σ_{max} and σ_{min}) and by the azimuths of the major semi-axis (ζ_{max} in degrees clockwise from north). The rotation rate uncertainty (σ_ω) is determined from a one-dimensional marginal distribution, whereas the lengths of the principal axes are determined from a two-dimensional marginal distribution. From D. F. Argus and R. G. Gordon, manuscript in preparation, 1994.

daries across which motion is inferred solely from data on other boundaries and on those boundaries having only sparse data. From space-geodetic data, the motion of several plates has been estimated from data spanning merely a decade. Before long the velocities of many of the major plates averaged over several years to a decade or two will be well known. The results to date strongly support the hypothesis that plate motion is very steady and extend the time range of plate kinematic predictions such that velocities inferred from data that average over millions of years can be used to predict motions observed over a time scale of just a few years.

In contrast, fundamental questions concerning the motion of the plates relative to a deep mantle reference frame remain unanswered. Accuracies for geologically recent absolute motion will always be far worse than for relative plate motion simply because the hotspot tracks that are the only likely recorders of such motion are trails that are far less precise recorders of motion than are transform faults and the magnetic anomalies that record reversals in the seafloor.

Many more measurements, like those made since 1986 in southern California [29], will be needed to obtain accurate descriptions of motions within wide plate boundary zones. A great success of plate tectonics has been in its statistically efficient description of the motion between the major plates. For example, in global plate motion model NUVEL-1, which describes the motion between 12 major plates, 1122 high-quality data are well described by 33 adjustable parameters [23]. This result implies that a model of rigid plates separated by narrow boundaries is useful, even if it may not apply to a significant minority (~15%) of Earth's surface. This success suggests that the same kinematic model of rigid plates could be applied to ever smaller crustal or lithospheric blocks or microplates. This approach has proved useful in many cases, for example, to the motion of the Turkish, Central Iranian, and South Caspian microplates in the deformation belts from the eastern Mediterranean to the Middle East [47, 59] and to the motion of the Sierra Nevada-Great Valley microplate in western North America [3]. However, as the number of required blocks increases and the size of these blocks decreases, as is needed for a complete description of the kinematics in all wide deforming zones, the number of parameters needed to specify the kinematics can quickly become too large to be useful.

This limitation and other considerations have led to alternative continuum formulations of the kinematics and dynamics of continental plate boundary zones [8, 28, 46, 60, 87, 88]. These formulations are motivated in part by the belief that the strongest part of continental crust lies not in the brittlely deforming upper crust but in the plastically deforming uppermost mantle and that the brittle upper crust may passively mimic the deeper continuous flow [59, 66]. If deformation is

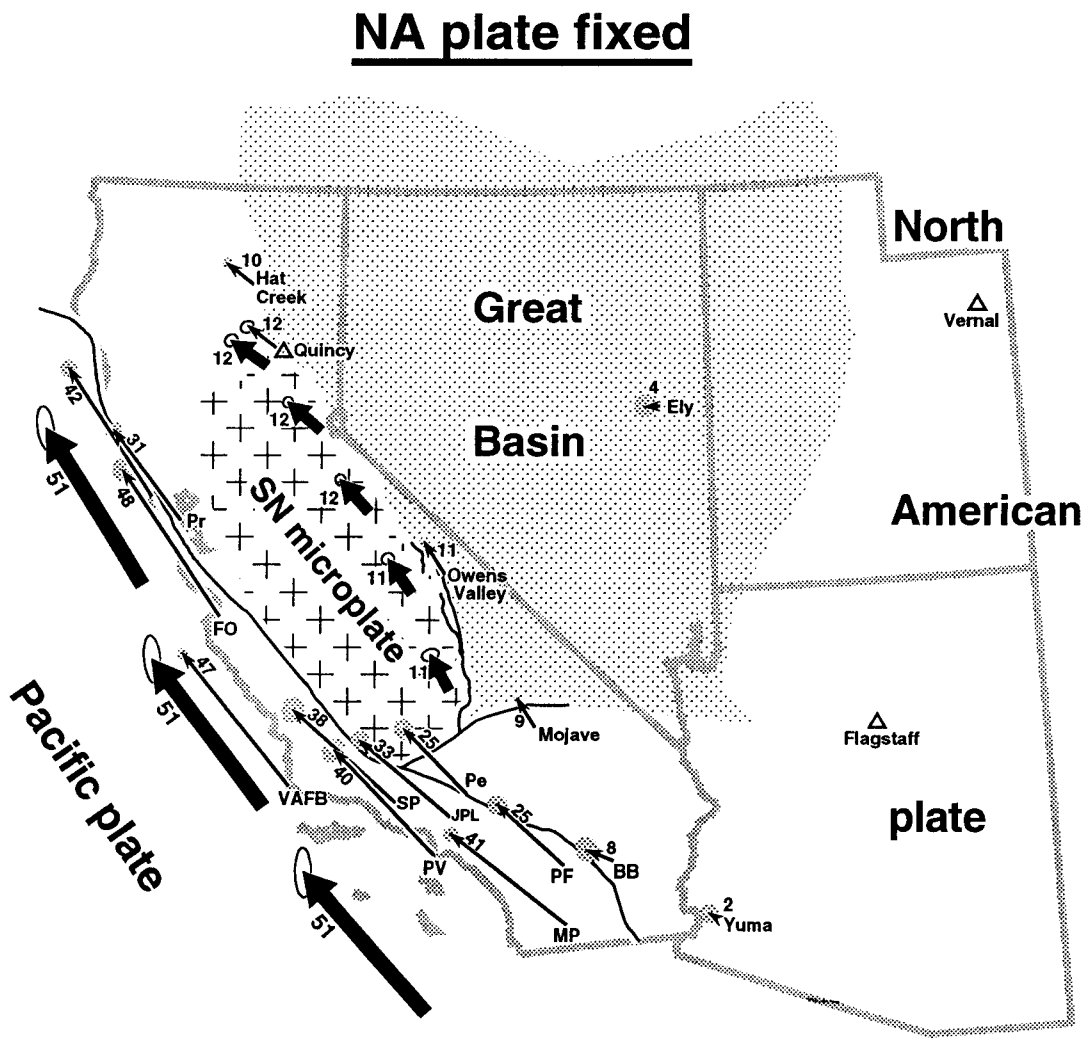

Fig. 4. Plate and site motions relative to North America estimated from VLBI geodetic data. Bold arrows show the motion of the Pacific plate and of the Sierra Nevada-Great Valley microplate relative to North America. Small arrows show the motion of individual radio telescope sites (not constrained to lie on a plate) relative to North America; ellipses centered on the tips of arrowheads are 95% confidence limits. Numerals adjacent to arrows give the velocities in millimeters per year. The lengths of the arrows are scaled to show displacements if each velocity was constant for two million years. "SN" is the Sierra Nevada-Great Valley microplate. From D. F. Argus and R. G. Gordon (manuscript in preparation, 1994).

homogeneous in a plate boundary zone, the kinematics can be specified by a constant horizontal velocity gradient tensor. Unfortunately, a velocity gradient tensor does not completely specify the motion of crustal blocks within a deforming zone [47], and additional parameters are needed to complete such a specification. Moreover, regionally averaged deformation is unlikely to be homogeneous in many plate boundary zones; thus further parameters will be needed to specify how the deformation varies [46, 65]. Future papers describing global crustal kinematics will need to describe not only the rotations of rigid plates, but will also need to specify velocity gradients, their spatial variations, and additional parameters specifying the velocity field within deforming zones.

In sum, plate tectonics is very successful in describ-

ing the kinematics and tectonics of the ~85% of Earth's surface covered by rigid plates separated by narrow boundaries. Carefully defined plate interiors appear rigid to within a few millimeters per year and possibly to much less. The geologically recent angular velocities specifying motion between nearly all the major plates are now accurately described, as are the angular velocities averaged over several years of several of these plates. The velocities of plates averaged over years are very similar to velocities averaged over millions of years. Plate tectonics fails to describe the 15% of Earth's surface covered with deforming lithosphere. These zones seem better interpreted as wide plate boundary zones than as zones of intraplate deformation. Many new observations will be needed before the kinematics of these deforming zones will be described with the same accuracy that plate velocities are now known.

Acknowledgments. I thank Clem Chase for a helpful review of this manuscript. Tom Shoberg made several improvements both to the idealized narrow plate boundaries and to the wide plate boundary zones shown in Figure 1, which was prepared by Shoberg. A similar figure, also prepared by Shoberg, was previously published in Gordon and Stein [36]. My plate motion research has recently been supported by NSF grants OCE-8900090 and OCE-9218541 and NASA grant NAG5-885.

REFERENCES

1. Anderson, H. A., and J. A. Jackson, Active tectonics of the Adriatic region, *Geophys. J. R. astron. Soc., 91,* 937–983, 1987.
2. Argus, D. F., and R. G. Gordon, Pacific-North American plate motion from very long baseline interferometry compared with motion inferred from magnetic anomalies, transform faults, and earthquake slip vectors, *J. Geophys. Res., 95,* 17,315–17,324, 1990.
3. Argus, D. F., and R. G. Gordon, Current Sierra Nevada-North America motion from very long baseline interferometry: Implications for the kinematics of the western United States, *Geology, 19,* 1085–1088, 1991a.
4. Argus, D. F., and R. G. Gordon, No-net-rotation model of current plate velocities incorporating plate motion model NUVEL-1, *Geophys. Res. Lett., 18,* 2038–2042, 1991b.
5. Argus, D. F., and R. G. Gordon, Tests of the rigid-plate hypothesis and bounds on plate rigidity using geodetic data from very long baseline interferometry, *J. Geophys. Res.,* submitted, 1993.
6. Argus, D. F., R. G. Gordon, C. DeMets, and S. Stein, Closure of the Africa-Eurasia-North America plate motion circuit and tectonics of the Gloria fault, *J. Geophys. Res., 94,* 5585–5602, 1989.
7. Baksi, A. K., V. Hsu, M. O. McWilliams, and E. Farrar, $^{40}Ar/^{39}Ar$ dating of the Brunhes-Matuyama geomagnetic field reversal, *Science, 256,* 356–357, 1992.
8. Bird, P., and K. Piper, Plane-stress finite-element models of the tectonic flow in southern California, *Phys. Earth Planet. Inter., 21,* 158–175, 1980.
9. Bowen, A. N., and R. S. White, Deep-Tow seismic profiles from the Vema transform and ridge-transform intersection, *J. Geol. Soc. London, 143,* 807–818, 1986.
10. Bull, J. M., Structural style of intra-plate deformation, Central Indian Ocean Basin: evidence for the role of fracture zones, *Tectonophysics, 184,* 213–228, 1990.
11. Bull, J. M., and R. A. Scrutton, Fault reactivation in the central Indian Ocean and the rheology of oceanic lithosphere, *Nature, 344,* 855–858, 1990.
12. Chamot-Rooke, N., B. de Voogd, J. Diebold, J. Dyment, F. Farcy, L. Fleitout, P. Huchon, F. Jestin, P. Liverpool, M. Munschy, A. Oshida, J.-Y. Royer, C. Truffert, J. K. Weissel, and A. Ziolkowski, Seismic reflection profiling across the central Indian ocean deformed lithosphere (abstract), *Eos Trans. AGU, 72,* Supplement, 488, 1991.
13. Chase, C. G., The *n*-plate problem of plate tectonics, *Geophys. J. R. astron. Soc., 29,* 117–122, 1972.
14. Chase, C. G., Plate kinematics: The Americas, East Africa, and the rest of the world, *Earth Planet. Sci. Lett., 37,* 355–368, 1978a.
15. Chase, C. G., Extension behind island arcs and motions relative to hot spots, *J. Geophys. Res., 83,* 5385–5387, 1978b.
16. Chase, C. G., Asthenospheric

counterflow: A kinematic model, *Geophys. J. R. astron. Soc., 56,* 1–18, 1979.
17. Clark, T. A., D. Gordon, W. E. Himwich, C. Ma, A. Mallama, and J. W. Ryan, Determination of relative site motions in the western United States using Mark III very long baseline radio interferometry, *J. Geophys. Res., 92,* 12,741–12,750, 1987.
18. Cox, A., R. R. Doell, and G. B. Dalrymple, Reversals of the Earth's magnetic field, *Science, 144,* 1537–1543, 1964.
19. Curray, J. R., and D. G. Moore, Growth of the Bengal Deep-Sea Fan and denudation in the Himalayas, *Geol. Soc. Am. Bull., 82,* 563–572, 1971.
20. Curray, J. R., and T. Munasinghe, Timing of intraplate deformation, northeastern Indian Ocean, *Earth Planet. Sci. Lett., 94,* 71–77, 1989.
21. DeMets, C., and S. Stein, Present-day kinematics of the Rivera plate and implications for tectonics of southwestern Mexico, *J. Geophys. Res., 95,* 21,931–21,948, 1990.
22. DeMets, C., R. G. Gordon, and D. F. Argus, Intraplate deformation and closure of the Australia-Antarctica-Africa plate circuit, *J. Geophys. Res., 93,* 11,877–11,897, 1988.
23. DeMets, C., R. G. Gordon, D. F. Argus, and S. Stein, Current plate motions, *Geophys. J. Int., 101,* 425–478, 1990.
24. DeMets, C., R. G. Gordon, and P. Vogt, Location of the Africa-Australia-India triple junction and motion between the Australian and Indian plates: Results from an aeromagnetic investigation of the Central Indian and Carlsberg ridges, *Geophys. J. Int.,* in press 1994.
25. DeMets, C., R. G. Gordon, D. F. Argus, and S. Stein, Effect of recent revision on the geomagnetic reversal time scale on estimates of current plate motions, *Geophys. Res. Lett.,* submitted 1994.
26. Eittreim, S., and J. Ewing, Midplate tectonics in the Indian Ocean, *J. Geophys. Res., 77,* 6413–6421, 1972.
27. Eittreim, S., and J. Ewing, Vema Fracture Zone transform fault, *Geology, 3,* 555–558, 1975.
28. England, P. C., and D. P. McKenzie, A thin viscous sheet model for continental deformation, *Geophys. J. R. astron. Soc., 70,* 295–321, 1982.
29. Feigl, K. L., D. C. Agnew, Y. Bock, D. Dong, A. Donnellan, B. H. Hager, T. A. Herring, D. D. Jackson, T. H. Jordan, R. W. King, S. Larsen, K. M. Larson, M. M. Murray, Z. Shen, and F. H. Webb, Space geodetic measurement of crustal deformation in Central and Southern California, 1984–1992, *J. Geophys. Res., 98,* 21677–21712, 1993.
30. Fitch, T. J., Plate convergence, transcurrent faults, and internal deformation adjacent to Southeast Asia and the western Pacific, *J. Geophys. Res., 77,* 4432–4460, 1972.
31. Fox, P. J., and D. G. Gallo, A tectonic model for ridge-transform-ridge plate boundaries: Implications for the structure of oceanic lithosphere, *Tectonophysics, 104,* 205–242, 1984.
32. Geller, C. A., J. K. Weissel, and R. N. Anderson, Heat transfer and intraplate deformation in the central Indian Ocean, *J. Geophys. Res., 88,* 1018–1032, 1983.
33. Gordon, R. G., Plate Motion, *Reviews of Geophysics,* Supplement, 748–758, 1991.
34. Gordon, R. G., Orbital dates and steady rates, *Nature, 364,* 760–761, 1993.
35. Gordon, R. G., and C. DeMets, Present-day motion along the Owen Fracture Zone and Dalrymple Trough in the Arabian Sea, *J. Geophys. Res., 94,* 5560–5570, 1989.
36. Gordon, R. G., and S. Stein, Global tectonics and space geodesy, *Science, 256,* 333–342, 1992.
37. Gordon, R. G., S. Stein, C. DeMets, and D. F. Argus, Statistical tests for closure of plate motion circuits, *Geophys. Res. Lett., 14,* 587–590, 1987.
38. Gordon, R. G., C. DeMets, and D. F. Argus, Kinematic constraints on distributed lithospheric deformation in the equatorial Indian Ocean from present motion between the Australian and Indian plates, *Tectonics, 9,* 409–422, 1990.
39. Gripp, A. E., and R. G. Gordon, Current plate velocities relative to the hotspots incorporating the NUVEL-1 global plate motion model, *Geophys. Res. Lett., 17,* 1109–1112, 1990.
40. Gutenberg, B., and C. F. Richter, *Seismicity of the Earth and Associated Phenomena (2nd ed.),* Princeton University Press, Princeton, NJ, 1954.
41. Harper, J. F., Mantle flow and plate motions, *Geophys. J. R. astron. Soc., 87,* 155–171, 1986.
42. Harrison, C. G. A., and N. B. Douglas, Satellite laser ranging and geological constraints on plate motion, *Tectonics, 9,* 935–952, 1990.
43. Haxby, W. F., *Gravity field of the world's oceans,* NOAA, Boulder, 1987.
44. Heki, K., Y. Takahashi, T. Kondo, N. Kawaguchi, F. Takahashi, and N. Kawano, The relative movement of the North American and Pacific plates in

1984–1985, detected by the Pacific VLBI network, *Tectonophysics, 144,* 151–158, 1987.
45. Hilgen, F. J., Extension of the astronomically calibrated (polarity) time scale to the Miocene/Pliocene boundary, *Earth Planet. Sci. Lett., 107,* 349–368, 1991.
46. Holt, W. E., and A. J. Haines, Velocity fields in deforming Asia from the inversion of earthquake-released strains, *Tectonics, 12,* 1–20, 1993.
47. Jackson, J., and D. McKenzie, The relationship between plate motions and seismic moment tensors, and the rates of active deformation in the Mediterranean and Middle East, *Geophys. J. R. astron. Soc., 93,* 45–73, 1988.
48. Jarrard, R. D., Relations among subduction parameters, *Rev. Geophys., 24,* 217–284, 1986.
49. Johnson, T., and P. Molnar, Focal mechanisms and plate tectonics of the Southwest Pacific, *J. Geophys. Res., 77,* 5000–5032, 1972.
50. Le Pichon, X., Sea-floor spreading and continental drift, *J. Geophys. Res., 73,* 3661–3697, 1968.
51. Lisowski, M., J. C. Savage, and W. H. Prescott, The velocity field along the San Andreas fault, *J. Geophys. Res., 96,* 8369–8389, 1991.
52. Ma, C., J. W. Ryan, and D. S. Caprette, *Crustal Dynamics Project Data Analysis—1991: VLBI geodetic results 1979–1990, NASA Technical Memorandum* 104552, 424 pp., NASA, Greenbelt, 1992.
53. Macdonald, K. C., The crest of the Mid-Atlantic Ridge: Models for crustal generation processes and tectonics, in *The Geology of North America, Volume M, The Western North Atlantic Region,* edited by P. R. Vogt and B. E. Tucholke, The Geological Society of America, Boulder, CO, 1986.
54. Macdonald, K. C., Tectonic and magmatic processes on the East Pacific rise, in *The Eastern Pacific Ocean and Hawaii, The Geology of North America N,* edited by E. L. Winterer, D. M. Hussong and R. W. Decker, pp. 93–110, Geological Society of America, Boulder, CO, 1989.
55. Marks, K. M., and J. M. Stock, High-precision location of fracture zones in Geosat data: The Macquarie triple junction region (abstract), *Eos Trans. AGU, 72,* Supplement, 444, 1991.
56. McAdoo, D. C., and D. T. Sandwell, Folding of oceanic lithosphere, *J. Geophys. Res., 90,* 8563–8569, 1985.
57. McCaffrey, R., Slip vectors and stretching of the Sumatran fore arc, *Geology, 19,* 881–884, 1991.
58. McDougall, I., and F. H. Chamalaun, Geomagnetic polarity scale of time, *Nature, 212,* 1415–1418, 1966.
59. McKenzie, D. P., Active tectonics of the Alpine-Himalayan belt—the Aegean Sea and surrounding regions, *Geophys. J. R. astron. Soc., 55,* 217–254, 1978.
60. McKenzie, D., and J. Jackson, The relationship between strain rates, crustal thickening, paleomagnetism, finite strain, and fault movements within a deforming zone, *Earth Planet. Sci. Lett., 65,* 182–202, 1983.
61. McKenzie, D., and R. L. Parker, The North Pacific: an example of tectonics on a sphere, *Nature, 216,* 1276–1280, 1967.
62. Minster, J. B., and T. H. Jordan, Present-day plate motions, *J. Geophys. Res., 83,* 5331–5354, 1978.
63. Minster, J. B., and T. H. Jordan, Vector constraints on western U. S. deformation from space geodesy, neotectonics, and plate motions, *J. Geophys. Res., 92,* 4798–4804, 1987.
64. Minster, J. B., T. H. Jordan, P. Molnar, and E. Haines, Numerical modeling of instantaneous plate tectonics, *Geophys. J. R. astron. Soc., 36,* 541–576, 1974.
65. Molnar, P., Continental tectonics in the aftermath of plate tectonics, *Nature, 335,* 131–137, 1988.
66. Molnar, P., Brace-Goetze strength profiles, the partitioning of strike-slip and thrust faulting at zones of oblique convergence and the stress-heat flow paradox of the San Andreas fault, in *Earthquake mechanics, Rock Deformation, and Transport Properties of Rocks: A Festscrift in Honor of W. F. Brace,* edited by B. Evans and T.-F. Wong, in press, Academic Press, London, 1992.
67. Molnar, P., and P. Tapponnier, Cenozoic tectonics of Asia: Effects of a continental collision, *Science, 189,* 419–426, 1975.
68. Morgan, W. J., Rises, trenches, great faults, and crustal blocks, *J. Geophys. Res., 73,* 1959–1982, 1968.
69. Morgan, W. J., Plate motions and deep mantle convection, *Geol. Soc. Am. Mem., 132,* 7–22, 1972.
70. Pelayo, A. M., and D. A. Wiens, Seismotectonics and relative plate motions in the Scotia Sea region, *J. Geophys. Res., 94,* 7293–7320, 1989.
71. Pitman, W. C., III, and J. R. Heirtzler, Magnetic anomalies over the Pacific-Antarctic ridge, *Science, 154,* 1164–1171, 1966.
72. Robbins, J. W., D. E. Smith, and C. Ma, Horizontal crustal deformation and large scale plate motions inferred from space geodetic techniques, in *Contribu-*

tions of Space Geodesy to Geodynamics: Crustal Dynamics, Geodynamic Series 23, edited by D. E. Smith and D. L. Turcotte, pp. 21–36, American Geophysical Union, Washington, 1993.

73. Royer, J.-Y., and T. Chang, Evidence for relative motions between the Indian and Australian plates during the last 20 Myr from plate tectonic reconstructions. Implications for the deformation of the Indo-Australian plate, *J. Geophys. Res., 96,* 11,779–11,802, 1991.
74. Ryan, J. W., C. Ma, and D. S. Caprette, *NASA Space Geodesy Program—GSFC Data Analysis—1992: Final Report of the Crustal Dynamics Project VLBI Geodetic Results 1979–91, NASA Technical Memorandum* 104572, 471 pp., National Aeronautics and Space Administration, Greenbelt, 1993.
75. Searle, R. C., GLORIA investigations of oceanic fracture zones: comparative study of the transform fault zone, *J. Geol. Soc. London, 143,* 743–756, 1986.
76. Seno, T., T. Moriyama, S. Stein, D. F. Woods, C. DeMets, D. Argus, and R. Gordon, Redetermination of the Philippine sea plate motion (abstract), *Eos Trans. AGU, 68,* 1474, 1987.
77. Shackleton, N. J., A. Berger, and W. R. Peltier, An alternative astronomical calibration of the lower Pleistocene timescale based on ODP Site 677, *Transactions of the Royal Society of Edinburgh: Earth Sciences, 81,* 251–261, 1990.
78. Silver, E. A., Tectonics of the Mendocino triple junction, *Geol. Soc. Am. Bull., 82,* 2965–2978, 1971.
79. Smith, D. E., R. Kolenkiewicz, P. J. Dunn, J. W. Robbins, M. H. Torrence, S. M. Klosko, R. G. Williamson, E. C. Pavlis, N. B. Douglas, and S. K. Fricke, Tectonic motion and deformation from satellite laser ranging to LAGEOS, *J. Geophys. Res., 95,* 22,013–22,041, 1990.
80. Solomon, S. C., and N. H. Sleep, Some simple physical models for absolute plate motions, *J. Geophys. Res., 79,* 2557–2567, 1974.
81. Stein, S., and R. G. Gordon, Statistical tests of additional plate boundaries from plate motion inversions, *Earth Planet. Sci. Lett., 69,* 401–412, 1984.
92. Stein, S., and E. A. Okal, Seismicity and tectonics of the Ninetyeast Ridge area: Evidence for internal deformation of the Indian plate, *J. Geophys. Res., 83,* 2233–2245, 1978.
83. Stein, C. A., S. Cloetingh, and R. Wortel, Seasat-derived gravity constraints on stress and deformation in the northeastern Indian Ocean, *Geophys. Res. Lett., 16,* 823–826, 1989.
84. Stoddard, P. R., A kinematic model for the evolution of the Gorda plate, *J. Geophys. Res., 92,* 11,524–11,532, 1987.
85. Stoddard, P. R., A comparison of brittle deformation models for the Gorda plate, *Tectonophysics, 187,* 205–214, 1991.
86. Sykes, L. R., Seismicity of the Indian Ocean and a possible nascent island arc between Ceylon and Australia, *J. Geophys. Res., 75,* 5041–5055, 1970.
87. Tapponnier, P., and P. Molnar, Slip-line field theory and large scale continental tectonics, *Nature, 294,* 319–324, 1976.
88. Vilotte, J. P., M. Daignieres, and R. Madariaga, Numerical modeling of intraplate deformation: simple mechanical models of continental collision., *J. Geophys. Res., 87,* 10,709–10,728, 1982.
89. Vine, F. J., Spreading of the ocean floor: new evidence, *Science, 154,* 1405–1415, 1966.
90. Vine, F. J., and D. H. Matthews, Magnetic anomalies over oceanic ridges, *Nature, 199,* 947–949, 1963.
91. Ward, S. N., Pacific-North America plate motions: New results from very long baseline interferometry, *J. Geophys. Res., 95,* 21,965–21,981, 1990.
92. Weissel, J. K., and R. N. Anderson, Is there a Caroline plate?, *Earth Planet. Sci. Lett., 41,* 143–158, 1978.
93. Weissel, J. K., R. N. Anderson, and C. A. Geller, Deformation of the Indo-Australian plate, *Nature, 287,* 284–291, 1980.
94. Wiens, D. A., C. DeMets, R. G. Gordon, S. Stein, D. Argus, J. F. Engeln, P. Lundgren, D. Quible, C. Stein, S. Weinstein, and D. F. Woods, A diffuse plate boundary model for Indian Ocean tectonics, *Geophys. Res. Lett., 12,* 429–432, 1985.
95. Wilson, D. S., A kinematic model for the Gorda deformation zone as a diffuse southern boundary of the Juan de Fuca plate, *J. Geophys. Res., 91,* 10,259–10,269, 1986.
96. Wilson, D. S., Tectonic history of the Juan de Fuca Ridge over the last 40 million years, *J. Geophys. Res., 93,* 11,863–11,876, 1988.
97. Wilson, D.S., Deformation of the so-called Gorda plate, *J. Geophys. Res., 94,* 3065–3075, 1989.
98. Wilson, J. T., Evidence from islands on the spreading of ocean floors, *Nature, 197,* 536–538, 1963a.
99. Wilson, J. T., A possible origin of the Hawaiian Islands, *Canadian J. of Physics, 41,* 863–870, 1963b.

Seismic Models of the Earth: Elastic and Anelastic

T. G. Masters and P. M. Shearer

1. INTRODUCTION

The intent of this chapter is to give a brief review of the current state of seismological modeling of the Earth's interior. The Earth is nearly spherically symmetric – we shall see below that departures from spherical symmetry in the deep Earth are only a few percent in magnitude – so it is useful to think of a spherical reference state with small perturbations superimposed. We write

$$\mathbf{m}(r,\theta,\phi) = \mathbf{m}_0(r) + \delta\mathbf{m}(r,\theta,\phi) \qquad (1)$$

where $\mathbf{m}$ denotes a vector of physical properties needed to define the seismic model. The spherical part of the model, $\mathbf{m}_0$ (sometimes called the "terrestrial monopole"), has been the subject of investigation for several decades and quite precise models have existed for nearly fifty years. Our knowledge of the aspherical part of the model, at least on a global scale, has improved dramatically in the last decade, largely as a result of the availability of high-quality digital data sets.

2. SPECIFICATION OF EARTH MODELS

What are the properties that comprise the vector $\mathbf{m}$? We consider first the spherical part of the model. The traditional data sets used to constrain $\mathbf{m}_0$ include free-oscillation frequencies, surface-wave phase velocity measurements, and travel times of body-waves. Free-oscillation frequencies have some sensitivity to density and, of course, all the data sets are sensitive to the seismic velocities. Until the mid-1970's, the terrestrial monopole was assumed to be perfectly elastic and isotropic. An isotropic model is specified by three functions of radius: density ρ, and the Lamé parameters, λ and μ (μ is also called the "rigidity" or "shear modulus"). Other combinations of elastic moduli in common usage for isotropic materials are

$$\left.\begin{aligned} K_s &= \lambda + \frac{2}{3}\mu \\ E &= \frac{\mu(3\lambda+2\mu)}{\lambda+\mu} \\ \sigma &= \frac{\lambda}{2(\lambda+\mu)} \end{aligned}\right\} \qquad (2)$$

where K_s is the adiabatic bulk modulus, E is Young's modulus, and σ is Poisson's ratio. The Earth's mantle has a Poisson's ratio close to 0.25 which is achieved when $\lambda = \mu$. The fluid outer core is often modeled as a perfectly elastic (inviscid) fluid where $\mu = 0$ so $\sigma = 0.5$. The elastic moduli can be cast in terms of the seismic velocities, V_p and V_s:

$$\left.\begin{aligned} \mu &= \rho V_s^2 \\ K_s &= \rho(V_p^2 - \frac{4}{3}V_s^2) \\ \lambda &= \rho(V_p^2 - 2V_s^2) \end{aligned}\right\} \qquad (3)$$

In the mid 70's it became clear that the weak attenuation of seismic energy in the Earth has a significant effect on the modeling of seismic data. In any attenuating body, the moduli must be frequency dependent (an effect called "physical dispersion") so that the Earth sensed by low-frequency free oscillations is different from that sensed by

T. G. Masters and R. Widmer, University of California, San Diego, IGPP, A025, La Jolla, CA 92093

Global Earth Physics
A Handbook of Physical Constants
AGU Reference Shelf 1

high-frequency body waves. In fact, it had been noticed that models made using free oscillations alone predicted travel-times which were offset from the observed travel-times. This difference was called the "baseline" effect and was originally ascribed to a continental bias to seismic travel times because of the distribution of seismic receivers. However, it is now clear that much of the baseline effect can be explained by physical dispersion.

Specification of a weakly attenuating Earth model is complicated by the fact that there are now a multitude of possible constitutive relationships to choose from. It is usual to choose some simple visco-elastic behavior to model real-Earth materials, with a standard linear solid (SLS) being a common choice. A SLS exhibits elastic-type instantaneous deformation when stressed but then relaxes with a characteristic time constant. Such a material preferentially attenuates seismic energy at a specific frequency. A composite body can be constructed which attenuates energy over a broad range of frequencies to produce an "absorption band" that mimics the observed absorption of energy in the Earth. The "elastic" moduli describing this behavior are now complex and frequency-dependent. For example, we can write the shear modulus as

$$\mu(\omega) = \mu_0 \left[1 + d_\mu(\omega) + iq_\mu(\omega)\right] \tag{4}$$

where d and q are small if attenuation is weak, and μ_0 is the "unrelaxed modulus" which describes the initial response of the material to loading. Conventionally, seismic attenuation is described using the "quality factor," Q, which is related to the amount of energy lost per cycle, ΔE when the material is stressed at frequency ω:

$$\frac{2\pi}{Q} = -\frac{\Delta E}{E}$$

and E is the peak strain energy. In terms of the complex modulus, the attenuation in shear, $1/Q_\mu(\omega)$, is defined as $Im(\mu(\omega))/Re(\mu(\omega))$. An equation similar to (4) can be defined for the bulk modulus and the quality of attenuation in compression, $Q_K(\omega)$. Q_μ and Q_K together provide a phenomenological description of attenuation in the Earth and must be specified as a function of depth and frequency. The fact that the elastic moduli are complex leads to complex frequencies of free oscillation which means simply that the oscillations decay. Observation of the decay rates of the oscillations can, in principle, be used to constrain Q_μ and Q_K as a function of depth and frequency, and we shall discuss this below.

The physical dispersion is controlled by $d(\omega)$ which can be computed from $q(\omega)$ if q is known for all frequencies [1, section 5.5]. Of course this is impossible, so further assumptions about the frequency dependence of q (or equivalently Q) must be made before the physical dispersion can be computed. Observations of attenuation over a broad range of frequencies are consistent with Q being roughly independent of frequency from periods of a few seconds down to periods of about an hour. With this constraint, $d(\omega)$ can be calculated and we find that the modulus at one frequency within the absorption band is related to the modulus at another frequency by

$$\frac{\mu(\omega_1)}{\mu(\omega_2)} = 1 + \frac{2}{\pi Q_\mu} \ln\left(\frac{\omega_1}{\omega_2}\right)$$

This means that seismic velocities change by about 1% for a period change of $1 \rightarrow 1000$ secs if $Q \simeq 200$. The number is increased to 4% if $Q \simeq 60$.

The next major evolution in spherical-Earth modeling came in the early 80's when it became clear that departures from elastic isotropy might be needed. A generally anisotropic model (with up to 21 elastic moduli) cannot exhibit spherical symmetry but a model with elastic velocities in the radial direction different from elastic velocities perpendicular to the radial direction can be spherically symmetric. Such a material is called *transversely isotropic*. There are now five independent elastic coefficients (as opposed to two for the isotropic case). In Love notation, these moduli are given the symbols A, C, N, L and F. An isotropic model can be thought of as a special case of the transversely isotropic model when $A=C=\lambda+2\mu$, $N=L=\mu$ and $F=\lambda$. In terms of the seismic velocities in the radial direction (V_{pv}, V_{sv}) and in the transverse direction (V_{ph}, V_{sh}), we have

$$\left.\begin{aligned} A &= \rho V_{ph}^2 \\ C &= \rho V_{pv}^2 \\ N &= \rho V_{sh}^2 \\ L &= \rho V_{sv}^2 \end{aligned}\right\} \tag{5}$$

The fifth constant, F, is a function of the velocities at intermediate incident angles [7].

Having decided upon the physical parameters to be included in the model, we must still decide how to parameterize the structure. Recently, it has become common to use polynomial representations of the density and seismic velocities as a function of frequency (IASP91, PREM). One difficulty is choosing the radial knots at which the polynomials are broken. There are several radii in the Earth at which there is clear evidence for a sharp change in structure of a global nature. The most prominent of these is the core-mantle boundary (CMB) followed by the

inner-core boundary (ICB) and Moho. There is now good evidence for the global nature of sharp changes in structure at depths of 410 km and 660 km [34] though there is also evidence for some variability in the depth and strength of these "discontinuities." Other radii have been proposed but the evidence for other discontinuities of global extent is weak. In particular, there is little evidence for a globally-coherent 220 km discontinuity, although it appears to be present in some locations. The top of the D″ region (roughly the bottom 250 km of the mantle) also shows evidence for a sharp change in structure in some locations but again its properties vary spatially. Section 4 discusses the discontinuities in more detail while section 5 discusses the parameterization of aspherical models.

3. SOME SPHERICAL MODELS

Modern spherical Earth models are built using large data sets of free-oscillation frequencies, surface-wave phase velocities, and the travel-times of body waves. All these data sets are, to some extent, contaminated by the effects of 3-dimensional structure and much effort has been expended in constructing data sets which are representative of the spherically-averaged structure. The free-oscillation and phase-velocity data sets are summarized elsewhere in this volume. These data sets sample the Earth at frequencies between 0.3 and 15 mHz so a model of the frequency-dependence of structure must also be included. The absorption band model described in section 2 is generally felt to be an adequate model for the long-period data but requires that Q be roughly independent of frequency in the band covered by the data. It is unlikely that such an attenuation model will be valid up to a period of about 1 second which is the dominant period of the P-wave body waves whose travel-times are compiled by the International Seismological Centre (ISC). This makes it difficult to include the absolute times of body waves in global inversions even though such data can enhance the depth resolution of structure in some parts of the Earth. Dziewonski and Anderson [7] circumvented this problem by using the shape of the travel time curve rather than the absolute times since, for teleseismic P-waves, it is likely that the effect of physical dispersion can be modeled by a baseline shift of the whole travel time curve.

Model PREM is shown Figure 1 and the isotropic version is listed in Table 1. This model has a pronounced 220 km discontinuity and is transversely isotropic above this depth. Montagner and Anderson [22] have experimented with the depth extent of anisotropy using a new compilation of free-oscillation frequencies. Their models, which do not have a 220 km discontinuity, show an interesting

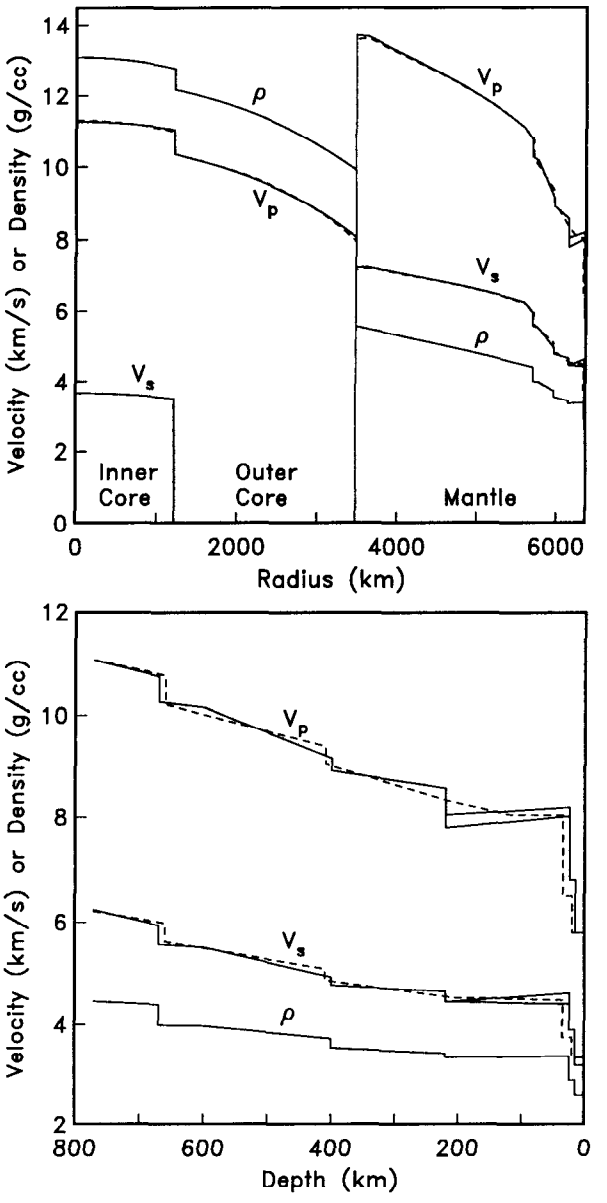

Fig. 1. Seismic velocities and density vs. radius for PREM [7] shown as solid lines, and SP6 [27], which is a modified version of the IASP91 model, shown as dashed lines. PREM and SP6 are in close agreement throughout the lower mantle and core, with the largest differences occuring in the gradients just above and below the core-mantle boundary. PREM contains transverse isotropy in the uppermost mantle between 24.4 and 220 km depth; the lines plotted show the minimum and maximum velocities. PREM has three major discontinuties in the upper mantle at depths of 220, 400 and 670 km, and an S-wave low-velocity zone between 80 and 220 km. SP6, like IASP91, contains upper-mantle discontinuities only at 410 and 660 km, with no low-velocity zone.

TABLE 1. Preliminary Reference Earth Model (isotropic version)

Radius (km)	Depth (km)	V_p (m/s)	V_s (m/s)	ρ (kg m^{-3})	Q_μ	Q_κ	K_s (GPa)	μ (GPa)	ν	P (GPa)	g (m s^{-2})
0.0	6371.0	11262.2	3667.8	13088.5	84.6	1327.7	1425.3	176.1	0.44	364.0	0.00
100.0	6271.0	11260.6	3666.7	13086.3	84.6	1327.7	1424.8	175.9	0.44	363.7	0.37
200.0	6171.0	11255.9	3663.4	13079.8	84.6	1327.7	1423.1	175.5	0.44	363.0	0.73
300.0	6071.0	11248.1	3657.9	13068.9	84.6	1327.7	1420.3	174.9	0.44	361.8	1.10
400.0	5971.0	11237.1	3650.3	13053.7	84.6	1327.7	1416.4	173.9	0.44	360.2	1.46
500.0	5871.0	11223.0	3640.4	13034.1	84.6	1327.7	1411.4	172.7	0.44	358.0	1.82
600.0	5771.0	11205.8	3628.4	13010.1	84.6	1327.7	1405.3	171.3	0.44	355.4	2.19
700.0	5671.0	11185.4	3614.1	12981.8	84.6	1327.7	1398.1	169.6	0.44	352.3	2.55
800.0	5571.0	11161.9	3597.7	12949.1	84.6	1327.7	1389.8	167.6	0.44	348.8	2.91
900.0	5471.0	11135.2	3579.0	12912.1	84.6	1327.7	1380.5	165.4	0.44	344.8	3.27
1000.0	5371.0	11105.4	3558.2	12870.8	84.6	1327.7	1370.1	163.0	0.44	340.4	3.62
1100.0	5271.0	11072.5	3535.2	12825.0	84.6	1327.7	1358.6	160.3	0.44	335.5	3.98
1200.0	5171.0	11036.4	3510.0	12775.0	84.6	1327.7	1346.2	157.4	0.44	330.2	4.33
1221.5	5149.5	11028.3	3504.3	12763.6	84.6	1327.7	1343.4	156.7	0.44	329.0	4.40
1221.5	5149.5	10355.7	0.0	12166.3	0.0	57823.0	1304.7	0.0	0.50	329.0	4.40
1300.0	5071.0	10309.7	0.0	12125.0	0.0	57823.0	1288.8	0.0	0.50	324.7	4.64
1400.0	4971.0	10249.6	0.0	12069.2	0.0	57823.0	1267.9	0.0	0.50	318.9	4.94
1500.0	4871.0	10187.5	0.0	12009.9	0.0	57823.0	1246.4	0.0	0.50	312.7	5.25
1600.0	4771.0	10122.9	0.0	11946.8	0.0	57823.0	1224.2	0.0	0.50	306.3	5.56
1700.0	4671.0	10055.8	0.0	11879.9	0.0	57823.0	1201.3	0.0	0.50	299.5	5.86
1800.0	4571.0	9985.6	0.0	11809.0	0.0	57823.0	1177.5	0.0	0.50	292.3	6.17
1900.0	4471.0	9912.1	0.0	11734.0	0.0	57823.0	1152.9	0.0	0.50	284.9	6.47
2000.0	4371.0	9835.0	0.0	11654.8	0.0	57823.0	1127.3	0.0	0.50	277.1	6.77
2100.0	4271.0	9754.0	0.0	11571.2	0.0	57823.0	1100.9	0.0	0.50	269.1	7.07
2200.0	4171.0	9668.7	0.0	11483.1	0.0	57823.0	1073.5	0.0	0.50	260.8	7.37
2300.0	4071.0	9578.8	0.0	11390.4	0.0	57823.0	1045.1	0.0	0.50	252.2	7.66
2400.0	3971.0	9484.1	0.0	11293.0	0.0	57823.0	1015.8	0.0	0.50	243.3	7.95
2500.0	3871.0	9384.2	0.0	11190.7	0.0	57823.0	985.5	0.0	0.50	234.2	8.23
2600.0	3771.0	9278.8	0.0	11083.4	0.0	57823.0	954.2	0.0	0.50	224.9	8.51
2700.0	3671.0	9167.6	0.0	10970.9	0.0	57823.0	922.0	0.0	0.50	215.4	8.78
2800.0	3571.0	9050.2	0.0	10853.2	0.0	57823.0	888.9	0.0	0.50	205.7	9.04
2900.0	3471.0	8926.4	0.0	10730.1	0.0	57823.0	855.0	0.0	0.50	195.8	9.31
3000.0	3371.0	8795.8	0.0	10601.5	0.0	57823.0	820.2	0.0	0.50	185.7	9.56
3100.0	3271.0	8658.1	0.0	10467.3	0.0	57823.0	784.7	0.0	0.50	175.5	9.81
3200.0	3171.0	8513.0	0.0	10327.3	0.0	57823.0	748.4	0.0	0.50	165.2	10.05
3300.0	3071.0	8360.2	0.0	10181.4	0.0	57823.0	711.6	0.0	0.50	154.8	10.28
3400.0	2971.0	8199.4	0.0	10029.4	0.0	57823.0	674.3	0.0	0.50	144.3	10.51
3480.0	2891.0	8064.8	0.0	9903.4	0.0	57823.0	644.1	0.0	0.50	135.8	10.69
3480.0	2891.0	13716.6	7264.7	5566.5	312.0	57823.0	655.6	293.8	0.31	135.8	10.69
3500.0	2871.0	13711.7	7264.9	5556.4	312.0	57823.0	653.7	293.3	0.30	134.6	10.66
3600.0	2771.0	13687.6	7265.7	5506.4	312.0	57823.0	644.0	290.7	0.30	128.8	10.52
3630.0	2741.0	13680.4	7266.0	5491.5	312.0	57823.0	641.2	289.9	0.30	127.0	10.49
3700.0	2671.0	13596.0	7234.0	5456.6	312.0	57823.0	627.9	285.5	0.30	123.0	10.41
3800.0	2571.0	13477.4	7188.9	5406.8	312.0	57823.0	609.5	279.4	0.30	117.4	10.31
3900.0	2471.0	13360.8	7144.2	5357.1	312.0	57823.0	591.7	273.4	0.30	111.9	10.23
4000.0	2371.0	13245.3	7099.7	5307.3	312.0	57823.0	574.4	267.5	0.30	106.4	10.16
4100.0	2271.0	13130.6	7055.2	5257.3	312.0	57823.0	557.5	261.7	0.30	101.1	10.10
4200.0	2171.0	13015.8	7010.5	5207.2	312.0	57823.0	540.9	255.9	0.30	95.8	10.06

TABLE 1. Continued

Radius (km)	Depth (km)	V_p (m/s)	V_s (m/s)	ρ (kg m^{-3})	Q_μ	Q_κ	K_s (GPa)	μ (GPa)	ν	P (GPa)	g (m s^{-2})
4300.0	2071.0	12900.5	6965.3	5156.7	312.0	57823.0	524.6	250.2	0.29	90.6	10.02
4400.0	1971.0	12783.9	6919.5	5105.9	312.0	57823.0	508.5	244.5	0.29	85.5	9.99
4500.0	1871.0	12665.5	6872.8	5054.7	312.0	57823.0	492.5	238.8	0.29	80.4	9.97
4600.0	1771.0	12544.7	6825.1	5003.0	312.0	57823.0	476.6	233.0	0.29	75.4	9.95
4700.0	1671.0	12420.8	6776.0	4950.8	312.0	57823.0	460.7	227.3	0.29	70.4	9.94
4800.0	1571.0	12293.2	6725.4	4897.9	312.0	57823.0	444.8	221.5	0.29	65.5	9.93
4900.0	1471.0	12161.3	6673.1	4844.3	312.0	57823.0	428.8	215.7	0.28	60.7	9.93
5000.0	1371.0	12024.5	6618.9	4789.9	312.0	57823.0	412.8	209.8	0.28	55.9	9.94
5100.0	1271.0	11882.1	6562.4	4734.6	312.0	57823.0	396.6	203.9	0.28	51.2	9.94
5200.0	1171.0	11733.6	6503.6	4678.5	312.0	57823.0	380.3	197.9	0.28	46.5	9.95
5300.0	1071.0	11578.3	6442.3	4621.3	312.0	57823.0	363.8	191.8	0.28	41.9	9.96
5400.0	971.0	11415.6	6378.1	4563.1	312.0	57823.0	347.1	185.6	0.27	37.3	9.97
5500.0	871.0	11244.9	6310.8	4503.8	312.0	57823.0	330.3	179.4	0.27	32.8	9.99
5600.0	771.0	11065.6	6240.4	4443.2	312.0	57823.0	313.4	173.0	0.27	28.3	10.00
5701.0	670.0	10751.3	5945.1	4380.7	312.0	57823.0	299.9	154.8	0.28	23.8	10.02
5701.0	670.0	10266.2	5570.2	3992.1	143.0	57823.0	255.6	123.9	0.29	23.8	10.02
5771.0	600.0	10157.8	5516.0	3975.8	143.0	57823.0	248.9	121.0	0.29	21.1	10.01
5771.0	600.0	10157.8	5515.9	3975.8	143.0	57823.0	248.9	121.0	0.29	21.1	10.01
5800.0	571.0	10009.4	5431.3	3939.3	143.0	57823.0	239.7	116.2	0.29	19.9	10.00
5900.0	471.0	9497.4	5139.6	3813.2	143.0	57823.0	209.7	100.7	0.29	16.0	9.99
5971.0	400.0	9133.9	4932.5	3723.7	143.0	57823.0	189.9	90.6	0.29	13.4	9.97
5971.0	400.0	8905.2	4769.9	3543.3	143.0	57823.0	173.5	80.6	0.30	13.4	9.97
6000.0	371.0	8849.5	4749.6	3525.9	143.0	57823.0	170.1	79.5	0.30	12.3	9.96
6100.0	271.0	8657.1	4679.6	3466.2	143.0	57823.0	158.6	75.9	0.29	8.9	9.93
6151.0	220.0	8558.9	4643.9	3435.8	143.0	57823.0	152.9	74.1	0.29	7.1	9.91
6151.0	220.0	7989.7	4418.9	3359.5	80.0	57823.0	127.0	65.6	0.28	7.1	9.91
6200.0	171.0	8020.0	4437.0	3364.8	80.0	57823.0	128.1	66.2	0.28	5.5	9.89
6291.0	80.0	8076.2	4470.5	3374.7	80.0	57823.0	130.2	67.4	0.28	2.5	9.86
6291.0	80.0	8076.2	4470.5	3374.7	600.0	57823.0	130.2	67.4	0.28	2.5	9.86
6300.0	71.0	8081.8	4473.8	3375.7	600.0	57823.0	130.4	67.6	0.28	2.2	9.86
6346.6	24.4	8110.6	4491.0	3380.7	600.0	57823.0	131.5	68.2	0.28	0.6	9.84
6346.6	24.4	6800.0	3900.0	2900.0	600.0	57823.0	75.3	44.1	0.25	0.6	9.84
6356.0	15.0	6800.0	3900.0	2900.0	600.0	57823.0	75.3	44.1	0.25	0.3	9.84
6356.0	15.0	5800.0	3200.0	2600.0	600.0	57823.0	52.0	26.6	0.28	0.3	9.84
6368.0	3.0	5800.0	3200.0	2600.0	600.0	57823.0	52.0	26.6	0.28	0.0	9.83
6368.0	3.0	1450.0	0.0	1020.0	0.0	57823.0	2.1	0.0	0.50	0.0	9.83
6371.0	0.0	1450.0	0.0	1020.0	0.0	57823.0	2.1	0.0	0.50	0.0	9.82

trade-off between the depth extent of anisotropy and the size of the shear velocity jump at the 410 km discontinuity. If anisotropy is allowed to extend to 400 km depth or greater, the shear velocity jump at the 410 km discontinuity becomes extremely small. This is inconsistent with the results of regional studies and suggests that global transverse isotropy should be confined to relatively shallow depths. In fact, some workers have suggested that the evidence for global transverse isotropy is sufficiently weak that it may not be a required feature of the spherically-averaged Earth.

Other spherical Earth models of seismic velocity alone have been generated from the ISC data set. Model IASP91, [15], has been designed to provide an optimal fit to the ISC times (see Kennett, this volume, for a detailed description). This may mean that IASP91 is not necessarily an unbiased estimate of the spherically-averaged Earth since the ISC data provide a non-uniform geographic sampling

of the Earth. Modifications to IASP91 have already been proposed, primarily in the velocities in the core [27 and Figure 1].

Free oscillation data have traditionally been used to infer the average Q structure of the Earth. Earlier compilations of mode Q's have been augmented with overtone measurements and new models of the attenuation characteristics of the Earth at low frequencies have been derived [e.g. 46]. All models are similar in the mantle (see Table 1) and the evidence now seems to prefer a relatively low Q ($Q_\mu \simeq 120$) for the inner core. This is in qualitative agreement with the high attenuation observed for body-waves which sample the upper part of the inner core. It should also be noted that there is some evidence for systematic differences between mean Q measurements made from the analysis of surface-waves and those made by fitting the spectra of free-oscillation peaks. Models based on surface-wave observations tend to have shear-Q values about 5% lower in the upper mantle than the mode models. The reason for this discrepancy is not yet clear.

4. A TOUR THROUGH THE EARTH

The gross structure of the Earth and its division into core, mantle and crust were determined by seismologists early in this century. More recently, attention has focused on the finer structure of the Earth and the evidence for lateral variations in properties. Generally, the largest variations in structure are found near the major discontinuities such as the surface and the core-mantle boundary (CMB), with comparatively smooth changes outside of these regions. We now take a closer look at Earth structure, starting at the center.

4.1. Inner Core

The radius of the inner core is defined by a small but sharp increase in P-wave velocity at a radius of about 1220 ± 10 km (see [19] for references to recent work on core structure). This velocity increase is constrained by travel time data to be about 0.7 ± 0.15 km/s and is required to explain the triplications in the direct body waves which travel through the core (PKP waves) and the observations of reflected arrivals from the inner-core boundary ($PKiKP$ waves). Arrival times and waveforms of $PKiKP$ at high frequencies provide the most direct constraints on the properties of the inner-core boundary (ICB). These data show that departures from the expected elliptical shape of the ICB are confined to a few kilometers and that the ICB transition must be complete in less than about 5 km. Waveform modeling experiments sampling different parts of the ICB have found velocity jumps varying from about 0.5 km/s to 0.8 km/s [e.g. 35] which may well reflect lateral variations in structure near the top of the inner core. Normal mode observations indicate a density jump at the ICB of about 0.55 g/cm^3, a result which is also consistent with $PKiKP$ amplitudes. The average P-wave velocity in the inner core is about 11.2 km/s as determined by PKP travel times and normal modes. Constraints on the S-wave velocity in the inner core are weaker. Claims of observations of a body wave with an S leg through the inner core ($PKJKP$) are now generally discarded but normal mode observations quite tightly constrain the average inner core shear velocity to be about 3.5 km/s. This gives a high Poisson ratio for the inner core of about 0.45 which has led some people to infer that this region may be close to its melting temperature. On the other hand, the high Poisson ratio may be simply a natural consequence of the fact that the ambient pressure is a significant fraction of the elastic moduli.

As noted in the previous section, studies of the decay of normal modes and pulse broadening in PKP waveforms that have traveled through the inner core indicates that at least the outer part of the inner core is highly attenuating [e.g. 3, 46]. There is now hard evidence that the inner core is also strongly anisotropic. Studies of $PKIKP$ with paths nearly parallel to the rotation axis show that the waves travel anomalously quickly in this direction relative to more equatorial paths [e.g. 24] and are characterized by low-amplitude, complicated waveforms [4, 36]. A simple model of anisotropy in the inner core can be found which goes a long way to simultaneously explaining the $PKIKP$ observations and the anomalous splitting of free-oscillations that sample the core [e.g. 42]. The physical cause of the anisotropy is not currently understood, though alignment of iron crystals by convective flow [13] or by the magnetic field [14] are contenders.

4.2. Outer Core

The outer core is assumed to be fluid since rapid convection is required to drive the geodynamo and no evidence has ever been found for outer-core shear waves. (It is possible that a very slow S-wave velocity ($<\sim$100 m/s) could escape seismic detection.) The P-wave velocity and density appear to increase smoothly with depth in the outer core, consistent with a well-mixed, vigorously convecting layer. However, there is some evidence for anomalous velocity gradients and/or weak heterogeneity in the uppermost 200 km [e.g., 18] and low velocity gradients close to the ICB [37, 35]. The region near the top of the core is particularly hard to study since few body waves turn here. The best data are mantle shear waves which convert to P-waves at the core-mantle boundary (e.g. SKS and

$SKKS$). Using such data, Lay and Young [18] find evidence for anomalously low velocities (by 1–2%) in a thin layer 50–100 km thick beneath the core-mantle boundary (CMB) under Alaska. Some studies have inferred weak lateral variation of structure in the outer core but $SmKS$ data can also be affected by rapid lateral variations of structure at the base of the mantle, a region we know to be strongly heterogeneous. It seems preferable to assume the outer core is laterally homogeneous until more compelling observational evidence becomes available.

The core-mantle boundary (CMB) is constrained by both body waves and normal modes to have a radius of 3483 $\pm$ 5 km. Attempts to resolve topography on the CMB from travel times of the reflected phase PcP [e.g., 25] have led to inconclusive results, primarily due to the difficulty in removing the effect of heterogeneity in the mantle on the travel times [31]. The PcP times suggest it is unlikely that the CMB deviates by more than about 10 km from its hydrostatic shape. Short-period PcP waveforms appear undistorted, consistent with a sharp, smooth interface at the CMB [44].

4.3. D″ Region

D″ is the name given to a region of reduced velocity gradients about 100 to 300 km thick immediately above the CMB. There is an extensive history of seismic exploration of the base of the mantle and a review of the great diversity of models proposed for this region can be found in [53]. It is also known that the D″ region is characterized by strong lateral heterogeneity covering a broad spectrum of wavelengths [16].

The existence of large-scale S velocity anomalies with variations of up to 3% near the base of the mantle now seems to be well-established. They have been found in studies of $ScS - S$ [e.g. 49] and diffracted S [51]. Such variations are also capable of explaining anomalous $SmKS$ differential times in some areas [10]. Observations of additional phases arriving slightly before ScS suggest the presence of a triplication caused by a velocity discontinuity about 280 km above the CMB [e.g., 17, 9]. The data can be modeled with either a first-order discontinuity with a velocity contrast of about 3% or as a zone of high velocity gradient up to 100 km wide. This discontinuity seems to vary in depth and is probably not a global feature since it is not seen in some areas. A sharp gradient in shear velocity is unlikely to be explained by temperature effects so it is probable that a compositional stratification or a new phase transformation will have to be invoked to explain the data. A similar triplication has occasionally been observed in P wave data with the size of the inferred P-wave jump also being about 2–3% [e.g., 45]. Again, this P wave discontinuity is unlikely to be a global feature since reflections from it are rarely observed even under favorable recording conditions. Lateral variations of about 3% in P at the base of the mantle have also been inferred by Young and Lay [54] in a study of short period amplitude profiles and by Wysession and Okal [52] using diffracted P.

Additionally, D″ appears to be a strong scatterer of body waves [e.g., 2]. The scatterers produce precursors to PKP and are of scale-length ~30 km and composed of roughly 1% variations in density and velocity (these scatterers could also be explained by a rough CMB boundary).

4.4. Lower Mantle

The lower mantle is usually taken to be all the mantle from the top of D″ to the 660-km discontinuity. Up to a depth of about 750 km, the lower mantle appear to be relatively homogeneous with no significant discontinuities in structure of global extent. Tomography results indicate shear-velocity variations of 1% or less. Above 750 km, we enter the region where upper mantle minerals are still undergoing phase changes to their high pressure forms and there may be an anomalously steep velocity gradient just below the 660-km discontinuity.

4.5. Transition Zone

This is usually taken to be the region between the two major seismic discontinuities in the upper mantle–the 410- and 660-km discontinuities. Most Earth models have first-order discontinuities at these depths with 4–7% jumps in velocity and density. Both discontinuities are now generally explained as resulting from phase changes in olivine, but controversy remains regarding whether small compositional changes might also occur. Most seismological observations of the discontinuities cannot distinguish between abrupt discontinuities and gradual transitions over a depth interval up to about 20 km. An exception are short-period precursors to the phase $PKPPKP$ (generally termed $P'P'$ which result from underside reflections off mantle discontinuities at near-vertical incidence. These observations suggest that, at least in some regions, a significant part of the velocity and density jumps at 410 and 660 km must occur within a depth interval of less than 5 km [e.g., 43].

Depths to the major discontinuities have varied between different studies and it now appears that at least some of this variation is due to topography on the discontinuities. Recent observations of long-period S-wave reflections from the discontinuities suggest depth variations of up to 30 km [30, 33]. These studies also indicate a minor discontinuity near 520 km depth.

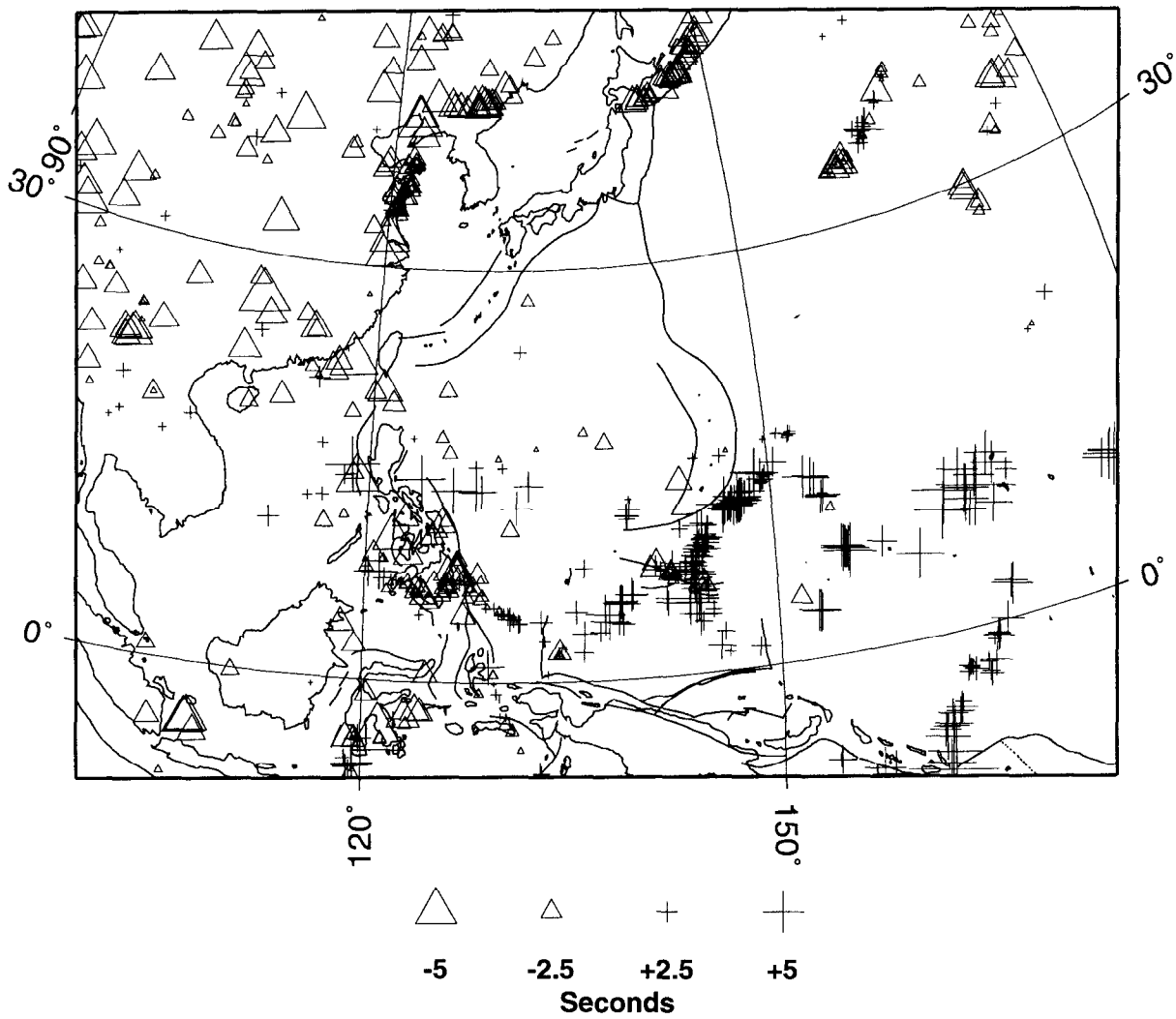

Fig. 2. Observed long-period $ScS - S$ residuals plotted at their bouncepoint positions on the core-mantle boundary. $ScS - S$ residuals are particularly sensitive to structure in the D'' region (the bottom few hundred kilometers of the mantle, just above the core-mantle boundary). Positive residuals indicate late ScS travel times relative to S, suggesting slow structure in D'', while negative residuals suggest fast structure. Large-scale coherent patterns are apparent in the residuals for this region,and are indicative of slow D'' structure beneath eastern China and fast D'' velocities in parts of the western Pacific. A more rigorous interpretation of these data that accounts for the possibility of velocity variations anywhere along the ray paths involves combining the $ScS - S$ data with other data into a general inversion for three-dimensional mantle structure.

4.6. Uppermost Mantle

This is the highly heterogeneous region between the crust and the 410-km discontinuity. In most models, the shear velocity (and sometimes the compressional velocity) decreases at a depth of 20–50 km beneath the oceans and at depth of greater than 150 km under the shields. The evidence for this low velocity zone (LVZ) comes from surface waves and body waves, the region above the LVZ is sometimes called the "lid." Isotropic models of the Earth require deep LVZs with velocity drops of 5–10% in shear velocity. Such models presumably imply that substantial partial melting is present, a result consistent with obser-

vations of high attenuation in surface waves that sample this region. The introduction of transverse isotropy can substantially reduce the magnitude of the inferred velocity drop of the LVZ at the cost of adding additional free parameters to the inversion (see Mitchell [21] for a discussion). A 220-km discontinuity, marking the bottom of the LVZ, has occasionally been observed (e.g. under Australia) and is a conspicuous feature of PREM (see Figure 1). However, in most areas such an interface is not seen, and recent stacks of long-period seismograms confirm that a 220-km discontinuity cannot be a global feature unless it is extremely variable in depth [33]. At the top of the lid is a sharp change in composition and seismic velocity (the Mohorovicic discontinuity or "Moho") which separates the mantle from the overlying crust. The oceanic crust is about 7 km thick, while continental crust varies from 20 to 70 km in thickness.

5. MODELS OF LARGE-SCALE THREE-DIMENSIONAL STRUCTURE

One of the most exciting achievements in seismology in the last decade has been the development of large-scale models of the three-dimensional velocity structure in the Earth's mantle. Although seismologists had long noted that there appeared to be lateral variations in structure, only in the 1980's did sufficient data and computing power become available to perform global inversions.

Returning to equation (1), we now consider the specification of the 3-dimensional term, $\delta\mathbf{m}(r,\theta,\phi)$. In general we should include anisotropic and anelastic terms in our 3D models, and some attempts have been made to do this, but most effort has been expended on the simpler problem of finding 3D variations in isotropic compressional velocity, $\delta V_p(r,\theta,\phi)$, and shear velocity, $\delta V_s(r,\theta,\phi)$. Parameterizations of the 3-dimensional velocity variation have generally involved either dividing the Earth into blocks or using a global basis such as spherical harmonics. In the latter case, for shear velocity variations we write

$$\delta V_s(r,\theta,\phi) = \sum_{l=0}^{l_{max}} \sum_{m=-l}^{l} c_l^m(r) Y_l^m(\theta,\phi) \qquad (6)$$

where $Y_l^m(\theta,\phi) = X_l^m(\theta)e^{im\phi}$ is a spherical harmonic of harmonic degree l and azimuthal order m [see e.g., 8]. Written in this way, the coefficients, c_l^m, are complex and satisfy the relation

$$c_l^{-m} = (-1)^m c_l^{m*} \qquad (7)$$

where the $*$ denotes complex conjugation. It is more common to expand in terms of sines and cosines giving

$$\delta V_s(r,\theta,\phi) = \sum_{l=0}^{l_{max}} \sum_{m=0}^{l} \left[A_l^m(r)\cos(m\phi) + B_l^m(r)\sin(m\phi)\right] p_l^m(\theta) \qquad (8)$$

where

$$Re(c_l^m) = (-1)^m\sqrt{2\pi}A_l^m$$
$$Im(c_l^m) = (-1)^{(m+1)}\sqrt{2\pi}B_l^m$$
$$c_l^0 = \sqrt{4\pi}A_l^0.$$

p_l^m is a normalized associated Legendre function with the normalization commonly used in geodesy (see Appendix C of Stacey [38]). $A_l^m(r)$ and $B_l^m(r)$ are usually expanded in basis functions in radius: Legendre poylnomials, Chebyshev polynomials, plane layers, B-splines, and linear interpolation between model knots have all been used.

For either a block model or a spherical harmonic expansion, some care is needed to ensure that the parameterization is adequate to model the data. In particular, an inappropriate choice of the maximum spherical harmonic degree, l_{max}, can lead to aliasing of short-wavelength structure into long-wavelength structure. There is now abundant evidence that the spectrum of 3-dimensional shear velocity structure in the Earth has power concentrated at long wavelengths where the amplitude of the structure is large (the low-amplitude structure in the mid-mantle may be quite white in spectral character). Often, the data can be plotted in a way designed to crudely reveal the underlying structure. For example, $ScS - S$ travel time residuals measured from long-period (20sec) data reveal large-scale coherent patterns when they are plotted at the bounce point of ScS on the core-mantle boundary (Figure 2). These differential times are insensitive to near-source and near-receiver structure and are mainly sensitive to structure at the base of the mantle [49]. A spectral analysis of the global pattern shows that it is dominantly of harmonic degree 2 with most of the power below $l = 6$. A similar analysis for $SS - S$ travel time residuals and SS absolute times again shows the dominance of low-order structure [50, 39] though now there is significant power up to about degree 10. Because of these observations, l_{max} has commonly been chosen to be between 8 and 12. The situation for the P-velocity models is a bit more complicated since the primary data source is the ISC compilation of short-period P arrival times which, in principle, are sensitive to structure of wavelength of a few kilometers. Models derived from the ISC data set have been quite variable and so we discuss the P velocity models separately from the S models.

Table 2 summarizes 12 models of mantle heterogeneity obtained by various groups. Some of the models apply only to the upper mantle (above the 670-discontinuity), others are for the lower mantle, and many recent inversions are for the whole mantle.

Figure 3 compares some of the different P-wave models at several depths in the mantle with the velocity perturbations shown in percent. One of the first inversions was done by Clayton and Comer in 1983 [see 11]. They used almost 2 million P-wave travel times as tabulated by the ISC from 1971 to 1980, and inverted for a perturbation model in which the mantle was discretized into 48,000 blocks. A year later, Dziewonski [6] inverted ISC P data for lower mantle structure, parameterized by spherical harmonics up to degree 6 and up to 5th order polynomials in depth (i.e. models LO2.45 and LO2.56). Comparison of the Clayton and Comer model with L02.56 showed that only the very longest wavelengths agree in shape (degrees 2 and 3) and even these were quite different in amplitude. These early models received considerable attention and also generated some criticism. The doubts regarding these models generally centered on questions regarding the reliability of the ISC data and the possibility of artifacts resulting from improper inversion procedures. However, the large-scale structures in more recent mantle heterogeneity models are in fair agreement with the early Harvard models, and it is now clear that the ISC data, with suitable averaging, can be useful in constraining mantle structure. In particular, a major feature of L02.56 is the ring of high velocities at the base of the mantle around the Pacific. This feature does not appear in all models generated from the ISC data set (Figure 3 and [29]) but is a robust feature of the shear-wave models.

The situation regarding global shear-wave models is more satisfactory, probably because lateral variations in shear velocity are significantly greater than those in compressional velocity, and because a greater variety of data sets have been brought to bear on the problem. Figure 4 compares some of the shear-wave models at three depths (some models are of the upper mantle only since the data they are constructed from are insensitive to the lower mantle). It is clear that although there is agreement between many of the models on the largest features, the overall shape and amplitude of the anomalies varies considerably between the models. The variability between models is largely a function of the data sets which went into their construction. For example, models based on surface-wave dispersion data alone have good lateral resolution in the upper mantle but relatively poor depth resolution and little sensitivity to structure deeper than 400 km. Models based solely on waveform fitting algorithms are probably biased in the lower mantle by inadequacies in the theory for modeling deep-turning waves. The latest models generally include data sets of many different types (e.g. absolute and differential travel times, surface-wave dispersion, free-oscillation splitting data, long-period waveforms). As more data are added, the models of different workers have converged and we now have reason to be-

TABLE 2. Three-dimensional Mantle Velocity Models

Model	Wave	Type	Max. Degree	Radial Function[a]	Data Types	Year	Ref. Number
LO2.56	P	lower	6	5 Lpoly	ISC[b] P picks	84	6
M84A	S	upper	8	4 Lpoly	Surface waves	84	47
M84C	S	upper	8	4 Lpoly	Surface waves	84	47
DSXRG	S	upper	8	10 layers	Surface waves	88	40
INOUE	P	whole	B[c]	11 layers	ISC P picks	90	12
MDLSH	S	whole	6	11 layers	S waveforms	90	41
V3	P	lower	6	5 Lpoly	ISC P picks	91	26
SH425	S	upper	8	4 Lpoly	S waveforms	92	39
	S	lower	8	5 Lpoly	S waveforms	92	39
RG5.5	S	upper	36	28 layers	Surface waves	92	55
WM13	S	whole	8	14 Cpoly	Surface waves + S, SS, ScS	92	48
SH10c17	S	whole	10	11 layers	Modes + S, SS, ScS	92	20
M12.love	S	whole	8	12 layers	Modes + Love + S, SS, ScS	93	-

Notes: a) Lpoly = Legendre Polynomials, Cpoly = Chebyshev Polynomials, the number indicates the order of the polynomial
b) ISC indicates the data set of phase arrival times collected and disseminated by the International Seismological Commission
c) The Inoue et al. [12] model is a block model

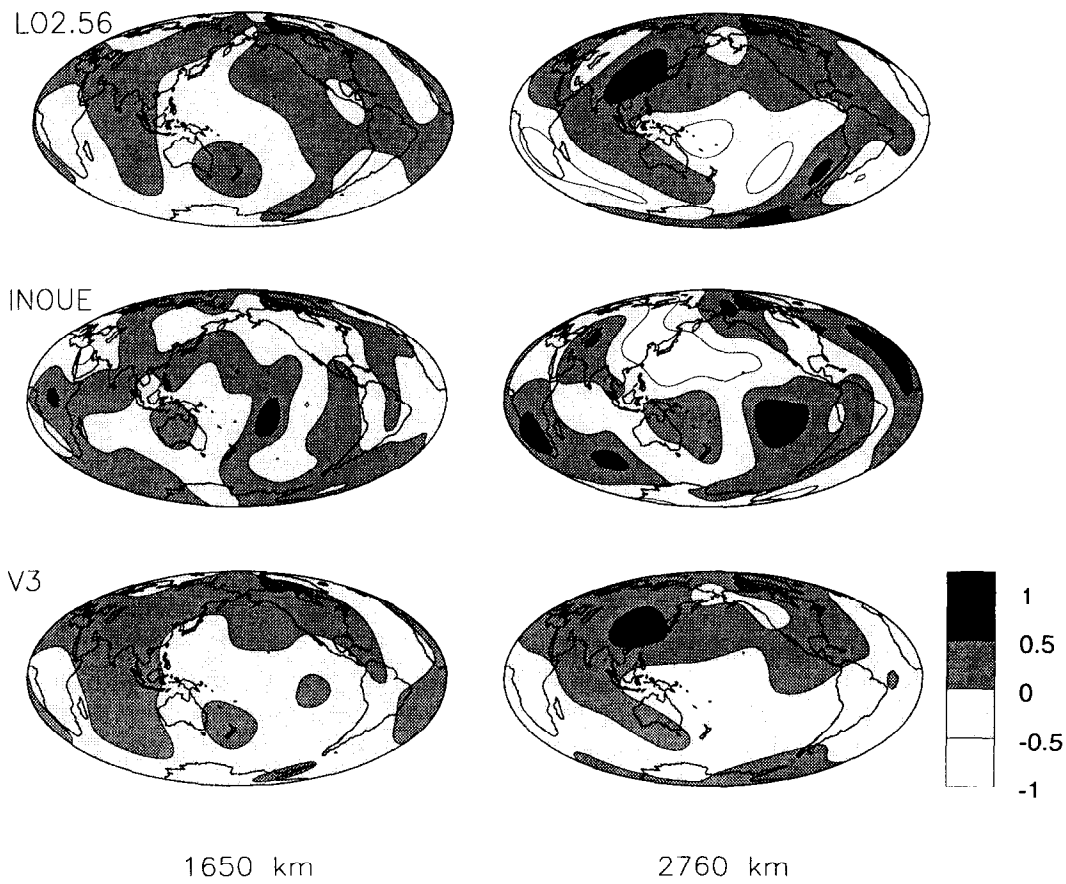

Fig. 3. A comparison between 3 different models of mantle P-velocity variations at depths of 1650 km (mid-mantle) and 2760 km (D″ region in the lowermost mantle). Perturbations are shown in percent; regions more than 0.5% fast are black, while regions more than 0.5% slow are white. Models LO2.56 and V3 were derived from ISC travel times by Dziewonski and co-workers at Harvard using a spherical harmonic expansion and smooth polynomial functions in depth. These models are in rough agreement, and were the first to show the fast circum-Pacific velocities (see also Figure 5). Model INOUE, which differs significantly from the Harvard models, used a block parameterization scheme. See Table 2 for additional details concerning these models.

lieve that the S velocity distribution is quite reliably determined for lateral wavelengths longer than about 5000 km over depth scales of about 200 km (Figure 5). This is particularly true of the uppermost and lowermost mantle where there is large-amplitude structure. The mid-mantle is characterized by low amplitude structure and is less reliably recovered.

The models discussed above are of isotropic perturbations in structure. The recovery of azimuthal anisotropy on a global-scale using long-period (70–250s) Love and Rayleigh waves has been undertaken by Montagner and Tanimoto [22, 23]. The authors solve for an azimuth-independent contribution to the phase velocity and a contribution which depends upon 2ψ and 4ψ (ψ is azimuth). The azimuth-independent term (essentially the isotropic contribution) dominates the signal and shows excellent correlation with surface tectonics. They also find that the directions of fast velocities for Rayleigh waves are well correlated with plate velocity directions. It seems that azimuthal anisotropy can be resolved from surface wave data at long wavelengths but that its amplitude is quite small (less than 1.3%). The depth extent of the anisotropic region is however very uncertain but anisotropy is apparently not required below 300 km.

The models listed in Table 2 were derived relative to a reference radial Earth model in which boundary pertur-

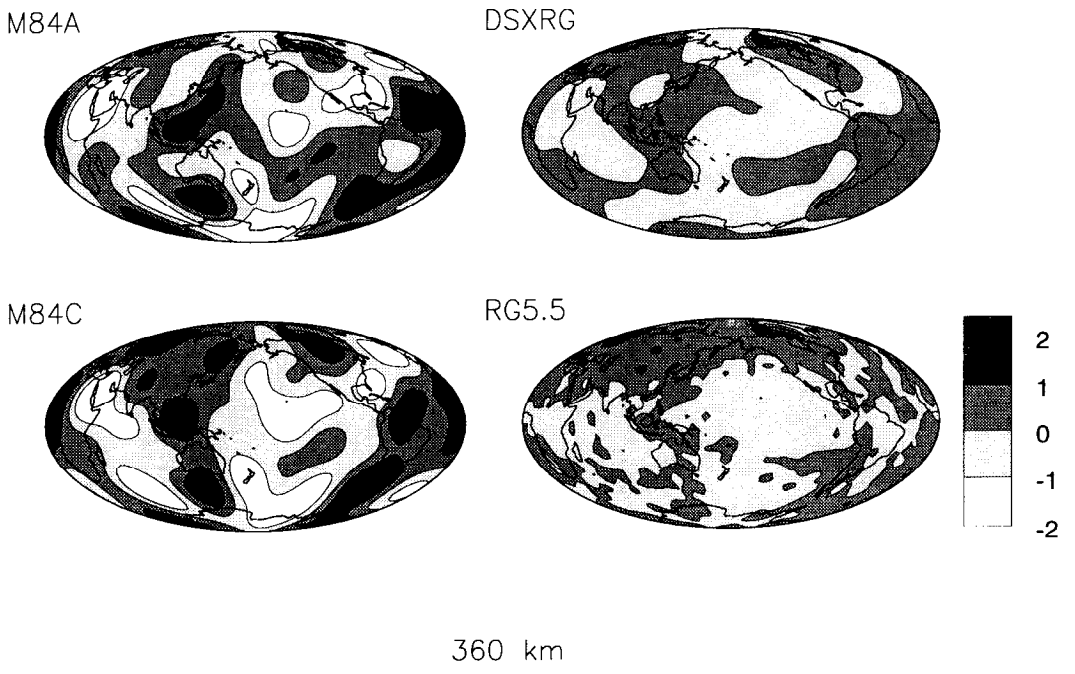

Fig. 4a. A comparison between 4 upper mantle models of S-velocity variations at a depth of 360 km. Perturbations are shown in percent; regions more than 1% fast are black while regions more than 1% slow are white. Models shown include M84a, M84c, DSXRG and RG5.5. The differences between M84a and M84c show the importance of correcting for variations in crustal thickness—M84a is the uncorrected model. M84c agrees fairly well with the more recent whole mantle S-velocity models (all of which are corrected for crustal thickness).

bations were not allowed. However, it is now becoming clear that 30 to 40 km of topography is present on the 410- and 660-km discontinuities. Figure 6 shows maps of these perturbations obtained using precursors to SS [34]. The calculated depths to the discontinuities are sensitive to the velocity structure in the upper mantle and these maps depend upon the tomography results discussed above. Ultimately it will become necessary to perform simultaneous inversions for both velocity structure and boundary perturbations to obtain the most accurate results.

6. CONCLUSIONS

This chapter has attempted to summarize the current state of 1-dimensional and 3-dimensional global Earth modeling. Though much progress has been made, the determination of finer-scale structure, 3-dimensional Q structure, the relative behavior of P and S velocities, and the elucidation of anisotropy remain very vigorous areas of research. The study of the particle motions of surface waves, for example, reveals a clear signal from large-scale anisotropy [28] and the study of the attenuation of surface wave packets is also beginning to reveal our first 3-dimensional views of Q structure in the upper mantle [5, 32].

The models generated by the structural seismologist are of importance to a large number of sub-disciplines in geophysics and geochemistry. In particular, the 3-dimensional models are being used to address key questions concerning the nature of the mantle convection that governs the evolution of our planet. Velocity variations can be related to temperature and density perturbations, and these results, together with the geoid and other geophysical constraints, provide insight into the mantle viscosity structure and current flow regime. Ten years ago, we knew almost nothing about the three-dimensional structure of the Earth, perhaps in the next ten years these models will have helped us to address some of the fundamental problems in global geophysics.

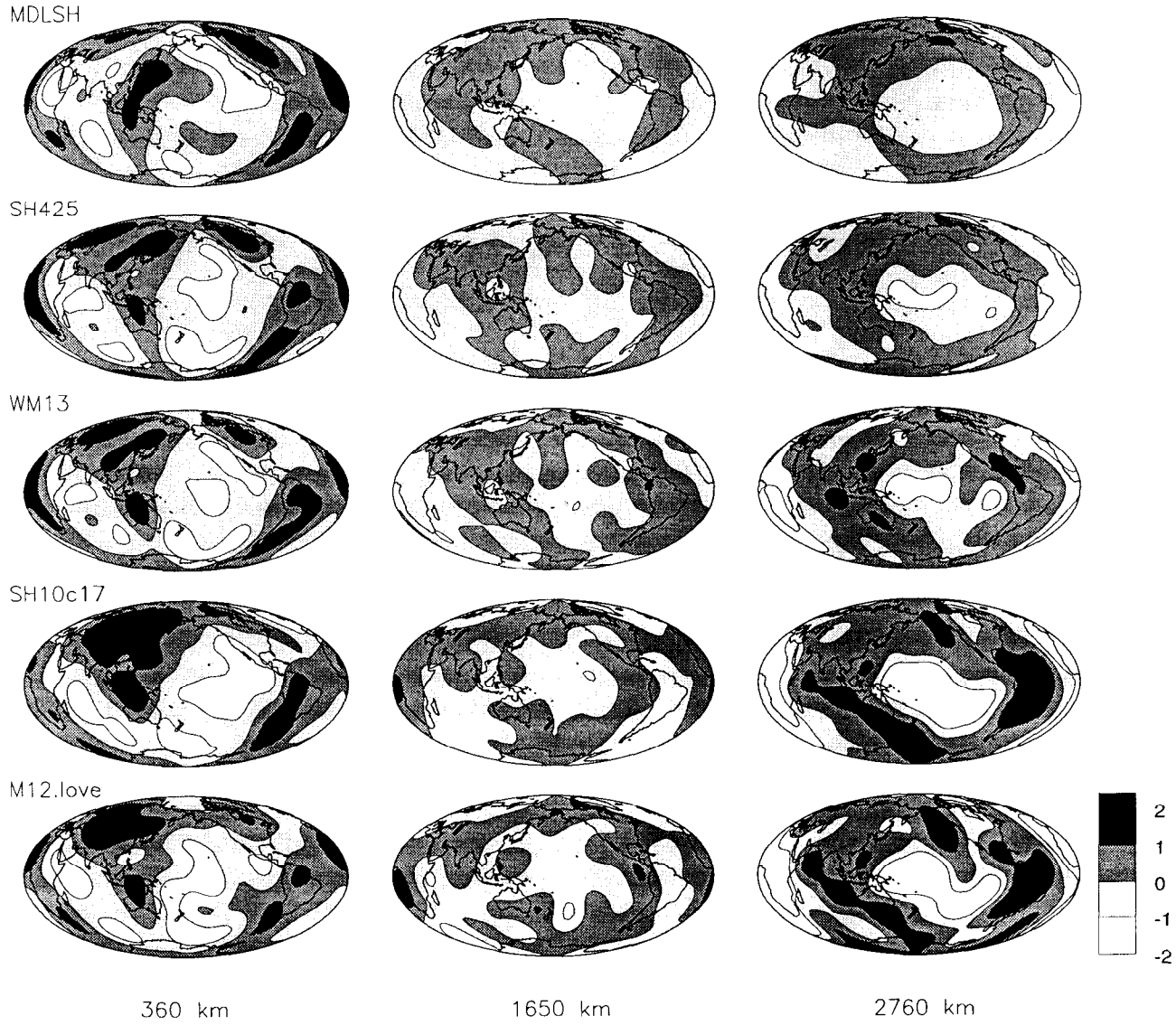

Fig. 4b. A comparison between 5 different whole-mantle models of S-velocity variations at depths of 360 km (upper mantle), 1650 km (mid-mantle) and 2760 km (D″ region). Perturbations are shown in percent; regions more than 1% fast are black while regions more than 1% slow are white. Models shown include MDSLH, SH425, WM13, SH10c17 and M12.love and are all corrected for crustal structure. The whole mantle models are in rough agreement, exhibiting reduced amplitudes in the mid-mantle and a ring of fast velocities around the Pacific in the deep mantle. The largest differences are the amplitude of the pattern within D″, with the models containing ScS and deep-turning S data showing the largest anomalies. See Table 2 for additional details concerning these models.

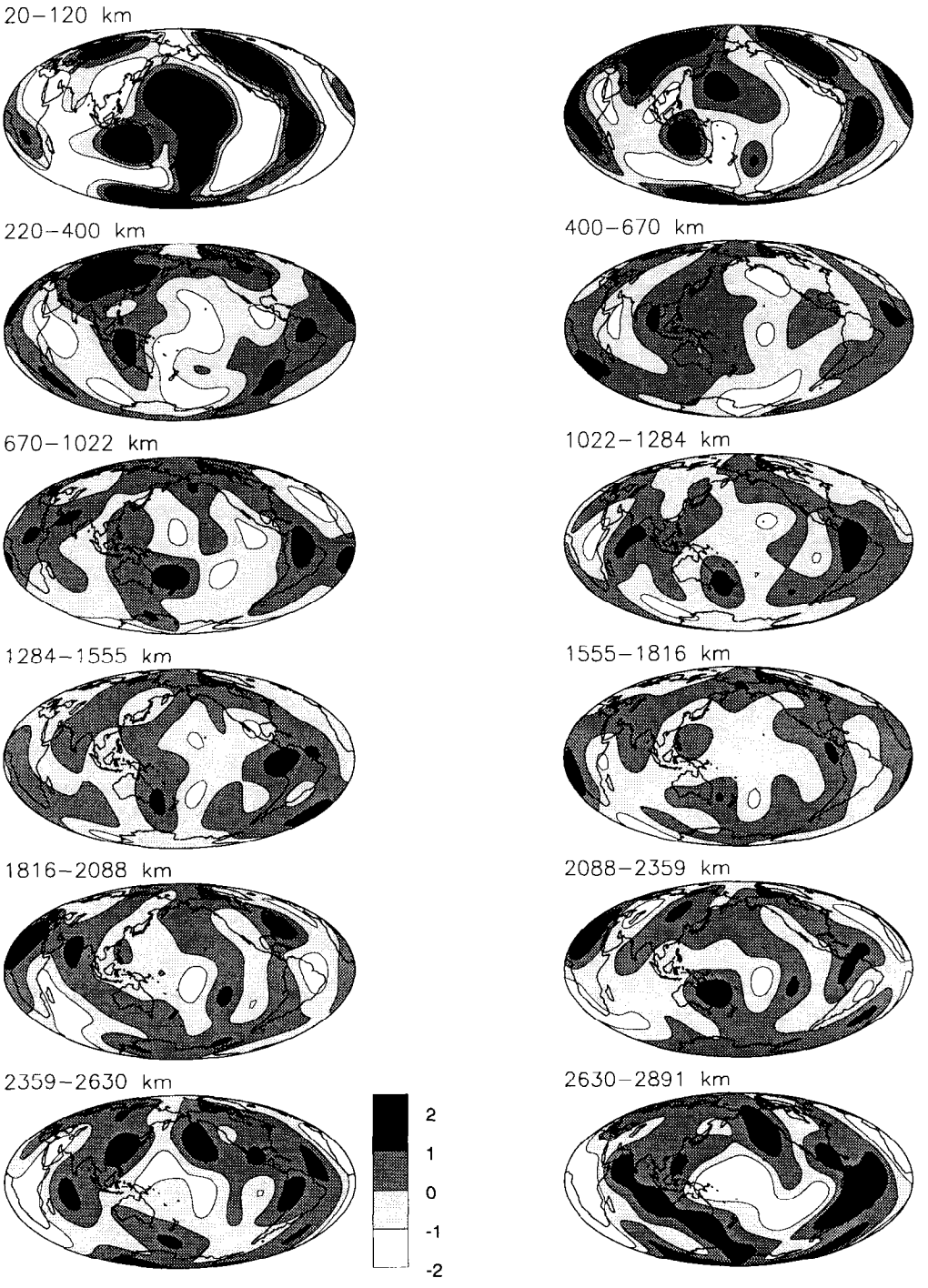

Fig. 5. The S-velocity variations within the 12 layers of model M12.love. This model is parameterized up to spherical harmonic degree 8 and is derived from long-period S, SS and ScS travel times and surface-wave data. Perturbations are shown in percent; regions more than 1% fast are black while regions more than 1% slow are white. Heterogeneity in this model, like most other whole-mantle S-wave models, is concentrated near the top and bottom of the mantle. Velocity anomalies within the uppermost layer are highly correlated with surface tectonics with the fastest velocities beneath old oceans and continental shields. Near the core-mantle boundary, the most significant feature is a ring of fast velocities around the Pacific.

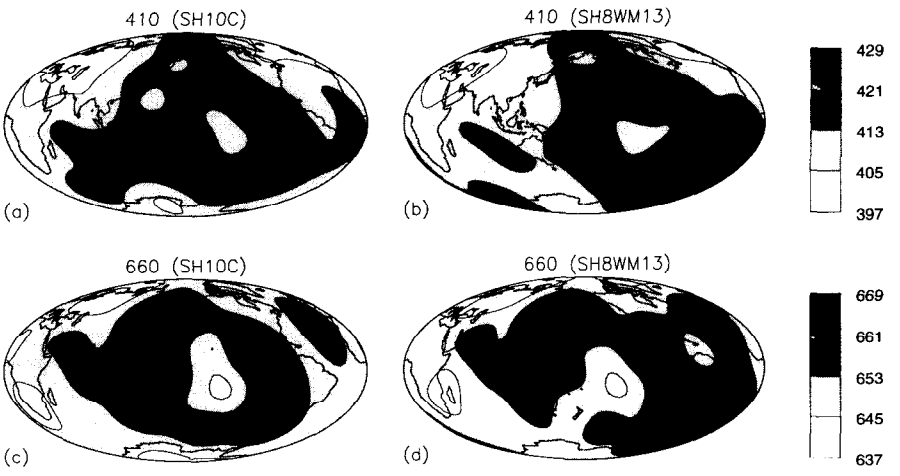

Fig.6. Maps of topography on the 410- and 660-km discontinuities obtained from long-period SS precursors [34]. Corrections for upper mantle heterogeniety were applied using model SH10c17 (left) and model WM13 (right). 30 to 40 km of topography (peak-to-trough) is observed.

Acknowledgments. This work was funded by grants from the National Science Foundation

REFERENCES

1. Aki, K., and P.G. Richards, *Quantitative Seismology: Theory and Methods, vol. 1.* W.H. Freeman, San Francisco, 1980.
2. Bataille, K., R-S. Wu, and S.M. Flatte, Inhomogeneities near the core-mantle boundary evidenced from scattered waves: A review. *Pageoph*, **132**, 151–173, 1990.
3. Bhattacharyya, J., P.M. Shearer, and G. Masters, Inner core attenuation from short period $PKP(BC)$ versus $PKP(DF)$ waveforms. *Geophys. J. Int.*, **114**, 1–11, 1993.
4. Creager, K.C., Anisotropy of the inner core from differential travel times of the phases PKP and $PKIKP$. *Nature*, **356**, 309–314, 1992.
5. Durek, J.J., M.H. Ritzwoller, and J.H. Woodhouse, Constraining upper mantle anelasticity using surface wave amplitude anomalies. *Geophys. J. Int.*, **114**, 249–272, 1993.
6. Dziewonski, A.M., Mapping the lower mantle: determination of lateral heterogeneity in P velocity up to degree and order 6. *J. Geophys. Res.*, **89**, 5929–5952, 1984.
7. Dziewonski, A.M., and D.L. Anderson, Preliminary reference Earth model. *Phys. Earth Planet. Inter.*, **25**, 297–356, 1981.
8. Edmonds, A.R., *Angular Momentum and Quantum Mechanics.* Princeton University Press, Princeton, N.J., 1960.
9. Gaherty, J.B., and T. Lay, Investigation of laterally heterogeneous shear velocity structure in D″ beneath Eurasia. *J. Geophys. Res.*, **97**, 417–435, 1992.
10. Garnero, E.J., and D.V. Helmberger, Travel times of S and SKS: Implications for three-dimensional lower mantle structure beneath the central Pacific. *J. Geophys. Res.*, **98**, 8225–8241, 1993.
11. Hager, B.H., and R.W. Clayton, Constraints on the structure of mantle convection using seismic observations, flow models, and the geoid. In: *Mantle Convection, ed W.R. Peltier, Gordon and Breach, New York*, pp.657–763, 1989.
12. Inoue, H., Y. Fukao, K. Tanabe, and Y. Ogata, Whole mantle P-wave travel time tomography. *Phys. Earth Planet. Inter.*, **59**, 294–328, 1990.
13. Jeanloz, R., and H.-R. Wenk, Convection and anisotropy of the inner core. *Geophys. Res. Lett.*, **15**, 72–75, 1988.
14. Karato, S., Inner core anisotropy due to magnetic field-induced preferred orientation of iron. *Science*, **262**, 1708–1711, 1993.
15. Kennett, B.L.N., and E.R. Engdahl, Treaveltimes for global earthquake location and phase identification. *Geophys. J. Int.*, **105**, 429–465, 1991.
16. Lay, T., Structure of the core-mantle transition zone: a chemical and thermal boundary layer. *Eos, Trans. AGU*, **70**, 49–59, 1989.
17. Lay, T., and D.V. Helmberger, A lower mantle S wave triplication and the shear velocity structure of D″. *Geophys. J. R. Astron. Soc.*, **75**, 799–837, 1983.
18. Lay, T., and C.J. Young, The stably-stratified outermost core revisited. *Geophys. Res. Lett.*, **17**, 2001–2004, 1990.
19. Masters, G., and P.M. Shearer, Summary of seismological constraints on the structure of the Earth's core. *J.*

Geophys. Res., **95**, 21,619–21,695, 1990.

20. Masters, G., H. Bolton, and P. Shearer, Large-scale 3-dimensional structure of the mantle. *EOS, Trans. AGU*, **73**, 201, 1992.
21. Mitchell, B.J., On the inversion of Love and Rayleigh wave dispersion and implications for earth structure and anisotropy. *Geophys. J. R. Astron. Soc.*, **76**, 233–241, 1984.
22. Montagner, J-P., and D.L. Anderson, Constrained reference mantle model. *Phys. Earth Planet. Inter.*, **58**, 205–227, 1989.
23. Montagner, J-P., and T. Tanimoto, Global anisotropy in the upper mantle inferred from the regionalization of phase velocities. *J. Geophys. Res.*, **95**, 4797–4819, 1990.
24. Morelli, A., A.M. Dziewonski, and J.H. Woodhouse, Anisotropy of the inner core inferred from $PKIKP$ travel times. *Geophys. Res. Lett.*, **13**, 1545–1548, 1986.
25. Morelli, A., and A.M. Dziewonski, Topography of the core-mantle boundary and lateral homogeneity of the liquid core. *Nature*, **325**, 678–683, 1987.
26. Morelli, A., and A.M. Dziewonski, Joint determination of lateral heterogeneity and earthquake location. In: *Glacial isostasy, sea level, and mantle rheology. Eds R.Sabadini, K. Lambeck, E. Boschi. NATO ASI Series*, pp.515–534, 1991.
27. Morelli, A., and A.M. Dziewonski, Body wave traveltimes and a spherically symmetric $P-$ and S-wave velocity model. *Geophys. J. Int.*, **112**, 178–194, 1993.
28. Park, J., and Y. Yu, Anisotropy and coupled free oscillations: simplified models and surface wave observations. *Geophys. J. Int.*, **110**, 401–420, 1992.
29. Pulliam, R.J., D.W. Vasco, and L.R. Johnson, Tomographic imversions for mantle P wave velocity structure based on the minimization of l^2 and l^1 norms of International Seismological Centre travel time residuals. *J. Geophys. Res.*, **98**, 699–734, 1993.
30. Revenaugh, J.S., and T.H. Jordan, Mantle layering from ScS reverberations: 1. Waveform inversion of zeroth-order reverberations. *J. Geophys. Res.*, **96**, 19,749–19,762, 1991.
31. Rodgers, A., and J. Wahr, Inference of core-mantle boundary topography from ISC PcP and PKP traveltimes. *Geophys. J. Int.*, **115**, 991–1011, 1993.
32. Romanowicz, B., The upper mantle degree 2: Constraints and inferences from global mantle wave attenuation measurements. *J. Geophys. Res.*, **95**, 11,051–11,071, 1990.
33. Shearer, P.M., Imaging global body wave phases by stacking long-period seismograms. *J. Geophys. Res.*, **96**, 20,353–20,364, 1991.
34. Shearer, P.M., Global mapping of upper mantle reflectors from long-period SS precursors. *Geophys. J. Int.*, **115**, 878–904, 1993.
35. Song, X., and D.V. Helmberger, Velocity structure near the inner core boundary from waveform modelling. *J. Geophys. Res.*, **97**, 6573–6586, 1992.
36. Song, X., and D.V. Helmberger, Anisotropy of the Earth's inner core. *Geophys. Res. Lett.*, **20**, 2591–2594, 1993.
37. Souriau, A., and G. Poupinet, The velocity profile at the base of the liquid core from $PKP(BC + C_{diff})$ data: An argument in favor of radial inhomogeneity. *Geophys. Res. Lett.*, **18**, 2023–2026, 1991.
38. Stacey, F.D., *Physics of the Earth*. Brookfield Press, Brisbane, 1992.
39. Su, W-J., and A.M. Dziewonski, Predominance of long-wavelength heterogeneity in the mantle. *Nature*, **352**, 121–126, 1991.
40. Tanimoto, T., The 3-D shear wave structure in the mantle by overtone waveform inversion. II, Inversion of X-waves, R-waves and G-waves. *Geophys. J.*, **93**, 321–333, 1988.
41. Tanimoto, T., Long-wavelength S-velocity structure throughout the mantle. *Geophys. J. Int.*, **100**, 327–336, 1990.
42. Tromp, J., Support for anisotropy of the Earth's inner core from free oscillations. *Nature*, **366**, 678–681, 1993.
43. Vidale, J.E., and H.M. Benz, Upper-mantle discontinuities and the thermal structure of transition zones. *Nature*, **356**, 678–681, 1992.
44. Vidale, J.E., and H.M. Benz, A sharp and flat section of the core-mantle boundary. *Nature*, **359**, 627–629, 1992.
45. Weber, M., P- and S-wave relections from anomalies in the lowermost mantle. *Geophys. J. Int.*, **115**, 183–210, 1993.
46. Widmer, R., G. Masters, and F. Gilbert, Spherically symmetric attenuation within the Earth from normal mode data. *Geophys. J. Int.*, **104**, 541–553, 1991.
47. Woodhouse, J.H., and A.M. Dziewonski, Mapping of the upper mantle: three-dimensional modeling of earth structure by inversion of seismic waveforms. *J. Geophys. Res.*, **89**, 5953–5986, 1984.
48. Woodward, R.L., A.M. Forte, W. Su, and A.M. Dziewonski, Constraints on the large-scale structure of the mantle. In: *Geophys. Monograph 74, IUGG, v14, Takahashi et al., eds. , AGU, Washington DC*, pp.89–109, 1992.
49. Woodward, R.L., and G. Masters, Lower mantle structure from $ScS - S$ differential travel times. *Nature*, **352**, 231–233, 1991.
50. Woodward, R.L., and G. Masters, Global upper mantle structure from long-period differential travel-times. *J. Geophys. Res.*, **96**, 6351–6377, 1991.
51. Wysession, M.E., and E.A. Okal, Evidence for lateral heterogeneity at the core-mantle boundary from the slowness of diffracted S profiles. In: *Structure and dynamics of the Earth's deep interior, AGU monograph 46*, pp.55–63, 1988.
52. Wysession, M.E., and E.A. Okal, Regional analysis of D″ velocities from the ray parameters of diffracted P profiles. *Geophys. Res. Lett.*, **16**, 1417–1420, 1989.
53. Young, C.J., and T. Lay, The core-mantle boundary. *Ann. Rev. Earth Planet. Sci.*, **15**, 25–46, 1987.
54. Young, C.J., and T. Lay, The core shadow zone boundary and lateral variations of the P-velocity structure of the lowermost mantle. *Phys. Earth Planet. Inter.*, **54**, 64–81, 1989.
55. Zhang, Y-S., and T. Tanimoto, Ridges, hotspots and their interactions as observed in seismic velocity maps. *Nature*, **355**, 45–49, 1992.

Free Oscillations: Frequencies and Attenuations

T. G. Masters and R. Widmer

1. INTRODUCTION

The displacement at any point on the surface of the Earth can be quite complicated but can be thought of as a sum of discrete modes of oscillation, each mode having a characteristic frequency and decay rate which are dependent upon the structure of the Earth. The initial amplitudes of the modes of free oscillation depend upon the source of excitation which, in free-oscillation seismology (or "normal mode" seismology), is usually an earthquake. Earthquakes are typically of relatively short duration. For example, a magnitude 6.5 earthquake will rupture for perhaps ten seconds after which the Earth is in free oscillation. Away from the immediate vicinity of the earthquake, the motions of the Earth are small in amplitude and the total displacement at a recording site can be written simply as a sum of decaying cosinusoids:

$$u(t) = \sum_k A_k \cos(\omega_k t + \phi_k) e^{-\alpha_k t}. \quad (1)$$

ω_k is the frequency of the k'th mode which has an initial amplitude A_k and an initial phase ϕ_k. α_k controls the decay rate of the k'th mode and is often written in terms of the "quality" of the mode, Q_k, where

$$Q_k = \frac{\omega_k}{2\alpha_k}. \quad (2)$$

When Q_k is large, α_k is small so the mode rings on for a long time. Conversely, low Q modes decay away quickly. In the Earth, attenuation of seismic energy is weak and the Q's of modes are typically between 100 and 6000. Thus modes of oscillation ring on for many cycles before being appreciably attenuated.

Long wavelengths are typically associated with low frequencies and free oscillation theory has usually been used to describe motions of the Earth with periods between about 100 seconds and 1 hour. The latter period corresponds to the frequency of the mode ${}_0S_2$ which is sometimes called the "football mode" of the Earth since it corresponds to a mode of deformation in which the Earth looks like an American football (Figure 1a). The notation ${}_nS_\ell$ arises from the fact that, on a spherically-symmetric Earth, free oscillations have displacement fields which are simply related to spherical harmonics: the ℓ is the harmonic degree of the relevant spherical harmonic which controls the number of nodes in the displacement field in latitude. n is the "overtone index". $n = 0$ corresponds to the lowest frequency mode of harmonic degree ℓ and is termed a "fundamental mode". Higher frequency modes, $n > 0$, are called "overtones". Finally, the S indicates that this mode is in the class of "spheroidal" modes. Spheroidal modes can have complicated displacement fields which involve compression of the Earth as well as shearing. These modes therefore affect (and are affected by) the gravitational field of the Earth and can be measured using gravimeters. The simplest case of a spheroidal mode is one in which the displacement is everywhere in the radial direction (Figure 1b). Such modes are called "radial" modes and the fundamental radial mode, ${}_0S_0$, has a period of about 20 minutes. An alternate class of modes is the "toroidal modes" which consist of shearing on concentric shells (e.g., Figure 1c) and are labelled ${}_nT_\ell$ in an analogous fashion to the

T. G. Masters and P. M. Shearer, University of California, San Diego, IGPP, A025, La Jolla, CA 92093

Global Earth Physics
A Handbook of Physical Constants
AGU Reference Shelf 1

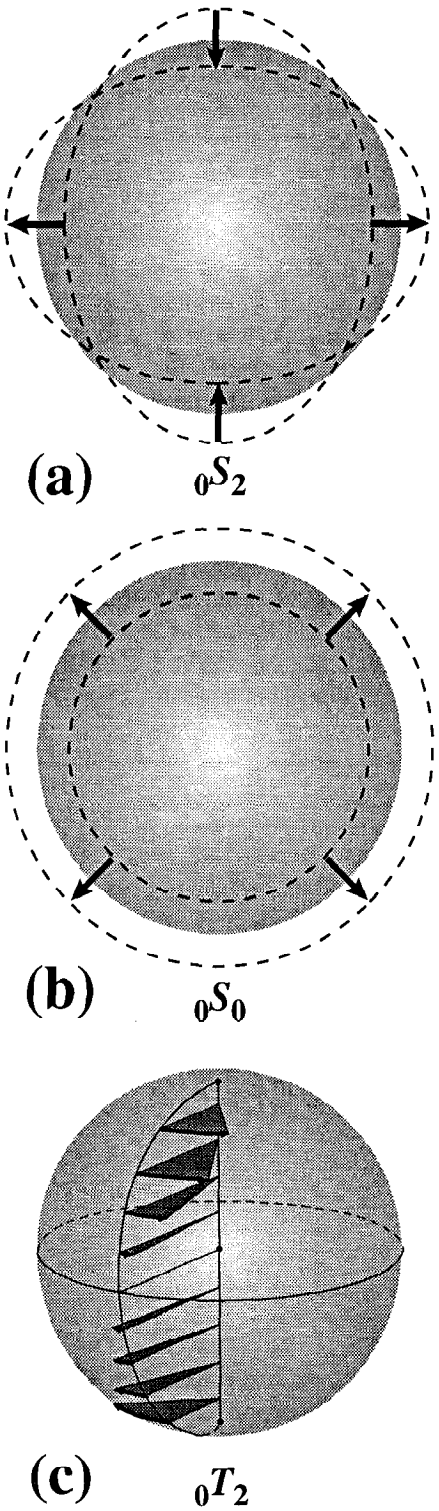

Fig. 1. Illustrations of the displacement fields of various modes of oscillation. a) ${}_0S_2$, the "football" mode of the Earth, b) ${}_0S_0$, the "breathing" mode of the Earth, and c) the toroidal mode ${}_0T_2$.

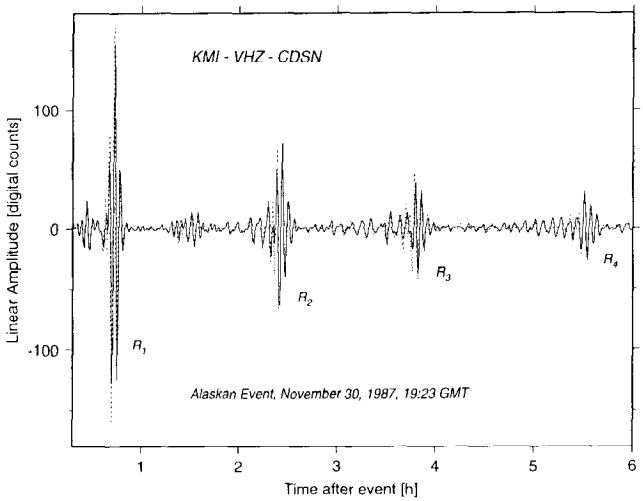

Fig. 2. Comparison of a synthetic seismogram with data for a vertical-component, long-period recording (VHZ) from a station of the Chinese Digital Seismic Network at Kunming (KMI). The dotted line is the synthetic made by mode summation and includes all modes with frequencies less then 8 mHz. The large wave packets labelled R_1–R_4 are Rayleigh wave surface waves. R_1 has travelled the minor arc from the source to receiver while R_2 has travelled in the opposite direction. The travel time to complete a full orbit is about 3 hours (R_3 is the same as R_1 but after one complete orbit).

spheroidal modes. The motion in a toroidal mode has no radial component and there is no compression or dilation so they are not recorded on gravimeters.

Low frequency disturbances are efficiently excited only by large earthquakes so the study of free oscillations has historically concerned the study of very large earthquakes. Modern networks can easily record free oscillations from earthquakes with surface wave magnitudes greater than about 6.5. There are roughly 20 such events per year so there are now many thousands of recordings available for free-oscillation research. An example of a long-period recording is shown in Figure 2 along with a "synthetic" seismogram made using equation (1). A model of the earthquake source is used to calculate the initial amplitude and phase (A_k and ϕ_k) of each mode and a model of the elastic and anelastic properties of the Earth is used to calculate the frequency and attenuation rate (ω_k and α_k) of each mode. Even though equation (1) is very simple, the interference between modes of oscillation gives a complicated waveform which agrees in detail with the observations. The large amplitude wave packets seen in the seismogram correspond to surface waves which travel around the surface of the Earth much like ripples on the

surface of a pond travelling away from some initial disturbance.

It is interesting to note that the particular Earth model used in this calculation is rather simple. In fact the model includes only radial variations of the elastic and anelastic parameters and completely ignores lateral variations such as continent/ocean differences. Such spherically-symmetric Earth models can quite accurately reproduce many seismic observations and provide useful starting approximations to more realistic calculations.

Much of the theory used to calculate the free oscillations of Earth models has been available for over a century but the observational history is much shorter. The initial "observation" was made by Benioff [3] who recorded a long-period disturbance of the Earth on a fused-quartz strainmeter after a large earthquake in Kamchatka in 1952. Benioff's interpretation of this record is almost certainly wrong but this work did reawake interest in the theoretical aspects of free-oscillations [e.g., 1]. Thus, in 1960, code for computing the free-oscillation frequencies of realistic Earth models existed just as the huge Chilean earthquake provided the first unambiguous recordings. Several groups presented observations of spheroidal modes measured on gravimeters and spheroidal and toroidal modes measured on strainmeters and the good agreement with the calculated frequencies gave strong support to the results (particularly convincing was the lack of peaks at the computed toroidal mode frequencies on the gravimeter recordings). Recordings from this event also provided the first observational evidence for splitting of the lowest frequency modes caused by the rotation of the Earth [2, 25].

The occurrence of several huge earthquakes throughout the 60's and the installation of the WWSSN (Worldwide Standardized Seismographic Network) in the early 60's resulted in many further observations of mode frequencies which are summarized in Derr [9] and were used in several attempts to make better Earth models.

The next major step forward came with the occurrence of the Columbian 1970 earthquake. This remarkable earthquake was as large as anything recorded digitally since but was at a depth of 650 km. Such deep earthquakes are incapable of exciting fundamental modes which normally dominate the seismogram and obscure the lower amplitude overtones. Consequently, the Colombian earthquake allowed a great number of overtones to be measured for the first time. These modes are important since they constrain the structure of the deep Earth. A gravimeter recording of this event was made at Payson Arizona by W. Farrell and the spectrum (see next section) is completely dominated by overtones, some of which have not been reliably observed since! It is this recording which provided the impetus to start the global IDA (International Deployment of Accelerometers) array in the mid-70's. Theoretical work by Gilbert in the early 70's also led to compact expressions for mode excitation and array processing algorithms which were eventually applied to hand-digitized WWSSN recordings of the Columbian earthquake [16]. The resulting explosion in the number and quality of degenerate frequency estimates led to a dataset which is essentially that used in the construction of current reference Earth models [e.g., 11]. Subsequent work using data from the modern digital arrays has led to the identification of large signals due to Earth rotation and 3-dimensional structure which must be assessed before accurate degenerate frequencies can be assigned.

2. FREE-OSCILLATION FREQUENCIES AND ATTENUATION RATES

The utility of the free-oscillation description of long-period seismic motion becomes apparent when we look at the spectrum of a seismic recording. Figure 3 shows the amplitude spectrum of 60 hours of the recording of Figure 2. The spectrum is clearly composed of discrete peaks, each peak corresponding to one (or more) mode of free

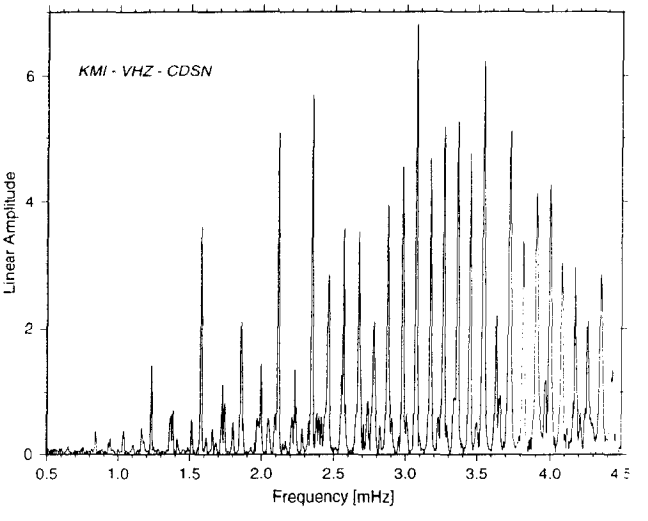

Fig. 3. Fourier amplitude spectrum of 60 hours of the recording shown in Figure 2. The record was Hanning-tapered to reduce spectral leakage effects. The spectrum (which is proportional to ground acceleration) is dominated by large peaks which are roughly uniformly spaced with a separation of about 0.1 mHz. These peaks correspond to fundamental spheroidal modes which compose the large amplitude Rayleigh wave packets seen in Figure 2.

oscillation. If a peak can be identified as a particular mode of oscillation and the peak frequency accurately measured, we can use the frequencies to improve our models of the Earth. The width of each spectral peak is also related to the attenuation of a mode – slowly attenuating modes have narrow spectral peaks while strongly attenuated modes have broad spectral peaks. We can, in principle, measure the attenuation rate of each mode and thus learn about the attenuation characteristics of the Earth.

The situation is much more complicated in practice due to the small departures from spherical symmetry in the real Earth. To understand this, we require some theory (the details are relegated to the Appendix). We find that, on a spherically symmetric Earth, there are two classes of oscillation: spheroidal and toroidal (see equations 15,16). The displacement fields are proportional to a spherical harmonic of degree ℓ or its lateral derivatives though the frequencies of free oscillation are independent of the azimuthal order number m. A consequence of this is that there are $2\ell+1$ modes of oscillation with exactly the same frequency. This group of $2\ell+1$ modes is called a "multiplet" while the individual members of the multiplet are called "singlets". Departures of the Earth from spherical symmetry remove the degeneracy and, in general, each singlet within a multiplet will have a slightly different frequency. This phenomonon is called "splitting".

Figure 4 shows the degenerate frequencies of toroidal and spheroidal oscillation for a typical spherically symmetric Earth model, PREM, for frequencies below 10 mHz. The large dots indicate those degenerate frequencies which can be reliably determined (see also Table 1). There is considerable structure in these diagrams and modes are often classified into various types to help describe their properties. Consider the simpler case of toroidal modes. Once the displacement field is known for a mode, it is straightforward to calculate the distribution of energy of the mode within the Earth (see Appendix). Figure 5 shows the elastic shear energy density for three different toroidal modes as a function of radius. The first is a fundamantal mode ($n = 0$) and the energy is confined close to the surface. If we use equation (1) to calculate a synthetic seismogram and include only fundamental modes, we generate a seismogram consisting of the large amplitude surface waves (actually Love waves). Fundamental modes are therefore called "surface-wave equivalent" modes. The second example is of a mode whose energy distribution is oscillatory part way through the mantle then becomes exponentially decaying. The depth at which the behavior changes from oscillatory to exponential is called the "turning point". If a seismogram is constructed of all modes with a turning point at this depth, we find that it looks like

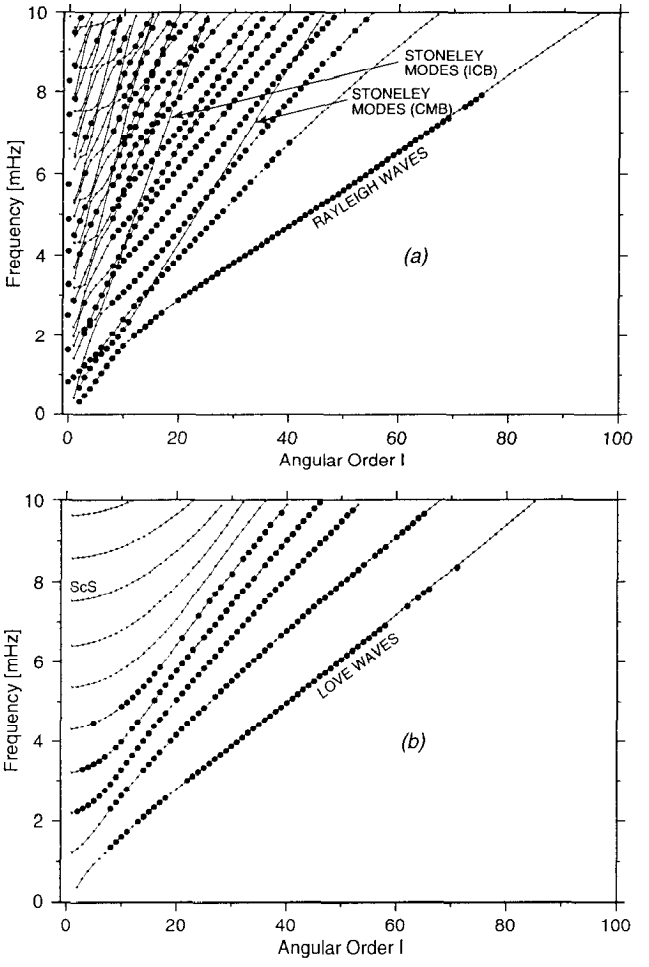

Fig. 4. Free-oscillation frequencies (dots) plotted as a function of harmonic degree for a) spheroidal modes and b) toroidal modes. The large dots indicate the modes for which a reliable degenerate frequency can be assigned (see Table 1). The solid lines join modes of the same overtone number and are called "branches". The fundamental mode branch is the lowest frequency branch and is equivalent to the dispersion curve for fundamental mode surface waves. Also marked in figure 4a are the pseudobranches corresponding to waves trapped on the CMB and on the ICB (a pseudobranch is made up of several segments of different overtone branches). The very steep pseudobranches in the top left of figure 4a are composed of modes which have their energy trapped inside the inner core while the nearly flat pseudobranches which cross them are composed of ScS-equivalent and PcP-equivalent modes.

a set of body wave S arrivals (e.g. S, SS, SSS, etc.) all of which have the same ray turning point. Such modes are called "mantle S-equivalent" modes. The final example is oscillatory all the way through the mantle. In fact, all

TABLE 1. Mode frequencies and attenuations

Mode	f_{obs} μHz	f_{PREM} μHz	q^a_{obs}	q_{PREM}	ref.[b]	Mode	f_{obs} μHz	f_{PREM} μHz	q_{obs}	q_{PREM}	ref.
${}_0S_2$	309.45 ± 0.15	309.28	1.23 ± .30	1.962	26[c]	${}_0T_{15}$	2212.15 ± 0.40	2210.34	5.96 ± .25	6.572	32[c]
${}_0T_2$	377.30 ± 0.80	379.17		3.994	37[c]	${}_7S_1$		2224.25		4.018	
${}_2S_1$		403.96		2.520		${}_2S_9$		2228.75		5.312	
${}_0S_3$	468.55 ± 0.15	468.56	2.63 ± .31	2.395	26[c]	${}_2T_2$		2230.84		4.878	
${}_0T_3$	587.60 ± 0.70	586.16		4.167	37[c]	${}_0S_{14}$	2229.60 ± 0.25	2231.40	3.02 ± .10	3.352	32[c]
${}_0S_4$	646.80 ± 0.20	647.07	2.74 ± .22	2.680	27[c]	${}_3S_5$		2234.54		11.122	I
${}_1S_2$	680.00 ± 0.30	679.85	2.71 ± .51	3.222	26[c]	${}_4S_4$	2279.65 ± 0.45	2279.60		3.446	26
${}_0T_4$	766.90 ± 0.40	765.66		4.382	37[c]	${}_1T_8$	2281.00 ± 2.50	2280.23		4.308	34
${}_0S_0$	814.39 ± 0.01	814.31	0.17 ± .01	0.188	21[c]	${}_2T_3$		2294.97		4.836	
${}_0S_5$	840.08 ± 0.10	840.42	2.86 ± .10	2.812	27	${}_0T_{16}$	2327.03 ± 0.40	2325.19	6.08 ± .23	6.690	32[c]
${}_0T_5$	928.55 ± 0.25	928.24	3.89 ± .25	4.621	37[c]	${}_0S_{15}$	2344.75 ± 0.20	2346.38	2.92 ± .08	3.463	32[c]
${}_2S_2$		937.85		10.432	I	${}_1S_{11}$	2346.50 ± 1.00	2347.54		2.674	34
${}_1S_3$	939.60 ± 0.25	939.83	3.01 ± .14	3.537	27	${}_5S_4$	2379.17 ± 0.20	2379.52	2.11 ± .12	2.044	27
${}_3S_1$	944.20 ± 0.30	943.95	1.25 ± .12	1.209	34[c]	${}_2T_4$		2379.86		4.775	
${}_0S_6$	1037.55 ± 0.10	1038.21	2.91 ± .13	2.879	27[c]	${}_2S_{10}$	2404.00 ± 0.70	2402.93	4.51 ± .10	5.518	32
${}_0T_6$	1078.90 ± 0.20	1078.83	4.01 ± .37	4.868	37[c]	${}_6S_2$		2410.68		10.788	I
${}_3S_2$	1106.00 ± 0.40	1106.21	2.66 ± .29	2.728	27[c]	${}_4S_5$		2411.43		3.541	
${}_1S_4$	1172.77 ± 0.10	1172.85	3.76 ± .18	3.689	27	${}_0T_{17}$	2441.35 ± 0.50	2439.09	5.42 ± .23	6.795	32[c]
${}_0T_7$	1221.50 ± 0.40	1220.70	4.65 ± .52	5.112	37	${}_1T_9$	2452.00 ± 1.00	2452.49		4.399	34
${}_0S_7$	1230.96 ± 0.20	1231.79	3.21 ± .15	2.923	27	${}_0S_{16}$	2456.80 ± 0.15	2458.22	3.08 ± .08	3.586	32[c]
${}_1T_1$		1236.11		3.847		${}_2T_5$		2485.09		4.693	
${}_2S_3$	1242.96 ± 0.10	1242.19	2.53 ± .20	2.407	27	${}_2S_0$	2507.90 ± 0.20	2510.48	0.56 ± .14	.805	21
${}_1T_2$		1320.13		3.901		${}_7S_2$		2517.29		2.929	
${}_0T_8$	1356.70 ± 0.30	1356.11	4.95 ± .33	5.346	34	${}_3S_6$		2549.64		3.629	
${}_1S_5$	1370.01 ± 0.20	1370.27	3.02 ± .27	3.426	27	${}_0T_{18}$	2554.40 ± 0.70	2552.22	6.18 ± .29	6.890	32[c]
${}_2S_4$	1379.60 ± 0.20	1379.20	2.55 ± .15	2.630	27	${}_1S_{12}$		2555.06		2.738	M
${}_4S_1$		1412.64		2.817		${}_0S_{17}$	2565.35 ± 0.30	2567.12		3.719	32[c]
${}_0S_8$	1412.74 ± 0.10	1413.51	2.92 ± .20	2.964	27[c]	${}_2S_{11}$		2572.16		5.676	
${}_3S_3$		1417.19		11.000	I	${}_2T_6$		2610.08		4.591	
${}_1T_3$		1439.13		3.955		${}_1T_{10}$	2619.00 ± 2.00	2620.02		4.479	34
${}_0T_9$	1487.30 ± 0.20	1486.61	5.24 ± .27	5.566	34[c]	${}_4S_6$		2626.93		11.136	I
${}_2S_5$	1515.27 ± 0.30	1514.93		3.309	27	${}_0T_{19}$		2664.71		6.974	
${}_1S_6$	1521.36 ± 0.40	1522.04	2.64 ± .35	2.893	27	${}_0S_{18}$		2673.30		3.860	
${}_0S_9$	1577.37 ± 0.20	1578.28	2.80 ± .12	3.005	27[c]	${}_3S_7$		2686.33		3.713	
${}_1T_4$		1585.50		4.006		${}_5S_5$	2703.67 ± 0.20	2703.36	1.89 ± .15	1.990	27
${}_0T_{10}$	1614.10 ± 0.45	1613.26	5.32 ± .29	5.773	34[c]	${}_2S_{12}$	2736.60 ± 0.50	2737.31	4.58 ± .10	5.769	32
${}_1S_0$	1631.36 ± 0.05	1631.34	0.54 ± .06	0.667	21[c]	${}_2T_7$		2753.73		4.476	
${}_1S_7$	1654.48 ± 0.20	1655.51	2.31 ± .08	2.687	27	${}_1S_{13}$		2766.24		2.895	M
${}_2S_6$	1681.17 ± 0.20	1680.84	3.38 ± .16	4.203	27	${}_0T_{20}$		2776.67		7.050	
${}_5S_1$		1713.79		11.019	I	${}_0S_{19}$		2776.98		4.006	
${}_4S_2$		1722.30		2.303		${}_1T_{11}$	2783.00 ± 1.00	2783.31		4.546	34
${}_0S_{10}$	1725.25 ± 0.20	1726.47	2.79 ± .10	3.050	32[c]	${}_3S_8$	2819.02 ± 0.30	2819.64	3.33 ± .17	3.794	27
${}_0T_{11}$	1738.25 ± 0.45	1736.85	5.06 ± .39	5.963	32[c]	${}_6S_3$	2821.87 ± 0.10	2821.72	2.23 ± .16	2.345	27
${}_1T_5$		1750.49		4.061		${}_8S_1$	2872.85 ± 0.15	2873.36	1.02 ± .16	1.075	26
${}_1S_8$	1797.76 ± 0.10	1799.30	2.31 ± .25	2.635	27	${}_0S_{20}$	2877.95 ± 0.20	2878.37	3.55 ± .08	4.154	33[c]
${}_3S_4$		1833.30		11.113	I	${}_0T_{21}$	2886.90 ± 0.70	2888.20	6.37 ± .20	7.118	32[c]
${}_0T_{12}$		1857.94		6.138		${}_2S_{13}$	2903.50 ± 2.00	2899.90		5.738	34
${}_0S_{11}$		1862.42		3.105		${}_2T_8$	2913.00 ± 4.50	2913.97		4.363	34
${}_2S_7$		1864.96		4.726		${}_1T_{12}$		2943.21		4.601	
${}_1T_6$	1925.51 ± 0.45	1925.61		4.129	37	${}_3S_9$	2951.50 ± 1.50	2951.58		3.865	34
${}_1S_9$	1961.72 ± 0.60	1963.74	2.37 ± .25	2.629	27	${}_1S_{14}$		2975.79		3.408	M
${}_0T_{13}$	1979.15 ± 0.45	1976.99	5.05 ± .27	6.297	32[c]	${}_0S_{21}$	2977.05 ± 0.15	2977.73	3.61 ± .06	4.303	33[c]
${}_6S_1$		1980.38		1.538		${}_0T_{22}$	2998.80 ± 0.70	2999.37	7.05 ± .27	7.178	32[c]
${}_0S_{12}$	1988.70 ± 0.30	1990.37	2.84 ± .10	3.173	32[c]	${}_5S_6$	3011.54 ± 0.20	3010.69	1.80 ± .08	1.975	27
${}_4S_3$	2048.11 ± 0.30	2048.97	1.60 ± .18	2.083	27	${}_4S_7$		3013.63		11.151	I
${}_2S_8$	2049.44 ± 0.30	2049.21	4.14 ± .10	5.057	27	${}_2S_{14}$	3062.00 ± 1.50	3063.60		5.322	34
${}_5S_2$		2091.28		3.146		${}_0S_{22}$	3074.60 ± 0.15	3075.27	3.87 ± .06	4.450	33[c]
${}_0T_{14}$	2096.25 ± 0.40	2094.36	5.55 ± .31	6.442	32[c]	${}_7S_3$		3082.21		11.190	I
${}_1T_7$		2103.79		4.214		${}_3S_{10}$	3081.50 ± 1.00	3084.79		3.933	34
${}_0S_{13}$	2111.55 ± 0.15	2112.94	2.84 ± .10	3.255	32[c]	${}_2T_9$	3092.00 ± 7.00	3087.52		4.265	34
${}_1S_{10}$	2150.00 ± 4.50	2148.42		2.643	34	${}_6S_4$		3092.11		2.894	
${}_5S_3$	2168.67 ± 0.20	2169.66	2.80 ± .23	3.420	27	${}_1T_{13}$		3100.46		4.648	
${}_2T_1$		2187.83		4.904		${}_0T_{23}$	3109.10 ± 0.70	3110.25	7.19 ± .23	7.232	33[c]

TABLE 1. continued

Mode	f_{obs} μHz	f_{PREM} μHz	q^a_{obs}	q_{PREM}	ref.[b]	Mode	f_{obs} μHz	f_{PREM} μHz	q_{obs}	q_{PREM}	ref.
${}_1S_{15}$	3169.00 ± 2.50	3170.55		4.922	34	${}_3T_9$	3843.00 ± 5.00	3853.78		4.276	34
${}_0S_{23}$	3170.65 ± 0.10	3171.26	3.86 ± .06	4.594	33[c]	${}_1T_{18}$		3859.82		4.874	
${}_9S_1$		3197.91		4.486		${}_4S_{10}$	3864.50 ± 2.00	3864.58		3.307	34
${}_3T_1$		3203.50		4.636		${}_2S_{18}$		3874.44		2.489	M
${}_8S_2$		3214.23		2.954		${}_9S_4$		3877.95		1.940	
${}_0T_{24}$	3222.00 ± 0.60	3220.90	7.37 ± .26	7.281	32[c]	${}_0T_{30}$	3883.00 ± 1.00	3881.75	7.23 ± .29	7.479	38
${}_3S_{11}$	3220.60 ± 0.70	3221.27		4.002	34	${}_0S_{31}$	3904.85 ± 0.20	3905.40	4.95 ± .08	5.571	33
${}_9S_2$		3231.75		2.456		${}_1S_{20}$	3944.50 ± 2.50	3941.56		6.434	34
${}_3T_2$		3234.09		4.615		${}_7S_6$		3958.72		1.983	
${}_2S_{15}$		3240.89		3.878	M	${}_6S_9$	3964.50 ± 2.00	3965.35		3.119	34
${}_1T_{14}$	3255.00 ± 1.50	3255.59		4.691	34	${}_3S_{16}$	3965.50 ± 1.50	3966.87		4.408	34
${}_0S_{24}$	3265.60 ± 0.10	3265.89	3.97 ± .06	4.734	33[c]	${}_0T_{31}$	3993.10 ± 1.50	3991.62		7.501	d
${}_6S_5$		3266.82		3.683		${}_0S_{32}$	3994.05 ± 0.15	3995.04	5.03 ± .10	5.671	33
${}_2T_{10}$	3267.50 ± 3.50	3270.21		4.193	34	${}_3T_{10}$	3990.00 ± 5.00	3996.61		4.218	34
${}_3S_0$	3272.70 ± 0.60	3271.18	0.71 ± .07	.923	21	${}_1T_{19}$	4006.00 ± 2.00	4007.17		4.930	34
${}_3T_3$		3279.74		4.585		${}_4S_{11}$	4009.00 ± 2.00	4010.47		3.513	34
${}_8S_3$		3283.64		3.916		${}_2T_{14}$	4011.00 ± 4.50	4016.39		4.155	34
${}_5S_7$	3291.88 ± 0.30	3290.76	1.91 ± .15	2.029	27	${}_{10}S_2$	4042.58 ± 0.20	4032.33	1.17 ± .15	5.217	27
${}_0T_{25}$	3332.40 ± 0.50	3331.35	7.26 ± .23	7.324	32[c]	${}_{11}S_2$		4058.47		7.638	I
${}_1S_{16}$	3341.00 ± 1.00	3338.62		6.024	34	${}_0S_{33}$	4082.95 ± 0.20	4084.52	5.24 ± .10	5.766	33
${}_3T_4$		3340.20		4.546		${}_1S_{21}$	4093.50 ± 2.50	4088.34		6.429	34
${}_0S_{25}$	3358.95 ± 0.10	3359.38	4.13 ± .08	4.869	33[c]	${}_2S_{19}$		4092.40		2.457	M
${}_3S_{12}$	3361.40 ± 0.45	3362.07		4.074	34	${}_0T_{32}$		4101.44		7.520	
${}_{10}S_1$		3394.09		11.213	I	${}_4S_0$	4106.20 ± 0.10	4105.76	0.82 ± .04	1.032	21
${}_4S_8$		3396.91		11.160	I	${}_3S_{17}$	4124.30 ± 0.90	4125.58		4.497	34
${}_6S_6$		3403.86		3.905		${}_3T_{11}$		4151.80		4.164	
${}_1T_{15}$	3407.00 ± 1.50	3408.95		4.733	34	${}_4S_{12}$	4150.00 ± 2.00	4152.98		3.643	34
${}_7S_4$		3413.23		2.996		${}_1T_{20}$	4152.00 ± 2.50	4153.05		4.990	34
${}_3T_5$		3415.15		4.500		${}_5S_{10}$		4157.00		11.175	I
${}_0T_{26}$	3442.80 ± 0.60	3441.64	7.18 ± .26	7.362	32[c]	${}_8S_5$	4165.61 ± 0.20	4166.20	1.63 ± .15	1.636	27
${}_2S_{16}$		3443.46		2.821	M	${}_0S_{34}$	4172.10 ± 0.25	4173.90	5.06 ± .08	5.857	33
${}_0S_{26}$	3451.40 ± 0.10	3451.91	4.29 ± .08	5.000	33[c]	${}_2T_{15}$	4190.00 ± 2.00	4196.12		4.180	34
${}_2T_{11}$	3456.00 ± 2.50	3457.67		4.150	34	${}_6S_{10}$	4211.11 ± 0.30	4210.76		2.822	34
${}_1S_{17}$	3495.50 ± 1.00	3493.94		6.309	34	${}_0T_{33}$		4211.23	7.52 ± .32	7.537	
${}_3T_6$		3504.29		4.449		${}_1S_{22}$	4228.50 ± 3.50	4234.40		6.418	34
${}_3S_{13}$	3506.20 ± 0.70	3507.44		4.152	34	${}_7S_7$		4237.85		2.409	
${}_5S_8$	3526.43 ± 0.70	3525.65		2.391	27	${}_0S_{35}$	4261.45 ± 0.20	4263.23	5.33 ± .10	5.945	33
${}_0S_{27}$	3543.10 ± 0.10	3543.65	4.36 ± .08	5.125	33	${}_3S_{18}$	4284.00 ± 1.00	4285.98		4.586	34
${}_0T_{27}$		3551.80		7.397		${}_4S_{13}$	4294.00 ± 2.00	4295.21		3.728	34
${}_6S_7$		3552.60		3.919		${}_1T_{21}$	4295.00 ± 1.00	4297.42		5.055	34
${}_9S_3$	3557.94 ± 0.50	3554.98	1.30 ± .15	1.286	27	${}_{12}S_1$		4300.34		4.466	
${}_1T_{16}$	3560.50 ± 1.00	3560.73		4.777	34	${}_{10}S_3$		4300.92		3.451	
${}_3T_7$		3607.30		4.393		${}_4T_1$		4304.57		4.528	
${}_0S_{28}$	3634.40 ± 0.10	3634.76	4.61 ± .08	5.244	33	${}_2S_{20}$		4310.64		2.440	M
${}_1S_{18}$	3642.50 ± 1.50	3644.94		6.395	34	${}_3T_{12}$	4317.00 ± 6.00	4318.29		4.120	34
${}_2T_{12}$	3640.50 ± 2.50	3646.13		4.134	34	${}_0T_{34}$	4322.00 ± 1.50	4321.00	7.52 ± .28	7.553	38
${}_3S_{14}$	3655.40 ± 0.60	3657.11		4.234	34	${}_9S_5$		4324.87		11.117	I
${}_2S_{17}$		3657.42		2.564	M	${}_4T_2$		4326.83		4.527	
${}_7S_5$		3659.75		2.095		${}_{12}S_2$		4330.16		4.357	
${}_0T_{28}$	3662.00 ± 0.60	3661.86	7.08 ± .26	7.427	32	${}_0S_{36}$	4351.15 ± 0.25	4352.53	5.43 ± .10	6.030	33
${}_{11}S_1$		3685.48		1.507		${}_4T_3$		4360.07		4.527	
${}_8S_4$		3702.73		10.692	I	${}_2T_{16}$	4367.00 ± 3.50	4372.15		4.211	34
${}_4S_9$	3707.50 ± 1.50	3708.76		2.950	34	${}_1S_{23}$	4379.00 ± 2.00	4379.84		6.405	34
${}_1T_{17}$	3710.00 ± 1.00	3711.01		4.824	34	${}_{10}S_4$		4381.16		4.217	
${}_3T_8$		3723.89		4.335		${}_4T_4$		4404.14		4.527	
${}_0S_{29}$	3724.75 ± 0.15	3725.34	4.50 ± .08	5.358	33	${}_0T_{35}$		4430.75	7.11 ± .24	7.566	
${}_6S_8$	3737.50 ± 1.00	3737.62		3.615	34	${}_8S_6$		4435.24		2.268	
${}_0T_{29}$	3772.50 ± 0.70	3771.84	7.39 ± .28	7.455	32	${}_4S_{14}$	4433.00 ± 1.50	4439.08		3.784	34
${}_5S_9$		3777.80		11.168	I	${}_1T_{22}$	4440.00 ± 2.00	4440.27		5.124	34
${}_1S_{19}$	3794.00 ± 1.50	3793.89		6.426	34	${}_0S_{37}$	4440.70 ± 0.35	4441.84	5.37 ± .10	6.111	33
${}_3S_{15}$	3809.80 ± 0.80	3810.48		4.319	34	${}_3S_{19}$	4447.00 ± 1.00	4447.56		4.675	34
${}_0S_{30}$	3814.85 ± 0.15	3815.52	4.75 ± .08	5.467	33	${}_7S_8$	4448.00 ± 1.00	4452.59		3.111	34
${}_2T_{13}$	3830.50 ± 3.50	3832.88		4.138	34	${}_5S_{11}$	4464.00 ± 2.00	4456.55		2.669	34

TABLE 1. continued

Mode	f_{obs} μHz	f_{PREM} μHz	q^a_{obs}	q_{PREM}	ref.[b]	Mode	f_{obs} μHz	f_{PREM} μHz	q_{obs}	q_{PREM}	ref.
${}_4T_5$		4458.81		4.526		${}_3T_{16}$	5040.00 ± 4.50	5054.35		4.121	34
${}_{11}S_3$		4462.42		2.235		${}_0S_{44}$	5069.05 ± 0.65	5069.01	6.03 ± .10	6.615	33
${}_{10}S_5$		4469.75		4.129		${}_7S_{12}$	5068.50 ± 2.50	5071.02		3.936	34
${}_3T_{13}$	4482.00 ± 7.00	4494.38		4.090	34	${}_{11}S_5$	5072.64 ± 0.20	5074.41	1.66 ± .10	1.503	27
${}_{13}S_1$	4490.00 ± 0.80	4495.73	0.94 ± .07	1.360	34	${}_0T_{41}$		5089.15	7.10 ± .30	7.617	
${}_4T_6$		4523.86		4.526		${}_1S_{28}$	5088.00 ± 5.00	5097.80		6.360	34
${}_1S_{24}$	4525.00 ± 3.00	4524.68		6.391	34	${}_3S_{23}$	5092.50 ± 2.00	5098.49		4.999	34
${}_2S_{21}$		4528.88		2.430	M	${}_4T_{12}$	5116.00 ± 6.00	5119.49		4.517	34
${}_0S_{38}$	4529.20 ± 0.20	4531.20	5.56 ± .10	6.190	33	${}_1T_{27}$	5129.00 ± 2.00	5131.50		5.525	34
${}_6S_{11}$		4534.94		11.182	I	${}_5S_{14}$	5138.00 ± 2.00	5136.81		2.691	34
${}_0T_{36}$	4542.00 ± 2.00	4540.49		7.578	38	${}_9S_8$	5138.50 ± 3.50	5144.45		2.117	34
${}_2T_{17}$	4543.00 ± 2.00	4544.86		4.245	34	${}_0S_{45}$	5157.20 ± 0.40	5159.01	6.01 ± .10	6.680	33
${}_1T_{23}$	4580.00 ± 2.00	4581.59		5.198	34	${}_2S_{24}$		5182.42		2.447	M
${}_4S_{15}$	4583.00 ± 1.50	4585.74		3.820	34	${}_{13}S_3$	5194.39 ± 0.10	5193.82	1.28 ± .10	1.101	27
${}_4T_7$		4599.04		4.527		${}_0T_{42}$	5200.00 ± 2.50	5198.89		7.621	38
${}_3S_{20}$	4606.00 ± 1.00	4609.89		4.761	34	${}_4S_{19}$	5201.00 ± 2.00	5206.51		3.862	34
${}_7S_9$	4612.00 ± 2.50	4617.95		3.548	34	${}_2T_{21}$	5202.00 ± 2.50	5210.67		4.399	34
${}_0S_{39}$	4618.65 ± 0.20	4620.61	5.58 ± .10	6.266	33	${}_8S_9$	5211.00 ± 2.00	5211.87		1.994	34
${}_9S_6$		4620.88		3.020		${}_6S_{13}$	5233.50 ± 2.50	5233.88		3.944	34
${}_0T_{37}$		4650.23	7.53 ± .33	7.588		${}_1S_{29}$		5239.29		6.363	
${}_8S_7$		4650.46		2.844		${}_3T_{17}$	5234.00 ± 8.00	5242.20		4.171	34
${}_1S_{25}$	4670.50 ± 3.00	4668.93		6.378	34	${}_0S_{46}$	5248.50 ± 0.50	5249.12	6.12 ± .10	6.743	32
${}_3T_{14}$		4677.69		4.078		${}_4T_{13}$	5243.00 ± 7.00	5251.78		4.505	34
${}_{12}S_3$		4683.62		11.585	I	${}_3S_{24}$	5262.50 ± 1.50	5261.42		5.050	34
${}_4T_8$		4684.10		4.527		${}_1T_{28}$	5264.50 ± 2.00	5265.22		5.611	34
${}_5S_{12}$	4700.00 ± 0.80	4695.98		2.593	34	${}_7S_{13}$		5288.15		11.194	I
${}_0S_{40}$	4707.70 ± 0.35	4710.10	5.66 ± .10	6.339	33	${}_{12}S_4$		5293.80		11.333	I
${}_2T_{18}$	4710.00 ± 2.50	4714.71		4.281	34	${}_{15}S_1$		5295.75		1.471	
${}_1T_{24}$	4721.00 ± 2.00	4721.36		5.276	34	${}_0T_{43}$		5308.63		7.625	
${}_4S_{16}$	4730.00 ± 2.50	4735.78		3.842	34	${}_5S_{15}$	5328.00 ± 2.00	5330.11		2.894	34
${}_2S_{22}$		4746.99		2.424	M	${}_0S_{47}$	5338.60 ± 0.50	5339.35	6.10 ± .12	6.804	32
${}_0T_{38}$	4762.00 ± 2.00	4759.96	7.02 ± .30	7.597	38	${}_{11}S_6$		5351.70		2.158	
${}_{11}S_4$	4765.79 ± 0.20	4766.86	1.35 ± .11	1.425	27	${}_5T_1$		5353.50		5.012	
${}_7S_{10}$	4763.50 ± 4.50	4767.76		3.756	34	${}_{16}S_1$		5355.04		4.984	
${}_3S_{21}$	4771.00 ± 1.50	4772.64		4.845	34	${}_4S_{20}$	5362.00 ± 2.50	5369.24		3.862	34
${}_4T_9$		4778.82		4.527		${}_5T_2$		5370.60		5.010	
${}_0S_{41}$	4798.10 ± 0.30	4799.67	5.88 ± .10	6.411	33	${}_2T_{22}$	5366.00 ± 2.50	5372.32		4.440	34
${}_1S_{26}$	4812.50 ± 3.00	4812.57		6.368	34	${}_{14}S_2$		5374.58		4.938	
${}_{13}S_2$	4844.60 ± 0.20	4845.26	1.00 ± .05	1.138	27	${}_1S_{30}$	5378.50 ± 4.00	5379.96		6.371	34
${}_1T_{25}$	4859.50 ± 2.00	4859.60		5.357	34	${}_9S_9$	5378.00 ± 3.50	5389.25		2.696	34
${}_3T_{15}$		4865.33		4.089		${}_4T_{14}$	5384.50 ± 4.50	5393.54		4.488	34
${}_0T_{39}$		4869.69	7.11 ± .30	7.605		${}_5T_3$		5396.19		5.007	
${}_9S_7$		4872.64		2.041		${}_1T_{29}$	5399.50 ± 2.50	5397.51		5.697	34
${}_2T_{19}$		4882.09		4.319		${}_2S_{25}$		5398.22		2.734	M
${}_4T_{10}$	4885.00 ± 5.00	4883.02		4.526	34	${}_{14}S_3$		5407.52		4.866	
${}_5S_0$	4889.10 ± 0.30	4884.17	0.80 ± .08	1.086	21	${}_6S_{14}$	5409.00 ± 2.00	5410.08		3.857	34
${}_0S_{42}$	4887.70 ± 0.35	4889.34	5.75 ± .10	6.481	33	${}_0T_{44}$		5418.38		7.627	
${}_4S_{17}$	4882.50 ± 2.00	4889.38		3.854	34	${}_3S_{25}$	5424.50 ± 2.50	5425.56		4.835	34
${}_8S_8$	4904.50 ± 2.50	4908.07		2.384	34	${}_3T_{18}$	5414.00 ± 7.00	5427.08		4.232	34
${}_6S_{12}$		4911.92		11.188	I	${}_0S_{48}$	5428.50 ± 0.50	5429.70	6.50 ± .16	6.865	32
${}_{10}S_6$		4914.11		11.470	I	${}_5T_4$		5430.22		5.002	
${}_7S_{11}$	4915.50 ± 3.00	4916.94		3.870	34	${}_{13}S_4$		5455.12		4.811	
${}_5S_{13}$	4927.50 ± 1.50	4924.40		2.590	34	${}_5T_5$		5472.60		4.996	
${}_{14}S_1$		4925.38		11.350	I	${}_{10}S_7$		5489.22		11.287	I
${}_3S_{22}$	4931.50 ± 1.50	4935.56		4.926	34	${}_5S_{16}$	5507.00 ± 2.00	5506.96		3.117	34
${}_1S_{27}$	4956.00 ± 6.00	4955.54		6.361	34	${}_8S_{10}$	5506.00 ± 2.00	5508.75		2.031	34
${}_2S_{23}$		4964.89		2.425	M	${}_1S_{31}$	5512.50 ± 4.50	5519.76		6.385	34
${}_0S_{43}$	4977.35 ± 0.40	4979.12	6.00 ± .12	6.549	33	${}_0S_{49}$	5518.70 ± 0.50	5520.16	6.61 ± .15	6.924	32
${}_0T_{40}$	4981.00 ± 2.00	4979.42	7.27 ± .30	7.611	d	${}_5T_6$		5523.25		4.987	
${}_1T_{26}$		4996.30		5.440		${}_{12}S_5$		5527.66		4.539	
${}_4T_{11}$	4993.50 ± 4.50	4996.59		4.523	34	${}_0T_{45}$	5529.00 ± 4.00	5528.13		7.630	38
${}_4S_{18}$	5043.00 ± 2.50	5046.41		3.860	34	${}_1T_{30}$	5527.50 ± 1.50	5528.40		5.783	34
${}_2T_{20}$	5044.50 ± 4.00	5047.32		4.359	34	${}_2T_{23}$	5525.50 ± 2.50	5532.41		4.481	34

TABLE 1. continued

Mode	f_{obs} μHz	f_{PREM} μHz	q^a_{obs}	q_{PREM}	ref.[b]	Mode	f_{obs} μHz	f_{PREM} μHz	q_{obs}	q_{PREM}	ref.
${}_4S_{21}$	5525.00 ± 2.00	5534.06		3.861	34	${}_7S_{15}$		6038.97		11.205	I
${}_{14}S_4$	5544.94 ± 0.79	5541.84	1.23 ± .06	1.346	34	${}_1T_{34}$	6039.50 ± 3.50	6039.22		6.113	34
${}_4T_{15}$	5538.00 ± 7.00	5544.83		4.462	34	${}_4T_{18}$		6051.83		4.362	
${}_{15}S_2$		5557.32		9.752	I	${}_3S_{28}$		6053.73		2.377	M
${}_{11}S_7$		5563.67		3.563		${}_{11}S_8$		6055.80		11.532	I
${}_5T_7$		5582.08		4.976		${}_0S_{55}$	6064.80 ± 1.50	6065.26	7.03 ± .14	7.255	34
${}_2S_{26}$	5579.00 ± 2.00	5582.65		5.148	34	${}_2S_{29}$	6068.50 ± 2.50	6066.18		5.460	34
${}_6S_{15}$	5606.50 ± 2.50	5602.51		3.673	34	${}_1S_{35}$		6069.14		6.494	
${}_3T_{19}$	5607.00 ± 4.50	5608.11		4.296	34	${}_0T_{50}$		6076.99		7.630	
${}_0S_{50}$	5609.70 ± 0.50	5610.73	6.77 ± .16	6.982	32	${}_5T_{13}$		6102.68		4.816	
${}_9S_{10}$	5604.50 ± 2.50	5610.93		3.127	34	${}_{17}S_1$		6129.05		1.396	
${}_3S_{26}$		5620.49		2.489	M	${}_3T_{22}$	6120.00 ± 6.00	6129.31		4.456	34
${}_0T_{46}$		5637.89		7.631		${}_{12}S_8$	6132.42 ± 0.55	6137.17	2.01 ± .11	1.763	34
${}_{12}S_6$		5646.58		3.743		${}_5S_{20}$	6152.00 ± 3.00	6155.98		3.579	34
${}_5T_8$		5649.00		4.961		${}_0S_{56}$	6158.90 ± 1.50	6156.48	7.13 ± .15	7.306	34
${}_1T_{31}$	5656.00 ± 3.00	5657.96		5.868	34	${}_2T_{27}$	6151.00 ± 6.00	6159.71		4.633	34
${}_1S_{32}$	5657.00 ± 8.00	5658.62		6.404	34	${}_{13}S_6$		6161.19		1.541	
${}_7S_{14}$		5663.80		11.200	I	${}_1T_{35}$	6166.00 ± 3.50	6164.06		6.189	34
${}_5S_{17}$	5669.00 ± 3.00	5673.69		3.295	34	${}_8S_{14}$	6169.00 ± 6.00	6170.65		3.904	34
${}_2T_{24}$	5684.50 ± 4.00	5691.09		4.522	34	${}_0T_{51}$		6186.78		7.628	
${}_{16}S_2$		5697.12		3.042		${}_9S_{12}$	6184.50 ± 2.00	6187.26		2.150	34
${}_4S_{22}$	5694.00 ± 2.50	5700.49		3.861	34	${}_{10}S_{10}$	6176.50 ± 2.50	6190.88		2.658	34
${}_0S_{51}$	5701.20 ± 0.60	5701.42	6.99 ± .16	7.039	32	${}_1S_{36}$	6200.00 ± 7.00	6203.83		6.534	34
${}_4T_{16}$	5709.00 ± 7.00	5705.48		4.431	34	${}_4S_{25}$	6199.00 ± 3.00	6204.82		3.868	34
${}_8S_{11}$	5715.50 ± 3.00	5717.48		3.095	34	${}_5T_{14}$		6217.17		4.768	
${}_5T_9$		5723.92		4.943		${}_{16}S_3$		6222.36		11.598	I
${}_{10}S_8$	5735.00 ± 7.00	5737.09		3.550	34	${}_2S_{30}$	6230.50 ± 2.50	6225.58		5.524	34
${}_6S_0$	5742.00 ± 0.20	5740.25	0.90 ± .18	1.095	34	${}_4T_{19}$		6234.50		4.334	
${}_2S_{27}$	5736.50 ± 2.50	5745.07		5.316	34	${}_6S_{18}$	6242.00 ± 2.00	6235.56		3.236	34
${}_0T_{47}$		5747.66		7.631		${}_0S_{57}$	6246.30 ± 1.30	6247.80	6.80 ± .13	7.357	34
${}_3T_{20}$	5785.00 ± 8.00	5785.19		4.357	34	${}_3S_{29}$		6270.74		2.372	M
${}_1T_{32}$	5786.50 ± 3.00	5786.24		5.952	34	${}_1T_{36}$	6287.50 ± 3.00	6287.87		6.263	34
${}_0S_{52}$	5792.30 ± 1.20	5792.22	6.85 ± .16	7.095	32	${}_0T_{52}$		6296.58		7.626	
${}_1S_{33}$	5798.00 ± 6.00	5796.49		6.429	34	${}_3T_{23}$	6299.00 ± 6.00	6297.60		4.491	34
${}_5T_{10}$		5806.78		4.919		${}_2T_{28}$	6309.50 ± 3.50	6313.75		4.667	34
${}_6S_{16}$	5811.50 ± 2.50	5808.40		3.474	34	${}_5S_{21}$	6312.50 ± 2.00	6316.82		3.632	34
${}_{13}S_5$		5834.28		4.079		${}_8S_{15}$	6306.50 ± 4.50	6317.11		3.990	34
${}_5S_{18}$	5831.00 ± 3.00	5835.59		3.422	34	${}_{15}S_4$		6332.35		2.507	
${}_3S_{27}$		5836.74		2.389	M	${}_1S_{37}$	6338.00 ± 6.00	6337.41		6.578	34
${}_2T_{25}$	5843.00 ± 3.50	5848.47		4.561	34	${}_0S_{58}$	6341.10 ± 1.50	6339.21	7.21 ± .16	7.406	34
${}_{12}S_7$		5855.88		2.360		${}_5T_{15}$		6339.76		4.713	
${}_0T_{48}$	5859.00 ± 4.00	5857.43		7.631	38	${}_4S_{26}$	6363.00 ± 3.50	6373.42		3.876	34
${}_4S_{23}$	5858.50 ± 2.00	5868.03		3.861	34	${}_2S_{31}$	6388.50 ± 2.00	6384.20		5.585	34
${}_4T_{17}$	5870.00 ± 9.00	5874.88		4.396	34	${}_{17}S_2$		6395.21		4.327	
${}_8S_{12}$	5874.50 ± 3.50	5876.05		3.565	34	${}_6T_1$		6397.86		4.955	
${}_0S_{53}$	5885.00 ± 1.50	5883.13	6.83 ± .15	7.149	32	${}_{13}S_7$		6398.97		2.613	
${}_9S_{11}$	5887.00 ± 7.00	5885.77		2.416	34	${}_{18}S_1$		6402.12		5.271	
${}_5T_{11}$		5897.53		4.891		${}_0T_{53}$	6408.00 ± 6.00	6406.38		7.623	38
${}_2S_{28}$	5904.00 ± 2.00	5906.03		5.393	34	${}_1T_{37}$	6412.50 ± 2.50	6410.74		6.333	34
${}_1T_{33}$	5915.00 ± 3.50	5913.31		6.034	34	${}_6T_2$		6412.65		4.948	
${}_{14}S_5$		5929.81		8.644	I	${}_7S_{16}$		6413.76		11.211	I
${}_1S_{34}$		5933.35		6.459		${}_4T_{20}$		6420.67		4.316	
${}_{10}S_9$	5939.00 ± 4.50	5941.76		3.125	34	${}_{19}S_1$		6427.44		11.165	I
${}_3T_{21}$	5955.00 ± 6.00	5958.71		4.411	34	${}_0S_{59}$	6436.30 ± 3.50	6430.72		7.454	34
${}_0T_{49}$	5969.50 ± 4.00	5967.21		7.631	d	${}_6T_3$		6434.81		4.938	
${}_0S_{54}$	5975.60 ± 1.40	5974.14	7.15 ± .14	7.203	32	${}_{11}S_9$	6437.50 ± 1.50	6437.12		1.594	34
${}_5S_{19}$	5989.50 ± 2.00	5995.82		3.513	34	${}_6S_{19}$	6453.50 ± 2.50	6447.44		3.197	34
${}_5T_{12}$		5996.15		4.856		${}_{17}S_3$		6452.27		4.679	
${}_2T_{26}$	6001.00 ± 4.50	6004.65		4.598	34	${}_{10}S_{11}$	6446.00 ± 6.00	6454.44		2.637	34
${}_6S_{17}$	6026.50 ± 2.00	6021.31		3.325	34	${}_3T_{24}$		6464.14		4.517	
${}_8S_{13}$	6016.00 ± 3.50	6024.43		3.778	34	${}_6T_4$		6464.29		4.924	
${}_{15}S_3$	6030.96 ± 0.35	6035.22	1.24 ± .16	1.241	34	${}_8S_{16}$	6471.00 ± 4.50	6464.75		4.057	34
${}_4S_{24}$	6025.50 ± 3.50	6036.26		3.864	34	${}_2T_{29}$	6464.50 ± 3.00	6466.83		4.698	34

TABLE 1. continued

Mode	f_{obs} μHz	f_{PREM} μHz	q^a_{obs}	q_{PREM}	ref.[b]	Mode	f_{obs} μHz	f_{PREM} μHz	q_{obs}	q_{PREM}	ref.
${}_1S_{38}$	6482.00 ± 9.00	6469.86		6.627	34	${}_{10}S_{13}$	6871.00 ± 9.00	6874.43		3.601	34
${}_5T_{16}$		6470.62		4.651		${}_4S_{29}$	6870.00 ± 2.00	6877.18		3.917	34
${}_{15}S_5$		6475.31		4.113		${}_0S_{64}$		6889.58		7.678	
${}_5S_{22}$	6480.00 ± 6.00	6478.57		3.678	34	${}_{18}S_3$	6888.00 ± 0.55	6891.93	1.21 ± .11	1.174	34
${}_9S_{13}$	6487.00 ± 1.50	6483.50		2.063	34	${}_1T_{41}$	6889.00 ± 6.00	6894.00		6.580	34
${}_3S_{30}$		6487.70		2.368	M	${}_5T_{19}$		6914.69		4.433	
${}_{14}S_6$		6493.51		11.069	I	${}_2T_{32}$	6911.00 ± 4.50	6920.90		4.784	34
${}_6T_5$		6501.07		4.907		${}_3S_{32}$		6921.36		2.363	M
${}_0T_{54}$		6516.18		7.620		${}_7S_{19}$	6919.00 ± 7.00	6921.84		4.175	34
${}_0S_{60}$	6526.00 ± 3.00	6522.32	7.11 ± .19	7.501	34	${}_{11}S_{11}$	6915.00 ± 9.00	6922.23		3.088	34
${}_1T_{38}$		6532.73		6.400		${}_{20}S_1$	6948.50 ± 0.60	6954.04	1.29 ± .15	1.141	34
${}_4S_{27}$	6532.00 ± 2.00	6541.80		3.886	34	${}_0T_{58}$	6959.00 ± 6.00	6955.42		7.604	d
${}_2S_{32}$	6548.50 ± 4.00	6542.03		5.643	34	${}_6T_{12}$		6956.77		4.714	
${}_6T_6$		6545.07		4.887		${}_3T_{27}$	6946.50 ± 3.50	6956.93		4.557	34
${}_{18}S_2$		6545.69		1.876		${}_5S_{25}$	6964.50 ± 3.50	6967.92		3.803	34
${}_{13}S_8$		6553.59		3.591		${}_4T_{23}$		6980.21		4.309	
${}_{16}S_4$		6568.64		3.389		${}_0S_{65}$	6985.00 ± 5.00	6981.61		7.720	d
${}_7S_0$	6580.00 ± 0.50	6580.71	1.26 ± 0.09	1.135		${}_1S_{42}$		6988.22		6.852	
${}_{15}S_6$		6595.93		4.489		${}_2S_{35}$	7015.00 ± 3.50	7010.52		5.800	34
${}_6T_7$		6596.24		4.864		${}_1T_{42}$	7013.50 ± 3.50	7013.05		6.633	34
${}_1S_{39}$		6601.16		6.679		${}_9S_{15}$	7028.00 ± 2.50	7029.82		2.325	34
${}_4T_{21}$	6594.00 ± 6.00	6608.12		4.307	34	${}_{10}S_{14}$	7027.00 ± 4.50	7038.76		3.859	34
${}_5T_{17}$		6609.94		4.583		${}_4S_{30}$	7034.00 ± 2.00	7043.91		3.938	34
${}_{12}S_9$		6610.23		11.602	I	${}_{14}S_8$	7039.00 ± 1.50	7047.89		2.070	34
${}_0S_{61}$		6614.00		7.547		${}_6S_{22}$	7053.50 ± 2.50	7048.18		3.324	34
${}_7S_{17}$	6611.00 ± 4.50	6614.22		4.110	34	${}_6T_{13}$		7049.19		4.680	
${}_2T_{30}$	6609.00 ± 3.50	6619.02		4.728	34	${}_0T_{59}$		7065.24		7.599	
${}_0T_{55}$		6625.98		7.617		${}_2T_{33}$	7066.00 ± 4.00	7070.65		4.811	34
${}_3T_{25}$	6622.50 ± 3.50	6629.35		4.536	34	${}_0S_{66}$		7073.71		7.760	
${}_5S_{23}$	6635.00 ± 3.50	6641.17		3.720	34	${}_{19}S_2$		7078.81		11.007	I
${}_1T_{39}$	6656.00 ± 6.00	6653.89		6.464	34	${}_5T_{20}$		7080.11		4.356	
${}_6S_{20}$	6659.50 ± 2.00	6654.48		3.202	34	${}_7S_{20}$	7085.00 ± 5.00	7081.96		4.182	34
${}_6T_8$		6654.50		4.838		${}_{15}S_7$		7085.82		11.488	I
${}_{13}S_9$		6686.16		3.861		${}_1S_{43}$		7115.01		6.914	
${}_{10}S_{12}$	6682.50 ± 3.00	6687.11		3.104	34	${}_3T_{28}$	7113.50 ± 3.50	7119.64		4.562	34
${}_2S_{33}$		6699.04		5.698		${}_5S_{26}$	7129.00 ± 2.00	7131.42		3.846	34
${}_3S_{31}$		6704.57		2.365	M	${}_1T_{43}$	7133.00 ± 5.00	7131.51		6.683	34
${}_0S_{62}$		6705.78		7.592		${}_3S_{33}$		7138.07		2.360	M
${}_4S_{28}$	6705.00 ± 1.50	6709.77		3.900	34	${}_{12}S_{11}$	7138.00 ± 1.50	7138.82		1.956	34
${}_{11}S_{10}$	6712.50 ± 3.50	6712.42		2.345	34	${}_6T_{14}$		7148.14		4.644	
${}_6T_9$		6719.78		4.810		${}_{11}S_{12}$	7144.00 ± 5.00	7149.61		2.725	34
${}_1S_{40}$	6739.00 ± 7.00	6731.31		6.734	34	${}_{16}S_6$	7149.13 ± 0.54	7153.68	1.72 ± .25	1.352	34
${}_0T_{56}$		6735.79		7.613		${}_{13}S_{10}$		7155.54		11.652	I
${}_5T_{18}$		6757.93		4.509		${}_8S_{18}$		7162.43		11.222	I
${}_7S_{18}$	6764.00 ± 6.00	6766.28		4.150	34	${}_4T_{24}$	7159.00 ± 8.00	7163.04		4.313	34
${}_9S_{14}$	6771.50 ± 1.00	6768.24		2.063	34	${}_2S_{36}$	7166.50 ± 3.00	7164.96		5.847	34
${}_2T_{31}$	6763.00 ± 4.50	6770.36		4.756	34	${}_0S_{67}$		7165.89		7.799	
${}_{14}S_7$		6772.89		3.026		${}_0T_{60}$		7175.06		7.594	
${}_1T_{40}$	6773.50 ± 4.50	6774.29		6.524	34	${}_{10}S_{15}$	7202.00 ± 5.00	7209.25		3.746	34
${}_8S_{17}$		6788.22		11.217	I	${}_4S_{31}$	7200.00 ± 2.00	7209.87		3.963	34
${}_6T_{10}$		6791.98		4.780		${}_2T_{34}$	7214.00 ± 6.00	7219.63		4.838	34
${}_3T_{26}$	6791.00 ± 7.00	6793.54		4.548	34	${}_6S_{23}$	7241.00 ± 2.00	7233.92		3.425	34
${}_4T_{22}$		6795.04		4.306		${}_9S_{16}$	7238.00 ± 3.00	7239.58		3.133	34
${}_0S_{63}$		6797.64		7.635		${}_1S_{44}$		7240.71		6.977	
${}_5S_{24}$	6802.00 ± 3.00	6804.39		3.761	34	${}_{18}S_4$	7238.25 ± 0.18	7241.00	1.08 ± .06	1.060	34
${}_{16}S_5$	6829.84 ± 1.44	6836.41	1.86 ± .15	1.720	34	${}_7S_{21}$	7238.50 ± 4.50	7247.61		4.166	34
${}_0T_{57}$		6845.61		7.609		${}_1T_{44}$	7249.50 ± 3.00	7249.42		6.730	34
${}_{17}S_4$		6854.04		11.690	I	${}_6T_{15}$		7253.56		4.609	
${}_6S_{21}$	6859.00 ± 2.00	6855.03		3.246	34	${}_5T_{21}$		7253.69		4.286	
${}_2S_{34}$		6855.21		5.750		${}_0S_{68}$		7258.14		7.838	
${}_1S_{41}$		6860.33		6.792		${}_3T_{29}$	7273.00 ± 4.50	7281.77		4.565	34
${}_{12}S_{10}$	6860.00 ± 5.00	6861.33		3.022	34	${}_0T_{61}$		7284.88		7.588	
${}_6T_{11}$		6871.01		4.748		${}_5S_{27}$		7294.59		3.892	

TABLE 1. continued

Mode	f_{obs} μHz	f_{PREM} μHz	q^a_{obs}	q_{PREM}	ref.[b]	Mode	f_{obs} μHz	f_{PREM} μHz	q_{obs}	q_{PREM}	ref.
${}_2S_{37}$	7314.50 ± 3.50	7318.53		5.890	34	${}_2T_{37}$	7653.00 ± 3.00	7661.93		4.924	34
${}_4T_{25}$		7343.40		4.318		${}_{15}S_8$		7664.98		11.231	I
${}_0S_{69}$		7350.47		7.875		${}_7T_7$		7667.63		4.741	
${}_{14}S_9$	7343.94 ± 0.61	7354.08		1.892	34	${}_{10}S_{17}$	7678.00 ± 1.50	7675.89		2.580	34
${}_3S_{34}$		7354.71		2.358	M	${}_{20}S_3$		7685.74		7.229	I
${}_{20}S_2$		7357.09		1.940		${}_{11}S_{14}$	7679.00 ± 3.50	7686.80		2.504	34
${}_1S_{45}$		7365.35		7.041		${}_{16}S_8$		7689.68		4.011	
${}_6T_{16}$		7365.37		4.574		${}_{13}S_{11}$		7693.02		11.669	I
${}_1T_{45}$	7362.50 ± 4.50	7366.83		6.773	34	${}_4T_{27}$	7694.00 ± 7.00	7697.46		4.326	34
${}_2T_{35}$	7362.00 ± 4.00	7367.85		4.865	34	${}_9S_{19}$	7695.00 ± 4.50	7698.29		4.030	34
${}_4S_{32}$	7366.00 ± 2.00	7374.98		3.992	34	${}_4S_{34}$	7691.00 ± 1.50	7702.48		4.062	34
${}_0T_{62}$		7394.70		7.582		${}_1T_{48}$	7713.50 ± 3.50	7716.44		6.886	34
${}_9S_{17}$	7390.00 ± 5.00	7403.56		3.675	34	${}_7T_8$		7717.14		4.735	
${}_6S_{24}$	7418.50 ± 2.00	7413.13		3.534	34	${}_0S_{73}$		7720.47		8.012	
${}_{11}S_{13}$	7411.50 ± 4.00	7417.49		2.379	34	${}_0T_{65}$		7724.15		7.563	
${}_7S_{22}$	7416.00 ± 6.00	7419.40		4.127	34	${}_1S_{48}$		7733.33		7.236	
${}_{10}S_{16}$	7423.00 ± 2.50	7422.64		3.038	34	${}_6T_{19}$		7738.59		4.474	
${}_8S_0$	7428.00 ± 1.50	7424.13	0.90 ± .22	1.174	34	${}_6S_{26}$	7756.00 ± 4.00	7757.89		3.733	34
${}_5T_{22}$		7434.43		4.226		${}_3T_{32}$	7757.50 ± 4.50	7764.94		4.572	34
${}_0S_{70}$		7442.86		7.911		${}_{15}S_9$		7771.75		4.008	
${}_3T_{30}$	7439.00 ± 4.50	7443.36		4.567	34	${}_7T_9$		7772.53		4.730	
${}_{12}S_{12}$	7451.50 ± 2.00	7455.08		1.754	34	${}_2S_{40}$	7776.00 ± 4.00	7773.95		6.005	34
${}_5S_{28}$	7450.50 ± 2.00	7457.18		3.939	34	${}_{12}S_{13}$	7771.00 ± 2.50	7777.00		1.758	34
${}_{17}S_5$		7461.22		10.212	I	${}_5S_{30}$	7776.50 ± 2.50	7780.00		4.034	34
${}_2S_{38}$	7476.00 ± 4.00	7471.21		5.931	34	${}_7S_{24}$	7788.00 ± 5.00	7780.08		4.013	34
${}_{16}S_7$	7470.04 ± 1.00	7474.14	1.50 ± .15	1.250	34	${}_3S_{36}$		7787.76		2.355	M
${}_6T_{17}$		7483.49		4.540		${}_{21}S_3$		7801.59		5.862	
${}_1T_{46}$	7483.50 ± 4.00	7483.78		6.813	34	${}_{17}S_8$		7805.05		1.838	
${}_1S_{46}$		7488.98		7.106		${}_2T_{38}$	7797.00 ± 4.00	7807.76		4.956	34
${}_{21}S_1$		7495.27		4.718		${}_5T_{24}$		7810.82		4.155	
${}_7T_1$		7498.57		4.762		${}_0S_{74}$		7813.15		8.043	
${}_0T_{63}$		7504.52		7.576		${}_{22}S_1$	7816.70 ± 0.40	7819.54	0.95 ± .05	1.304	34
${}_{19}S_3$		7504.81		4.384		${}_{14}S_{11}$	7803.00 ± 6.00	7823.54		3.769	34
${}_7T_2$		7511.20		4.760		${}_1T_{49}$	7830.00 ± 6.00	7832.22		6.918	34
${}_{21}S_2$		7514.86		4.577		${}_7T_{10}$		7833.70		4.725	
${}_2T_{36}$	7505.00 ± 5.00	7515.28		4.894	34	${}_0T_{66}$		7833.97		7.555	
${}_{18}S_5$		7517.39		4.365		${}_8S_{20}$	7848.00 ± 6.00	7843.35		4.106	34
${}_4T_{26}$	7512.00 ± 6.00	7521.46		4.322	34	${}_1S_{49}$		7854.14		7.300	
${}_7T_3$		7530.11		4.758		${}_4S_{35}$	7856.00 ± 1.50	7864.82		4.102	34
${}_0S_{71}$		7535.33		7.946		${}_4T_{28}$	7863.00 ± 8.00	7871.66		4.331	34
${}_8S_{19}$		7536.41		11.229	I	${}_6T_{20}$		7875.57		4.443	
${}_4S_{33}$	7532.00 ± 1.50	7539.19		4.025	34	${}_{15}S_{10}$	7893.00 ± 6.00	7897.49		3.224	34
${}_{19}S_4$		7540.90		4.538		${}_{23}S_1$		7899.09		11.631	I
${}_9S_{18}$	7551.00 ± 5.00	7552.78		3.907	34	${}_7T_{11}$		7900.55		4.720	
${}_7T_4$		7555.27		4.754		${}_0S_{75}$		7905.88		8.074	
${}_3S_{35}$		7571.27		2.357	M	${}_9S_{20}$		7910.21		11.235	I
${}_{17}S_6$		7580.67		4.230		${}_{11}S_{15}$		7919.06		3.012	
${}_7T_5$		7586.61		4.750		${}_2S_{41}$	7917.50 ± 6.00	7924.01		6.038	34
${}_6S_{25}$	7590.00 ± 1.50	7587.27		3.640	34	${}_3T_{33}$	7914.50 ± 4.50	7924.89		4.576	34
${}_7S_{23}$	7598.00 ± 3.50	7597.20		4.073	34	${}_6S_{27}$	7929.00 ± 7.00	7926.36		3.810	34
${}_1T_{47}$	7594.00 ± 5.00	7600.31		6.851	34	${}_{10}S_{18}$	7940.50 ± 2.50	7938.48		2.434	34
${}_3T_{31}$	7605.00 ± 5.00	7604.42		4.569	34	${}_5S_{31}$	7939.00 ± 1.50	7940.16		4.080	34
${}_6T_{18}$		7607.90		4.506		${}_0T_{67}$	7950.00 ± 8.00	7943.78		7.548	d
${}_1S_{47}$		7611.63		7.171		${}_1T_{50}$	7948.50 ± 3.50	7947.68		6.947	34
${}_0T_{64}$		7614.33		7.569		${}_2T_{39}$	7943.50 ± 3.00	7952.75		4.990	34
${}_5S_{29}$	7616.00 ± 2.50	7619.01		3.987	34	${}_{13}S_{12}$	7954.50 ± 5.50	7955.03		4.043	34
${}_5T_{23}$		7620.80		4.181		${}_{18}S_6$		7957.04		2.530	
${}_2S_{39}$	7627.00 ± 4.00	7623.02		5.970	34	${}_7S_{25}$	7968.00 ± 3.50	7966.58		3.960	34
${}_7T_6$		7624.09		4.746		${}_7T_{12}$		7972.96		4.715	
${}_0S_{72}$		7627.87		7.979		${}_1S_{50}$		7974.10		7.363	
${}_{17}S_7$		7635.12		4.372		${}_8S_{21}$		7989.31		4.156	
${}_{14}S_{10}$	7624.00 ± 4.00	7635.75		2.574	34	${}_0S_{76}$	8015.00 ± 8.00	7998.68		8.103	d
${}_{19}S_5$		7661.84		2.726		${}_5T_{25}$		8002.38		4.148	

TABLE 1. continued

Mode	f_{obs} μHz	f_{PREM} μHz	q^a_{obs}	q_{PREM}	ref.[b]	Mode	f_{obs} μHz	f_{PREM} μHz	q_{obs}	q_{PREM}	ref.
${}_3S_{37}$		8004.19		2.353	M	${}_4T_{31}$		8385.31		4.361	
${}_6T_{21}$		8018.91		4.413		${}_3T_{36}$	8395.00 ± 10.0	8401.09		4.598	34
${}_4S_{36}$	8015.50 ± 3.50	8026.22		4.146	34	${}_1T_{54}$	8400.00 ± 10.0	8406.75		7.044	34
${}_4T_{29}$		8044.29		4.339		${}_{12}S_{15}$	8402.00 ± 9.00	8411.28		1.840	34
${}_7T_{13}$		8050.83		4.711		${}_7T_{17}$		8414.71		4.696	
${}_0T_{68}$		8053.59		7.540		${}_5S_{34}$	8410.00 ± 4.00	8416.62		4.191	34
${}_1T_{51}$	8059.00 ± 6.00	8062.83		6.975	34	${}_{11}S_{18}$	8424.00 ± 8.00	8418.49		3.976	34
${}_2S_{42}$	8065.00 ± 8.00	8073.21		6.069	34	${}_6S_{30}$	8417.00 ± 6.00	8427.41		3.952	34
${}_3T_{34}$	8080.00 ± 5.00	8084.26		4.581	34	${}_{15}S_{12}$	8432.50 ± 3.00	8432.73		1.747	34
${}_{13}S_{13}$		8091.46		3.907		${}_3S_{39}$		8436.86		2.350	M
${}_0S_{77}$		8091.55		8.131		${}_{16}S_{10}$	8433.00 ± 3.00	8437.72		1.291	34
${}_{19}S_6$		8093.14		10.515	I	${}_8S_{24}$	8431.00 ± 8.00	8440.00		4.211	34
${}_1S_{51}$		8093.25		7.425		${}_1S_{54}$		8446.31		7.603	
${}_6S_{28}$	8094.00 ± 5.00	8093.69		3.871	34	${}_{10}S_{20}$	8451.50 ± 2.50	8446.66		2.560	34
${}_2T_{40}$	8089.00 ± 5.00	8096.87		5.027	34	${}_0S_{81}$		8463.61		8.232	
${}_{12}S_{14}$	8093.00 ± 2.50	8097.37		1.809	34	${}_{20}S_5$	8464.65 ± 0.84	8471.58		1.571	34
${}_5S_{32}$	8098.00 ± 5.00	8099.56		4.122	34	${}_{13}S_{15}$	8462.00 ± 9.00	8474.42		2.968	34
${}_{11}S_{16}$	8100.00 ± 10.0	8107.03		3.514	34	${}_6T_{24}$		8487.69		4.332	
${}_{20}S_4$		8116.77		1.278		${}_0T_{72}$		8492.80		7.507	
${}_{16}S_9$	8116.00 ± 2.00	8117.59		1.392	34	${}_4S_{39}$	8492.50 ± 3.00	8504.92		4.293	34
${}_{15}S_{11}$	8132.00 ± 6.00	8130.95		1.999	34	${}_2S_{45}$	8515.00 ± 8.00	8515.75		6.150	34
${}_7T_{14}$		8134.04		4.707		${}_7T_{18}$		8518.35		4.691	
${}_8S_{22}$	8135.00 ± 8.00	8136.99		4.188	34	${}_1T_{55}$		8520.94		7.063	
${}_7S_{26}$	8152.00 ± 8.00	8155.16		3.919	34	${}_2T_{43}$	8507.00 ± 8.00	8523.66		5.153	34
${}_0T_{69}$		8163.40		7.533		${}_7S_{28}$	8536.00 ± 9.00	8533.66		3.876	34
${}_6T_{22}$		8168.68		4.385		${}_{24}S_1$		8550.62		4.963	
${}_1T_{52}$	8170.00 ± 8.00	8177.72		7.000	34	${}_8T_1$		8551.15		4.975	
${}_0S_{78}$		8184.47		8.158		${}_4T_{32}$	8548.00 ± 7.00	8553.86		4.377	34
${}_4S_{37}$	8177.50 ± 3.00	8186.69		4.192	34	${}_0S_{82}$		8556.77		8.254	
${}_5T_{26}$		8193.48		4.159		${}_3T_{37}$	8548.00 ± 5.00	8558.49		4.609	34
${}_{10}S_{19}$	8200.00 ± 3.50	8197.96		2.428	34	${}_{22}S_3$		8559.91		3.686	
${}_{22}S_2$		8207.04		1.397		${}_{23}S_2$		8561.36		5.004	
${}_1S_{52}$		8211.63		7.486		${}_8T_2$		8561.68		4.974	
${}_4T_{30}$	8195.00 ± 10.0	8215.47		4.348	34	${}_1S_{55}$		8562.68		7.659	
${}_3S_{38}$		8220.55		2.352	M	${}_{11}S_{19}$		8568.59		4.020	
${}_2S_{43}$	8213.00 ± 7.00	8221.56		6.098	34	${}_5T_{28}$		8568.60		4.218	
${}_7T_{15}$		8222.48		4.703		${}_5S_{35}$	8570.50 ± 3.50	8574.62		4.218	34
${}_{14}S_{12}$		8224.06		11.684	I	${}_8T_3$		8577.46		4.973	
${}_2T_{41}$	8230.00 ± 8.00	8240.08		5.066	34	${}_{24}S_2$		8585.28		11.454	I
${}_3T_{35}$		8243.00		4.589		${}_6S_{31}$	8589.00 ± 5.00	8594.46		3.975	34
${}_{17}S_9$		8248.53		11.488	I	${}_8S_{25}$	8582.00 ± 6.00	8596.24		4.205	34
${}_5S_{33}$	8253.50 ± 3.50	8258.32		4.159	34	${}_{22}S_4$		8598.40		4.877	
${}_{13}S_{14}$	8265.00 ± 8.00	8258.94		3.502	34	${}_8T_4$		8598.47		4.970	
${}_6S_{29}$	8257.50 ± 4.00	8260.57		3.918	34	${}_{18}S_8$		8599.27		2.423	
${}_9S_0$	8269.50 ± 1.00	8262.64	0.82 ± .20	1.190	34	${}_0T_{73}$		8602.59		7.499	
${}_{11}S_{17}$	8265.00 ± 8.00	8268.00		3.821	34	${}_{23}S_3$		8602.59		2.605	
${}_0T_{70}$		8273.20		7.524		${}_8T_5$		8624.69		4.967	
${}_0S_{79}$		8277.46		8.184		${}_7T_{19}$		8626.95		4.685	
${}_9S_{21}$		8283.85		11.241	I	${}_1T_{56}$	8627.00 ± 8.00	8634.93		7.081	34
${}_8S_{23}$	8273.00 ± 7.00	8287.05		4.205	34	${}_{21}S_5$		8639.18		4.429	
${}_1T_{53}$	8278.00 ± 7.00	8292.35		7.023	34	${}_{20}S_6$		8642.79		4.644	
${}_{18}S_7$		8301.04		1.444		${}_0S_{83}$		8649.99		8.275	
${}_7T_{16}$		8316.07		4.700		${}_3S_{40}$		8653.08		2.360	M
${}_6T_{23}$		8324.95		4.358		${}_{25}S_1$	8652.50 ± 0.40	8655.17	1.02 ± .07	1.185	34
${}_1S_{53}$		8329.31		7.545		${}_8T_6$		8656.08		4.964	
${}_7S_{27}$	8347.00 ± 6.00	8344.50		3.892	34	${}_6T_{25}$		8656.69		4.309	
${}_4S_{38}$	8336.00 ± 2.00	8346.24		4.242	34	${}_9S_{22}$		8657.36		11.248	I
${}_2S_{44}$	8367.00 ± 6.00	8369.08		6.124	34	${}_2S_{46}$	8682.00 ± 6.00	8661.61		6.173	34
${}_0S_{80}$		8370.50		8.208		${}_4S_{40}$	8651.50 ± 3.00	8662.79		4.335	34
${}_{21}S_4$		8373.62		11.544	I	${}_2T_{44}$	8661.00 ± 9.00	8663.95		5.200	34
${}_2T_{42}$	8370.00 ± 10.0	8382.36		5.108	34	${}_{19}S_7$		8671.41		10.411	I
${}_5T_{27}$		8382.56		4.183		${}_{10}S_{21}$	8669.00 ± 4.50	8673.48		2.922	34
${}_0T_{71}$		8383.00		7.516		${}_1S_{56}$		8678.47		7.713	

TABLE 1. continued

Mode	f_{obs} μHz	f_{PREM} μHz	q^a_{obs}	q_{PREM}	ref.[b]	Mode	f_{obs} μHz	f_{PREM} μHz	q_{obs}	q_{PREM}	ref.
${}_{12}S_{16}$	8689.50 ± 4.00	8691.79		2.225	34	${}_{8}T_{13}$		9017.75		4.900	
${}_{8}T_{7}$		8692.62		4.959		${}_{1}S_{59}$		9022.73		7.864	
${}_{20}S_{7}$		8706.24		5.731		${}_{25}S_{2}$	9026.51 ± 0.69	9022.91	1.22 ± .11	1.269	34
${}_{0}T_{74}$		8712.37		7.489		${}_{0}S_{87}$		9023.43		8.350	
${}_{3}T_{38}$	8697.00 ± 8.00	8715.17		4.622	34	${}_{3}T_{40}$	9020.00 ± 10.0	9026.32		4.653	34
${}_{4}T_{33}$	8718.00 ± 4.50	8721.15		4.395	34	${}_{9}S_{23}$		9030.75		11.255	I
${}_{7}S_{29}$		8722.02		3.870		${}_{10}S_{23}$	9025.00 ± 10.0	9038.42		3.756	34
${}_{11}S_{20}$	8715.00 ± 10.0	8726.69		3.927	34	${}_{0}T_{77}$	9050.00 ± 8.00	9041.69		7.461	d
${}_{5}S_{36}$	8726.50 ± 3.50	8732.50		4.237	34	${}_{19}S_{9}$	9038.00 ± 8.00	9047.16		1.632	34
${}_{8}T_{8}$		8734.26		4.953		${}_{5}S_{38}$	9035.50 ± 4.50	9048.53		4.258	34
${}_{14}S_{13}$	8724.50 ± 4.00	8734.78		2.097	34	${}_{4}T_{35}$	9050.00 ± 5.00	9052.02		4.438	34
${}_{16}S_{11}$	8729.00 ± 5.00	8736.47		1.816	34	${}_{10}S_{0}$		9056.12		1.206	
${}_{7}T_{20}$		8740.51		4.677		${}_{13}S_{17}$	9055.50 ± 4.00	9063.12		2.083	34
${}_{0}S_{84}$		8743.27		8.296		${}_{2}T_{47}$	9069.00 ± 8.00	9078.56		5.359	34
${}_{18}S_{9}$	8735.00 ± 7.00	8747.40		4.299	34	${}_{4}S_{42}$		9085.50		2.346	M
${}_{1}T_{57}$	8740.00 ± 10.0	8748.74		7.097	34	${}_{8}S_{28}$		9086.85		4.143	
${}_{15}S_{13}$		8749.54		11.679	I	${}_{1}T_{60}$	9083.00 ± 9.00	9089.22		7.137	34
${}_{5}T_{29}$		8751.14		4.257		${}_{8}T_{14}$		9089.28		4.882	
${}_{13}S_{16}$	8746.00 ± 5.00	8752.25		2.313	34	${}_{2}S_{49}$	9093.00 ± 9.00	9094.25		6.239	34
${}_{8}S_{26}$	8760.00 ± 9.00	8756.06		4.191	34	${}_{7}S_{31}$	9107.00 ± 8.00	9095.12		3.875	34
${}_{6}S_{32}$	8755.00 ± 5.00	8761.80		3.991	34	${}_{16}S_{13}$		9095.71		3.627	
${}_{8}T_{9}$		8780.96		4.946		${}_{6}S_{34}$	9100.00 ± 10.0	9097.31		4.004	34
${}_{1}S_{57}$		8793.72		7.765		${}_{5}T_{31}$		9105.98		4.337	
${}_{19}S_{8}$		8797.85		3.536		${}_{11}S_{22}$	9101.50 ± 4.50	9111.59		3.153	34
${}_{2}T_{45}$	8785.00 ± 6.00	8803.22		5.250	34	${}_{7}T_{23}$		9111.72		4.629	
${}_{2}S_{47}$		8806.64		6.196		${}_{0}S_{88}$		9116.92		8.365	
${}_{17}S_{10}$		8817.00		11.146	I	${}_{3}S_{43}$	9120.50 ± 2.00	9131.62		4.510	34
${}_{3}S_{41}$	8816.50 ± 2.50	8819.77		4.400	34	${}_{1}S_{60}$		9136.57		7.911	
${}_{0}T_{75}$		8822.15		7.480		${}_{12}S_{18}$		9145.99		3.073	
${}_{6}T_{26}$		8831.46		4.290		${}_{17}S_{12}$	9146.00 ± 5.00	9151.28		2.163	34
${}_{8}T_{10}$		8832.70		4.937		${}_{0}T_{78}$		9151.46		7.451	
${}_{18}S_{10}$		8836.23		4.985		${}_{8}T_{15}$		9165.71		4.862	
${}_{0}S_{85}$		8836.60		8.315		${}_{14}S_{15}$		9168.47		3.598	
${}_{21}S_{6}$	8848.57 ± 0.71	8850.77	1.60 ± .20	1.351	34	${}_{21}S_{7}$	9167.79 ± 0.53	9173.79	1.58 ± .20	1.250	34
${}_{7}T_{21}$		8859.08		4.665		${}_{3}T_{41}$	9166.00 ± 8.00	9180.76		4.670	34
${}_{1}T_{58}$	8851.00 ± 9.00	8862.38		7.112	34	${}_{6}T_{28}$		9194.29		4.271	
${}_{10}S_{22}$	8868.00 ± 7.00	8868.46		3.417	34	${}_{9}S_{24}$	9175.00 ± 10.0	9196.93		3.929	34
${}_{4}S_{41}$		8869.34		2.348	M	${}_{1}T_{61}$	9197.00 ± 8.00	9202.44		7.148	34
${}_{3}T_{39}$	8858.00 ± 8.00	8871.12		4.637	34	${}_{5}S_{39}$	9195.00 ± 4.50	9206.92		4.259	34
${}_{4}T_{34}$	8873.00 ± 6.00	8887.20		4.416	34	${}_{0}S_{89}$		9210.47		8.380	
${}_{8}T_{11}$		8889.44		4.927		${}_{2}T_{48}$	9204.00 ± 8.00	9214.61		5.416	34
${}_{5}S_{37}$	8882.50 ± 2.00	8890.43		4.250	34	${}_{4}T_{36}$	9210.00 ± 8.00	9215.65		4.462	34
${}_{11}S_{21}$		8904.37		3.606		${}_{24}S_{3}$		9218.64		10.287	I
${}_{1}S_{58}$		8908.46		7.816		${}_{2}S_{50}$		9236.83		6.261	
${}_{7}S_{30}$		8909.23		3.870		${}_{7}T_{24}$		9246.21		4.601	
${}_{8}S_{27}$	8912.00 ± 6.00	8919.60		4.170	34	${}_{8}T_{16}$		9247.01		4.839	
${}_{6}S_{33}$	8929.00 ± 6.00	8929.44		4.000	34	${}_{1}S_{61}$		9250.01		7.955	
${}_{0}S_{86}$	8955.00 ± 8.00	8929.99		8.333	d	${}_{8}S_{29}$	9258.00 ± 9.00	9257.65		4.114	34
${}_{5}T_{30}$		8930.17		4.298		${}_{0}T_{79}$		9261.21		7.441	
${}_{0}T_{76}$		8931.93		7.471		${}_{20}S_{8}$		9262.17		11.298	I
${}_{12}S_{17}$	8929.00 ± 5.00	8933.91		2.612	34	${}_{6}S_{35}$		9265.32		4.006	
${}_{2}T_{46}$	8932.00 ± 7.00	8941.43		5.303	34	${}_{15}S_{14}$		9270.16		11.706	I
${}_{23}S_{4}$	8934.36 ± 0.70	8941.57	1.34 ± .15	1.235	34	${}_{5}T_{32}$		9279.00		4.372	
${}_{17}S_{11}$		8942.70		3.946		${}_{7}S_{32}$		9279.63		3.882	
${}_{16}S_{12}$		8944.33		3.522		${}_{3}S_{44}$	9275.00 ± 3.50	9286.52		4.564	34
${}_{2}S_{48}$	8955.00 ± 10.0	8950.86		6.218	34	${}_{23}S_{5}$	9289.53 ± 0.30	9289.58	1.12 ± .17	1.112	34
${}_{8}T_{12}$		8951.13		4.914		${}_{4}S_{43}$		9301.61		2.345	M
${}_{1}T_{59}$		8975.87		7.125		${}_{0}S_{90}$		9304.07		8.394	
${}_{3}S_{42}$	8966.50 ± 2.50	8976.05		4.455	34	${}_{16}S_{14}$		9304.36		2.698	
${}_{7}T_{22}$		8982.76		4.650		${}_{1}T_{62}$	9307.00 ± 7.00	9315.53		7.157	34
${}_{14}S_{14}$	8978.00 ± 6.00	8985.12		3.019	34	${}_{12}S_{19}$	9341.00 ± 8.00	9329.10		3.469	34
${}_{22}S_{5}$		9005.25		11.708	I	${}_{8}T_{17}$		9333.20		4.813	
${}_{6}T_{27}$		9011.09		4.277		${}_{3}T_{42}$	9323.00 ± 8.00	9334.44		4.688	34

TABLE 1. continued

Mode	f_{obs} μHz	f_{PREM} μHz	q^a_{obs}	q_{PREM}	ref.[b]	Mode	f_{obs} μHz	f_{PREM} μHz	q_{obs}	q_{PREM}	ref.
${}_{14}S_{16}$		9337.18		3.543		${}_{9}T_{4}$		9621.48		4.773	
${}_{11}S_{23}$	9333.00 ± 5.00	9341.10		2.863	34	${}_{3}T_{44}$	9615.00 ± 7.00	9639.58		4.723	34
${}_{2}T_{49}$	9333.00 ± 8.00	9349.55		5.475	34	${}_{7}S_{34}$	9651.00 ± 5.00	9644.54		3.899	34
${}_{9}S_{25}$		9351.55		4.017		${}_{9}T_{5}$		9645.80		4.762	
${}_{19}S_{10}$	9343.00 ± 5.00	9357.39		1.479	34	${}_{23}S_{6}$		9646.41		7.094	I
${}_{1}S_{62}$		9363.08		7.997		${}_{12}S_{21}$	9646.00 ± 7.00	9647.81		3.867	34
${}_{26}S_{1}$		9364.82		11.554	I	${}_{24}S_{5}$		9647.92		4.675	
${}_{5}S_{40}$	9353.50 ± 3.00	9365.67		4.256	34	${}_{19}S_{11}$		9653.75		1.872	
${}_{0}T_{80}$		9370.95		7.430		${}_{1}T_{65}$	9648.00 ± 4.00	9654.15		7.180	34
${}_{13}S_{18}$	9366.00 ± 6.00	9371.79		2.038	34	${}_{2}S_{53}$		9659.62		6.326	
${}_{4}T_{37}$	9390.00 ± 7.00	9378.12		4.485	34	${}_{9}S_{27}$		9660.38		4.088	
${}_{2}S_{51}$		9378.59		6.282		${}_{13}S_{19}$	9668.00 ± 7.00	9671.80		2.054	34
${}_{6}T_{29}$		9379.50		4.272		${}_{9}T_{6}$		9674.96		4.750	
${}_{18}S_{11}$		9384.31		11.660	I	${}_{0}S_{94}$		9678.99		8.438	
${}_{7}T_{25}$		9386.54		4.564		${}_{5}S_{42}$	9666.00 ± 3.00	9684.42		4.239	34
${}_{0}S_{91}$		9397.73		8.407		${}_{7}T_{27}$		9686.26		4.465	
${}_{10}S_{24}$		9404.05		11.263	I	${}_{4}T_{39}$	9679.00 ± 9.00	9699.82		4.530	34
${}_{8}T_{18}$		9424.29		4.783		${}_{0}T_{83}$		9700.14		7.398	
${}_{25}S_{3}$		9424.61		2.646		${}_{24}S_{6}$		9700.17		4.089	
${}_{1}T_{63}$	9420.00 ± 10.0	9428.51		7.166	34	${}_{1}S_{65}$		9700.36		8.113	
${}_{8}S_{30}$	9413.00 ± 9.00	9431.74		4.083	34	${}_{9}T_{7}$		9708.96		4.735	
${}_{6}S_{36}$	9420.00 ± 6.00	9433.35		4.005	34	${}_{17}S_{14}$	9705.00 ± 6.00	9709.08		2.165	34
${}_{17}S_{13}$	9430.00 ± 6.00	9435.93		1.804	34	${}_{22}S_{7}$		9716.00		4.489	
${}_{3}S_{45}$	9424.00 ± 4.50	9440.80		4.618	34	${}_{8}T_{21}$		9727.24		4.671	
${}_{5}T_{33}$		9449.69		4.402		${}_{4}S_{45}$		9733.71		2.343	M
${}_{7}S_{33}$	9464.00 ± 9.00	9462.76		3.890	34	${}_{3}S_{47}$	9729.00 ± 6.00	9747.60		4.724	34
${}_{1}S_{63}$		9475.81		8.038		${}_{9}T_{8}$		9747.78		4.719	
${}_{0}T_{81}$		9480.69		7.420		${}_{2}T_{52}$	9745.00 ± 10.0	9747.83		5.661	34
${}_{2}T_{50}$	9475.00 ± 10.0	9483.40		5.536	34	${}_{14}S_{18}$	9725.00 ± 10.0	9748.85		2.707	34
${}_{27}S_{1}$	9484.00 ± 0.50	9485.84	1.35 ± .24	1.542	34	${}_{25}S_{4}$		9749.46		3.347	
${}_{3}T_{43}$	9472.00 ± 7.00	9487.38		4.706	34	${}_{6}T_{31}$		9750.03		4.287	
${}_{0}S_{92}$		9491.43		8.418		${}_{1}T_{66}$		9766.83		7.187	
${}_{12}S_{20}$	9486.00 ± 9.00	9493.18		3.724	34	${}_{22}S_{8}$		9766.99		4.488	
${}_{21}S_{8}$	9489.93 ± 1.20	9496.96	1.50 ± .09	1.497	34	${}_{6}S_{38}$		9768.94		4.004	
${}_{9}S_{26}$	9502.00 ± 8.00	9505.55		4.063	34	${}_{0}S_{95}$		9772.85		8.447	
${}_{4}S_{44}$		9517.68		2.344	M	${}_{10}S_{25}$		9777.27		11.271	I
${}_{2}S_{52}$	9538.00 ± 8.00	9519.52		6.304	34	${}_{5}T_{35}$		9785.86		4.443	
${}_{8}T_{19}$		9520.30		4.749		${}_{16}S_{15}$		9786.62		11.714	I
${}_{5}S_{41}$	9512.50 ± 4.50	9524.84		4.249	34	${}_{8}S_{32}$		9788.23		4.023	
${}_{14}S_{17}$		9526.65		3.162		${}_{20}S_{9}$	9810.00 ± 10.0	9790.64		3.485	34
${}_{7}T_{26}$		9533.08		4.519		${}_{3}T_{45}$	9782.00 ± 9.00	9791.08		4.741	34
${}_{4}T_{38}$		9539.49		4.509		${}_{9}T_{9}$		9791.40		4.700	
${}_{1}T_{64}$	9539.00 ± 8.00	9541.38		7.174	34	${}_{2}S_{54}$	9820.00 ± 10.0	9798.87		6.348	34
${}_{6}T_{30}$		9565.17		4.279		${}_{12}S_{22}$		9799.02		3.939	
${}_{9}T_{1}$		9577.68		4.792		${}_{0}T_{84}$		9809.85		7.387	
${}_{11}S_{24}$	9576.50 ± 4.50	9578.38		2.757	34	${}_{1}S_{66}$		9812.22		8.148	
${}_{28}S_{1}$		9579.07		4.744		${}_{11}S_{25}$	9811.00 ± 5.00	9814.25		2.769	34
${}_{0}S_{93}$		9585.19		8.429		${}_{9}S_{28}$		9816.78		4.100	
${}_{26}S_{2}$		9586.48		4.754		${}_{7}S_{35}$	9827.00 ± 9.00	9824.99		3.908	34
${}_{9}T_{2}$		9587.42		4.788		${}_{21}S_{9}$		9828.72		4.309	
${}_{1}S_{64}$		9588.23		8.077		${}_{8}T_{22}$		9838.26		4.626	
${}_{0}T_{82}$		9590.42		7.409		${}_{9}T_{10}$		9839.82		4.680	
${}_{3}S_{46}$	9575.50 ± 4.50	9594.48		4.672	34	${}_{5}S_{43}$	9826.00 ± 7.00	9844.43		4.227	34
${}_{15}S_{15}$	9599.00 ± 7.00	9597.78		2.004	34	${}_{7}T_{28}$		9846.40		4.402	
${}_{6}S_{37}$	9597.50 ± 6.50	9601.27		4.005	34	${}_{4}T_{40}$		9859.20		4.550	
${}_{9}T_{3}$		9602.02		4.781		${}_{27}S_{2}$	9869.31 ± 1.00	9865.33	1.32 ± .10	1.266	34
${}_{22}S_{6}$		9603.76		6.315		${}_{0}S_{96}$		9866.75		8.455	
${}_{26}S_{3}$		9604.98		4.727		${}_{22}S_{9}$		9871.01		9.425	I
${}_{8}S_{31}$	9596.00 ± 8.00	9608.74		4.052	34	${}_{2}T_{53}$		9878.43		5.725	
${}_{24}S_{4}$		9615.50		4.537		${}_{1}T_{67}$		9879.42		7.192	
${}_{2}T_{51}$	9615.00 ± 10.0	9616.16		5.598	34	${}_{11}S_{0}$		9887.92		1.202	
${}_{5}T_{34}$		9618.51		4.426		${}_{9}T_{11}$		9893.01		4.658	
${}_{8}T_{20}$		9621.27		4.712		${}_{18}S_{12}$		9894.79		2.975	

TABLE 1. continued

Mode	f_{obs} μHz	f_{PREM} μHz	q^a_{obs}	q_{PREM}	ref.[b]	Mode	f_{obs} μHz	f_{PREM} μHz	q_{obs}	q_{PREM}	ref.
$_{20}S_{10}$		9900.15		4.259		$_{4}S_{46}$		9949.71		2.343	M
$_{3}S_{48}$	9877.00 ± 6.00	9900.17		4.775	34	$_{12}S_{23}$		9950.43		3.965	
$_{26}S_{4}$		9910.84		9.693	I	$_{9}T_{12}$		9950.95		4.634	
$_{0}T_{85}$	9930.00 ± 10.0	9919.55		7.376	d	$_{5}T_{36}$		9952.11		4.453	
$_{1}S_{67}$		9923.84		8.182		$_{8}T_{23}$		9954.41		4.579	
$_{15}S_{16}$		9926.89		1.857		$_{0}S_{97}$	9998.00 ± 10.0	9960.70		8.461	d
$_{6}T_{32}$		9933.27		4.293		$_{13}S_{20}$		9961.02		2.114	
$_{6}S_{39}$		9936.22		4.004		$_{8}S_{33}$		9969.78		3.997	
$_{2}S_{55}$		9937.26		6.372		$_{9}S_{29}$		9975.13		4.106	
$_{17}S_{15}$		9938.07		2.835		$_{23}S_{7}$		9983.94		1.497	
$_{3}T_{46}$	9926.00 ± 7.00	9941.90		4.758	34	$_{1}T_{68}$		9991.93		7.197	
$_{19}S_{12}$		9945.85		11.627	I	$_{14}S_{19}$		9994.61		2.461	

a) $q \equiv 1000/Q$; b) Reference number or mode type; c) Coriolis or second order rotation correction applied.
d) Preliminary estimates from surface-wave dispersion (see text)
I denotes a mode a mode whose energy is trapped within the inner core or on the inner-core boundary (unlikely to be observed).
M denotes a Stoneley mode trapped on the core-mantle boundary (unlikely to be observed).

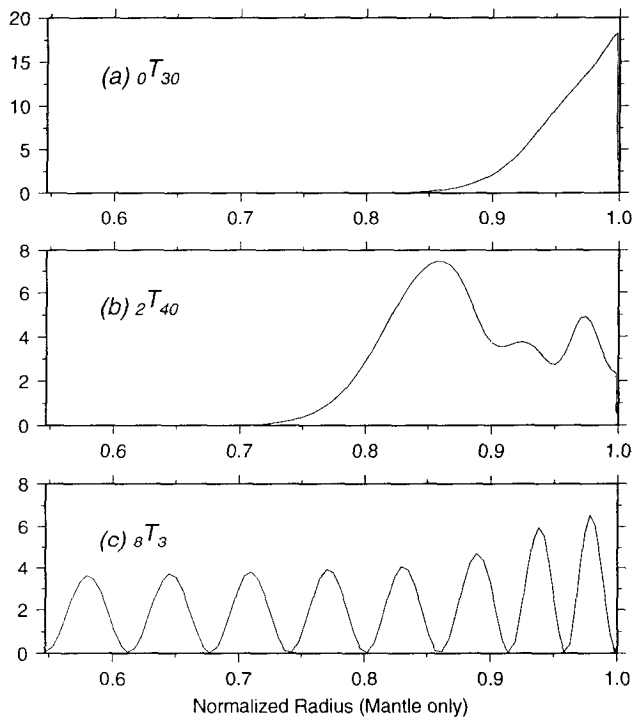

Fig. 5. Shear-energy density as a function of radius in the mantle (R = 1 is the surface). The energy has been normalized so that the total potential energy of the mode is unity. Panel (a) is a fundamental toroidal mode demonstrating how surface-wave equivalent modes have their sensitivity concentrated near the surface of the Earth. Panel (b) is a "mantle S-equivalent" mode – the turning point is at about R = 0.85. Panel (c) is an "ScS-equivalent" mode which is oscillatory throughout the mantle.

modes in the upper left triangle of Figure 4 are like this and, when added together using equation (1), make a seismogram which corresponds to the body wave arrival ScS and its multiples. Such modes are called "ScS-equivalent". Adding all the modes together gives a complete seismogram.

A similar analysis can be carried out for spheroidal modes and Figure 6 shows the elastic compressional and shear energy densities for a variety of modes. Since spheroidal modes are not confined to the mantle, it is now possible to get modes which are interface waves trapped at the core mantle boundary and the inner core boundary. Such modes are called Stoneley modes. Fundamental spheroidal modes are the free-surface equivalent of these and are called surface-wave equivalent modes (Rayleigh waves). Other modes are considered to be equivalent to various kinds of body waves depending upon the location of their turning points and the distributions of compressional and shear energy. It is the great variety of ways in which free oscillations sample the Earth that makes them extremely powerful at constraining the structure of the Earth.

Returning to Figure 3, the clear large-amplitude peaks which are roughly evenly spaced in frequency about 0.1 mHz apart are fundamental spheroidal modes which comprise the large amplitude surface waves in the time domain. Figure 3 is typical for the spectrum of a shallow event. By way of contrast, Figure 7 shows the spectrum of the Payson recording of the deep 1970 Columbian earthquake which, because of the absence of fundamental modes, is completely dominated by overtones. Each peak in Figure 3 and 7 is actually a multiplet composed of $2\ell + 1$ singlets. The singlets are too close together to be resolved since they are broadened by attenuation and finite record

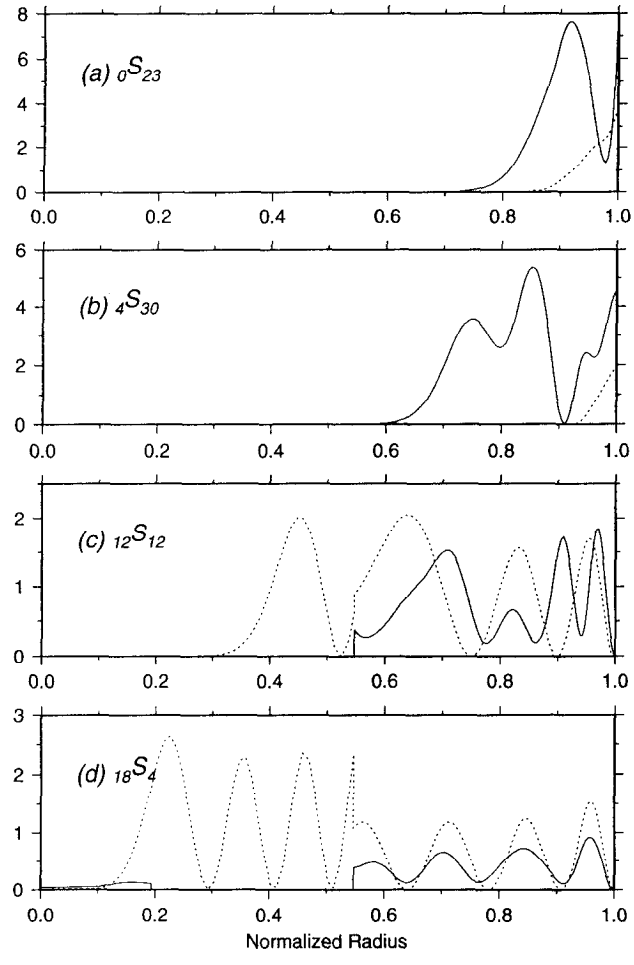

Fig. 6. Shear-energy density (solid line) and compressional energy density (dashed line) for selected spheroidal modes. Panel (a) is a surface-wave equivalent mode, panel (b) is a mantle S-equivalent mode, panel (c) is a PKP-equivalent mode, and panel (d) is a $PKIKP$-equivalent mode. Note that the inner-core boundary is at a normalized radius of 0.19 and the core-mantle boundary is at a normalized radius of 0.55.

length effects. This is not always the case, particularly if we choose low ℓ, high Q multiplets since there are then only a few narrow peaks. Very-low frequency modes are also resolvably split because of their strong sensitivity to the rotation of the Earth (Figure 8).

A traditional way of measuring mode frequencies involves simply picking the peak of the Fourier amplitude spectrum. This can lead to bias if there are nearby interfering modes and also gives no estimate of error. Similarly, the traditional way of measuring attenuation is to perform a "time lapse" analysis where the amplitude of a mode is

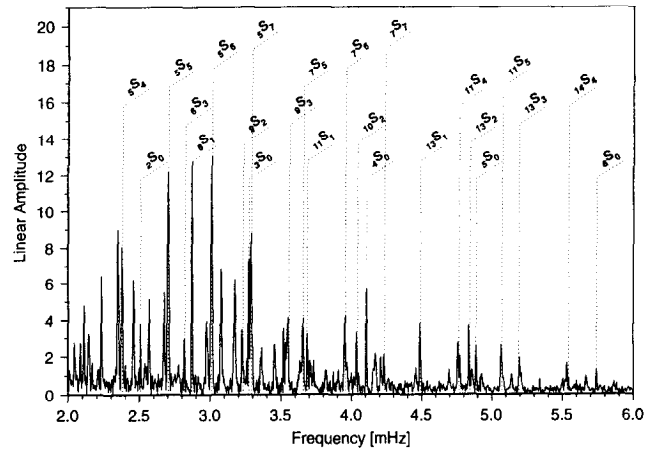

Fig. 7. Linear amplitude spectrum of 67 hours of recording of the large 1970 Colombian earthquake (depth 650 km) made by a modified LaCoste gravimeter sited at Payson, Arizona. This event was too deep to excite large surface waves so the spectrum is very different from that of Figure 3. Nearly all peaks are overtone modes of oscillation some of which (e.g., $_{11}S_1$) have not been strongly excited since.

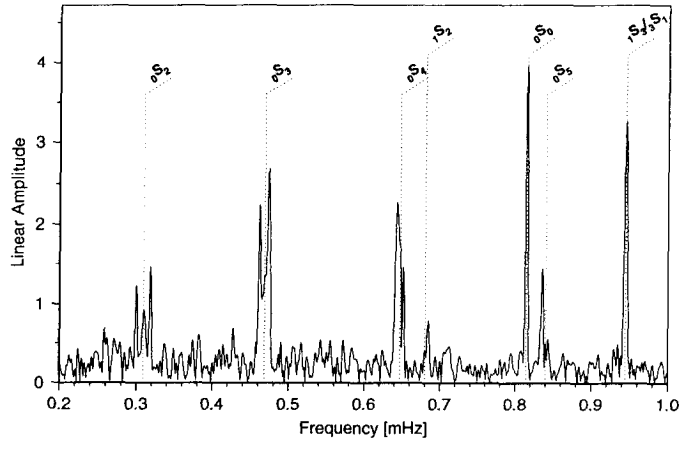

Fig. 8. A spectrum of 150 hours of recording of the 1977 Sumbawa earthquake (the largest earthquake to be digitally recorded since 1975) at station BDF (Brazilia). The very-low frequency part of the spectrum is shown illustrating that the multiplets are now visibly split into multiple peaks. In this frequency band, the "splitting" is dominantly due to the rotation of the Earth. The multiplets $_1S_3$ and $_3S_1$ overlap in frequency.

measured from the spectra of successive time windows and attenuation is estimated from the resulting amplitude decay. It turns out that this method is also biased if there are nearby modes and is an inefficient estimator (in a statistical sense) of the attenuation rate. Several methods which can simultaneously estimate the properties of closely spaced modes have been developed [21, 5, 17]. An example of simple least-squares fitting of a resonance function to the observed spectrum using an iterative technique is shown in Figure 9 where the original amplitude spectrum around a mode of interest is shown along with a residual spectrum after removal of the best-fitting resonance function. An alternative technique based upon the autoregressive character of equation (1) allows determination of a mode frequency and decay rate in a single step.

Most of the Q measurements given in Table 1 are the means of many hundreds of mode measurements. The reason that we must use many measurements to get an accurate estimate of the mean attenuation rate is that the spectral width of a multiplet is greatly influenced by the interference between singlets within that multiplet due to the splitting caused by 3-dimensional structure. The values in Table 1 are based on the assumption that the mean width of the multiplet is related to the attenuation rate that the multiplet would have if it were not split. There is some theoretical justification for this [7] and it seems to be supported by experiments with synthetic data [8] though there is still some controversy as to whether the resulting Q values are unbiased [10].

Most of the techniques discussed above are capable of simultaneous estimation of the properties of more than one mode from a single recording. This is useful but there are often severe tradeoffs when multi-mode estimation is attempted. To circumvent this, we often add records together in various ways to enhance a particular mode of interest. Consider equation (1) but now written in the frequency domain as

$$u_j(\omega) = \sum_k a_{kj} C_k(\omega) \tag{3}$$

where a_{kj} is a complex number with

$$A_k = |a_{kj}| \quad \text{and} \quad \phi_k = \tan^{-1}\left[\frac{Im(a_{kj})}{Re(a_{kj})}\right]$$

and $C_k(\omega)$ is the spectrum of a decaying cosinusoid. We have used the j index to indicate that this recording is for the j'th source-receiver pair. Suppose we have many recordings of a multiplet at a particular frequency ω and suppose we can estimate the initial amplitude and phase

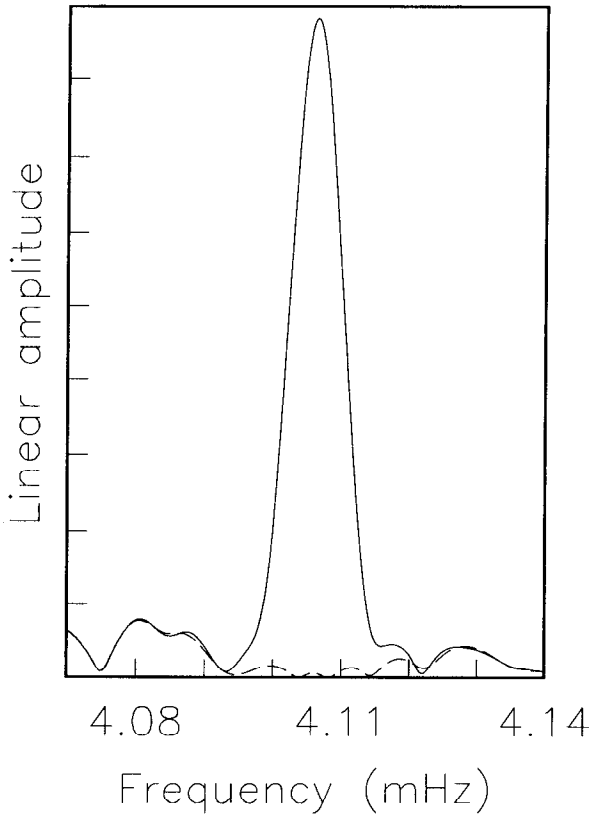

Fig. 9. A close-up of the spectrum shown in Figure 7 around the mode ${}_4S_0$. The dashed line shows the residual after the best-fitting resonance function has been fit to the data. This process gives a center frequency of 4.1062 mHz and a Q value of 1210.

of the k'th mode (A_{kj}, ϕ_{kj}) based on a model of the source mechanism. We can then use the equation to estimate the resonance function of the k'th mode at frequency ω:

$$\mathbf{C}(\omega) = \mathbf{a}^{-1}\mathbf{u}(\omega) \tag{4}$$

Solving this system at a number of frequencies in a narrow frequency band encompassing several modes allows the resonance function of those modes to be estimated (Figure 10). The properties of those modes (e.g. center frequency and decay rate) can then be determined from the recovered resonance functions. This technique, called "stripping" by Gilbert and Dziewonski [16], can be applied to isolate singlets within multiplets as well as to isolate multiplets from other multiplets. Most of the multiplet frequencies given in Table 1 were measured from strips of several thousands of recordings.

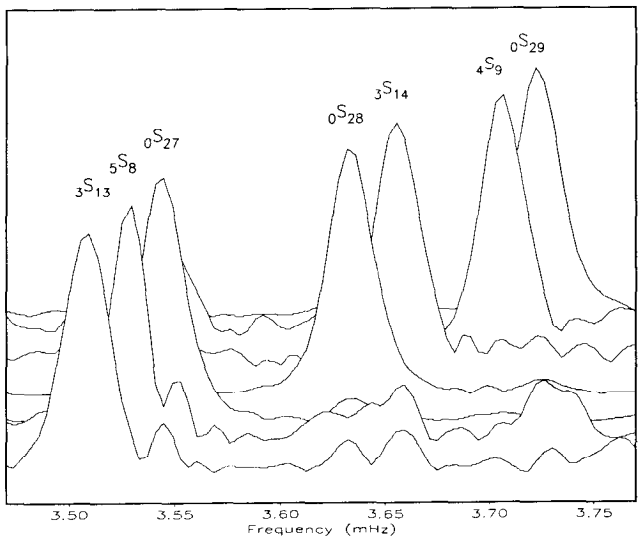

Fig. 10. The results of multiplet stripping in a small frequency band which includes the fundamental spheroidal modes $_0S_{27}$ and $_0S_{28}$. The target multiplets are (front to back) $_3S_{13}$, $_5S_8$, $_0S_{27}$, $_0S_{28}$, $_3S_{14}$, $_4S_9$ and $_0S_{29}$. Note that overtones such as $_3S_{14}$ are clearly separated from the highly excited fundamental modes.

3. MODE SPLITTING AND COUPLING

A theoretical treatment of mode splitting and coupling is beyond the scope of this paper but this section tries to give a flavor of the effects upon the observations and, in particular, how they can bias degenerate frequency estimates.

For many purposes, coupling between multiplets is sufficiently weak to be neglected and we can consider the mode to be "isolated". We divide the splitting of isolated multiplets up into two categories: 1) resolvably split multiplets where we can attempt to isolate individual singlets of a multiplet and 2) unresolvably split multiplets where it is not possible to analyze individual singlets but the spectrum of a multiplet varies in a systematic way depending upon source/receiver orientation. All fundamental modes above about $\ell = 10$ fall in the latter category since there are so many broad singlets in the multiplet which completely overlap in the frequency domain. Inspection of several recordings of an unresolvably split multiplet reveals that the multiplet looks like a single resonance function but the peak appears to move around. Theoretical work in the late 70's showed that the phenomenon is a result of interference between the singlets within the multiplet and that the apparent peak frequency is dominantly a function of the structure underlying the great circle joining source and receiver. Thus, the spectral peak of a multiplet for a fast great-circle path is at an apparently high frequency while a slow great-circle path produces a low frequency peak. In the limit that the wavelength of the structure is much longer than the wavelength of the multiplet, Jordan [18] showed that the observed peak shift is given by:

$$\delta\omega = \sum_s P_s(0) \sum_t c_s^t Y_s^t(\Theta, \Phi) \tag{5}$$

where the c_s^t are the so-called "structure coefficients" and the Y_s^t are spherical harmonics defined in equation (12). Θ and Φ are the colatitude and longitude of the pole of the great circle joining the source and receiver. Plotting the peak shift of a multiplet for many different recordings at the appropriate great-circle pole positions reveals a large-scale pattern [22] which is dominated by structure of harmonic degree 2 (Figure 11).

The structure coefficients are simply related to 3-dimensional structure. In particular, if 3-dimensional structure is expanded as

$$m(r, \theta, \phi) = \bar{m}(r) + \delta m(r, \theta, \phi) \tag{6}$$

where

$$\delta m(r, \theta, \phi) = \sum_{s,t} \delta m_s^t(r) Y_s^t(\theta, \phi)$$

and $\bar{m}$ is the spherically averaged model then the structure coefficients are related to the model expansion coefficients by an equation of the form:

$$c_s^t = \int_0^a M_s(r) \delta m_s^t(r) r^2 dr \tag{7}$$

(See Woodhouse and Dahlen [39] for the form of the integral kernels M_s.) Clearly, observations of peak shifts can be used to determine structure coefficients which in turn can be inverted for the 3-dimensional structure expansion coefficients [e.g., 33]. Unfortunately, multiplet peak shift data can constrain only the even degree ($s = 2, 4, 6...$) part of the structure. This is because the mode spectrum includes many orbits of surface waves and such data effectively average out the odd-degree part of the 3-dimensional structure. Using equation (5) to find structure coefficients which fit the observed peak shifts also results in refined estimates of the degenerate frequency and it is these frequencies which are given in Table 1 when available.

One final comment about Table 1 is necessary. Explicit accounting for the effects of 3-dimensional structure as in the studies described above can lead to extremely precise

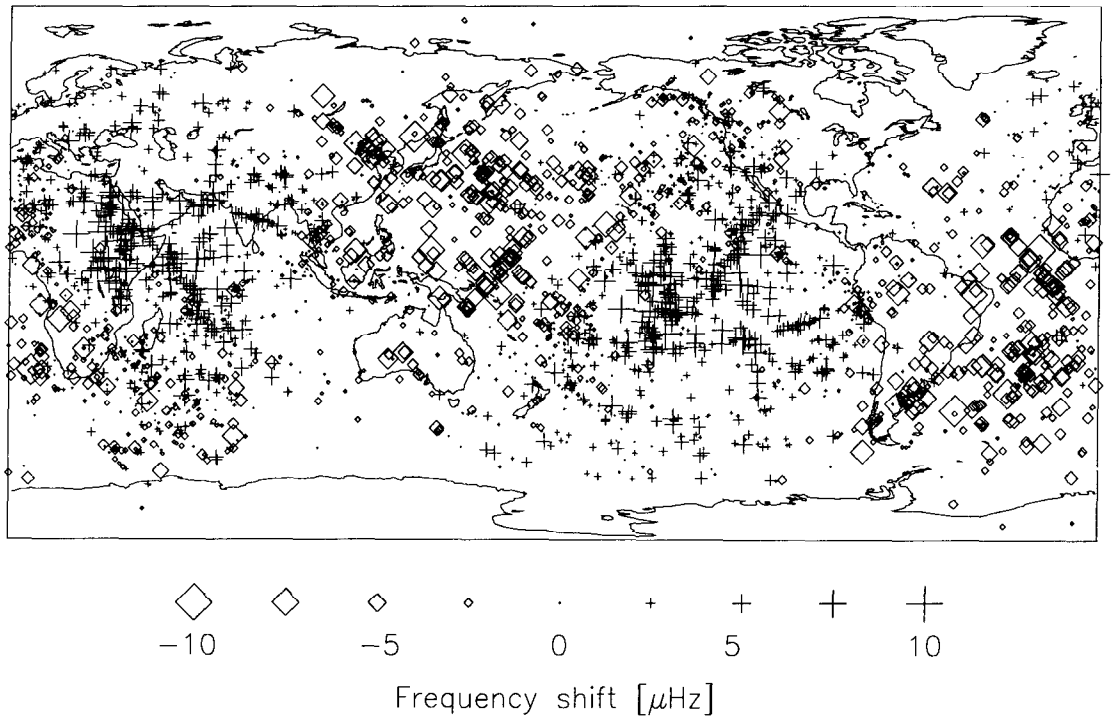

Fig. 11. Fundamental mode peak shifts for the mode ${}_0S_{23}$ from Smith and Masters [33]. The symbols are plotted at the pole of the great circle joining the source and the receiver locations. Plus symbols (+) indicate an anomalously high frequency corresponding to a fast great-circle path on average. Converseley diamonds (◇) plot at the poles of slow great-circle paths. The size of the symbols reflects the magnitude of the frequency shift which varies by $\pm 10\mu$Hz. Note the coherent degree 2 pattern which is caused by 3D-structure in the upper mantle and transition zone.

mean frequency estimates for a multiplet but it is not always true that this is a reliable estimate of the degenerate frequency of the multiplet. The reason is that coupling of one mode to another through rotation or 3-dimensional structure can lead to an effective shifting of the mean frequency. A clear example of mode-coupling is the coupling of toroidal fundamental modes to spheroidal fundamental modes in the frequency band 1.8 – 3.3 mHz by the Coriolis force [23]. In this case, the shift of the apparent mode frequency can be computed and the data in Table 1 have been corrected for this effect.

4. SUMMARY

Table 1 represents our latest compilation of reliable degenerate frequency estimates. One single method cannot give accurate degenerate frequencies for all modes and, in fact, we have used four methods of degenerate frequency estimation:

1) Histogram analysis of peak-frequency measurements from single recordings. The measurements must be corrected for the signal from 3-dimensional structure [31, 21, 29, 28, 8, 33, 32, 30].
2) Multiple-record analysis to isolate the individual singlets of a multiplet so that a reliable mean can be estimated [4, 26, 36, 39].
3) Fitting of the spectra of split multiplets including the effects of aspherical structure as well as a perturbation to the degenerate frequency [14,15, 26, 27, 20, 36, 39].
4) Multiple-record analysis ignoring 3-dimensional structure [16, 34].

Many of our measurements have been determined using more than one of these techniques allowing some sources of bias to be estimated. Slightly over 600 mode frequencies are listed which is significantly less than the 1064 frequencies reported by Gilbert and Dziewonski [16]. Some of the high-frequency fundamental toroidal and spheroidal measurements are absent from the current list since precise mean values from a global study are not yet available. Several research groups are actively studying global

surface-wave dispersion and we give some preliminary values based on the results of Wong [38] and unpublished results of Dr J-P. Montagner and of Dr. G. Laske. Also missing are degenerate frequency estimates for some high Q, low-ℓ modes which were originally identified using a simple histogram analysis [12, 13]. Strong splitting of such modes is very common and great care must be taken to get unbiased degenerate frequency estimates. It will probably take another earthquake like the 1970 Columbian event before we have the recordings to significantly expand the dataset.

5. APPENDIX

This appendix describes some basic theoretical results – a more complete treatment can be found in Lapwood and Usami [19].

Since departures from spherical symmetry are small (particularly in the deep Earth), it is useful to consider an approximate Earth model which is spherically symmetric, non-rotating, and elastically isotropic. Departures from this state (i.e. anelasticity, anisotropy, rotation and three-dimensional structure) are supposed sufficiently small that they can be treated by perturbation theory. The model is assumed to be initially quiescent and in a state of hydrostatic equilibrium. The equations governing the small oscillations of such a body are given by:

$$\rho_0 \frac{\partial^2 \mathbf{s}}{\partial t^2} = \nabla \cdot \mathbf{T} - \nabla(s_r \rho_0 g_0) - \rho_0 \nabla \phi_1 + \hat{\mathbf{r}} g_0 \nabla \cdot (\rho_0 \mathbf{s}) + \mathbf{f} \quad (8)$$

and

$$\nabla^2 \phi_1 = -4\pi G \nabla \cdot (\rho_0 \mathbf{s}) \quad (9)$$

Equation (8) is the linearized equation for conservation of momentum. ρ_0 is the unperturbed density and $\mathbf{s}$ is the displacement field. The acceleration due to gravity is given by $\mathbf{g}(r) = -\hat{\mathbf{r}} g_0(r)$, $\mathbf{T}$ is the elastic stress tensor and $\mathbf{f}$ is a body force density used to represent the earthquake source ($\mathbf{f} = 0$ when the Earth is in free oscillation). Since the motion of the earth causes a disturbance of the gravitational potential which in turn affects the motion, we must also solve Poisson's equation (equation 9) where ϕ_1 is the perturbation in the gravitational potential associated with the motion. Considering the linearized the momentum equation, the force densities contributing to the acceleration of material at a fixed point in space are respectively: 1) elastic forces caused by the deformation of the body, 2) motion of material in the initial stress field, 3) forces due to the change in gravitational potential, and 4) forces due to motion within the initial gravitational field.

We seek solutions to equation 8 and 9 which satisfy certain boundary conditions on the displacement field and the tractions acting on interfaces (the traction acting on a surface with normal $\hat{\mathbf{n}}$ is $\mathbf{T} \cdot \hat{\mathbf{n}}$). In particular, the displacement field must be continuous everywhere except at a fluid-solid boundary where slip is allowed. The tractions on horizontal surfaces must be continuous at all interfaces and must vanish at the free surface. The usual way to proceed is to use separation of variables and expand the displacement field in vector spherical harmonics. We recognize that there may be more than one solution to equation 8 and 9 and designate the k'th solution by $\mathbf{s}_k$ where:

$$\mathbf{s}_k = \hat{\mathbf{r}}\, {}_kU + \nabla_1\, {}_kV - \hat{\mathbf{r}} \times (\nabla_1\, {}_kW) \quad (10)$$

$\nabla_1 = \hat{\boldsymbol{\theta}} \partial_\theta + \hat{\boldsymbol{\phi}} \operatorname{cosec} \theta \partial_\phi$ is the horizontal gradient operator and ${}_kU$, ${}_kV$ and ${}_kW$ are scalar functions of position. We now expand ${}_kU$, ${}_kV$ and ${}_kW$ in ordinary spherical harmonics as well as ϕ_{1k}. Each of these functions have an expansion of the form

$$\left.\begin{aligned} {}_kU &= \sum_{l=0}^{\infty} \sum_{m=-l}^{l} {}_kU_l^m(r) Y_l^m(\theta, \phi) \\ {}_kV &= \sum_{l=0}^{\infty} \sum_{m=-l}^{l} {}_kV_l^m(r) Y_l^m(\theta, \phi), \quad \text{etc.} \end{aligned}\right\} \quad (11)$$

where the $Y_l^m(\theta, \phi)$ are fully normalized spherical harmonics:

$$Y_l^m(\theta, \phi) = (-1)^m \left[\frac{2l+1}{4\pi} \frac{(l-m)!}{(l+m)!}\right]^{\frac{1}{2}} P_l^m(\cos\theta) e^{im\phi} \quad (12)$$

and the P_l^m are associated Legendre functions.

To proceed, we adopt a constitutive relation for the material to relate $\mathbf{T}$ to the deformation of the body. In the simplest case, a perfectly elastic relation is adopted (the weak attenuation being amenable to treatment by perturbation theory) and $\mathbf{T} = \mathbf{C} : \boldsymbol{\epsilon}$ where $\boldsymbol{\epsilon}$ is the strain tensor and $\mathbf{C}$ is a fourth-order tensor of elastic moduli. In component form, the constitutive relation is

$$T_{ij} = C_{ijkl} \epsilon_{kl}$$

where summation over repeated indices is implied. The

most general elastic Earth exhibiting spherical symmetry is "transversely isotropic" (i.e. seismic velocities in the radial direction are different from velocities in the tangent plane) and is described by five elastic moduli which, in Love notation, are: A, C, L, N, and F. An elastically isotropic body is described by two elastic moduli: λ and μ where μ is known as the shear modulus or rigidity. The results for an isotropic body can be recovered from those for a transversely isotropic body using the substitutions: A = C = $\lambda + 2\mu$, F = λ, and L = N = μ.

Substitution of these forms into equation 8 and 9 results in four coupled second-order ordinary differential equations governing the radial dependence of the scalars in equation 11. (For clarity, we drop the subscripts on U, V, W, and Φ so, in the next equation $U \equiv {}_kU_l^m$ etc.)

$$\left.\begin{aligned}
&\frac{1}{r^2}\left(\frac{d}{dr}\, r^2 \frac{d\Phi_1}{dr}\right) - l(l+1)\frac{\Phi_1}{r^2} = \\
&\qquad -4\pi G\left[\frac{d}{dr}(\rho_0 U) + \rho_0 F\right] \\
&-\rho_0\omega_k^2 U = \frac{d}{dr}\left(CU' + FF\right) \\
&-\frac{1}{r}\left[2(F-C)U' + 2(A-N-F)F + l(l+1)LX\right] \\
&\qquad -\rho_0\Phi_1' + g_0\left((\rho_0 U)' + \rho_0 F\right) - (\rho_0 g_0 U)' \\
&-\rho_0\omega_k^2 V = \frac{d}{dr}(LX) \\
&+\frac{1}{r}\left[(A-N)F + FU' + 3LX - \frac{NV}{r}(l+2)(l-1)\right] \\
&\qquad -\frac{\rho_0\Phi_1}{r} - \frac{\rho_0 g_0 U}{r}
\end{aligned}\right\} \tag{13}$$

$$\begin{aligned}
-\rho_0\omega_k^2 W &= \frac{d}{dr}(LZ) \\
&+\frac{1}{r}\left[3LZ - \frac{NW}{r}(l+2)(l-1)\right]
\end{aligned} \tag{14}$$

where

$$\begin{aligned}
X &= V' + \frac{U-V}{r} \\
Z &= W' - \frac{W}{r} \\
F &= \frac{1}{r}(2U - l(l+1)V)
\end{aligned}$$

and a prime denotes radial derivative. Note that the equations are dependent upon harmonic degree (ℓ) but are independent of azimuthal order number m. Consider equation 14. For a chosen harmonic degree and frequency, the solution to these equations will not necessarily match the boundary conditions (notably vanishing of traction at the free surface). There are however, discrete frequencies for each ℓ when solutions $W(r)$ can be found which match all boundary conditions. Such frequencies are the frequencies of free toroidal oscillation of the Earth. For a particular ℓ, the mode with the lowest frequency of free oscillation is labelled ${}_0T_\ell$, the next highest is ${}_1T_\ell$ and so on. The displacement field of the n'th mode ${}_nT_\ell$ which has frequency ${}_n\omega_\ell$ say is proportional to

$${}_n\mathbf{s}_l^m = \left[\hat{\boldsymbol{\theta}}\,\mathrm{cosec}\,\theta\; {}_nW_l(r)\frac{\partial Y_l^m}{\partial\phi} - \hat{\boldsymbol{\phi}}\; {}_nW_l(r)\frac{\partial Y_l^m}{\partial\theta}\right] e^{i\,{}_n\omega_l t} \tag{15}$$

for $-l \le m \le l$. This kind of motion is called toroidal because it consists of twisting on concentric shells. Toroidal motion can be sustained only in a solid so toroidal modes are confined to the mantle (another class is confined to the inner core but cannot be observed at the surface). Note that there is no radial component of motion and no compression or dilation so there is no perturbation to the gravitational field. This is not true for solutions to the other three coupled ODEs (equation 13). Again there are discrete frequencies for a fixed harmonic degree where solutions can be found which match all boundary conditions. These are the frequencies of free spheroidal motion (sometimes called poloidal motion). For a particular ℓ, the mode with the lowest frequency of free oscillation is labelled ${}_0S_\ell$, the next highest is ${}_1S_\ell$ and so on. The displacement field of the n'th mode ${}_nS_\ell$ which has frequency ${}_n\omega_\ell$ say is proportional to

$$\begin{aligned}
{}_n\mathbf{s}_l^m = \Big[&\hat{\mathbf{r}}\; {}_nU_l(r)Y_l^m(\theta,\phi) + \hat{\boldsymbol{\theta}}\; {}_nV_l(r)\frac{\partial Y_l^m}{\partial\theta}(\theta,\phi) \\
&+ \mathrm{cosec}\,\theta\hat{\boldsymbol{\phi}}\; {}_nV_l(r)\frac{\partial Y_l^m}{\partial\phi}(\theta,\phi)\Big] e^{i{}_n\omega_l t}
\end{aligned} \tag{16}$$

Note that in both equations 15 and 16, for each n and ℓ there are $2\ell+1$ modes of oscillation with exactly the same frequency (since the governing equations don't depend upon m). This is the phenomenon of degeneracy which is a consequence of the assumed symmetry of the Earth model. This group of $2\ell+1$ modes is called a "multiplet" while the individual members of the multiplet are called "singlets". Departures of the Earth from spherical sym-

metry remove the degeneracy and, in general, each singlet within a multiplet will have a slightly different frequency.

We can also use the results given above to compute the elastic energy density of a mode. The total elastic energy of a mode is:

$$E = \int_V \epsilon^* \cdot\cdot \mathbf{C} : \epsilon \, dV \tag{17}$$

where the double dots indicate tensor contraction. This can be written in terms of the mode scalars as:

$$E = \int \left[l(l+1)(l-1)(l+2)\frac{\mathrm{N}}{r^2}W^2 + l(l+1)\mathrm{L}Z^2 \right] r^2 \, dr \tag{18}$$

for toroidal modes, and

$$E = \int \left[l(l+1)(l-1)(l+2)\frac{\mathrm{N}}{r^2}V^2 + l(l+1)\mathrm{L}X^2 + 2\mathrm{F}U'F + (\mathrm{A}-\mathrm{N})F^2 + CU'^2 \right] r^2 \, dr \tag{19}$$

for spheroidal modes. For an elastically isotropic material, we can divide the elastic energy into its shear and compressional components by substituting the bulk modulus K_s for λ using the relationship $K_s = \lambda + 2/3\mu$ yielding

$$E = \int \left[\frac{\mu}{r^2} l(l+1)(l-1)(l+2)W^2 + \mu l(l+1)Z^2 \right] r^2 \, dr \tag{20}$$

for toroidal modes, and

$$E = \int \left[\frac{\mu}{r^2} l(l+1)(l-1)(l+2)V^2 + \mu l(l+1)X^2 + \frac{\mu}{3}(2U' - F)^2 + K_s(U'+F)^2 \right] r^2 \, dr \tag{21}$$

for spheroidal modes. The integrands are plotted in Figures 5 and 6 for some representative modes of oscillation.

Acknowledgments. This work was funded by grants from the National Science Foundation. Dr. G. Laske and Dr. J-P. Montagner kindly made available some unpublished results on global surface-wave dispersion.

REFERENCES

1. Z. Alterman, H. Jarosch, and C.L. Pekeris, Oscillations of the Earth. *Proc. Roy. Soc.*, **A252**, 80–95, 1959.
2. G.E. Backus, and J.F. Gilbert, The rotational splitting of the free oscillations of the earth. *Proc. Natl. Acad. Sci.*, **47**, 362–371, 1961.
3. H. Benioff, Long waves observed in the Kamchatka earthquake of November 4, 1952. *J. Geophys. Res.*, **63**, 589–593, 1958.
4. R. Buland, J. Berger, and F. Gilbert, Observations from the IDA network of attenuation and splitting during a recent earthquake. *Nature*, **277**, 358–362, 1979.
5. B.F. Chao, and F. Gilbert, Autoregressive estimation of complex eigenfrequencies in low frequency seismic spectra. *Geophys. J. R. Astron. Soc.*, **63**, 641–657, 1980.
6. F.A. Dahlen, The spectra of unresolved split normal mode multiplets. *Geophys. J. R. Astron. Soc.*, **58**, 1–33, 1979.
7. F.A. Dahlen, The free oscillations of an anelastic aspherical earth. *Geophys. J. R. Astron. Soc.*, **66**, 1–22, 1981.
8. J.P. Davis, Local eigenfrequency and its uncertainty inferred from fundamental spheroidal mode frequency shifts. *Geophys. J. R. Astron. Soc.*, **88**, 693–722, 1987.
9. J.S. Derr, Free oscillation observations through 1968. *Bull. Seismol. Soc. Am.*, **59**, 2079–2099, 1969.
10. J.J. Durek, and G. Ekström, Differences between observations of fundamental mode attenuation. *EOS Trans. AGU*, **73**, 402, 1992.
11. A.M. Dziewonski, and D.L. Anderson, Preliminary reference Earth model. *Phys. Earth Planet. Inter.*, **25**, 297–356, 1981.
12. A.M. Dziewonski, and J.F. Gilbert, Observations of normal modes from 84 recordings of the Alaskan earthquake of 28 March 1964. *Geophys. J. R. Astron. Soc.*, **27**, 393–446, 1972.
13. A.M. Dziewonski, and J.F. Gilbert, Observations of normal modes from 84 recordings of the Alaskan earthquake of 28 March 1964 II. *Geophys. J. R. Astron. Soc.*, **35**, 401–437, 1973.
14. D. Giardini, X.-D. Li, and J.H. Woodhouse, Three-dimensional structure of the earth from splitting in free oscillation spectra. *Nature*, **325**, 405–411, 1987.
15. D. Giardini, X.-D. Li, and J.H. Woodhouse, Splitting functions of long period normal modes of the earth. *J. Geophys. Res.*, **93**, 13,716–13,742, 1988.
16. F. Gilbert, and A.M. Dziewonski, An application of normal mode theory to the retrieval of structural parameters and source mechanisms from seismic spectra. *Phil. Trans. R. Soc. Lond.*, **A278**, 187–269, 1975.
17. S. Hori, Y. Fukao, M. Kumazawa, M. Furumoto, and A. Yamamoto, A new method of spectral analysis and its application to the Earth's free oscillations: The "Sompi" method. *J. Geo-*

phys. Res., **94**, 7537–7553, 1989.
18. T.H. Jordan, A procedure for estimating lateral variations from low-frequency eigenspectra data. *Geophys. J. R. Astron. Soc.*, **52**, 441–455, 1978.
19. E.R. Lapwood, and T. Usami, *Free Oscillations of the Earth.* Cambridge University Press, New York, 1981.
20. X.-D. Li, D. Giardini, and J.H. Woodhouse, Large-scale, three-dimensional, even degree structure of the Earth from splitting of long-period normal modes. *J. Geophys. Res.*, **96**, 551–577, 1991.
21. G. Masters, and F. Gilbert, Attenuation in the earth at low frequencies. *Phil. Trans. R. Soc. Lond.*, **A308**, 479–522, 1983.
22. G. Masters, T.H. Jordan, P.G. Silver, and F. Gilbert, Aspherical earth structure from fundamental spheroidal-mode data. *Nature*, **298**, 609–613, 1982.
23. G. Masters, J. Park, and F. Gilbert, Observations of coupled spheroidal and toroidal modes. *J. Geophys. Res.*, **88**, 10,285–10,298, 1983.
24. J. Park, C.R. Lindberg, and D. Thomson, Multiple-taper spectral analysis of terrestrial free oscillations: Part I. *Geophys. J. R. Astron. Soc.*, **91**, 755–794, 1987.
25. C.L. Pekeris, Z. Alterman, and H. Jarosch, Rotational multiplets in the spectrum of the earth. *Phys. Rev.*, **122**, 1692–1700, 1961.
26. M. Ritzwoller, G. Masters, and F. Gilbert, Observations of anomalous splitting and their interpretation in terms of aspherical structure. *J. Geophys. Res.*, **91**, 10,203–10,228, 1986.
27. M. Ritzwoller, G. Masters, and F. Gilbert, Constraining aspherical structure with low frequency interaction coefficients: Application to uncoupled multiplets. *J. Geophys. Res.*, **93**, 6369–6396, 1988.
28. B. Romanowicz, G. Roult, and T. Kohl, The upper mantle degree two pattern: constraints from GEOSCOPE fundamental spheroidal mode eigenfrequency and attenuation measurements. *Geophys. Res. Lett.*, **14**, 1219–1222, 1987.
29. G. Roult, and B. Romanowicz, Very long-period data from the geoscope network: Preliminary results on great circle averages of fundamental and higher Rayleigh and Love modes. *Bull. Seismol. Soc. Am.*, **74**, 2221–2243, 1984.
30. G. Roult, B. Romanowicz, and J.P. Montagner, 3-D upper mantle shear velocity and attenuation from fundamental mode free oscillation data. *Geophys. J. Int.*, **101**, 61–80, 1990.
31. P.G. Silver, and T.H. Jordan, Fundamental spheroidal mode observations of aspherical heterogeneity. *Geophys. J. R. Astron. Soc.*, **64**, 605–634, 1981.
32. M.F. Smith, *Imaging the Earth's aspherical structure with free oscillation frequency and attenuation measurements.* Ph.D Thesis, Univ. Cal. San Diego, La Jolla, CA, 1989.
33. M.F. Smith, and G. Masters, Aspherical structure constraints from free oscillation frequency and attenuation measurements. *J. Geophys. Res.*, **94**, 1953–1976, 1989.
34. R. Widmer, *The large-scale structure of the deep Earth as constrained by free oscillation observations.* Ph.D. Thesis Univ. Cal. San Diego., 1991.
35. R. Widmer, G. Masters, and F. Gilbert, Spherically symmetric attenuation within the Earth from normal mode data. *Geophys. J. Int.*, **104**, 541–553, 1991.
36. R. Widmer, G. Masters, and F. Gilbert, Observably split multiplets – data analysis and interpretation in terms of large-scale aspherical structure. *Geophys. J. Int.*, **111**, 559–576, 1992.
37. Widmer, R. W. Zürn, and G. Masters, Observations of low order toroidal modes from the 1989 Macquarie Rise event. *Geophys. J. Int.*, **111**, 226–236, 1992.
38. Y.K. Wong, *Upper mantle heterogeneity from phase and amplitude data of mantle waves.* Ph.D Thesis, Harvard University, Cambridge, 1989.
39. J.H. Woodhouse, and F.A. Dahlen, The effect of a general aspherical perturbation on the free oscillations of the earth. *Geophys. J. R. Astron. Soc.*, **53**, 335–354, 1978.

Seismic Traveltime Tables

B.L.N. Kennett

1. INTRODUCTION

The location of earthquakes requires a knowledge of the traveltimes of observed seismic phases along the path from source to receiver. Such traveltimes themselves have to be derived from the observations of the arrival times of different phases. A collection of traveltime tables for the major phases was published by Jeffreys and Bullen [4] based on the the method of "uniform reduction" - a major advance introduced by Jeffreys [3] to deal with discordant readings. Subsequently the "1968 Tables for P phases" [2] made use of accurate timing information from nuclear explosions to help constrain the traveltimes for P waves.

Recently the "IASPEI 1991 Seismological Tables" [6] have been prepared for a wide range of P and S seismic phases. This work has been based on the large digital database of arrival times prepared by the International Seismological Centre since 1964. Kennett and Engdahl [5] describe the construction and testing of the radial velocity model *iasp91* from which the traveltimes are calculated.

The upper mantle model for the *iasp91* model is constructed to provide a good summary behaviour for the characteristics of the traveltime distribution for P and S waves out to 30°. The radial velocity model has a crust and mantle representative of continental regions, since the vast majority of seismic stations lie on the continents, and includes the major discontinuities near 410 and 660 km in the upper mantle. The velocity is specified by a sequence of linear gradients in radius in the upper mantle and a cubic in radius through most of the lower mantle (for depths between 760 and 2740 km). The velocities in the lowermost mantle are taken as a linear gradient in radius down to the core-mantle boundary. In the core and inner core the velocity functions are specified as quadratics in radius. The model is tabulated in parametric form in Table 1 and illustrated in Figure 1.

The *iasp91* velocity model is designed to represent 'average', primarily continental, behaviour in the upper mantle and so is unlikely to be appropriate for detailed studies in any particular region. The constraints on the P wave distribution are strong and regional effects, although undoubtedly important, still allow the definition of a satisfactory summary travel time curve. For S waves the situation is more complex, the variations in S wave travel times from different regions are much larger than for P particularly for distances less than 20°. The *iasp91* model is probably biased slightly towards a 'tectonic' structure for S, but contains no low velocity zone since this feature is subject to considerable regional variation and is less pronounced beneath continents. With the simple form of velocity distribution adopted it is possible to generate an S arrival for all combinations of depth and epicentral distance.

For P waves at telescismic distances, the *iasp91* tables are about 0.7 seconds slower than the 1968 P-tables [2]

B. L. N. Kennett, Australian National University, RSES, GPO 4, Canberra, 2601, Australia

Global Earth Physics
A Handbook of Physical Constants
AGU Reference Shelf 1

TABLE 1: Parameterised form of *iasp91* model. α is the P wave velocity, β is the shear velocity.

Depth z [km]	Radius r [km]	α [km/s]	β [km/s]
6371 - 5153.9	0 - 1217.1	11.24094 - 4.09689 x^2	3.56454 - 3.45241 x^2
5153.9 - 2889	1217.1 - 3482	10.03904 3.75665 x - 13.67046 x^2	0
2889 - 2740	3482 - 3631	14.49470 - 1.47089 x	8.16616 - 1.58206 x
2740 - 760	3631 - 5611	25.1486 - 41.1538 x + 51.9932 x^2 - 26.6083 x^3	12.9303 - 21.2590 x + 27.8988 x^2 - 14.1080 x^3
760 - 660	5611 - 5711	25.96984 - 16.93412 x	20.76890 - 16.53147 x
660 - 410	5711 - 5961	29.38896 - 21.40656 x	17.70732 - 13.50652 x
410 - 210	5961 - 6161	30.78765 - 23.25415 x	15.24213 - 11.08552 x
210 - 120	6161 - 6251	25.41389 - 17.69722 x	5.75020 - 1.27420 x
120 - 35	6251 - 6336	8.78541 - 0.74953 x	6.706231 - 2248585 x
35 - 20	6336 - 6351	6.50	3.75
20 - 0	6351 - 6371	5.80	3.36

x normalised radius r/a (a = 6371 km)

and on average about 1.8 seconds faster than the Jeffreys & Bullen [4] tables. For S waves the teleseismic times lie between those of the JB tables and the results of Randall [7]. Because the times for all phases are derived from the same velocity model, there is complete consistency between the travel times for different branches at different hypocentral depths.

The effect of three-dimensional structure within the earth is to produce detectable differences in the travel times of P and S waves on different paths compared with the tables. The r.m.s. error would be about 1.3 s for P and 4 s for S. The differences in travel times for different source-receiver combinations can be used to build up three-dimensional models of the velocity structure within the earth (see e.g. Inoue et al [8]).

2. CALCULATION SCHEMES FOR GENERATING TRAVELTIMES

2.1 Interpolation

For the attached tables of traveltimes for surface sources derived from the *iasp91* model, a convenient and accurate interpolation formula exploits the tabulated slownesses. When the epicentral distance Δ is bracketed by tabulated values at Δ_1 and Δ_2, the travel time can be found from

$$T(\Delta) = \tfrac{1}{2}[T_1+T_2] + \tfrac{1}{2}[(\Delta-\Delta_1)p_1+(\Delta-\Delta_2)p_2] + (1/4)[(\Delta-\Delta_1)^2+(\Delta-\Delta_2)^2](p_2-p_1)/(\Delta_2-\Delta_1) \quad (1)$$

The subscripts for the times T and slowness p refer to

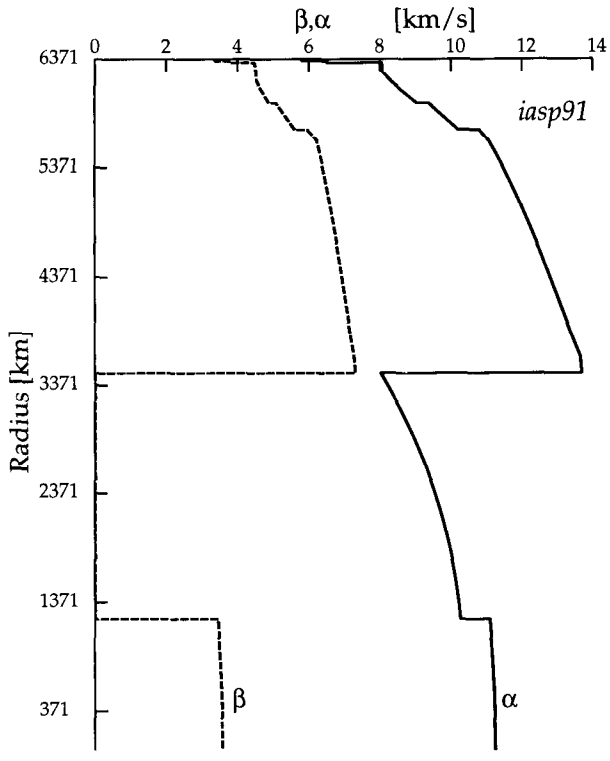

Fig 1. The radial velocity model *iasp91*, α is the P wave velocity, β is the shear velocity.

the appropriate epicentral distances. With the relatively close 1 degree tabulation in Tables 2, 3 the only significant errors (about 0.04 s) arise for the branches associated with the upper mantle transition zone where the slowness can be discontinuous between successive tabulated values.

Traveltimes and slownesses for sources at different depths are represented in Figures 3-8. Comprehensive tables for the Iasp91 model, including multiple source depths are presented in the "IASPEI 1991 Seismological Tables" [6].

2.2 Tau spline calculations

The calculation scheme adopted to generate the traveltime tables and charts for the *iasp91* model is that proposed by Buland & Chapman [1]. Tables of delay time τ as a function of slowness are stored and interpolated using a specially designed tau-spline system which takes care of square-root singularities in the derivatives of the travel times curves at certain critical slownesses. With this representation it is straightforward to find the travel time explicitly for a given epicentral distance once the depth is specified.

For slowness (ray parameter) p, the delay time

$$\tau(p) = T(p) - p\,\Delta(p), \tag{2}$$

in terms of the traveltime $T(p)$ and distance $\Delta(p)$. To find the traveltime for a particular distance δ, it is convenient to introduce the theta function

$$\theta(p,\delta) = \tau(p) + p\,\delta = T(p) - p\,[\delta - \Delta(p)]. \tag{3}$$

The stationary points of $\theta(p,\delta)$ as a function of slowness p correspond to geometrical arrivals at the distance δ, i.e.

$$\left.\frac{\partial\theta(p,\delta)}{\partial p}\right|_{p_\delta} = 0, \quad \text{when} \quad \delta = \Delta(p_\delta). \tag{4}$$

This property is exploited by Buland & Chapman [1], who introduce a novel form of spline representation for the $\tau(p)$ behaviour of a traveltime branch to take care of the square root singularity in the derivatives of $\tau(p)$ at the highest slowness along the branch. The traveltime can then be found for distance δ by solving a quadratic for the geometric slowness p_δ and then using the delay time for that slowness:

$$T(x) = \tau(p_\delta) + p_\delta\,\delta. \tag{5}$$

This process has the advantage of yielding traveltime as an explicit function of range.

The first stage in the construction of the requisite $\tau(p)$ tables is a discretization of the slowness domain and also the establishment of a set of depths between which the τ integrals over the velocity model will be calculated. It is convenient to sample the model at the discrete slowness grid used in the representation of the τ branches. The slownesses just above and below each first order discontinuity, and the slowness at any discontinuity in velocity gradient or local slowness extrema need to be sampled exactly. The discretisation between critical points is arranged so that the range for the τ branch is sampled at approximately equal intervals.

The calculation of the $\tau(p)$ distribution along each branch is carried out by summing the analytic results for segments of the model represented as linear slowness gradients. The τ values for a surface source are calculated for the full range of ray parameters, and also the τ-segments for upgoing waves for a range of source depths down to 760 km. The surface τ results are

organised into mantle, core and inner core contributions. The full range of upgoing, downgoing and surface reflected phases can then be assembled by suitable addition and subtraction of segments of the ray paths. For an arbitrary source depth, the corrections to the τ values for the nearest standard source depths can be readily found and so a precise tau-spline can be generated for any depth.

3. TRAVELTIME TABLES FOR SEISMIC PHASES

3.1 Convention for Seismological Phases

The naming convention used to identify the different types of seismic phases is based on the division of the earth into three major zones: the mantle, outer core, and inner core. The nature of the ray path traversed by the wave is used to construct the code for the particular phase. A compressional wave leg in the mantle is denoted by P, and a shear wave leg by S. A compressional wave leg in the outer core is indicated by K and I is used for compressional waves in the inner core. Sample raypaths and codes for the phases illustrated in the tables are shown in Figure 2.

The codes P, S are used for paths which pass once through the mantle. Reflection at the free surface is indicated by adding another letter depending on the nature of the second ray leg to give PP, SS, PS, SP. For sources at depth lower case letters are used to indicate upward travelling energy from the source. The reflected wave which left the source as compressional energy, was reflected at the free surface and then propagated as P in the mantle is designated by pP, if the initial leg was as a shear wave the code would be sP. Waves reflected from internal boundaries include a lower case letter to indicate the point of reflection, thus PcP is a P wave reflected from the core-mantle boundary, and SKiKS would be a S wave in the mantle converted to P in the core and then reflected from the inner-core boundary. Pdiff and Sdiff refer to waves which are diffracted around the core before return through the mantle.

The phase PKP corresponds to P waves which enter the core and then are refracted back by the velocity increase with depth to re-emerge into the mantle at large epicentral distance. The reduction of P wave velocity on entry into the core leads to refraction towards the vertical and a rather complex pattern of travel time branches. Individual segments are designated by their limit points e.g. PKPab. The waves refracted through the inner core (PKIKP) form part of the PKP system and are often indicated by PKPdf. Because the P wave velocity in the core is higher than the S wave velocity at the base of the mantle, the phase SKS overtakes S at about 80° epicentral distance. A more detailed discussion of the behaviour of different phases can be found in seismological texts such as Bullen and Bolt [9].

3.2 Traveltime Tables

The Tables (2, 3) that follow provide a summary of the traveltimes and slownesses for a number of important seismic phases as a function of epicentral distance for a surface focus for the *iasp91* model. These are accompanied by charts for surface sources and source depths of 300 and 600 km which display the travel times and slowness as a function of epicentral distance for a wide variety of seismic phases (Figures 3-8). The slowness values for each phase are shown in italics in Tables 2 and 3 with units s/deg.

The traveltimes in Tables 2 and 3 are appropriate for waves with a frequency close to 1 Hz. For lower frequency waves a correction needs to be made for the frequency dispersion associated with anelastic attenuation (see e.g. Aki and Richards [10]). The tabulated times are for a spherical earth. The actual traveltimes between a source and a receiver differ from those tabulated due to the ellipticity of the earth. The corrections for ellipticity depend on the ray path followed by each seismic phase.

A more comprehensive form of the traveltime tables, including times for sources at depth and ellipticity correction tables, has been published by the Research School of Earth Sciences, Australian National University as the "IASPEI 1991 Seismological Tables" and is available for purchase from Bibliotech Pty. Ltd., Canberra ACT 0200, Australia.

A convenient set of computer software which allows the determination of the traveltimes of many different seismic phases for a given depth and epicentral distance is available from the National Earthquake Information Center, Golden, Colorado. This software makes use of the Buland & Chapman [1] tau-spline algorithm to provide rapid and accurate access to the traveltimes.

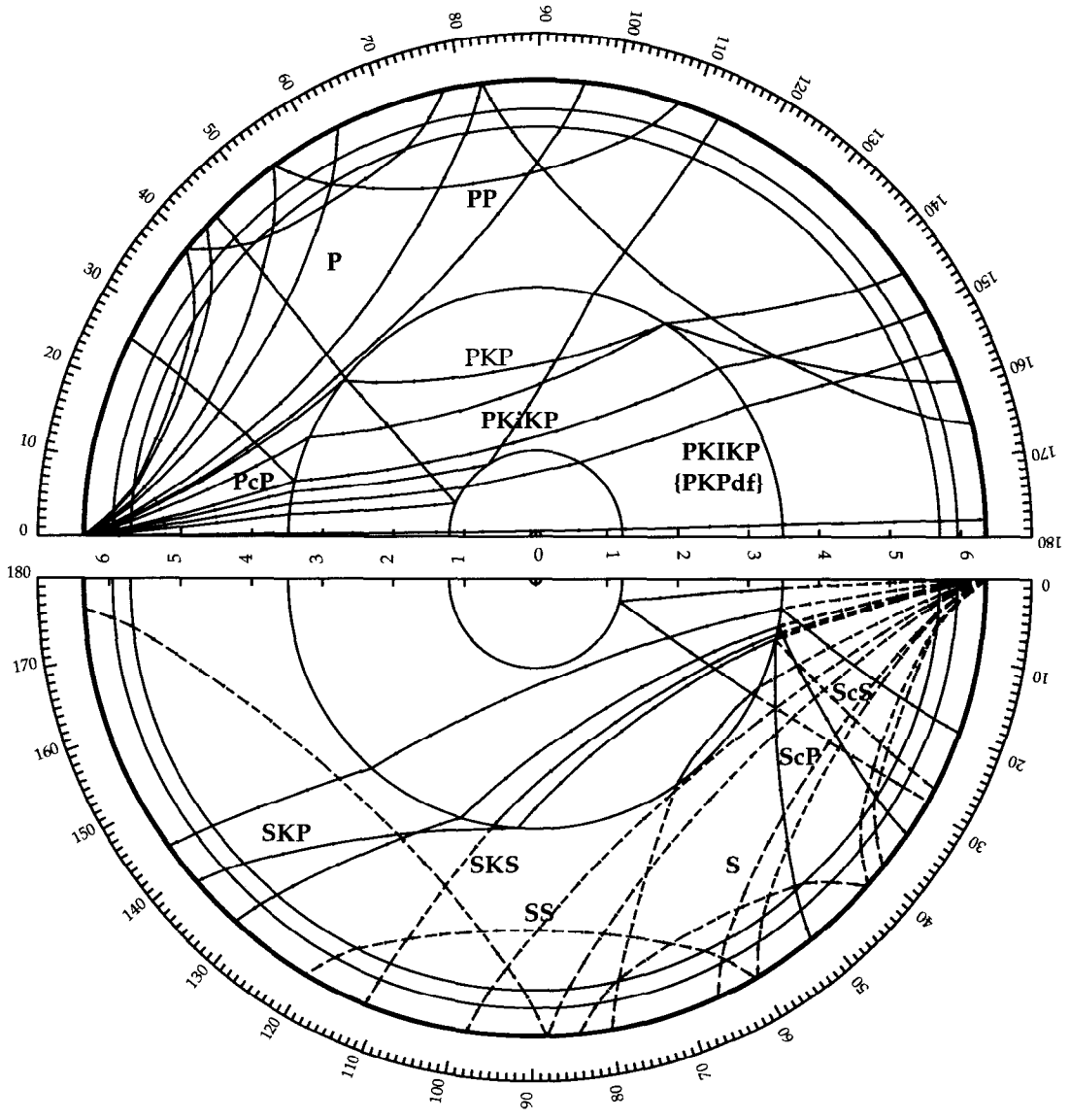

Fig 2. Ray paths corresponding to the principal seismic phases

TABLE 2. Travel times for principal seismic phases to 124°.
For each phase the slowness in s/deg is shown in italics.

Δ	P	PP	PcP	S	SS	ScS	ScP	SKSac
deg	min s	min s	min s	min s	min s	min s	min s	min s
0.0	0.00	0.00	8 31.28	0.00	0.00	15 35.57	12 03.43	
	19.17	*19.17*	*0.00*	*33.09*	*33.09*	*0.00*	*0.00*	
1.0	0 19.17	0 19.17	8 31.33	0 33.09	0 33.09	15 35.66	12 03.49	
	19.17	*19.17*	*0.10*	*33.09*	*33.09*	*0.18*	*0.12*	
2.0	0 35.03	0 38.34	8 31.47	1 01.73	1 06.19	15 35.93	12 03.68	
	13.75	*19.17*	*0.19*	*24.74*	*33.09*	*0.35*	*0.25*	
3.0	0 48.78	0 56.30	8 31.71	1 26.47	1 38.73	15 36.37	12 03.99	
	13.75	*13.75*	*0.29*	*24.73*	*24.74*	*0.53*	*0.37*	
4.0	1 02.53	1 10.05	8 32.05	1 51.19	2 03.47	15 36.99	12 04.42	
	13.75	*13.75*	*0.38*	*24.72*	*24.74*	*0.71*	*0.50*	
5.0	1 16.27	1 23.81	8 32.48	2 15.90	2 28.20	15 37.79	12 04.98	
	13.74	*13.75*	*0.48*	*24.70*	*24.73*	*0.88*	*0.62*	
6.0	1 30.01	1 37.56	8 33.01	2 40.59	2 52.94	15 38.76	12 05.66	
	13.74	*13.75*	*0.57*	*24.68*	*24.73*	*1.06*	*0.74*	
7.0	1 43.75	1 51.31	8 33.63	3 05.26	3 17.66	15 39.90	12 06.47	
	13.73	*13.75*	*0.67*	*24.66*	*24.72*	*1.23*	*0.87*	
8.0	1 57.47	2 05.06	8 34.35	3 29.91	3 42.38	15 41.22	12 07.40	
	13.72	*13.75*	*0.76*	*24.63*	*24.72*	*1.41*	*0.99*	
9.0	2 11.19	2 18.80	8 35.16	3 54.52	4 07.10	15 42.72	12 08.44	
	13.71	*13.75*	*0.86*	*24.60*	*24.71*	*1.58*	*1.11*	
10.0	2 24.90	2 32.55	8 36.06	4 19.10	4 31.80	15 44.38	12 09.61	
	13.70	*13.74*	*0.95*	*24.56*	*24.70*	*1.75*	*1.23*	
11.0	2 38.59	2 46.29	8 37.05	4 43.64	4 56.50	15 46.22	12 10.90	
	13.69	*13.74*	*1.04*	*24.52*	*24.69*	*1.92*	*1.35*	
12.0	2 52.27	3 00.03	8 38.14	5 08.14	5 21.19	15 48.22	12 12.30	
	13.67	*13.74*	*1.13*	*24.47*	*24.68*	*2.09*	*1.46*	
13.0	3 05.94	3 13.76	8 39.32	5 32.59	5 45.87	15 50.40	12 13.82	
	13.66	*13.73*	*1.22*	*24.43*	*24.67*	*2.26*	*1.58*	
14.0	3 19.59	3 27.49	8 40.59	5 56.99	6 10.53	15 52.74	12 15.46	
	13.64	*13.73*	*1.31*	*24.37*	*24.66*	*2.42*	*1.69*	
15.0	3 33.23	3 41.22	8 41.95	6 21.33	6 35.18	15 55.24	12 17.20	
	13.63	*13.73*	*1.40*	*24.31*	*24.64*	*2.59*	*1.80*	
16.0	3 46.38	3 54.95	8 43.39	6 45.62	6 59.82	15 57.91	12 19.06	
	12.92	*13.72*	*1.49*	*24.26*	*24.63*	*2.75*	*1.91*	
17.0	3 59.13	4 08.66	8 44.93	7 09.86	7 24.44	16 00.73	12 21.03	
	12.58	*13.72*	*1.58*	*24.22*	*24.61*	*2.91*	*2.02*	
18.0	4 11.58	4 22.38	8 46.54	7 34.06	7 49.05	16 03.72	12 23.11	
	12.33	*13.71*	*1.66*	*24.18*	*24.60*	*3.07*	*2.13*	
19.0	4 23.16	4 36.09	8 48.25	7 58.22	8 13.64	16 06.86	12 25.29	
	10.98	*13.71*	*1.75*	*24.14*	*24.58*	*3.22*	*2.24*	
20.0	4 34.10	4 49.79	8 50.04	8 20.86	8 38.21	16 10.16	12 27.58	
	10.90	*13.70*	*1.83*	*20.05*	*24.56*	*3.38*	*2.34*	
21.0	4 44.95	5 03.49	8 51.91	8 40.80	9 02.76	16 13.61	12 30.00	
	10.81	*13.69*	*1.91*	*19.82*	*24.54*	*3.53*	*2.44*	
22.0	4 55.71	5 17.18	8 53.86	9 00.49	9 27.29	16 17.22	12 32.46	
	10.70	*13.69*	*1.99*	*19.55*	*24.52*	*3.68*	*2.54*	
23.0	5 06.34	5 30.87	8 55.89	9 19.14	9 51.80	16 20.97	12 35.04	
	10.57	*13.68*	*2.07*	*16.35*	*24.50*	*3.82*	*2.64*	
24.0	5 16.31	5 44.54	8 58.00	9 35.41	10 16.28	16 24.86	12 37.73	
	9.14	*13.67*	*2.15*	*16.20*	*24.47*	*3.97*	*2.73*	

TABLE 2. (continued)

Δ	P	PP	PcP	S	SS	ScS	ScP	SKSac
deg	min s	min s	min s	min s	min s	min s	min s	min s
25.0	5 25.43	5 58.22	9 00.19	9 51.46	10 40.75	16 28.90	12 40.50	
	9.10	*13.67*	*2.23*	*15.89*	*24.45*	*4.11*	*2.82*	
26.0	5 34.51	6 11.88	9 02.45	10 07.31	11 05.18	16 33.08	12 43.37	
	9.06	*13.66*	*2.30*	*15.82*	*24.43*	*4.25*	*2.91*	
27.0	5 43.54	6 25.54	9 04.79	10 23.11	11 29.60	16 37.40	12 46.32	
	9.00	*13.65*	*2.37*	*15.77*	*24.40*	*4.39*	*3.00*	
28.0	5 52.50	6 39.18	9 07.20	10 38.86	11 53.99	16 41.85	12 49.37	
	8.93	*13.64*	*2.45*	*15.74*	*24.37*	*4.52*	*3.08*	
29.0	6 01.41	6 52.83	9 09.68	10 54.58	12 18.34	16 46.43	12 52.49	
	8.88	*13.64*	*2.52*	*15.70*	*24.34*	*4.65*	*3.17*	
30.0	6 10.27	7 06.46	9 12.23	11 10.27	12 42.66	16 51.15	12 55.70	
	8.85	*13.63*	*2.59*	*15.67*	*24.31*	*4.78*	*3.25*	
31.0	6 19.10	7 19.76	9 14.86	11 25.92	13 06.96	16 55.99	12 58.98	
	8.81	*13.08*	*2.66*	*15.62*	*24.28*	*4.91*	*3.32*	
32.0	6 27.89	7 32.76	9 17.55	11 41.51	13 31.23	17 00.96	13 02.34	
	8.77	*12.92*	*2.72*	*15.57*	*24.26*	*5.03*	*3.40*	
33.0	6 36.64	7 45.60	9 20.30	11 57.05	13 55.49	17 06.06	13 05.78	
	8.72	*12.74*	*2.79*	*15.51*	*24.24*	*5.15*	*3.47*	
34.0	6 45.34	7 58.25	9 23.12	12 12.52	14 19.72	17 11.27	13 09.28	
	8.67	*12.58*	*2.85*	*15.44*	*24.22*	*5.27*	*3.54*	
35.0	6 53.98	8 10.77	9 26.00	12 27.93	14 43.93	17 16.59	13 12.85	
	8.62	*12.45*	*2.91*	*15.37*	*24.20*	*5.39*	*3.61*	
36.0	7 02.57	8 23.15	9 28.95	12 43.26	15 08.12	17 22.04	13 16.49	
	8.56	*12.33*	*2.97*	*15.29*	*24.18*	*5.50*	*3.67*	
37.0	7 11.09	8 35.33	9 31.95	12 58.52	15 32.30	17 27.59	13 20.19	
	8.50	*11.01*	*3.03*	*15.22*	*24.16*	*5.61*	*3.73*	
38.0	7 19.56	8 46.32	9 35.01	13 13.69	15 56.44	17 33.25	13 23.95	
	8.44	*10.98*	*3.09*	*15.13*	*24.14*	*5.72*	*3.79*	
39.0	7 27.96	8 57.28	9 38.13	13 28.78	16 20.57	17 39.02	13 27.77	
	8.37	*10.94*	*3.15*	*15.05*	*24.11*	*5.82*	*3.85*	
40.0	7 36.30	9 08.20	9 41.30	13 43.79	16 41.71	17 44.89	13 31.64	
	8.30	*10.90*	*3.20*	*14.96*	*20.05*	*5.92*	*3.90*	
41.0	7 44.57	9 19.08	9 44.53	13 58.70	17 01.71	17 50.87	13 35.57	
	8.24	*10.86*	*3.25*	*14.87*	*19.94*	*6.02*	*3.95*	
42.0	7 52.78	9 29.91	9 47.81	14 13.52	17 21.59	17 56.94	13 39.54	
	8.17	*10.81*	*3.31*	*14.77*	*19.82*	*6.12*	*4.00*	
43.0	8 00.91	9 40.69	9 51.14	14 28.25	17 41.35	18 03.11	13 43.56	
	8.10	*10.75*	*3.36*	*14.68*	*19.69*	*6.21*	*4.04*	
44.0	8 08.98	9 51.42	9 54.52	14 42.87	18 00.97	18 09.37	13 47.62	
	8.03	*10.70*	*3.40*	*14.58*	*19.55*	*6.31*	*4.08*	
45.0	8 16.97	10 02.08	9 57.95	14 57.41	18 20.45	18 15.72	13 51.73	
	7.96	*10.64*	*3.45*	*14.48*	*19.40*	*6.39*	*4.12*	
46.0	8 24.90	10 12.69	10 01.43	15 11.84	18 38.27	18 22.15	13 55.87	
	7.89	*10.57*	*3.50*	*14.38*	*16.35*	*6.48*	*4.16*	
47.0	8 32.75	10 23.22	10 04.95	15 26.16	18 54.59	18 28.68	14 00.05	
	7.82	*10.50*	*3.54*	*14.28*	*16.27*	*6.56*	*4.20*	
48.0	8 40.54	10 32.62	10 08.51	15 40.39	19 10.82	18 35.28	14 04.26	
	7.75	*9.14*	*3.59*	*14.17*	*16.20*	*6.65*	*4.23*	
49.0	8 48.25	10 41.75	10 12.12	15 54.51	19 26.98	18 41.97	14 08.51	
	7.68	*9.12*	*3.63*	*14.07*	*16.10*	*6.73*	*4.26*	

TABLE 2. (continued)

Δ deg	P min s	PP min s	PcP min s	S min s	SS min s	ScS min s	ScP min s	SKSac min s
50.0	8 55.89	10 50.86	10 15.76	16 08.53	19 42.93	18 48.73	14 12.78	
	7.60	*9.10*	*3.67*	*13.96*	*15.89*	*6.80*	*4.29*	
51.0	9 03.45	10 59.95	10 19.45	16 22.44	19 58.79	18 55.57	14 17.08	
	7.53	*9.08*	*3.71*	*13.86*	*15.85*	*6.88*	*4.31*	
52.0	9 10.95	11 09.01	10 23.18	16 36.24	20 14.63	19 02.48	14 21.40	
	7.46	*9.06*	*3.74*	*13.75*	*15.82*	*6.95*	*4.33*	
53.0	9 18.37	11 18.06	10 26.94	16 49.94	20 30.43	19 09.47	14 25.74	
	7.39	*9.03*	*3.78*	*13.64*	*15.80*	*7.02*	*4.35*	
54.0	9 25.72	11 27.07	10 30.74	17 03.52	20 46.22	19 16.52	14 30.10	
	7.31	*9.00*	*3.82*	*13.53*	*15.77*	*7.08*	*4.37*	
55.0	9 32.99	11 36.06	10 34.57	17 17.00	21 01.98	19 23.63	14 34.48	
	7.24	*8.96*	*3.85*	*13.42*	*15.75*	*7.15*	*4.39*	
56.0	9 40.20	11 45.00	10 38.44	17 30.37	21 17.73	19 30.81	14 38.87	
	7.17	*8.93*	*3.88*	*13.31*	*15.74*	*7.21*	*4.40*	
57.0	9 47.33	11 53.92	10 42.34	17 43.63	21 33.46	19 38.06	14 43.28	
	7.10	*8.91*	*3.92*	*13.20*	*15.72*	*7.27*	*4.41*	
58.0	9 54.39	12 02.82	10 46.27	17 56.78	21 49.17	19 45.36	14 47.69	
	7.02	*8.88*	*3.95*	*13.09*	*15.70*	*7.33*	*4.42*	
59.0	10 01.38	12 11.69	10 50.23	18 09.82	22 04.86	19 52.72	14 52.12	
	6.95	*8.86*	*3.97*	*12.98*	*15.69*	*7.39*	*4.43*	
60.0	10 08.29	12 20.55	10 54.22	18 22.74	22 20.54	20 00.13	14 56.55	
	6.88	*8.85*	*4.00*	*12.87*	*15.67*	*7.44*	*4.43*	
61.0	10 15.13	12 29.39	10 58.24	18 35.55	22 36.20	20 07.60	15 00.98	
	6.81	*8.83*	*4.03*	*12.76*	*15.65*	*7.49*	*4.44*	
62.0	10 21.90	12 38.20	11 02.28	18 48.25	22 51.84	20 15.12	15 05.42	
	6.73	*8.81*	*4.06*	*12.64*	*15.62*	*7.54*	*4.44*	
63.0	10 28.60	12 47.00	11 06.35	19 00.84	23 07.44	20 22.69		20 22.69
	6.66	*8.79*	*4.08*	*12.53*	*15.60*	*7.59*		*7.59*
64.0	10 35.22	12 55.79	11 10.44	19 13.31	23 23.03	20 30.30		20 30.27
	6.59	*8.77*	*4.10*	*12.42*	*15.57*	*7.64*		*7.59*
65.0	10 41.77	13 04.54	11 14.56	19 25.67	23 38.58	20 37.96		20 37.86
	6.51	*8.75*	*4.13*	*12.30*	*15.54*	*7.68*		*7.58*
66.0	10 48.25	13 13.28	11 18.70	19 37.92	23 54.10	20 45.67		20 45.44
	6.44	*8.72*	*4.15*	*12.19*	*15.51*	*7.73*		*7.58*
67.0	10 54.66	13 21.99	11 22.86	19 50.05	24 09.59	20 53.41		20 53.02
	6.37	*8.70*	*4.17*	*12.07*	*15.47*	*7.77*		*7.57*
68.0	11 00.99	13 30.67	11 27.04	20 02.07	24 25.05	21 01.20		21 00.58
	6.30	*8.67*	*4.19*	*11.96*	*15.44*	*7.80*		*7.56*
69.0	11 07.25	13 39.33	11 31.23	20 13.97	24 40.47	21 09.02		21 08.13
	6.22	*8.64*	*4.21*	*11.84*	*15.41*	*7.84*		*7.54*
70.0	11 13.43	13 47.96	11 35.45	20 25.75	24 55.86	21 16.88		21 15.67
	6.15	*8.62*	*4.23*	*11.73*	*15.37*	*7.88*		*7.53*
71.0	11 19.55	13 56.56	11 39.69	20 37.42	25 11.21	21 24.78		21 23.18
	6.08	*8.59*	*4.24*	*11.61*	*15.33*	*7.91*		*7.50*
72.0	11 25.59	14 05.13	11 43.94	20 48.97	25 26.52	21 32.70		21 30.67
	6.00	*8.56*	*4.26*	*11.49*	*15.29*	*7.94*		*7.47*
73.0	11 31.55	14 13.68	11 48.21	21 00.40	25 41.80	21 40.66		21 38.13
	5.93	*8.53*	*4.27*	*11.37*	*15.26*	*7.97*		*7.44*
74.0	11 37.45	14 22.19	11 52.49	21 11.71	25 57.03	21 48.65		21 45.55
	5.86	*8.50*	*4.29*	*11.25*	*15.22*	*8.00*		*7.40*

TABLE 2. (continued)

Δ deg	P min s	PP min s	PcP min s	S min s	SS min s	ScS min s	ScP min s	SKSac min s
75.0	11 43.26	14 30.67	11 56.78	21 22.90	26 12.23	21 56.67		21 52.92
	5.78	*8.47*	*4.30*	*11.13*	*15.17*	*8.03*		*7.35*
76.0	11 49.01	14 39.12	12 01.09	21 33.98	26 27.38	22 04.71		22 00.24
	5.71	*8.44*	*4.32*	*11.01*	*15.13*	*8.06*		*7.29*
77.0	11 54.68	14 47.54	12 05.41	21 44.93	26 42.49	22 12.78		22 07.49
	5.63	*8.40*	*4.33*	*10.89*	*15.09*	*8.08*		*7.22*
78.0	12 00.27	14 55.93	12 09.75	21 55.76	26 57.56	22 20.88		22 14.67
	5.56	*8.37*	*4.34*	*10.77*	*15.05*	*8.11*		*7.14*
79.0	12 05.79	15 04.28	12 14.09	22 06.47	27 12.59	22 28.99		22 21.77
	5.48	*8.34*	*4.35*	*10.65*	*15.00*	*8.13*		*7.05*
80.0	12 11.23	15 12.60	12 18.45	22 17.05	27 27.57	22 37.13		22 28.78
	5.40	*8.30*	*4.36*	*10.52*	*14.96*	*8.15*		*6.96*
81.0	12 16.60	15 20.89	12 22.81	22 27.51	27 42.51	22 45.29		22 35.69
	5.33	*8.27*	*4.37*	*10.40*	*14.91*	*8.17*		*6.86*
82.0	12 21.88	15 29.15	12 27.19	22 37.84	27 57.40	22 53.47		22 42.50
	5.25	*8.24*	*4.38*	*10.27*	*14.87*	*8.19*		*6.75*
83.0	12 27.10	15 37.37	12 31.57	22 48.05	28 12.24	23 01.66		22 49.20
	5.17	*8.20*	*4.39*	*10.14*	*14.82*	*8.20*		*6.64*
84.0	12 32.23	15 45.55	12 35.96	22 58.12	28 27.04	23 09.87		22 55.78
	5.09	*8.17*	*4.39*	*10.01*	*14.77*	*8.22*		*6.53*
85.0	12 37.28	15 53.71	12 40.35	23 08.07	28 41.79	23 18.09		23 02.26
	5.01	*8.14*	*4.40*	*9.88*	*14.73*	*8.23*		*6.42*
86.0	12 42.26	16 01.82	12 44.75	23 17.88	28 56.49	23 26.33		23 08.62
	4.94	*8.10*	*4.41*	*9.75*	*14.68*	*8.24*		*6.31*
87.0	12 47.16	16 09.91	12 49.16	23 27.56	29 11.14	23 34.58		23 14.88
	4.86	*8.07*	*4.41*	*9.61*	*14.63*	*8.26*		*6.20*
88.0	12 51.96	16 17.96	12 53.58	23 37.10	29 25.75	23 42.85		23 21.02
	4.74	*8.03*	*4.42*	*9.48*	*14.58*	*8.27*		*6.09*
89.0	12 56.67	16 25.97	12 57.99	23 46.51	29 40.30	23 51.12		23 27.05
	4.69	*8.00*	*4.42*	*9.34*	*14.53*	*8.28*		*5.98*
90.0	13 01.35	16 33.95	13 02.42	23 55.78	29 54.81	23 59.40		23 32.98
	4.66	*7.96*	*4.42*	*9.20*	*14.48*	*8.29*		*5.87*
91.0	13 06.00	16 41.89	13 06.84	24 04.91	30 09.27	24 07.69		23 38.80
	4.64	*7.93*	*4.43*	*9.06*	*14.43*	*8.29*		*5.77*
92.0	13 10.62	16 49.80	13 11.27	24 13.90	30 23.67	24 15.99		23 44.52
	4.61	*7.89*	*4.43*	*8.91*	*14.38*	*8.30*		*5.67*
93.0	13 15.23	16 57.67	13 15.70	24 22.73	30 38.03	24 24.29		23 50.14
	4.60	*7.85*	*4.43*	*8.77*	*14.33*	*8.31*		*5.57*
94.0	13 19.81	17 05.51	13 20.14	24 31.47	30 52.33	24 32.60		23 55.65
	4.58	*7.82*	*4.44*	*8.70*	*14.28*	*8.31*		*5.47*
95.0	13 24.38	17 13.31	13 24.57	24 40.15	31 06.58	24 40.92		24 01.07
	4.55	*7.78*	*4.44*	*8.66*	*14.23*	*8.32*		*5.37*
96.0	13 28.91	17 21.07	13 29.01	24 48.78	31 20.78	24 49.23		24 06.40
	4.52	*7.75*	*4.44*	*8.60*	*14.17*	*8.32*		*5.28*
97.0	13 33.41	17 28.80	13 33.45	24 57.33	31 34.93	24 57.55		24 11.63
	4.49	*7.71*	*4.44*	*8.52*	*14.12*	*8.32*		*5.19*
98.0	13 37.89	17 36.50	13 37.89	25 05.81	31 49.02	25 05.88		24 16.78
	4.45	*7.68*	*4.44*	*8.43*	*14.07*	*8.32*		*5.10*
99.0	13 42.33	17 44.15		25 14.20	32 03.07	25 14.20		24 21.83
	4.44	*7.64*		*8.34*	*14.02*	*8.32*		*5.01*

TABLE 2. (continued)

Δ deg	Pdiff min s	PP min s	PcP min s	Sdiff min s	SS min s	ScS min s	ScP min s	SKSac min s
100.0	13 46.77	17 51.77		25 22.52	32 17.06			24 26.79
	4.44	*7.60*		*8.32*	*13.96*			*4.92*
101.0	13 51.20	17 59.36		25 30.85	32 31.00			24 31.67
	4.44	*7.57*		*8.32*	*13.91*			*4.84*
102.0	13 55.64	18 06.91		25 39.17	32 44.88			24 36.46
	4.44	*7.53*		*8.32*	*13.86*			*4.75*
103.0	14 00.08	18 14.42		25 47.49	32 58.71			24 41.17
	4.44	*7.49*		*8.32*	*13.80*			*4.67*
104.0	14 04.52	18 21.89		25 55.82	33 12.49			24 45.80
	4.44	*7.46*		*8.32*	*13.75*			*4.59*
105.0	14 08.96	18 29.33		26 04.14	33 26.21			24 50.35
	4.44	*7.42*		*8.32*	*13.69*			*4.51*
106.0	14 13.40	18 36.74		26 12.46	33 39.87			24 54.82
	4.44	*7.39*		*8.32*	*13.64*			*4.43*
107.0	14 17.84	18 44.10		26 20.79	33 53.49			24 59.22
	4.44	*7.35*		*8.32*	*13.59*			*4.36*
108.0	14 22.28	18 51.44		26 29.11	34 07.05			25 03.54
	4.44	*7.31*		*8.32*	*13.53*			*4.28*
109.0	14 26.72	18 58.73		26 37.43	34 20.55			25 07.78
	4.44	*7.28*		*8.32*	*13.48*			*4.21*
110.0	14 31.16	19 05.99		26 45.76	34 34.00			25 11.95
	4.44	*7.24*		*8.32*	*13.42*			*4.13*
111.0	14 35.59	19 13.21		26 54.08	34 47.40			25 16.05
	4.44	*7.20*		*8.32*	*13.37*			*4.06*
112.0	14 40.03	19 20.40		27 02.40	35 00.74			25 20.08
	4.44	*7.17*		*8.32*	*13.31*			*3.99*
113.0	14 44.47	19 27.55		27 10.73	35 14.03			25 24.03
	4.44	*7.13*		*8.32*	*13.26*			*3.92*
114.0	14 48.91	19 34.66		27 19.05	35 27.26			25 27.92
	4.44	*7.10*		*8.32*	*13.20*			*3.85*
115.0	14 53.35	19 41.74		27 27.37	35 40.44			25 31.74
	4.44	*7.06*		*8.32*	*13.15*			*3.79*
116.0	14 57.79	19 48.78		27 35.70	35 53.56			25 35.50
	4.44	*7.02*		*8.32*	*13.09*			*3.72*
117.0	15 02.23	19 55.79		27 44.02	36 06.62			25 39.18
	4.44	*6.99*		*8.32*	*13.04*			*3.65*
118.0	15 06.67	20 02.75		27 52.34	36 19.63			25 42.80
	4.44	*6.95*		*8.32*	*12.98*			*3.59*
119.0	15 11.11	20 09.69		28 00.67	36 32.58			25 46.36
	4.44	*6.91*		*8.32*	*12.92*			*3.52*
120.0	15 15.54	20 16.58		28 08.99	36 45.48			25 49.85
	4.44	*6.88*		*8.32*	*12.87*			*3.46*
121.0	15 20.00	20 23.44		28 17.31	36 58.32			25 53.28
	4.44	*6.84*		*8.32*	*12.81*			*3.40*
122.0	15 24.42	20 30.27		28 25.64	37 11.11			25 56.65
	4.44	*6.81*		*8.32*	*12.76*			*3.33*
123.0	15 28.86	20 37.05		28 33.96	37 23.83			25 59.95
	4.44	*6.77*		*8.32*	*12.70*			*3.27*
124.0	15 33.30	20 43.80		28 42.28	37 36.51			26 03.19
	4.44	*6.73*		*8.32*	*12.64*			*3.21*

TABLE 3. Travel times for seismic phases beyond 110°.
For each phase the slowness in s/deg is shown in italics.

Δ	PKPab	PKPbc	PKPdf	PP	SKSac	SKSdf	SKP	SS
deg	min s	min s	min s	min s	min s	min s	min s	min s
110.0				19 05.99	25 11.95	25 46.63	22 09.91	34 34.00
				7.24	*4.13*	*1.91*	*1.92*	*13.42*
111.0				19 13.21	25 16.05	25 48.55	22 11.82	34 47.40
				7.20	*4.06*	*1.91*	*1.91*	*13.37*
112.0				19 20.40	25 20.08	25 50.46	22 13.74	35 00.74
				7.17	*3.99*	*1.91*	*1.91*	*13.31*
113.0				19 27.55	25 24.03	25 52.36	22 15.65	35 14.03
				7.13	*3.92*	*1.91*	*1.91*	*13.26*
114.0			18 40.84	19 34.66	25 27.92	25 54.27	22 17.57	35 27.26
			1.92	*7.10*	*3.85*	*1.90*	*1.91*	*13.20*
115.0			18 42.75	19 41.74	25 31.74	25 56.17	22 19.48	35 40.44
			1.92	*7.06*	*3.79*	*1.90*	*1.91*	*13.15*
116.0			18 44.67	19 48.78	25 35.50	25 58.07	22 21.39	35 53.56
			1.91	*7.02*	*3.72*	*1.90*	*1.91*	*13.09*
117.0			18 46.58	19 55.79	25 39.18	25 60.00	22 23.30	36 06.62
			1.91	*6.99*	*3.65*	*1.90*	*1.91*	*13.04*
118.0			18 48.50	20 02.75	25 42.80	26 01.87	22 25.21	36 19.63
			1.91	*6.95*	*3.59*	*1.89*	*1.91*	*12.98*
119.0			18 50.41	20 09.69	25 46.36	26 03.76	22 27.11	36 32.58
			1.91	*6.91*	*3.52*	*1.89*	*1.90*	*12.92*
120.0			18 52.32	20 16.58	25 49.85	26 05.64	22 29.02	36 45.48
			1.91	*6.88*	*3.46*	*1.88*	*1.90*	*12.87*
121.0			18 54.23	20 23.44	25 53.28	26 07.53	22 30.92	36 58.32
			1.91	*6.84*	*3.40*	*1.88*	*1.90*	*12.81*
122.0			18 56.14	20 30.27	25 56.65	26 09.40	22 32.82	37 11.11
			1.91	*6.81*	*3.33*	*1.87*	*1.90*	*12.76*
123.0			18 58.05	20 37.05	25 59.95	26 11.27	22 34.71	37 23.83
			1.91	*6.77*	*3.27*	*1.87*	*1.89*	*12.70*
124.0			18 59.96	20 43.80	26 03.19	26 13.14	22 36.60	37 36.51
			1.90	*6.73*	*3.21*	*1.86*	*1.89*	*12.64*
125.0			19 01.86	20 50.52	26 06.38	26 14.99	22 38.49	37 49.12
			1.90	*6.70*	*3.15*	*1.85*	*1.88*	*12.59*
126.0			19 03.76	20 57.20	26 09.50	26 16.84	22 40.37	38 01.68
			1.90	*6.66*	*3.09*	*1.85*	*1.88*	*12.53*
127.0			19 05.66	21 03.84	26 12.56	26 18.69	22 42.24	38 14.18
			1.90	*6.62*	*3.03*	*1.84*	*1.87*	*12.47*
128.0			19 07.55	21 10.44	26 15.56	26 20.52	22 44.11	38 26.63
			1.89	*6.59*	*2.97*	*1.83*	*1.87*	*12.42*
129.0			19 09.44	21 17.01	26 18.51	26 22.34	22 45.98	38 39.02
			1.89	*6.55*	*2.92*	*1.82*	*1.86*	*12.36*
130.0			19 11.33	21 23.55	26 21.40	26 24.15	22 34.73	38 51.35
			1.88	*6.51*	*2.86*	*1.80*	*3.84*	*12.30*
131.0			19 13.21	21 30.04	26 24.23	26 25.95	22 38.46	39 03.62
			1.88	*6.48*	*2.80*	*1.79*	*3.64*	*12.25*
132.0			19 15.09	21 36.50	26 27.00	26 27.73	22 42.02	39 15.84
			1.87	*6.44*	*2.74*	*1.78*	*3.50*	*12.19*
133.0			19 16.96	21 42.93	26 29.72	26 29.50	22 45.46	39 28.00
			1.87	*6.41*	*2.69*	*1.76*	*3.38*	*12.13*
134.0			19 18.82	21 49.31	26 32.38	26 31.25	22 48.79	39 40.10
			1.86	*6.37*	*2.63*	*1.75*	*3.28*	*12.07*

TABLE 3. (continued)

Δ deg	PKPab min s	PKPbc min s	PKPdf min s	PP min s	SKSac min s	SKSdf min s	SKP min s	SS min s
135.0			19 20.68	21 55.66	26 34.98	26 32.99	22 52.01	39 52.15
			1.85	*6.33*	*2.58*	*1.73*	*3.18*	*12.02*
136.0			19 22.52	22 01.98	26 37.53	26 34.71	22 55.14	40 04.14
			1.84	*6.30*	*2.52*	*1.71*	*3.09*	*11.96*
137.0			19 24.36	22 08.25	26 40.03	26 36.41	22 58.19	40 16.06
			1.83	*6.26*	*2.47*	*1.69*	*3.00*	*11.90*
138.0			19 26.19	22 14.50	26 42.47	26 38.08	23 01.14	40 27.94
			1.82	*6.22*	*2.41*	*1.67*	*2.92*	*11.84*
139.0			19 28.00	22 20.70	26 44.86	26 39.74	23 04.02	40 39.75
			1.81	*6.19*	*2.36*	*1.64*	*2.84*	*11.78*
140.0			19 29.80	22 26.87	26 47.19	26 41.37	23 05.78	40 51.50
			1.80	*6.15*	*2.31*	*1.62*	*1.72*	*11.73*
141.0			19 31.59	22 33.00	26 49.47	26 42.98	23 07.49	41 03.20
			1.78	*6.11*	*2.25*	*1.59*	*1.70*	*11.67*
142.0			19 33.36	22 39.10	26 51.69	26 44.56	23 09.17	41 14.84
			1.76	*6.08*	*2.20*	*1.57*	*1.67*	*11.61*
143.0			19 35.12	22 45.15	26 53.86	26 46.11	23 10.84	41 26.42
			1.75	*6.04*	*2.15*	*1.54*	*1.65*	*11.55*
144.0			19 36.85	22 51.17	26 55.98	26 47.63	23 12.47	41 37.94
			1.73	*6.00*	*2.09*	*1.51*	*1.62*	*11.49*
145.0	19 37.74	19 37.62	19 38.57	22 57.16		26 49.13	23 14.08	41 49.40
	3.71	*3.28*	*1.70*	*5.97*		*1.48*	*1.60*	*11.43*
146.0	19 41.54	19 40.79	19 40.26	23 03.11		26 50.59	23 15.66	42 00.80
	3.87	*3.07*	*1.68*	*5.93*		*1.45*	*1.57*	*11.37*
147.0	19 45.45	19 43.78	19 41.93	23 09.02		26 52.02	23 17.21	42 12.14
	3.96	*2.92*	*1.65*	*5.89*		*1.41*	*1.53*	*11.31*
148.0	19 49.45	19 46.63	19 43.57	23 14.89		26 53.41	23 18.73	42 23.42
	4.03	*2.79*	*1.63*	*5.86*		*1.38*	*1.50*	*11.25*
149.0	19 53.50	19 49.36	19 45.18	23 20.73		26 54.77	23 20.22	42 34.65
	4.08	*2.67*	*1.60*	*5.82*		*1.34*	*1.47*	*11.19*
150.0	19 57.61	19 51.98	19 46.77	23 26.53		26 56.10	23 21.67	42 45.81
	4.13	*2.57*	*1.57*	*5.78*		*1.31*	*1.43*	*11.13*
151.0	20 01.76	19 54.49	19 48.31	23 32.29		26 57.39	23 23.08	42 56.91
	4.17	*2.47*	*1.53*	*5.74*		*1.27*	*1.40*	*11.07*
152.0	20 05.94	19 56.92	19 49.83	23 38.01		26 58.64	23 24.46	43 07.96
	4.20	*2.37*	*1.49*	*5.71*		*1.23*	*1.36*	*11.01*
153.0	20 10.16	19 59.25	19 51.30	23 43.70		26 59.85	23 25.79	43 18.94
	4.23	*2.28*	*1.46*	*5.67*		*1.19*	*1.32*	*10.95*
154.0	20 14.40	20 01.49	19 52.74	23 49.35		27 01.03	23 27.09	43 29.86
	4.25	*2.20*	*1.42*	*5.63*		*1.15*	*1.28*	*10.89*
155.0	20 18.66	20 03.64	19 54.13	23 54.96		27 02.16	23 28.35	43 40.72
	4.28	*2.11*	*1.37*	*5.59*		*1.11*	*1.23*	*10.83*
156.0	20 22.95		19 55.49	24 00.54		27 03.26	23 29.56	43 51.52
	4.30		*1.33*	*5.56*		*1.07*	*1.19*	*10.77*
157.0	20 27.26		19 56.79	24 06.08		27 04.31	23 30.73	44 02.26
	4.32		*1.28*	*5.52*		*1.03*	*1.15*	*10.71*
158.0	20 31.58		19 58.06	24 11.57		27 05.32	23 31.86	44 12.93
	4.33		*1.24*	*5.48*		*0.99*	*1.10*	*10.65*
159.0	20 35.92		19 59.27	24 17.04		27 06.29	23 32.94	44 23.55
	4.35		*1.19*	*5.44*		*0.95*	*1.06*	*10.58*

TABLE 3. (continued)

Δ deg	PKPab min s	PKPbc min s	PKPdf min s	PP min s	SKSac min s	SKSdf min s	SKP min s	SS min s
160.0	20 40.27		20 00.43	24 22.46		27 07.22	23 33.97	44 34.10
	4.36		*1.14*	*5.40*		*0.91*	*1.01*	*10.52*
161.0	20 44.64		20 01.55	24 27.84		27 08.11	23 34.96	44 44.59
	4.37		*1.09*	*5.37*		*0.86*	*0.96*	*10.46*
162.0	20 49.01		20 02.61	24 33.19		27 08.95	23 35.90	44 55.02
	4.38		*1.04*	*5.33*		*0.82*	*0.92*	*10.40*
163.0	20 53.39		20 03.62	24 38.50		27 09.75	23 36.79	45 05.38
	4.39		*0.98*	*5.29*		*0.78*	*0.87*	*10.33*
164.0	20 57.79		20 04.58	24 43.77		27 10.50	23 37.64	45 15.68
	4.40		*0.93*	*5.25*		*0.73*	*0.82*	*10.27*
165.0	21 02.19		20 05.48	24 49.00		27 11.21	23 38.43	45 25.92
	4.40		*0.87*	*5.21*		*0.69*	*0.77*	*10.20*
166.0	21 06.60		20 06.32	24 54.19		27 11.88	23 39.18	45 36.09
	4.41		*0.82*	*5.17*		*0.64*	*0.72*	*10.14*
167.0	21 11.01		20 07.11	24 59.35		27 12.50	23 39.87	45 46.20
	4.42		*0.76*	*5.13*		*0.60*	*0.67*	*10.08*
168.0	21 15.43		20 07.85	25 04.46		27 13.07	23 40.52	45 56.24
	4.42		*0.71*	*5.09*		*0.55*	*0.62*	*10.01*
169.0	21 19.85		20 08.53	25 09.53		27 13.60	23 41.11	46 06.22
	4.43		*0.65*	*5.05*		*0.51*	*0.57*	*9.95*
170.0	21 24.28		20 09.15	25 14.56		27 14.09	23 41.66	46 16.13
	4.43		*0.59*	*5.01*		*0.46*	*0.52*	*9.88*
171.0	21 28.71		20 09.71	25 19.56		27 14.53	23 42.15	46 25.98
	4.43		*0.53*	*4.98*		*0.42*	*0.47*	*9.81*
172.0	21 33.14		20 10.21	25 24.52		27 14.92	23 42.59	46 35.76
	4.43		*0.47*	*4.94*		*0.37*	*0.42*	*9.75*
173.0	21 37.57		20 10.66	25 29.44		27 15.27	23 42.98	46 45.47
	4.44		*0.42*	*4.90*		*0.32*	*0.36*	*9.68*
174.0	21 42.01		20 11.04	25 34.32		27 15.57	23 43.32	46 55.12
	4.44		*0.36*	*4.86*		*0.28*	*0.31*	*9.61*
175.0	21 46.45		20 11.37	25 39.15		27 15.83	23 43.61	47 04.69
	4.44		*0.30*	*4.79*		*0.23*	*0.26*	*9.54*
176.0	21 50.89		20 11.64	25 43.91		27 16.04	23 43.84	47 14.20
	4.44		*0.24*	*4.74*		*0.19*	*0.21*	*9.48*
177.0			20 11.85	25 48.64		27 16.20	23 44.03	47 23.65
			0.18	*4.71*		*0.14*	*0.16*	*9.41*
178.0			20 12.00	25 53.34		27 16.31	23 44.16	47 33.02
			0.12	*4.69*		*0.09*	*0.10*	*9.34*
179.0			20 12.09	25 58.03		27 16.38	23 44.23	47 42.33
			0.06	*4.68*		*0.05*	*0.05*	*9.27*
180.0			20 12.12	26 02.70		27 16.41	23 44.26	47 51.56
			0.00	*4.66*		*0.00*	*0.00*	*9.20*

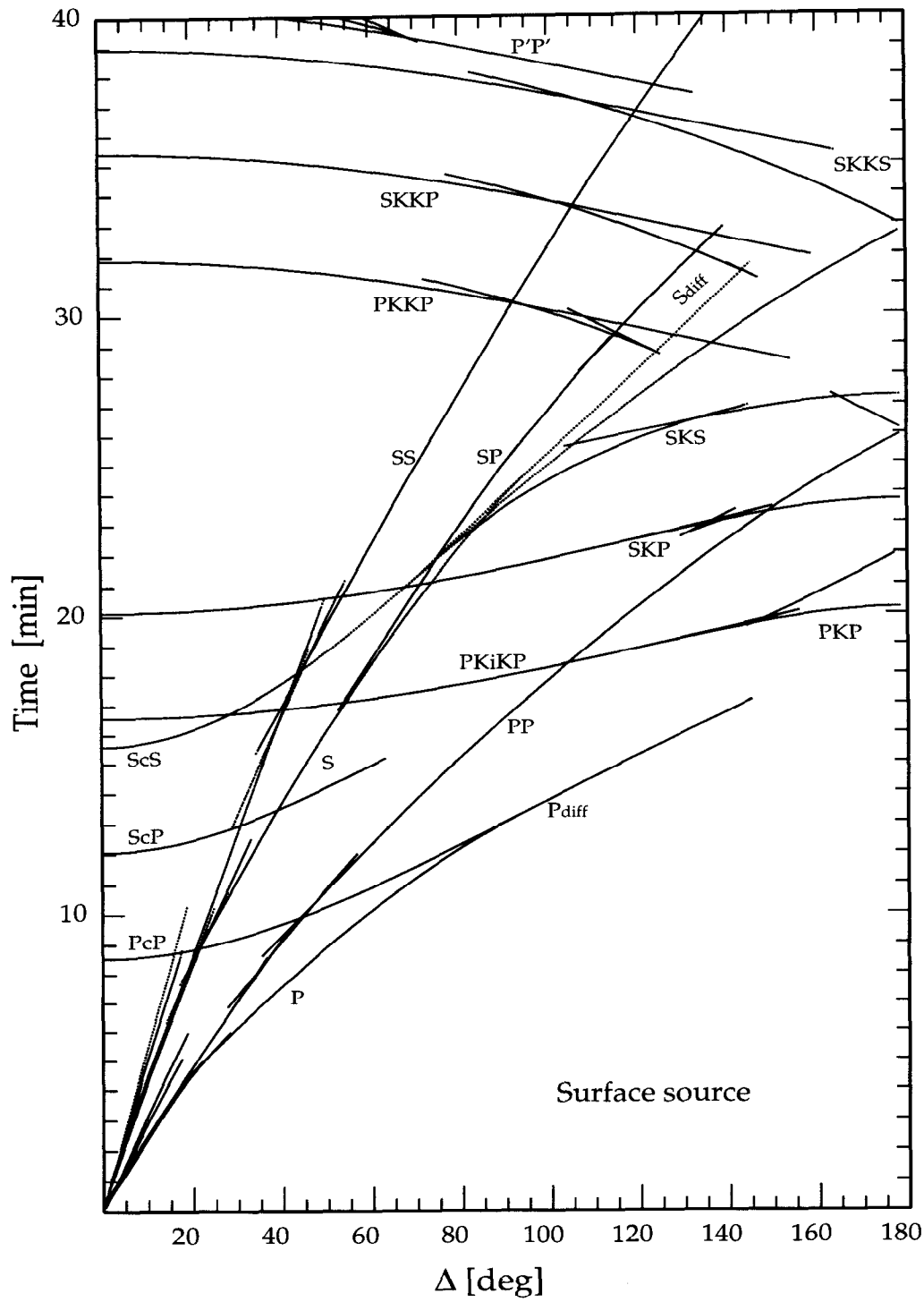

Fig 3. Traveltime curves for the *iasp91* model for surface source. Dashed lines indicated phases received as S waves.

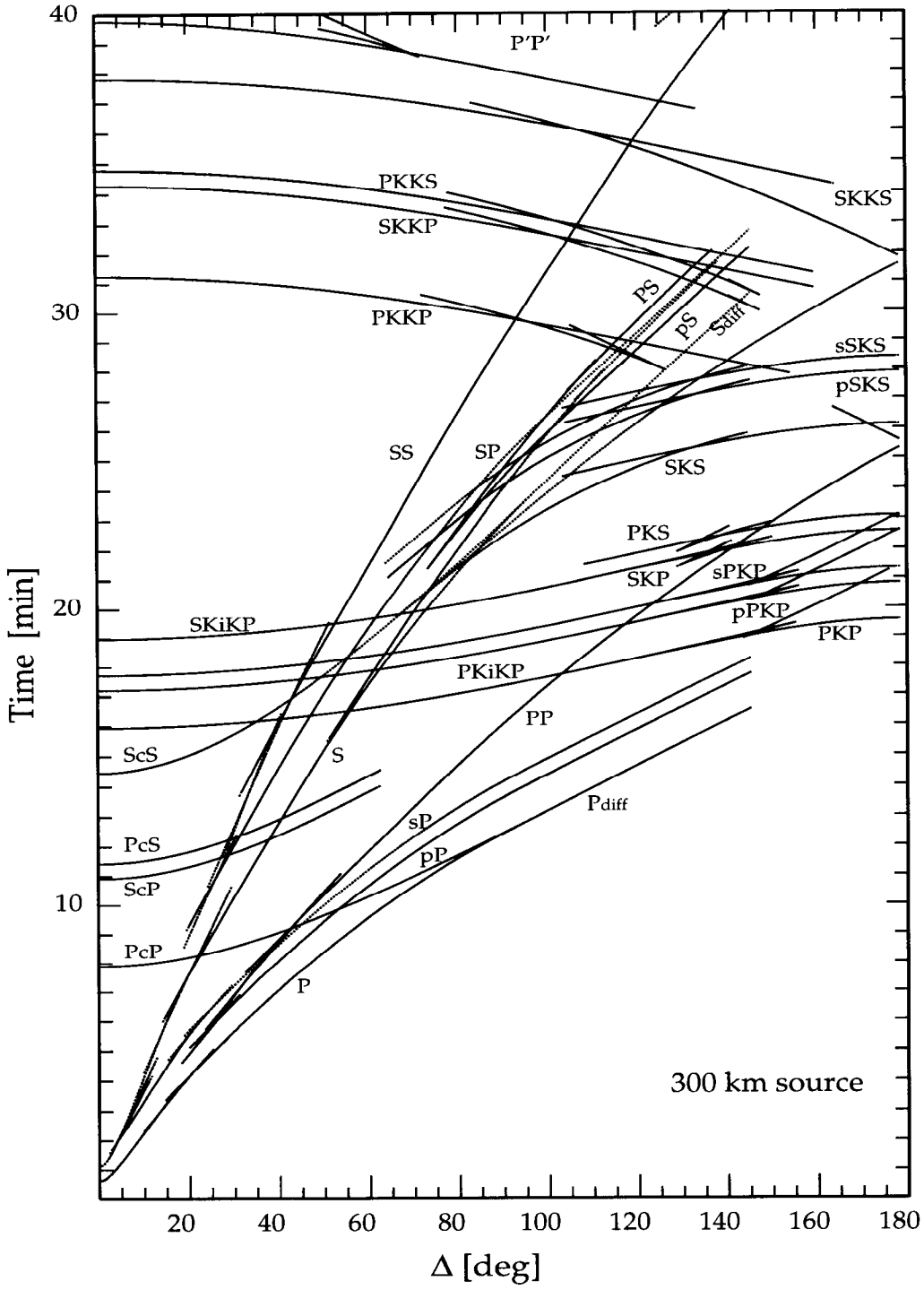

Fig 4. Traveltime curves for the *iasp91* model for 300 km source depth.

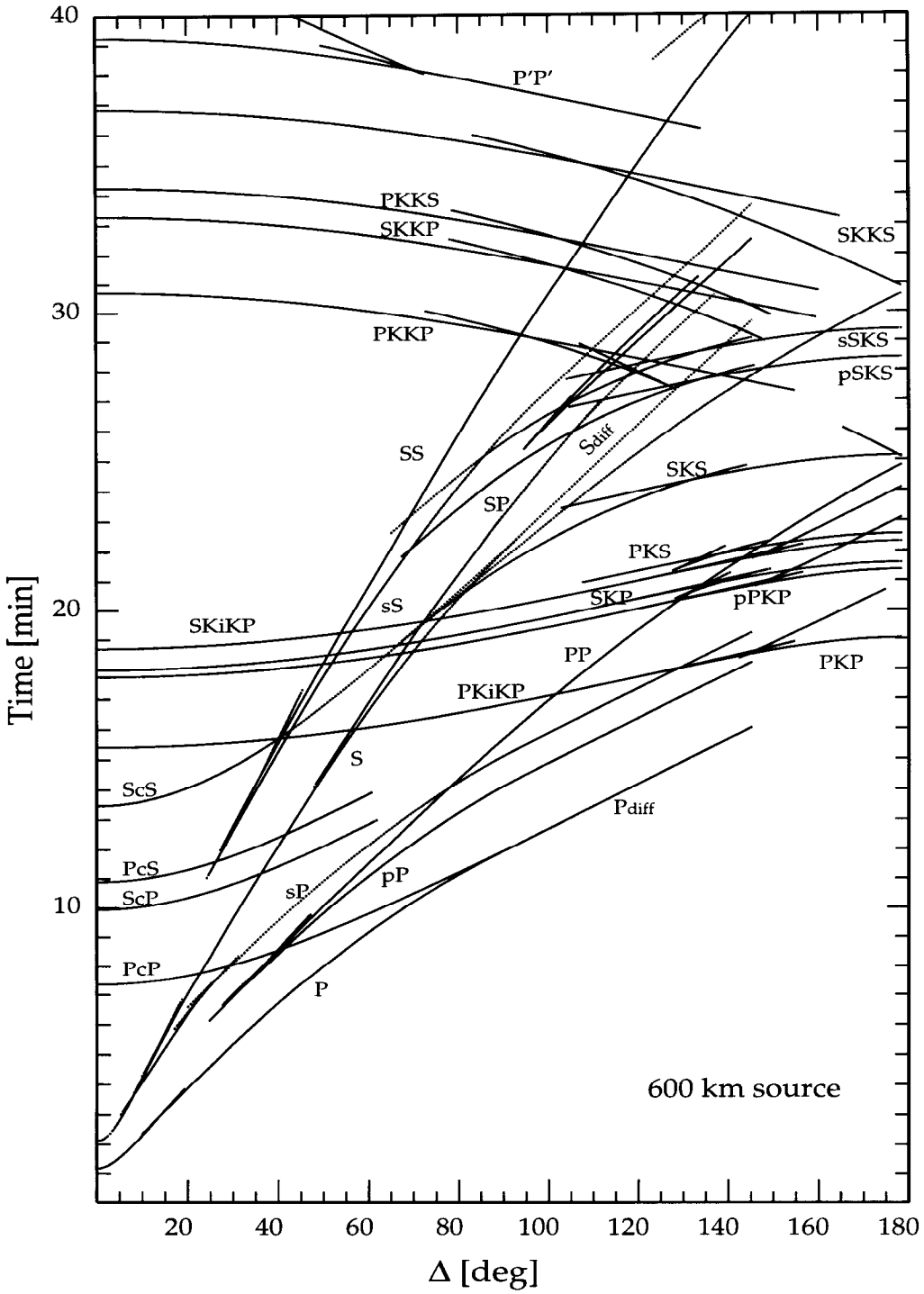

Fig 5. Traveltime curves for the *iasp91* model for 600 km source depth.

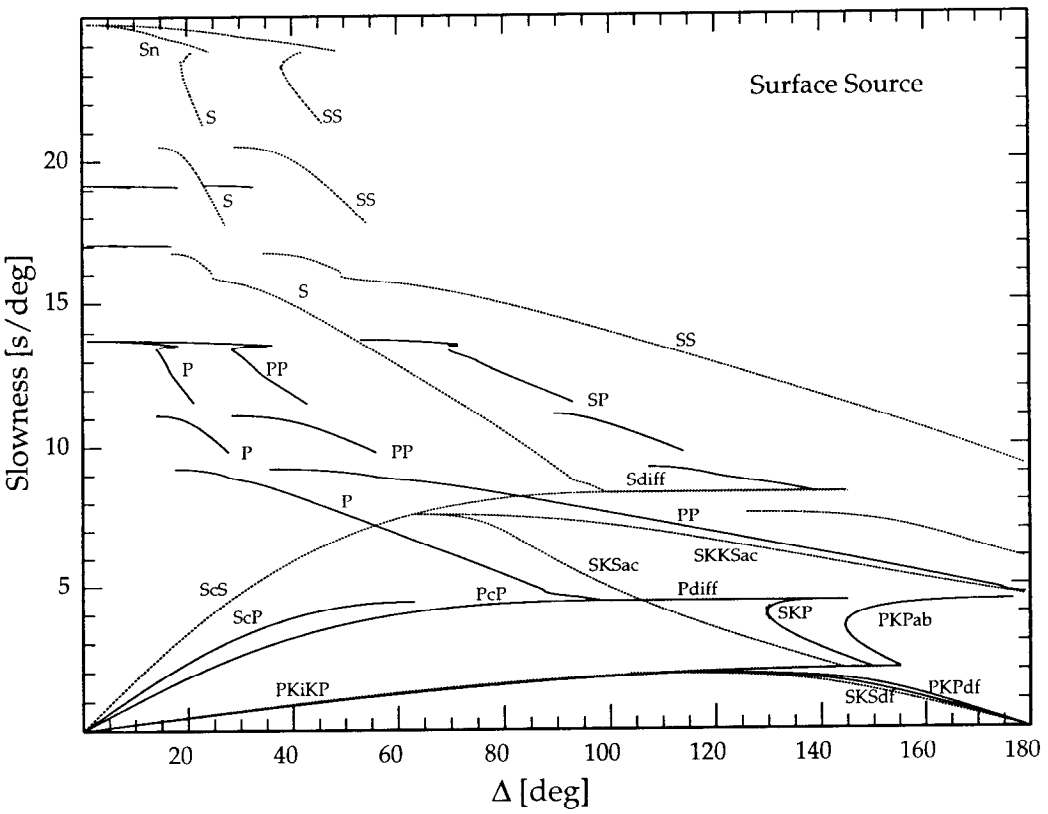

Fig 6. Slowness as a function of epicentral distance for the *iasp91* model for surface source.

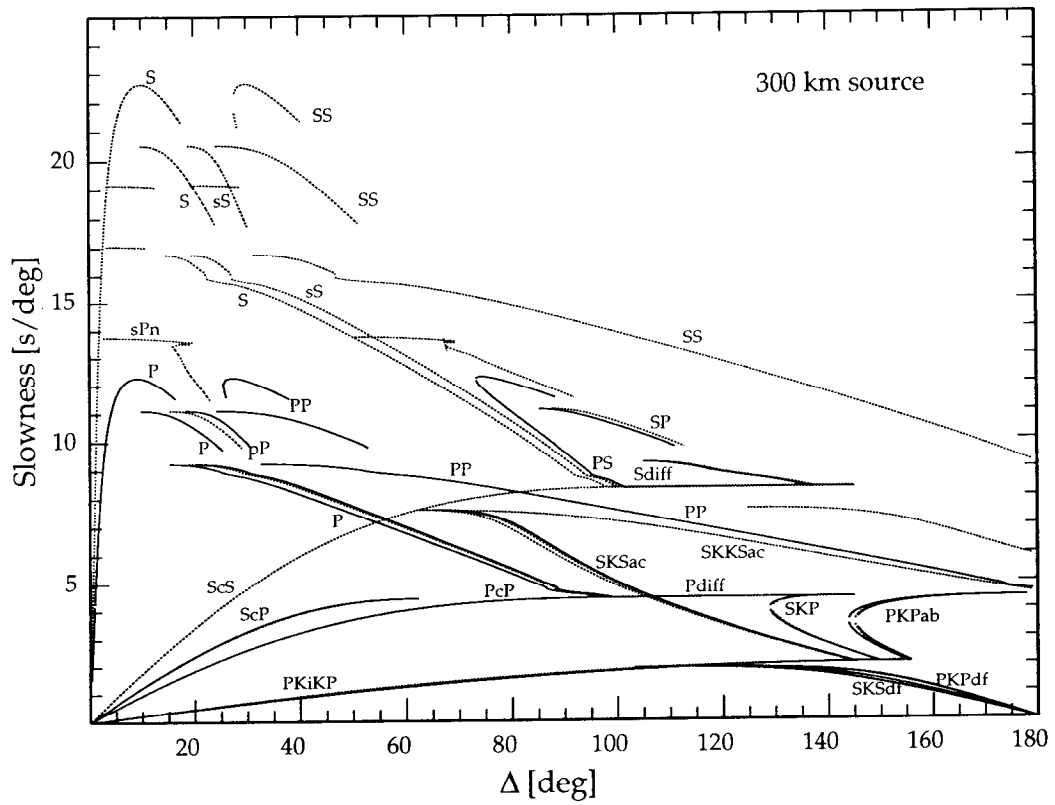

Fig 7. Slowness as a function of epicentral distance for the *iasp91* model for 300 km source depth.

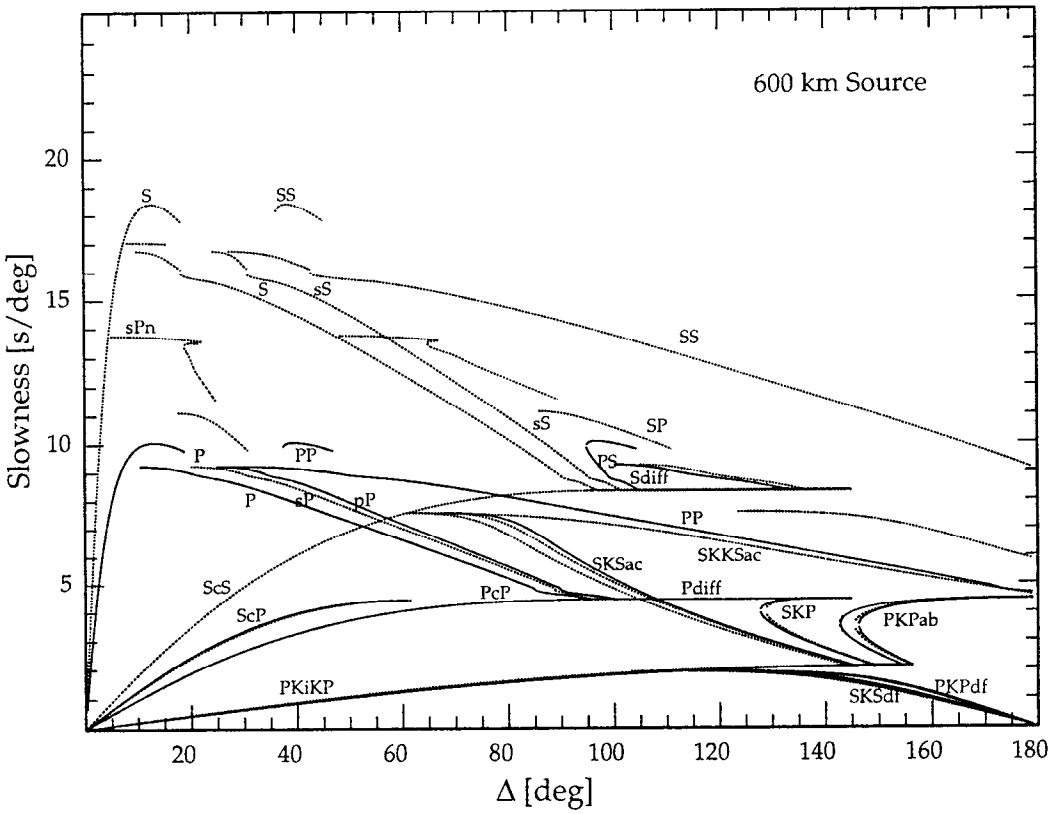

Fig 8. Slowness as a function of epicentral distance for the *iasp91* model for 600 km source depth.

REFERENCES

1 Buland. R and C.H. Chapman, The computation of seismic travel times, *Bull. Seism. Soc. Am*, 73, 1271-1302, 1983.

2 Herrin E., Introduction to '1968 Seismological tables for P-phases', *Bull. Seism. Soc. Am*, 58, 1193-1195, 1968.

3 Jeffreys H., An alternative to the rejection of observations, *Proc. R. Soc. Lond.*, A, 137, 78-87, 1932.

4 Jeffreys H. and K.E. Bullen, *Seismological Tables*, British Association for the Advancement of Science, London.

5 Kennett B.L.N. and E.R. Engdahl, Traveltimes for global earthquake location and phase identification, *Geophys. J. Int.*, 105, 429-465, 1991.

6 Kennett B.L.N., *IASPEI 1991 Seismological Tables*, Research School of Earth Sciences, Canberra, 1991.

7 Randall M.J., A revised travel-time table for S, *Geophys. J. R. astr. Soc.*, 22, 229-234, 1971.

8 Inoue H., Y. Fukao, K. Tanabe and Y. Ogata., Whole-mantle P-wave travel time tomography, *Phys. Earth Planet. Int.*, 59, 294-328.

9 Bullen K.E. and B.A. Bolt, *An introduction to the theory of Seismology*, Cambridge University Press, Cambridge.

10 Aki K. and P. Richards, *Quantitative Seismology*, W.H. Freeman, San Francisco.

Heat Flow of the Earth

Carol A. Stein

1. INTRODUCTION

1.1 Background

Earth's evolution reflects the history of heat transfer from the interior [53, 110] via the fundamental processes of plate tectonics, conduction through continental lithosphere, and hotspot volcanism [103]. As a result, considerable attention has been directed toward understanding Earth's thermal history, the variation in the temperature field in space and time. The primary directly observable quantity for heat flow is the temperature gradient near the surface, which is in turn used to estimate the flow of heat from the interior and hence draw inferences about the thermal structure and evolution.

The challenge is the classical one of using the measured temperature and temperature gradient at an object's surface to infer the temperature field within the body, T(x,t), a function of position x and time t. Near the earth's surface, the temperature gradient is essentially vertical, so the outward heat flow q_s is

$$q_s = k\frac{dT(z)}{dz}\Big|_{z=0}, \qquad (1)$$

the product of the vertical gradient of the temperature T(z), which is most everywhere positive downwards (temperature increases with depth z), and the measured or estimated thermal conductivity of the material, k. Such heat flow measurements (or more precisely estimates based on the measured gradient) are the primary boundary conditions used to find the temperature field via the heat equation,

$$\rho C_p\left[\frac{\partial \mathbf{T}}{\partial t} + \mathbf{v}\cdot\nabla\mathbf{T}\right] = \nabla\cdot(\mathbf{k}\nabla\mathbf{T}) + \mathbf{A}, \qquad (2)$$

where ρ is the density, C_p is the specific heat, A is the heat generation, and v is the velocity of the moving material [e.g 25, 108]. This equation balances the change in the heat content of a body of material with the heat transferred by conduction, brought in by material motion, and generated within the body.

Solution of this equation, and hence deduction of temperature structure from heat flow, is a difficult and nonunique inverse problem. The variation in physical properties with depth is significant but uncertain. The expected solid state convection in the mantle has major thermal effects [e.g. 93]. As a result, although some inferences about temperature structure can be drawn based largely on heat flow, considerable additional information is drawn from seismological studies [e.g. 96], laboratory and theoretical studies of the physical properties of earth materials [e.g. 2], and modeling of convection in the earth [e.g. 48].

The measurement of heat flow has thus long been an active research area. The first reported heat flow measurements were made in oceanic lithosphere by Revelle and Maxwell [92] and in the continental lithosphere by Benfield [13] and Bullard [23]. The 1966 edition of *The Handbook of Physical Constants* [65] listed about 2000 measurements. Since then, the number of heat flow sites included in successive compilations [51, 72, 102] has increased to about 25,000 listed in the most

C. A. Stein, Department of Geological Sciences, University of Illinois at Chicago, 845 W. Taylor Street, Chicago, IL 60607-7059

Global Earth Physics
A Handbook of Physical Constants
AGU Reference Shelf 1

recent compilation [87]. Typical values of the surface temperature gradient, conductivity, radioactive heat generation, and heat flow for continents and oceans are listed in Table 1.

1.2 Measurements and Techniques

Despite its conceptual simplicity, the process of deducing heat flow from a measured gradient and conductivity values has surprising complexity. Aspects of the problem, including the historical development, are reviewed by various authors: see Louden and Wright [73] for marine studies, Beck [9] and Clauser and Huenges [30] for thermal conductivity, Beck and Balling [11] for temperatures, and Jessop [50] for both temperatures and thermal conductivity.

The vertical temperature gradient is computed from temperatures measured at known depths below the surface. However, the process of penetrating the surface to measure the temperatures disturbs the thermal structure. For marine measurements, thrusting a probe into the sediments to depths of about 5 m results in frictional heating, which takes from 5 to 30 minutes to dissipate depending mostly on the probe diameter. Prior to 1975 most heat flow values were based on single measurements, which were typically spaced about 200 km apart. Subsequently, digital instrumentation has resulted in both better temperature determinations and the capability to make closely-spaced seafloor ("pogo") penetrations more rapidly than before. Hence, local variations in the heat flux can be better identified and their cause determined. For measurements on land, temperatures are measured in drill holes using down-hole instruments lowered on a cable. For either measurements on land, or in marine boreholes (such as for the Deep-Sea Drilling Project or the Ocean Drilling Program), calculating the undisturbed temperatures is more complicated. The drilling process produces thermal perturbations due to the exchange of heat between the walls of the hole and the drilling fluid in addition to that due to the friction of drilling. With time, the temperatures slowly return to the undisturbed state. Temperature is determined either by waiting sufficient time for the site to return to the presumed equilibrium state, or measuring the change in temperature with time and then calculating an assumed equilibrium temperature [11].

Table 1. Important Parameters for Heat Flow

Property, Symbol	Approximate Range
Heat flow, q	0 - 125 mW m^{-2}
Vertical temperature gradient, dT/dz	10 to 80 °C/km
Thermal conductivity, k	
marine sediments	0.6 - 1.2 W m^{-1} K^{-1}
continental sediments	1 - 5 W m^{-1} K^{-1}
heat generation, A	0-8 10^{-6} W m^{-3}
Specific heat, C_p	0.85-1.25 kJ $kg^{-1}°C^{-1}$
Density of crustal rocks and lithosphere, ρ	2200 to 3400 kg m^{-2}

In some cases the thermal conductivity is measured either *in situ* or on a sample of the rock recovered and measured in a laboratory. In others, it is estimated based on either the known lithology or values measured from nearby sites. Initially measurements were made on recovered samples with corrections made for the differences in pressures and temperatures between the laboratory and the depth from which the sample was recovered [e.g. 91]. For marine studies the *in situ* and corrected shipboard thermal conductivity measurements agree within about 5% [49]. *In situ* determinations are preferred because the sediments have not been disturbed (especially due to water loss) by the coring and transportation. Generally, no attempt is made to measure or correct for the possibility of anisotropic values of conductivity, resulting mainly from the anisotropic structure of minerals and rocks. The anisotropy of near-surface marine sediments is negligibly small.

Typically the heat flow is calculated from the product of the average thermal conductivity and the thermal gradient. If there are significant variations of the conductivity and thermal gradient with depth (typically due to variations in lithology) the heat flow is estimated. The two most commonly used techniques are the interval method and the Bullard method [90]. The interval method can be used if there is a sufficient density of measurements with depth to assign intervals over which the values of the thermal gradient and conductivity are relatively constant. For each interval, a heat flow is calculated from the product of the average temperature gradient and an average conductivity. Then the overall mean heat flow is determined from these interval values. Alternatively, the Bullard method relies on the assumption that in the absence of significant heat sources or sinks and with one-dimensional, steady-state, conductive heat flow, the subsurface temperature T(z) is:

$$T(z) = T_0 + q_0 \sum_{i=1}^{N} (\Delta z_i / k_i), \quad (3)$$

where T_0 is the surface temperature, q_0 is the constant heat flow, and k_i is the conductivity over the ith depth

interval Δz_i. For each temperature measurement point, the thermal depth, $\sum(\Delta z_i/k_i)$, can be calculated. Then, a least-squares fit is made to the data of T(z) with the thermal depth and the slope of the line is equal to the constant heat flow.

1.3 Corrections and Climatic Effects

The goal of measuring heat flow is to determine the steady-state transfer of heat flow from below. However, the simpliest assumptions that the only uncertainties are from measurement error, the site has uniform horizontal properties and is in a thermal steady state with only conductive heat transfer, are often not the case. Local factors such as topography, sedimentation rates, and surface temperature changes, may disturb the heat flux. Given sufficient information, corrections can be made for these factors. Horizontal variations in topography and lithology cause lateral variations in the temperature and, hence surface heat flow. For the oceans, variable sediment thickness and the rough basaltic surface near the measurement site may result in a horizontal component of heat flow, largely due to the contrast between the lower conductivity of the sediments and the higher values for the basalt [e.g. 14, 54, 112]. For the marine setting the seafloor temperature usually may be assumed to be constant, but for continents the variation of the air-temperature with elevation is frequently included in modeling the steady-state vertical heat flow [e.g. 17, 44]. Another cause of non-steady state behavior is sedimentation or erosion. Rapid sedimentation conductively blankets the surface leading to lower measured heat flow [45, 63, 112]. Conversely, erosion leads to higher measured heat flow.

The magnitude and duration of surface temperature fluctuations control the magnitude and depth of the perturbation of the geotherm. Daily, annual, or climatic ($\sim 10^3$ years) time periods affect the temperatures below the land surface to order one meter, ten meters, and several hundred meters respectively. Hence, for continental regions, the depth of measurements should be greater than about 300 meters to obtain temperatures unaffected by climatic changes. The effects of surface temperature variations over time will be superimposed on the near-surface geotherm. However, higher frequency variations are suppressed relative to longer period changes. A number of techniques have been used to either correct the geotherm for a known temperature variation or to invert for long-term temperature variations [e.g. 10, 26]. For regions where historical temperature information is not available inverting for the surface temperature variations is useful. For example, geotherms from the Alaskan permafrost indicate warming trends in this century [57]. Studies for North America indicate a warming trend this century and a cooler period corresponding to the Little Ice Age that began in the 1400s and lasted into the 1800s [12, 28, 101, 115]. Given the thick water column, the bottom of the ocean is, in general, thermally stable, so variations of sea surface temperatures even as long as climatic time periods do not affect the sub-seafloor temperatures. Most of the deep ocean has sufficiently stable temperatures at the seafloor for accurate heat flow measurements without corrections [46]. However, changes in bottom water temperatures in some regions can affect the temperatures in the uppermost few meters of the sediment [e.g. 56].

2. MARINE HEAT FLOW

2.1 Background

Seafloor heat flow (Figure 1) is highest at midocean ridges, and decreases with the age of the lithosphere [62, 97, 112]. This variation is one of the key features in the models of plate tectonics, where the oceanic lithosphere cools as it spreads away from midocean ridges and reheats upon returning to the mantle at subduction zones. This cycle is a surface manifestation of terrestrial convection [e.g. 48, 83] and the primary mode of heat transfer from the earth's interior [27, 34, 99].

Average heat flow (Figure 1) is greater than about 100 mW m^{-2} for the youngest (<10 Ma) lithosphere. The mean values rapidly decrease from about 0 to 30 million years. The standard deviations are large for young lithosphere, but decrease with increasing lithospheric age. Although heat flow data is "noisy" and scattered, it is required to develop average thermal models of oceanic lithosphere. The magnitudes of depth and heat flow anomalies (the difference between observed and predicted) implicitly depend on how well the reference model reflects the average thermal state, but this is often not explicitly stated. This is especially important for models based on observed anomalies for hotspots and hydrothermal circulation.

2.2 Thermal Models

The primary constraints on models of thermal evolution are ocean depth and heat flow versus age data. The two sets of data jointly reflect the evolution with age of the geotherm in the lithosphere, because the bathymetry depends on the temperature integrated over depth and the heat flow depends on the temperature gradient at the

sea floor. The key features of the data, the decrease in heat flow and increase in seafloor depth with age, prompted two classes of models. One is the half-space model [37], where depth and heat flow vary as the square root of age and the reciprocal of the square root of age, respectively. The second is the plate model [62, 75], where the lithosphere behaves as a cooling boundary layer until it reaches ages at which the effects of the lower boundary cause the depth and heat flow curves to flatten and vary more slowly with age. The asymptotic plate thickness to which the lithosphere evolves corresponds to the depth at which the additional heat is supplied from below to prevent the continuation of half-space cooling for older ages, and above which temperature changes cause bathymetric variations.

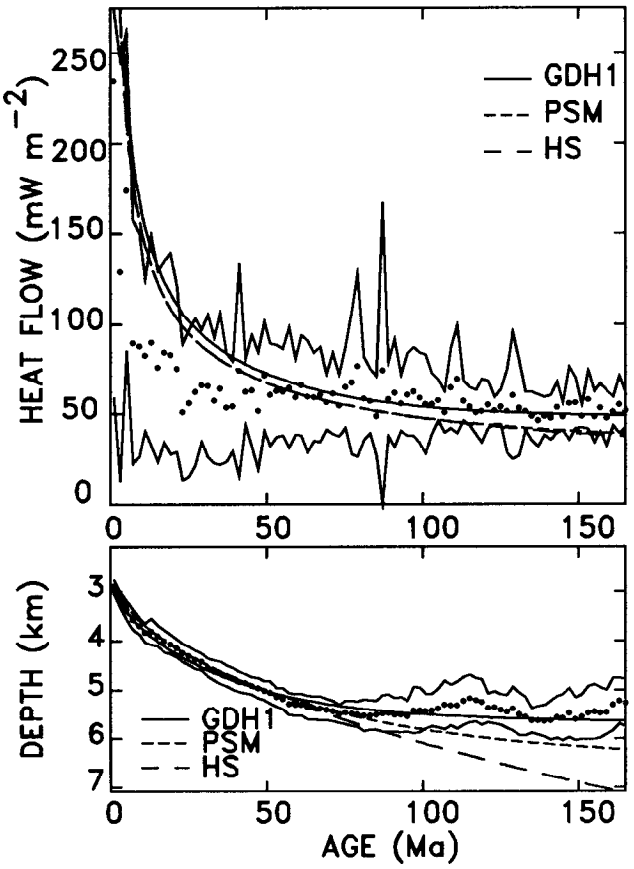

Fig. 1. Oceanic data, for the north Pacific and northwestern Atlantic Oceans, and models for heat flow and depth as a function of age. The data were averaged in two-m.y. bins, and one standard deviation about the mean value for each is shown by the envelope. The models shown are the plate model of Parsons and Sclater [84] (PSM), a cooling half-space model with the same thermal parameters (HS), and the GDH1 plate model. GDH1 (Global Depth and Heat flow), derived by joint fitting of this heat flow and bathymetry fits the data significantly better than earlier models, including the data from older lithosphere previously treated as anomalous. The improved fits imply that the oceanic lithosphere is thinner and hotter at depth than previously thought. From Stein and Stein [105].

Because of the observed flattening of depths and heat flow for older lithospheric ages, the plate model appears to be a better overall model to describe the data. Two different sets of parameters for the plate model (Table 2) have been used by Parsons and Sclater [84] (hereafter termed PSM) and Stein and Stein [105] (hereafter termed GDH1). GDH1 provides a somewhat better fit to the average depth-age and heat flow-age data using a hotter, thinner lithosphere compared to PSM (Figure 1). The heat flow predictions for GDH1 are conveniently and accurately approximated using a half-space model with the same parameters for young lithosphere, and with the first term of the series solution for older lithosphere [84]. The heat flow q (mW m^{-2}) is related to the age t (Ma) by $q(t) = 510\ t^{-1/2}$ for ages less than or equal to 55 Ma and $48 + 96 \exp(-0.0278\ t)$ for ages greater than 55 Ma. Table 3 lists the average observed heat flow for the major oceanic basins and predicted heat flow from the GDH1 model with lithospheric age.

2.3 Hydrothermal Circulation

Regardless of which thermal model is used to represent the heat flow with oceanic age, a significant discrepancy exists between the heat flow measured at the sea floor and the higher values predicted for ages 0-70 Ma (Figure 2). This is attributed to hydrothermal circulation with advective interchange between pore waters in the crust and sediments and sea water, rather than the conductive cooling assumed in the models [e.g. 68, 81]. The first detailed measurements at a ridge crest, the Galapagos Spreading Center [118], showed the convection pattern with high heat flow associated with upwelling zones located above topographic basement highs and low heat flow associated with down-flowing water above topographic basement lows, in accord with modeling [e.g. 74]. Often at sites with up-flowing water the temperature versus depth profiles are non-linear, concave upward, and at sites with down-flowing water are non-linear, concave downward [6, 19]. Subsequent studies indicate that in young lithosphere the high scatter in the values of individual heat flow measurements are presumably related to the variations in sedi-

Table 2: Plate model parameters

		GDH1	PSM
a	plate thickness	95 km	125 km
T_m	basal temperature	1450°C	1350°C
α	thermal expansion coefficient	3.1×10^{-5} °C^{-1}	3.28×10^{-5} °C^{-1}
k	thermal conductivity	3.138 W m^{-1} °C^{-1}	3.138 W m^{-1} °C^{-1}
C_p	specific heat	1.171 kJ kg^{-1} °C^{-1}	1.171 kJ kg^{-1} °C^{-1}
ρ_m	mantle density	3330 kg m^{-3}	3330 kg m^{-3}
ρ_w	water density	1000 kg m^{-3}	1000 kg m^{-3}
d_r	ridge depth	2600 m	2500 m

GDH1 model parameters from Stein and Stein [105]; PSM from Parsons and Sclater [84]

ment distribution, topographic basement relief, and local hydrological effects [1, 35, 41, 60]. Perhaps the most spectacular evidence for hydrothermal circulation is found in the "black smoker" vents of superheated water (at ~350°C) at the ridge crest with the associated biological communities [e.g. 31]. The circulation is thought to be divided into two primary stages [39, 69]. Near the ridge axis, "active" circulation occurs, during which water cools and cracks the rock, and heat is extracted rapidly by high temperature water flow [40, 85]. Once cracking ceases, "passive" circulation transports lower temperature water.

The amount of convective heat transport can be estimated from the difference between the observed and predicted heat flow [119]. Of the predicted global oceanic heat flux of 32×10^{12} W, $11 \pm 4 \times 10^{12}$ W or 34 ± 12% occurs by hydrothermal flow [107]. On a global basis ~26% of the hydrothermal heat flux occurs for ages less than 1 Ma and ~33% occurs for ages greater than 9 Ma (Table 4).

The hydrothermal water flux decreases with age and then is assumed to stop at the sealing age, defined when the observed and predicted heat flow are approximately equal. The fraction of mean observed heat flow to that expected for cooling plate models gradually rises from about .4 for the youngest lithosphere to about 1 in an approximately linear fashion until the sealing age at which it remains 1 thereafter. For the global heat flow data the sealing age is estimated at 65 ± 10 Ma (Figure 2) [107]. Because the sealing age is an average value, some water circulation may persist beyond it [e.g. 7], although the heat transfer is assumed to be primarily conductive. Within the uncertainties there are no differences for the sealing age between the major ocean basins [107].

Two mechanisms that may cause hydrothermal circulation to cease are sufficient overlying sediment to seal off the crustal convective system (and hence which no exchange of water between the crust and ocean due to the integrated permeability of the sediment column) and age-dependent properties resulting in decreasing porosity and hence permeability of the crust due to hydrothermal deposition of minerals, which also is assumed to change seismic velocity in the uppermost layer of the crust [5, 47]. It was proposed that to reach the sealing age for a given heat flow site either about 150-200 m of

Table 3. Oceanic Heat Flow Predicted from a Plate Model and Observed with Given Uncertainties due only to Data Scatter

Age (Ma)	Average Heat Flow (mW m^{-2}) Predicted (GDH1 Model)	Observed	No. Data
0-1	1020	131 ± 93	79
0-2	721	136 ± 99	195
0-4	510	128 ± 98	338
4-9	204	103 ± 80	382
9-20	136	82 ± 52	658
20-35	98	64 ± 40	535
35-52	77	60 ± 34	277
52-65	66	62 ± 26	247
65-80	60	61 ± 27	398
80-95	56	59 ± 43	443
95-110	53	57 ± 20	230
110-125	51	53 ± 13	417
125-140	50	52 ± 20	224
140-160	49	51 ± 14	242
160-180	48	52 ± 10	67

from Stein and Stein [107]

sediment covering the basement rock is required [4] or the region about the site should be well sedimented (as characterized by the sedimentary environment classification of Sclater et al. [98]). The heat flow fraction for the global data set for either sites with less than 200 m of sediment or more, or for those within the 4 categories of sedimentary environments (from poorly to well-sedimented sites) show the same linear trend of increasing heat flow fraction with age, and within the uncertainties the same sealing age [107]. Hence, probably neither ~200 m of sediment nor well sedimented sites are necessary or sufficient for crustal sealing; the effect of overlying sediment appears instead to be secondary, and is probably most important for the young lithosphere.

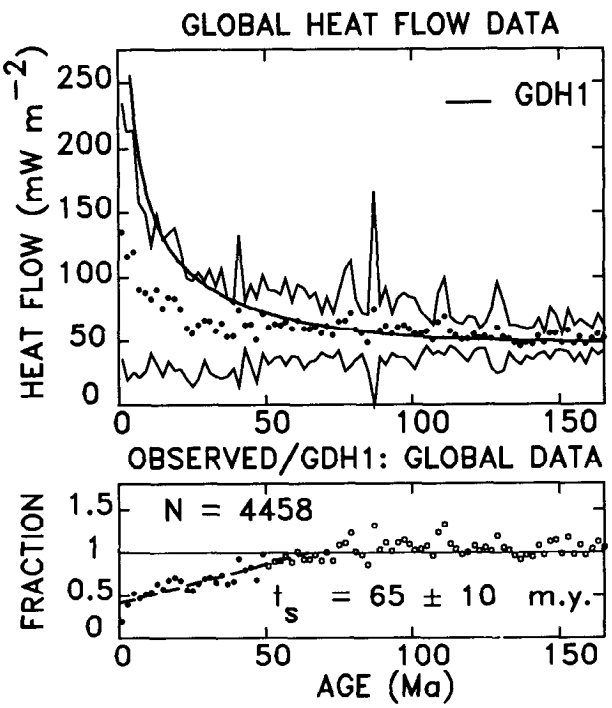

Fig. 2. Observed heat flow versus age for the global data set from the major ocean basins and predictions of the GDH1 model, shown in raw form (*top*) and fraction (*bottom*). Data are averaged in 2-m.y. bins. The discrepancy for ages < 50-70 Ma presumably indicates the fraction of the heat transported by hydrothermal flow. The fractions for ages < 50 Ma (closed circles), which were not used in deriving GDH1, are fit by a least squares line. The sealing age, where the line reaches one, is 65 ± 10 Ma [107].

The hydrothermal circulation has profound implications for the chemistry of the oceans, because sea water reacts with the crust, giving rise to hydrothermal fluid of significantly different composition [119, 120]. The primary geochemical effects are thought to result from the high temperature water flow observed at ridge axes [e.g. 31]. Nonetheless, the persistence of the heat flow discrepancy to ages of 50-70 Ma indicates that much of the hydrothermal heat flux occurs away from the ridge axis. This lower temperature off-axial flow is thought to have a much smaller geochemical effect than the near-axis flow, based on the major element chemistry of the fluid [8].

2.4 Back-Arc Spreading, Subduction Zones and Accretionary Prisms

Heat flow measurements across western Pacific subduction zones show patterns of low values from the trench axis to the volcanic arc, high and variable values over the volcanic zone and values in the back arc region similar to those for the major ocean basins of the same lithospheric age [3, 116]. However, the depths of marginal basins range from that expected to ~1 km deeper than predicted for their lithospheric ages [71, 82, 116]. Some of these depth anomalies may be due to lateral transport of heat for very small ocean basins or those formed with a short axis of spreading (<200 km) [18]. Alternatively, secondary convection associated with back-arc spreading may cause greater seafloor depths.

Accretionary prisms contain accumulations of water-saturated sediment. Initial studies with sparsely spaced measurements suggested that heat flow was lower than average [61, 116]. More recent surveys [e.g. 36, 42, 64, 122] with densely-spaced measurements indicate that heat flow is highly variable, both within a given prism and for different prisms. Many regions of high heat flow are associated with upward advection of pore fluids, typically found along faults and the bottom decollement. This process is probably a factor controlling the prism's mechanical deformation.

2.5 Hot Spots

Hawaii is the type example for hotspot studies, because of its size and isolation from other perturbing processes (including ridges and other hotspots). The observation that heat flow on the Hawaiian swell was higher than that predicted for the Parsons and Sclater [84] model was initially treated as consistent with the elevated heat flow expected for a reheating model [113] but subsequent measurements showed that its heat flow hardly differs from that for lithosphere of comparable

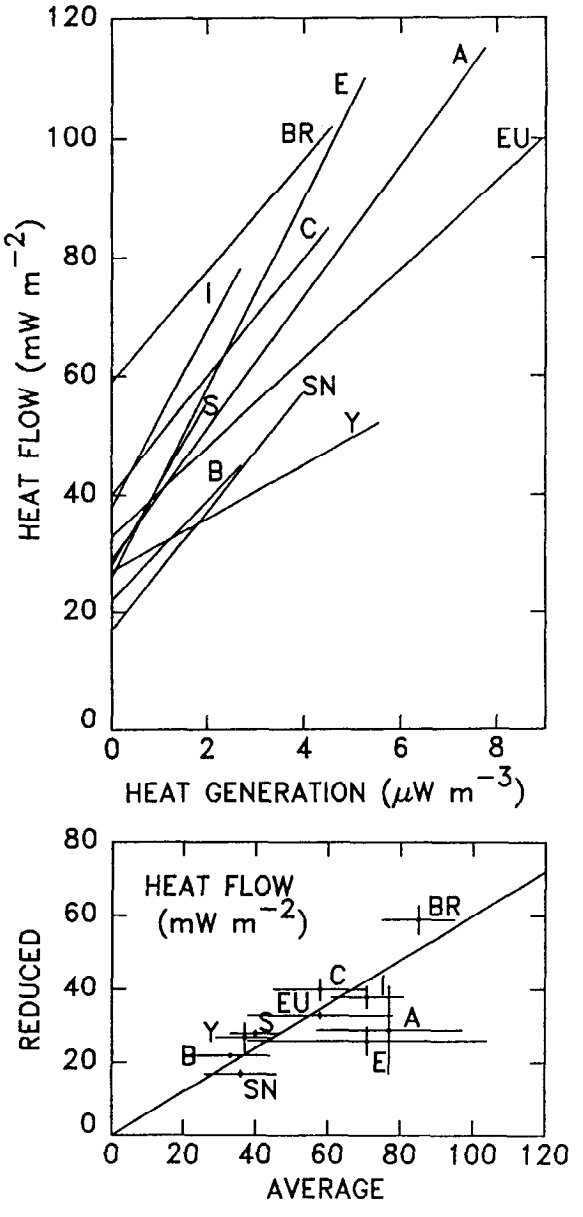

Fig. 3. (*top*) Heat flow and heat generation for various heat-flow provinces. The intercept is the reduced heat flow and the slope is "D" value. (*bottom*) Plot of reduced heat flow against average surface heat flow for the same heat-flow provinces as above. Error bars show standard deviation of the data sets. The diagonal line indicated reduced heat flow of 60% of the average heat flow, as indicated by the theory of Pollack and Chapman [82]. A=Central Australia; B=Baltic Shield; BR=Basin and Range Province; C=Atlantic Canada; E=England and Wales; EU=Eastern U.S.A.; I=India; S=Superior Province; SN=Sierra Nevada; Y=Yilgarn Block (Australia). After Jessop [50].

ages [114] and is only slightly above that expected for GDH1 [106]. A similar situation for the heat flow anomalies applies for the Bermuda [38], Cape Verde [33] and, Crozet [32] hotspots. Using the GDH1 reference model, the small heat flow anomaly thus favors a primarily dynamic origin [e.g. 70] for these swells rather than a largely thermal origin [e.g. 113]. The interpretation favoring a dynamic model is consistent with seismological data, which shows no evidence for a low velocity zone under the Hawaiian swell [121].

3. CONTINENTAL HEAT FLOW

3.1 Background

Because the oceanic lithosphere is relatively uniform in composition, and little heat is generated within it by radioactivity, oceanic heat flow is essentially a simple function of age described by the cooling plate model. In contrast, continental lithosphere is quite heterogeneous in composition, due to its much longer tectonic history. Moreover, the heat flow depends critically on radioactive heat production in the crust. The two primary effects are thus that continental heat flow is proportional to the surface crustal radioactivity in a given region, and decreases with the time since the last major tectonic event.

3.2 Radioactive (Crustal) Heat Production

The continental crust contains a relatively high density of radioactive isotopes, primarily those of uranium, thorium, and potassium [109]. Hence, within a region the heat flow depends on (1) radioactivity in the crust, (2) tectonic setting, and (3) heat flux from the mantle below. For a given area, termed a heat-flow province, the measured heat flow q varies linearly with the near-surface radioactive heat production A_o [15, 94]. Thus we define heat flow provinces characterized by q_r, the reduced heat flow, and a slope D, such that the heat flow

$$q = q_r + DA_o \tag{4}$$

(Figure 3). Initially it was suggested that the D value represents a slab of uniform heat production [94]. However, because differential erosion within the region would invalidate this explanation, the radioactive heat production is often treated as exponentially distributed with depth, z, or

$$A(z) = A_o e^{-(z/D)} \tag{5}$$

[55]. The reduced heat flow appears to be relatively uni-

Table 4. Oceanic Cumulative Heat Flux with Uncertainties due only to Data Scatter

Age (Ma)	Cumulative Heat Flux (10^{12} W) Predicted	Observed	Hydrothermal
1	3.6	0.4 ± 0.3	3.2 ± 0.3
2	5.1	1.0 ± 0.7	4.1 ± 0.7
4	7.2	1.8 ± 1.4	5.4 ± 1.4
9	11.3	3.8 ± 2.1	7.4 ± 2.1
20	15.6	6.5 ± 2.7	9.1 ± 2.7
35	19.8	9.2 ± 3.2	10.5 ± 3.2
52	22.7	11.5 ± 3.4	11.2 ± 3.4
65	24.6	13.3 ± 3.5	11.3 ± 3.5
80	26.9	15.6 ± 3.7	11.3 ± 3.7
95	28.5	17.3 ± 3.9	11.2 ± 3.9
110	29.8	18.7 ± 3.9	11.1 ± 3.9
125	30.6	19.5 ± 3.9	11.1 ± 3.9
140	31.5	20.4 ± 3.9	11.1 ± 3.9
160	31.9	20.8 ± 3.9	11.1 ± 3.9
180	32.0	21.0 ± 3.9	11.0 ± 3.9

from Stein and Stein [107]

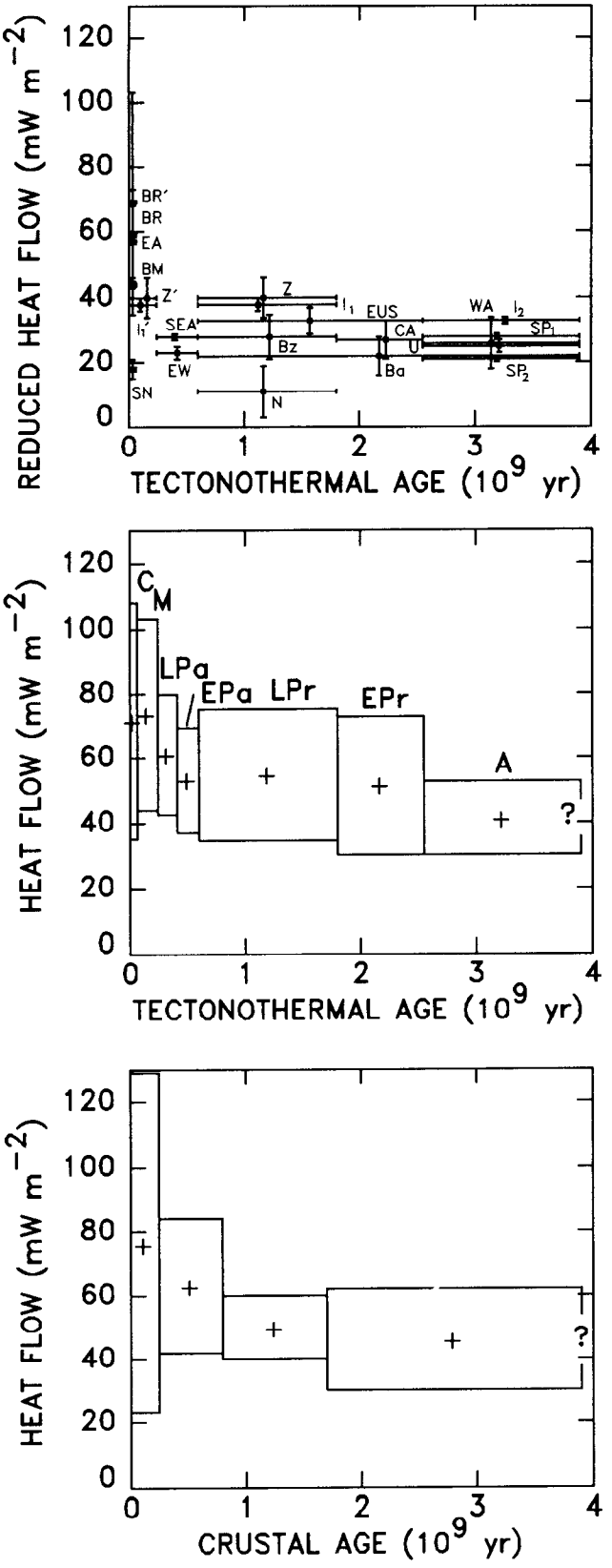

Fig. 4. For the continental heat flow data set: (*top*) Reduced heat flow as a function of age since the last tectonothermal event, for different heat flow provinces. Heat flow error bars are the uncertainties in reduced heat flow and age. BR=Basin and Range; BR'=Basin and Range; SEA=SE Appalachians; SN=Sierra Nevada; EUS=Eastern US; SP_2=Superior; SP_1=Superior, corrected; Bz=Brazilian coastal shield; Ba=Baltic shield; BM=Bohemian Massif; U=Ukraine; EW=England and Wales; N=Niger; Z=Zambia; Z'=Zambia; WA=Western Australia; CA=Central Australia; EA=Eastern Australia; I_1=Indian Shield; I'_1=Indian Shield; I_2=Archean Indian Shield. BR', EA, N, Z, and Z' were derived from assumed heat production values. (*middle*) Heat flow data averaged in groups according to age of the last tectonothermal event at each site. C=Cenozoic, M=Mesozoic, LPa=Late Paleozoic, EPa=Early Paleozoic, LPr=Late Proterozoic, EPr=Early Proterozoic, and A=Archean. (*bottom*) Heat flow data averaged in groups according to radiometric crustal age at each site. In each plot, mean heat flow values in each group are plotted as crosses at the mid-point of the age range; Boxes around the crosses indicate the age ranges for the data and standard deviations of the means. The number of data in each group are indicated by each box in parentheses. After Morgan [78].

form within the heat-flow province and can be interpreted as representing the flux from deep crustal regions or at the Moho. On average, the reduced heat flow for a province is about 0.6 of the average heat flow (Figure 3, bottom), suggesting that about 60% of the flux comes from the lower crust or below [86].

3.3 Continental Heat Flux with Age

Lee and Uyeda [66] first suggested that the continental heat flow was age dependent. Subsequent work [e.g. 89; 111] better demonstrated this relationship (Table 5). The heat flow within a given continent generally decreases with age [99]. The decrease is even clearer when the age used is the time since the last tectonothermal event (Figure 4). As with oceanic heat flow, continental measurements show a relatively large standard deviation. Local conditions such as variations in radioactive heat production, sedimentation, erosion, topography, water circulation and climate variability add to the uncertainties. One method of attempting to remove the radioactive signal is to consider the reduced heat flux versus age. This parameter rapidly decreases with tectonothermal ages from 0 and 300 Ma (Figure 4, top). For older ages (Paleozoic and Pre-Cambrian) the reduced heat flow appears to be a relatively constant, about 25 mW m^{-2} (.6 HFU) [78, 99].

3.4 Water Circulation

In contrast to the oceanic lithosphere, in which little is known about water circulation, water circulation in the continental crust has been intensively studied. Most water flow is driven by hydraulic gradients associated with variations in water table elevation and location of aquifers [e.g. 67]. Near-surface hydrothermal circulation in the continental crust can also extensively redistribute heat (for example in Iceland), thus complicating analysis of heat flow data. For example, analysis of heat flow values for the Snake River Plateau/Yellowstone hotspot are complicated by extensive ground water circulation [e.g. 20].

3.5 Extension, Hotspots and Frictional Heating

Transient heating of the continental lithosphere can occur due to tectonic processes including extension, hotspot reheating, and fault motion. Unlike oceanic hotspots where heat flow anomalies are calculated relative to that expected for the lithospheric age, continental anomalies are relative to the surrounding lithosphere not affected by the tectonic event. For example, the Snake River Plain, a topographic feature resulting from intraplate volcanism and massive magmatic intrusions in the uppermost crust starting about 16 Ma, is thought to mark the passage of the Yellowstone hotspot. Heat flow systematically increases eastward towards the recent volcanism from about 75-90 mW m^{-2} to 90-110 mW m^{-2}, well above the average North American values [16]. In Yellowstone National Park, heat flow measurements [79] and geochemical analysis [43] imply high heat loss and upper crustal temperatures in the most recently active region of volcanism.

During extension or rifting of continental lithosphere, additional heat is added to the near surface by both upward advection of heat by magmatic intrusions and volcanism, and overall thinning of the crust. The higher geotherm, subsidence, and typically rapid sedimentation, as the lithosphere cools, facilitates the production of

Table 5. Continental Heat Flow

Age (Ma)	Average heat flow (mW m^{-2})	No. Data
Subaqueous continental undifferentiated (lakes, continental shelf and slope)	77.7 ± 53.6	295
Cenozoic sedimentary and metamorphic	63.9 ± 27.5	2912
Cenozoic igneous	97.0 ± 66.9	3705
Mesozoic sedimentary and metamorphic	63.7 ± 28.2	1359
Mesozoic igneous	64.2 ± 28.8	1591
Paleozoic sedimentary and metamorphic	61.0 ± 30.2	403
Paleozoic igneous	57.7 ± 20.5	1810
Proterozoic	58.3 ± 23.6	260
Archean	51.5 ± 25.6	963

From Pollack et al. [88].

fossil fuels. Regions currently undergoing extension, such as the Basin and Range province in the western U. S. have higher average heat flow [e.g. 58, 77] and reduced heat flow compared to sites with the same average radioactive heat generation (Figures 3 and 4). High heat flow is also found where Cenozoic rifting has formed passive margins or substantially thinned continental crust prior to the onset of seafloor spreading [e.g. 22]. The effect of recent volcanism is apparent when comparing the average heat flow of Cenozoic igneous regions to Cenozoic sedimentary and metamorphic regions. Simple models of the process of lithospheric extension, which may produce a rifted continental margin or sedimentary basin [e.g. 76, 95], suggest that although heat is added to the crust, the additional heat flow will almost completely dissipate within less than 100 m.y. Hence, it is not surprising that heat flow for igneous regions are similar to that for sedimentary and metamorphic regions of Mesozoic or Paleozoic ages (Table 5).

It has been proposed that frictional heating during faulting may provide an additional source of heat to the lithosphere, proportional to the product of the velocity of the motion and the fault stress. The first such study for the San Andreas fault [21] suggested that the absence of a significant heat flow anomaly implied relatively low stresses (about 100 bars) over long periods of time. More recent heat flow measurements and modeling [58] and recent drilling results for the Cajon Pass site [59] support the initial conclusion.

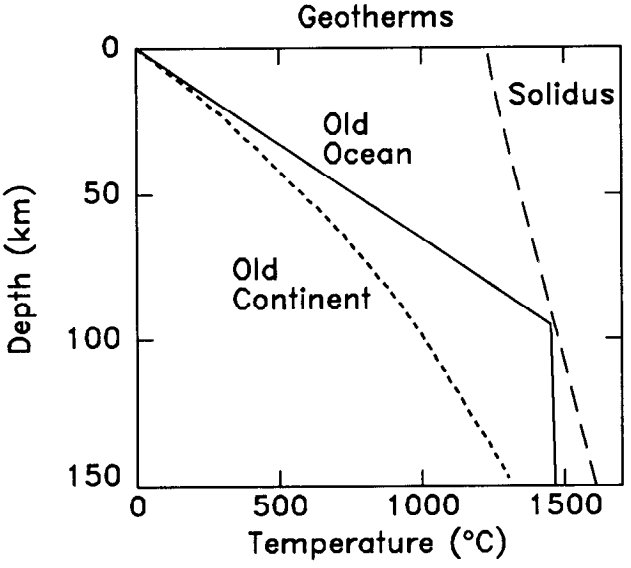

Fig. 5: Geotherms for old oceanic [105] and old continental lithosphere assuming a 50 mW m^{-2} surface heat flow [86], and a solidus [104]. Radioactive heat production in continental crust results in lower temperatures at a given depth compared with the oceanic geotherm. Continental geotherm is calculated assuming only conduction, but other modes of heat transfer may be increasingly significant at depths greater than about 70 km [86].

4. GEOTHERMS

Continental and oceanic lithosphere are composed of very different materials with different tectonic histories. The lithospheric thickness, which presumably varies as a function of age and tectonic history, can be defined based on different properties [e.g. 52], such as mechanical strength [e.g. 24], seismic velocity [e.g. 80], or thermal behavior. Possible thermal definitions include the region where conduction is the major heat transfer mechanism [e.g. 78], or the region at which temperature are less than some fraction of the expected solidus.

An interesting fact is that the average heat flow for old oceanic lithosphere and the oldest continental lithosphere is approximately the same, about 50 mW m^{-2} (Tables 3 and 5). Whether this approximate equality is a coincidence or reflects a fundamental tectonic fact is an interesting question. The issue is complicated by the challenge of estimating the geotherm given the surface heat flow. The oceanic geotherm within the lithosphere is thought to be a straightforward calculation from the cooling plate model. The geotherm changes with age until it reaches a steady state, at which time the geotherm is essentially linear with depth, with a slope equal to the surface heat flow divided by the thermal conductivity (Figure 5), because the radioactive heat production is small. Beneath the plate a shallow adiabatic gradient, ~0.3°C/km, is generally assumed [108]. The continental geotherm, however, depends on the assumed the variation of radioactive heat production with depth. Assuming only conductive heat transfer, steady-state conditions and given two boundary conditions, the surface heat flow q_s and a surface temperature T_s, the geotherm T(z) is

$$T(z) = T_s + \frac{q_s}{k}z - \frac{\rho A}{2k}z^2. \quad (6)$$

Hence for a given surface heat flow and temperature, the temperatures at depth will be lower the higher the radioactive heat production. The continental geotherm in Figure 5 [86] assumes a heat production of 2.5

10^{-6}Wm^{-3} for the upper 8 km, an order of magnitude less for the lower crust and even less for the mantle below. The resulting geotherm suggests that the thermal thickness of old continental lithosphere exceeds that of old oceanic lithosphere. These relative thicknesses agree with some assessments [e.g. 52] but is opposite the conclusions of Sclater et al. [99, 100] who suggested approximate equality of the geotherms, in part due to their cooler oceanic model. Given the uncertainties in the estimated geotherms, due in large part to the largely unknown variation in both heat production and other physical properties with depth, the question of what the equality of old continental and oceanic heat flow means remains unresolved and possibly even unresolvable.

5. GLOBAL HEAT LOSS

Prior to the development of plate tectonics, it was thought that the average oceanic heat flow might be lower than that for the continents because the basalt of the oceanic crust has less radioactive isotopes compared to continental material. In fact, the average oceanic heat flow (101 mW m^{-2}) is higher than for continents (65 mW m^{-2}) because of the plate cooling process. Thus oceanic and continental heat flow account for about 70% and 30% respectively of the integrated surface heat flux (Table 6), yielding a global average of 87 mW m^{-2}

Table 6. Global Heat Flow

Region	Mean heat flow (mW m^{-2})	No. Data
Oceanic	101 ± 2.2	9864
Continental	65 ± 1.6	10337
Global	87 ± 2.0	20201

Total global heat loss= 4.42 ± 0.10 × 10^{13} W
From Pollack et al. [88].

or a total heat loss of 4.42 × 10^{13} W [88]. These values are about 4-8% higher than previous analyses of the global heat flow data set [e.g. 34, 99, 117]. The more difficult to estimate total heat production within the earth, 27.5 × 10^{12} W (from 3.47 × 10^{-8} cal g^{-1} yr^{-1} [Table 10; 109]), is often divided by the global heat loss, giving a value of about 0.6. This quantity, known as the Urey ratio, indicates that radioactivity can account for about 60% of the earth's heat output, and hence is important for modeling the thermal evolution of the earth [29].

Acknowledgments: I thank Henry Pollack for providing a preprint of his paper and Seth Stein and an anonymous reviewer for useful comments. This research was supported by NSF grant EAR-9219302.

REFERENCES

1. Abbott, D. H., C. A. Stein, and O. Diachok, Topographic relief and sediment thickness: their effects on the thermal evolution of oceanic lithosphere, *Geophys. Res. Lett., 19,* 1975-1978, 1992.
2. Akaogi, M., E. Ito, and A. Navrotsky, Experimental and thermodynamic constraints on phase transitions of mantle minerals (abstract), *Abstr. 28th Internat. Geol. Cong., 1,* 26, 1989.
3. Anderson, R. N., 1980 Update of heat flow in the East and Southeast Asian seas, in *The Tectonic and Geologic Evolution of Southeast Asian Seas and Islands, Geophysical Monograph Series, 23,* edited by D. E. Hayes, pp. 319–326, Am. Geophys. Un., Washington, D. C., 1980.
4. Anderson, R. N., and M. A. Hobart, The relation between heat flow, sediment thickness, and age in the eastern Pacific, *J. Geophys. Res., 81,* 2968–2989, 1976.
5. Anderson, R. N., M. G. Langseth, and J. G. Sclater, The mechanisms of heat transfer through the floor on the Indian Ocean, *J. Geophys. Res., 82,* 3391–3409, 1977.
6. Anderson, R. N., M. G. Langseth, and M. A. Hobart, Geothermal convection through oceanic crust and sediments in the Indian Ocean, *Science, 204,* 828–832, 1979.
7. Anderson, R. N., and J. N. Skilbeck, Oceanic heat flow, in *The Oceanic Lithosphere, The Seas 7,* edited by C. Emiliani, pp. 489–523, Wiley-Interscience, New York, 1981.
8. Baker, P. A., P. M. Stout, M. Kastner, and H. Elderfield, Large-scale lateral advection of seawater through oceanic crust in the central equatorial Pacific, *Earth Planet. Sci. Lett., 105,* 522–533, 1991.
9. Beck, A. E., Methods for determining thermal conductivity and thermal diffusivity, in *Handbook of terrestrial heat-flow density determination,* edited by R. Haenel, L. Rybach and L. Stegena, pp. 87–124, Kluwer Academic Publishers, Dordrecht, 1988.
10. Beck, A. E., Inferring past climate change from subsurface temperature profiles: some problems and methods, *Palaeography, Palaeoclimatology, Palaeoecology (Global and Planetary Change Section), 98,* 73–80, 1992.
11. Beck, A. E., and N. Balling, Deter-

mination of virgin rock temperatures, in *Handbook of terrestrial heat-flow density determination,* edited by R. Haenel, L. Rybach and L. Stegena, pp. 59–85, Kluwer Academic Publishers, Dordrecht, 1988.

12. Beltrami, H., and J-C Mareshal, Ground temperature histories for central and eastern Canada from geothermal measurements: Little Ice Age signature, *Geophys. Res. Lett., 19,* 689–692, 1992.
13. Benfield, A. E., Terrestrial heat flow in Great Britian, *Proc. Roy. Soc. London, A, 173,* 428–450, 1939.
14. Birch, F., Low values of oceanic heat flow, *J. Geophys. Res., 72,* 2261–2262, 1967.
15. Birch, F., R. F. Roy, and E. R. Decker, Heat flow and the thermal history in New England and New York, in *Studies of Appalachian geology, northern and maritime,* edited by E. Zen, W. S. White, J. B. Hadley and J. B. Thompson, pp. 437–451, Interscience, 1968.
16. Blackwell, D. D., Regional implications of heat flow of the Snake River Plain, Northwestern United States, *Tectonophysics, 164,* 323–343, 1989.
17. Blackwell, D. D., J. L. Steele, and C. A. Brott, The terrain effect on terrestrial heat flow, *J. Geophys. Res., 85,* 4757–4772, 1980.
18. Boerner, S. T., and J. G. Sclater, Approximate solutions for heat loss in small marginal basins, in *CRC Handbook of Seafloor Heat Flow,* edited by J. A. Wright and K. E. Louden, pp. 231–255, CRC Press, Inc., Boca Raton, 1989.
19. Bredehoeft, J.D., and I.S. Papadopulos, Rates of vertical groundwater movement estimated from the earth's thermal profile, *Water Resour. Res., 2,* 325–328, 1965.
20. Brott, C. A., D. D. Blackwell, and J. P. Ziagos, Thermal and tectonic implications of heat flow in the Eastern Snake River Plain, Idaho, *J. Geophys. Res., 86,* 11,709–11,734, 1981.
21. Brune, J. N., T. L. Henyey, and R. F. Roy, Heat flow, stress, and rate of slip along the San Andreas Fault, California, *J. Geophys. Res., 74,* 3821–3827, 1969.
22. Buck, W. R., F. Martinez, M. S. Steckler, and J. R. Cochran, Thermal consequences of lithospheric extension: pure and simple, *Tectonics, 7,* 213–234, 1988.
23. Bullard, E. C., Heat flow in South Africa, *Proc. Roy. Soc. London, A, 173,* 474–502, 1939.
24. Calmant, S., J. Francheteau, and A. Cazenave, Elastic layer thickening with age of the oceanic lithosphere a tool for prediction of age of volcanoes or oceanic crust, *Geophys. J. Int., 100,* 59–67, 1990.
25. Carslaw, H. S., and J. C. Jaeger, *Conduction of heat in solids,* Oxford University Press, Oxford, 510 pp., 1959.
26. Cermak, V., Underground temperature and inferred climatic temperature of the past millennium, *Palaeogeogr., Palaeoclimatol., Palaeoceol., 10,* 1–19, 1971.
27. Chapman, D. S., and H. N. Pollack, Global heat flow: a new look, *Earth Planet. Sci. Lett., 28,* 23–32, 1975.
28. Chapman, D. S., T. J. Chisholm, and R. N. Harris, Combining borehole temperature and meteorological data to constrain past climate change, *Palaeography, Palaeoclimatology, Palaeoecology (Global and Planetary Change Section), 98,* 269–281, 1992.
29. Christensen, U., The energy budget of the earth, in *The encyclopedia of solid earth geophysics, Encyclopedia of Earth Sciences,* edited by D. E. James, pp. 372–378, Van Nostrand Reinhold Company, New York, 1989.
30. Clauser, C., and E. Huenges, Thermal conductivity of rocks and minerals, *AGU Handbook of Physical Constants,*, Ed., edited by T. J. Ahrens, Am. Geophys. Un., Washington, D.C., this volume, 1994.
31. Corliss, J. B., J. Dymond, L. I. Gordon, J. M. Edmond, R. P. Von Herzen, R. D. Ballard, K. L. Green, D. Williams, A. L. Brainbridge, K. Crane, and T. H. van Andel, Submarine thermal springs on the Galapagos rift, *Science, 203,* 1073–1083, 1979.
32. Courtney, R. C., and M. Recq, Anomalous heat flow near the Crozet Plateau and mantle convection, *Earth Planet. Sci. Lett., 79,* 373–384, 1986.
33. Courtney, R. C., and R. S. White, Anomalous heat flow and geoid across the Cape Verde Rise: evidence for dynamic support from a thermal plume in the mantle, *Geophys. J. R. astron. Soc., 87,* 815–867, 1986.
34. Davies, G. F., Review of oceanic and global heat flow estimates, *Rev. Geophys. Space Phys., 18,* 718–722, 1980.
35. Davis, E. E., D. S. Chapman, C. B. Forster, and H. Villinger, Heat-flow variations correlated with buried basement topography on the Juan de Fuca Ridge, *Nature, 342,* 533–537, 1989.
36. Davis, E. E., R. D. Hyndman, and H. Villinger, Rates of fluid expulsion across the northern Cascadia accretionary prism: Constraints from new heat flow and multichannel seismic reflection data, *J. Geophys. Res., 95,* 8869–8890, 1990.
37. Davis, E. E., and C. R. B. Lister, Fundamentals of ridge crest topography, *Earth Planet. Sci. Lett., 21,* 405–413, 1974.
38. Detrick, R. S., R. P. Von Herzen, B. Parsons, D. Sandwell, and M. Dougherty, Heat flow observations on the Bermuda Rise and thermal models of midplate swells, *J. Geophys. Res., 91,* 3701–3723, 1986.
39. Fehn, U., and L. M. Cathles, The influence of plate movement on the evolution of hydrothermal convection cells in the oceanic crust, *Tectonophysics, 125,* 289–312, 1986.
40. Fehn, U., K. E. Green, R. P. Von Herzen, and L. M. Cathles, Numerical models for the hydrothermal field at the Galapagos spreading center, *J. Geophys. Res., 88,* 1033–1048, 1983.
41. Fisher, A. T., Becker, K., and T. N. Narasimhan, Off-axis hydrothermal circulation: parametric tests of a refined model of processes at Deep

Sea Drilling Project/Ocean Drilling Program site 504, J. Geophys. Res., 99, 3097-3121, 1994.

42. Foucher, J. P., X. Le Pichon, S. Lallemant, M. A. Hobart, P. Henry, M. Benedetti, G. K. Westbrook, and M. G. Langseth, Heat flow, tectonics, and fluid circulation at the toe of the Barbados Ridge accretionary prism, *J. Geophys. Res., 95,* 8859–8867, 1990.
43. Fournier, R. O, Geochemistry and dynamics of the Yellowstone National Park hydrothermal system, in *Ann. Rev. Earth Planet. Sci., 17,* edited by G. W. Wetherill, A. L. Albee and F. G. Stehli, pp. 13–53, 1989.
44. Henry, S. G., and H. N. Pollack, Heat flow in the presence of topography: numerical analysis of data ensembles, *Geophysics, 50,* 1335–1341, 1985.
45. Hutchison, I., The effects of sedimentation and compaction on oceanic heat flow, *Geophys. J. R. astr. Soc., 82,* 439–459, 1985.
46. Hyndman, R. D., M. G. Langseth, and R. P. Von Herzen, Deep Sea Drilling project geothermal measurements: a review, *Rev. Geophys., 25,* 1563-1582, 1987.
47. Jacobson, R. S., Impact of crustal evolution on changes of the seismic properties of the uppermost ocean crust, *Rev. Geophysics, 30,* 23–42, 1992.
48. Jarvis, G. T., and W. R. Peltier, Convection models and geophysical observations, in *Mantle Convection,* edited by W. R. Peltier, pp. 479–594, Gordon and Breach, New York, 1989.
49. Jemsek, J., and R.P. Von Herzen, Measurement of *in situ* sediment thermal conductivity: continuous-heating method with outrigged probes, in *Handbook of seafloor heat flow,* edited by J.A. Wright and K.E. Louden, pp. 91–120, CRC Press, Inc., Boca Raton, Florida, 1989.
50. Jessop, A. M., *Thermal geophysics, Developments in solid earth geophysics* 17, 306 pp., Elsevier Science Publishers B. V., Amsterdam, 1990.
51. Jessop, A. M., M. A. Hobart, and J. G. Sclater, *The world heat flow data collection-- 1975, Geothermal Series 5,* Energy, Mines and Resources, Earth Physics Branch, Ottawa, Canada, 1976.
52. Jordan, T. H., Global tectonic regionalization for seismological data analysis, *Bull. Seismol. Soc. Am., 71,* 1131–1141, 1981.
53. Kaula, W. M., Absolute plate motions by boundary velocity minizations, *J. Geophys. Res., 80,* 244–248, 1975.
54. Lachenbruch, A.H., Rapid estimation of the topographic disturbances to superficial thermal gradients, *Rev. Geophys. Space Phys., 6,* 365–400, 1968.
55. Lachenbruch, A. H., Crustal temperature and heat production: Implications of the linear heat-flow relation, *J. Geophys. Res., 75,* 3291–3300, 1970.
56. Lachenbruch, A. H., and B. V. Marshall, Heat flow and water temperature fluctuations in the Denmark Strait, *J. Geophys. Res., 73,* 5829–5842, 1968.
57. Lachenbruch, A. H., and B. V. Marshall, Changing climate: geothermal evidence from permafrost in the Alaskan Arctic, *Science, 234,* 689–696, 1986.
58. Lachenbruch, A. H., and J. H. Sass, Heat flow and energetics of the San Andreas Fault zone, *J. Geophys. Res., 85,* 6185–6223, 1980.
59. Lachenbruch, A. H., and J. H. Sass, Heat flow from Cajon Pass, fault strength, and tectonic implications, *J. Geophys. Res., 97,* 4995–5015, 1992.
60. Langseth, M., K. Becker, R. P. Von Herzen, and P. Schultheiss, Heat and fluid flux through sediment on the flank of the mid-Atlantic ridge, *Geophys. Res. Lett., 19,* 517–520, 1992.
61. Langseth, M. G., and R. P. Von Herzen, Heat flow through the floor of the world oceans, in *The Sea, 4,* edited by A. E. Maxwell, pp. 299–352, Interscience, New York, 1970.
62. Langseth, M. G., X. Le Pichon, and M. Ewing, Crustal structure of the mid-ocean ridges, 5, Heat flow through the Atlantic Ocean floor and convection currents, *J. Geophys. Res., 71,* 5321–5355, 1966.
63. Langseth, M. G., M. A. Hobart, and K. Horai, Heat flow in the Bering Sea, *J. Geophys. Res., 85,* 3740–3750, 1980.
64. Le Pichon, X., P. Henry, and S. Lallemant, Accretion and erosion in subduction zones: The role of fluids, in *Annu. Rev. Earth Planet. Sci., 21,* edited by G. W. Wetherill, A. L. Albee and K. C. Burke, pp. 307–331, 1993.
65. Lee, W. H. K., and S. P. Clark, Jr., Heat flow and volcanic temperatures, in *Handbook of Physical Constants, Geol. Soc. Am. Mem. 97,* edited by S. P. Clark, Jr., pp. 483–511, 1966.
66. Lee, W. H. K., and S. Uyeda, Review of heat flow data, in *Terrestrial heat flow, Geophys. Monograph 8* edited by W. H. K. Lee, pp. 87–190, American Geophysical Union, Washington, D.C., 1965.
67. Lewis, T. J., and A. E. Beck, Analysis of heat-flow data- detailed observations in many holes in a small area, *Tectonophys., 41,* 41–59, 1977.
68. Lister, C. R. B., On the thermal balance of a mid-ocean ridge, *Geophys. J. R. astron. Soc., 26,* 515–535, 1972.
69. Lister, C. R. B., "Active" and "passive" hydrothermal systems in the oceanic crust: predicted physical conditions, in *The dynamic environment of the ocean floor,* edited by K. A. Fanning and F. T. Manheim, pp. 441–470, University of Miami, 1982.
70. Liu, M., and C. G. Chase, Evolution of midplate hotspot swells: numerical solutions, *J. Geophys. Res., 94,* 5571–5584, 1989.
71. Louden, K. E., The crustal and lithospheric thickness of the Philippine Sea as compared to the Pacific, *Earth Planet. Sci. Lett., 50,* 275–288, 1980.
72. Louden, K. E., Marine heat flow

data listing, Appendix B, in *Handbook of seafloor heat flow,* edited by J. A. Wright and K. E. Louden, pp. 325–485, CRC Press, Inc., Boca Raton, Florida, 1989.

73. Louden, K. E., and J. A. Wright, Marine heat flow data: A new compilation of observations and brief review of its analysis, in *CRC Handbook of Seafloor Heat Flow,* edited by J. A. Wright and K. E. Louden, pp. 3–67, CRC Press, Inc., Boca Raton, 1989.
74. Lowell, R. P., Topographically driven subcritical hydrothermal convection in the oceanic crust, *Earth Planet. Sci. Lett., 49,* 21–28, 1980.
75. McKenzie, D. P., Some remarks on heat flow and gravity anomalies, *J. Geophys. Res., 72,* 6261–6273, 1967.
76. McKenzie, D. P., Some remarks on the development of sedimentary basins, *Earth Planet. Sci. Lett., 40,* 25–32, 1978.
77. Morgan, P., Constraints on rift thermal processes from heat flow and uplift, *Tectonophysics, 94,* 277–298, 1983.
78. Morgan, P., The thermal structure and thermal evolution of the continental lithosphere, in *Structure and evolution of the continental lithosphere, Physics and chemistry of the earth 15,* edited by H. N. Pollack and V. R. Murthy, pp. 107–193, Pergamon Press, Oxford, 1984.
79. Morgan, P., D. D. Blackwell, R. E. Spafford, and R. B. Smith, Heat flow measurements in Yellowstone Lake and the thermal structure of the Yellowstone Caldera, *J. Geophys. Res., 82,* 3719–3732, 1977.
80. Nishimura, C., and D. Forsyth, The anisotropic structure of the upper mantle in the Pacific, *Geophys. J. R. Astr. Soc., 96,* 203–226, 1989.
81. Palmason, G., On heat flow in Iceland in relation to the Mid-Atlantic Ridge, *Iceland and mid-ocean ridges- Report of a symposium,* pp. 111–127, Geoscience Society of Iceland, Reykjavik, 1967, Reykjavik, Iceland, 1967.
82. Park, C.-H., K. Tamaki, and K. Kobayashi, Age-depth correlation of the Philippine Sea back-arc basins and other marginal basins in the world, *Tectonophys., 181,* 351–371, 1990.
83. Parsons, B., and F. M. Richter, Mantle convection and the oceanic lithosphere, in *Oceanic Lithosphere, (The Sea, vol. 7),* edited by C. Emiliani, pp. 73–117, Wiley-Interscience, New York, 1981.
84. Parsons, B., and J. G. Sclater, An analysis of the variation of ocean floor bathymetry and heat flow with age, *J. Geophys. Res., 82,* 803–827, 1977.
85. Patterson, P. L., and R. P. Lowell, Numerical models of hydrothermal circulation for the intrusion zone at an ocean ridge axis, in *The Dynamic Environment of the Ocean Floor,* edited by K. A. Fanning and F. T. Manheim, pp. 471–492, University of Miami, 1982.
86. Pollack, H. N., and D. S. Chapman, On the regional variation of heat flow, geotherms, and the thickness of the lithosphere, *Tectonophysics, 38,* 279–296, 1977.
87. Pollack, H. N., S. J. Hurter, and J. R. Johnston, Global heat flow data set, World Data Center A for Solid Earth Geophysics, NOAA E/GCI, 325 Broadway, Boulder, CO 80303, USA, 1992.
88. Pollack, H. N., S. J. Hurter, and J. R. Johnston, Heat loss from the earth's interior: analysis of the global data set, *Rev. Geophys., 31,* 267–280, 1993.
89. Polyak, B. G., and Y. A. Smirnov, Relationship between terrestrial heat flow and the tectonics of continents, *Geotectonics, 4,* 205–213, 1968.
90. Powell, W. G., D. S. Chapman, N. Balling, and A. E. Beck, Continental heat-flow density, in *Handbook of Terrestrial Heat-Flow Determination,* edited by R. Haenel, L. Rybach and L. Stegena, pp. 167–222, Kluwer Academic Publishers, Hordrecht, 1988.
91. Ratcliffe, E. H., The thermal conductivities of ocean sediments, *J. Geophys. Res., 65,* 1535–1541, 1960.
92. Revelle, R., and A. E. Maxwell, Heat flow through the floor of the eastern north Pacific Ocean, *Nature, 170,* 199–200, 1952.
93. Richter, F. M., Kelvin and the age of the earth, *J. Geol., 94,* 395–401, 1986.
94. Roy, R. F., D. D. Blackwell, and F. Birch, Heat generation of plutonic rocks and continental heat flow provinces, *Earth Planet. Sci. Lett., 5,* 1–12, 1968.
95. Royden, L., and C. E. Keen, Rifting process and thermal evolution of the continental margin of eastern Canada determined from subsidence curves, *Earth Planet. Sci. Lett., 51,* 343–361, 1980.
96. Sato, H., I. S. Sacks, and T. Murase, Use of laboratory velocity data for estimating temperature and partial melt fraction in the low velocity zone: comparison with heat flow and electrical conductivity studies, *J. Geophys. Res., 94,* 5689–5704, 1989.
97. Sclater, J. G., and J. Francheteau, The implications of terrestrial heat flow observations on current tectonic and geochemical models of the crust and upper mantle of the Earth, *Geophys. J. R. astron. Soc., 20,* 509–542, 1970.
98. Sclater, J. G., J. Crowe, and R. N. Anderson, On the reliability of oceanic heat flow averages, *J. Geophys. Res., 81,* 2997–3006, 1976.
99. Sclater, J. G., C. Jaupart, and D. Galson, The heat flow through oceanic and continental crust and the heat loss of the Earth, *Rev. Geophys. Space Phys., 18,* 269–311, 1980.
100. Sclater, J. G., B. Parsons, and C. Jaupart, Oceans and continents: Similarities and differences in the mechanisms of heat loss, *J. Geophys. Res., 86,* 11,535–11,552, 1981.
101. Shen, P. Y., and A. E. Beck, Paleoclimate change and heat flow density inferred from temperature data in the Superior Province of the Canadian Shield, *Palaeography, Palaeoclimatology, Palaeoecology (Global and Planetary Change Section), 98,* 143–165, 1992.

102. Simmons, G., and K. Horai, Heat flow data, 2, *J. Geophys. Res., 73,* 6608–6629, 1968.
103. Solomon, S. C., and J. W. Head, Mechanisms for lithospheric heat transport on Venus: Implications for tectonic style and volcanism, *J. Geophys. Res., 87,* 9236–9246, 1982.
104. Stacey, F. D., *Physics of the Earth (3rd Edition),* Brookfield Press, Kenmore, 1992.
105. Stein, C. A., and S. Stein, A model for the global variation in oceanic depth and heat flow with lithospheric age, *Nature, 359,* 123–129, 1992.
106. Stein, C. A., and S. Stein, Constraints on Pacific midplate swells from global depth-age and heat flow-age models, in *The Mesozoic Pacific, Geophys. Monogr. Ser. vol. 77,* edited by M. Pringle, W. W. Sager, W. Sliter and S. Stein, pp. 53–76, AGU, Washington, D. C., 1993.
107. Stein, C. A., and S. Stein, Constraints on hydrothermal heat flux through the oceanic lithosphere from global heat flow, *J. Geophys. Res., 99,* 3081-3095, 1994.
108. Turcotte, D. L., and G. Schubert, *Geodynamics: applications of continuum physics to geological problems,* John Wiley, New York, 1982.
109. Van Schmus, W. R., Natural radioactivity of the crust and mantle, *AGU Handbook of Physical Constants,* , Ed., edited by T. J. Ahrens, Am. Geophys. Un., Washington, D.C., this volume, 1994.
110. Verhoogen, J., *Energetics of the Earth,* National Academy of Sciences, Washington, D.C., 1980.
111. Vitorello, I., and H. N. Pollack, On the variation of continental heat flow with age and the thermal evolution of continents, *J. Geophys. Res., 85,* 983–995, 1980.
112. Von Herzen, R. P., and S. Uyeda, Heat flow through the eastern Pacific ocean floor, *J. Geophys. Res., 68,* 4219–4250, 1963.
113. Von Herzen, R. P., R. S. Detrick, S. T. Crough, D. Epp, and U. Fehn, Thermal origin of the Hawaiian swell: Heat flow evidence and thermal models, *J. Geophys. Res., 87,* 6711–6723, 1982.
114. Von Herzen, R. P., M. J. Cordery, R. S. Detrick, and C. Fang, Heat flow and the thermal origin of hotspot swells: the Hawaiian swell revisited, *J. Geophys. Res., 94,* 13,783–13,799, 1989.
115. Wang, K., T. J. Lewis, and A. M. Jessop, Climatic changes in central and eastern Canada inferred from deep borehole temperature data, *Palaeogeolgraphy, Palaeoclimatology, Palaeocology (Global and Planetary Change Section), 98,* 129–141, 1992.
116. Watanabe, T., M. G. Langseth, and R. N. Anderson, Heat flow in back-arc basins of the western Pacific, in *Island Arcs, Deep Sea Trenches, and Back-Arc Basins,* edited by M. Talwani and W. Pitman, III, pp. 137–162, American Geophysical Union, Washington, D.C., 1977.
117. Williams, D. L., and R. P. Von Herzen, Heat loss from the earth: New estimate, *Geology, 2,* 327–328, 1974.
118. Williams, D. L., R. P. Von Herzen, J. G. Sclater, and R. N. Anderson, The Galapagos spreading centre: Lithospheric cooling and hydrothermal circulation, *Geophys. J. R. astr. Soc., 38,* 587–608, 1974.
119. Wolery, T. J., and N. H. Sleep, Hydrothermal circulation and geochemical flux at mid-ocean ridges, *J. Geol., 84,* 249–275, 1976.
120. Wolery, T. J., and N. H. Sleep, Interactions of geochemical cycles with the mantle, in *Chemical Cycles in the Evolution of the Earth,* edited by C. B. Gregor, R. M. Garrels, F. T. Mackenzie and J. B. Maynard, pp. 77–103, John Wiley and Sons, Inc., New York, 1988.
121. Woods, M. T., J.-J. Leveque, E. A. Okal, and M. Cara, Two-station measurements of Rayleigh wave group velocity along the Hawai'ian swell, *Geophys. Res. Lett., 18,* 105–108, 1991.
122. Yamano, M., J. P. Foucher, M. Kinoshita, A. Fisher, and R. D. Hyndman, Heat flow and fluid flow regime in the western Nankai accretionary prism, *Earth Planet. Sci. Lett., 109,* 451–462, 1992.

Composition of the Solar System, Planets, Meteorites, and Major Terrestrial Reservoirs

Horton E. Newsom

1. INTRODUCTION

The compositions of the Sun, meteorites and planets provide important clues to the origin and evolution of the solar system, and the major fractionations involved in the formation of the planets. This article tabulates and discusses the current compilations of elemental abundances for the solar system, meteorites, and some of the terrestrial planets. Planetary compositions are only reported for bodies from which actual samples were analyzed or chemical data have been obtained by other means. Estimates of several authors are usually tabulated because the data sets used, and the approaches taken, are often dramatically different. The variability among the estimates, therefore, provides some idea of the uncertainties in the estimates.

2. SOLAR SYSTEM ABUNDANCES

The composition of the solar system was established by astrophysical processes, starting with the light elements, such as H, He and Li, produced in the Big Bang, approximately 20 Ga ago. The heavier elements were produced over time by processes involving the evolution and destruction of massive stars (primarily stars greater than 9 solar masses), and processes in novae, both of which enriched the galactic annulus containing the sun by the time the solar system was formed [86,19]. The formation of the solar system is best dated at 4.559 ± 0.004 Ga ago, the Pb isotope age of calcium aluminum rich inclusions from the Allende CV chondrite meteorite [73]. The formation of the solar system occurred by collapse of a dense molecular cloud core which contained the material that now makes up the planets, meteorites and the Sun. This relationship is indicated by the similarity between elemental abundance ratios for non-gaseous elements in the CI carbonaceous chondrites and abundance ratios in the sun [4, Figure 1]. The CI chondrites are volatile-rich meteorites that consist largely of clay-like minerals, which have the most solar-like chemical compositions of all the primitive meteorite types (Table 1). The sun contains more than 99.99% of the mass of the solar system, and abundance ratios for many non-gaseous elements have been measured in the sun by spectroscopic techniques, and by measurements of the composition of the solar wind and solar energetic particles (Table 2). The composition of dust from comet P/Halley, as measured by the Vega and Giotto spacecraft is similar to CI chondrites, but enriched in the volatile elements H, C and N, making this the most primitive meteoritic material [46]. Comets are thought to have formed in the Uranus-Neptune zone or just beyond.

Recent work on the abundances in CI meteorites by Dreibus et al. [22] and Spettel et al. [64] have provided improvements for some elements to the compilation by Anders and Grevesse [4], and Wasson and Kallemeyn [80]. The average sulfur content of CI meteorites reported by Anders and Grevesse [4] of 6.25% is high because of the inclusion of data for Ivuna, Alais and Tonk. The S abundance for Orgeil of 5.41 wt% (Table 1), however, is consistent with the S/Se ratio for all groups of carbonaceous chondrites [22]. Compared to the Anders and Grevesse [4] compilation, data from Mainz and UCLA for the elements Se, Au, and Ir [averaged in Table 1 as the Spettel et al., 1993[64] compilation] show good agreement and are probably

H. E. Newsom, University of New Mexico, Department of Geology, Albuquerque, NM 87131

Global Earth Physics
A Handbook of Physical Constants
AGU Reference Shelf 1

somewhat better. Agreement between the averaged Mainz data and UCLA data, and the Anders and Grevesse [4] data for most of the elements is generally better than plus or minus 3%. Earlier compilations of CI data include Anders and Ebihara [3], and Palme et al. [51].

The isotopic composition of the solar system reported by Clark [18] has also been updated by Anders and Grevesse [4, Table 3]. Some solar system material contains elements whose isotopic systems exhibit anomalies or evidence of extinct radionuclides, which have been interpreted in terms of different presolar contributions to the solar nebula [e.g. 39]. The origin by nuclear or chemical processes of the most widespread of the isotopic anomalies, the variations in oxygen isotopes, is still in doubt [71]. Clayton et al. [20] argued that two gaseous reservoirs, one "terrestrial", one ^{16}O rich, are required to explain the O-isotope variations in meteorites. Whatever their origin, the variations in the ratios of $^{17}O/^{16}O$ and $^{18}O/^{16}O$ (Figure 2) is the most useful system for distinguishing different planetary materials. The terrestrial fractionation line is due to mass fractionation of the O isotopes in terrestrial materials. The carbonaceous chondrite anhydrous minerals line may represent mixing between different components. The Earth and Moon fall on the same fractionation line, possibly indicating a close relationship between the two bodies.

During the formation of the solar system, the material now in the terrestrial planets and meteorites lost substantial amounts of the gaseous elements, such as H and He. Great diversity in different meteorite types was established due to variable oxidation states in different nebula reservoirs, and because fractionations of different solid components led to other chemical variations. Much of the material was also thermally processed, resulting in chemical signatures of evaporation and condensation that are recorded in the meteorites and planets. Some of the thermal events were of a transient nature, resulting in the formation of the round silicate chondrules characteristic of most chondritic meteorites. Surprisingly, the CI chondrites do not contain chondrules, but they do contain fragments of what are interpreted to have originally been chondrules. The thermal events resulted in chemical fractionations that can be best characterized by the calculated condensation temperature, which is a measure of volatility. These condensation temperatures represent the temperature at which 50% of the element would be condensed from a system with a bulk solar system composition at a given pressure (Table 1).

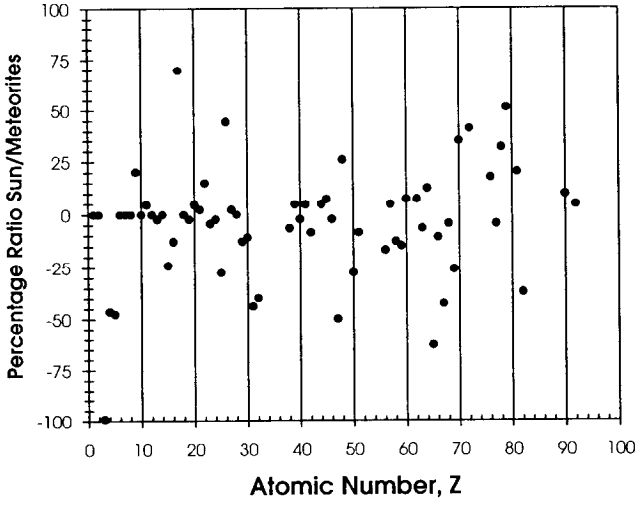

Fig. 1. Comparison of photospheric ("solar") and solar-system ("meteoritic") abundances from [4] with permission.

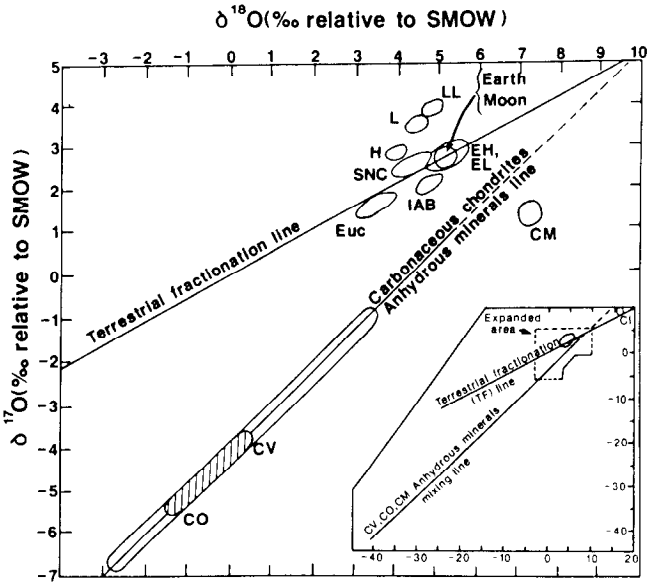

Fig. 2. The relationship between $\delta^{17}O$ and $\delta^{18}O$ for the Earth, Moon, and meteorites from [69] with permission. The terms $\delta^{17}O$ (‰ relative to SMOW) and $\delta^{18}O$ (‰ relative to SMOW) refer to the ratios of $^{17}O/^{16}O$ and $^{18}O/^{16}O$, expressed in parts per thousand relative to Standard Mean Ocean Water.

The chemical elements can be classified based on their condensation temperature [50, Table 1]: 1. The refractory elements (Ca, Al, Ti, Zr, REE, Ir, Os, etc.) make up about 5% of the total condensible matter. 2. Mg-silicates (forsterite Mg_2SiO_4, enstatite $MgSiO_3$) and metal (FeNi) represent the major fraction of condensible matter. 3. Moderately volatile elements (Na, K, Cu, Zn, etc.) have condensation temperatures, from below Mg-silicate and FeNi, down to S (as FeS). 4. Highly volatile elements (In, Cd, Pb, etc) have

condensation temperatures below FeS. Variations in the abundances of these different groups of elements are also characteristic of the different meteorite groups.

Meteorites can be divided into two major types, chondrites, which never experienced wholesale melting after accretion from the solar nebula, and achondrites, which are igneous rocks that are thought to be the result of melting and crystallization on their parent asteroids. Classification schemes from Wasson [79] are shown in Tables 4 and 5, and also discussed by Sears and Dodd [62]. Data for some types of chondritic meteorites other than CI are listed in Table 6. [80]. The CI, CM, CO, CK and CV chondrites are called carbonaceous chondrites, because of their dark appearance and high C content. These meteorites are also highly oxidized, The CI chondrites contain essentially no iron metal. The H, L and LL chondrites are called the ordinary chondrites because they are the most abundant types of meteorites in the world's collections; they are also intermediate in oxidation state. The EH and EL chondrites are highly reduced enstatite chondrites, which contain essentially no oxidized iron. Several new types of chondritic meteorites are in the process of being characterized. Data for a limited number of elements for the CK (Karoonda-type) carbonaceous chondrites are listed in Table 6 [36]. The CK meteorites have refractory enrichments intermediate between the CV and CO, CM classes. Their oxygen isotopes are similar to CO chondrites, and the olivine compositions range from Fa 29-33 [36]. Other groups of chondrites are the CR (Renazzo-type) carbonaceous chondrites [83, 13], the R (Carlisle Lakes) chondrites, which have more affinities with ordinary and enstatite chondrites [61], the Kakangari-type chondrites [84] and the Bencubbin-Weatherford chondrites [85]. The CH chondrites (ALH85085, ACFER 182, and paired samples ACFER 207 and ACFER 214) are enriched in Fe metal and siderophile elements [13].

Chondritic meteorites provide information about the chemical fractionations and processes that occurred in the solar nebula, and the nature of the building blocks for the planets [37, part 7]. Solar system material has been affected by different fractionation processes during the formation of the solar system, and within the terrestrial planets [50]. These fractionations were caused by variations in the abundance of refractory components, olivine, iron metal, and loss of volatile elements during condensation or heating. Refractory elements vary by a factor of two within chondritic meteorites due to variations in high temperature condensates, such as Ca, Al-rich inclusions in carbonaceous chondrites. Variations of Mg/Si ratios by 30% in chondrites are ascribed to fractionation of olivine. The depletion of volatile elements relative to CI chondrite abundances is observed in chondritic meteorites, and in the compositions of differentiated planets and asteroids. The abundances of siderophile elements (elements with an affinity for iron metal) are enriched or depleted by a factor of two between the metal-depleted LL chondrites and the metal-enriched CH chondrites [13]. Siderophile element abundances are often depleted in differentiated bodies because of core formation. Figure 3 illustrates the depletions of volatile elements in the CM chondrites and the Bulk Silicate Earth (BSE) composition. The additional depletion of siderophile elements (both refractory and volatile) in the BSE due to core formation is evident in Figure 3.

3. ASTEROIDS

Meteorites are thought to come from parent bodies in the asteroid belt between Mars and Jupiter (exceptions include the SNC meteorites, probably from Mars, see below, and lunar meteorites). Spectrophotometry of asteroids has resulted in the development of classification schemes which reflect the chemical and mineralogical nature of the asteroids. The possible connection between known meteorite types and asteroid spectral types is described in Table 7. An unanswered question is whether these meteorites originally accreted in the asteroid belt, or whether their parent asteroids were transported from other parts of the solar system to the asteroid belt and stored in their present location? The regular distribution of asteroid types in the asteroid belt (Figure 4) suggests that the asteroids have *not*

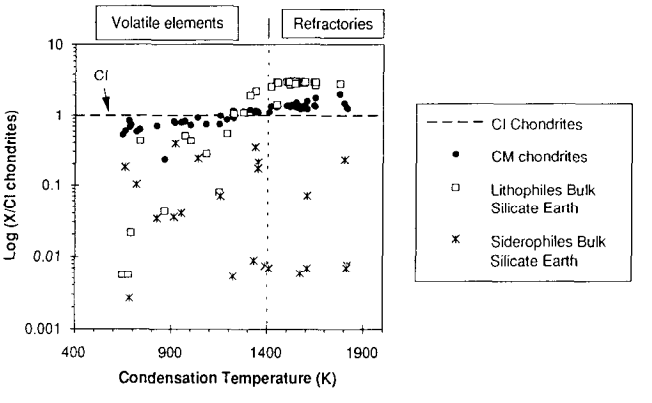

Fig. 3 Plot of the log ratio of the abundance of all elements in CM chondrites (Table 2) and in the Bulk Silicate Earth [56, Table 7], normalized to CI chondrites [4, Table 1], and plotted versus the 50% condensation temperature of the elements at 10^{-4} atm total pressure, a measure of the volatility of the elements [80]. The figure illustrates the depletion of volatile elements in the CM chondrites and the Bulk Silicate Earth, as well as the additional depletion of siderophile elements in the Bulk Silicate Earth.

been widely transported, which implies that the meteorites in our collections are probably originally derived from a limited portion of the solar system.

The achondrite meteorites are igneous rocks and include several varieties. The Howardite, Eucrite and Diogenite clan, which are thought to come from the same parent body, called either the HED parent body, or the Eucrite Parent Body (EPB). The Eucrite meteorites are basalts containing plagioclase and pyroxene, the Diogenites are ultramafic rocks containing pyroxene and olivine, while the Howardites are brecciated mixtures of material similar to Eucrites and Diogenites. Thus the EPB meteorites represent portions of the parent bodies' crust. The EPB meteorites record evidence of core formation and igneous processes that occurred soon after the formation of the solar system [30]. Lead isotope data suggest that the EPB samples crystallized shortly after the formation of the most primitive meteorites. For example, data for the Juvinas eucrite suggests a melting age of 4.539 ± 0.004 Ga, only 20 Ma after the formation of the Allende carbonaceous chondrite.

The bulk composition of the Eucrite Parent Body has been estimated (Table 8), although the lack of mantle rocks from the EPB is a great handicap. Dreibus and Wänke [23] estimated the bulk composition by using mixing diagrams for EPB meteorites to obtain a composition with chondritic ratios of the refractory elements, which was then added to an olivine composition. The Vizgirda and Anders [74] and Hertogen et al. [29], and Morgan et al. [45] compositions were obtained by using fractionation factors from the Moon and Earth, which relate the composition of basalts to the bulk composition by the processes of core and crust formation. Consolmagno and Drake [21] calculated a metal free bulk composition based on trace element constraints for the mode of the eucrite source regions and mineral compositions from the work of Stolper [66]. Jones [33] modeled the bulk composition as a mixture of 25% eucrite and 75% olivine. Estimates of the amount of metal in the parent body, based on the depletions of siderophile elements in eucrites, include: 8% Hertogen et al. [29], 12.9% Morgan et al. [45], and 20% - 40% Hewins and Newsom [30].

4. TERRESTRIAL PLANET COMPOSITIONS

In-situ chemical measurements have been made for all of the terrestrial planets except Mercury. Several Soviet Venera and Vega landers made chemical analyses of the surface of Venus. For the Moon, we have samples returned by United States manned and Soviet unmanned spacecraft, as well as lunar meteorites. For Mars we have the United States Viking lander measurements, and the SNC meteorites, which are thought to come from Mars. The properties of the Moons of Mars: density, albedo, color and spectral reflectivity are similar to C-type asteroids, although their origin as captured asteroids is not completely certain [16]. The relationship between the esitimated compositions of the planets and the solar system composition, provide clues to the formation of the planets. For example, the high metal/silicate ratio for Mercury and the low ratio for the Moon suggests the role of giant impacts.

4.1. Mercury, Venus

The compositions of Mercury and Venus are not well known (Table 9). For Mercury the available data includes density information and very limited spectroscopic information suggesting a low FeO content (< 5.5 wt%) [26]. The high mean density of Mercury (5.43 g cm^{-3}) sets this planet apart from the other terrestrial planets, and implies an iron rich core making up 65 wt% to 68 wt% of the planet [7]. Based on this information and cosmochemical constraints, several authors have come to the conclusion that the high density probably cannot have been produced by a simple

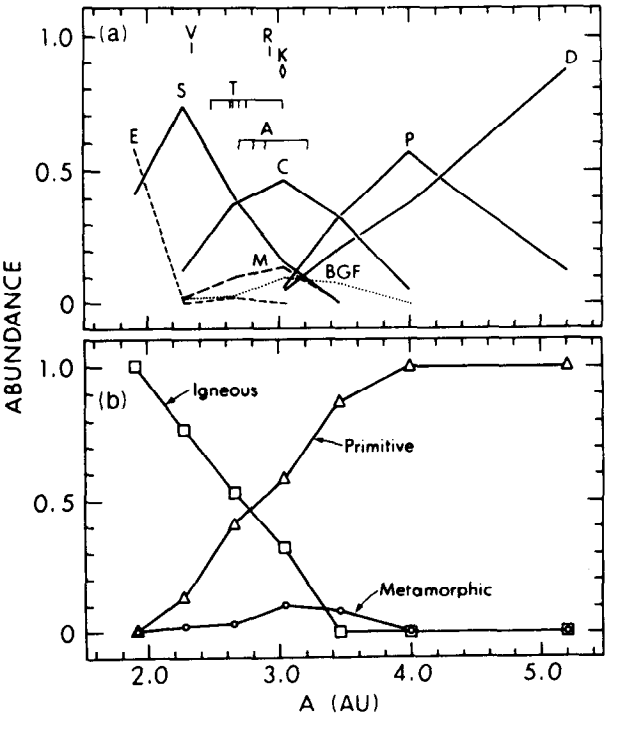

Fig. 4. Occurrence in the asteroid belt of asteroid spectral types from [12] with permission. (a) Distribution of the taxonomic types of Tholen [72], plus K class of Bell [11]. The actual heliocentric locations of the individual V, T, A, R and K asteroids are indicated by tick marks. (b) Distribution in the asteroid belt of the asteroid superclasses of Bell [10]. The assumption, however, that the S-type meteorites are differentiated, and that T, B, G and F types are metamorphic is still very speculative.

accretion model [e.g. 40, 25]. This has led to giant impact models, such as the vaporization model of Fegley and Cameron [25] which involves a giant impact that strips off much of the silicate mantle of Mercury.

An estimate of the bulk composition of Venus based on cosmochemical grounds [44] is also listed in Table 9. Chemical analyses of the Venus surface have been obtained by spacecraft of the former Soviet Union and the chemistry of the surface has been considered at length [8, 24], but this data has not yet been incorporated into models of the bulk planetary composition. Goettel [26] has also estimated the composition of the core of Mercury as 88-91 wt% Fe, 6.5-7.5 wt% Ni, and 0.5-5 wt% S.

4.2. Mars (SNC parent body)

Information on the composition of the silicate portion of Mars is based on cosmochemical models, and on the composition of the Shergottite, Nakhlite and Chassignite meteorites (SNC's) (Table 10). The martian origin of the SNC's is strongly supported by their young ages (about 1.3 B.Y.), and the similarity of their trapped Ar and Xe isotopic compositions to measurements of the martian atmosphere by Viking [52]. The composition of Wänke and Dreibus [76] is based on element ratios in the SNC meteorites. Anderson's model [5] is based on a mixture of 75% type 3 carbonaceous chondrites and 25% ordinary chondrites, which was chosen in order to obtain a metal core composition consistent with geophysical parameters for Mars. Morgan and Anders [55] used the abundances of index elements obtained from orbital gamma-ray observations, Viking observations, and geophysical constraints, in order to relate the composition of the planet to chondrites via four nebular fractionation processes. The composition of Ringwood [55] consists of a mixture of 30% of a low-temperature condensate, represented by the Orgeuil CI chondrite, and 70% of a high-temperature devolatilized metal-rich component. For additional data on Mars, including mineralogical models, see Longhi et al. [41].

4.3. Moon

The chemistry of the Moon has been extensively studied based on remote sensing and on the lunar samples returned from the Moon by the Apollo astronauts, the unmanned Luna probes by the former U.S.S.R. and from lunar meteorites. Detailed chemical information for a large number of different types of lunar material is summarized in the *Lunar Source Book* [28]. Compared to the Earth, the Moon has a very low volatile element content and a higher FeO content. The Moon has a low mean density of 3.34 g cm^{-3} implying a low iron content. The existence of a lunar metal core has not been conclusively proven, although substantial indirect geophysical data supports the presence of a small core of 350-500 km radius [35]. Constraints due to the lunar properties mentioned above, and the angular momentum of the Earth-Moon system have led to a theory for the origin of the Moon by a giant impact of a Mars-sized planet into the Earth [48]. Table 11 contains estimates of the bulk silicate composition of the Moon, and an estimate of the composition of the lunar highlands crust. Anders [2] used a cosmochemical approach involving 6 components to estimate the bulk Moon composition, and estimated a metal content of 6.1% and a troilite content of 1.1%. The O'Neill [49] composition consists of 82.5% of the present Earth's mantle, 0.2% of "Hadean matte" (Fe-Ni-S-O liquid), 13.3% volatile free CI material, and 4% H chondrite material. The Taylor [68] composition is based on heat flow, density data, the composition of the highland crust, and elemental ratios in lunar samples. Taylor [68] also estimated a metal content of 2.3%. Wänke et al. [78] used a mixing model for lunar highlands samples between lunar anorthosites and a "primary component". The primary component consists of a refractory and non-refractory component in the ratio of 21 to 79. For the bulk Moon, a composition was derived consisting of a 50-50 mixture (constrained by the lunar K/La ratio) of the refractory and non-refractory portions. The metal content was also estimated at 1.5%. The bulk silicate composition estimated by Jones and Delano [34] is based on a mixture of an early olivine residuum, a later olivine cumulate, and a primitive liquid composition from pristine lunar glasses. Ringwood et al. [57] used a mixture of a komatiite component (essentially the primary component of Wänke et al. [78]), and its liquidus olivine composition.

4.4. Earth

The Earth is the best studied planet, although the composition of the bulk Earth, and its major parts are still uncertain for many elements. The bulk composition of the silicate portion of the Earth is broadly chondritic in composition, but no presently identified chondrite type represents an exact match [69]. The Earth is divided into several major parts, including the core (32 wt%), lower mantle (48 wt%), upper mantle (20 wt%), and continental crust (0.4 wt%). The composition of the Bulk Silicate Earth is based on samples available for chemical analysis from the upper mantle and crust. The continental crust can also be divided into upper and lower parts. The composition of the ancient continental crust has also been investigated in order to study the chemical evolution of the crust with time. The compositions of the different reservoirs in the Earth provides clues to the major processes involved in the evolution of the Earth, such as core formation and the formation of the continental crust. The composition of the continental crust is also important for determining the bulk abundance in the Earth because many incompatible elements, which are

concentrated in the continental crust. The continental crust, for example, may contain more than 80% of the highly mobile elements Cs, Cl, and Br [77]. This type of data has even been extended by some authors to include estimates of the enrichment of some elements in ore deposits relative to the continental crust [15,42].

4.4.1. Core. The Earth's core consists largely of Fe-metal, along with Ni and Co, in the same ratio to Fe as observed in solar system material, such as the CI chondrites (approximately 5.8 wt% Ni, 0.3 wt% Co, Table 12). These compositions are observed in iron meteorites, which are thought to be the cores of melted asteroids that formed at relatively low pressures. However, geophysical evidence indicates that the Earth's metal core is 10% less dense than pure Fe-Ni-Co, indicating the presence of a significant amount of a light element which is not observed in iron meteorites. The presence of the light element may be due to processes that only occur at very high pressures within the Earth. The nature of this light element is currently controversial, with the main candidates being oxygen or sulfur. A recent estimate of Ahrens and Jeanloz [1] assuming sulfur is the light element, gives a sulfur content of 11 ± 2%, based on experimental evidence. Experimental work at pressures approximating the core mantle boundary has shown that high pressure mantle minerals, such as (Mg, Fe)SiO_2 perovskite, will react chemically with iron to form alloys [38]. This experimental result may explain the light element component, and the existence of the D" (D-double-prime) layer at the core mantle boundary observed in seismic studies. Such reactions could be changing the composition of the core over time.

4.4.2 Bulk Silicate Earth (primitive mantle). The composition of the silicate portion of the Earth (the mantle plus crust) has been estimated based on measurements of upper mantle and crustal rocks (Table 13). The composition of the upper mantle is surprisingly homogeneous for many elements. Elements that are compatible in mantle minerals, such as Co and Ni, have abundances in primitive mantle nodules that do not vary by more than plus or minus 10% [65]. The abundances of poorly known incompatible elements can be determined relative to well known incompatible elements. For example, Mo is constant within plus or minus a factor of two relative to the light rare earth element Ce in terrestrial basalts [47]. The composition of Anderson [6] is a mixture of five components, ultramafic rocks, orthopyroxene, Mid-ocean Ridge Basalt (MORB), the continental crust, and kimberlite, combined to achieve chondritic relative abundances of refractory elements. Taylor and McLennan [70] used a mixture of cosmochemical components for refractory elements, crustal data for volatile elements and mantle nodule data for siderophile element data. The Ringwood [56] "pyrolite" primitive mantle composition is based on complementary compositions of melts and residual mantle material. A similar approach was used by Sun [67]. Wänke et al. [77], updating Jagoutz et al. [32] have used the composition of mantle nodules to represent the depleted upper mantle, combined with a continental crust composition. Zindler and Hart [89] used ratios of refractory elements in lherzolites together with cosmochemical constraints. The bulk Earth composition of Morgan and Anders [44] used 7 cosmochemical components constrained by the mass of the core, the U and Fe abundance, and the ratios K/U, Tl/U, FeO/MnO.

4.4.3. Bulk Continental Crust. Estimates of the composition of the continental crust are listed in Table 14. The bulk continental crustal composition of Taylor and McLennan [70] (their Table 3.5) is comprised of 75% of their Archean crustal composition (Table 9) and 25% of their Andesite model (Table 9), to represent the relative contributions of Archean and Post-Archean crustal growth processes. A similar approach was taken by Weaver and Tarney [81], who combined composition estimates for the upper crust, Archean middle crust, Archean lower crust and post-Archean middle and lower crust in the proportions 8:3:9:4.

Other estimates of the composition of the continental crust include those of Holland and Lambert [31], Poldevaart [53], Ronov and Yaroshevsky [59], Ronov and Migdisov [60], and Wedepohl [82]. For a summary of other major element estimates of the composition of the bulk continental crust see Table 3.4 in Taylor and McLennan [70].

4.4.4 Other crustal abundances. The continental crust can be broken down into other divisions that provide useful constraints in terms of the formation of the continental crust (Table 15). The composition of the upper continental crust estimated by Taylor and McLennan [70] is based on sampling programs in the Canadian shield for major elements, and analyses of sedimentary rocks for trace elements. Rare-earth distributions of a composite of 40 North American shales were compiled by Haskin et al. [27] to approximate the composition of the upper continental crust. The lower continental crust composition of Taylor and McLennan [70] is based on their bulk continental crustal composition, from which their upper continental crustal composition (Table 15) has been subtracted. The composition of the bulk Archean continental crust estimated by Taylor and McLennan [70], is based on a mixture of basic and felsic rocks consistent with the observed heat flow. Taylor and McLennan [70] present a composition for the post-Archean continental crust, the "Andesite model", which is based on the average composition of erupted material at island arcs.

TABLE 1. Solar-System abundances of the Elements Based on Meteorites and Condensation Temperatures

Element		Solar System atoms/10^6Si Anders & Grevesse [1989][4]	Uncertainity s (%)	CI Chondr. Anders & Grevesse [1989][4]		CI Chondr. Wasson & Kallemeyn [1988][80]	CI Chondr. Spettel et al. [1993][64]	Calculated Condensation Temp at 10^{-4} atm Wasson [1985][79]
1	H	2.79×10^{10}	----	----	----	2	----	----
2	He	2.72×10^{9}	----	----	----	----	----	----
3	Li	57.1	9.2	1.5	ppm	1.57	----	1225 K
4	Be	0.73	9.5	24.9	ppb	27	----	----
5	B	21.2	10	870	ppb	1200	----	----
6	C	1.01×10^{7}	----	----	----	3.2	----	----
7	N	3.13×10^{6}	----	----	----	1500	----	----
8	O	2.38×10^{7}	10	----	----	46.0	----	----
9	F	843	15	60.7	ppm	64	----	736 K
10	Ne	3.44×10^{6}	14	----	----	----	----	----
11	Na	5.74×10^{4}	7.1	5000	ppm	4900	4982	970 K
12	Mg	1.074×10^{6}	3.8	9.89	%	9.7	9.6	1340 K
13	Al	8.49×10^{4}	3.6	8680	ppm	8600	8650	1650 K
14	Si	1.00×10^{6}	4.4	10.64	%	10.5	----	1311 K
15	P	1.04×10^{4}	10	1220	ppm	1020	----	1151 K
16	S	5.15×10^{5}	13	6.25	%	5.9	5.41	648 K
17	Cl	5240	15	704	ppm	680	----	863 K
18	Ar	1.01×10^{5}	6	----	----	----	----	----
19	K	3770	7.7	558	ppm	560	544	1000 K
20	Ca	6.11×10^{4}	7.1	9280	ppm	9200	9510	1518 K
21	Sc	34.2	8.6	5.82	ppm	5.8	5.9	1644 K
22	Ti	2400	5.0	436	ppm	420	----	1549 K
23	V	293	5.1	56.5	ppm	55	54.3	~1450 K
24	Cr	1.35×10^{4}	7.6	2660	ppm	2650	2646	1277 K
25	Mn	9550	9.6	1990	ppm	1900	1933	1190 K
26	Fe	9.00×10^{5}	2.7	19.04	%	18.2	18.23	1336 K
27	Co	2250	6.6	502	ppm	508	506	1351 K
28	Ni	4.93×10^{4}	5.1	1.10	%	1.07	1.077	1354 K
29	Cu	522	11	126	ppm	121	----	1037 K
30	Zn	1260	4.4	312	ppm	312	323	660 K
31	Ga	37.8	6.9	10.0	ppm	9.8	9.71	918 K
32	Ge	119	9.6	32.7	ppm	33	----	825 K
33	As	6.56	12	1.86	ppm	1.84	1.81	1157 K
34	Se	62.1	6.4	18.6	ppm	19.6	21.3	684 K
35	Br	11.8	19	3.57	ppm	3.6	3.5	~690 K
36	Kr	45	18	----	----	----	----	----
37	Rb	7.09	6.6	2.30	ppm	2.22	----	~1080 K
38	Sr	23.5	8.1	7.80	ppm	7.9	----	----
39	Y	4.64	6.0	1.56	ppm	1.44	----	1592 K
40	Zr	11.4	6.4	3.94	ppm	3.8	----	~1780 K
41	Nb	0.698	1.4	246	ppb	270	----	~1550 K
42	Mo	2.55	5.5	928	ppb	920	----	1608 K
44	Ru	1.86	5.4	712	ppb	710	----	1573 K

TABLE 1. (Continued)

Element		Solar System atoms/10^6Si Anders & Grevesse [1989][4]	Uncertainity s (%)	CI Chondr. Anders & Grevesse [1989][4]		CI Chondr. Wasson & Kallemeyn [1988][8]	CI Chondr. Spettel et al. [1993][7]	Calculated Condensation Temp at 10^{-4} atm Wasson [1985][16]
45	Rh	0.344	8	134	ppb	134	----	1391 K
46	Pd	1.39	6.6	560	ppb	560	----	1334 K
47	Ag	0.486	2.9	199	ppb	208	----	952 K
48	Cd	1.61	6.5	686	ppb	650	----	----
49	In	0.184	6.4	80	ppb	80	----	----
50	Sn	3.82	9.4	1720	ppb	1720	----	720 K
51	Sb	0.309	18	142	ppb	153	----	912 K
52	Te	4.81	10	2320	ppb	2400	----	680 K
53	I	0.90	21	433	ppb	500	----	----
54	Xe	4.7	20	----	----	----	----	----
55	Cs	0.372	5.6	187	ppb	183	----	----
56	Ba	4.49	6.3	2340	ppb	2300	----	----
57	La	0.4460	2.0	234.7	ppb	236	247	1520 K
58	Ce	1.136	1.7	603.2	ppb	616	----	1500 K
59	Pr	0.1669	2.4	89.1	ppb	92.9	----	1532 K
60	Nd	0.8279	1.3	452.4	ppb	457	----	1510 K
62	Sm	0.2582	1.3	147.1	ppb	149	145	1515 K
63	Eu	0.0973	1.6	56.0	ppb	56.0	57	1450 K
64	Gd	0.3300	1.4	196.6	ppb	197	----	1545 K
65	Tb	0.0603	2.2	36.3	ppb	35.5	----	1560 K
66	Dy	0.3942	1.4	242.7	ppb	245	253	1571 K
67	Ho	0.0889	2.4	55.6	ppb	54.7	----	1568 K
68	Er	0.2508	1.3	158.9	ppb	160	----	1590 K
69	Tm	0.0378	2.3	24.2	ppb	24.7	----	1545 K
70	Yb	0.2479	1.6	162.5	ppb	159	162	1455 K
71	Lu	0.0367	1.3	24.3	ppb	24.5	26	1597 K
72	Hf	0.154	(1.9)	104	ppb	120	----	1652 K
73	Ta	0.0207	1.8	14.2	ppb	16	----	~1550 K
74	W	0.133	5.1	92.6	ppb	100	----	1802 K
75	Re	0.0517	9.4	36.5	ppb	37	----	1819 K
76	Os	0.675	6.3	486	ppb	490	486	1814 K
77	Ir	0.661	6.1	481	ppb	460	459	1610 K
78	Pt	1.34	7.4	990	ppb	990	----	1411 K
79	Au	0.187	15	140	ppb	144	152	1225 K
80	Hg	0.34	12	258	ppb	390	----	----
81	Tl	0.184	9.4	142	ppb	142	----	----
82	Pb	3.15	7.8	2470	ppb	2400	----	----
83	Bi	0.144	8.2	114	ppb	110	----	----
90	Th	0.0335	5.7	29.4	ppb	29	----	1545 K
92	U	0.0090	8.4	8.1	ppb	8.2	----	1420 K

TABLE 2. Abundances in the Solar Photosphere
($\log N_H=12$)[4]

Element		Photosphere*		Meteorites†	Phot.-Met*
1	H	12.00	----	[12.00]	----
2	He	[10.99	±0.035]	[10.99]	----
3	Li	1.16	±0.1	3.31 ±0.04	-2.15
4	Be	1.15	±0.10	1.42 ±0.04	-0.27
5	B	(2.6	±0.3)	2.88 ±0.04	(-0.28)
6	C	8.56	±0.04	[8.56]	----
7	N	8.05	±0.04	[8.05]	----
8	O	8.93	±0.035	[8.93]	----
9	F	4.56	±0.3	4.48 ±0.06	+0.08
10	Ne	[8.09	±0.10]	[8.09 ±0.10]	----
11	Na	6.33	±0.03	6.31 ±0.03	+0.02
12	Mg	7.58	±0.05	7.58 ±0.02	0.00
13	Al	6.47	±0.07	6.48 ±0.02	-0.01
14	Si	7.55	±0.05	7.55 ±0.02	0.00
15	P	5.45	±(0.04)	5.57 ±0.04	-0.12
16	S	7.21	±0.06	7.27 ±0.05	-0.06
17	Cl	5.5	±0.3	5.27 ±0.06	+0.23
18	Ar	[6.56	±0.10]	[6.56 ±-0.10]	----
19	K	5.12	±0.13	5.13 ±0.03	-0.01
20	Ca	6.36	±0.02	6.34 ±0.03	+0.02
21	Sc	3.10	±(0.09)	3.09 ±0.04	+0.01
22	Ti	4.99	±0.02	4.93 ±0.02	+0.06
23	V	4.00	±0.02	4.02 ±0.02	-0.02
24	Cr	5.67	±0.03	5.68 ±0.03	-0.01
25	Mn	5.39	±0.03	5.53 ±0.04	-0.14
26	Fe	7.67	±0.03	7.51 ±0.01	+0.16
27	Co	4.92	±0.04	4.91 ±0.03	+0.01
28	Ni	6.25	±0.04	6.25 ±0.02	0.00
29	Cu	4.21	±0.04	4.27 ±0.05	-0.06
30	Zn	4.60	±0.08	4.65 ±0.02	-0.05
31	Ga	2.88	±(0.10)	3.13 ±0.03	-0.25
32	Ge	3.41	±0.14	3.63 ±0.04	-0.22
33	As	----	----	2.37 ±0.05	----
34	Se	----	----	3.35 ±0.03	----
35	Br	----	----	2.63 ±0.08	----
36	Kr	----	----	3.23 ±0.07	----
37	Rb	2.60	±(0.15)	2.40 ±0.03	+0.20
38	Sr	2.90	±0.06	2.93 ±0.03	-0.03
39	Y	2.24	±0.03	2.22 ±0.02	+0.02
40	Zr	2.60	±0.03	2.61 ±0.03	-0.01
41	Nb	1.42	±0.06	1.40 ±0.01	+0.02
42	Mo	1.92	±0.05	1.96 ±0.02	-0.04
44	Ru	1.84	±0.07	1.82 ±0.02	+0.02
45	Rh	1.12	±0.12	1.09 ±0.03	+0.03
46	Pd	1.69	±0.04	1.70 ±0.03	-0.01
47	Ag	(0.94	±0.25)	1.24 ±0.01	(-0.30)
48	Cd	1.86	±0.15	1.76 ±0.03	+0.10
49	In	(1.66	±0.15)	0.82 ±0.03	(+0.84)
50	Sn	2.0	±(0.3)	2.14 ±0.04	-0.14
51	Sb	1.0	±(0.3)	1.04 ±0.07	-0.04

TABLE 2. (Continued)

Element		Photosphere*		Meteorites†	Phot.-Met*
52	Te	----	----	2.24 ±0.04	----
53	I	----	----	1.51 ±0.08	----
54	Xe	----	----	2.23 ±0.08	----
55	Cs	----	----	1.12 ±0.02	----
56	Ba	2.13	±0.05	2.21 ±0.03	-0.08
57	La	1.22	±0.09	1.20 ±0.01	+0.02
58	Ce	1.55	±0.20	1.61 ±0.01	-0.06
59	Pr	0.71	±0.08	0.78 ±0.01	-0.07
60	Nd	1.50	±0.06	1.47 ±0.01	+0.03
62	Sm	1.00	±0.08	0.97 ±0.01	-0.03
63	Eu	0.51	±0.08	0.54 ±0.01	-0.03
64	Gd	1.12	±0.04	1.07 ±0.01	+0.05
65	Tb	(-0.1	±0.3)	0.33 ±0.01	(-0.43)
66	Dy	1.1	±0.15	1.15 ±0.01	-0.05
67	Ho	(0.26	±0.16)	0.50 ±0.01	(-0.24)
68	Er	0.93	±0.06	0.95 ±0.01	-0.02
69	Tm	(0.00	±0.15)	0.13 ±0.01	(-0.13)
70	Yb	1.08	±(0.15)	0.95 ±0.01	+0.13
71	Lu	(0.76	±0.30)	0.12 ±0.01	(+0.64)
72	Hf	0.88	±(0.08)	0.73 ±0.01	+0.15
73	Ta	----	----	0.13 ±0.01	----
74	W	(1.11	±0.15)	0.68 ±0.02	(+0.43)
75	Re	----	----	0.27 ±0.04	----
76	Os	1.45	±0.10	1.38 ±0.03	+0.07
77	Ir	1.35	±(0.10)	1.37 ±0.03	-0.02
78	Pt	1.8	±0.3	1.68 ±0.03	+0.12
79	Au	(1.01	±0.15)	0.83 ±0.06	(+0.18)
80	Hg	----		1.09 ±0.05	----
81	Tl	(0.9	±0.2)	0.82 ±0.04	(+0.08)
82	Pb	1.85	±0.05	2.05 ±0.03	-0.20
83	Bi	----	----	0.71 ±0.03	----
90	Th	0.12	±(0.06)	0.08 ±0.02	+0.04
92	U	(<-0.47)	-0.49 ±0.04	----	----

* Values in parentheses are uncertain.
† Values in brackets are based on solar or other astronomical data.

TABLE 3. Abundance of the Nuclides (Atoms/10^6 Si)[4]

Element, A		Atom Percent	Process*	Abund.†	Element, A		Atom Percent	Process*	Abund.†
1 H	1	99.9966	----	2.79×10^{10}		42	0.647	Ex,O	395
	2	0.0034	U	9.49×10^{5}		43	0.135	Ex,C,S	82.5
2 He	3	0.0142	U,h?	3.86×10^{5}		44	2.086	Ex,S	1275
	4	99.9858	U,h	2.72×10^{9}		46	0.004	Ex,C,Ne	2.4
3 Li	6	7.5	X	4.28		48	0.187	E,Ex	114
	7	92.5	U,x,h	52.82	21 Sc	45	100	Ex,Ne,E	34.2
4 Be	9	100	X	0.73	22 Ti	46	8.0	Ex	192
5 B	10	19.9	X	4.22		47	7.3	Ex	175
	11	80.1	X	16.98		48	73.8	Ex	1771
6 C	12	98.90	He	9.99×10^{6}		49	5.5	Ex	132
	13	1.10	H,N	1.11×10^{5}		50	5.4	E	130
7 N	14	99.634	H	3.12×10^{6}	23 V	50	0.250	Ex,E	0.732
	15	0.366	H,N	1.15×10^{4}		51	99.750	Ex	292
8 O	16	99.762	He	2.37×10^{7}	24 Cr	50	4.345	Ex	587
	17	0.038	N,H	9.04×10^{3}		52	83.789	Ex	1.131×10^{4}
	18	0.200	He,N	4.76×10^{4}		53	9.501	Ex	1283
9 F	19	100	N	843		54	2.365	E	319
10 Ne	20	92.99	C	3.20×10^{6}	25 Mn	55	100	Ex,E	9550
	21	0.226	C,Ex	7.77×10^{3}	26 Fe	54	5.8	Ex	5.22×10^{4}
	22	6.79	He,N	2.34×10^{5}		56	91.72	Ex,E	8.25×10^{5}
11 Na	23	100	C,Ne,Ex	5.74×10^{4}		57	2.2	E,Ex	1.98×10^{4}
12 Mg	24	78.99	N,Ex	8.48×10^{5}		58	0.28	He,E,C	2.52×10^{3}
	25	10.00	Ne,Ex,C	1.07×10^{5}	27 Co	59	100	E,C	2250
	26	11.01	Ne,Ex,C	1.18×10^{5}	28 Ni	58	68.27	E,Ex	3.37×10^{4}
13 Al	27	100	Ne,Ex	8.49×10^{4}		60	26.10	E	1.29×10^{4}
14 Si	28	92.23	O,Ex	9.22×10^{5}		61	1.13	E,Ex,C	557
	29	4.67	Ne,Ex	4.67×10^{4}		62	3.59	E,Ex,O	1770
	30	3.10	Ne,Ex	3.10×10^{4}		64	0.91	Ex	449
15 P	31	100	Ne,Ex	1.04×10^{4}	29 Cu	63	69.17	Ex,C	361
16 S	32	95.02	O,Ex	4.89×10^{5}		65	30.83	Ex	161
	33	0.75	Ex	3.86×10^{3}	30 Zn	64	48.63	Ex,E	613
	34	4.21	O,Ex	2.17×10^{4}		66	27.90	E	352
	36	0.02	Ex,Ne,S	1.03×10^{2}		67	4.10	E,S	51.7
17 Cl	35	75.77	Ex	2860		68	18.75	E,S	236
	37	24.23	Ex,C,S	913		70	0.62	E,S	7.8
18 Ar	36	84.2	Ex	8.50×10^{4}	31 Ga	69	60.108	S,c,r	22.7
	38	15.8	O,Ex	1.60×10^{4}		71	39.892	S,e,r	15.1
	40	----	S,Ne	26	32 Ge	70	20.5	S,e	24.4
	40	-----	----	*25±14*		72	27.4	S,e,r	32.6
19 K	39	93.2581	Ex	3516		73	7.8	e,s,r	9.28
	40	0.01167	S,Ex,Ne	0.440		74	36.5	e,s,r	43.4
	40	----	----	*5.48*		76	7.8	E	9.28
	41	6.7302	Ex	253.7	33 As	75	100	R,s	6.56
20 Ca	40	96.941	Ex	5.92×10^{4}	34 Se	74	0.88	P	0.55

TABLE 3. (Continued)

Element, A		Atom Percent	Process*	Abund.†	Element, A		Atom Percent	Process*	Abund.†
	76	9.0	S,p	5.6		104	11.14	S	0.155
	77	7.6	R,s	4.7		105	22.33	R,s	0.310
	78	23.6	R,s	14.7		106	27.33	R,S	0.380
	80	49.7	R,s	30.9		108	26.46	R,S	0.368
	82	9.2	R	5.7		110	11.72	R	0.163
35 Br	79	50.69	R,s	5.98	47 Ag	107	51.839	R,s	0.252
	81	49.31	R,s	5.82		109	48.161	R,s	0.234
36 Kr	78	0.339	P	0.153	48 Cd	106	1.25	P	0.0201
	80	2.22	S,p	0.999		108	0.89	P	0.0143
	82	11.45	S	5.15		110	12.49	S	0.201
	83	11.47	R,s	5.16		111	12.80	R,S	0.206
	84	57.11	R,S	25.70		112	24.13	S,R	0.388
	86	17.42	S,r	7.84		113	12.22	R,S	0.197
37 Rb	85	72.165	R,s	5.12		114	28.73	S,R	0.463
	87	27.835	S	1.97		116	7.49	R	0.121
	87	----	----	*2.11*	49 In	113	4.3	p,s,r	0.0079
38 Sr	84	0.56	P	0.132		115	95.7	R,S	0.176
	86	9.86	S	2.32	50 Sn	112	0.973	P	0.0372
	87	7.00	S	1.64		114	0.659	P,s	0.0252
	87	----	----	*1.51*		115	0.339	p,s,r	0.0129
	88	82.58	S,r	19.41		116	14.538	S,r	0.555
39 Y	89	100	S	4.64		117	7.672	R,S	0.293
40 Zr	90	51.45	S	5.87		118	24.217	S,r	0.925
	91	11.22	S	1.28		119	8.587	S,R	0.328
	92	17.15	S	1.96		120	32.596	S,R	1.245
	94	17.38	S	1.98		122	4.632	R	0.177
	96	2.80	R	0.320		124	5.787	R	0.221
41 Nb	93	100	S	0.698	51 Sb	121	57.362	R,s	0.177
42 Mo	92	14.84	P	0.378		123	42.638	R	0.132
	94	9.25	P	0.236	52 Te	120	0.09	P	0.0043
	95	15.92	R,s	0.406		122	2.57	S	0.124
	96	16.68	S	0.425		123	0.89	S	0.0428
	97	9.55	R,s	0.244		124	4.76	S	0.229
	98	24.13	R,s	0.615		125	7.10	R,s	0.342
	100	9.63	R	0.246		126	18.89	R,S	0.909
44 Ru	96	5.52	P	0.103		128	31.73	R	1.526
	98	1.88	P	0.0350		130	33.97	R	1.634
	99	12.7	R,s	0.236	53 I	127	100	R	0.90
	100	12.6	S	0.234	54 Xe	124	0.121	P	0.00571
	101	17.0	R,s	0.316		126	0.108	P	0.00509
	102	31.6	R,S	0.588		128	2.19	S	0.103
	104	18.7	R	0.348		129	27.34	R	1.28
45 Rh	103	100	R,s	0.344		130	4.35	S	0.205
46 Pd	102	1.020	P	0.0142		131	21.69	R	1.02
	132	26.50	R,s	1.24		160	21.86	R	0.0721
	134	9.76	R	0.459	65 Tb	159	100	R	0.0603
	136	7.94	R	0.373	66 Dy	156	0.056	P	0.000221
55 Cs	133	100	R,s	0.372		158	0.096	P	0.000378
56 Ba	130	0.106	P	0.00476		160	2.34	S	0.00922
	132	0.101	P	0.00453		161	18.91	R	0.0745
	134	2.417	S	0.109		162	25.51	R,s	0.101

TABLE 3. (Continued)

Element, A		Atom Percent	Process*	Abund.†
	135	6.592	R,s	0.296
	136	7.854	S	0.353
	137	11.23	S,r	0.504
	138	71.70	S	3.22
57 La	138	0.089	P	0.000397
	138	----	----	*0.000409*
	139	99.911	S,r	0.446
58 Ce	136	0.19	P	0.00216
	138	0.25	P	0.00284
	138	----	----	*0.00283*
	140	88.48	S,r	1.005
	142	11.08	R	0.126
59 Pr	141	100	R,S	0.167
60 Nd	142	27.13	S	0.225
	143	12.18	R,S	0.101
	143	----	----	*0.100*
	144	23.80	S,R	0.197
	145	8.30	R,s	0.0687
	146	17.19	R,S	0.142
	148	5.76	R	0.0477
	150	5.64	R	0.0467
62 Sm	144	3.1	P	0.00800
	147	15.0	R,s	0.0387
	147	----	----	*0.0399*
	148	11.3	S	0.0292
	149	13.8	R,S	0.0356
	150	7.4	S	0.0191
	152	26.7	R,S	0.0689
	154	22.7	R	0.0586
63 Eu	151	47.8	R,s	0.0465
	153	52.2	R,s	0.0508
64 Gd	152	0.20	P,s	0.00066
	154	2.18	S	0.00719
	155	14.80	R,s	0.0488
	156	20.47	R,s	0.0676
	157	15.65	R,s	0.0516
	158	24.84	R,s	0.0820
76 Os	184	0.018	P	0.000122
	186	1.58	S	0.0107
	187	1.6	S	0.0108
	187	----	----	*0.00807*
	188	13.3	R,s	0.0898
	189	16.1	R	0.109
	190	26.4	R	0.178
	192	41.0	R	0.277
77 Ir	191	37.3	R	0.247
	193	62.7	R	0.414
78 Pt	190	0.0127	P	0.000170
	192	0.78	S	0.0105
	194	32.9	R	0.441
	195	33.8	R	0.453
	163	24.90	R	0.0982
	164	28.19	R,S	0.0111
67 Ho	165	100	R	0.0889
68 Er	162	0.14	P	0.000351
	164	1.61	P,S	0.00404
	166	33.6	R,s	0.0843
	167	22.95	R	0.0576
	168	26.8	R,S	0.0672
	170	14.9	R	0.0374
69 Tm	169	100	R,s	0.0378
70 Yb	168	0.13	P	0.000322
	170	3.05	S	0.00756
	171	14.3	R,s	0.0354
	172	21.9	R,S	0.0543
	173	16.12	R,s	0.0400
	174	31.8	S,R	0.0788
	176	12.7	R	0.0315
71 Lu	175	97.41	R,s	0.0357
	176	2.59	S	0.000951
	176	----	---	*0.001035*
72 Hf	174	0.162	P	0.000249
	176	5.206	S	0.00802
	176	----	----	*0.00793*
	177	18.606	R,s	0.0287
	178	27.297	R,S	0.0420
	179	13.629	R,s	0.0210
	180	35.100	S,R	0.0541
73 Ta	180	0.012	p,s,r	2.48×10^{-6}
	181	99.988	R,S	0.0207
74 W	180	0.13	P	0.000173
	182	26.3	R,s	0.0350
	183	14.3	R,s	0.0190
	184	30.67	R,s	0.0408
	186	28.6	R	0.0380
75 Re	185	37.40	R,s	0.0193
	187	62.60	R	0.0324
	187	----	----	*0.0351*

TABLE 3. (Continued)

Element, A		Atom Percent	Process*	Abund.†
	196	25.2	R	0.338
	198	7.19	R	0.0963
79 Au	197	100	R	0.187
80 Hg	196	0.1534	P	0.00052
	198	9.968	S	0.0339
	199	16.873	R,S	0.0574
	200	23.096	S,r	0.0785
	201	13.181	S	0.0448
	202	29.863	S,r	0.1015
	204	6.865	R	0.0233
81 Tl	203	29.524	R,S	0.0543
	205	70.476	S,R	0.1297
82 Pb	204	1.94	S	0.0611
	206	19.12	R,S	0.602
	206	----	----	*0.593*
	207	20.62	R,S	0.650
	207	----	----	*0.644*
	208	58.31	R,s	1.837
	208	----	----	*1.828*
83 Bi	209	100	R,s	0.144
90 Th	232	100	RA	0.0335
	232	----	----	*0.0420*
92 U	235	0.7200	RA	6.48×10^{-5}
	235	-----	----	*0.00573*
	238	99.2745	RA	0.00893
	238	----	----	*0.0181*

*Assignments to nucleosynthetic processes are from Cameron [1982][17], Schramm (private communication, 1982), Walter et al. [1986][75], Woosley and Hoffman [1986, 1989][87,88], and Beer and Penzhorn [1987][9]. Processes are listed in the order of importance, with minor processes (10-30% for r-and s-processes) shown in lower case. See above references for details. U = cosmological nucleosynthesis, H = hydrogen burning, N = hot or explosive hydrogen burning, He = helium burning, C = carbon burning, O = oxygen burning, Ne = neon burning, Ex = explosive nucleosynthesis, E = nuclear statistical equilibrium, S = s-process, R = r-process, RA = r-process producing actinides, P = p-process, X = cosmic-ray spallation. †Italicized values refer to abundances 4.55×10^9 yr ago.

TABLE 4. Properties of Chondrite Groups[a]

Clan	Group	refr[c]	Fe[c]	FeO[c]	Fe met[c]	Mafic min.	$\delta^{18}O$	$\Delta^{17}O$	Chondrule		Fall
	Si	Si	FeO+MgO	Si	Comp.[h]		(‰)	(‰)	size[d]	freq[e]	freq[f]
Carbon-aceous	CV	1.35	0.87	35	0.6-19	----	1.5	-3.6	0.9	46	0.72
	CO	1.10	0.90	35	2.3-15	----	-0.9	-4.5	0.3	18	0.60
	CK[i]	----	----	----	----	Fa 29-33	-0.9	-4.5	----	----	----
	CM	1.13	0.93	43	0.1-0.5	----	7	-3	0.3	12	2.17
	CI	1.00	1.00	45	<0.1	----	17	+1	----	<0.1	0.60
Ordinary	LL	0.76	0.62	27	2.7-11	Fa 26-32	4.9	1.3	0.8	70	7.95
	L	0.77	0.66	22	17-22	Fa 21-25	4.6	1.1	0.6	70	38.43
	H	0.79	0.93	17	46-52	Fa 17-19	4.2	0.8	0.5	70	33.25
IAB inclusion	IAB	~0.7	~0.70	6	~50	Fs 4-8	5.0	5.0	----	----	0.95
Enstatite	EL	0.60	0.76	0.05	47-57	Fs ~0.05	5.6	0.0	≤1.0	≥12	0.84
	EH[g]	0.59	1.13	0.05	68-72		5.3	0.0	0.5	20	0.72

[a]Table after Wasson [1985][79]

[b]Refractory lithophile and bulk Fe abundances are Cl-normalized.

[c]Atom or mole ratios x 100.

[d]Median diameter in mm.

[e]Median diameter in mm.

[f]Percent of observed falls.

[g]EH chondrites are unequilibrated; although their mean FeO/(FeO+MgO) ratios range up to 0.2 mol%, they have more metallic Si in the metal than EL chondrites.

[h]Atom or mole ratios x 100. Mafic-mineral (olivine, Fa, or low-calcium pyroxene, Fs) compositions given only for equilibrated meteorites.

[i]Data for CK from Kallemeyn et al. [1991][36]; some parameters are not reported.

TABLE 5. Properties of Differentiated Silicate-Rich Meteorites

Group	Major mafic mineral			Fe-Ni	$\delta^{18}O$	$\Delta^{17}O$	Breccia type
	Name	Conc.	FeO/(FeO+MgO) (mol%)	(mg/g)	(‰)	(‰)	
Eucrites	Pigeonite	40-80	45-70	<10	3.2-3.8	-0.2	Monomict[b]
Howardites	Orthopyroxene	40-80	25-40	~10	3.2-3.8	-0.2	Polymict
Diogenites	Orthopyroxene	~95	25-27	<10	3.2-3.8	-0.2	Monomict
Mesosiderites	Orthopyroxene	40-80	23-27	300-550	3.2-3.8	-0.2	Polymict
Pallasites	Olivine	~98	11-14	280-880	3.2-3.8	-0.3	Monomict[c]
Aubrites	Low-calcium-clinopyroxene	~97	0.01-0.03	~10	5.1-5.5	0.0	Polymict
Ureilites	Olivine	~85	10-25	10-60	7.6-8.0	-1.0	Polymict

[a] As fraction of silicates

[b] Ibitira is an unbrecciated eucrite

[c] Pallastic silicates monomict; metal and silicates probably originally separate in core and mantle, repectively.

TABLE 6. Compositions of Chondrite Meteorite Groups

Element		CM	CO	CK	CV	H	L	LL	EH	EL
1 H	%	1.4	.07	----	.28	----	----	----	----	----
3 Li	ppm	1.36	1.2	----	1.24	1.7	1.8	2.1	2.1	0.58
4 Be	ppb	----	----	----	----	51	43	51	----	----
5 B	ppb	600	----	----	300	500	400	----	----	----
6 C	%	2.2	.45	----	.56	.11	.09	.12	.40	.36
7 N	ppm	1520	90	----	80	48	43	70	----	----
8 O	%	43.2	37.0	----	37.0	35.7	37.7	40.0	28.0	31.0
9 F	ppm	38	30	----	24	32	41	63	238	180
11 Na	ppm	4100	4100	3190	3300	6400	7000	7000	6800	5800
12 Mg	%	11.7	14.5	14.8	14.5	14.0	14.9	15.3	10.6	14.1
13 Al	ppm	11800	14300	16100	17500	11300	12200	11900	8100	10500
14 Si	%	12.9	15.9	----	15.6	16.9	18.5	18.9	16.7	18.6
15 P	ppm	900	1040	----	990	1080	950	850	2000	1170
16 S	%	3.3	2.0	----	2.2	2.0	2.2	2.3	5.8	3.3
17 Cl	ppm	160	240	----	210	80	76	130	660	210
19 K	ppm	400	345	285	310	780	825	790	800	735
20 Ca	ppm	12700	15800	17200	19000	12500	13100	13000	8500	10100
21 Sc	ppm	8.2	9.6	11.0	11.4	7.9	8.6	8.4	5.7	7.4
22 Ti	ppm	580	780	----	980	600	630	620	450	580
23 V	ppm	75	92	96	96	74	77	75	54	60
24 Cr	ppm	3050	3550	3660	3600	3660	3880	3740	3150	3050
25 Mn	ppm	1700	1650	1460	1450	2320	2570	2620	2200	1630
26 Fe	%	21.0	24.8	23.6	23.5	27.5	21.5	18.5	29.0	22.0
27 Co	ppm	575	688	637	655	810	590	490	840	670
28 Ni	%	1.20	1.40	1.27	1.34	1.60	1.20	1.02	1.75	1.30
29 Cu	ppm	115	125	----	100	82	90	80	185	110
30 Zn	ppm	185	100	98	116	47	50	46	250	17
31 Ga	ppm	7.8	7.1	5.5	6.0	6.0	5.7	5.0	16	11
32 Ge	ppm	23	21	----	17	13	10	9.0	42	28
33 As	ppm	1.80	1.95	1.48	1.60	2.05	1.55	1.35	3.45	2.20
34 Se	ppm	12.7	7.6	6.9	8.3	7.7	9.0	9.9	25.5	13.5
35 Br	ppm	2.6	1.3	0.4	1.5	0.5	0.8	0.6	2.4	0.8
37 Rb	ppm	1.7	1.45	----	1.25	2.9	3.1	3.1	2.6	2.5
38 Sr	ppm	10.1	12.7	----	15.3	10.0	11.1	11.1	7.2	8.2
39 Y	ppm	2.0	2.4	----	2.4	2.2	2.1	2.0	1.3	----
40 Zr	ppm	8.0	7.8	----	8.3	6.3	5.9	5.9	4.9	5.2
41 Nb	ppb	(370)	(450)	----	(540)	(360)	(390)	(370)	(250)	----
42 Mo	ppb	1500	1900	----	2100	1700	1300	1100	----	----
44 Ru	ppb	883	1090	1110	1130	1100	750	----	915	831
45 Rh	ppb	----	----	----	250	220	----	----	----	----
46 Pd	ppb	640	703	----	705	870	560	530	885	690
47 Ag	ppb	157	97	----	107	45	65	72	236	23
48 Cd	ppb	368	8	----	373	17	11	37	484	27
49 In	ppb	50	25	----	33	11	7.0	12	58	2.3
50 Sn	ppb	1010	890	----	900	860	710	----	800	----
51 Sb	ppb	115	105	70	85	70	68	60	196	90
52 Te	ppb	1910	900	----	1020	260	480	490	2230	800
53 I	ppb	425	200	----	188	68	53	----	150	53
55 Cs	ppb	125	80	----	95	120	280	180	200	100
56 Ba	ppb	3300	4290	----	4900	4200	3700	4800	2600	----
57 La	ppb	317	387	462	486	295	310	315	235	190

TABLE 6. (Continued)

Element		CM	CO	CK	CV	H	L	LL	EH	EL
58 Ce	ppb	838	1020	----	1290	830	900	907	660	300
59 Pr	ppb	129	157	----	200	123	132	122	94	----
60 Nd	ppb	631	772	----	990	628	682	659	460	233
62 Sm	ppb	200	240	284	295	185	195	200	140	135
63 Eu	ppb	76	94	108	113	73	78	76	54	54
64 Gd	ppb	276	337	----	415	299	310	303	214	107
65 Tb	ppb	47	57	----	65	53	57	48	35	----
66 Dy	ppb	330	404	----	475	343	366	351	240	139
67 Ho	ppb	77	94	----	110	73	81	77	50	----
68 Er	ppb	218	266	----	315	226	248	234	166	97
69 Tm	ppb	33	40	----	45	39	39	34	25	----
70 Yb	ppb	222	270	311	322	205	220	220	160	165
71 Lu	ppb	33	40	44	48	31	33	33	24	24
72 Hf	ppb	186	178	----	194	180	170	150	140	150
73 Ta	ppb	(22)	(27)	----	(32)	22	23	(22)	(15)	----
74 W	ppb	140	160	----	190	160	110	----	----	----
75 Re	ppb	46	55	----	65	70	40	33	52	47
76 Os	ppb	640	790	813	825	820	515	400	654	589
77 Ir	ppb	595	735	767	760	760	490	360	565	525
78 Pt	ppb	1100	1200	----	1250	1400	1050	850	1200	----
79 Au	ppb	165	184	136	144	215	162	140	330	225
80 Hg	ppb	----	----	----	----	----	----	----	----	----
81 Tl	ppb	92	42	----	46	3.7	2.0	7.2	103	5.0
82 Pb	ppb	1700	2200	----	1400	240	370	----	1100	----
83 Bi	ppb	75	33	----	48	17	14	16	88	12
90 Th	ppb	40	(45)	----	60	42	43	43	30	35
92 U	ppb	11	13	----	17	12	13	13	9	10

Data from Wasson and Kallemeyn [1988][80], & Kallemeyn et al. [1991][36] (CK). Values in parentheses for Nb and Ta are inferred by assuming they are unfractionated relative to well-determined refractory lithophiles.

TABLE 7. Compositional Interpretations of Asteroid Taxonomic Types

Bell [1986][10] Superclass	Tholen [1984][72] Class	Inferred Minerals	Analogous Meteorities
Primitive	D	organics + ? (ice??)	(none)
	P	organics + ? (ice??)	(none)
	C	clays, C, organics	CI, CM chondrites
	K	ol, pyx, carbon	CV, CO chondrites
	Q	pyx, ol, gray NiFe	H, L, LL chondrites ?
	?	Fe-free pyx, gray NiFe	EH, EL chondrites
Metamorphic	T	?	highly altered C Cs ??
	B+G+F	clays, opaques	high altered C Cs ?

TABLE 7. (Continued)

Bell [1986][10] Superclass	Tholen [1984][72] Class	Inferred Minerals	Analogous Meteorities
Igneous	V	plag, pyx, ol	basaltic achondrites
	R	ol, pyx	ol-rich achondrites?
	S	pyx, ol, red NiFe	pallasites, lodranites, irons ?
	A	ol	brachinites
	M	NiFe	irons
	E	Fe-free pyx	aubrites
	(Mars)		(SNC meteorites)
	(Moon)		(lunar meteorites)

Table from Bell et al. [1989][12].

TABLE 8. Estimated Composition of the Silicate Portion of the Parent Body of the Eucrite Meteorites

		Dreibus and Wänke [1980][23]	Jones [1984][33]	Consolmagno & Drake [1977][21]	Morgan et al. [1978][45]	Vizgirda and Anders [1976][74]	Hertogen et al. [1977][29]
Li	ppm	2.7	----	----	----	----	----
F	ppm	4.8	----	----	----	----	----
Na	ppm	830	820	450	370	520	520
Mg	%	19.0	16.7	16.9	17.2	21.1	17.7
Al	ppm	17300	16,900	13,500	13,200	12,200	12,700
Si	%	21.59	18.8	19.3	18.6	23.0	19.2
P	ppm	97	96	----	----	----	----
Cl	ppm	4.6	----	----	----	----	----
K	ppm	76	83	----	33	83	33
Ca	ppm	18400	19,000	13,200	14,700	14,000	14,000
Sc	ppm	12.4	----	----	----	----	----
Ti	ppm	960	960	----	780	720	720
V	ppm	91	----	----	----	----	----
Cr	ppm	5980	2,300	----	----	----	----
Mn	ppm	3290	4,900	----	139	2,300	3,600
Fe	%	11.50	19.6	20.4	20.7	8.55	18.6
Co	ppm	13	----	----	----	----	----
Ni	%	0.0038	30-80	----	----	----	----
Ga	ppm	0.67	----	----	----	----	----
Br	ppm	0.03	----	----	----	----	----
Sr	ppm	19.1	----	----	----	----	----
Zr	ppm	9.9	----	----	----	----	----
Ba	ppb	6000	----	----	----	----	----
La	ppb	650	----	----	----	----	----
Sm	ppb	380	----	----	----	----	----
Eu	ppb	140	----	----	----	----	----

TABLE 8. (Continued)

		Dreibus and Wänke [1980][23]	Jones [1984][33]	Consolmagno & Drake [1977][21]	Morgan et al. [1978][45]	Vizgirda and Anders [1976][74]	Hertogen et al. [1977][29]
Yb	ppb	430	----	----	----	----	----
Hf	ppb	290	----	----	----	----	----
Ta	ppb	31	----	----	----	----	----
W	ppb	14	----	----	----	----	----
U	ppb	22	----	----	----	----	----

TABLE 9. Mercury & Venus

Element			Fegley & Cameron [1987][25] Mercury	Goettel [1988][26] Mercury	Morgan & Anders [1980][44] Mercury	Morgan & Anders [1980][44] Venus
1	H	ppm	----	----	0.4	35
3	Li	ppm	----	----	0.87	1.94
4	Be	ppb	----	----	34	47
5	B	ppb	----	----	0.11	10.0
6	C	%	----	----	0.00051	0.0
7	N	ppm	----	----	0.046	4.3
8	O	%	----	----	14.44	30.9
9	F	ppm	----	----	2.2	15
11	Na	ppm	----	0.1-0.7	200	1390
12	Mg	%	25.5	19-23	6.5	14.54
13	Al	ppm	8.99	1.9-3.7	10,800	14,800
14	Si	%	12.1	18-22	7.05	15.82
15	P	ppm	----	----	390	1860
16	S	%	----	----	0.24	1.62
17	Cl	ppm	----	----	0.23	20.9
19	K	ppm	0	----	22	150
20	Ca	ppm	9.80	2.4-5.0	11,800	16,610
21	Sc	ppm	----	----	7.4	10.1
22	Ti	ppm	0.479	0.09-0.18	630	850
23	V	ppm	----	----	63	86
24	Cr	ppm	----	----	7180	4060
25	Mn	ppm	----	----	150	460
26	Fe	%	0.3	0.4-4.0	64.47	31.17
27	Co	ppm	----	----	1690	820
28	Ni	%	----	----	3.66	1.77
29	Cu	ppm	----	----	5.1	35
30	Zn	ppm	----	----	12.1	82
31	Ga	ppm	----	----	0.50	3.4
32	Ge	ppm	----	----	1.24	8.4
33	As	ppm	----	----	6.4	3.1
34	Se	ppm	----	----	0.79	5.4
35	Br	ppm	----	----	0.0012	0.111
37	Rb	ppm	----	----	0.075	0.509
38	Sr	ppm	----	----	1.11	15.2

TABLE 9. (Continued)

Element			Fegley & Cameron [1987][25] Mercury	Goettel [1988][26] Mercury	Morgan & Anders [1980][44] Mercury	[1980][44] Venus
39	Y	ppm	----	----	2.01	2.74
40	Zr	ppm	----	----	5.5	7.5
41	Nb	ppb	----	----	610	840
42	Mo	ppb	----	----	1.81	2.47
44	Ru	ppb	----	----	910	1230
45	Rh	ppb	----	----	194	265
46	Pd	ppb	----	----	1790	870
47	Ag	ppb	----	----	7.2	49
48	Cd	ppb	----	----	0.19	17.2
49	In	ppb	----	----	0.024	2.24
50	Sn	ppb	----	----	64	430
51	Sb	ppb	----	----	5.7	39
52	Te	ppb	----	----	122	830
53	I	ppb	----	----	0.16	14.3
55	Cs	ppb	----	----	2.5	17.0
56	Ba	ppb	----	----	3.1	4.2
57	La	ppb	----	----	291	397
58	Ce	ppb	----	----	780	1060
59	Pr	ppb	----	----	99	135
60	Nd	ppb	----	----	530	723
62	Sm	ppb	----	----	160	218
63	Eu	ppb	----	----	61	83
64	Gd	ppb	----	----	220	300
65	Tb	ppb	----	----	41	56
66	Dy	ppb	----	----	280	382
67	Ho	ppb	----	----	61	84
68	Er	ppb	----	----	177	242
69	Tm	ppb	----	----	27	37
70	Yb	ppb	----	----	176	240
71	Lu	ppb	----	----	297	405
72	Hf	ppb	----	----	177	241
73	Ta	ppb	----	----	17.9	24.4
74	W	ppb	----	----	139	189
75	Re	ppb	----	----	46	64
76	Os	ppb	----	----	670	920
77	Ir	ppb	----	----	650	890
78	Pt	ppb	----	----	1.29	1.76
79	Au	ppb	----	----	516	250
80	Hg	ppb	----	----	0.09	8.3
81	Tl	ppb	----	----	0.044	4.05
82	Pb	ppb	----	----	0.018	1.66
83	Bi	ppb	----	----	0.034	3.08
90	Th	ppb	377	----	39.4	53.7
92	U	ppb	0	----	11.0	15.0

TABLE 10. Compositions of the silicate portion of Mars

		Anderson [1972][6]	Morgan & Anders [1979][43]	Ringwood [1981][55]	Wänke & Dreibus [1988][76]
Mantle + Crust					
MgO	%	27.4	29.8	29.9	30.2
Al_2O_3	%	3.1	6.4	3.1	3.02
SiO_2	%	40.0	41.6	36.8	44.4
CaO	%	2.5	5.2	2.4	2.45
TiO_2	%	0.1	0.3	0.2	0.14
FeO	%	24.3	15.8	26.8	17.9
Na_2O	%	0.8	0.1	0.2	0.50
P_2O_5	%	---	---	---	0.16
Cr_2O_3	%	0.6	0.6	0.4	0.76
MnO	%	0.2	0.15	0.1	0.46
K	ppm	573	77	218	305
Rb	ppm	----	0.258	----	1.06
Cs	ppm	----	0.026	----	0.07
F	ppm	----	24	----	32
Cl	ppm	----	0.88	----	38
Br	ppb	----	4.7	----	145
I	ppb	----	0.59	----	32
Co	ppm	----	----	----	68
Ni	%	----	----	----	0.04
Cu	ppm	----	----	----	5.5
Zn	ppm	----	42	----	62
Ga	ppm	----	2.4	----	6.6
Mo	ppb	----	----	----	118
In	ppb	----	0.095	----	14
Tl	ppb	----	0.17	----	3.6
W	ppb	----	----	----	105
Th	ppb	77	113	60	56
U	ppb	17	33	17	16
Core					
Fe	%	72	88.1	63.7	77.8
Ni	%	9.3	8.0	8.2	7.6
Co	%	----	----	----	0.36
S	%	18.6	3.5	9.3	14.24
O	%	----	----	18.7	----
Core Mass	%	11.9	19.0	18.2	21.7

TABLE 11. Compositions of the Silicate Portion of the Moon

Element			Anders [1977][2]	Jones & Delano [1989][34]	O'Neill [1991][49]	Taylor [1982][68]	Wänke et al. [1977][78]	Ringwood et al. [1986][57]	Taylor [1982][68] Highlands Crust
1	H	ppm	2.34	----	----	----	----	----	----
3	Li	ppm	9.27	----	1.9	0.850	----	----	----
4	Be	ppb	198	----	----	184	----	----	----
5	B	ppb	13.9	----	----	553	----	----	----
6	C	ppm	10.5	----	----	----	----	----	----
7	N	ppm	0.277	----	----	----	----	----	----
8	O	%	44.11	----	----	----	42.6	----	----
9	F	ppm	32.0	----	1.3	----	----	----	----
11	Na	ppm	960	----	260	614	1520	450	3300
12	Mg	%	18.5	22.4	20.8	19.8	12.8	22.22	4.1
13	Al	ppm	62100	19600	20400	32500	86300	19700	130000
14	Si	%	19.83	19.9	20.5	20.8	18.7	20.19	----
15	P	ppm	573	----	43	----	----	----	----
16	S	%	0.415	----	0.08	----	0.193	----	----
17	Cl	ppm	0.746	----	----	----	----	----	----
18	Ar		39.4	----	----	----	----	----	----
19	K	ppm	102	----	31	85.0	178	----	600
20	Ca	ppm	67800	----	23100	33000	91400	21700	113000
21	Sc	ppm	42.6	----	15.4	19.5	60.9	14	10
22	Ti	ppm	3600	1140	1220	1840	4670	1800	3350
23	V	ppm	362	----	81	154	315	79	24
24	Cr	ppm	1280	----	3140	4300	2030	2200	680
25	Mn	ppm	352	1500	1310	1230	914	1200	----
26	Fe	%	3.09	10.6	9.9	8.3	7.0	9.51	5.1
27	Co	ppm	256	----	220	----	----	95	15
28	Ni	%	0.543	----	0.472	----	0.0914	0.2487	.010
29	Cu	ppm	7.35	----	3.3	----	----	----	----
30	Zn	ppm	21.2	----	1.9	----	----	----	----
31	Ga	ppm	0.703	----	0.24	----	----	----	----
32	Ge	ppm	1.77	----	0.52	----	----	----	----
33	As	ppm	0.959	----	0.082	----	----	----	----
34	Se	ppm	1.39	----	----	----	----	----	----
35	Br	ppm	0.00405	----	----	----	----	----	----
36	Kr		0.192	----	----	----	----	----	----
37	Rb	ppm	0.352	----	0.12	0.287	0.406	----	1.7
38	Sr	ppm	63.9	----	----	30.7	66.0	----	120
39	Y	ppm	11.6	----	----	5.22	17.3	----	13.4
40	Zr	ppm	69.2	----	----	14.3	47.7	----	63
41	Nb	ppb	3520	----	----	1130	3350	----	4500
42	Mo	ppb	10400	----	68	----	----	----	----
44	Ru	ppb	5220	----	----	----	----	----	----
45	Rh	ppb	1120	----	----	----	----	----	----
46	Pd	ppb	266	----	----	----	----	----	----
47	Ag	ppb	10.2	----	----	----	----	----	----
48	Cd	ppb	0.618	----	----	----	----	----	----
49	In	ppb	0.0799	----	0.4	----	----	----	----
50	Sn	ppb	90.5	----	34	----	----	----	----
51	Sb	ppb	8.09	----	2.8	----	----	----	----
52	Te	ppb	213	----	----	----	----	----	----

TABLE 11. (Continued)

Element			Anders [1977][2]	Jones & Delano [1989][34]	O'Neill [1991][49]	Taylor [1982][68]	Wänke et al. [1977][78]	Ringwood et al. [1986][57]	Taylor [1982][68] Highlands Crust
53	I	ppb	0.511	----	----	----	----	----	----
55	Cs	ppb	35.2	----	4.8	12.3	20.3	----	70
56	Ba	ppb	17900	----	----	9010	24400	----	66000
57	La	ppb	16700	----	----	922	2540	----	5300
58	Ce	ppb	4470	----	----	2400	----	----	12000
59	Pr	ppb	565	----	----	348	----	----	1600
60	Nd	ppb	3090	----	----	1780	----	----	7400
62	Sm	ppb	916	----	----	584	----	----	2000
63	Eu	ppb	352	----	----	215	579	----	1000
64	Gd	ppb	1260	----	----	768	----	----	2300
65	Tb	ppb	234	----	----	143	----	----	410
66	Dy	ppb	1590	----	----	952	----	----	2600
67	Ho	ppb	352	----	----	215	----	----	530
68	Er	ppb	1020	----	----	625	----	----	1510
69	Tm	ppb	154	----	----	90.1	----	----	220
70	Yb	ppb	1010	----	----	62.5	----	----	1400
71	Lu	ppb	170	----	----	95.2	----	----	210
72	Hf	ppb	1010	----	----	430	----	----	1400
73	Ta	ppb	102	----	----	----	132	----	----
74	W	ppb	799	----	41	758	----	----	----
75	Re	ppb	266	----	16	----	----	----	----
76	Os	ppb	3830	----	----	----	----	----	----
77	Ir	ppb	3730	----	210	----	----	----	----
78	Pt	ppb	7350	----	----	----	----	----	----
79	Au	ppb	76.7	----	----	----	----	----	----
80	Hg	ppb	0.298	----	----	----	----	----	----
81	Tl	ppb	0.128	----	----	----	----	----	----
82	Pb	ppb	----	----	----	----	----	----	----
83	Bi	ppb	0.111	----	----	----	----	----	----
90	Th	ppb	224	----	----	128	223	----	900
92	U	ppb	62.8	----	19	33.8	60.9	----	240

Noble gasses 10^{-10} cm^3 s.t.p./g.

TABLE 12. Composition of the Earth's Core

	Ringwood [1977][54], Ringwood & Kesson [1977][58]	Morgan & Anders [1980][44]	Wänke et al. [1984][77]
Fe wt % of core	86.2	84.5	80.27
Ni wt % of core	4.8	5.6	5.46
Co wt % of core	---	---	0.27
S wt % of core	1.0	9.0	---
O wt % of core	8.0	---	---
Si, Mn, Cr	---	---	14.00
core wt % of Earth	31.2	32.4	33.5

TABLE 13. Composition of Bulk Silicate Earth (Primitive Mantle), Depleted Mantle and the Bulk Earth (Core + Mantle + Crust)

Element		Anderson [1983][7]	Ringwood [1991][56]	Sun [1982][67]	Taylor & McLennan [1985][7]	Wänke et al. [1984][77]	Zindler & Hart [1986][89]	Wänke et al. [1984][77] Depleted mantle	Morgan & Anders [1980][44] Bulk Earth
1 H	ppm	----	----	----	----	----	----	----	33
3 Li	ppm	2.09	1.6	1.4	0.83	2.15	----	2.07	1.85
4 Be	ppb	----	80	----	60	----	----	----	45
5 B	ppb	----	500	----	600	----	----	----	9.6
6 C	ppm	----	250	----	----	46.2	----	24	446
7 N	ppm	4.1	----	----	----	----	----	----	4.1
8 O	%	----	----	----	----	----	----	----	30.12
9 F	ppm	28	26	26	----	19.4	----	16.3	13.5
11 Na	ppm	2040	2545	2890	2500	2889	----	2745	1250
12 Mg	%	20.52	22.45	22.9	21.2	22.23	22.8	22.22	13.90
13 Al	ppm	20200	23600	22800	19300	22200	21500	21700	14100
14 Si	%	22.40	20.93	20.8	23.3	21.48	21.5	21.31	15.12
15 P	ppm	57	95	92	----	64.5	----	60	1920
16 S	%	0.0048	.035	.035-0.1	----	0.00132	----	0.0008	2.92
17 Cl	ppm	8	30	21-38	----	11.8	----	.50	19.9
19 K	ppm	151	240	230	180	231	----	127	135
20 Ca	ppm	22000	25730	25000	20700	25300	23400	25000	15400
21 Sc	ppm	15	17.34	----	13	17.0	----	16.9	9.6
22 Ti	ppm	1225	1280	1300	960	1350	----	1320	820
23 V	ppm	77	82	87	128	82.1	----	81.3	82
24 Cr	ppm	2342	2935	3000	3000	3011	----	3010	4120
25 Mn	ppm	1016	1080	1100	1000	1021	----	1016	750
26 Fe	%	6.11	6.53	6.5	6.22	5.89	----	5.86	32.07
27 Co	ppm	101	105	110	100	105	----	105	840
28 Ni	%	0.1961	0.1890	0.2	0.2	0.2108	----	0.2108	1.82
29 Cu	ppm	29	30	30	28	28.5	----	28.2	31

TABLE 13. (Continued)

Element	Anderson [1983][7]	Ringwood [1991][56]	Sun [1982][67]	Taylor & McLennan [1985][7]	Wänke et al. [1984][77]	Zindler & Hart [1986][89]	Wänke et al. [1984][77] Depleted mantle	Morgan & Anders [1980][44] Bulk Earth
30 Zn ppm	37	56	56	50	48.5	----	48	74
31 Ga ppm	4	3.9	4.5 - 5.0	3	3.8	----	3.7	3.1
32 Ge ppm	1.13	1.1	----	1.2	1.32	----	1.31	7.6
33 As ppm	----	0.13	----	0.10	0.152	----	0.14	3.2
34 Se ppm	0.02	0.05	----	0.041	0.0135	----	0.0126	9.6
35 Br ppm	----	0.075	0.060-0.090	----	0.0456	----	0.0046	0.106
37 Rb ppm	0.39	0.635	0.66	0.55	0.742	----	0.276	0.458
38 Sr ppm	16.2	21.05	----	17.8	27.7	19.6	26.0	14.5
39 Y ppm	3.26	4.55	----	3.4	----	----	----	2.62
40 Zr ppm	13	11.22	----	8.3	----	----	----	7.2
41 Nb ppb	970	713	----	560	----	----	----	800
42 Mo ppm	----	0.065	----	0.059	----	----	----	2.35
44 Ru ppm	----	0.0042	----	0.0043	----	----	----	1.18
45 Rh ppb	----	1	----	1.7	1.18	----	----	252
46 Pd ppb	----	5	----	3.9	----	----	----	890
47 Ag ppb	3	8	5-10	19	2.92	----	2.51	44
48 Cd ppb	20	40	----	40	26.1	----	25.5	16.4
49 In ppb	6	13	10-15	18	18.5	----	18.1	2.14
50 Sn ppb	600	175	----	600	----	----	----	390
51 Sb ppb	----	5	3-6	25	5.7	----	4.5	35
52 Te ppb	----	13	----	22	19.9	----	19.9	1490
53 I ppb	----	11	----	----	13.3	----	4.2	13.6
55 Cs ppb	20	33	8-17	18	9.14	----	1.44	15.3
56 Ba ppb	5220	6989	----	5100	5600	----	2400	4000
57 La ppb	570	708	----	551	520	----	350	379
58 Ce ppb	1400	1833	----	1436	1730	----	1410	1010
59 Pr ppb	----	278	----	206	----	----	----	129
60 Nd ppb	1020	1366	----	1067	1430	1170	1280	690
62 Sm ppb	320	444	----	347	520	380	490	208
63 Eu ppb	130	168	----	131	188	----	180	79
64 Gd ppb	----	595	----	459	740	----	690	286
65 Tb ppb	90	108	----	87	126	----	120	54
66 Dy ppb	----	737	----	572	766	----	730	364
67 Ho ppb	----	163	----	128	181	----	170	80
68 Er ppb	----	479	----	374	460	----	440	231
69 Tm ppb	----	74	----	54	----	----	----	35
70 Yb ppb	320	481	----	372	490	420	470	229
71 Lu ppb	60	73.7	----	57	74	----	71	386
72 Hf ppb	330	309	----	270	280	----	260	230
73 Ta ppb	40	41	----	40	25.6	----	12.6	23.3
74 W ppb	----	21	(21)	16	24.1	----	16.4	180
75 Re ppb	0.21	0.28	----	0.25	0.236	----	0.23	60
76 Os ppb	2.90	3.4	----	3.8	3.106	----	3.1	880
77 Ir ppb	2.97	3.3	----	3.2	2.81	----	2.8	840
78 Pt ppb	----	6.8	----	8.7	----	----	----	1670
79 Au ppb	0.50	0.75	----	1.3	0.524	----	0.50	257
80 Hg ppb	----	10	----	----	----	----	----	7.9

TABLE 13. (Continued)

Element			Anderson [1983][7]	Ringwood [1991][56]	Sun [1982][67]	Taylor & McLennan [1985][7]	Wänke et al. [1984][77]	Zindler & Hart [1986][89]	Wänke et al. [1984][77] Depleted mantle	Morgan & Anders [1980][44] Bulk Earth
81	Tl	ppb	10	7	4-6	6	----	----	----	3.86
82	Pb	ppb	120	185	----	120	----	----	----	----
83	Bi	ppb	3.3	2.5	1-4	10	----	----	----	2.94
90	Th	ppb	76.5	84.1	----	64	----	----	----	51.2
92	U	ppb	19.6	21	----	18	29.3	20.8	22.2	14.3

TABLE 14. Bulk Continental Crust

Element			Taylor & McLennan [1985][70]	Wänke et al. [1984][77]	Weaver & Tarney [1984][81]
3	Li	ppm	13	13.7	----
4	Be	ppb	1500	----	----
5	B	ppb	10000	----	----
6	C	%	----	0.376	----
9	F	ppm	----	525	----
11	Na	ppm	23000	24400	31000
12	Mg	%	3.20	2.37	1.69
13	Al	ppm	84100	83050	85200
14	Si	%	26.77	28.1	29.5
15	P	ppm	----	763	830
16	S	%	----	0.0881	----
17	Cl	ppm	----	1900	----
19	K	ppm	9100	17600	17000
20	Ca	ppm	52900	49200	34000
21	Sc	ppm	30	21.4	----
22	Ti	ppm	5400	5250	3600
23	V	ppm	230	134	----
24	Cr	ppm	185	146	56
25	Mn	ppm	1400	847	1000
26	Fe	%	7.07	4.92	3.8
27	Co	ppm	29	25.4	----
28	Ni	%	0.0105	0.00695	0.0035
29	Cu	ppm	75	47	----
30	Zn	ppm	80	76	----
31	Ga	ppm	18	18.6	----
32	Ge	ppm	1.6	1.32	----
33	As	ppm	1.0	2.03	----
34	Se	ppm	0.05	0.153	----
35	Br	ppm	----	6.95	----
37	Rb	ppm	32	79.0	61

TABLE 14. (continued)

Element			Taylor & McLennan [1985][70]	Wänke et al. [1984][77]	Weaver & Tarney [1984][81]
38	Sr	ppm	260	293	503
39	Y	ppm	20	----	14
40	Zr	ppm	100	----	210
41	Nb	ppb	11000	----	13000
42	Mo	ppb	1000	----	----
46	Pd	ppb	1.0	----	----
47	Ag	ppb	80	69.5	----
48	Cd	ppb	98	100	----
49	In	ppb	50	69.5	----
50	Sn	ppb	2500	----	----
51	Sb	ppb	200	203	----
52	Te	ppb	----	2.03	----
53	I	ppb	----	1540	----
55	Cs	ppb	1000	1310	----
56	Ba	ppb	250000	542000	707000
57	La	ppb	16000	29000	28000
58	Ce	ppb	33000	54200	57000
59	Pr	ppb	3900	----	----
60	Nd	ppb	16000	25400	23000
62	Sm	ppb	3500	5590	4100
63	Eu	ppb	1100	1407	1090
64	Gd	ppb	3300	8140	----
65	Tb	ppb	600	1020	530
66	Dy	ppb	3700	6102	----
67	Ho	ppb	780	1860	----
68	Er	ppb	2200	3390	----
69	Tm	ppb	320	----	240
70	Yb	ppb	2200	3390	1530
71	Lu	ppb	300	576	230
72	Hf	ppb	3000	3460	4700
73	Ta	ppb	1000	2203	----
74	W	ppb	1000	1310	----
75	Re	ppb	0.5	1.02	----
76	Os	ppb	----	1.02	----
77	Ir	ppb	0.1	1.02	----
79	Au	ppb	3.0	4.07	----
81	Tl	ppb	360	----	----
82	Pb	ppb	8000	----	15000
83	Bi	ppb	60	----	----
90	Th	ppb	3500	----	5700
92	U	ppb	910	1200	1300

TABLE 15. Compositions of the Upper Continental Crust, Lower Continental Crust and Archean Continental Crusts

Element			Upper Continental Crust		North American Shale	Lower Continental Crust	Archean Continental Crust		Post-Archean Continental Crust
			(1)	(2)	(3)	(1)	Upper (1)	Total (1)	(1)
3	Li	ppm	20	22	----	11	----	----	10
4	Be	ppb	3000	----	----	1000	----	----	1500
5	B	ppb	15000	----	----	8300	----	----	----
11	Na	%	2.89	2.57	----	2.08	2.45	2.23	2.6
12	Mg	%	1.33	1.35	----	3.80	2.83	3.56	2.11
13	Al	ppm	80400	77400	----	8.52	8.10	8.04	9.5
14	Si	%	30.8	30.4	----	25.42	28.08	26.63	27.1
19	K	ppm	28000	25700	----	2800	15000	7500	12500
20	Ca	ppm	30000	29500	----	60700	44300	52200	53600
21	Sc	ppm	11	7	----	36	14	30	30
22	Ti	ppm	3000	3120	----	6000	5000	6000	4800
23	V	ppm	60	53	----	285	195	245	175
24	Cr	ppm	35	35	----	235	180	230	55
25	Mn	ppm	600	527	----	1670	1400	1500	1100
26	Fe	%	3.50	3.09	----	8.24	6.22	7.46	5.83
27	Co	ppm	10	12	----	35	25	30	25
28	Ni	%	0.002	0.0019	----	0.0135	0.0105	0.0130	0.0030
29	Cu	ppm	25	14	----	90	----	80	60
30	Zn	ppm	71	52	----	83	----	----	----
31	Ga	ppm	17	14	----	18	----	----	18
32	Ge	ppm	1.6	----	----	1.6	----	----	----
33	As	ppm	1.5	----	----	0.8	----	----	----
34	Se	ppm	0.05	----	----	0.05	----	----	----
37	Rb	ppm	112	110	----	5.3	50	28	42
38	Sr	ppm	350	316	----	230	240	215	400
39	Y	ppm	22	21	35	19	18	19	22
40	Zr	ppm	190	240	----	70	125	100	100
41	Nb	ppb	25000	26000	----	6000	----	----	11000
42	Mo	ppb	1500	----	----	800	----	----	----
46	Pd	ppb	0.5	----	----	1	----	----	----
47	Ag	ppb	50	----	----	90	----	----	----
48	Cd	ppb	98	----	----	98	----	----	----
49	In	ppb	50	----	----	50	----	----	----
50	Sn	ppb	5500	----	----	1500	----	----	----
51	Sb	ppb	200	----	----	200	----	----	----
55	Cs	ppb	3700	----	----	100	----	----	1700
56	Ba	ppb	550000	1070000	----	150000	265000	220000	350000
57	La	ppb	30000	3200	39000	11000	20000	15000	19000
58	Ce	ppb	64000	65000	76000	23000	42000	31000	38000
59	Pr	ppb	7100	----	103000	2800	4900	3700	4300
60	Nd	ppb	26000	26000	37000	12700	20000	16000	16000
62	Sm	ppb	4500	4500	70000	3170	4000	3400	3700
63	Eu	ppb	880	940	20000	1170	1200	1100	1100
64	Gd	ppb	3800	2800	61000	3130	3400	3200	3600
65	Tb	ppb	640	480	130000	590	570	590	640
66	Dy	ppb	3500	----	----	3600	3400	3600	3700
67	Ho	ppb	800	620	140000	770	740	770	820
68	Er	ppb	2300	----	40000	2200	2100	2200	2300
69	Tm	ppb	330	----	58000	320	300	320	320

TABLE 15 (continued)

Element			Upper Continental Crust		North American Shale	Lower Continental Crust	Archean Continental Crust		Post-Archean Continental Crust
			(1)	(2)	(3)	(1)	Upper (1)	Total (1)	(1)
70	Yb	ppb	2200	1500	34000	2200	2000	2200	2200
71	Lu	ppb	320	230	60000	290	310	330	300
72	Hf	ppb	5800	5800	----	2100	3000	3000	3000
73	Ta	ppb	2200	----	----	600	----	----	----
74	W	ppb	2000	----	----	700	----	----	----
75	Re	ppb	0.5	----	----	0.5	----	----	----
77	Ir	ppb	0.02	----	----	0.13	----	----	----
79	Au	ppb	1.8	----	----	3.4320	----	----	----
81	Tl	ppb	750	520	----	230	----	----	----
82	Pb	ppb	20000	17000	----	4000	----	----	10000
83	Bi	ppb	127	----	----	38	----	----	----
90	Th	ppb	10700	10000	----	1060	5700	2900	4800
92	U	ppb	2800	2500	----	280	1500	750	1250

Refs: (1) Taylor and McLennan [1985][70], (2) Shaw, D.M. [1976][63], (3) Haskin et al. [1966][27]

Acknowledgments. I wish to thank S. Maehr for assistance with the tables, and T.J. Ahrens, A.J. Brearley, and R.H. Jones for helpful comments. This work was supported by NSF grants EAR 9005199, EAR 9209641, and the Institute of Meteoritics, Univ. of New Mexico.

REFERENCES

1. Ahrens, T.J., and R. Jeanloz, Pyrite: shock compression, isentropic release, and composition of the Earth's core, *J. Geophys. Res., 92*, 10,363-10,375, 1987.
2. Anders, E., Chemical compositions of the Moon, Earth, and eucrite parent body, *Phil. Trans. Roy. Soc. A285*, 23-40, 1977.
3. Anders, E., and M. Ebihara, Solar-system abundances of the elements, *Geochim. Cosmochim. Acta, 46*, 2,363-2,380, 1982.
4. Anders, E., and N. Grevesse, Abundances of the elements: Meteoritic and solar, *Geochim. Cosmochim. Acta, 53*, 197-214, 1989.
5. Anderson, D.L., Internal constitution of Mars, *J. Geophys. Res. 77*, 789-795, 1972.
6. Anderson, D.L., Chemical composition of the mantle, *J. Geophys. Res., 88*, B41-B52, 1983.
7. Basaltic Volcanism Study Group, *Basaltic Volcanism on the Terrestrial Planets*, Lunar and Planetary Institute, Houston, 1981.
8. Basilevsky, A.T., O.V. Nikolaeva, and C.M. Weitz, Geology of the Venera 8 Landing site region from Magellan Data: Morphological and geochemical considerations, *J. Geophys. Res. 97*, 16,315-16,335, 1992.
9. Beere, H. and R.D. Penzhorn, Measurement of the neutron capture cross section of ^{40}Ar and an s-process analysis from ^{34}S to ^{42}Ca, *Astron Astrophysics, 174*, 323-328, 1987.
10. Bell, J.F., Mineralogical evolution of meteorite parent bodies, *Lunar and Planet. Sci. XVII*, 985-986, 1986.
11. Bell, J.F., A probable asteroidal parent body for the CV or CO chondrites, *Meteoritics 23*, 256-257, 1988.
12. Bell, J.F., D.R. Davis, W.K. Hartmann, and M.J. Gaffey, Asteroids: the big picture, in *Asteroids II*, edited by R.P. Binzel, T. Gehrels, and M.S. Matthews, pp. 921-945, Univ. of Arizona Press, Tucson, A.Z., 1989.
13. Bischoff, A., Palme, H., Schultz, L., Weber, D., and B. Spettel, Acfer 182 and paired samples, an iron-rich carbonaceous chondrite: Similarities with ALH85085 and relationship to CR chondrites, *Geochim. Cosmochim. Acta, 57*, 2631-2648, 1993b.
14. Bischoff, A., Palme, H., Ash, R.D., Clayton, R.N., Schultz, L., Herpers, U., Stöffler, D., Grady, M.M., Pillinger, C.T., Spettel, B., Weber, H., Grund, T., Endress, M., and D. Weber, Paired Renazzo-type (CR) carbonaceous chondrites from the Sahara, *Geochim. Cosmochim. Acta, 57*, 1587-1603, 1993.
15. Brimhall, Jr., G.H., Preliminary fractionation patterns of ore metal through Earth history, *Chem. Geol., 64*, 1-16, 1987.
16. Burns, J.A., Contradictory clues as to the origin of the Martian Moons, in *Mars*, edited by H.H. Kieffer, B.M. Jakosky, C.W. Snyder and M.S. Matthews, pp. 1283-1301, Univ. of Arizona Press, Tucson, A.Z., 1992.
17. Cameron, A.G.W., Elemental and nuclidic abundances in the solar system, in *Essays in Nuclear Astrophysics*, edited by C.A. Barnes, D.D. Clayton, D.N. Schramm, pp. 23-43, Cambridge Univ. Press, Cambridge, 1982.
18. Clark, Jr., S.P., Isotopic abundances and atomic weights, *Handbook of Physical Constants, Revised Edition, Geol. Soc., Amer. Memoir, 97*, 12-17, (Table 3-1), 1966.
19. Clayton, D.D., Stellar nucleosynthesis and chemical evolution of the solar neighborhood, in *Meteorites and the Early Solar System*, edited by J.F. Kerridge and M.S. Matthews, pp. 1021-1062, Univ. of Arizona Press, Tucson, A.Z., 1988.
20. Clayton, R.N., Mayeda, T.K. and C.A. Molini-Velsko, Isotopic variations in solar system material: Evaporation and condensation of silicates, in *Protostars and Planets II*, edited by D.C. Black, and M.S. Matthews, pp. 755-771, Univ. of Arizona Press, Tucson, A.Z., 1985.

21. Consolmagno, G.J. and M.J. Drake, Composition and evolution of the eucrite parent body: evidence from rare earth elements, *Geochim. Cosmochim. Acta, 41*, 1,271-1,282, 1977.
22. Dreibus, G., Palme, H., Spettel, B. and H. Wänke, Sulfur and selenium in chondritic meteorites, *Meteoritics 28*, 343, 1993.
23. Dreibus, G., and H. Wänke, The bulk composition of the eucrite parent asteroid and its bearing on planetary evolution, *Z. Naturforsch, 35a*, 204-216, 1980.
24. Fegley, B., Jr., Venus surface mineralogy: Observational and theoretical constraints, *Proceedings of Lunar and Planetary Science 22*, Lunar and Planetary Institute, Houston, 3-19, 1992.
25. Fegley, B., Jr., and A.G.W. Cameron, A vaporization model for iron/silicate fractionation in the Mercury protoplanet, *Earth Planet. Sci. Lett. 82*, 207-222, 1987.
26. Goettel, K.A., Present bounds on the bulk composition of Mercury: implications for planetary formation processes, in *Mercury*, edited by F. Vilas, C.R. Chapman, and M.S. Matthews, pp. 613-621, Univ. of Arizona Press, Tucson, A.Z., 1988.
27. Haskin, L.A. Frey, F.A., Schmitt, R.A. and R.H. Smith, Meteoritic, solar and terrestrial rare-earth distributions, in *Physics and Chemistry of the Earth, 7*, edited by L.H. Ahrens, F. Press, S.K. Runcorn, and H.C. Urey, pp. 167-321, Pergamon Press, Oxford, 1966.
28. Heiken, G.H., Vaniman, D.T. and B.M. French, editors, *Lunar Source Book*, Cambridge, 736 pp., 1991.
29. Hertogen, J., J. Vizgirda, and E. Anders, Composition of the parent body of the eucrite meteorites (abstract), *Bull. Amer. Astron. Soc., 9*, 458-459, 1977.
30. Hewins, R.H., and H.E. Newsom, Igneous activity in the early solar system, in *Meteorites and the Early Solar System*, edited by J.F. Kerridge and M. Matthews, pp. 73-101, University of Arizona Press, Tucson, A.Z., 1988.
31. Holland, J.G., and R.St.J. Lambert, Major element chemical composition of shields and the continental crust, *Geochim. Cosmochim. Acta, 36*, 673-683, 1972.
32. Jagoutz, E., Palme, H., Baddenhausen, H., Blum, K., Cendales, M., Dreibus, G., Spettel, B. Lorentz, V. and H. Wänke, The abundances of major, minor and trace elements in the Earth's mantle as derived from primitive ultramafic nodules, *Proc. 10th Lunar Planet. Sci. Conf., Geochim. Cosmochim. Acta, Suppl., 11*, 2031-2050, 1979.
33. Jones, J., The composition of the mantle of the eucrite parent body and the origin of eucrites, *Geochim. Cosmochim. Acta, 48*, 641-648, 1984.
34. Jones, J.H., and J.W. Delano, A three component model for the bulk composition of the Moon, *Geochim Cosmochim. Acta, 53*, 513-528, 1989.
35. Jones, J.H. and L.L. Hood, Does the Moon have the same chemical composition as the Earth's upper mantle?, in *Origin of the Earth*, edited by H.E. Newsom and J.H. Jones, pp. 85-98, Oxford Press, N.Y., 1990.
36. Kallemeyn, G.W., Rubin, A.E., and J.T. Wasson, The compositional classification of chondrites: V. The Karoonda (CK) group of carbonaceous chondrites, *Geochim Cosmochim. Acta, 55*, 881-892, 1991.
37. Kerridge, J.F. and M.S. Matthews, editors, *Meteorites and the Early Solar System*, Univ. of Arizona Press, Tucson, A.Z., pp. 1269, 1988.
38. Knittle, E. and R. Jeanloz, Simulating the core-mantle boundary: an experimental study of high-pressure reactions between silicates and liquid iron, *Geophys. Res. Lett., 16*, 609-612, 1989.
39. Lee, T. Implications of isotopic anomalies for nucleosynthesis, in *Meteorites and the Early Solar System*, edited by J.F. Kerridge and M.S. Matthews, pp. 1063-1089, Univ. of Arizona Press, Tucson, A.Z., 1988.
40. Lewis, J.S., Origin and composition of Mercury, in *Mercury*, edited by F. Vilas, C.R. Chapman, and M.S. Matthews, pp. 651-669, Univ. of Arizona Press, Tucson, A.Z., 1988.
41. Longhi, J., Knittle, E., Holloway, J.R., and H. Wänke, The bulk composition, mineralogy and internal structure of Mars, in *Mars*, edited by H.H. Kieffer, B.M. Jakosky, C.W. Snyder and M.S. Matthews, pp. 184-208, Univ. of Arizona Press, Tucson, A.Z., 1992.
42. Mason, B., Concentration Clarkes for ore bodies of the commoner metals, in *Principles of Geochemistry*, Wiley, 310 pp., 1982.
43. Morgan, J.W. and E. Anders, Chemical composition of Mars, *Geochim Cosmochim Acta, 43*, 1,601-1,610, 1979.
44. Morgan, J., and W.E. Anders, Chemical composition of Earth, Venus, and Mercury, *Proc. Nat. Acad. Sci., 77*, 6,973-6,977, 1980.
45. Morgan, J.W., H. Higuchi, H. Takahashi, and J. Hertogen, A "chondritic" eucrite parent body: inference from trace elements, *Geochim. Cosmochim. Acta, 42*, 27-38, 1978.
46. Mumma, M.J., Weissman, P.R., and S.A. Stern, Comets and the origin of the solar system: Reading the Rosetta Stone, in *Protostars and Planets III*, edited by E.H. Levy and J.I. Lunine, pp. 1177-1252, Univ. of Arizona Press, Tucson, A.Z., 1993.
47. Newsom, H.E., Noll, P.D. Jr., Slane, F.A. and T.B. Beserra, Siderophile element abundances and behavior. In *Lunar Planet. Sci. XXIII*, 983-984, 1992.
48. Newsom, H.E. and S.R. Taylor, The single impact origin of the Moon, *Nature 338*, 29-34, 1989.
49. O'Neill, H.St.C., The origin of the Moon and the early history of the Earth - A chemical model. Part 1: The Moon, *Geochim. Cosmochim. Acta, 55*, 1,135-1,157, 1991.
50. Palme, H., and W.V. Boynton, Meteoritic Constraints on Conditions in the Solar Nebula, in *Protostars and Planets III*, edited by E.H. Levy and J.I. Lunine, pp. 979-1004, Univ. of Arizona Press, Tucson, A.Z., 1993.
51. Palme, H., H.E. Suess, and H.D. Zeh, Abundances of the elements in the solar system, *Landolt-Bornstein, VI, 2 pt. a*, Springer-Verlag, New York, 257-272, 1981.
52. Pepin, R.O. and M.H. Carr, Major issues and outstanding questions, in *Mars*, edited by H.H. Kieffer, B.M. Jakosky, C.W. Snyder and M.S. Matthews, pp. 120-143, Univ. of Arizona Press, Tucson, A.Z., 1992.
53. Poldevaart, A., Chemistry of the Earth's Crust, *Geol. Soc. Am., Spec. Pap., 62*, 119-154, 1955.
54. Ringwood, A.E., Basaltic magmatism and the composition of the Moon I: Major and heat producing elements, *The Moon, 16*, 389-423, 1977.
55. Ringwood, A.E., The Canberra model of planet formation, in *Basaltic Volcanism on the Terrestrial Planets*, pp. 653-656, Lunar and Planetary Institute, Houston, T.X., 1981.
56. Ringwood, A.E., Phase transformations and their bearing on the constitution and dynamics of the mantle, *Geochim. Cosmochim. Acta, 55*, 2,083-2,110, 1991.
57. Ringwood, A.E., S. Seifert, and H. Wänke, A komatiite component in Apollo 16 highland breccias: implications for the nickel-cobalt systematics and bulk composition of the Moon, *Earth and Planetary Science Letters, 81*, 105-117, 1986.
58. Ringwood, A.E., and S.E. Kesson, Basaltic magmatism and the bulk composition of the Moon, II. Siderophile and volatile elements in Moon, Earth and chondrites: Implications for lunar origin, *The Moon, 16*, 425-464, 1977.
59. Ronov, A.B., and A.A. Yaroshevsky, Chemical composition of the Earth crust, in *The Earth's Crust and Upper Mantle, Am. Geophys. Union, Mono., 13*, 37-57, 1969.
60. Ronov, A.B., and A.A. Migdisov, Geochemical history of the crystalline basement and the sedimentary cover of the Russian and North American platforms, *Sedimentology, 16*, 137-185, 1971.
61. Rubin, A.E., and G.W. Kallemeyn, Carlisle Lakes Chondrites: Relationship to other chondrite groups, *Meteoritics 28*, 424-425,

1993.

62. Sears, D.W.G., and R.T. Dodd, Overview and classification of meteorites, in *Meteorites and the Early Solar System*, edited by J.F. Kerridge and M.S. Matthews, pp. 3-31, Univ. of Arizona Press, Tucson, A.Z., 1988.
63. Shaw, D.M., Dostal, J., and R.R. Keays, Additional estimates of continental surface Precambrian shield composition in Canada, *Geochim. Cosmochim. Acta, 40*, 73-83, 1976.
64. Spettel, B., Palme, H., Dreibus, G. and H. Wänke, New analyses of CI chondrites: refinement of solar system abundances, *Meteoritics 28*, 440-441, 1993.
65. Spettel, B., Palme, H., Ionov, D.A., and L.N. Kogarko, Variations in the iridium content of the upper mantle of the Earth, *Lunar Planet. Sci. XXII*, 1301-1302, 1991.
66. Stolper, E., Experimental petrology of eucritic meteorites, *Geochim. Cosmochim. Acta, 41*, 587-611, 1977.
67. Sun, S-S, Chemical composition and origin of the Earth's primitive mantle, *Geochim. Cosmochim. Acta, 46*, 179-192, 1982.
68. Taylor, S.R., *Planetary Science: A Lunar Perspective*, 481 pp., Lunar and Planetary Inst., Houston, 1982.
69. Taylor, S.R., Planetary compositions, in *Meteorites and the Early Solar System*, edited by J.F. Kerridge and M.S. Matthews, pp. 512-534, Univ. of Arizona Press, Tucson, A.Z., 1988.
70. Taylor, S.R., and S.M. McLennan, *The continental crust: Its composition and evolution*, Blackwell Sci. Publ., Oxford, 330 pp, 1985.
71. Thiemens, M.H. , Heterogeneity in the nebula: evidence from stable isotopes, in *Meteorites and the Early Solar System*, edited by J.F. Kerridge and M. Matthews, pp. 899-923, University of Arizona Press, Tucson, A.Z., 1988.
72. Tholen, D.J., *Asteroid taxonomy from cluster analysis of photometry*, Ph.D. Thesis, University of Arizona, 1984.
73. Tilton, G.R., Age of the solar system, in *Meteorites and the Early Solar System*, edited by J.F. Kerridge and M.S. Matthews, pp. 259-275, Univ. of Arizona Press, Tucson, A.Z., 1988.
74. Vizgirda, J., and E. Anders, Composition of the eucrite parent body, *Lunar Science VII*, 898-900, 1976.
75. Walter, G., Beer, H., Käppler, F., Reffo, G. and F. Fabbri, The s-process branching at ^{79}Se, *Astron. Astrophys. 167*, 186-199, 1986.
76. Wänke, H., and G. Dreibus, Chemical composition and accretion history of terrestrial planets, *Phil. Trans. Roy. Soc., A325*, 545--557, 1988.
77. Wänke, H., G. Dreibus, and E. Jagoutz, Mantle chemistry and accretion history of the Earth, in *Archean Geochemistry*, edited by A. Kröner, G.N. Hanson, and A.M. Goodwin, pp. 1-24, Springer- Verlag, Berlin, 1984.
78. Wänke, H., H. Palme, H. Baddenhausen, H. Kruse, and B. Spettel, Element correlations and the bulk composition of the Moon, *Phil. Trans. Roy. Soc., A285*, 41-48, 1977.
79. Wasson, J.T., *Meteorites*, Freeman, 267 pp., 1985.
80. Wasson, J.T., and G.W. Kallemeyn, Composition of chondrites, *Phil. Trans. Roy. Soc., A325*, 535-544, 1988.
81. Weaver, B.L., and J. Tarney, Major and trace element composition of the continental lithosphere, in *Physics and Chemistry of the Earth, 15*, edited by H.N Pollack and V.R. Murthy, pp. 39-68, Pergamon, Oxford, 1984.
82. Wedepohl, K.H., Der Primäre Erdmantel (Mp) und die durch die Krustenbildung verarmte Mantelzusammensetzung (Md), *Fortschr. Miner., 59*, 203-205, 1981.
83. Weisberg, M.K., Prinz, M., Clayton, R.N., and T.K. Mayeda, The CR (Renazzo-type) carbonaceous chondrite group and its implications, *Geochim. Cosmochim. Acta, 57*, 1567-1586, 1993.
84. Weisberg, M.K., Prinz, M., Clayton, R.N., Mayeda, Grady, M.M. and I.A. Franchi, Petrology and stable isotopes of LEW 8723-2, a new Kakangari-type chondrite, *Meteoritics 28*, 458-459, 1993.
85. Weisberg, M.K., Prinz, M., and C.E. Nehru, The Bencubbin chondrite breccia and its relationship to CR chondrites and the ALH8-5085 chondrite, *Meteoritics 25*, 269-280, 1990.
86. Woolum, D.S., Solar-System Abundances and Processes of Nucleosynthesis, in *Meteorites and the Early Solar System*, edited by J.F. Kerridge and M.S. Matthews, pp. 995-1020, Univ. of Arizona Press, Tucson, A.Z., 1988.
87. Woosley, S.E. and R.D. Hoffman, 16th advanced course, in *Nucleosynthesis and Chemical Evolution*, edited by B. Hauck, A. Maeder, and G. Meynet, Saas-Fee, 1986.
88. Woosley, S.E. and R.D. Hoffman, Parameterized studies of nucleosynthesis, *Astrophys. J. Suppl.*, 1989.
89. Zindler, A., and S. Hart, Chemical Geodynamics, *Ann. Rev. Earth Planet. Sci., 14*, 493-571, 1986.

Electrical Conductivity Models of the Crust and Mantle

John F. Hermance

1. ELECTRICAL CONDUCTIVITY AS A GEOPHYSICAL (AND PETROLOGICAL) PARAMETER

Of all geophysical parameters — seismic velocity, density, magnetization, etc. — the electrical conductivity, σ (or, its inverse, the resistivity, $\rho = 1/\sigma$), is one of the most sensitive to the composition and temperature of earth materials, and is particularly sensitive to the presence and character of interstitial fluids in the crust and upper mantle. The fluids can be either ion-bearing aqueous phases, or accumulations of partial melt distributed along the pores and cracks of the host rock matrix. Thus, characterizing the distribution of the bulk conductivity of geologic materials in the earth's interior can often place significant bounds on the physical state and processes in the crust and mantle.

To a very good degree, one can represent the bulk or total conductivity of a representative elemental volume in the earth's interior by two parallel branches [20]: conductance through the host matrix (the solid fabric of the rock or mineral) and conductance through materials distributed in the interstitial volume (cracks, pores, joints, etc.) of the rock. In some situations (particularly for certain metamorphic zones in the crust), this interstitial component may consist of interconnected graphite and/or sulfide minerals [28], but in most cases (such as sedimentary basins, unmetamorphosed crystalline basement, etc.), the interstitial component will consist of fluid phases (usually ion-bearing water at crustal depths; but perhaps magma at mantle depth — or at crustal depths in volcanically active areas).

The matrix materials of most rocks and minerals are electrical semiconductors, so that the bulk conductivity of the host medium over a limited range of temperatures generally follows an Arrhenius type relation of the form:

$$\sigma = \sigma_0 \, e^{-E/kT} \tag{1}$$

where σ_0 is a constant depending on the number and mobility of charge carriers, E is an activation energy, k is the Maxwell-Boltzmann constant, and T is the temperature in ^{o}K. Most rocks, if dry, are essentially insulators at temperatures less than several hundred degrees Celsius. Small amounts of pore fluids, however, can substantially increase the bulk conductivity of the composite material.

A rough rule-of-thumb for the bulk electrical conductivity of fluid-saturated rocks (where the fluid can be either an aqueous phase or melt) is the empirical relation known as Archie's Law [28], which in simple form [20] can be expressed as

$$\sigma_{bulk} = \sigma_{fluid} \, P^2, \tag{2}$$

where σ_{bulk} is the bulk conductivity of the rock (the inverse of the bulk resistivity), σ_{fluid} is the conductivity of the fluid contained in the pores and cracks, and P is the fractional porosity of the interconnected pathways. The intrinsic conductivity of the fluid can be represented by the sum

$$\sigma_{fluid} = \Sigma_i \, n_i \, |eZ_i| \, u_i \tag{3}$$

where the index i ranges over all ionic species present in the fluid, n_i is the number of ions of the ith species per unit volume, e is the unit electronic charge, Z_i is the ionization number (or ionic valence) of the particular ionic

J. F. Hermance, Brown University, Environmental Geophysics/ Hydrology, Providence, RI 02912-1846

Global Earth Physics
A Handbook of Physical Constants
AGU Reference Shelf 1

species (so that $|eZ_i|$ is the absolute total charge of the ith ion), and u_i is the mobility of the ith ionic species. Among other factors, an ion's mobility depends inversely on its radius and the viscosity of the fluid. As the temperature increases, the viscosity of the fluid decreases, the mobility of ions increases, and the total conductivity increases. This would be the case, for example, in the earth's crust providing that the effective pore pressure is sufficient to prevent cracks and pores from closing with depth. Figure 1 shows a conceptual model of the expected behavior of conductivity with depth in the earth.

At temperatures above 400-500°C, however, the dielectric properties of water begin to break down, so that ions in aqueous phases begin to associate; as the concentration of free ions decreases (or as n_i in the above expression decreases), σ_{fluid} correspondingly decreases.

As temperatures increase above 600-700°C, since most rocks fall into the class of ionic or electronic semiconductors, conduction of ionic species through the solid fabric of the rock itself starts to become significant, and at temperatures of 1000°C and greater, solid conduction clearly dominates conduction by aqueous phases in cracks and pores. At these temperatures, however, either because the rock itself may begin to melt, or because magma may locally accumulate from sources elsewhere, molten material may appear along grain boundaries. Because ions are so mobile in liquid phases, fluid conduction may again dominate the electrical properties of the bulk rock.

At higher pressures, mineral structures may collapse to denser forms (e.g. olivine to spinel), which might account for some or all of the rapid increase in conductivity associated with the seismic transition zones at depths of 400 to 650 km in the upper mantle [1]. This association, however, is not clear cut from field evidence and is under active study by a number of workers [26, 33, 40, 41].

2. PROCEDURES FOR ESTIMATING CONDUCTIVITIES IN THE CRUST AND MANTLE

The most effective means for studying the earth's electrical conductivity at crust and upper mantle depths is provided by analyzing natural magnetic field transient disturbances from sources in the ionosphere and magnetosphere. An example of a world-wide magnetic "storm" simultaneously recorded at a number of mid latitude standard observatories is shown in Figure 2. A filtered version (T = 1 hr) is shown for comparison in Figure 3 to emphasize some of the large scale correlation patterns (and lack thereof) discussed later.

These magnetic fluctuations induce electromotive forces in the conducting earth and oceans, causing broad-scale eddy currents to flow, which in turn cause secondary magnetic fields over a wide range of amplitudes. (Solid earth workers typically record natural signals having amplitudes from .01 to 10^3 nT and periods from 10^{-4} to 10^5 s; although usually not in the same experiment). Workers can employ the three components of the magnetic field for geomagnetic deep sounding (GDS) or for the magnetic variation (MV) method to obtain one, two, and three dimensional images of the electrical resistivity structure of the Earth's interior [16, 17, 39, 40]. If, in addition, the two horizontal components of the electric field (called the telluric field by electromagneticians) are also measured at various sites, additional constraints on the interpretation may be obtained from employing the conventional 5 component magnetotelluric (MT) method [5, 25, 46].

At periods of 10^{-4} to 1.0 s (or frequencies of 10 kHz to 1 Hz), natural electromagnetic methods employ the propagation of extremely low-frequency, natural electromagnetic energy from distant transient sources in the troposphere due to lightning activity. At periods of 1.0 to 10^5s (or frequencies of 1 Hz to 10^{-2} mHz), the method employs sources in the ionosphere and magnetosphere due to substorms, pulsations and diurnal variations (discussed below).

3. DYNAMICAL CHARACTERISTICS OF NATURAL EXTERNAL SOURCE FIELDS

3.1. Solar-Terrestrial Interactions

The sun constantly emits a stream of neutral plasma which hydromagnetically interacts with the Earth's magnetic field to cause a dew-dropped, or comet-shaped, magnetosphere (Figure 4).

As the Earth rotates through this imposed distortion, electromotive forces are created, and stress, energy and momentum are exchanged between the solar wind and the various elements within the geospace environment: the deep magnetosphere, the plasmasphere, the ionosphere, and even the neutral atmosphere.

3.2. Field Aligned Currents

In the presence of a magnetic field **B**, an electric charge q, moving with a velocity v in an ionized gas, will tend to be deflected perpendicular to the direction of any ambient magnetic field through the body force

$$\mathbf{F} = q\mathbf{v} \times \mathbf{B} \tag{4}$$

The result is that in the absence of collisions, charges are effectively prevented from traveling in straight paths perpendicular to field lines. On the other hand, charges can readily travel along field lines, so the sum total effect is that electric currents experience a much lower resistance when flowing parallel to magnetic field lines than when forced to cross them. This is the primary reason why

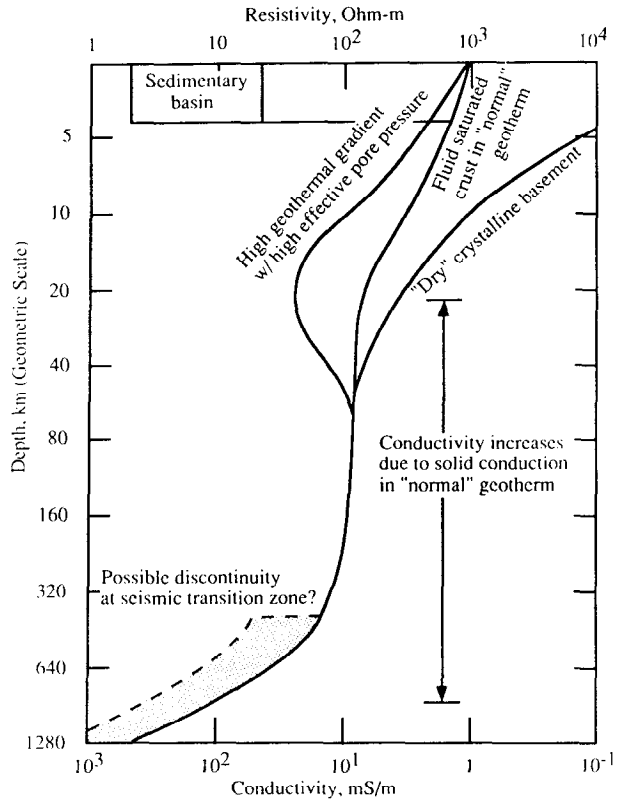

Fig. 1. A conceptual model for the resistivity (conductivity) structure of the earth's crust and upper mantle (from the surface to 1600 km). The units for conductivity, here and in other figures, are millisiemens/meter (mS/m).

electric charges accelerated in the deeper magnetosphere are so readily transferred along field lines into the high latitude auroral zone. These "field aligned currents" (as shown in Figure 5) provide a major mechanism for transferring energy from the deep magnetosphere to the high latitude ionosphere [29, 38].

Because the earth's rotation in the solar wind is a steady state process, field aligned currents are a steady-state feature of the high latitude thermosphere, and provide a significant contribution to the high latitude quiet time magnetic variation field at the earth's surface. During disturbed intervals (triggered by transient perturbations in the solar wind), the intensity of these currents can increase dramatically, and the current systems become very complex in space and time.

At one end of their path, field aligned currents close through horizontal currents in the auroral zone ionosphere, where magnetic field fluctuations of 500 nT or more over time scales of 0.5 hr or less are not unusual in the vicinity of the auroral electrojets. At the other end of their path, field aligned currents close in the equatorial plane at 4-6 earth radii. A number of workers have suggested that the magnetic field signature of these currents may have effects at much lower latitudes — certainly to latitudes as low as 40°, perhaps to the equator. Since a substantial fraction of the magnetic disturbance field at sub auroral, mid and even low latitudes

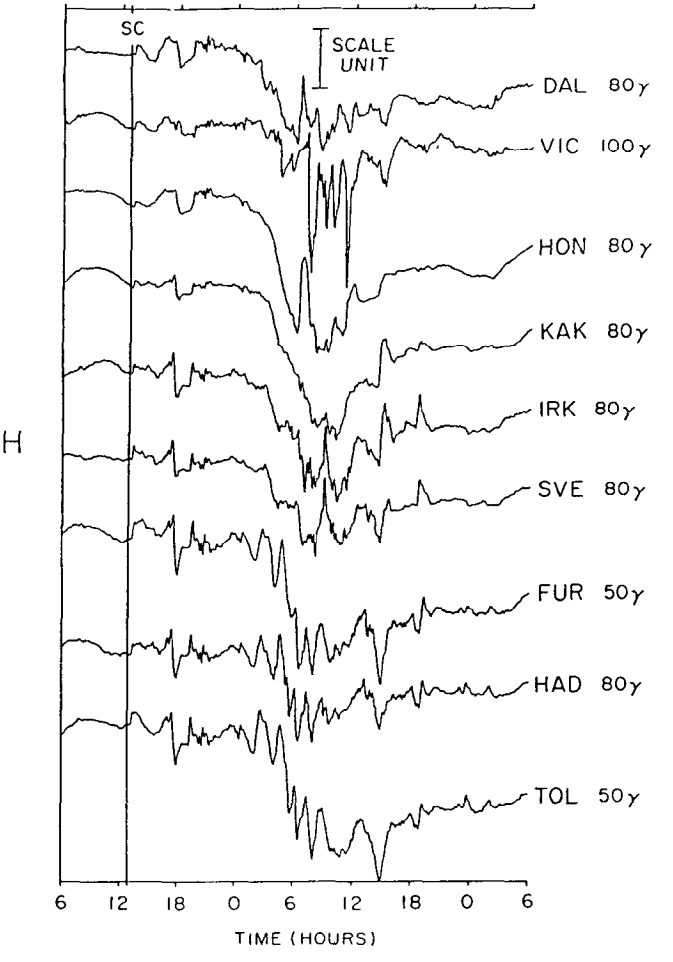

Fig. 2. Magnetograms for the H (magnetic north) component from a magnetic storm recorded from 0600 hrs (UT) April 17, 1965 to 0600 hrs (UT) April 19, 1965 at a number of standard global observatories. Top to bottom (east to west geographic longitude): Dallas, Texas (33°N; 263°E); Victoria, British Columbia (48°N; 237°E); Honolulu, Hawaii (21°N; 202°E); Kakioka, Japan (36°N; 140°E); Irkutsk, Siberia (52°N; 104°E); Svedlovsk, Siberia (57°N; 61°E); Furstenfeldbruck, Germany (48°N; 11°E); Hartland, England (51°N; 356°E); Toledo, Spain (40°N; 356°E). Each magnetogram is scaled so that the number to the right of each trace corresponds to the amplitude in nT (or gammas) of the scale at the top.

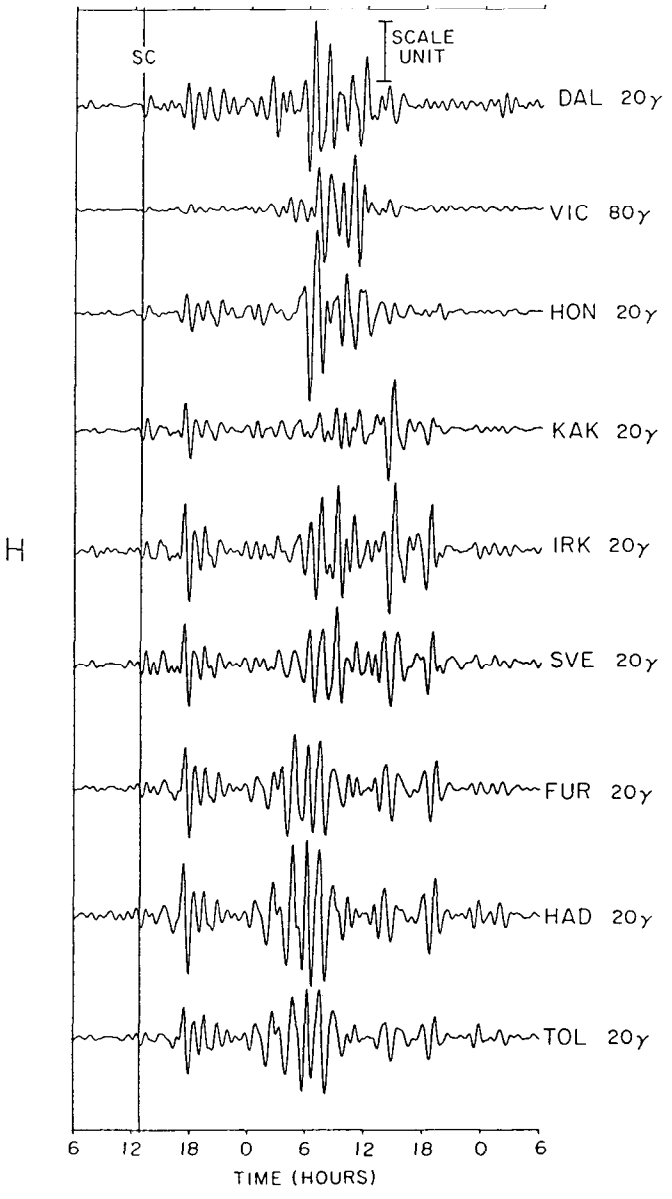

Fig. 3. The time series from Figure 3 numerically bandpassed filtered with a selectivity of 0.3 at a period of 3600 s (1 hr). Note global correlation in some "events" (such as the sudden commencement: SC), and correlation restricted to specific longitude sectors for other events.

may be due to such field aligned currents, there are significant implications for characterizing the source field for solid earth induction studies.

3.3. Quiet Time Magnetic Variations

A daily, or diurnal, variation in the magnetic field strength with an amplitude of approximately 50 nT at mid latitudes on the earth's surface has been recognized for two and a half centuries. At low to sub tropical latitudes,

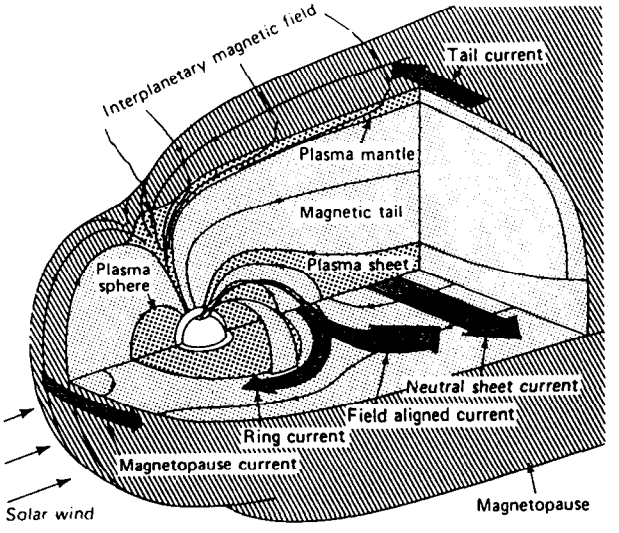

Fig. 4. A generalized view of the Earth's magnetosphere. The innermost sphere is the ionosphere at an altitude of approximately 110 km [29, 38].

most of this variation is caused by the magnetic field of ionospheric electric currents (see Figure 5) from a dynamo in which the highly conducting ionosphere is driven though the earth's magnetic field by solar heating of the atmosphere. In the equatorial zone, the unique electrodynamical setting causes the ionospheric current to locally concentrate to form the equatorial electrojet — an east-directed electric current intensification perhaps 5° wide, extending in longitude over a number of hours around local noon. It is responsible for magnetic field perturbations in excess of 100 nT in a belt perhaps 500 to 1000 km wide.

At latitudes higher than 45°, there is increasing evidence for a significant quiet-time contribution from the earth rotating under steady-state field-aligned currents entering and closing in the auroral zone and the polar cap, driven by processes in the deeper magnetosphere.

3.4. Magnetospheric/Ionospheric Coupling to the Solar Wind

The magnetosphere, ionosphere and upper atmosphere provide a variety of pathways for energy and momentum to be transferred from the solar wind to the Earth's atmosphere. Current systems in the magnetosphere result from global convection systems created by solar wind drag on the Earth's magnetic field. Large-scale instabilities in this system are known as magnetospheric substorms, during which there is a strong intensification of the field-aligned currents — coupling the solar wind and magnetosphere to the ionosphere. (Some of the stronger 0.5 to 1 hr impulses during the storm of Figures 2 and 3 are the low and mid latitude signatures of superimposed substorms at high latitude.) During such substorms, there

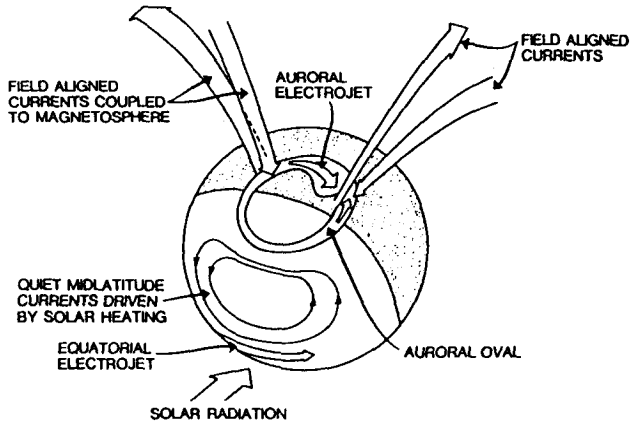

Fig. 5. Field aligned currents in the magnetosphere entering the high latitude ionosphere. The spherical surface corresponds to the global ionosphere at an altitude of approximately 110 km, with the north geomagnetic pole approximately located at the center of the auroral oval so that the Earth's rotation is counterclockwise from this view. The westward electrojet is shown in the midnight (shaded) sector, the eastward electrojet is shown in the late afternoon-evening sector. Also shown is the mid to low latitude quiet time Sq current system in the ionosphere (beneath which the Earth rotates), and its associated equatorial electrojet. [29, 38.]

is a dramatic increase in the number and energy of particles "trapped" in the Van Allen radiation belts at 3 to 6 earth radii.

The general view is that the drift of these trapped particles around the Earth produces a hypothetical ring of electric current at 3 to 6 earth radii that many workers believe is principally responsible for the long term (many hours to days) transient magnetic field observed on the ground during the main phase and the recovery phase of a magnetic storm. This "ring current" has been assumed by many solid Earth workers to be the dominant source of the storm-time Dst signal used for global induction studies (the so-called P_1^0 source term) at periods of hours to many days. A most compelling plot is that of Eckhardt et al. (Figure 6) which shows the geomagnetic colatitude dependence of the horizontal and vertical field amplitudes at a period of 9.8 days from analyzing several years of observatory data. The appropriate theoretical P_1^0 terms, shown as solid lines in the figure, compare favorably (i.e. to first order) to their respective field components.

3.5. Pulsations

Geomagnetic pulsations are quasi-periodic or aperiodic variations in the geomagnetic field with characteristic periods of 0.1 to 600 s, and amplitudes from a fraction of a nanotesla (nT) to as much as tens of nT. Pulsations having periods in the range 10 - 150 s (commonly known as Pc 3,4 pulsations) are ubiquitously observed at all dayside latitudes, and are primarily driven by the interaction of the magnetosphere with the solar wind.

Pi 2 pulsations ($T \approx 40$-150 s) seem to originate from instabilities in the field aligned current system associated with the onset of auroral zone magnetic substorms. Because substorms are nightside phenomena, Pi 2 pulsations are dominant during the night time at subauroral and mid latitudes. Analysis of magnetic pulsations observed by meridional chains of magnetometers in Greenland which span invariant latitudes 66^o to 86^o, have shown that the spatial characteristics of the disturbances can be modeled as the result of ionospheric current vortices associated with field-aligned currents. Pc 3,4 and Pi 2 pulsations provide a rich source of natural electromagnetic energy for the kinds of solid earth studies discussed below.

4. GEOMAGNETIC DEEP SOUNDING USING POTENTIAL SEPARATION

Geomagnetic depth sounding (GDS) involves determining the vertical distribution of electrical conductivity using observations of the magnetic field components alone. The classical approach employs potential field theory to separate fields of internal and external origin, and implies knowledge of the magnetic field over the entire surface of the earth.

One of the most profound contributions of 19th century physics was the recognition that measurements of magnetic field variations on the surface of the earth could be decomposed into contributions from sources outside the earth (external fields) and sources inside the earth (internal fields). Originally applied by Gauss to show that the earth's main magnetic field was of internal origin, workers in the late 19th and early 20th century applied such procedures to magnetic field transients for a range of characteristic phenomena [3, 6, 7, 10, 40, 41].

Since, for the present application, the magnetic flux density **B** in the atmosphere can be assumed to be curl-free (i.e. conduction currents are minimal in the highly resistive atmosphere, and we can neglect the contribution of the displacement field, $\partial D/\partial t$, at the low frequencies of interest), **B** can be represented as the gradient of a scalar potential such that $\mathbf{B} = -\nabla U$. Moreover, the divergence of **B** is zero, so that the scalar potential U is a solution of Laplace's equation

$$\nabla^2 U = 0 \qquad (5)$$

The fact that the magnetic field in the atmosphere can be represented as a potential field (with its intrinsic ambiguity regarding source field distributions) means that for solid earth studies, we do not need to know the true

distribution of currents in the magnetosphere, only the distribution of the global or regional source field at the Earth's surface, or the "equivalent" current system mapped onto, say, the base of the ionosphere.

An appropriate solution to Laplace's equation (5) in the atmosphere is given by

$$U = U_0 \exp\{i[\omega t - k_x x - k_y y] \pm kz\} \quad (6)$$

where ω is the radian frequency, t is the time, and k_x and k_y are the spatial wavenumbers of the source field in the horizontal directions x and y, respectively, and are related to the characteristic spatial wavelengths λ_x and λ_y of the source field through $k_x = 2\pi/\lambda_x$ and $k_y = 2\pi/\lambda_y$. In addition, for (6) to be a solution to (5), it is required that $k = [k_x^2 + k_y^2]^{1/2}$. Without loss of generality, one can write (6) in the form

$$U = [U_e \exp\{- kz\} + U_i \exp\{+ kz\}] \exp\{i(\omega t - k_x x - k_y y)\} \quad (7)$$

where the subscripts e and i are used to denote the coefficients for the external field and the internal field, respectively — an association prompted by the fact that $U_e \exp\{- kz\}$ is a term that decreases in the positive z or downward direction (representing sources from above), whereas $U_i \exp\{+ kz\}$ is a term that decreases in the negative z or upward direction (representing sources from below).

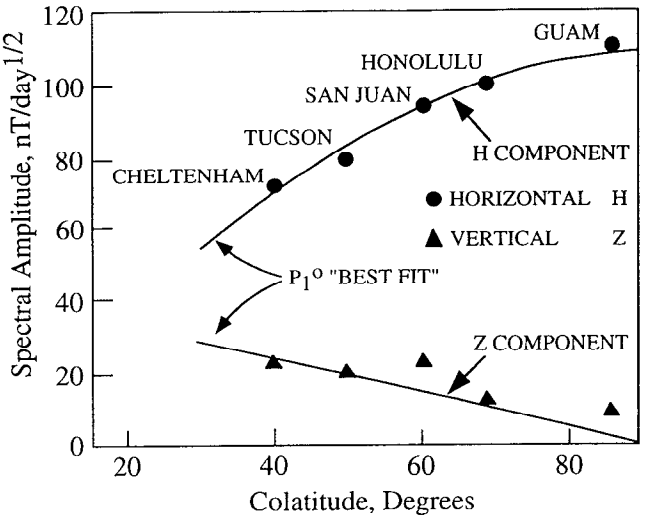

Fig. 6. Plot of horizontal (H) and vertical (Z) magnetic field spectral amplitudes as a function of geomagnetic colatitude at a period of 9.8 days from analyzing observatory daily mean values for 1957-58. P_1^0 mode terms, shown as solid lines in the figure, are least squares fits to their respective field components. [After 10.]

Differentiating U in (7) according to $\mathbf{B} = -\nabla U$, at the earth's surface (z = 0), we obtain for each characteristic wavenumber

$$B_x = - \partial U/\partial x = ik_x [U_e + U_i] \quad (8)$$

$$B_y = - \partial U/\partial y = ik_y [U_e + U_i] \quad (9)$$

$$B_z = - \partial U/\partial z = k [U_e - U_i] \quad (10)$$

where we have suppressed the common factor $\exp\{i(\omega t - k_x x - k_y y)\}$. Since, in principle, the left hand side of each of the above expressions is known (i.e. each corresponds to the observed value for the respective field component, or more strictly to its Fourier coefficient), the set of equations (8) and (10), or, alternatively, the set (9) and (10), can be simultaneously solved for the coefficients U_e and U_i representing the external potential field and the internal potential field, respectively. This is what is properly termed a "potential field separation" — in the case of transient magnetic variations, we have separated the field into its external (or source) and internal.(or induced) field contributions. The problem now reduces to determining a conductivity structure for the earth's interior (usually assumed to vary only in the vertical direction) which when "illuminated" by the corresponding source field, leads to the correct ratio of $Q = U_i / U_e$ for a given range of frequencies.

The range of Q is quite restricted: for a flat earth (i.e. where the wavenumber is much larger than $1/R_e$), $0 \le Q \le 1$, whereas for a round earth (i.e. where the wavenumber is much smaller than $1/R_e$), $0 \le Q \le 0.5$. A major contribution of early global induction studies involved demonstrating that, to first order, long term transients from global magnetic storm disturbances could be represented by a potential field comprised of the single P_1^0 surface harmonic. In addition, workers showed that the ratio of internal to external fields had typical values of $Q \approx 0.3$ to 0.4. They inferred this to imply a substantial increase in conductivity at depths of 400 km or more in the mantle (see Figure 7 where the results from a number of investigations are compared).

Many attempted to associate this rise in conductivity with the seismic transition zones thought to represent phase transitions at 400 and 650 km depth — a possibility which found support from laboratory experiments on materials analogous to those supposed to be present in the earth's interior [1]. The laboratory work showed an order of magnitude increase in the electrical conductivity associated with a solid-solid phase transition of olivine to spinel in a fayalite (Fe_2SiO_4) specimen (a mineralogic analog of forsterite, Mg_2SiO_4, which is thought to dominate the composition of the upper mantle).

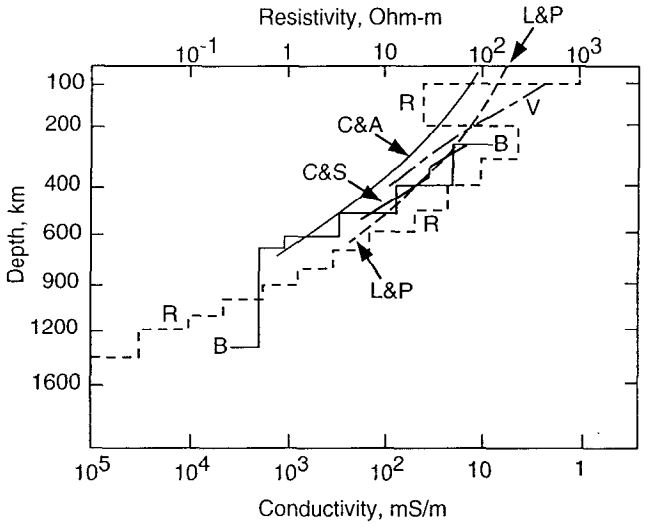

Fig. 7. The results of various global induction studies using quiet time diurnal variations and disturbed time magnetic storm variations. L&P: Lahiri and Price (1939); B: Banks (1972); V: Van'yan (1981); R: Rokityansky (1982); C&A: Campbell and Anderssen (1983), for North America; C&S: Campbell and Schiffmacher (1988), for the Australian region. [After 33.]

5. MAGNETOTELLURICS

5.1. Fundamental Relations

A magnetotelluric survey involves the measurement of orthogonal electric and magnetic field variations at single sites sequentially, or at a number of sites simultaneously [5, 25, 28, 46]. The electric field is measured quite simply as the voltage difference between two electrodes buried in the ground a hundred meters or so apart. The magnetic field can be measured with a variety of sensors: induction coils (known as "search coils" in space physics), superconducting SQUIDS, or flux-gate magnetometers.

A wave component (a horizontal magnetic field in this case) propagating in the positive (vertically downward) direction has the form

$$B_x(z,t) = B_x \exp(-\gamma z) \exp(i\omega t) \tag{11}$$

where $\gamma = [k^2 + i\omega\mu\sigma]^{1/2}$, and σ is the total conductivity given by $\sigma = \sigma_{dc} + i\omega\varepsilon$. For source fields of large horizontal spatial dimensions, the characteristic spatial wavelengths λ_x and λ_y approach infinity, and $k_x \approx k_y \approx 0$; so that $\gamma \approx [i\omega\mu\sigma]^{1/2}$.

At low frequencies, in conductors where the displacement currents become negligible compared to conduction currents, $\sigma \approx \sigma_{dc}$, and γ reduces to

$$\gamma = (1 + i)(\omega\mu\sigma_{dc}/2)^{1/2} \tag{12}$$

5.2. Depth of penetration

We define a parameter $\delta = [\,2/(\omega\mu\sigma_{dc})]^{1/2}$, so that, at the low frequencies used for crust and upper mantle studies, the magnetic field can be represented as the product of two spatial factors:

$$B_x(z,t) = B_{xo} \exp(-z/\delta) \bullet \exp(i\omega t - i\, z/\delta). \tag{13}$$

The first term in (13) represents a monotonic exponential attenuation with depth; the second term represents a harmonic signal traveling in the +z (downward) direction. The first term attenuates in such a way that the field decreases to 1/eth of its value at a depth δ which is termed the "skin depth" or the "depth of penetration" in classical physics. This phenomena is illustrated in Figure 8, which illustrates the "damping" of $B_x(z,t)$ at two periods — 10 s and 1000 s — in a 40 ohm-m homogeneous halfspace. In either case, a unit amplitude field (B_{xo} = unity) is assumed at the surface, and (13) is plotted as a function of depth at an instant of time, t = 0 (actually the real part of $B_x(z,t)$ given by (13) at t = 0).

5.3. Poynting Vector, Characteristic Impedance, and Apparent Resistivity

According to the classical theory of electromagnetic propagation in a linear homogeneous isotropic medium, a uniform plane wave propagates such that the electric field **E** and the magnetic field **H** are orthogonal (recall that **E**×**H** is the Poynting Vector, or the power flow along the direction of propagation). In addition, the ratio of an electric field component to the magnetic field intensity in an orthogonal direction is a characteristic measure of the electromagnetic properties of the medium, often called the characteristic impedance, and denoted by Z where

$$Z = E_x/H_y \tag{14}$$

$$Z = -E_y/H_x \tag{15}$$

$$= i\omega\mu/\gamma. \tag{16}$$

In free-space, where $\sigma_{dc} \approx 0$, the induction parameter becomes $\gamma = (-\omega\varepsilon\mu)^{1/2}$, where μ is the permeability of free space and ε is the permittivity. In this case, the expression for the characteristic impedance given by (16) becomes the well-known form $Z = (\mu/\varepsilon)^{1/2}$,. However, in the more general case of a lossy medium such as the Earth,

$$Z = (i\omega\mu/\sigma)^{1/2}, \tag{17}$$

where $\sigma = \sigma_{dc} + i\omega\varepsilon$, or, in terms of the resistivity $\rho = 1/\sigma$,

$$Z = (i\omega\mu\rho)^{1/2}. \quad (18)$$

Procedurally, simultaneous measurements of natural electric and magnetic field variations at the earth's surface can be Fourier analyzed into appropriate frequency contributions, and, upon forming the ratios of orthogonal component pairs (e.g. E_x and H_y, or E_y and $-H_x$) at appropriate frequencies ω, can be used in (14) and/or (15) to determine the impedance Z of the earth. The relation between the impedance and the actual resistivity of the medium can then be factored to yield

$$\rho_a = (i/\omega\mu)|Z|^2, \quad (19)$$

or, in terms of the actual electric and magnetic field components measured at the earth's surface, one could determine a measure of the depth averaged resistivity

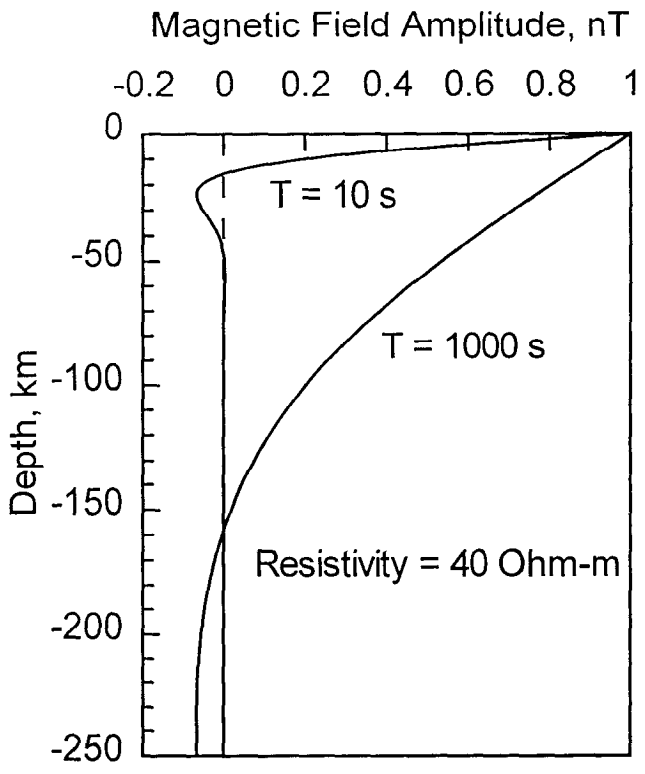

Fig. 8. Comparing the penetration of a unit amplitude (1 nT) magnetic field signal $B_x(z,t)$ in a 40 ohm m homogeneous halfspace at periods of 10 s (corresponding to δ = 10.07 km), and 1000 s (corresponding to δ = 100.7 km), respectively. For this specific case, the field decreases with depth more rapidly than the exponential damping would suggest because of the second spatial factor in (13) which, at t = 0, has the form $\cos(z/\delta)$.

$$\rho_a = (i/\omega\mu)|E_x/H_y|^2, \quad (20)$$

$$= (i/\omega\mu)|E_y/H_x|^2. \quad (21)$$

The subscript "a" is used in these expressions to denote that the left hand terms are an "apparent" resistivity, since, for a heterogeneous earth, a particular value calculated from this relation may represent some type of volumetric average of two or more "true" resistivities.

6. PRINCIPLE OF "DEPTH SOUNDING" METHODS

The fundamental principle on which natural electromagnetic methods are based involves the concept of "skin depth" or the "depth of penetration", $\delta = (2/\omega\mu\sigma_{dc})^{1/2}$, of electromagnetic fields in a lossy electrical medium (such as the solid earth). As shown in the last section, for a medium of given conductivity, lower frequency (longer period) signals propagate to greater depths than higher frequency (shorter period) signals. Therefore by estimating the response of the earth at increasingly longer periods, one can obtain a measure of the electrical conductivity of the earth's interior at progressively greater depths. Typical periods employed by MT workers to study the crust and upper mantle extend from 10^{-3} to 10^4 s (although several special studies have gone to 10^5 s, and longer).

At a period of 10 s, and for a resistivity of the earth of 10 ohm-m (a period typical of pulsations and a resistivity typical of sedimentary basins), we obtain a depth of penetration of approximately 5 km. If, instead of a period of 10 s, one used a period of 10^4 s, and instead of a resistivity of 10 ohm-m, the earth had a resistivity of 10^2 ohm-m (typical of the earth's upper mantle), then the depth of penetration would increase to 500 km — the depth of penetration goes as the square root of the product of the resistivity of the medium and the period of the signal.

To illustrate the concept of "depth sounding," consider a simple two-layered earth. The skin-depth phenomenon will cause observations at short period to lead to a response function (the apparent resistivity) asymptotic to that associated with the true resistivity of the upper layer. Whereas at long periods the skin depth will be large and the observations will asymptotically approach the true resistivity of the deeper layer. The magnetotelluric response for such a two-layered earth model is shown in Figure 9.

For the case used here, the resistivity of the upper layer is 10 ohm-m (corresponding to a surface layer of conductive sediments), and the resistivity of the lower half space is 1000 ohm-m (corresponding to more resistive crystalline basement). The response is shown for various

earth models in which the depth to the interface between the two layers is progressively larger (from 100 to 2000 m, respectively). As seen in this figure, the response for the model corresponding to each depth is associated with a particular range of periods over which the observed apparent resistivity changes from values characteristic of layer 1 (ρ_1 = 10 ohm-m) to values characteristic of layer 2 (ρ_2 = 1000 ohm-m). As the interface gets deeper, this transition in apparent resistivity occurs at longer periods. Thus a magnetotelluric "sounding" in such a setting will yield *three* essential pieces of information on the structure: ρ_1, ρ_2 and the depth to the interface between the two layers. In this way, one can use increasingly longer periods to "sound" the earth to progressively greater depths.

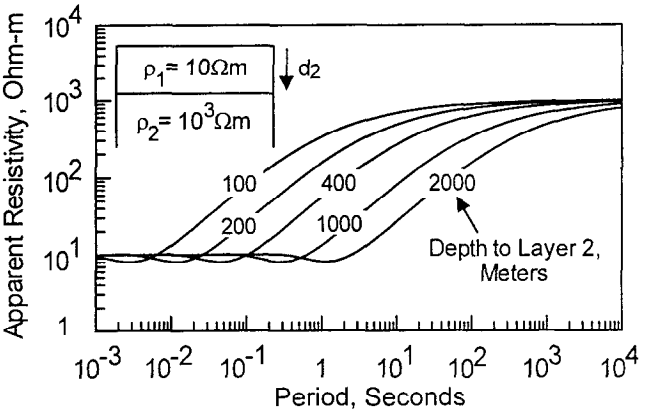

Fig. 9. The theoretical magnetotelluric (MT) response at the surface of a two layered earth for various depths to the lower interface. The resistivity of layer one is 10 ohm-m, and that for layer two is 1000 ohm-m. The magnetotelluric apparent resistivity is plotted as a function of the period for the case of five different earth models corresponding to depths to layer two (d_2) of 100, 200, 400, 1000, and 2000 m, respectively.

7. MAGNETIC GRADIOMETRIC METHOD

While potential field separation is the classical method for global induction studies, more recently one of the more widely used geomagnetic depth sounding (GDS) approaches is the magnetic gradiometric method [4, 30, 39, 40]. This technique estimates the conductivity of the underlying medium given observations of the vertical field, B_Z, and the horizontal divergence of the horizontal magnetic field components, $[\partial B_X/\partial x + \partial B_y/\partial y]$, at the earth's surface.

Solutions to the dissipative Helmholtz equation for **B** in a medium having conductivity σ can have the form

$$\mathbf{B} = \mathbf{B}_0 \exp\{i[\omega t - k_x x - k_y y] \pm \gamma z\} \quad (22)$$

where, as before (Section 5.1), γ is the induction parameter defined by $\gamma = [k^2 + i\omega\mu\sigma]^{1/2}$, where $k = [k_x^2 + k_y^2]^{1/2}$. The term $\exp(-\gamma z)$ represents downward traveling functions from primary source fields above, whereas the term $\exp(+\gamma z)$ represents upward traveling functions from secondary induced sources below.

Upon rearranging the non-divergence of **B** ($\nabla\cdot\mathbf{B} = 0$), one obtains

$$[\partial B_X/\partial x + \partial B_y/\partial y] = -\partial B_Z/\partial z. \quad (23)$$

Assume, for the moment, a homogeneous earth where one has only downward propagating waves corresponding to the exp $(-\gamma z)$ term in (22). One can calculate the vertical derivative of the B_Z component of that expression to show that

$$\partial B_Z/\partial z = -\gamma B_Z. \quad (24)$$

Upon substituting (24) for the right side of (23), and rearranging to solve for $1/\gamma$, one obtains what some workers refer to as a complex induction length given by

$$C = 1/\gamma = B_Z / [\partial B_X/\partial x + \partial B_y/\partial y]. \quad (25)$$

Just as in the magnetotelluric case, where the definition of the resistivity for a homogeneous half-space is generalized to the concept of the *apparent resistivity* of an arbitrarily layered medium, so too has the concept of the complex induction length been generalized to include the multi-layered case.

8. ZERO WAVENUMBER APPROXIMATION

Under the assumption $k^2 << |i\omega\mu\sigma|$, the induction parameter $\gamma = [k^2 + i\omega\mu\sigma]^{1/2}$ becomes

$$\gamma \approx [i\omega\mu\sigma]^{1/2} \quad (26)$$

and, upon again neglecting displacement currents so that $\sigma \approx \sigma_{dc}$, the complex induction length $1/\gamma$ for a homogeneous earth given by (25) becomes

$$C = 1/[i\omega\mu\sigma]^{1/2} = [1 - i]\,\delta_0/2, \quad (27)$$

where $\delta_0 = (2/\omega\mu\sigma)^{1/2}$ is the conventional "skin depth" or "depth of penetration" of a plane wave in a homogeneous medium, and the subscript "o" on δ_0 denotes the zero wavenumber or plane wave case. (Note, however, that the source field for the gradiometric method

can never be exactly uniform, or k will be identically 0, and the horizontal derivatives in the denominator of the last term in (25) will vanish.)

Expression (27) shows that for a homogeneous Earth, the parameter C is directly proportional to the depth of penetration (hence the concept of induction "length"), and has a phase of -45°. This relation can be easily rewritten to provide the following form for estimating the resistivity of the underlying medium,

$$\rho = \omega\mu\,|C|^2 \qquad (28)$$

where, observationally, C is given above by the last term in (25). The magnetic gradiometric approach is quite analogous to the magnetotelluric method described above with ρ calculated from (28) serving the same role as the magnetotelluric apparent resistivity calculated from (19).

As in the magnetotelluric case considered above in Section 5.3, when the earth is not homogeneous, but can be represented by a resistivity function that varies with depth, one determines a volumetrically averaged "apparent" resistivity, ρ_a, and an "effective" induction length, C. In such a case, C (still assuming $k \approx 0$) is given at the surface of the earth for a particular frequency, ω, by

$$C = (1/\gamma)[(I - R) / (I + R)], \qquad (30)$$

where $\gamma \approx (i\omega\mu\sigma_{dc})^{1/2}$, I is a coefficient representing the strength of the incident wave function, and R is a coefficient representing the strength of the function "reflected" from the various layers at depth within the earth, so is dependent on the frequency, as well as the resistivity and thickness of each layer. The parameter C from (30) can be substituted into (29) and, in principle, one can solve for an apparent resistivity analogous to the MT case, but without the need to explicitly employ electric field information.

9. THE "SOURCE EFFECT" ON GDS AND MT STUDIES

Traditionally, the magnetic gradiometric method has been developed — as was the MT method — for the quasi zero wavenumber case (i.e. $k \approx 0$). However, even when the source field has a finite wavenumber (i.e. when the approximation $k \approx 0$ is no longer valid), it continues to be useful to define an apparent resistivity

$$\rho_a = \omega\mu\,|C|^2 \qquad (31)$$

where C is still theoretically given by the form (30), but now γ, I and R are all functions of the characteristic wave number k of the source field [26].

The fundamental principle on which natural electromagnetic methods are based involves the concept of depth of penetration, which, as given above for a plane wave incident on a homogeneous earth, is $\delta_o = (2/\omega\mu\sigma)^{1/2}$. As discussed above in Section 6, in a medium of given conductivity for the zero wavenumber case, lower frequency signals propagate to greater depths than higher frequency signals. However, if "source effects" dominate (i.e. if the spatial wave number is so large that the induction parameter $\gamma = [k^2 + i\omega\mu\sigma]^{1/2}$ is dominated by $k^2 >> i\omega\mu\sigma$, so that $\gamma \approx k$), then the depth of penetration is not governed by the resistivity of the earth at all, but becomes asymptotic to $\delta_k = 1/k$ (where the subscript "k" denotes the large wave number limit). Thus, at large wavenumbers, the behavior of the electromagnetic field is governed by the dimensions of the source field, rather than the electrical conductivity structure of the solid Earth.

As an example, for a typical source field dimension of 6000 km, the source effect may become important when one is studying the Earth at depths on the order of 1000 km ($k = 2\pi/6000$), or greater. This underscores the importance of explicitly accounting for the nature of source/earth coupling phenomena for solid earth induction studies [19, 26, 37, 47].

The point of the above discussion is two-fold. First, the horizontal gradient of the source field at the earth's surface can be used along with the vertical field to infer the gross electrical structure of the earth's interior. Second, in deriving the simple zero wavenumber form for the parameter C as was done in Section 8, an implied condition was that $\lambda_x >> \delta_o$ and $\lambda_y >> \delta_o$. If this is not the case, but rather the spatial wavelength of the source field is on the order of, or less than, a characteristic depth of penetration, then the estimate of the apparent resistivity will be biased by what is known as the "source effect".

10. HORIZONTAL MAGNETIC VARIATION PROFILING

Three component magnetic field variations at each field site along a profile can be reduced to complex magnetic transfer coefficients in the frequency domain [39]. This assumes a linear relationship at a particular site between the spectral coefficients for the vertical magnetic field component, B_Z, and the two horizontal field components, B_X(north) and B_Y(east), having the form:

$$B_Z = M_{ZX}B_X + M_{ZY}B_Y\,. \qquad (32)$$

One can loosely think of M_{ZX} and M_{ZY} as representing vector components of **M**, itself. However **M** is generally complex, so that there are "directions" of **M** associated with both its real and imaginary parts. In 2-D, these

directions will be collinear (i.e. parallel or antiparallel), but in 3-D situations the real and imaginary "induction vectors" are often not aligned. The amplitude of **M** projected on to the local principal direction is a measure of the dip of the anomalous magnetic field perturbation below the horizontal [since the tangent of the dip angle θ is equivalent to B(vertical)/B(horizontal)].

In a strictly 2-D situation one can rotate their measuring coordinate system such that the two horizontal directions are oriented parallel (the new x direction, say) and perpendicular (the new y direction) to the strike of electric current flow. In this case, plotting observed values of M_{zy} along a profile perpendicular to strike provides a graphic measure of local distortions of the magnetic field variations. And by analyzing M_{zy} over a range of periods, one can use the depth of penetration phenomena to separate near surface features from deeper features. The application of magnetic variation profiling to a transect of the Rio Grande rift in the vicinity of the Socorro magma body is shown in Figure 10.

This figure shows

a) The original data (shown as points in each panel) reduced to complex (real and imaginary) spectral estimates at periods of 63 s and 625 s, respectively,
b) A resistivity model determined using generalized inverse theory,
c) The real and imaginary components of the predicted model response at the two periods (shown as solid lines in each panel).

Contrary to what a number of non-specialists apparently believe, electromagnetic induction methods are not potential field methods in the classical sense, and do not suffer from the nonuniqueness usually associated with those techniques — by using data over a range of frequencies (and from a number of sites for the 2-D and 3-D cases), the depth of penetration phenomenon allows one to unequivocally separate the effects of shallow features from deeper features.

11. OVERVIEW OF RESULTS FROM NATURAL ELECTROMAGNETIC STUDIES

We conclude our discussion with a generalized 1-D view of the earth (see Figure 11) which, while over-simplified, provides the conceptual paradigm for many electromagnetic studies. We then apply these concepts to two contrasting tectonic environments: extensional and collisional regimes. For more specific information, the reader is directed, for global scale studies, to [33] and [40], and for regional MT and MV studies from various tectonic regimes, to the comprehensive reviews of [11], [17], [22], [23] and [36].

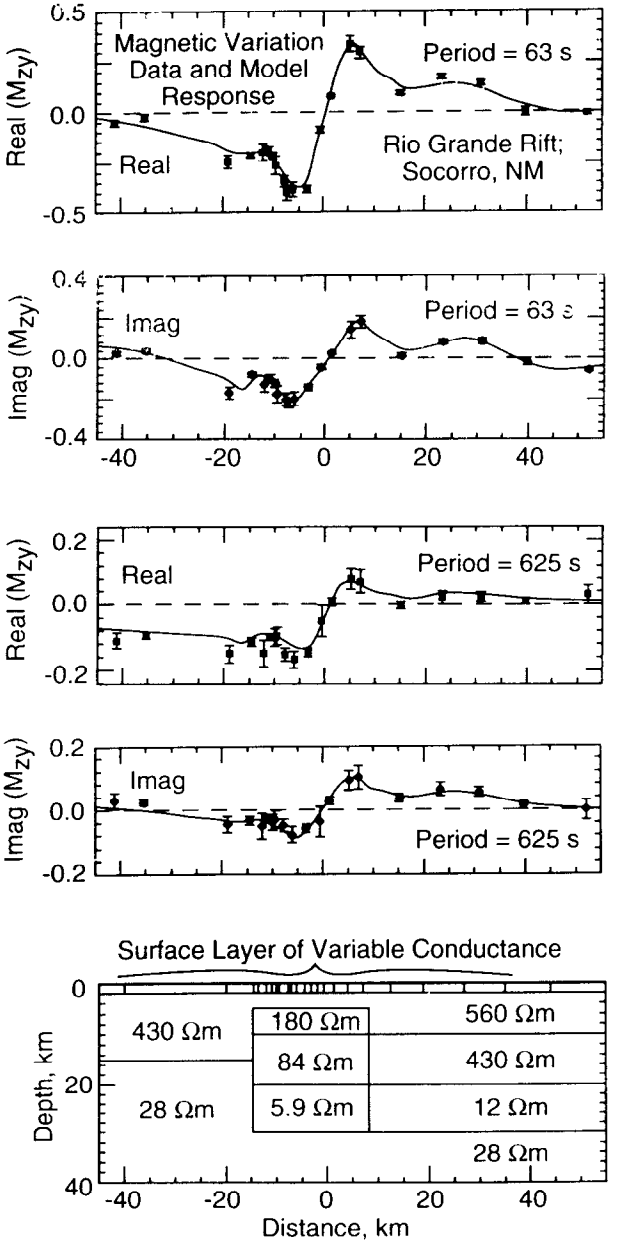

Fig. 10. Magnetic variation (MV) parameters from a profile of sites along an east-west line transecting the Rio Grande rift at a point centered 10 km south of Socorro, New Mexico (along a latitude of approx. 34°N). The original data are shown as points in each panel, reduced to complex (real and imaginary) spectral estimates at periods of 63 s and 625 s, respectively. The bottom panel shows a resistivity model determined using generalized inverse theory, and the real and imaginary components of the predicted model response at the two periods are shown as solid lines in each panel. [After 24.]

11.1. A Synoptic Model

In general, at periods of 10^{-2} to 10^{3} s, magnetotelluric and magnetic variation profiling surveys can be of great value in the reconnaissance of sedimentary basins. Because sediments tend to have a relatively high porosity (10-20%), and to be saturated with ground water having a relatively high concentration of ions, their resistivity is typically quite low (2-20 ohm-m; see Figure 11).

In contrast, the crystalline basement that outcrops nearby, or underlies the sediments, tends to have a much lower porosity (less than 1%). This results in far fewer connected pathways along which ions (the major charge carriers for the electric current) can flow. Consequently, crystalline and metamorphic basement materials tend to have a much higher resistivity (10^{3} - 10^{4} ohm-m). Thus as shown in Figure 11, to a first order approximation a sedimentary basin can, in some sense, be characterized as a single layer of low resistivity sediments (2-20 ohm-m), underlain by a highly resistive crystalline basement (10^{3} - 10^{4} ohm-m). Determining the depth to basement is often a key objective in many geophysical studies; a parameter which was readily determined for the idealized, two layered case considered above in Section 6 (see Figure 9).

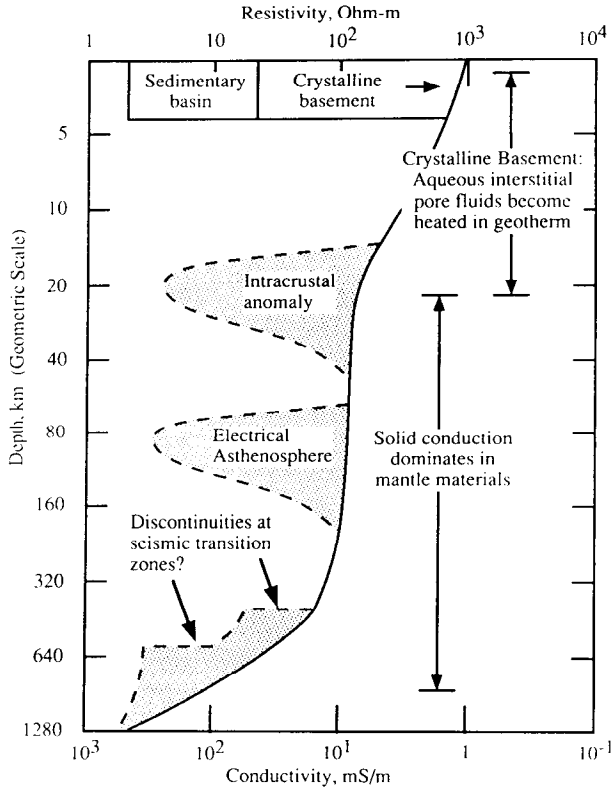

Fig. 11. A generalized 1-D conceptual model of the earth emphasizing various "targets" of interest to electromagnetic studies: sedimentary basins, intracrustal conductivity anomalies, the "electrical asthenosphere" and the transition zones at (circa) 400 and 650 km. The units for the conductivity are millisiemens/m (mS/m).

Another parameter which is readily determined from natural electromagnetic studies is the depth to a conductor. This is often the objective in regional surveys when one is investigating large scale thermo-mechanical processes at depth in the lithosphere or asthenosphere, particularly in tectonically active areas, where surface thermal gradients may be quite high. While the low temperature electrical conductivity of the crystalline basement at depths of a few km is usually limited by conduction in pore fluids and is relatively resistive in the range of 10^{3} - 10^{4} ohm-m, at greater depth where thermal gradients may lead to temperatures of several hundred degrees or so, interstitial aqueous phases may lead to bulk resistivities as low as 10 ohm-m.

At still higher temperatures, say 800°C or so, semiconduction mechanisms in the bulk material itself cause the resistivity of even crystalline rock to drop to values of only a few tens of ohm-meters — molten rock typically has a resistivity on the order of 1 ohm-m or less. Thus it is typical for MT surveys in active tectonic areas to indicate a resistive upper crust (10^{3} - 10^{4} ohm-m), underlain at a depth of 15-20 km by a zone having a bulk resistivity significantly less than 10^{2} ohm-m (Figure 11). Most workers feel that this low resistivity material represents conductive interstitial fluid — either ion-bearing aqueous phases or accumulations of partial melt — in a relatively resistive matrix [20].

At greater depth (approx. 100 km, as shown in Figure 11), in many areas there seems to be evidence of an anomalously low resistivity associated with the asthenosphere, perhaps due to small fractions of partial melt or melt accumulations [44]. This highly conducting (up to 4,000 S) "electrical asthenosphere" is a common feature of many seafloor experiments [2, 9, 12, 13], but does not appear to be a ubiquitous (at least resolvable) feature of global nor continental-scale interpretations [36, 45].

There is, on the other hand, substantial evidence for a sharp increase in electrical conductivity on a global scale at a depth between 400 and 800 km (see Figure 11 as a generalization of Figure 7) which many believe is associated with the so-called "transition zones" in the upper mantle, inferred through seismic studies to be solid-solid phase transitions. The present evidence, however, for the collocation of sharp changes in electrical conductivity with the upper mantle seismic discontinuities, while suggestive, is not compelling [26, 33, 41].

11.2. Extensional Regimes

Figure 12 is a conceptual model representing an

electrical cross-section of western North America along a latitude of approximately 36°N from the Sierra Nevada Mountains in the west to the High Plains in the east. The Basin and Range province of Eastern California, Nevada and Utah, and the Rio Grande Rift of Central New Mexico are presently zones of active extension.

The Sierra Nevada block to the west has been recently uplifted by over 4 km along a series of major normal faults along its eastern front. The Colorado Plateau is a relatively stable province that too has been uplifted several km in the last 10 million years. The High Plains province has been gently uplifted to the west and slopes to the east, relatively undeformed, to the Mississippi River and beyond.

Seismicity and high heat flow are associated with active extension in the Basin and Range and the Rio Grande Rift, and both provinces are underlain by zones of anomalously low resistivity at mid-levels (15-20 km) in the crust (Figure 12) — a feature commonly found in many rift zones of the earth [22]. This electrical anomaly — thought to represent conductive fluid phases in an otherwise resistive solid matrix — is generally associated with a zone of seismic attenuation or low seismic velocity — hence it has been termed the intracrustal geophysical anomaly [22]. This electrical feature is well-bounded having a reasonably well-resolved depth to its top, a conductance (conductivity-thickness product) of several thousand Siemens, and a resolved maximum depth to bottom, below which the resistivity increases [21]. The intracrustal anomaly does not seem to be present beneath the Colorado Plateau (although the crust is significantly conductive [34]), and its effect is substantially attenuated beneath the High Plains to the east where its conductance may be only several hundred Siemens. There is evidence that the anomaly is sharply truncated at the face of the Sierras to the west.

Superimposed on this ubiquitous relatively flat-lying mid-crustal feature are modulations in the magnitude and

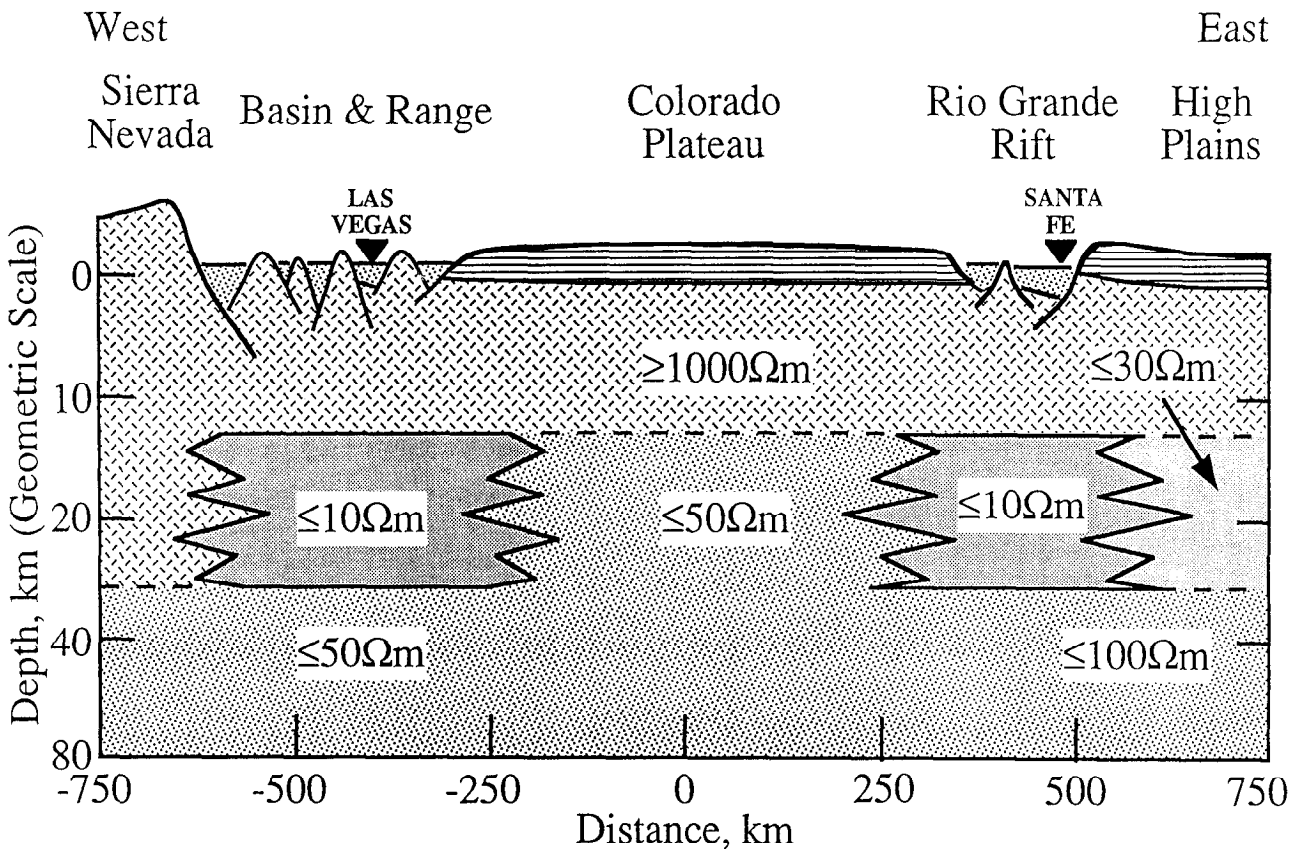

Fig. 12. A two-dimensional conceptual model of western North America from west to east along a latitude of approximately 36°N emphasizing the relation of an intracrustal conductivity anomaly to the extensional regimes of the Basin and Range province of southern California and Nevada, and the Rio Grande Rift of Central New Mexico. For reference, the approximate locations of Las Vegas, Nevada, and Santa Fe, New Mexico, are indicated.

distribution of conductivity associated with local perturbations in the thermal regime, such as the Socorro "magma body" ([24]; see Figure 10 and its related discussion above).

11.3. Collisional Regimes

A generalized composite section representing oceanic lithosphere colliding and subducting beneath continental lithosphere from electromagnetic studies in several regions is illustrated in Figure 13. Subduction of the Pacific plate beneath New Zealand was studied using land-based MT and MV data from New Zealand [27].

Subduction of the Juan de Fuca plate beneath the northwest United States and southwest Canada was studied by a number of investigators: MT data from a series of parallel east-west profiles in the Cascade Volcanic Belt of Washington and Oregon were interpreted by [43]; MT data from Vancouver Island were interpreted by [31]. Perhaps the most comprehensive single experiment in this region involved the simultaneous deployment of an array of land-based and ocean floor MT and MV instruments over this entire area during Project EMSLAB (Electromagnetic Studies of the Lithosphere and Below; see the review of MT interpretations by [48] and MV results by [18, 23]. Among the lessons learned from the studies of [18, 43] should be the great variability of these features along strike — a point the reader should keep in mind when viewing the generalized 2-D section in Figure 13.

While the present evidence is not overwhelming, several MT workers have suggested the presence of a relatively conductive zone (50 ohm-m or less) being subducted directly at the continental margin (from -200 to +100 km) beneath both New Zealand and western North America. If in fact present, this conductive (≤50 ohm-m) feature is likely to be sediments and/or shallow ocean basement saturated with sea water, and appears to be underlain by a more resistive (≥500 ohm-m) layer representing relatively impermeable lower crust and upper mantle. Beneath the resistive section, the mantle becomes more conductive. Figure 13 more closely represents the situation for western North America where the subduction zone (and

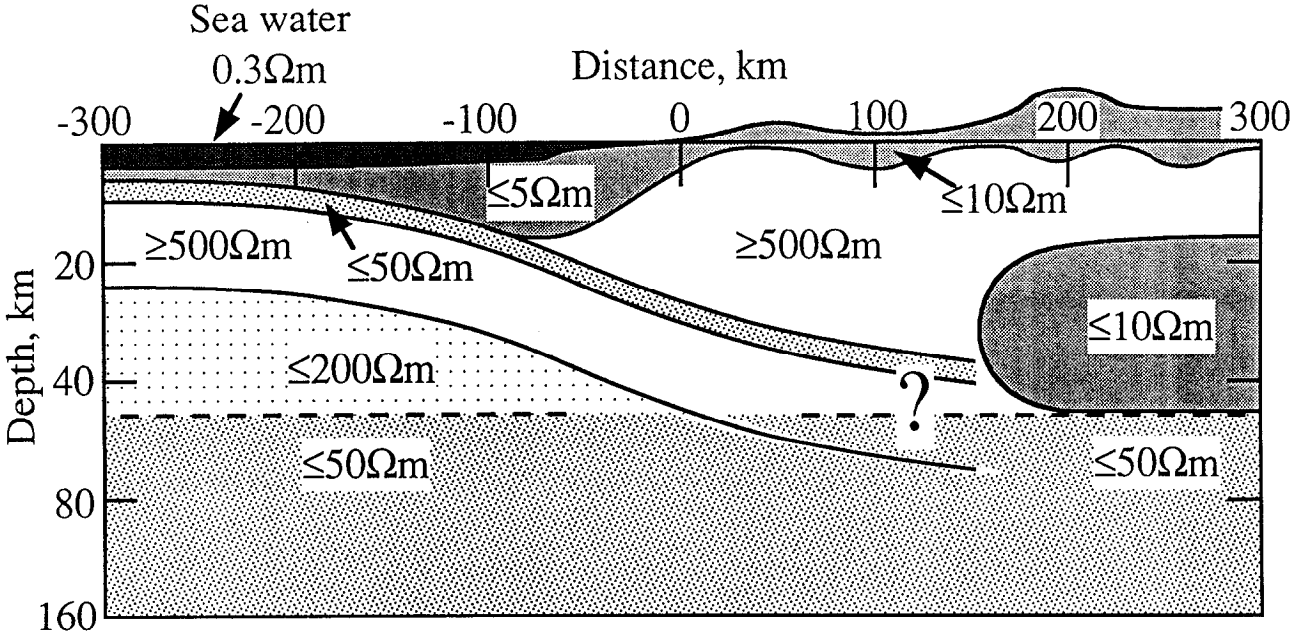

Fig. 13. A generalized composite section representing oceanic lithosphere colliding and subducting beneath continental lithosphere based on electromagnetic studies from several regions of the Pacific: New Zealand employing a series of seafloor MT stations along a 190 km SE-NW (from left to right in the figure) profile centered at approx. 41S lat. and 175.5E long.; Vancouver Island in southwest Canada using land MT stations along an 80 km SW-NE profile centered at 49N lat. and 124.5E long.; the Pacific Northwest of the United States (from seafloor and land MT stations along a 350 km W-E profile at a latitude of 45N, crossing the coast 30 km north of Newport, Oregon. A relatively conductive (50 ohm-m or less) zone dipping from left to right is likely to be sea water saturated sediments and/or shallow ocean basement subducted with the oceanic plate. A unique feature of the Pacific Northwest (as compared to the New Zealand subduction zone) is a profound electrical anomaly (≤10 ohm-m) subtending the volcanically active High Cascades at a depth of 15-20 km, extending to the east to the Basin and Range province.

continental margin) is relatively close to the spreading center along the Juan de Fuca ridge. Recent advected mantle material is hotter and more conductive (perhaps ≤50 ohm-m at 50 km depth) beneath western North America than the older, colder plate being subducted beneath New Zealand (perhaps ≥100 ohm-m above a depth of 150 km).

A unique feature of the Pacific Northwest (as compared to the New Zealand subduction zone) is a profound electrical anomaly (≤10 ohm-m) subtending the volcanically active High Cascades at a depth of 15-20 km, extending to the east to the Basin and Range province. Some workers have suggested that features associated with Basin and Range extension are being imprinted on processes beneath the Cascades [e.g. 23]. In fact, [43] likened the High Cascades intracrustal anomaly to a similar feature beneath the Rio Grande rift (discussed above). As indicated in Figure 13, the behavior of the subducted oceanic conductor (≤50 ohm-m) is not clear in the vicinity of the High Cascades intracrustal anomaly (≤10 ohm-m).

REFERENCES

1. Akimoto, S. I. and H. Fujisawa, Demonstration of the electrical conductivity jump produced by the olivine-spinel transition, *J. Geophys. Res., 70*, 443-449, 1965.
2. Bahr, K. and J. H. Filloux, Local Sq response functions from EMSLAB data, *J. Geophys. Res., 94*, 1989.
3. Banks, R. J., Geomagnetic variations and the electrical conductivity of the upper mantle, *Geophys. J. R. astr. Soc., 17*, 457-487, 1969.
4. Berdichevskiy, M. N., L. L. Vanyan and E. B. Faynberg, Magnetic variation sounding using space derivatives of the field, *Geomag. Aeron., 9*, 299-301, 1969.
5. Cagniard, L., Basic theory of the magnetotelluric method of geophysical prospecting, *Geophysics, 18*, 605-635, 1953.
6. Campbell, W. H. and R. S. Andersen, Conductivity of the sub-continental upper mantle: An analysis using quiet-day geomagnetic records of North America, *J. Geomag. Geoelectr., 35*, 367-382, 1983.
7. Campbell, W. H. and E. R. Schiffmacher, Upper mantle electrical conductivity for seven subcontinental regions of the Earth, *J. Geomag. Geoelectr., 40*, 1387-1406, 1988.
8. Chapman, S., The solar and lunar diurnal variations of terrestrial magnetism, *Phil. Trans. R. Soc. Lond. A, 218*, 1-118, 1919.
9. Chave, A. D., R. P. Von Herzen, K. A. Poehls and C. S. Cox, Electromagnetic induction fields in the deep ocean north-east of Hawaii: Implications for mantle conductivity and source fields, *Geophys. J. Roy. Astr. Soc., 66*, 379-406, 1981.
10. Eckhardt, D., K. Larner and T. Madden, Long period magnetic fluctuations and mantle conductivity estimates, *J. Geophys. Res., 68*, 6279-6286, 1963.
11. ERCEUGT (Electrical Resistivity along the Central Segment of the European Geotraverse) Group), An electrical resistivity crustal section from the Alps to the Baltic Sea (central segment of the EGT), *Tectonophys., 207*, 123-140, 1992.
12. Ferguson, I. J., F. E. M. Lilley and J. H. Filloux, Geomagnetic induction tin the Tasman Sea and electrical conductivity structure beneath the Tasman Seafloor, *Geophys. J. Int., 102*, 299-312, 1990.
13. Filloux, J. H., Magnetotelluric and related electromagnetic investigations in geophysics, *Rev. Geophys. and Space Phys., 17*, 282-294, 1979.
14. Filloux, J. H., L. K. Law, T. Yukutake, J. Segawa, Y. Hamano, H. Utada, A. White, A. Chave. P. Tarits and A. W. Green, OFFSHORE EMSLAB: Objectives, experimental phase and early results, *Phys. Earth and Planet. Int., 53*, 422-431, 1989.
15. Gamble, T. D., W. M. Goubau and J. Clarke, Error analysis for remote reference magnetotellurics, *Geophysics, 44*, 959-968, 1979.
16. Gough, D.I. and M.R. Ingham, Interpretation methods for magnetometer arrays, *Rev. Geophys. Space Phys.*, 21, 805-827, 1983.
17. Gough, D.I., Magnetometer array studies, earth structure, and tectonic processes, *Rev. Geophysics*, 21, 805-827, 1989.
18. Gough, D. I., D. M. McKirdy, D. V. Woods and H. Geiger, Conductive structures and tectonics beneath the EMSLAB land array, *J. Geophys. Res., 94*, 14,099-14,110, 1989.
19. Hermance, J. F., Electromagnetic induction by moving ionospheric current systems, *Geophys. J. Roy. Astron. Soc., 55*, 557, 1978.
20. Hermance, J. F., The electrical conductivity of materials containing partial melt: A simple model from Archie's Law, *Geophys. Res. Letters, 6*, 613-616, 1979.
21. Hermance, J. F. and J. Pedersen, The deep structure of the Rio Grande Rift: A magnetotelluric study, *J. Geophys. Res., 85*, 3899-3912, 1980.
22. Hermance, J. F., Magnetotelluric and geomagnetic deep sounding studies in rifts and adjacent area: Constraints on physical processes in the crust and upper mantle, *Special Volume on Continental and Ocean Rifts, 8*, 169-192, International Commission on Geodynamics, AGU, Washington, DC, 1982.
23. Hermance, J.F., S. Lusi, W. Slocum, G.A. Neumann, and A.W. Green, Jr., A high density remote reference magnetic variation profile in the Pacific Northwest of North America, *Phys. Earth Planet. Int., 53*, 305-319, 1989.
24. Hermance, J.F. and G.A. Neumann, The Rio Grande Rift: New electromagnetic constraints on the Socorro magma body, *Phys. Earth Planet. Int., 66*, 101-117, 1990.
25. Hermance, J.F., The magnetotelluric method: Fundamental considerations, in *Encyclopedia of Geophysics*, edited by David James, 746 -

770, Van Nostrand Reinhold Co., New York, 1989.
26. Hermance, J. F. and W. Wang, "Mode-blind" estimates of deep earth resistivity, *J. Geomag. Geoelec., 44*, 373-389, 1992.
27. Ingham, M. R., A magnetotelluric and magnetovariational traverse across the New Zealand subducton Zone, *Geophys. J., 92*, 495-504, 1988.
28. Jones, A. G., Electrical conductivity of the continental crust, Chapter 3 in *Continental Lower Crust,* edited by D. M. Fountain, R. J. Arculus and R. W. Kay, pp. 81-143, Elsevier, 1992.
29. Kelley, M. C., *The Earth's Ionosphere*, 487 pp., Academic Press, New York, 1989.
30. Kuckes, A., Relations between electrical conductivity of a mantle and fluctuating magnetic fields, *Geophys. J. R. astro. Soc., 32,* 119-131, 1973.
31. Kurtz, R. D., J. M. DeLaurier and J. C. Gupta, The electrical conductivity distribution beneath Vancouver Island: A region of active Plate subduction, *J. Geophy. Res., 95*, 10,929-10,946, 1990.
32. Lilley, F. E. M., D. V. Woods and M. N. Sloane, Electrical conductivity from Australian magnetometer arrays using spatial gradient data, *Phys. Earth and Plan. Int., 25*, 202-209, 1981.
33. Parkinson, W. D., and V. R. S. Hutton, The Electrical Conductivity of the Earth, Chapter 4 in *Geomagnetism, Vol. 3*, edited by J. A. Jacobs, 261-321, Academic Press, San Diego, CA, 1989.
34. Pedersen, J. and J. F. Hermance, Deep electrical structure of the Colorado Plateau as determined from magnetotelluric measurements, *J. Geophys. Res., 86*, 1849-1857, 1981.
35. Pedersen, J. and J. F. Hermance, Least squares inversion of one-dimensional magnetotelluric data: An assessment of procedures employed by Brown University, *Surveys in Geophysics, 8*, 187-231, 1986.
36. Praus, O., J. Pecova, V. Petr, V. Babuska and J. Plomerova, Magnetotelluric and seismological determination of the lithosphere-asthenosphere transition in Central Europe, *Phys. Earth Planet. Int., 60*, 212-228, 1990.
37. Price, A.T., The theory of magnetotelluric methods when the source field is considered, *J. Geophys. Res., 67*, 1907-1918, 1962.
38. Richmond, A. D., Upper-atmosphere electric-field sources, in *The Earth's Electrical Environment*, 195-205, Nat. Acad. Press, Washingtion. D. C.., 1986.
39. Schmucker, U., Anomalies of geomagnetic variations in the southwest United States, *Bull. Scripps. Inst. Oceanogr., 13*, 165 pp., 1970.
40. Schmucker, U. Depth distribution of the electrical conductivity, in *Geophysics of the Solid Earth, the Moon and the Planets*, Landolt-Bornstein, Vol.2, edited by K. -H. Hellwege and O. Madelung, 370-397, Springer, Berlin, 1985.
41. Schultz, A. and J. C. Larsen, On the electrical conductivity of the mid-mantle -- I. Calculation of equivalent scalar magnetotelluric response functions, *Geophys. J. R. astr. Soc., 88*, 733-761, 1987.
42. Schuster, A., The diurnal variation of terrestrial magnetism, *Phil. Trans. Roy. Soc. Lond. A, 180*, 467-518, 1889.
43. Stanley, W. D., W. D. Mooney and G. S. Fuis, Deep crustal structure of the Cascade Range and surrounding regions from seismic refraction and magnetotelluric data, *J. Geophys. Res., 95*, 19,419-19,438, 1990.
44. Van'yan, L. L., Progress report on Electrical Conductivity of the Asthenosphere project, *Int. Assoc. Geomagn. Aeron. News, No. 19*, 73-84, 1980.
45. Van'yan, L. L., Deep geoelectrical models: geological and electromagnetic principles, *Phys. Earth Planet. Int., 25*, 273-279, 1981.
46. Vozoff, K. (Ed.), *Magnetotelluric Methods*, 763 pp., Soc. Explor. Geophys., Tulsa, OK, 1986.
47. Wait, J.R., On the relation between telluric currents and the earth's magnetic field, *Geophysics, 19*, 281-289, 1954.
48. Wannamaker, P. E., J. R. Booker, A. G. Jones, A. D. Chave, J. H. Filloux, H. S. Waff, and L. K. Law, Resistivity cross section through the Juan de Fuca subduction system and its tectonic implications, *J. Geophys. Res., 94*, 14,127-14,144, 1989.

Magnitudes and Moments of Earthquakes

Katsuyuki Abe

1. EARTHQUAKE MAGNITUDE

Charles Richter's [29] original magnitude scale, called the local magnitude M_L, was designed to provide a relative measure of the size of waves recorded in southern California from local earthquakes, i.e.,

$$M_L = \log A + B \quad (1)$$

where A is the maximum trace amplitude (in mm) on records of specific Wood-Anderson torsion seismographs and B is the distance correction. The predominant period of the waves used is usually 0.1-3 s. To generalize the restrictive range of earthquakes that could be quantified with M_L, Gutenberg [17] used the amplitude of distant surface waves in his definition of the surface-wave magnitude M_s, and he thus extended the Richter's scale to observations at any distance. M_s is defined as

$$M_s = \log A + 1.656\log D + 1.818 \quad (2)$$

where A is the maximum combined horizontal ground amplitude (in microns) for surface waves with periods of about 20 s and D is the angular epicentral distance (in degrees). Gutenberg [18] and Gutenberg and Richter [20] also used the maximum amplitude of body waves to define the body-wave magnitude, m_B:

$$m_B = \log (A/T) + Q \quad (3)$$

K. Abe, Earthquake Research Institute, University of Tokyo
Yayoi 1-1-1, Bunkyo-ku, Tokyo, Japan 113

Global Earth Physics
A Handbook of Physical Constants
AGU Reference Shelf 1

where A is the maximum ground amplitude (in microns), T is the corresponding period (in s), and Q is the correction function for the type of body-wave phase (P, PP and S), epicentral distance and focal depth. Usually the period of the waves used ranges from 4-20 s [8].

Since these formulas were established, many variations of these scales have been proposed for different regions, magnitude ranges and instruments by many investigators. Several tens of the existing relations are compiled by Bath [12]. These scales have not always been calibrated well against the original scale, and mixed use of inhomogeneous magnitude values requires some caution [3, 25]. There is significant inhomogeneity in the existing magnitude catalogs [16, 3]. For example, the single magnitude values in the famous catalog of Gutenberg and Richter [19] are basically M_s for large shocks shallower than 40 km, but are m_B or modified m_B for large shocks deeper than 40 km [3, 5].

The body-wave magnitude of current use, denoted by m_b, is determined routinely from the amplitude in the first few cycles of 1-s period P waves on "narrow-band" instruments. Owing to the substantial difference in the wave period and the way the maximum amplitude is measured, m_b and m_B are distinct and should not be used as the same scale.

Extensive studies by Gutenberg and Richter suggested that M_s, m_B and M_L are related to each other and can be used to represent the total energy (E) released in seismic waves. Through repeated revisions, Gutenberg and Richter [20] derived empirical relations:

$$m_B = 1.7 + 0.8M_L - 0.01M_L^2 \quad (4)$$

$$m_B = 0.63M_s + 2.5$$

$$\text{or equivalently } M_s = 1.59m_B - 3.97 \quad (5)$$

$$\log E(\text{J}) = 2.9 + 1.9M_L - 0.024M_L^2 \quad (6)$$

$$\log E(\text{J}) = 1.5M_s + 4.8 \quad (7)$$

Since then, a large number of relations have been proposed for different magnitude scales [e.g., 12]. Recently Kikuchi and Fukao [27] claimed that the seismic wave energy from equation (7) is systematically large, by one order of magnitude, than that from a waveform inversion of body waves of large earthquakes.

The general distribution of earthquakes over the observed range of magnitude M can be represented simply by

$$\log N = a - bM \tag{8}$$

where a and b are constants, and N is the number of earthquakes in a certain magnitude range or the number of earthquakes larger than M [e.g., 19]. The value b for shallow earthquakes in the world is very close to unity. This implies that for shallow shocks a decrease of one unit in magnitude corresponds to an approximately ten-fold increase in frequency.

Since the magnitude is determined empirically from observed records at a given period without due consideration to the physics of the earthquake process, its physical significance in terms of earthquake size is somewhat vague. This is particularly so for large earthquakes in which the source dimension is much larger than the wave length of seismic waves used for the magnitude determination, and consequently the scale saturates owing to the magnitude-period dependence [10]; in other words, magnitudes can sometimes badly underestimate true earthquake size for large earthquakes. For example, M_s is determined from surface waves with a period of about 20 s and suffers saturation at M_s greater than about 8. m_b from 1-s period body waves suffers saturation at m_b greater than about 6.5.

Table 1 lists the values of surface-wave magnitude M_s of large shallow earthquakes of 1899-1990 with M_s = 7.9 or over, and broad-band body-wave magnitude m_B for large deep earthquakes with m_B = 7.6 or over. Earthquakes with depths below 70 km are called here deep earthquakes. The epicenters from this table are mapped on Figure 1. For smaller earthquakes, see the references in the table.

2. SEISMIC MOMENT

The quantification of earthquakes has been a problem with a very complex history, because of difficulty in representing earthquake size by a single parameter. Recent progress in seismology provided more quantitative scales than the magnitude. According to elastic dislocation theory, an earthquake can be modeled by shear faulting. In this model, energy and potency are physically meaningful parameterizations of earthquake size even in a heterogeneous medium [13, 22]. The other parameterization is seismic moment M_o [9], which is of currently wide use. M_o can be related to the faulting by the relation:

$$M_o = \mu DS \tag{9}$$

where μ is the rigidity of the material surrounding the fault, D is the average dislocation on the fault plane, and S is the surface area of the fault. S can often be approximated by $S = LW$ where L and W are the length and width of the fault, respectively. Since the seismic moment is proportional to the amplitude of seismic waves at periods sufficiently longer than the time scale of the faulting process, it can be reliably measured from observational data.

Kanamori [24] related M_o to the energy released in earthquakes and introduced a new magnitude scale M_w:

$$M_w = (\log M_o(\mathrm{Nm}) - 9.1)/1.5 \tag{10}$$
$$\log W = 1.5M_w + 4.8 \tag{11}$$

where W gives the minimum estimate of the strain energy drop (difference in strain energy before and after an earthquake). M_w is often called moment magnitude [21]. Since M_o does not suffer from saturation as the size of earthquake faulting increases, the M_w scale can be used as a natural con-tinuation of the M_s scale for great earthquakes. The 1960 Chilean earthquake has the largest M_w, 9.5. In much the same way as M_w, a moment magnitude for deep earthquakes is defined from M_o [4, 25]:

$$m_w = (\log M_o(\mathrm{Nm}) - 3.1)/2.4 \tag{12}$$

A remarkable linearity between $\log M_o$ and $\log S$ is suggested for large and great shallow earthquakes [1]:

$$\log M_o\ (\mathrm{Nm}) = 1.5\log S + 15.1 \tag{13}$$

where S is in km^2. This linearity is interpreted in terms of constant average stress drop [11].

In recent studies, the seismic moments have been derived from moment tensor analyses of long-period seismic waves [e.g., 14]. The values of M_o for major earthquakes have been available on a routine basis in *Monthly Listing of Preliminary Determination of Epicenters* by U.S. Geological Survey since July, 1981.

Table 2 lists a selection of the values of surface-wave magnitude M_s, seismic moment M_o, fault length L, fault width W and average dislocation on the fault D for shallow earthquakes. The selection illustrates variation of source parameters over a wide range of the magnitude. For an

TABLE 1. Magnitudes of Large Shallow Earthquakes with M_s = 7.9 or over and Deep Earthquakes with m_B = 7.6 or over from 1899 to 1990 [3, 5, 7]

Year	Mo Dy	Hr Mn	Lat	Long	M_s	m_B	Depth (km)	Epicenter
1899	9 04	0022	60.0	-142.0	7.9	-	-	S. Alaska
1899	9 10	2141	60.0	-140.0	8.0	-	-	S. Alaska
1901	8 9	1301	-22.0	170.0	7.9	-	-	Loyalty Is.
1906	1 31	1536	1.0	-81.5	8.2	-	-	Ecuador
1906	8 17	0040	-33.0	-72.0	8.1	-	-	Central Chile
1909	2 22	0921	-18.0	-179.0	-	7.6	550	W. of Tonga Is.
1909	3 13	1429	31.5	142.5	-	7.6	80	S. of Honshu, Japan
1909	7 7	2137	36.5	70.5	-	7.6	230	Hindu Kush
1910	4 12	0022	25.5	122.5	-	7.6	200	Taiwan
1910	6 16	0630	-19.0	169.5	-	7.9	100	Vanuatu Is.
1911	6 15	1426	29.0	129.0	-	8.1	160	Ryukyu Is.
1913	3 14	0845	4.5	126.5	7.9	-	-	Talaud Is.
1913	10 14	0808	-19.5	169.0	-	7.6	230	Vanuatu Is.
1914	5 26	1422	-2.0	137.0	8.0	-	-	W. New Guinea
1914	11 24	1153	22.0	143.0	-	7.9	110	Volcano Is.
1915	5 1	0500	47.0	155.0	8.0	-	-	Kurile Is.
1917	5 1	1826	-29.0	-177.0	7.9	-	-	Kermadec Is.
1917	6 26	0549	-15.5	-173.0	8.4	-	-	Tonga Is.
1918	5 20	1755	-28.5	-71.5	-	7.6	80	Central Chile
1918	8 15	1218	5.5	123.0	8.0	-	-	Mindanao, Philippines
1918	9 7	1716	45.5	151.5	8.2	-	-	Kurile Is.
1919	1 1	0259	-19.5	-176.5	-	7.7	180	W. of Tonga Is.
1919	4 30	0717	-19.0	-172.5	8.2	-	-	Tonga Is.
1919	5 6	1941	-5.0	154.0	7.9	-	-	Solomon Is.
1920	6 5	0421	23.5	122.0	8.0	-	-	Taiwan
1920	9 20	1439	-20.0	168.0	7.9	-	-	Loyalty Is.
1920	12 16	1205	36.0	105.0	8.6	-	-	Northern China
1921	11 15	2036	36.5	70.5	-	7.6	215	Hindu Kush
1922	11 11	0432	-28.5	-70.0	8.3	-	-	Central Chile
1923	2 3	1601	54.0	161.0	8.3	-	-	Kamchatka
1923	9 1	0258	35.3	139.5	8.2	-	-	Honshu, Japan
1924	4 14	1620	6.5	126.5	8.3	-	-	Mindanao, Philippines
1926	6 26	1946	36.5	27.5	-	7.7	100	Dodecanese Is.
1927	5 22	2232	36.8	102.0	7.9	-	-	Tsinghai Prov., China
1928	12 1	0406	-35.0	-72.0	8.0	-	-	Central Chile
1931	8 10	2118	47.0	90.0	7.9	-	-	Sinkiang Prov., China
1931	10 3	1913	-10.5	161.8	7.9	-	-	Solomon Is.
1932	5 14	1311	0.5	126.0	8.0	-	-	Molucca Passage
1932	6 3	1036	19.5	-104.3	8.2	-	-	Jalisco, Mexico
1933	3 2	1730	39.3	144.5	8.5	-	-	Honshu, Japan
1934	1 15	0843	26.5	86.5	8.3	-	-	Nepal-India
1934	7 18	1940	-11.8	166.5	8.1	-	-	Santa Cruz Is.
1935	9 20	0146	-3.5	141.8	7.9	-	-	New Guinea
1938	2 1	1904	-5.3	130.5	8.2	-	-	Banda Sea
1938	11 10	2018	55.5	-158.0	8.3	-	-	Alaska Peninsula
1939	4 30	0255	-10.5	158.5	8.0	-	-	Solomon Is.
1939	12 21	2100	0.0	123.0	-	7.8	150	N. Celebes
1940	5 24	1633	-10.5	-77.0	7.9	-	-	Peru
1941	11 25	1803	37.5	-18.5	8.2	-	-	N. Atlantic Ocean

TABLE 1. (continued)

Year	Mo Dy	Hr Mn	Lat	Long	M_s	m_B	Depth (km)	Epicenter
1942	5 14	0213	-0.8	-81.5	7.9	-	-	Ecuador
1942	8 6	2336	14.0	-91.0	7.9	-	-	Guatemala
1942	8 24	2250	-15.0	-76.0	8.2	-	-	Peru
1942	11 10	1141	-49.5	32.0	7.9	-	-	Prince Edward Is.
1943	4 6	1607	-30.8	-72.0	7.9	-	-	Central Chile
1943	7 23	1453	-9.5	110.0	-	7.6	90	S. of Java
1944	12 7	0435	33.8	136.0	8.0	-	-	S. Honshu, Japan
1945	11 27	2156	24.5	63.0	8.0	-	-	West Pakistan
1946	8 4	1751	19.3	-69.0	8.0	-	-	Dominican Rep.
1946	12 20	1919	32.5	134.5	8.2	-	-	Shikoku, Japan
1948	1 24	1746	10.5	122.0	8.2	-	-	Panay, Philippines
1949	8 22	0401	53.8	-133.3	8.1	-	-	Queen Charlotte Is.
1950	8 15	1409	28.5	96.5	8.6	-	-	India-China
1950	12 9	2138	-23.5	-67.5	-	7.7	100	Chile-Argentina
1951	11 18	0935	30.5	91.0	8.0	-	-	Tibet
1952	3 4	0122	42.5	143.0	8.3	-	-	Hokkaido, Japan
1952	11 4	1658	52.8	159.5	8.2	-	-	Kamchatka
1953	11 25	1748	34.0	141.5	7.9	-	-	Honshu, Japan
1957	3 9	1422	51.3	-175.8	8.1	-	-	Aleutian Is.
1957	12 4	0337	45.2	99.2	8.0	-	-	Mongolia
1958	7 10	0615	58.3	-136.5	7.9	-	-	S. Alaska
1958	11 6	2258	44.4	148.6	8.1	-	-	Kurile Is.
1960	5 21	1002	-37.6	-73.1	7.9	-	-	Central Chile
1960	5 22	1911	-38.2	-72.6	8.5	-	-	Central Chile
1961	9 8	1126	-56.3	-27.1	-	7.6	125	South Sandwich Is.
1963	10 13	0517	44.9	149.6	8.1	-	-	Kurile Is.
1963	11 4	0117	-6.9	129.5	-	7.8	108	Banda Sea
1964	3 28	0336	61.1	-147.5	8.4	-	-	S. Alaska
1965	2 4	0501	51.3	178.6	8.2	-	-	Aleutian Is.
1966	12 31	1823	-11.9	166.4	7.9	-	-	Santa Cruz Is.
1968	5 16	0048	40.9	143.4	8.1	-	-	Honshu, Japan
1971	1 10	0717	-3.2	139.7	7.9	-	-	W. New Guinea
1976	1 14	1647	-29.0	-177.4	7.9	-	-	Kermadec Is.
1977	8 19	0608	-11.2	118.4	8.1	-	-	S. of Sumbawa Is.
1985	9 19	1317	18.2	-102.5	8.1	-	-	Michoacan, Mexico
1986	10 20	0646	-28.1	-176.4	8.1	-	-	Kermadec Is.
1989	5 23	1054	-52.3	160.6	8.2	-	-	Macquarie Is.
1990	None							

Here "deep" is used for focal depths larger than 70 km. For 1981-1990, the M_s values are taken from *Preliminary Determination of Epicenters* of U.S. Geological Survey.

extensive compilation, see Purcaru and Berckhemer [28]. Relations involving seismic moment, magnitude, energy and fault dimension are discussed on the basis of this kind of the data set and dislocation models [26, 15]. Table 3 lists a selection of values of broad-band body-wave magnitude m_B, short-period body-wave magnitude m_b and seismic moment M_0 of large deep earthquakes.

3. TSUNAMI MAGNITUDE

Like long-period seismic waves, tsunami waves carry the information of the source displacement having a long time constant of 300-3000 s. With this in mind, the tsunami magnitude scale M_t for an tsunamigenic earthquake was introduced;

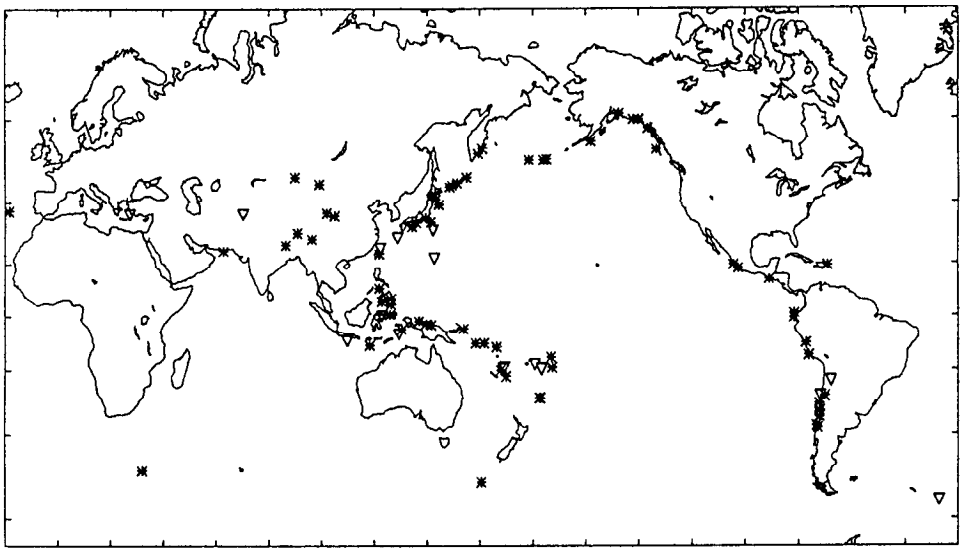

Fig. 1. Large earthquakes for the period from 1899 to 1990. Asterisks denote shallow shocks with M_s = 7.9 or over, and triangles denote large shocks deeper than 70 km with m_B = 7.6 or over.

TABLE 2. Seismic Moments and Source Parameters of Shallow Earthquakes [15]

Year	Mo	Dy	Epicenter	M_s	M_0 (10^{20} Nm)	L (km)	W (km)	D (m)
1923	9	1	Kanto	8.2	7.6	130	70	2.1
1927	3	7	Tango	7.6	0.46	35	13	3
1930	11	25	Kita-Izu	7.2	0.2	20	11	3
1931	9	21	Saitama	6.7	0.068	20	10	1
1933	3	2	Sanriku	8.5	43	185	100	3.3
1933	3	11	Long Beach	6.2	0.028	30	15	0.2
1940	5	19	Imperial Valley	7.1	0.48	70	11	2
1943	9	10	Tottori	7.4	0.36	33	13	2.5
1944	12	7	Tonankai	8.0	15	120	80	3.1
1945	1	12	Mikawa	6.8	0.087	12	11	2.2
1946	12	20	Nankaido	8.2	15	120	80	3.1
1948	6	28	Fukui	7.3	0.33	30	13	2
1952	3	4	Tokachi-Oki	8.3	17	180	100	1.9
1952	7	21	Kern County	7.8	2	60	18	4.6
1954	12	16	Fairview	7.1	0.13	36	6	2
1960	5	22	Chile	8.5	2700	800	200	24
1961	8	19	Kitamino	6.9	0.09	12	10	2.5
1963	3	27	Wakasa Bay	6.8	0.033	20	8	0.6
1963	8	3	North Atlantic	6.9	0.12	32	11	1
1963	10	13	Kurile Is.	8.1	75	250	150	3
1963	11	17	North Atlantic	6.5	0.038	27	9	0.48
1964	3	15	Spain	6.8	0.13	95	10	0.42
1964	3	28	Alaska	8.4	750	500	300	7
1964	6	16	Niigata	7.5	3.2	80	30	3.3
1965	2	4	Rat Is.	8.2	140	500	150	2.5
1965	3	30	Rat Is.	7.4	3.4	50	80	1.2

TABLE 2. (continued)

Year	Mo	Dy	Epicenter	M_s	M_o (10^{20} Nm)	L (km)	W (km)	D (m)
1966	6	28	Parkfield	5.9	0.032	26	7	0.6
1966	7	4	Aleutian	6.8	0.226	35	12	1.6
1966	9	12	Truckee	6.3	0.0083	10	10	0.3
1966	10	17	Peru	7.8	20	80	140	2.6
1967	7	22	Turkey	7.1	0.83	80	20	1.7
1968	4	9	Borrego	7.0	0.063	33	11	0.58
1968	5	16	Tokachi-Oki	8.1	28	150	100	4.1
1968	7	1	Saitama	5.4	0.019	10	6	0.92
1968	8	31	Iran	7.1	1	80	20	2.1
1969	2	28	Portuguese	7.8	5.5	80	50	2.5
1969	8	11	Kurile Is.	7.8	22	180	85	2.9
1969	9	9	Gifu	6.6	0.035	18	10	0.6
1970	5	31	Peru	7.6	10	130	70	1.6
1971	2	9	San Fernando	6.6	0.12	20	14	1.4
1973	6	17	Nemuro-Oki	7.7	6.7	60	100	1.6

The M_s values are taken from Abe [3] and other sources. Slight changes for the 1960 Chilean, the 1964 Alaskan, and the 1963 Kurile Islands earthquakes have been made according to the original references.

TABLE 3. Magnitudes and Seismic Moments of Large Deep Earthquakes [4]

Year	Mo	Dy	Epicenter	Depth (km)	m_B	m_b	M_o (10^{18} Nm)
1954	3	29	Spain	640	7.0	-	700
1957	11	29	Bolivia	170	7.4	-	650
1958	7	26	Bolivia	620	7.2	-	280
1959	6	14	Chile	100	7.5	-	87
1960	1	15	Peru	150	6.9	-	50
1961	8	31	Brazil	626	7.0	-	83
1962	12	8	Argentina	620	6.9	-	79
1963	7	4	Tonga Is.	158	6.9	-	15
1963	8	15	Peru	543	7.3	-	690
1963	8	25	Fiji	557	6.8	-	88
1963	11	4	Banda Sea	108	7.8	-	3100
1963	11	9	Peru	576	7.2	-	310
1964	1	20	New Hebrides	139	6.9	6.1	30
1964	3	21	Banda Sea	373	6.6	5.8	8.7
1964	4	24	New Guinea	99	6.9	6.3	18
1964	5	26	S.Sandwich Is.	114	7.5	5.8	620
1965	3	18	Tonga Is.	219	6.3	5.4	3.5
1965	11	3	Brazil	587	6.7	5.9	25
1965	11	18	Tonga Is.	417	6.1	5.6	3.9
1965	12	8	New Zealand	153	6.1	5.6	2.0
1966	2	4	New Hebrides	183	6.5	5.6	16
1966	3	17	Tonga Is.	627	6.2	5.9	21

TABLE 3. (continued)

Year	Mo	Dy	Epicenter	Depth (km)	m_B	m_b	M_o (10^{18} Nm)
1966	6	22	Banda Sea	523	6.7	6.1	7
1966	7	21	Tonga Is.	589	6.1	5.6	4.0
1967	8	12	Fiji Is.	144	6.5	5.7	11
1967	9	4	Kermadec Is.	223	6.4	5.6	4.0
1967	10	9	Tonga Is.	605	7.1	6.2	57
1967	12	1	Kurile Is.	144	6.4	5.9	7.1
1968	1	20	Kermadec Is.	352	6.0	5.7	2.8
1968	2	28	Japan	348	6.4	5.7	3.6
1968	3	11	Tonga Is.	87	6.3	5.9	5.8
1968	5	14	Ryukyu Is.	162	6.5	5.9	16
1968	9	26	Tonga Is.	202	6.0	5.7	1.9
1968	10	7	Bonin Is.	518	7.2	6.1	160
1969	1	19	Japan	238	7.3	6.3	91
1969	3	31	Japan Sea	397	6.6	5.7	17
1969	12	18	Sakhalin	329	6.4	5.9	10
1970	5	27	Bonin Is.	406	7.1	6.0	80
1970	7	31	Colombia	653	7.5	6.5	2200
1970	8	30	Okhotsk Sea	643	7.2	6.5	110
1971	1	29	Okhotsk Sea	515	6.9	6.0	28
1972	3	30	Fiji Is.	479	6.9	6.1	37
1973	9	10	Vladivostok	552	6.5	5.8	15
1973	9	29	Vladivostok	567	7.4	6.3	640
1975	2	22	Fiji Is.	338	6.8	6.1	21

TABLE 4. Magnitudes of Super-Great Tsunamigenic Earthquakes and Maximum Tsunami Heights [2]

Year	Mo	Dy	Epicenter	M_w	M_s	M_t	Maximum height
1960	5	22	Chile	9.5	8.5	9.4	25 m, Isla Mocha
1946	4	1	Aleutians	-	7.3	9.3	30 m, Unimak Is.
1837	11	7	Chile	-	-	9.3	6 m, Hilo, Hawaii
1964	3	28	Alaska	9.2	8.4	9.1	30 m, Valdes Inlet
1841	5	17	Kamchatka	-	-	9.0	4.6 m, Hilo, Hawaii
1868	8	13	Chile	-	-	9.0	14 m, Arica
1877	5	10	Chile	-	-	9.0	21 m, Mejillones
1952	11	4	Kamchatka	9.0	8.2	9.0	18 m, Paramushir Is.
1957	3	9	Aleutians	9.1	8.1	9.0	12 m, Unimak Is.
1923	2	3	Kamchatka	-	8.3	8.8	8 m, Kolgir Bay
1906	1	31	Ecuador	8.8	8.2	8.7	3.6 m, Hilo, Hawaii
1918	9	7	Kurile Is.	-	8.2	8.7	12 m, Urup Is.
1922	11	11	Chile	8.5	8.3	8.7	9 m, Chanaral
1896	6	15	Japan	-	-	8.6	38 m, Ryori, Japan
1965	2	4	Aleutians	8.7	8.2	8.6	10 m, Semya Is.
1755	11	1	Lisbon	-	-	8.6	18 m, Cadiz, Spain

$$M_t = \log H + B \quad (14)$$

where H is the maximum amplitude of tsunami waves (in m) measured by tide gages and B is the distance correction [2, 6]. The scale is calibrated against M_w. M_t provides a useful scale for distinguishing tsunami earthquakes from ordinary earthquakes by M_s-M_t disparity. The tsunami earthquake refers to an earthquake which generates disproportionately large tsunamis for the relatively small M_s, while the tsunamigenic earthquake simply means an earthquake with tsunamis. A recent example of such a tsunami earthquake is the Kurile Islands earthquake of June 10, 1975 (M_s = 6.8, M_t = 7.9).

Table 4 lists the values of moment magnitude M_w, surface-wave magnitude M_s, tsunami magnitude M_t, and the maximum run-up heights for historically super-great tsunamigenic earthquakes with M_t = 8.6 and above. The 1946 Aleutian Islands and the 1896 Sanriku events are known as the devastating tsunami earthquakes [23]. It can be seen that the M_s scale suffers saturation for these great events, i.e., $M_s << M_w$.

Acknowledgments. I thank Thomas Heaton for helpful comments to improve the manuscript. Satoshi Ide helped with preparation of the final camera copy.

REFERENCES

1. Abe, K., Reliable estimation of the seismic moment of large earthquakes, *J. Phys. Earth, 23,* 381-390, 1975.
2. Abe, K., Size of great earthquakes of 1837-1974 inferred from tsunami data, *J. Geophys. Res., 84,* 1561-1568, 1979.
3. Abe, K., Magnitudes of large shallow earthquakes from 1904 to 1980, *Phys. Earth Planet. Inter., 27,* 72-92, 1981.
4. Abe, K., Magnitude, seismic moment and apparent stress for major deep earthquakes, *J. Phys. Earth, 30,* 321-330, 1982.
5. Abe, K., Compliments to "Magnitudes of large shallow earthquakes from 1904 to 1980", *Phys. Earth Planet. Inter., 34,* 17-23, 1984.
6. Abe, K., Quantification of tsunamigenic earthquakes by the Mt scale, *Tectonophys., 166,* 27-34, 1989.
7. Abe, K. and S. Noguchi, Revision of magnitudes of large shallow earthquakes, 1897-1912, *Phys. Earth Planet. Inter., 33,* 1-11, 1983.
8. Abe, K., and H. Kanamori, Temporal variation of the activity of intermediate and deep focus earthquakes, *J. Geophys. Res., 84,* 3589-3595, 1979.
9. Aki, K., Generation and propagation of G waves from the Niigata earthquake of June 16, 1964, *Bull. Earthquake Res. Inst. Tokyo Univ., 44,* 23-88, 1966.
10. Aki, K., Scaling law of seismic spectrum, *J. Geophys. Res., 72,* 1217-1231, 1967.
11. Aki, K., Earthquake mechanism, *Tectonophys., 13,* 423-446, 1972.
12. Bath, M., Earthquake magnitude - Recent research and current trends, *Earth-Sci. Rev., 17,* 315-398, 1981.
13. Ben-Menahem, A., Renormalization of the magnitude scale, *Phys. Earth Planet Inter., 15,* 315-340, 1977.
14. Ekstrom, G., and A.M. Dziewonski, Evidence of bias in estimations of earthquake size, *Nature, 332,* 319-323, 1988.
15. Geller, R.J., Scaling relations for earthquake source parameters and magnitudes, *Bull. Seismol. Soc. Am., 66,* 1501-1523, 1976.
16. Geller, R.J., and H. Kanamori, Magnitudes of great shallow earthquakes from 1904 to 1952, *Bull. Seismol. Soc. Am., 67,* 587-598, 1977.
17. Gutenberg, B., Amplitudes of surface waves and magnitudes of shallow earthquakes, *Bull. Seis-mol. Soc. Am., 35,* 3-12, 1945*a*.
18. Gutenberg, B., Amplitudes of P, PP and S and magnitudes of shallow earthquakes, *Bull. Seismol. Soc. Am., 35,* 57-69, 1945*b*.
19. Gutenberg, B., and C.F. Richter, *Seismicity of the Earth and Associated Phenomena,* Princeton Univ. Press, Princeton, NJ, 2nd edn., 310pp., 1954.
20. Gutenberg, B., and C.F. Richter, Magnitude and energy of earthquakes, *Ann. Geofis. (Rome), 9,* 1-15, 1956.
21. Hanks, T.C., and H. Kanamori, A moment magnitude scale, *J. Geophys. Res., 84,* 2348-2350, 1979.
22. Heaton, T.H., and R. E. Heaton, Static deformations from point forces and force couples located in welded elastic Poissonian half-spaces: Implications for seismic moment tensors, *Bull. Seismol. Soc. Am., 79,* 813-841, 1989.
23. Kanamori, H., Mechanism of tsunami earthquakes, *Phys. Earth Planet. Inter., 6,* 346-359, 1972.
24. Kanamori, H., The energy release in great earthquakes, *J. Geophys. Res., 82,* 2981-2987, 1977.
25. Kanamori, H., Magnitude scale and quantification of earthquakes, *Tectonophys., 93,* 185-199, 1983.
26. Kanamori, H., and Don L. Anderson, Theoretical basis of some empirical relations in seismology, *Bull. Seismol. Soc. Am., 65,* 1073-1095, 1975.
27. Kikuchi, M., and Y. Fukao, Seismic wave energy inferred from long-period body wave inversion, *Bull. Seismol. Soc. Am., 78,* 1707-1724, 1988.
28. Purcaru, G., and H. Berckhemer, Quantitative relations of seismic source parameters and a classification of earthquakes, *Tectonophys., 84,* 57-128, 1982.
29. Richter, C.F., An instrumental earthquake magnitude scale, *Bull. Seismol. Soc. Am., 25,* 1-32, 1935.

Crustal Structure of the Earth

Toshiro Tanimoto

1. INTRODUCTION

The boundary between the crust and the mantle was discovered by Mohorovicic in 1909 under the European continent. Subsquent research in this century established the major differences between the continental and oceanic crust; a typical thickness for the continental crust is 30-50 km while a typical thickness for the oceanic crusts is 6 km. In terms of history the continental crust contains a much longer history of 4 billion years, whereas the oceanic crust contains at most 200 million years of history because of recycling of oceanic plates.

Because of its long history, the continental crust has been subjected to various tectonic processes, such as repeated episodes of partial melting, metamorphism, intrusion, faulting and folding. It is thus easier to find systematic relationships between age and structure of oceanic crusts. However, the existence of hotspots as well as changing patterns of plate motion complicate oceanic crustal structure. In this section, we assemble crustal thickness data from various tectonic provinces and discuss their implications.

T. Tanimoto, Department of Geological Sciences, University of California, Santa Barbara, Santa Barbara, CA 93106

Present Address: T. Tanimoto, Tokyo Institute of Technology, Earth and Planetary Sciences, Ookayama 2-12-1 Meguro-ku, Tokyo 152, Japan

Global Earth Physics
A Handbook of Physical Constants
AGU Reference Shelf 1

2. OCEANIC CRUSTS

2.1. Classic Subdivision and Mean Crustal Thickness

The oceanic crust is classically divided into three layers [52]; Layer 1 is the sedimentary layer, whose thickness varies widely according to sediment sources, and Layer 2 has a thickness of 1.5-2.0 km and P-wave velocity of 4.5-5.6 km/s and Layer 3 has a thickness of 4.5-5.0 km and P-wave velocity of 6.5-7.0 km/s. Combined thickness of layer 2 and 3 is often referred to as the oceanic crustal thickness and we adopt this convention. For the continental crust, we define the thickness from the surface to the Mohorovicic discontinuity (Moho).

The interpretation of oceanic velocity structure is based on two independent sources of information; one is by comparison of seismic velocities in laboratory measurements of rocks from ocean drilling cores with the velocities measured in seismic refraction experiments. The other is based on analogy with structures in ophiolite complexes. A commonly held view (e.g.,[65]) is that Layer 2 starts with extrusive volcanic rocks at shallow depths which grade downward from pillow basalts into sheeted dikes. There is a transition zone at the top of Layer 2 which shows interfingering of extrusive basaltic rocks and sheeted dikes. Layer 3 has properties appropriate to the massive to cumulate gabbro layer seen in ophiolite complexes. The top of Layer 3 has a transitional layer which shows interfingering of sheeted dikes (at the bottom of Layer 2) and isotropic gabbro (at the top of Layer 3). The isotropic gabbro layer is underlain by layered gabbro and harzburgite successively.

The traditional seismic modelling used a few homogeneous layers, which has been replaced by layers which contain velocity gradients in recent studies (e.g., [66]). If the assumption of a few stack of homogeneous

TABLE 1. Average thickness (km) and P-wave velocity (km/s) of layer 2 and 3 in oceanic crusts

	Raitt [52]	Shor et al. [59]	Christensen and Salisbury [9]	White et al.[70]
Thickness				
Layer 2	1.7±0.8	1.5±1.0	1.4±0.5	2.1±0.6
Layer 3	4.9±1.4	4.6±1.3	5.0±1.3	5.0±0.9
P-Wave velocity				
Layer 2	5.1±0.6	5.2±0.6	5.0±0.7	
Layer 3	6.7±0.3	6.8±0.2	6.7±0.2	

layers are used in regions of steep velocity gradient, estimates of crustal thickness can be misleading. Table 1 quotes the thicknesses of layer 2 and 3 from four studies during the last few decades. They are from P-wave velocity structure by refraction studies. Typically, thickness of layer 2 is 1.5-2.0 km and that of layer 3 is 4.5-5.0 km. Table 2 shows a compilation of mean crustal thickness, a sum of layer 2 and layer 3 thicknesses, which is almost uniformly 6 km. The most recent study [70] claims a somewhat higher value of 7.1 km and attributes this difference to underestimation of older studies. They claim that a travel time slope-intercept method of interpretation in previous studies may significantly underestimate the true thickness because it usually does not take into account the velocity gradients. Synthetic seismogram technique alleviates this problem. Note, however, that the difference is relatively small, up to 1 km, although it may be systematic. We thus summarize that the oceanic crustal thickness (excluding layer 1) is 6-7 km.

2.2 Age Dependence

In general, age dependence of crustal thickness is considered to be weak. In fact, constancy of crustal thickness has been regarded as almost a fact. While it is true that oceanic crust has fairly constant thickness everywhere in the ocean, there exist a few studies which claimed to have discovered the age dependence. Table 3 shows comparisons for crustal thickness between young oceanic region (younger than 30 million years old) and old oceanic region (older than 30 my). There are differences of 0.3-0.6 km between these two regions. Physical mechanism for the age dependence is not clear, however. It indicates somewhat thicker crustal generation in older oceans or gradual evolution of oceanic crust, but detailed mechanism for them are not available. Also, care must be taken before interpreting this difference, since there are a large number of seamounts in the old oceans which tend to biase the estimate toward thicker crusts. In that case, older oceans simply have anomalous crustal thickness due to seamounts and may not have thicker crusts uniformly.

2.3. Regions of Thin Crust

There are three regions where oceanic crust is reported to be thin; they are (i) a slow spreading rate (less than 2 cm/year) region, (ii) non-volcanic rifted margin which underwent extensional tectonics at some point in history and (iii) fracture zones (Table 4). The region (i) probably reflects the fact that an amount of partial melt is small under slow spreading ridges and thus crustal material is not transported from the mantle to shallow depths. Sleep [61] has shown that magma body under slow spreading ridges (less than 1 cm/y) may not be stable due to lateral conduction of heat. A seismic body wave study by Sheehan and Solomon [58] and a surface wave study by Zhang and Tanimoto [74] also showed the evidences for relatively fast seismic velocity under slow spreading ridges which indicate lack of or very little amount of melt under ridge axes. The region (ii) corresponds to an area where extreme extension had occurred in history. An example for this region is near the continental edge of (Central) Atlantic Ocean where extension played the major part in the continental break-up. The reason for thin crusts under fracture zones was recently shown to be caused by an extremely thin layer 3 or a lack of it under fracture zones [68] at least on the slow-spreading, Mid-Atlantic Ridge. This supports the idea that accretion and upwelling at slow-spreading ridges are focused near the center of segments rather than close to fracture zones. Bouger gravity anomaly also shows the so-called Bull's eye (low) gravity anomaly near the center of segments

TABLE 2. Mean Crustal Thickness

	Thickness (km)	Region
Raitt [52]	6.6±1.6	Pacific
Shor et al. [59]	6.1±1.6	Pacific
Houtz [24]	5.6±1.3	Atlantic
McClain [36]	5.8±0.9	Pacific
McClain and Atallah [37]	5.9±0.9	Pacific
Keen et al. [29]	5.8±1.1	Atlantic, Pacific
White et al. [70]	7.1±0.8	Atlantic,Indian,Pacific

TABLE 3. Age dependence of crustal thickness

	younger than 30 my	older than 30 my	Region
McClain and Atallah [37]	5.7±0.9	6.0±0.9	Pacific
White et al [70]	6.5±0.8	6.9±0.3	Pacific
White et al [70]	7.0±0.6	7.6±0.5	Atlantic

TABLE 4. Thin crust regions

	Oceanic Crustal Thickness (km)
Slow spreading region (less than 2 cm/y)	2.1±0.6[a]
Non-volcanic rifted margin	4.9±1.5[b]
Fracture zones	4.0±1.3[c]

Note:
a. Jackson et al. [26]
b. Ginzburg et al. [19]
Horsefield et al. [23]
Pinheiro et al. [46]
White et al. [70]
c. Minshull et al. [40]
Whitmarsh et al. [71]
Cormier et al. [11]
Sinha nd Louden [60]
Potts et al. [48][47]
Louden et al. [33]
Detrick et al. [15]

TABLE 5. Oceanic crustal thickness in plume affected regions

Region	Thickness (km)	
Madagascar	21.2	Sinha et al. [60]
Kerguelen	18.5, 20.5	Recq et al. [53]
S. Iceland	20.24	Bjarnason et al. [70][a]

Note: a. as referenced in White et al. [70]

because of thickness variations of layer 3.

2.3. Regions of Thick Crust

Thick oceanic crusts are found where hotspots (plumes) were or are currently under the ridge axes (Table 5). A typical crustal thickness reaches 20 km in such regions. Increased amount of partial melt due to high temperature in the hotspot regions must have been the reason. Some studies report a value of about 10 km, which is higher than the average value of 6-7 km. This can be explained that hotspots were not exactly under the ridge axes but were only in the neighborhood.

Many oceanic plateaus, such as the Ontong-Java plateau, also have thick crusts due to a large amount of melt by mantle plumes at the time of its generation. In this case, ridges may not have existed close by but the plume could have had a large flux and melt.

3. CONTINENTAL CRUSTS

3.1. Classical Division

Various tectonic activities have produced a wide range of continental crust during its long history. Structure within a continental crust is complex both in P-wave velocity variations and rock types. There are, however, approximately four layers within the crust and identification is often done with P-wave velocity. The first layer consists of sediment, characterized by P-wave velocity lower than 5.7 km/s. The second layer has P-wave velocity of 5.7-6.4 km/s, the majority of which is considered to be granite and low-grade gneisses. The third layer has P-wave velocity of 6.4-7.1 km/s and the fourth layer has 7.1-7.6 km/s. There are many candidates for the compositions of layers 3 and 4. The P-wave velocity of 7.6 km/s is typically the lowest end of P-wave velocity expected at the uppermost mantle (Pn velocity). Thus a layer with P-wave velocity of 7.6 km/s or higher is considered to be in the mantle. Crustal thickness or depth to Moho is 39 km on average, but it has some variations according to its regions. Conrad discontinuity, which is often found under continents in the mid-crust (about 15 km depth), is found between the first and the second layer in some regions, but it is not universal.

3.2. Shields and Platforms

Shields and platforms have generally thick crusts, typically exceeding 40 km. There are some variations among different regions (Table 6) and among different age provinces within a shield. They have relatively thick lower crust, which often lack clear signals in seismic reflection data (with occasional exceptions). Also the lower crust seems to have smooth velocity transitions from deep seismic sounding studies [38]. They suggest a lack of discontinuities in the lower crust. These features are usually interpreted as moderate level of differentiation in the lower crust.

3.3. Paleozoic and Mesozoic Regions

This region typically has crustal thickness of about 30 km (Table 7). The fourth layer in the classical division (a layer with P-wave velocity 7.1-7.6 km/s) is almost always missing in this region. Consequently, P-wave velocity makes a sharp velocity jump at the Moho. Wide angle reflection from Moho (PmP) is often strong because of it. Also, the Conrad discontinuity is often found in this region. However, most data are biased to European continents, thus requiring some care in generalizing its features.

3.4. Mountain Belts in the Cenozoic Era

The Alpine-Himalaya orogenic belts and the Rocky mountains are the typical regions in this category. Crustal thickness in this region varies between 40 and 70 km (Table 8). Crustal roots which compensate high mountains are found quite often. A thick upper crust which is detached from below, due to low-viscosity lower crust, is often suggested in understanding the tectonics of this region.

3.5. Island Arcs

The data is almost entirely biased to observation from Japan. Crustal thickness is about 20-30 km, which is slightly smaller than the value for the Paleozoic and Mesozoic regions. The region is underlain by a low velocity mantle with Pn velocity of about 7.5-7.8 km/s (Table 9), which indicates a higher temperature under island arcs. A recent tomographic study (e.g., [75]) clearly depicts slow velocity anomalies under volcanic chain in the crust, thus there are some three-dimensional variations being elucidated within the crust in recent studies.

3.6. Hotspots

Afar is one of the few regions studied so far and shows a thin crustal thickness, 15-20 km (Table 9). This is relatively thin for a continental crust, but it is about the same with the crusts under hotspots in the oceanic regions. Since it is at the edge of the continental boundary where the break-up of the two oceans (the Red Sea and the Gulf of Aden) are occuring, it may be natural to have the oceanic structure. Yellowstone hotspot has a normal crustal thickness, but it is substantially smaller than Afar hotspot. It is underlain by a thermal anomaly (e.g. [25]).

TABLE 6. Crustal Thickness in Shields and Platform

Shields and Platforms	Thickness (km)	
Baltic Shield	38,39,40,42	Hirschleher et al.[22]
	45	Korhonen and Parkka [31]
	41,45,47	Meissner [38]
North American Shield	41,45	Cohen and Meyer [10]
	50	Roller and Jackson [55]
	35,40,52	Steinhart and Meyer [67]
	37,38,43,44	Berry and Fuchs[7]
	42	Smith et al. [62]
Australian Shield	32,34,40,41	Hales and Rynn [21]
	50,55	Finlayson [17]
	38,44,,46	Mathur [35]
Indian Shield	40	Hales and Rynn [21]
	34,40,42	Kaila et al. [28]
Western Eurasia (except Baltic)	32	Alekseev et al. [1]
	36,50	Jentsch [27]
	39,46	Sollogub [64]
	39,47	Kosminskaya and Pavlenkova[32]

TABLE 7. Paleozoic and Mesozoic areas

Paleozoic and Mesozoic areas	Thickness (km)	
Caledonian structure (Scotland and Norway)		
	28,32	Assumpcao and Mabform [4]
	29,32,34	Bamford et al. [5]
	28	Payo [44]
Spain	27	Dagniereo et al. [12]
	32	Banda et al. [6]
	28,29,32	Sapin and Hirn [57]
France	28	Ansorge et al. [3]
Germany	26,29	Grubbe [20]
	23,24,25,29	Edel et al [16]
	28	Deichmann and Ansorge [14]
	29,30	Angenheister and Pohl [2]
	30	Meissner at al [39]
	28,30,31	Mooney and Prodehl [42]

TABLE 8. Cenozoic Mountain Belts

Cenozoic Mountain Belts	Thickness (km)	
Alps	38,39	Will [72]
	40,43,45,54	Giese and Prodehl [18]
Caucasus	42,43,44,55	Kondorskaya et al. [30]
Himalaya	66	
Mishra [41]		
	60,64,70	Volvovsky et al. [69]
Rocky	47,51	Prodehl and Pakiser [49]

3.7. Rifts

Various kinds of rift areas show somewhat thinner crust of 20-38 km (Table 9). Recent three-dimensional studies indicate existence of slow anomalies under some rifts, such as East African rift and the Rio Grande rift, while lack of such an anomaly was confirmed under others such as the Rhine Graben (e.g.,[13]).

3.8. Two Well-Studied Continents

Detailed crustal thickness variations have been published for Europe (Figure 1)[38] and for the United States (Figure 2)[8]. Crustal thickness variation within Europe shows thick crust under Scandinavia (the Baltic Shield), thick crust under Alpine-Caucasus orogenic zone, average crustal thickness for Paleozoic and Mesozoic regions (Spain, France and Germany) and relatively thin crust behind the subduction zone (West of Italy). Crustal thickness in the United States has three major peaks; one in the east in the Appalatian mountain region, one in the mid-continent and also the one in the Sierra-Nevada region. There is also a hint of thick crust under the Canadian Shield region, but this map shows only a small portion of it. The Basin and Range region shows a well-known thin crust, a result of extensional tectonics in this region.

For the United States, the map of Pn velocity has been published (Figure 3)[8]. It is not as detailed as the crustal thickness map because the work was done some time ago, but the large scale features in the variations are reliable. Fast Pn velocities are found in mid-continent where the crusts are thick and slow velocities are found in the western United States where the crusts are relatively thin. This of course applies to a large scale feature such as the Basin and Range and the Sierra Nevada mountains show thick crusts due to isostatic compensation.

4. SYNTHESIS

Synthesis of regional studies to construct a global crustal thicness variation map has been attempted by Soller et al. [63]. Their map (Figure 4) has been widely used by global seismologists, because it has been the only one easily accessible. This map, expanded in spherical harmonics up to degree and order 20, shows the depth to Moho, whose global average is 24 km depth. The boundary between the white and dark regions correspond to this depth. Contours

Table 9: Sundry Tectonically Active Regions

Region	Thickness (km)	
Japan(Island Arc)	24,33	Research Group[54]
	30	Yamashina [73]
Afar(Hotspot)	14,15,22,23	Pilger and Rosler [45]
	13,17,25	Ruegg [56]
Baikal (Rift)	28	Puzyrev et al. [50]
	28	Puzyrev et al. [51]
Red Sea (Rift)	32	Makris et al. [34]

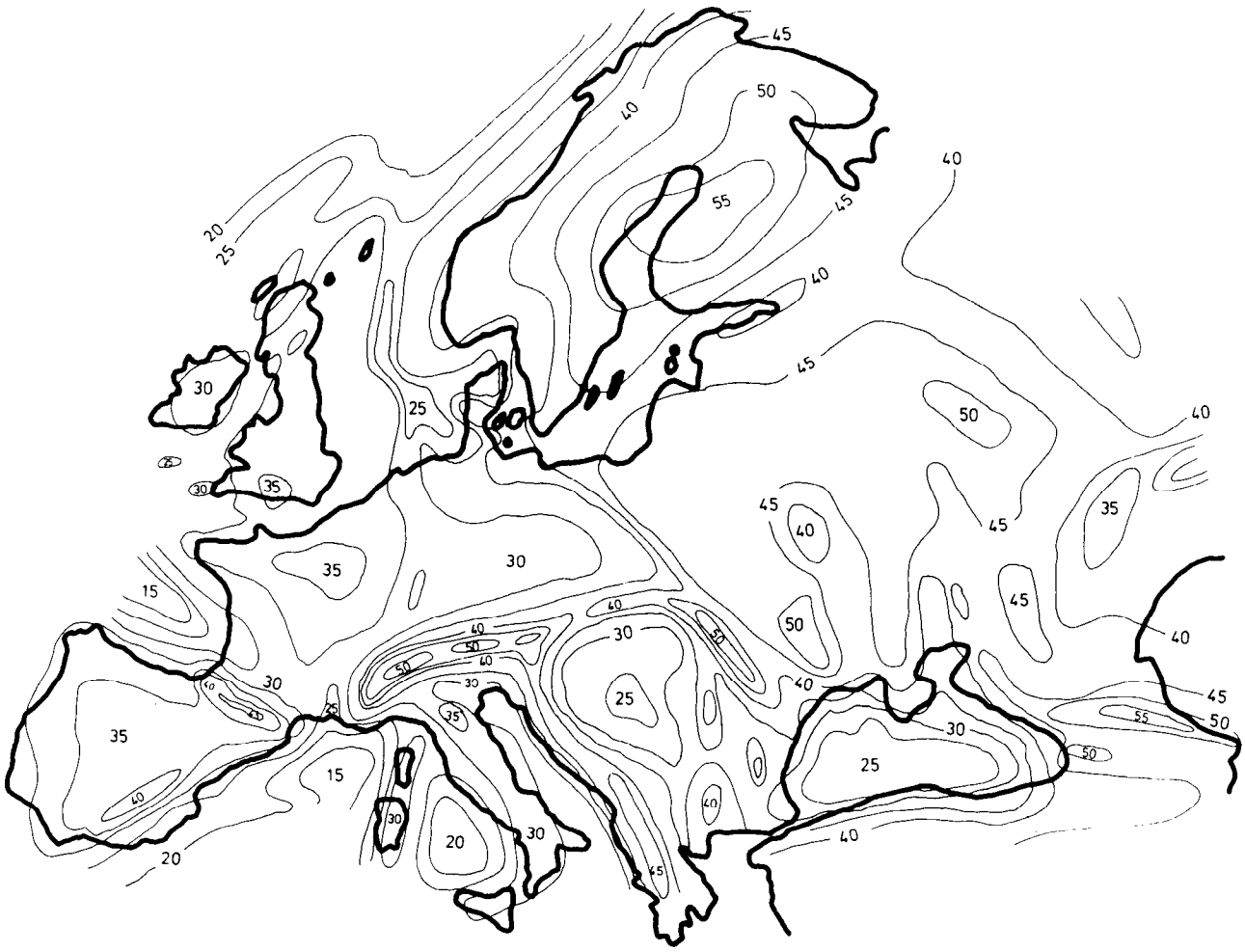

Fig. 1: Crustal thickness variations under Europe (after Meissner [38])

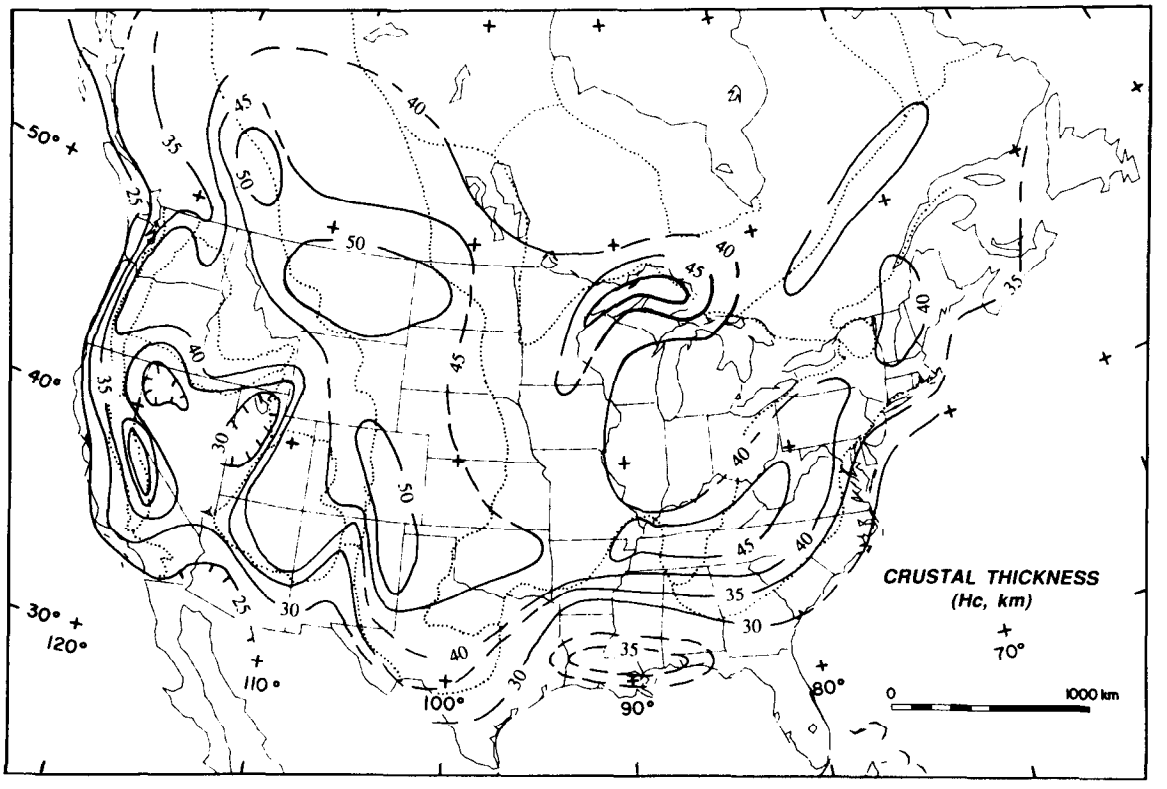

Fig. 2: Crustal thickness variations under the United States (after Braile et al. [8]

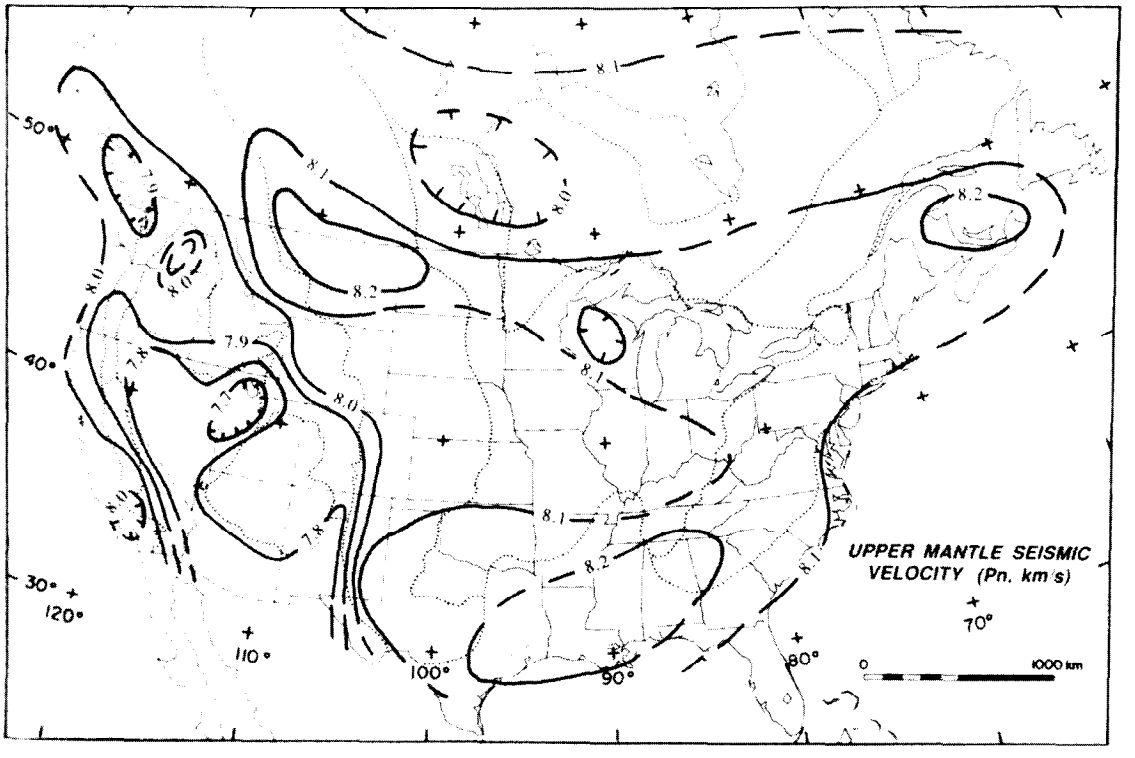

Fig. 3: Pn velocity variations under the United States (after Braile et al. [8])

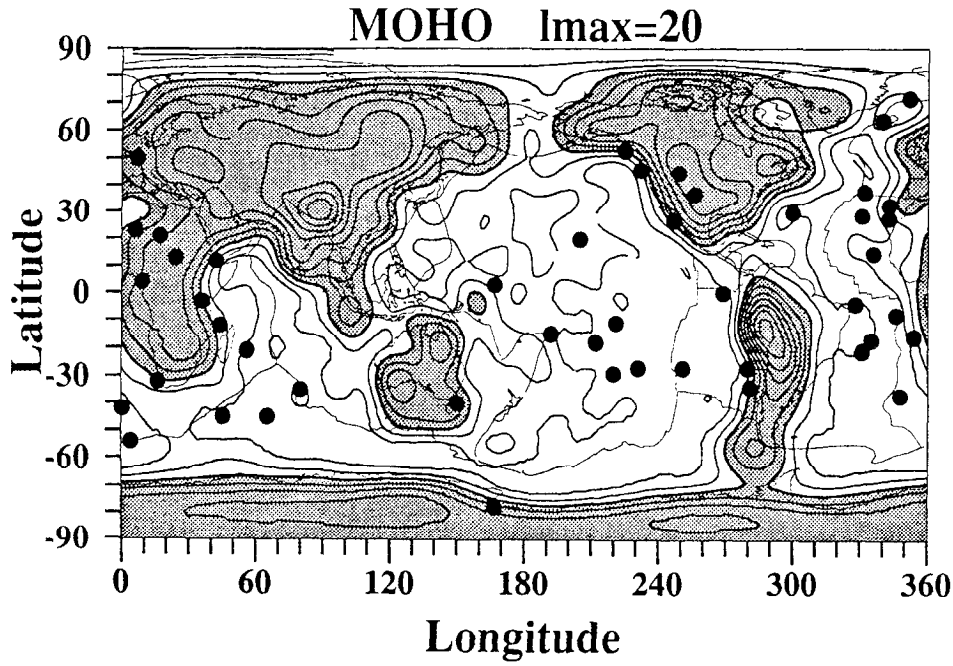

Fig. 4: Global Moho depth variations. Contours are at 5 km interval. The boundary between dark (thicker) regions and white regions is 24 km depth. Filled circles are locations of hotspots from the list of Morgan [43].

are given every 5 km. The peak at Himalaya, for example, corresponds to 65 km in depth. Some precaution in interpreting this map is required, since there are regions that have not been studied and the map contains some extrapolated results. Further work is clearly desired to improve this situation.

REFERENCES

1. Alekseev, A. S., A. V. Belonosova, I. A. Burmakov, G.V. Krasnopeterteva, N. N. Matveeva, N. I. Pavlenkova, V. G. Romanov, and V. Z. Ryaboy, Seismic studies of low-velocity layers and horizontal inhomogeneities within the crust and upper mantle on the territory of the U.S.S.R., *Tectonophysics*, *20*, 47-56, 1973.
2. Angenheister, G., and J. Pohl, in *"Explosion Seismology in Central Europe"*, edited by P. Giese, C. Prodehl and A. Stein, pp. 290-302, Springer-Verlag, Berlin and New York, 1976.
3. Ansorge, J., D. Emter, K. Fuchs, J. Lauer, S. Mueller, and E. Peterschmitt, in *"Graben Problems"*, edited by H. Illies and S. Mueller, pp. 190-197, Schweizerbart, Stuttgart, 1970.
4. Assumpcao, M., and D. Bamford, LISPB-V studies of crustal shear waves, *Geophys. J. R. Astron. Soc.*, *54*, 61-73, 1978.
5. Bamford, D., K. Nunn, C. Prodehl, and B. Jacob, LISPB-IV crustal structure of Northern Britain, *Geophys. J. R. Astron. Soc.*, *54*, 43-60, 1978.
6. Banda, E., E. Surinach, A. Aparicio, J. Sierra, and E. Ruiz De La Parte, Crustal and upper mantle structure of the central Iberian Mesета (Spain), *Geophys. J. R. Astron. Soc.*, *67*, 779-789, 1981.
7. Berry, M. J., and K. Fuchs, Crustal structure of the superior and Grenville Provences of the Northeastern Canadian shield, *Bull. Seism. Soc. Am.*, *63*, 1393-1432, 1973.
8. Braile, L. W., W. J. Hinze, R. R. B. von Frese, and G. R. Keller, Seismic properties of the crust and uppermost mantle of the conterminous United States and adjacent Canada, *Mem. Geol. Soc. Am.*, *172*, 655-680, 1989.
9. Christensen, N. I., and M. H. Salisbury, Structure and composition of the lower oceanic crust, *Rev. Geophys.*, *13*, 57-86, 1975.
10. Cohen, T., and R. Meyer, The Earth Beneath the Continents, vol. 10, edited by J. Steinhart and T. Smith, pp. 150-156, American Geophysical Union, Washington D.C., 1966.
11. Cormier, M. H., R. S. Detrick, and G. M. Purdy, Anomalously thin crust in oceanic fracture zones: New seismic constraints from the Kane fracture zone, *J. Geophys. Res.*, *89*, 10,249-10,266, 1984.
12. Daignieres, M., J. Gallert, E. Banda, and A. Hirn, Implications of the seismic structure for the orogenic evolution of the Pyrenean Range, *Earth Planet. Sci. Lett.*, *57*, 88-100, 1982.

13. Davis, P. M., S. Slack, H. A. Dahlheim, W. V. Green, R. P. Meyer, U. Achaur, A. Glahu, and M. Granet, Teleseismic tomography of continental rift zones, in *Seismic Tomography: Theory and Practice*, edited by H. M. Iyer, K. Hirahara, Chapman and Hall, 1993.
14. Deichmann, N., and J. Ansorge, Evidence for lamination in the lower Continental crust beneath the Black Forest (Southwestern Germany), *J. Geophys.*, *52*, 109-118, 1983.
15. Detrick, R. S., M. H. Cormier, R. A. Prince, D. W. Forsyth, and E. L. Ambos, Seismic constraints on the crustal structure within the Verma fracture zone, *J. Geophys. Res.*, *87*, 10,599-10,612, 1982.
16. Edel, J., K. Fuchs, C. Gelbke, and C. Prodehl, Deep structure of the Southern Rinegraben area from seismic refraction investigation, *J. Geophys.*, *41*, 333-356, 1975.
17. Finlayson, D. M., Seismic crustal structure of the Proterozoic North Australian Craton between Tennant Creek and Mount Isa, *J. Geophys. Res.*, *87*, 10569-10578, 1982.
18. Giese, P., and C. Prodehl, "Explosion Seismology in Central Europe", edited by P. Giese, C. Prodehl and A. Stein, pp. 347-376, Springer-Verlag, Berlin and New York, 1976.
19. Ginzburg, A., R. B. Whitmarsh, D. G. Roberts, L. Montaderi, A. Camus, and F. Avedik, The deep seismic structure of the northern continental margin of the Bay of Biscay, *Ann. Geophys.*, *3*, 499-510, 1985.
20. Grubbe, K., edited by P. Giese, C. Prodehl and A. Stein, pp. 268-282, Springer-Verlag, Berlin and New York, 1970.
21. Hales, A. L., and J. M. Rynn, A long-range, controlled source seismic profile in Northern Australia, *Geophys. J. R. Astron. Soc.*, *55*, 633-644, 1978.
22. Hirschleber, H., B. Lund, C. E. Meissner, R. Vogel, and W. Weinrebe, Seismic investigations along the Scandinavian "Blue Road" traverse, *J. Geophys.*, *41*, 135-148, 1975.
23. Horsefield, S. J., R. B. Whitmarsh, R. S. White, and J. C. Sibuet, Crustal structure of the Goban Spur passive continental margin, North Atlantic - Results of a detailed seismic refraction survey, *Geophys. J. Int.*, 1992, in press.
24. Houts, R. E., Crustal structure of the North Atlantic on the basis of large airgun-sonobuoy data, *Geol. Soc. Am Bull.*, *91*, 406-413, 1980.
25. Iyer, H. M., and P. B. Dawson, Imaging volcanoes using teleseismic tomography, in *Seismic Tomography: Theory and Practice*, edited by H. M. Iyer, K. Hirahara, Chapman and Hall, 1993.
26. Jackson, H. R., I. Reid, and R. K. H. Falconer, Crustal structure near the Arctic mid-ocean ridge, *J. Geophys. Res.*, *87*, 1773-1783, 1982.
27. Jentsch, M., Reinterpretation of a deep-seismic-sounding profile on the Ukrainian shield, *J. Geophys*, *45*, 355-372, 1978-79.
28. Kaila, K. L., P. R. K. Murty, V. K. Rao, and G. E. Kharetchko, Crustal structure from deep seismic soundings along the Kayna II (Kelsi-Loni) profile in the Deccan Trap area, India, *Tectonophysics*, *73*, 365-384, 1981b.
29. Keen, M. J., R. Courtney, J. McClain, and G. M. Purdy, Ocean-ridge crustal thickness correlated with paleobathymetry, *(abstract), EOS Trans. AGU*, *71*, 1573, 1990.
30. Kondorskaya, N., L. Slavina, N. Pivovarora, B. Baavadse, M. Alexidse, S. Gotsadse, G. Marusidse, D. Sicharaulidse, N. Pavienkova, E. Khromatskaya, and G. Krasnopertseva, Investigation of the Earth's crustal structure using earthquake and deep seismic sounding data obtained for the Carapathians, *Pure Appl. Geophys.*, *119*, 1157-1179, 1981.
31. Korhonen, H., and M. T. Parkka, The structure of the Baltic Shield Region on the basis of DSS and earthquake data, *Pure Appl. Geophys.*, *119*, 1093-1099, 1981.
32. Kosminskaya, I. P., and N. I. Pawlenkova, Seismic models of inner parts of the Euro-Asian continent and its margins, *Tectonophysics*, *59*, 307-320, 1979.
33. Louden, K. E., R. S. White, C. G. Potts, and D. W. Forsyth, Structure and seismotectonics of the Verma fracture zone, Atlantic *143*, 795-805, 1986.
34. Makris, J., Z. Ben Abraham, A. Behle, A. Ginzberg, P. Giese, L. Steinmetz, R. B. Whitmarch, and S. Elefthesion, Seismic refraction profiles between Cyprus and Israel and their interpretation, *Geophys. J. R. Astr. Soc.*, *75*, 575-591, 1983.
35. Mathur, S. P., Crustal structure in Southwestern Australia from seismic and gravity data, *Tectonophysics*, *24*, 151-182, 1974.
36. McClain, J. S., On long-term thickening of the oceanic crust, *Geophys. Res. Lett.*, *8*, 1191-1194, 1981.
37. McClain, J. S., and C. A. Atallah, Thickening of the oceanic crust with age, *Geology*, *14*, 574-576, 1986.
38. Meissner, R. (Ed.), *The Continental Crust, A Geophysical Approach*, International Geophysics Series, vol. 34, Academic Press, 1986.
39. Meissner, R., H. Bartelsen, A. Glocke, and W. Kaminski (Ed.), "Explosion Seismology in Central Europe", pp. 1245-251, Springer-Verlag, Berlin and New York, 1986.
40. Minshull, T. A., R. S. White, J. C. Mutter, P. Buhl, R. S. Detrick, C. A. Williams, and E. Morris, Crustal structure at the Blake Spur fracture zone from expanding spread profiles, *J. Geophys. Res.*, *96*, 9955-9984, 1991.
41. Mishra, D. C., Crustal structure and dynamics under Himalaya and Pamir ranges, *Earth Planet. Sci. Lett.*, *57*, 415-420, 1982.
42. Mooney, W. D., and C. Prodehl, Crustal structure of the Rhenish Massif and adjacent areas: a reinterpretation of existing seismic-refraction data, *J. Geophys.*, *44*, 573-601, 1978.
43. Morgan, W. J., Hotspot tracks and the opening of the Atlantic pp. 443-487, Wiley-Interscience, New York, 1981.
44. Payo, G., Crustal mantle velocities in the Iberian peninsula and tectonic implications of the seismicity in this

area, *Geophys. J. R. Astron. Soc.*, *30*, 85-99, 1972.

45. Pilger, A., and A. Rosler (Ed.), "Afar Depression of Ethiopia", Schweizerbart, Stuttgart, 1975.
46. Pinheiro, L. M., R. B. Whitmarsh, and P. R. Miles, The ocean continent boundary off the western continental margin of Iberia, part II, Crustal structure in the Tagus Abyssal Plain, *109*, 106-124, 1992.
47. Potts, C. G., A. J. Calvert, and R. S. White, Crustal structure of Atlantic fracture zones, III, The Tydeman fracture zone, *Geophys. J. R. Astron. Soc.*, *86*, 909-942, 1986b.
48. Potts, C. G., R. S. White, and K. E. Louden, Crustal structure of the Atlantic fracture zones, II, The Vema fracture zone and transverse ridge, *J. R. Astron. Soc.*, *86*, 491-513, 1986a.
49. Prodehl, C., and L. C. Pakiser, Crustal structure of the Southern Rocky Mountains from seismic measurements, *Geo. Soc. Am. Bull.*, *91*, 147-155, 1980.
50. Puzyrev, N. N., M. Mandelbaum, S. Krylov, B. Mishenkin, G. Krupskaya, and G. Petrik, Deep seismic investigations in the Baikal Rift Zone, *Tectonophysics*, *20*, 85-95, 1973.
51. Puzyrev, N. N., M. Mandelbaum, S. Krylov, B. Mishenkin, and G. Petrik, Deep structure of the Baikal and other Continental Rift Zones from seismic data, *Tectonophysics*, *45*, 15-22, 1978.
52. Raitt, R. W., The crustal rocks, in *The Sea*, vol. 3, edited by M. N. Hill, pp. 85-102, Wiley-Interscience, New York, 1963.
53. Recq, M., D. Brefort, J. Malod, and J. L. Veinaute, The Kerguelan Isles (Souxheru Indian Ocean): New results on deep structure from refraction profiles, *Tectonophysics*, *182*, 227-248, 1990.
54. Research Group for Explosion Seismology, "The Earth Beneath the Continents", vol. 10, pp. 334-348, Geophysics Monograph, American Geophysical Union, Washington, D.C., 1966.
55. Roller, J., and W. Jackson, In "The Earth Beneath the Continents", vol. 10, edited by J. S. Steinhart and T. J. Smith, pp. 270-275, American Geophysical Union, Washington, D.C., 1966.
56. Ruegg, J. C., In "Afar Depression in Ethiopia", edited by A. Pilger and A. Roesler, pp. 120-134, Schweizerbart, Stuttgart, 1975b.
57. Sapin, M., and A. Hirn, Results of explosion seismology in the Southern Rhone Valley, *Ann. Geophys.*, *30*, 181-202, 1974.
58. Sheehan, A. F., and S. C. Solomon, Joint inversion of shear wave travel time residuals and geoid and depth anomalies for long-wavelength variations in upper mantle temperature and composition along the Mid-Atlantic Ridge, *J. Geophys. Res.*, *96*, 19981-20009, 1991.
59. Shor, G. G., Jr., H. W. Menard, and R. S. Raitt, Structure of the Pacific Basin, in *The Sea*, vol. 4, edited by A. E. Maxwell, pp. 3-27, Wiley-Interscience, New York, 1970.
60. Sinha, M. C., and K. E. Louden, The Oceanographer Fracture Zone, I, Crustal Structure from seismic refraction studies, *Geophys. J. R. Astron. Soc.*, *75*, 713-736, 1983.
61. Sleep, N. H., Formation of oceanic crust: Some thermal constraint, *J. Geophys. Res.*, *80*, 4037-4042, 1975.
62. Smith, T., J. Steinhart, and L. Aldrich, "The Earth Beneath the Continents", in *Geophysics Monograph Series, Series 10*, edited by J. S. Steinhart and T. J. Smith, pp. 181-197, American Geophysical Union, Washington, D.C., 1966.
63. Soller, D. R., R. D. Ray, and R. D. Brown, A New Global Crustal Thickness Map, in *Tectonics*, vol. 1, pp. 125-149, 1982.
64. Sollogub, V. B., In "The Earth's Crust and Upper Mantle", edited by P. J. Hart, pp. 189-194, Geophysics Monograph Series 13, American Geophysical Union, Washington, D.C., 1969.
65. Solomon, S. C., and D. R. Toomey, The structure of mid-ocean ridges, *Annu. Rev. Earth Planet. Sci.*, *20*, 329-364, 1992.
66. Spudich, P., and J. Orcutt, A new look at the seismic velocity structure of the oceanic crust, *Rev. Geophys.*, *18*, 627-645, 1980.
67. Steinhart, J., and R. Meyer, "Explosion Studies of Continental Structure", Publication 622, Carnegie Institute, Washington, D.C., 1961.
68. Tolstoy, M., A. J. Harding, and J.A. Orcutt, Crustal thickness on the Mid-Atlantic Ridge: Bull's-eye gravity anomalies and focused accretion, *Science*, *262*, 726-729, 1993.
69. Volvovsky, B. S., I. S. Volvovsky, and N. S. Kombarov, Geodynamics and seismicity of the Pamir-Himalayas region, *Phys. Earth Planet. Inter.*, *31*, 307-312, 1983.
70. White, R. S., S. D. McKenzie, and R. K. O'Nions, Oceanic Crustal thickness from Seismic Measurements and Rare Earth Element Inversions, *J. Geophys. Res.*, *97*, 19683-19715, 1992.
71. Whitmarsh, R. B., and A. J. Calvert, Crustal Structure of Atlantic Fracture Zones, I. the Charlie Gibbs F.Z., *Geophys. J. R. Astr. Soc.*, *85*, 107-138, 1986.
72. Will, M., in *"Explosion Seismology in Central Europe"*, edited by P. Giese, C. Prodehl and A. Stein, pp. 168-177, Springer-Verlag, Berlin and New York, 1976.
73. Yamashina, K., Induced earthquakes in the Izu Peninsula by the Izu-Hanto-Oki earthquake of 1974, Japan, *Tectonophysics*, *51*, 139-154, 1978.
74. Zhang, Y. S., and T. Tanimoto, Global love wave phase velocity variation and its significance to plate tectonics, *Phys. Earth Planet. Inter*, *66*, 160-202, 1991.
75. Zhao, D., A. Hasegawa and S. Horiuchi, Tomographic Imaging of P and S wave Velocity Structure beneath Northeastern Japan, *J. Geophys. Res.*, *97*, 19908-19928, 1992.

Mean Paleomagnetic Poles for the Major Continents and the Pacific Plate

Richard G. Gordon and Rob Van der Voo

1. ABSTRACT

Apparent polar wander is the motion of Earth's spin axis relative to a reference frame that is usually fixed relative to a tectonic plate or stable interior of a continent. The main method for estimating the past position of Earth's spin axis is through paleomagnetism, the investigation of the magnetic memory of rocks. Mean paleomagnetic poles, which average poles over about half a geologic period and typically differ in mean age by ~20 to 30 millions of years, are presented for the major cratons over Phanerozoic time and are presented for more closely spaced ages for the Pacific plate since Late Jurassic time.

2. INTRODUCTION

Paleomagnetism is the study of Earth's past magnetic field through investigation of the magnetic memory of rocks. Among the branches of geophysics, paleomagnetism holds a special place for several reasons, not least of which was its pivotal role in providing support for the theory of continental drift. It is also special because most of the central problems of paleomagnetism are not concerned merely with the present Earth, as are most branches of geophysics, but with the history of Earth's solid surface over millions, tens of millions, hundreds of millions, or billions of years. Paleomagnetism is a tool for quantitative investigations of the tectonic history of Earth. Almost every modern paleomagnetic analysis is ultimately concerned with whether an estimated (i.e., observed) paleomagnetic direction differs significantly either from a known or hypothesized direction or from some other estimated direction.

In this chapter we briefly summarize what is known about the apparent polar wander (APW) paths of the stable portions of major continents over Phanerozoic time and of the Pacific plate since Late Jurassic time. With many caveats, including some discussed below, the paleomagnetic poles and their associated confidence limits can reasonably be considered a set of constraints on the crustal and mantle history of Earth.

What we cannot do here at all in this highly compact format is give any of the documentation of our sources of data, much less report on any of the field or laboratory investigations upon which these data rest, or discuss specific ambiguities in the data. The main data source used here for continental paleomagnetic poles and confidence limits is Van der Voo [46]. Sources for Pacific plate data are cited herein.

2.1 Apparent Polar Wander

APW is the position as a function of time of the intersection of Earth's spin axis with its surface as viewed from a reference frame attached to a finite-sized and stable portion of the surface of the solid Earth, which is most commonly a major craton, such as the stable interior of North America. This definition has some inherent problems, some trivial and some profound. The Earth's spin axis intersects its surface at two places, the north and south poles. Herein we use

R. G. Gordon, Department of Geological Sciences, Northwestern University, Evanston, IL 60208-2150

R. Van der Voo, Department of Geological Sciences, University of Michigan, Ann Arbor, Michigan 48109-1063

Global Earth Physics
A Handbook of Physical Constants
AGU Reference Shelf 1

only the north pole as a reference. This can be a non-trivial ambiguity for ancient APW when sparse sampling in time, combined with the unknown polarity of Earth's paleomagnetic field, makes unclear whether a pole is a north pole or a south pole. A less important ambiguity, negligible for present purposes, is that on short time scales of about a year, the spin axis transiently differs from Earth's axis of maximum moment of inertia, through the annual- and Chandler-wobble.

The key assumption in going from paleomagnetic observations to APW is the axial geocentric dipole hypothesis, that the time-average of Earth's magnetic field is that of a geocentric dipole aligned with Earth's spin axis. Paleomagnetists uniformly view APW as a continuous curve, provided that each point is understood to represent an average over an interval long enough (tens of thousands of years or longer) to sample the full range of geomagnetic secular variation.

It is convenient to think of APW as consisting of two parts— the motion of the plates relative to the deep mantle and true polar wander, i.e., the motion of the whole earth relative to the spin axis by the process described by Goldreich and Toomre [10]. For example, if one were completely confident that true polar wandering was negligible, it might be possible therefore to use what is known about plate motion to specify long time intervals of APW with just a few adjustable parameters, as Gordon et al. [15] and May and Butler [26] have attempted with very simple models.

2.1.1. Path construction. Many methods have been used for specifying APW paths or segments of APW paths. Here we specify a sequence of point estimates differing in age typically by 20 or 30 million years. This approach is most valid for intervals in which APW was small, that is, small in comparison with the dispersion of individual paleomagnetic poles due to uncertainty in pole position and small in comparison with the confidence limits of the resulting pole. A key advantage of this approach is simplicity of application— once the data in the interval have been identified, the pole and confidence limits can be calculated either using the oceanic plate method of Gordon and Cox [11] or, more commonly, by the application of Fisher statistics [8].

There are several disadvantages to this approach, as there are for all the alternatives. First, over time intervals as long as half a period, APW is non-negligible, successive poles from continents typically being separated by ~10° [46]. Thus, for accuracies better than ~10°, the pole cannot be thought of as representative of the entire half-period-long interval. Either the true age of the estimated pole is uncertain to about half a period or the true error in pole position for any precisely stated age is much more uncertain than implied by the confidence limits of the pole. If APW during the half-period was very smooth, if the pole moved along a great circle at a constant velocity, and if the included paleomagnetic poles have an average age near the middle of the interval, then the mean pole could be a good estimate of the average position of the pole during the half-period. However, if APW were more complex during the interval, e.g., reversing direction half-way through the interval as the North American pole appears to have done about 200 Ma [15, 26], then this method gives a biased estimate of the pole position and tends to give estimates of the rate and total length of APW that are less than the true rate and length.

Thus, readers who use these APW paths presented herein should be aware that what is presented are not the data, but a reduction of these data that is valid only insofar as the underlying assumptions discussed above are valid. It is not uncommon to see APW paths referred to as "data", but we emphasize that they are models having a large number of adjustable parameters.

2.1.2. Data selection. Although two-thirds of Earth's surface is covered by oceanic crust, the available data are dominated by those from the continents for two reasons. First, it is impractical to obtain oriented samples from oceanic crust except in oceanic islands, which are nearly always very young. Second, the oldest seafloor is very young (~170 Ma) relative to the oldest continental surface (> 3 Ga).

Various sets of criteria for minimum reliability or for data selection, all with similar intent, are in use by different workers in paleomagnetism. The data incorporated into the estimation of the continental paths described herein were filtered using seven criteria set forth by Van der Voo [46 and work cited therein]: (1) The rock age is well determined and the magnetization can reasonably be assumed to be the same age as the rock. (2) There are enough samples, small enough dispersion, and small enough confidence limits on the mean, specifically there are more than 25 samples, the precision parameter is at least 10 (corresponding to a two-dimensional angular standard deviation of at most 25.6°), and the radius of the cone of 95% confidence is 16° or less. (3) The samples have been adequately demagnetized and vector subtraction or principal component analysis have been used to analyze the demagnetization data. (4) Field tests constrain the age of magnetization. (5) There is sufficient structural control to correct the magnetization for post-magnetization

changes in orientation and there is enough evidence to indicate that the sampling sites are tectonically coherent with the relevant craton or block. (6) Reversals are present. (7) The paleomagnetic poles do not resemble any poles that are younger by more than a period.

The filter used by Van der Voo [46], whose paths are reproduced herein, are that only data meeting at least 3 of these criteria are included. See Van der Voo [46] for further details including the very long tables of data on which these paths are based. Acton and Gordon [3] describe a different approach for selection and rejection of continental paleomagnetic poles, which would reject more poles than does Van der Voo's filter. The difference in filter mainly reflects the difference in intended applications and the level of accuracy and resolution both desired and attainable from the more recent, better studied intervals investigated by Acton and Gordon.

For Pacific plate APW, the criteria of data selection usually have a similar intent, but are qualitatively different because Pacific plate data are qualitatively different. In a few special cases the requirement of well-determined rock age has been relaxed. Numbers of samples, precision of magnetization directions, and demagnetization are considered only when the magnetic results are based on oriented samples instead of measurements of the magnetic field intensity at the sea surface. Structural control and tectonic coherence are in nearly every case negligible problems for Pacific plate paleomagnetism [cf., 3].

2.2 APW Paths of the Major Continents

The major continents are North America, Greenland, Europe, Siberia, North and South China, and the Gondwana elements of South America, Africa, Madagascar, India, Australia, and Antarctica. All continents consist of older Precambrian nuclei on which Paleozoic and younger sediments were deposited. In this section we present the Phanerozoic APW paths of these continents. Results herein have not been compiled for post-Eocene times. Readers in search of Oligocene paleomagnetic poles are referred to Acton and Gordon [3]. This section follows chapter 5 of Van der Voo [46], to which the reader is referred for further details.

2.2.1. North America, Greenland, and Europe. North America and Europe are paleomagnetically the best studied continents of the world with 400 individual paleomagnetic poles for the Cambrian through Eocene periods [46]. Poles incorporated from North America come from the craton and its disturbed margin. Poles from displaced terranes, i.e., terranes known to have moved relative to stable North America in the distant past, are incorporated only for those intervals since those terranes became firmly attached to North America. Hence, poles for Appalachian displaced terranes north of New York City (41°N) have been included only for Devonian and younger times. Similarly, poles for Appalachian displaced terranes south of New York City have been included only for Late Carboniferous and younger times. Results from terranes in Mexico, in the western North American cordilleras, and in Alaska have been excluded. For two regions of the disturbed margin, the Colorado Plateau (including its surroundings in Colorado, Arizona, and New Mexico) and the northern part of the Pennsylvania Salient in the Appalachian fold and thrust belt, a correction for inferred rotation relative to the stable interior of North America has been applied to the poles before their incorporation into the path. The resulting individual poles have been combined to obtain a set of mean paleomagnetic poles for North America and Europe for time intervals from Early Cambrian to early Tertiary (Table 1). Some of these are shown in Figure 1 with and without correction for the opening of the Atlantic.

The European craton was taken as that part of the continent now found in Scandinavia, as well as the Russian Platform between the Urals and the Paleozoic or younger mobile belts at the surface or buried in Denmark, Germany, Poland, western Podolia (Ukraine), Romania, and Bulgaria. The European cratonic part during Paleozoic time is called Baltica. A second ancient element in Europe lies in the northern part of the British Isles. This area of Scotland and northern Ireland throughout the Paleozoic is thought to have formed part of the combined North American-Greenland continent (called Laurentia) and includes what is called the Lewisian basement that used to be continuous with Greenland. Pre-Late Silurian results from the northern British Isles may not be representative of Baltica (="Stable" Europe). From other terranes, only latest Silurian and younger results were included from the Midland Craton and its margins, only latest Carboniferous and younger results were included from Hercynian Europe, and no results were included from Alpine Europe including the large Hercynian massifs therein and the Moesian Platform (in Romania and Bulgaria).

Poles from Greenland are so sparse that only a very sparse APW path can be constructed for it. See Van der Voo [46] and Acton and Gordon [3] for a discussion of the relatively abundant early Tertiary paleomagnetic

Table 1. Mean Paleopoles from North America and Europe

Age interval	North America				Stable Europe			
	Pole	N	K	A_{95}	Pole	N	K	A_{95}
Tl (37–66)	82, 168	17	63	5	78, 177	20	75	4
†Tl (37–66)	†77, 173	26	43	4				
Ku (67–97)	68, 192	5	250	5	72, 154	5	146	6
†Ku (67–97)	†68, 192	7	227	4				
Kl (98–144)	69, 194	8	149	5	70, 193	4	41	15
Ju, uJm (145–176)	67, 133	8	44	9	66, 191	3	73	15
lJm, Jl (177–195)	68, 93	10	193	4	70, 126	4	86	10
Tru/Jl (196–215)	61, 81	15	68	5				
Tru, uTrm (216–232)	52, 96	7	180	5	52, 133	5	29	14
Trl/m, Trl (233–245)	52, 110	11	190	3	52, 150	13	103	4
Pu (246–266)	52, 120	5	371	4	50, 160	6	85	7
Pl (267–281)	45, 123	14	218	3	47, 164	21	134	3
Cu/Pl, Cu (282–308)	40, 128	15	314	2	41, 169	21	165	3
Cm, Cl, Du/Cl (309–365)	29, 131	20	49	5	25, 159	5	45	12
Du, Dm/Du (366–378)	30, 110	8	20	13	27, 151	6	38	10
Dm, Dl (379–397)	24, 108	5	23	16	24, 151	5	82	8
Su/Dl (398–414)	4, 95	4	75	11	3, 135	14	24	8
†Su/Dl (398–414)	†4, 97	5	78	9				
Su, Sm (415–429)	18, 127	2	-	-	20, 161	11	44	6
Ou/Sl, Ou, Om (430–467)	18, 146	9	16	13				
*Same, N. Britain only					*13, 181	9	24	10
Ol/m, Ol (468–505)	17, 152	3	31	23	-24, 230	2	-	-
*Same, N. Britain only					*16, 212	1	-	-
Cu, Cm, C (506–542)	9, 158	8	28	11				
Cl (543–575)	5, 170	6	22	15	11, 231	2	-	-

Mean north paleopoles for each continent are given in their own reference frames [46]. The mean paleopoles were determined from individual poles that are listed in Van der Voo [46] and meet 3 or more of 7 criteria (described in the text). Age abbreviations: T=Tertiary, K=Cretaceous, J=Jurassic, Tr=Triassic, P=Permian, C=Carboniferous, D=Devonian, S=Silurian, O=Ordovician, C=Cambrian, l=early, m=middle, u=late. Ages in millions of years before present are given in parentheses and are from the time scale of the Decade of North American Geology [28]. N, K, and A_{95} respectively are the number of individual paleopoles averaged, the precision parameter, and the radius of the cone of 95% confidence about the mean pole [8]. Pole positions are given in latitude (positive when north, negative when south) and east longitude.

* Great Britain north of the Iapetus suture only. For pre-Middle Silurian times the Baltic Shield and Russian Platform, exclusive of Caledonian Europe, are listed separately without an asterisk.

† Includes also the results from Greenland (rotated into the North American reference frame).

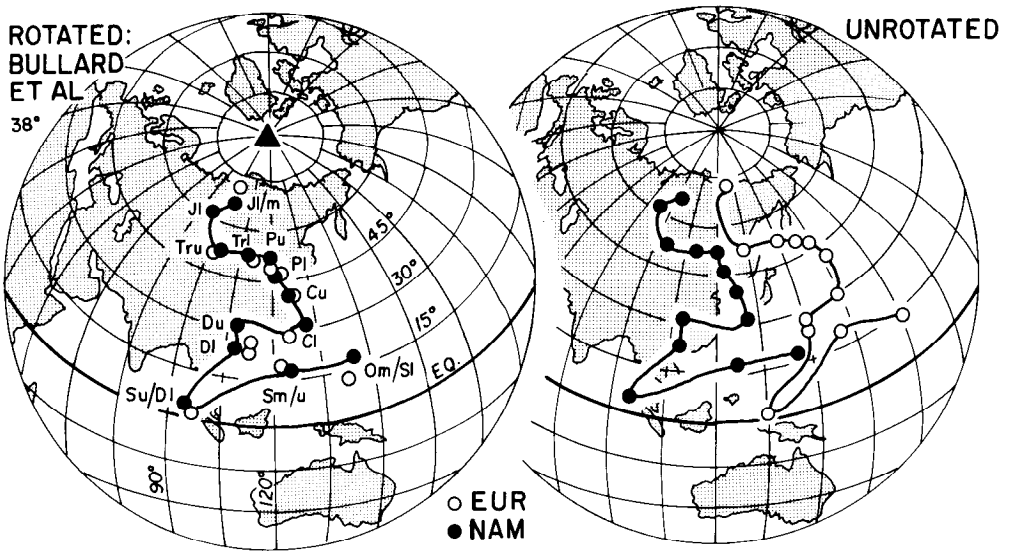

Fig. 1. Apparent polar wander paths (north poles) for Europe and North America for the interval from Middle Ordovician through Early Jurassic time. The plot on the right shows the North American poles in a reference frame attached to the present location of North America and shows the European poles in a reference frame attached to the present location of Europe. The left-hand side identically repeats the North American path but shows the European path reconstructed into the North American reference frame using the reconstruction of Bullard et al. [4]. The large triangle is the Euler pole of this rotation; the rotation angle is 38°. Age abbreviations are explained in Table 1. For pre-Middle Silurian times, only European paleomagnetic poles from northern Britain have been used. From Van der Voo [46].

poles from Greenland.

2.2.2. The Gondwana continents. Paleomagnetic poles for the Gondwana continents total less than 350 for Africa, South America, Antarctica, Australia, India, and Madagascar combined [46]. A major part of this paleo-supercontinent is cratonic including most of Africa, most of South America, Madagascar, India south of the Himalayan Front, Australia west of the eastern fold belts, and East Antarctica. The break-up of Gondwana is well documented and thought to have been initiated in Middle Jurassic time. In contrast, the timing of the assembly of Gondwana is poorly known. Much of cratonic Gondwana was last deformed or displaced relative to adjacent cratonic elements by the late Precambrian to early Paleozoic Pan-African orogeny, which formed (pre-Ordovician) mobile belts around and between the older Archean and earlier Proterozoic nuclei [46]. There remain many unanswered questions about the APW path of Gondwana, especially for Paleozoic time.

Each pole for each of the six now separate elements are given in its present reference frame in Table 2a. The Cambrian to earliest Jurassic subset of these poles is given in Table 2b after reconstruction into a common northwest African reference frame. The errors and precisions quoted in Table 2b are identical to those in 2a and neglect the presumably significant errors induced by the reconstruction.

Table 3 gives the Early Cambrian to Early Jurassic Gondwana paleomagnetic poles combined in the northwest African reference frame. Readers should note how very large some of the confidence limits are on these combined poles. Figure 2 shows a smooth curve drawn through the Late Carboniferous to Early Jurassic mean Gondwana poles, as well as the individual mean poles from each continent. Individual poles from the Gondwana continents are plotted in their separate reference frames attached to the present positions of their host cratons (Figure 3a) and are also plotted after rotation into a common northwest African reference frame (Figure 3b). The large decrease in dispersion of the data when reconstructed into the northwest African reference frame gives strong support to the Gondwana hypothesis, though the data cannot decisively distinguish between different Gondwana reconstructions that have been proposed. Figure 4 shows the individual

Table 2a. Mean Paleopoles for the Phanerozoic of Gondwana

Age Group	Africa				South America				India				Australia				Antarctica				Madagascar			
	Pole	N	K	A_{95}	Pole	N	K	A_{95}	Pole	N	K	A_{95}	Pole	N	K	A_{95}	Pole	N	K	A_{95}	Pole	N	K	A_{95}
Tl (37–66)	81, 185	4	77	11	79, 76	2			43, 285	10	24	10	61, 301	7	38	10								
Ku(67–97)	67, 245	12	60	6	85, 214	6	56	9	21, 295	7	47	9	56, 318	1							68, 231	6	103	7
Kl (98–144)	56, 263	6	105	7	84, 224	7	107	6	12, 299	2			41, 338	6	17	17								
Ju(145–176)	57, 251	7	22	13	85, 73	3	293	7	2, 310	2			48, 349	6	29	13	52, 30	6	89	7				
Jl (177–195)	72, 249	10	108	5									48, 357	3	562	5	49, 46	4	125	8				
Jl/Tru(196–215)	71, 214	2			71, 74	2			10, 310	1											74, 277	1		
Tru(216–232)	56, 253	2			79, 78	6	45	10					32, 350	1										
Trl (233–245)					63, 149	1			-6, 305	3	321	7	31, 338	2							66, 292	1		
Pu(246–266)					80, 110	5	77	9	4, 283	1			36, 321	3	37	21								
Pl (267–281)	32, 246	5	51	11	62, 174	3	399	6					46, 302	1										
Cu(282–308)	40, 217	3	20	28	54, 165	9	42	8	-18, 291	1			62, 322	2										
Cl (309–365)	21, 227	4	20	21									84, 141	1										
Du(366–378)	5, 197	2											62, 203	6	19	16								
Dl (379–397)					12, 130	2							77, 80	3	5	60								
Dl/Su (398–414)																								
Sm/Su(415–429)	43, 189	1											58, 173	3	4	68								
Sl/Om (430–467)	-35, 158	2											-2, 215	2										
Ol (468–505)	-38, 189	3	15	33	-4, 122	1							18, 199	3	22	27	9, 202	5	39	12				
€u(506–542)	-61, 162	5	3	50	-49, 194	3	15	33					18, 203	8	13	16								
€l (543–575)	-17, 90	2							35, 219	5	28	15	28, 178	4	12	27								

Mean north paleopoles for each of the Gondwana continents are given in their own reference frames [46]. The mean paleopoles were determined from individual poles that are listed in Van der Voo [46] and meet 3 or more of 7 criteria. Abbreviations and convention are the same as in Table 1.

Table 2b. Rotated Mean Paleopoles for the Phanerozoic of Gondwana

Age Group	Africa				South America				India				Australia*				Antarctica				Madagascar			
	Pole	N	K	A_{95}	Pole	N	K	A_{95}	Pole	N	K	A_{95}	Pole	N	K	A_{95}	Pole	N	K	A_{95}	Pole	N	K	A_{95}
Jl (177–195)	72, 249	10	108	5									63, 259	3	562	5	74, 272	4	125	8				
Tru/Jl(196–215)	71, 214	2			71, 217	2			67, 251	1											68, 232	1		
Tru(216–232)	56, 253	2			67, 236	6	45	10					52, 283	1										
Trl (233–245)					43, 222	1			50, 259	3	321	7	43, 276	2							65, 254	1		
Pu(246–266)					61, 236	5	77	9	43, 224	1			34, 261	3	37	21								
Pl (267–281)	32, 246	5	51	11	36, 234	3	399	6					28, 242	1										
Cu(282–308)	40, 217	3	20	28	31, 225	9	42	8	33, 251	1			45, 230	2										
Cl (309–365)	21, 227	4	20	21									43, 182	1										
Du(366–378)	5, 197	2											17, 184	6	19	16								
Dl (379–397)					7, 177	2							53, 175	3	5	60								
Su/Dl (398–414)																								
Sm-u(415–429)	43, 189	1											19, 168	3	4	68								
Om-Sl (430–467)	-35, 158	2											-48, 189	2										
Ol (468–505)	-38, 189	3	15	33	-2, 162	1							-26, 172	3	22	27	-30, 183	5	39	12				
€u(506–542)	-61, 162	5	3	50	-74, 200	3	15	33					-26, 176	8	13	16								
€l (543–575)	-17, 90	2							5, 162	5	28	15	-10, 157	4	12	27								

Mean north paleopoles for each of the Gondwana continents are given in the Northwest Africa reference frame [46]. The mean paleopoles were determined from individual poles that are listed in Van der Voo [46] and meet 3 or more of 7 criteria. Abbreviations and conventions are as in Table 1. The rotation parameters are from Lottes and Rowley [25] and for pre-Middle Jurassic times as follows: South America to Northwest Africa, Euler pole at 53°N, 325°E, angle 51.01° counterclockwise; India to Northwest Africa, Euler pole at 26.67°N, 37.29°E, angle 69.37° clockwise; Australia to Northwest Africa, Euler pole at 28.13°S, 66.79°W, angle 52.06° counterclockwise; Antarctica to Northwest Africa, Euler pole at 12.36°S, 33.81°W, angle 53.29° counterclockwise, and Madagascar to Northwest Africa, Euler pole at 14.9°S, 82.35°W, angle 15.7° counterclockwise.

* Australian means include Paleozoic results from the eastern foldbelt.

Table 3. Overall Mean Poles For Gondwana in Different Reconstructions

Age Interval	Pole[1]	N	K	A_{95}	Pole[2]	N	K	A_{95}	Pole[3]	N	K	A_{95}
J1 (177–195)	70, 260	3	138	11	65, 258	3	137	11	67, 250	3	162	10
Tru/Jl (196–215)	70, 230	4	163	7	67, 230	4	102	9	64, 256	4	23	20
Tru(216–232)	60, 261	3	32	22	58, 261	3	29	23	56, 260	3	75	14
Trl (233–245)	52, 253	4	20	21	50, 250	4	19	22	45, 264	4	13	26
Pu(246–266)	47, 242	3	17	31	44, 243	3	15	33	43, 256	3	48	18
Pl (267–281)	32, 241	3	156	10	30, 242	3	88	13	27, 244	3	176	9
Cu(282–308)	38, 231	4	37	15	34, 233	4	37	15	32, 239	4	14	25
Cl (309–365)	34, 207	2			31, 209	2			27, 210	2		
Du(366–378)	11, 191	2			9, 192	2			5, 196	2		
Dl (379–397)	30, 176	2			28, 179	2			25, 182	2		
Su/Dl (398–414)												
Sm-u(415–429)	31, 177	2			29, 179	2			25, 183	2		
Om-Sl (430–467)	-43, 172	2			-44, 170	2			-48, 175	2		
Ol (468–505)	-25, 176	4	19	22	-26, 175	4	19	22	-30, 180	4	12	27
€u(506–542)	-55, 176	3	10	42	-55, 173	3	11	40	-58, 172	3	16	32
€l (543–575)	-9, 138	3	4	71	-7, 140	3	4	73	-1, 144	3	3	110

Mean north paleopoles for each of the Gondwana continents (Table 2a and Van der Voo [46]) are given in the Northwest Africa reference frame for different reconstructions. (1) Rotation parameters of Lottes and Rowley [25]; Africa is assumed to have been composed of three distinct plates; see the legend of Table 2b for rotation parameters for the other continents. (2) Rotation parameters of Scotese and McKerrow [38]; Africa is assumed to have been a single plate; all rotations are counterclockwise (ccw) and with respect to Africa: South America, Euler pole at 45.5°N, 327.8°E, angle 58.2°; India, 28.1°S, 213.3°E, angle 66.5°; Australia, 24.63°S, 297.36°E, angle 55.92°; Antarctica, 9.68°S, 328.19°E, angle 58.54°; Madagascar, 1.7°S, 272.2°E, angle 22.2°. (3) Rotation parameters of Smith and Hallam [39]; Africa is assumed to have been a single plate; South America to Africa, Euler pole at 44°N, 329.4°E, angle 57° ccw; India to Africa, 25.5°S, 201.34°E, angle 44.97° ccw; Australia to Africa, 11.92°S, 294.59°E, angle 58.51° ccw; Antarctica to Africa, 1.3°N, 324°E, angle 58.4° ccw; Madagascar to Africa, 9°S, 313°E, angle 15° ccw.

Gondwana poles and a combined smoothed path from Early Cambrian to early Carboniferous time in a northwest African reference frame. There is a broad range of opinions of how the Ordovician poles are connected during Silurian and Devonian time to the late Paleozoic poles; some of these options imply very fast rates of APW of ~4° per million years (cf. figure 5.15 of Van der Voo [46]). Van der Voo [46] concludes that there will be no simple solution for this ambiguity until many more reliable poles are obtained from cratonic Gondwana from Silurian and Devonian rocks.

2.2.3. Siberia. Late Cambrian and younger poles for Siberia have thus far been obtained almost entirely by paleomagnetists from Russia. Unfortunately many of the original publications are not directly accessible, and non-Russian paleomagnetists must rely on published summaries for the available paleomagnetic poles [27, 42, 21, and pers. comm. from A. N. Khramov to RVdV, 1990]. Many results are apparently not fully based on directional analysis, and details of demagnetization and field tests are generally unreported. Thus, the summary poles (Table 4) should be treated with caution, if not skepticism.

For post-Permian poles, readers are advised to use the European reference poles because Eurasia—including stable Europe, Kazakhstan, and Siberia—was a single continent since the formation of the Urals, which formed in a collision of Europe, Kazakhstan, and Siberia no later than in Permian time, and perhaps earlier [17, 50, 49]. Apparently reliable and well-clustered groupings of paleomagnetic poles are available for Late Cambrian and Ordovician times from Siberia. The Silurian and Devonian poles from Siberia suggest that it drifted northward, but the Devonian poles are suspected of being secondary magnetizations [46].

2.2.4. North and South China. Poles for South China lie in the Pacific Ocean when plotted in the reference frame of South China (Figure 5, Table 5). The

Fig. 2. Mean paleomagnetic north poles for each Gondwana continent and combined Gondwana apparent polar wander path for late Carboniferous through Early Jurassic time (in northwest African coordinates from Tables 2b and 3). From Van der Voo [46].

North China paleomagnetic poles for Triassic and Permian time mainly fall in Europe and northern Africa when plotted in the reference frame of North China (Figure 5, Table 5). Recently obtained Silurian and Devonian poles for North China indicate a mid-Paleozoic path different from that sketched in Figure 5, with poles lying in the Pacific Ocean southwest of North America [48]. The Late Permian paleomagnetic poles of the two blocks appear well determined and provide strong evidence for post-Permian movement between the two blocks. Paleomagnetic poles from the two blocks for Cretaceous time are more or less consistent with one another and are consistent with those from Siberia, Europe, and North America rotated into a Eurasian reference frame. The available poles for both North China and South China indicate low to equatorial paleolatitudes.

2.3 APW of the Pacific Plate

All the APW paths presented above have been for continents or components of continents. Here we present an APW path for the Pacific plate (Figure 6, Table 6), which is nearly entirely oceanic. Because the oldest seafloor in the Pacific, ~175 Ma, is much younger than the oldest rocks on continents, the Pacific APW path cannot span nearly as long an interval.

Current estimates of Pacific APW come from several types of data: (1) seamount poles, (2) paleocolatitudes from azimuthally unoriented cores, (3) identification of equatorial sediment facies in drill cores, and (4) the shapes and amplitudes of marine magnetic

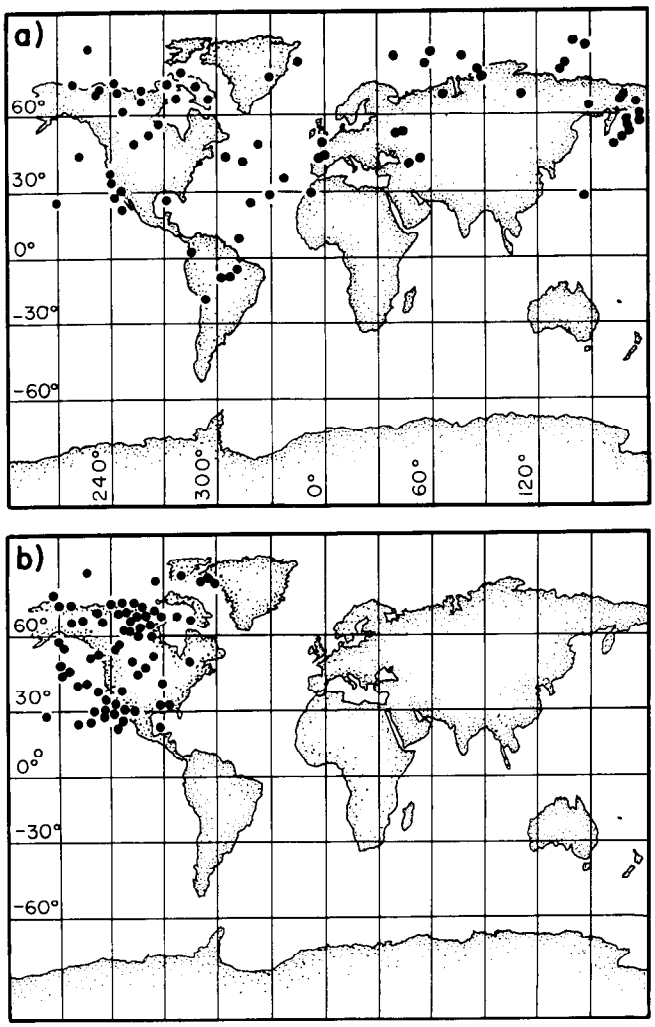

Fig. 3. a) Individual late Carboniferous through Early Jurassic paleomagnetic north poles from each of the Gondwana continents with each pole plotted in the reference frame fixed relative to the present location of its continent. b) Individual late Carboniferous through Early Jurassic paleomagnetic north poles from each of the Gondwana continents rotated into the West African reference frame using the reconstruction of Lottes and Rowley [25]. From Van der Voo [46].

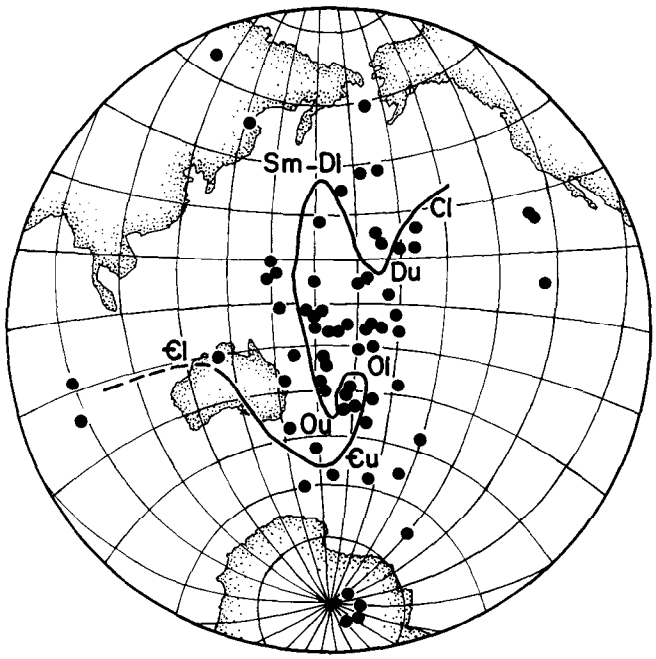

Fig. 4. Individual Cambrian through early Carboniferous paleomagnetic north poles from each of the Gondwana continents reconstructed into the West African reference frame using the reconstruction of Lottes and Rowley [25]. Also shown is the best estimate of the apparent polar wander path. From Van der Voo [46].

anomalies caused by the alternating polarity of seafloor magnetization recorded as the seafloor spreads away from mid-ocean ridges.

Most of the information about Pacific APW during Cretaceous time comes from seamount poles [43, 43, 9, 19, 33, 34, 35, 36, 20]. Most of these poles have been determined using a linear least-squares analysis and by assuming that the seamount is uniformly magnetized. R. Parker and colleagues have demonstrated that the observed anomalies over seamounts are inconsistent with uniform magnetization and have developed promising alternative methods for analyzing seamount magnetism [e.g., 29, 30], which have replaced uniform-magnetization approaches as the method of choice. The results from these new methods have provided bounds on how the magnetization is really distributed, but the pole positions are on average not very different from those from the uniform magnetization approach [e.g., 20]. In early work on seamount magnetism, seamounts lying close to one another were assumed to be of about the same age, and their poles were averaged together. This work indicated that seamount poles had large dispersions, with two-dimensional angular standard deviations of 6° to 11° [19]. Later work, building on more precise age dates, indicates that the dispersions are somewhat smaller, with two-dimensional angular standard deviations of 5° to 8° [11, 14, 34, 36]. The many seamount poles now available, in large part due to the work of W. Sager, renders the random error on averages of seamount poles small.

The main weakness of seamount poles for determining the Pacific APW path is that so few of them are precisely dated that they are not very useful in problems requiring a fine age resolution, which is critical, for example, for study over intervals of rapid APW. A

Table 4. Mean Palepoles for Siberia

Age or Interval	Pole	N	K	A_{95}	Ref.
Tl (45)	70, 162	4	39	11	1
Tl (59)	62, 146	5	46	9	1
Ku(88)	64, 151	4	108	7	1
Kl (121)	70, 167	5	234	4	1
Ju/Kl (142)	70, 150	6	42	9	1
Ju(151)	69, 131	5	49	9	1
Jm (173)	65, 132	6	29	11	1
Jl (195) *	63, 110	4	21	21	1
Tru/Jl (207)	56, 129	6	48	8	1
Tru(222)	55, 138	6	38	9	1
Trm (238)	52, 150	7	58	7	2
Trl (245)	52, 156	9	113	4	2
Pu(253)	42, 161	6	61	7	2
Pl (268)	38, 159	5	48	9	2
Cu/Pl (288)	34, 158	5	31	11	2
Devonian (360–408)	28, 151	7	65	8	3
Silurian (408–438)	-4, 121	8	-	19	4
M. Ordovician (458–478)	-22, 130	11	-	4	4
E. Ordovician (479–505)	-40, 132	12	-	7	4
L. Cambrian (505–523)	-36, 127	14	141	3	3
M. Cambrian (523–540)	-44, 157	4	61	12	3
E. Cambrian (540–575)	-35, 188	4	16	24	3

Mean north paleopoles for Siberia are given in the (Eur-)Asian reference frame [46]. The mean paleopoles were determined from individual poles that are listed in Van der Voo [46] and meet 3 or more of 7 criteria. Abbreviations and conventions are as in Table 1. References: 1 = Khramov [21 and pers. comm., 1990], with running mean averages in 20-Myr windows of all data from the U.S.S.R. part of Eurasia; 2 = Khramov [21 and pers. comm., 1990] with running mean averages in 20-Myr windows of the data from the Siberian Platform only; 3 = from McElhinny [27, table 20], conventional Fisher averages; 4 = Tarling [42, table 9.3], conventional Fisher averages.

* Calculated without running mean average, for the time of the peak of the polar wander path cusp (see also the discussion of North American paleopoles).

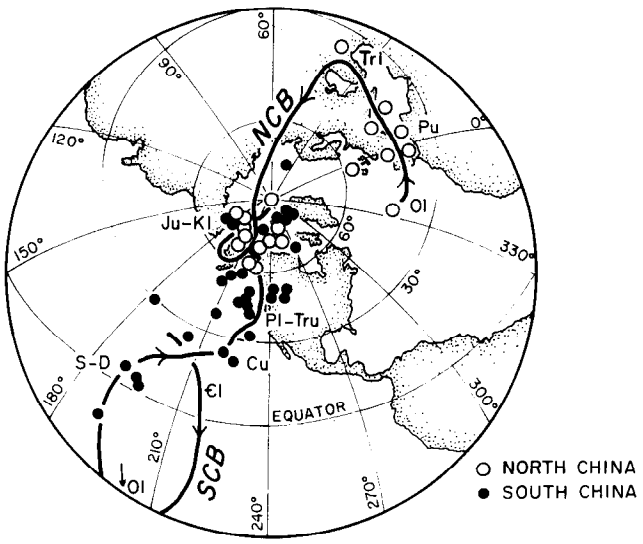

Fig. 5. Individual paleomagnetic north poles from South and North China, as well as best estimates of their paths of apparent polar wander. From Van der Voo [46].

lesser problem, which is undiminished by estimating poles for more seamounts, is that seamount poles must have a small poorly known bias or systematic error due to an induced magnetization or to a mainly Brunhes-age overprint. In a laboratory-based paleomagnetic study the former would be eliminated by making measurements in magnetic field-free space whereas the latter would be removed by alternating-field cleaning, thermal cleaning, or both. A final limitation to seamount poles is that it is unlikely that many, if any, useful poles can be obtained for time intervals when the geomagnetic field was reversing frequently because a seamount is unlikely to form entirely during a single short polarity interval. Consequently, few useful seamount poles have been obtained for the past 75 Ma when the interval between reversals was short, although many useful seamount poles have been obtained for mid- to Late Cretaceous time when the interval between reversals was long [see, Ogg, this volume].

Drill-core data also provide much useful information (see, for example, the review of deep sea drilling results by Cox and Gordon [6] and the many paleomagnetic results presented by Hammond et al. [18] and Epp et al. [7]). The most useful data are from igneous rocks recovered by deep-sea drilling and for sedimentary rocks recovered by piston cores. Paleomagnetic inclinations from sedimentary rocks recovered by deep-sea drilling are shallowly biased and are not of much use for the determination of accurate poles [16, 41]. The main weaknesses of unbiased drill core data are that the data are sparse and that the cores are azimuthally unoriented and therefore inclinations but not declinations are obtained. Results from widely separated sites can be combined to obtain unique pole positions, but the resulting poles are always much more narrowly

Table 5. Mean Paleopoles for the North and South China Blocks

Age Interval	South China Block				North China Block			
	Pole	N	K	A_{95}	Pole	N	K	A_{95}
Ku (67–97)	84, 213	2			80, 170	1		
Kl (98–144)	76, 201	2			77, 213	2		
Ju, uJm (145–176)					71, 224	7	102	6
Tru, uTrm (216–232)	45, 224	1						
Trl/m, Trl (233–245)	46, 215	8	26	11	42, 26	2		
Pu (246–266)	47, 232	12	30	8	46, 3	5	73	9
Cu/Pl, Cu (282–308)	22, 225	1						
Dm, Dl (379–397)	-9, 190	1						
Su, Sm (415–429)	5, 195	1						
Ol/m, Ol (468–505)	-39, 236	1			43, 333	1		
€l (543–575)	37, 206	4	4	53				

Mean north paleopoles for North and South China continents are given in their own reference frames [46]. The mean paleopoles were determined from individual poles that are listed in Van der Voo [46] and meet 3 or more of 7 criteria. Abbreviations and conventions are as in Table 1.

bounded in latitude than in longitude. Equatorial sediment facies have also provided useful information [45, 40, 12].

The fourth source of information comes from the shapes and amplitudes of marine magnetic anomalies. Pioneering studies of Larson and Chase [22] and of Cande [5, 37] provided useful constraints on Pacific APW. Cande's work, however, also showed a limitation caused by a systematic difference between the anomaly shape observed and that expected from simple crustal magnetization models that assume vertical boundaries between crust magnetized in opposite directions. This difference is referred to as anomalous skewness and has been observed in many studies. If no correction is made for anomalous skewness, the apparent effective inclination of the remanent magnetization of the seafloor is systematically in error. Recently, Petronotis et al. [31] have developed a method for estimating paleomagnetic poles with compact confidence limits from analysis of the shapes of Pacific plate anomalies despite the complication of anomalous skewness. Insofar as this approach proves successful, the skewness approach has many attractions: (1) There are typically one hundred or more magnetic profiles that cross each Tertiary and Late Cretaceous anomaly on the Pacific plate. (2) The available sites are widely distributed; on the Pacific plate, for example, some crossings of Tertiary and Late Cretaceous anomalies are separated by distances exceeding 10,000 km. (3) The age of the anomalies is (by definition) exactly correlated with the reversal time scale and in a useful and important sense the age of magnetization is exactly known. (4) Insofar as induced magnetizations, viscous magnetizations, and overprinted remanent magnetizations are widespread and well approximated by an infinite sheet, they produce no measurable influence on the observed magnetic anomalies or the inferred direction of magnetization.

Pioneering studies of seamount magnetism and of anomaly skewness showed that the Pacific plate has moved northward by 30°–35° since middle Early Cretaceous time (~125 Ma; Figure 6) [e.g., 44, 9, 22]. Additional studies showed that nearly all the northward motion has occurred since 80–85 Ma (Figure 6) with mid- and Early Cretaceous APW moving along a nearly constant line of latitude corresponding to a clockwise rotation of the Pacific plate with indeterminate east-west motion [11, 14]. Later work indicates that the Pacific plate mainly rotated clockwise from about late Middle Jurassic time (~155 Ma) to about mid-Cretaceous time possibly superposed on modest southward motion during Late Jurassic and part of Early Cretaceous time (Figure

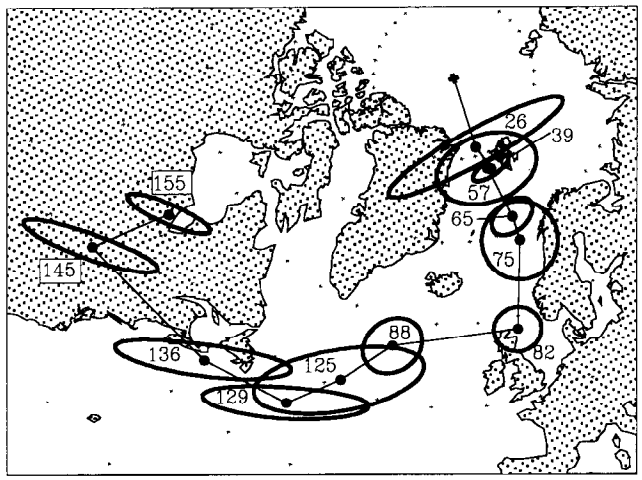

Fig. 6. Observed paleomagnetic north poles for the Pacific plate. Solid squares and surrounding open ellipses are the Pacific plate paleomagnetic poles and 95% confidence limits (Table 6). Stereographic projection.

Table 6. Pacific Plate Apparent Polar Wander Path

Age (Ma)	Pole	Major Semi-Axis	Minor Semi-Axis	Az	Ref
26	81.1, 2.4	12.3	2.1	80	1
39	78.0, 7.1	4.5	1.6	80	2
57	78.2, 4.8	6.4	4.1	93	3
65	71.6, 7.9	2.9	1.8	75	4
75	68.6, 7.2	4.7	4.7	--	5
82	58.4, 359.0	2.9	2.7	91	6
88	56.6, 330.7	3.8	3.1	41	6
125	50.9, 322.6	10.0	3.6	60	7
129	46.0, 315.6	9.4	1.8	67	8
136	44.9, 300.8	9.9	1.8	57	8
145	42.7, 276.5	7.6	1.3	45	8
155	51.9, 277.4	5.1	1.1	49	8

Mean north paleopoles for the Pacific plate. Ages are given in millions of years before present (Ma). Each 95% confidence limit is an ellipse, which is specified by the length in great circle degrees of the major semi-axis and of the minor semi-axis, and by the azimuth ("Az") in degrees clockwise from north of the major semi-axis. Sources and references ("Ref") are as follows: (1) Acton and Gordon [3], (2) Calculated by Acton and Gordon [3] from the data of Sager [35], (3) Petronotis et al. [32], (4) Acton and Gordon [1], (5) Calculated from three poles (dated as being from chron 33n) from the data of Sager and Pringle [36], (6) Sager and Pringle [36], (7) Petronotis et al. [31], and (8) Larson and Sager [23] (using their calculations with non-zero, adjustable anomalous skewness).

6) [23, 24].

Work building on the results of Cande [5] showed that much (~15°) of the post-mid-Cretaceous northward motion occurred between 80–85 Ma and ~65 Ma [13, 33], whereas paleomagnetic results from piston cores [18, 7] showed substantial (~10°) northward motion during the past 25–30 millions years. These results indicate that little APW occurred between ~65 and 25 Ma and later results, especially those of Sager [34], have started to fill in the details. Recently, Petronotis et al. [32] have determined a 57 Ma pole (Figure 6, Table 6) that indicates rapid APW continued after 65 Ma until 57 Ma, but that only insignificant APW occurred between 57 and 39 Ma. An important application of Pacific APW is to test the plate motion circuit used to estimate the motion of the Pacific plate relative to the continents [2].

Acknowledgments. Most of this manuscript was written while RGG was at the Laboratoire de Géodynamique Sous Marine in Villefranche sur Mer, while on a research leave of absence from Northwestern University. Our research in paleomagnetism is currently supported by NSF grants EAR-9005679 (RGG) and EAR-9118021 (RVdV).

REFERENCES

1. Acton, G. D., and R. G. Gordon, A 65 Ma palaeomagnetic pole for the Pacific Plate from the skewness of magnetic anomalies 27r-31, *Geoph. J. Int., 106,* 407–420, 1991.
2. Acton, G. D., and R. G. Gordon, Paleomagnetic tests of Pacific plate reconstructions and implications for motion between hotspots, *Science, 263,* 1246–1254, 1994a.
3. Acton, G. D., and R. G. Gordon, Paleomagnetic tests of plate motion circuits and the geocentric axial dipole hypothesis over the past 73 million years, *Geophys. J. Int.,* to be submitted, 1994b.
4. Bullard, E. C., J. E. Everett, and A. G. Smith, A symposium on continental drift—IV. The fit of the continents around the Atlantic, *Trans. Royal Soc. London, 258,* 41–51, 1965.
5. Cande, S. C., A palaeomagnetic pole from Late Cretaceous marine magnetic anomalies in the Pacific, *Geophys. J. R. astron. Soc., 44,* 547–566, 1976.
6. Cox, A., and R. G. Gordon, Paleolatitudes determined from paleomagnetic data from vertical cores, *Rev. Geophys. Space Phys., 22,* 47–72, 1984.
7. Epp, D., W. W. Sager, F. Theyer, and S. R. Hammond, Hotspot-spin axis motion or magnetic far-sided effect?, *Nature, 303,* 318–320, 1983.
8. Fisher, R. A., Dispersion on a sphere, *Proc. R. Soc. London, Ser. A, 217,* 295–305, 1953.
9. Francheteau, J., C. G. A. Harrison, J. G. Sclater, and M. L. Richards, Magnetization of Pacific Seamounts: A Preliminary Polar Curve for the Northeastern Pacific, *J. Geophys. Res., 75,* 2035–2063, 1970.
10. Goldreich, P., and A. Toomre, Some remarks on polar wandering, *J. Geophys. Res., 74,* 2555–2567, 1969.
11. Gordon, R. G., and A. Cox, Calculating palaeomagnetic poles for oceanic plates, *Geophys. J. R. astron. Soc., 63,* 619–640, 1980.
12. Gordon, R. G., and C. D. Cape, Cenozoic latitudinal shift of the Hawaiian hotspot and its implications for true polar wander, *Earth Planet. Sci. Lett., 55,* 37–47, 1981.
13. Gordon, R. G., The late Maastrichtian palaeomagnetic pole of the Pacific plate, *Geophys. J. R. astron. Soc., 70,* 129–140, 1982.
14. Gordon, R. G., Late Cretaceous apparent polar wander of the Pacific plate: Evidence for a rapid shift of the Pacific hotspots with respect to the spin axis, *Geophys. Res. Lett., 10,* 709–712, 1983.
15. Gordon, R. G., A. Cox, and S. O'Hare, Paleomagnetic Euler poles and the apparent polar wander and absolute motion of North America since the Carboniferous, *Tectonics, 3,* 499–537, 1984.
16. Gordon, R. G., Test for bias in paleomagnetically determined paleolatitudes from Pacific plate Deep Sea Drilling Project sediments, *J. Geophys. Res., 95,* 8397–8404, 1990.
17. Hamilton, W. B., The Uralides and the motion of the Russian and Siberian platforms, *Geol. Soc. Am. Bull., 81,* 2553–2576, 1970.
18. Hammond, S. R., D. Epp, and F. Theyer, Neogene relative plate motion between the Pacific plate, the mantle, and the Earth's spin axis, *Nature, 278,* 309–312, 1979.
19. Harrison, C. G. A., R. D. Jarrard, V. Vacquier, and R. L. Larson, Palaeomagnetism of Cretaceous Pacific seamounts, *Geophys. J. R. astron. Soc., 42,*

859–882, 1975.
20. Hildebrand, J. A., and R. L. Parker, Paleomagnetism of Cretaceous Pacific seamounts revisited, *J. Geophys. Res., 92,* 12,695–12,712, 1987.
21. Khramov, A. N., Paleomagnetism and the problems of accretional tectonics of the north-west segment of the Pacific belt (in Russian), *Paleomagnetism and Accretional Tectonics,* pp. 141–153, VNIGRI, Leningrad, 1988.
22. Larson, R. L., and C. G. Chase, Late Mesozoic evolution of the western Pacific Ocean, *Geol. Soc. Am. Bull., 83,* 3627–3643, 1972.
23. Larson, R. L., and W. W. Sager, Skewness of magnetic anomalies M0 to M29 in the northwestern Pacific, *Proc. ODP, Sci. Results, 129,* edited by R. L. Larson, Y. Lancelot, et al., pp. 471–481, Ocean Drilling Program, College Station, TX, 1992.
24. Larson, R. L., M. B. Steiner, E. Erba, and Y. Lancelot, Paleolatitudes and tectonic reconstructions of the oldest portion of the Pacific plate: Comparative study, *Proc. ODP, Sci. Results, 129,* edited by R. L. Larson, Y. Lancelot, et al., pp. 615–631, Ocean Drilling Program, College Station, TX, 1992.
25. Lottes, A. L., and D. B. Rowley, Early and Late Permian reconstructions of Pangaea, in *Palaeozoic Palaeogeography and Biogeography, Geol. Soc. London Memoir 12,* edited by W. S. McKerrow and C. R. Scotese, pp. 383–95, Geological Society of London, London, 1990.
26. May, S. R., and R. F. Butler, North American Jurassic apparent polar wander: Implications for plate motion, paleogeography and Cordilleran tectonics, *J. Geophys. Res., 91,* 11,519–11,544, 1986.
27. McElhinny, M. W., Mantle plumes, palaeomagnetism, and polar wandering, *Nature, 241,* 523–524, 1973.
28. Palmer, A. R., The Decade of North American Geology 1983 geologic time scale, *Geology, 11,* 503–504, 1983.
29. Parker, R. L., L. Shure, and J. A. Hildebrand, The application of inverse theory to seamount magnetism, *Reviews of Geophysics, 25,* 17–40, 1987.
30. Parker, R. L., A statistical theory of seamount magnetism, *J. Geophys. Res., 93,* 3105–3115, 1988.
31. Petronotis, K. E., R. G. Gordon, and G. D. Acton, Determining palaeomagnetic poles and anomalous skewness from marine magnetic anomaly skewness data from a single plate, *Geophys. J. Int., 109,* 209–224, 1992.
32. Petronotis, K. E., R. G. Gordon, and G. D. Acton, A 57 Ma Pacific plate palaeomagnetic pole determined from a skewness analysis of crossings of marine magnetic anomaly 25r, *Geophys. J. Int.,* in press, 1994.
33. Sager, W. W., Seamount Paleomagnetism and Pacific Plate Tectonics, Ph.D. thesis, University of Hawaii, Honolulu, 472 pp., 1983a.
34. Sager, W. W., A late Eocene paleomagnetic pole for the Pacific plate, *Earth Planet. Sci. Lett., 63,* 408–422, 1983b.
35. Sager, W. W., Late Eocene and Maastrichtian paleomagnetic poles for the Pacific plate: implications for the validity of seamount paleomagnetic data, *Tectonophysics, 144,* 301–314, 1987.
36. Sager, W. W., and M. S. Pringle, Mid-Cretaceous to early Tertiary apparent polar wander path of the Pacific plate, *J. Geophys. Res., 93,* 11,753–11,771, 1988.
37. Schouten, H., and S. C. Cande, Palaeomagnetic poles from marine magnetic anomalies, *Geophys. J. R. astron. Soc., 44,* 567–575, 1976.
38. Scotese, C. R., and W. S. McKerrow, Ordovician plate tectonic reconstructions, in *Advances in Ordovician Geology, Geol. Survey Canada Paper 90-9* edited by C. R. Barnes and S. H. Williams, pp. 271–282, 1991.
39. Smith, A. G., and A. Hallam, The fit of the southern continents, *Nature, 225,* 139–149, 1970.
40. Suárez, G., and P. Molnar, Paleomagnetic data and pelagic sediment facies and the motion of the Pacific plate relative to the spin axis since the Late Cretaceous, *J. Geophys. Res., 85,* 5257–5280, 1980.
41. Tarduno, J. A., Absolute inclination values from deep sea sediments: A reexamination of the Cretaceous Pacific record, *Geophys. Res. Lett., 17,* 101–104, 1990.
42. Tarling, D. H., *Palaeomagnetism, Principles and Applications in Geology, Geophysics and Archaeology,* Chapman and Hall, London, 1983.
43. Uyeda, S., and M. Richards, Magnetization of four seamounts near the Japanese islands, *Bull. Earthquake Res. Inst. Tokyo Univ., 44,* 179–213, 1966.
44. Vacquier, V., and S. Uyeda, Palaeomagnetism of nine seamounts in the western Pacific and of three volcanoes in Japan, *Bull. Earthquake Res. Inst. Tokyo Univ., 45,* 815–848, 1967.
45. van Andel, T. H., Cenozoic migration of the Pacific plate,

northward shift of the axis of deposition and paleobathymetry of the central equatorial Pacific, *Geology, 1,* 507–510, 1974.
46. Van der Voo, R., *Paleomagnetism of the Atlantic, Tethys and Iapetus Oceans,* 411 pp., Cambridge University Press, Cambridge, 1993.
47. Windley, B. F., *The Evolving Continents,* John Wiley and Sons, New York, 1977.
48. Zhao, X., R. Coe, H. Wu, and Z. Zhao, Silurian and Devonian paleomagnetic poles from North China and implications for Gondwana, *Earth Planet. Sci. Lett., 117,* 497–506, 1993.
49. Ziegler, P., *Evolution of the Arctic-North Atlantic and the western Tethys, Memoir* 43, 198 pp., Am. Assoc. Petrol. Geol., Tulsa, 1988.
50. Zonenshain, L. P., V. G. Korinevsky, V. G. Kazmin, and C. M. Pechersky, Plate tectonic model of the south Urals development, *Tectonophysics, 109,* 95–135, 1984.

Magnetic Polarity Time Scale of the Phanerozoic

James G. Ogg

1. GEOMAGNETIC FIELD REVERSALS AND THE MAGNETIC POLARITY TIME SCALE

Reversals of the polarity of the main geomagnetic dipole field are geologically rapid events, typically less than 5000 years in duration, which occur at random intervals. These geologically rapid events are recorded by iron oxides within volcanic and sedimentary rocks. The pattern of polarity reversals commonly provides a unique "fingerprint" for correlating rock strata among diverse depositional and faunal realms, and this magneto-stratigraphy allows marine magnetic anomalies to be dated through correlation to fossiliferous sedimentary deposits. The long-term average frequency of these magnetic reversals varies over geological time.

The magnetic polarity time scale has been constructed through a combination of marine magnetic anomaly patterns and of paleomagnetic analysis of various sedimentary sections having detailed biostratigraphy and igneous rocks with radiometric dates. This magnetic polarity time scale, especially the Mesozoic and Paleozoic portions, will continue to evolve as further precise magnetostratigraphic correlations to the geological time scale are obtained.

2. NOMENCLATURE

"Polarity chrons" are intervals of geological time having a constant magnetic field polarity delimited by reversals [39]. A "polarity zone" is the corresponding interval in a stratigraphic section deposited during the polarity chron. Magnetic polarity is called "normal" if the geomagnetic field orientation is similar to the present dipole polarity, and "reversed" if it is opposite in orientation. Some magnetostratigraphic publications have referred to a "polarity chron" as a "chron", but "chron" in the International Stratigraphic Guide designates a formal subdivision of a geological stage (e.g., "Planula chron" within the Oxfordian stage); therefore the prefix "polarity" should always be included for clarity.

Nomenclature for late Mesozoic and Cenozoic polarity chrons is derived from the numbering of the corresponding marine magnetic anomaly series, with oldest polarity chrons given the highest numbers. The latest Cretaceous through Cenozoic magnetic polarity time scale consists of the "C" series (or, often used without a preceding letter identifier),.and the late Jurassic through early Cretaceous scale consists of the "M" series. Each numbered polarity chron within the main "C" and "M" magnetic polarity time scales consists of a pair of an older reversed-polarity chron and a younger normal-polarity chron. As details of the magnetic polarity record became known, especially within the Cenozoic, the nomenclature became progressively more awkward, but a complete renumbering [e.g., 25] would probably introduce even more confusion.

A nomenclature system for the "M" and "C" series was proposed by Alan Cox [29]. A polarity chron has "n" or "r" following its number to indicate normal or reversed polarity, respectively. When a major numbered polarity chron has been further subdivided, the resulting subchrons are denoted by a suffix of a corresponding numbered polarity chron. For example, "M22n.2n" is the

J. G. Ogg, Purdue University, Department of Earth and Atmospheric Sciences, West Lafayette, IN 47907

Global Earth Physics
A Handbook of Physical Constants
AGU Reference Shelf 1

second-oldest normal-polarity subchron which comprises normal-polarity chron M22n. In some cases, further subdivisions have been made to previously published polarity subchrons, so these sub-subchrons are denoted by an additional suffix.

The relative timing of an event with a polarity chron or zone can be indicated by appending a decimal fraction to the polarity chron name [27, 29, 72]. For example, the relative timing of the Cretaceous/Tertiary boundary is at polarity chron C29r.7, indicating that 70% of reversed-polarity chron C29r preceded the event. For clarity in this paper, the decimal fraction is placed after the polarity chron name (e.g., Early/Middle Miocene boundary is at C5C.1n.8), rather than within the name (e.g., C5C.1.8n) as used in some scales [29, 72].

Pre-Late Jurassic portions of the magnetic polarity time scale are derived entirely from paleomagnetic analysis of stratigraphic sections; therefore the polarity chrons do not have a corresponding marine magnetic anomaly sequence to provide an independent nomenclature system. Some published magnetostratigraphic sections have designated individual polarity zones by stratigraphic numbering or lettering (upward or downward). Until the completeness and relative pattern of these various polarity zone series have been verified from coeval stratigraphic successions, it is premature to attempt any systematic nomenclature.

The pre-"M-sequence" magnetic polarity time scale in this paper displays possible polarity chron patterns according to composite sections (e.g., Early Triassic from the Canadian Arctic) or as recorded in a "biostratigraphically complete" section (e.g., Toarcian stage in Breggia Gorge, Switzerland), with rescaling to be consistent with the Decade of North American Geology (DNAG) time scale [78]. Within the Paleozoic, Soviet workers have proposed a series of "superzones" or "hyperzones" characterized by a dominant magnetic polarity or frequency of reversals [e.g., 46].

3. CENOZOIC AND LATE MESOZOIC

3.1. Pleistocene-Pliocene Time Scale

Absolute ages of geological time boundaries and magnetic polarity chrons within the Pleistocene and Pliocene epochs (Tables 1 and 2; Figure 1) are determined from correlation of Milankovitch orbital periodicities to pelagic sections having magnetostratigraphy, biostratigraphy, and detailed isotope or cycle stratigraphy. This astronomical tuning yields ages accurate to a single orbital precessional cycle or approximately 20,000 years. The Pleistocene magnetic polarity scale is calibrated from Ocean Drilling Program Site 677 in the equatorial Pacific [87], and the Pliocene polarity scale is derived from independent studies at Site 677 and in magnetostratigraphic sections near the Pliocene stage stratotypes in southern Italy [34, 35]. The astronomical-tuned age of the base of polarity chron C1n (Brunhes/Matuyama boundary) agrees with $^{40}Ar/^{39}Ar$ ages of lavas spanning this magnetic reversal [2].

The Pliocene-Pleistocene has a parallel nomenclature system in which the polarity chrons are also named for famous geomagnetists or for the geographic location where the polarity zone was first observed (Figure 1).

3.1.1. Pleistocene/Pliocene boundary. The boundary between the Pleistocene and Pliocene epochs is just prior to the end of polarity chron C2n (Olduvai Normal) and has an astronomically tuned age of 1.81 Ma.

3.1.2. Early/Late Pliocene boundary. The Early/Late Pliocene boundary is at the boundary between the Zanclian and Piacenzian stages in southern Italy, but recognition of this stage boundary within the "type" formations varies among biostratigraphic markers. Therefore this stage boundary has been placed at the beginning of the Gauss Normal Polarity Chron (beginning of polarity chron C2An) where the different biostratigraphy definitions appear to converge [34, 35].

3.2. Miocene-Campanian Magnetic Polarity Time Scale

The "C-sequence" polarity pattern for the Late Cretaceous through Miocene (Table 2, Figure 2) is derived by Cande and Kent [9] from a synthetic South Atlantic magnetic anomaly block model with additional details derived from Pacific and Indian Ocean magnetic profiles. Previous magnetic anomaly patterns and corresponding magnetic polarity time scales [3, 4, 29, 49, 62] had been based upon a "representative" South Atlantic magnetic profile [31]. The main magnetic anomalies in their new composite scale [9] are identical to previous scales, but the internal subdivisions and relative durations of normal- and reversed-polarity components are different.

In addition to the main polarity pattern, there are numerous "tiny wiggles" in the marine magnetic anomaly profiles and corresponding "cryptochrons" in the magnetic polarity time scale, especially within the interval of polarity chrons C1 through C13 and C24 through C28 [9]. These features may represent paleointensity fluctuations, brief polarity subchrons, or geomagnetic field excursions [10].

Absolute ages are assigned to this C-sequence of polarity chrons through a spine fit with nine magneto-

TABLE 1. Geologic Time Scale of the Phanerozoic

Geological Age ERA Period Epoch Sub-Epoch or Stage	Age of Top of Sub-Epoch or Stage (Ma)	 Polarity Chron
CENOZOIC		
Quaternary		
Holocene (Recent)	0.00	
Pleistocene	0.01	
Tertiary		
[Neogene]		
Pliocene		
Late (Piacenzian)	1.81	C2n.9
Early (Zanclean)	3.58	C2An.0
Miocene		
Late (Messinian, Tortonian)	5.32	C3r.85
Middle (Serravallian, Langhian)	10.86	C5n.2n.05
Early (Burdigalian, Aquitanian)	16.04	C5Br.0
[Paleogene]		
Oligocene		
Late (Chattian)	23.80	C6Cn.2n.0
Early (Rupelian)	28.48	C10n.1n.0
Eocene		
Late (Pribonian)	33.70	C13r.86
Middle (Bartonian, Lutetian)	37.60	C17n.1n.5
Early (Ypresian)	48.98	C22n.95
Paleocene		
Late (Thanetian)	55.00	C24r.36
Early (Danian)	60.20	C26r.25
MESOZOIC		
Cretaceous		
Late		
Maestrichtian	65.00	C29r.7
Campanian	71.30	C31r.05
Santonian	83.50	C33r.0
Coniacian	86.30	
Turonian	88.70	
Cenomanian	93.30	
Early		
Albian	98.50	
Aptian	113.00	
Barremian	119.00	M1n.9
Hauterivian	127.34	M6r.0
Valanginian	131.55	M10Nr.5
Berriasian	138.77	M15n.4
Jurassic		
Late		
Tithonian	144.75	M18r.0

TABLE 1. (continued)

Geological Age ERA Period Epoch Sub-Epoch or Stage	Age of Top of Sub-Epoch or Stage (Ma)	 Polarity Chron
Kimmeridgian	152.84	M22Ar.0
Oxfordian	156.00	M24Br.0
Callovian	163.00	
Middle		
Bathonian	169.00	
Bajocian	176.00	
Aalenian	183.00	
Early		
Toarcian	187.00	
Pliensbachian	193.00	
Sinemurian	199.00	
Hettangian	204.00	
Triassic		
Late		
Rhaetian	208.00	
Norian	211.50	
Carnian	225.00	
Middle	230.00	
Ladinian		
Anisian	235.00	
Early	240.00	
Olenekian (Smithian)		
(Spathian)	241.26	
Induan (Dienerian)	242.34	
(Griesbachian)	243.45	
PALEOZOIC		
Permian		
Late		
Tatarian	245.00	
Ufimian-Kasanian	253.00	
Early		
Kungurian	258.00	
Artinskian	263.00	
Sakmarian	268.00	
Asselian	277.00	
Carboniferous		
Late (Pennsylvanian)		
Kasimovian, Gzelian	286.00	
Moscovian	295.00	
Bashkirian	305.00	
Early (Mississippian)		
Serpukhovian	320.00	
Visean	333.00	

TABLE 1. (continued)

Geological Age	Age of Top of Sub-Epoch or Stage	
ERA		
Period	(Ma)	Polarity Chron
Epoch		
Sub-Epoch or Stage		
Tournaisian	352.00	
Devonian		
Late		
Famennian	360.00	
Frasnian	367.00	
Middle	374.00	
Givetian		
Eifelian	380.00	
Early	387.00	
Emsian		
Siegenian	394.00	
Gedinnian	401.00	
Silurian		
Late	408.00	
Pridolian		
Ludlovian	414.00	
Early	421.00	
Wenlockian		
Llandoverian	428.00	
Ordovician		
Late		
Ashgillian	438.00	
Caradocian	448.00	
Middle		
Llandelian	458.00	
Llanvirnian	468.00	
Early		
Arenigian	478.00	
Tremadocian	488.00	
Cambrian		
Late		
Trempealeauan	505.00	
Franconian	511.00	
Dresbachian	517.00	
Middle	523.00	
Early		
Lenaian	540.00	
Atdabanian	550.00	
Tommotian	560.00	
PROTEROZOIC		
Vedian		
Poundian	570.00	

TABLE 2. Cenozoic and Late Mesozoic Polarity Time Scale ("C-Sequence" and "M-Sequence")

Polarity Chrons within Geological Stages	Subchron[a]	Age (in Ma)[b]		
		Top	Bottom	Duration
"C-Sequence"[c]				
Holocene-Pleistocene		0.00		
C1[d]	C1n	0.00	0.78	0.78
	C1r.1n	0.99	1.07	0.08
	C1r.2n	1.19	1.20	0.01
C2	C2n	1.79	1.95	0.16
Pliocene (Late)		1.81		
	C2r.1n	2.14	2.15	0.01
	C2r.2n	2.22	2.23	0.01
C2A[e]	C2An.1n	2.60	3.04	0.44
	C2An.2n	3.11	3.22	0.11
	C2An.3n	3.33	3.58	0.25
Pliocene (Early)		3.58		
C3	C3n.1n	4.18	4.29	0.11
	C3n.2n	4.48	4.62	0.14
	C3n.3n	4.80	4.89	0.09
	C3n.4n	4.98	5.23	0.25
Miocene (Late)		5.32		
C3A	C3An.1n	5.88	6.11	0.24
	C3An.2n	6.24	6.53	0.29
C3B	C3Bn	6.90	7.05	0.15
	C3Br.1n	7.09	7.13	0.03
	C3Br.2n	7.30	7.33	0.03
C4	C4n.1n	7.39	7.52	0.13
	C4n.2n	7.60	8.02	0.42
	C4r.1n	8.17	8.21	0.03
C4A	C4An	8.65	8.97	0.33
	C4Ar.1n	9.18	9.26	0.08
	C4Ar.2n	9.53	9.59	0.06
C5	C5n.1n	9.69	9.83	0.14
	C5n.2n	9.87	10.91	1.04
Miocene (Middle)		10.86		
	C5r.1n	11.01	11.06	0.05
	C5r.2n	11.44	11.50	0.05
C5A	C5An.1n	11.91	12.05	0.15
	C5An.2n	12.16	12.38	0.22
	C5Ar.1n	12.66	12.69	0.03
	C5Ar.2n	12.76	12.80	0.05
C5AA	C5AAn	12.98	13.13	0.15
C5AB	C5ABn	13.29	13.50	0.21
C5AC	C5ACn	13.70	14.07	0.38
C5AD	C5ADn	14.18	14.61	0.44
C5B	C5Bn.1n	14.80	14.89	0.09
	C5Bn.2n	15.04	15.16	0.12

Table 2. (continued)

Polarity Chrons within Geological Stages	Subchron	Age (in Ma)		
		Top	Bottom	Duration
Miocene (Early)		16.04		
C5C	C5Cn.1n	16.04	16.32	0.28
	C5Cn.2n	16.35	16.52	0.16
	C5Cn.3n	16.58	16.76	0.17
C5D	C5Dn	17.31	17.65	0.34
C5E	C5En	18.32	18.82	0.50
C6	C6n	19.08	20.16	1.08
C6A	C6An.1n	20.55	20.75	0.21
	C6An.2n	21.02	21.34	0.32
C6AA	C6AAn	21.79	21.88	0.09
	C6AAr.1n	22.17	22.26	0.10
	C6AAr.2n	22.47	22.51	0.03
C6B	C6Bn.1n	22.60	22.76	0.16
	C6Bn.2n	22.81	23.08	0.26
C6C	C6Cn.1n	23.36	23.54	0.18
	C6Cn.2n	23.68	23.80	0.12
Oligocene (Late)		23.80		
	C6Cn.3n	24.00	24.12	0.12
C7	C7n.1n	24.72	24.77	0.05
	C7n.2n	24.83	25.17	0.34
C7A	C7An	25.48	25.63	0.15
C8	C8n.1n	25.81	25.93	0.13
	C8n.2n	25.97	26.53	0.56
C9	C9n	27.00	27.95	0.94
C10	C10n.1n	28.26	28.48	0.23
Oligocene (Early)		28.48		
	C10n.2n	28.55	28.72	0.17
C11	C11n.1n	29.37	29.63	0.26
	C11n.2n	29.74	30.07	0.33
C12	C12n	30.45	30.92	0.46
C13	C13n	33.05	33.54	0.49
Eocene (Late)		33.70		
C15[f]	C15n	34.67	34.96	0.29
C16	C16n.1n	35.37	35.55	0.19
	C16n.2n	35.72	36.38	0.67
C17	C17n.1n	36.67	37.53	0.87
Eocene (Middle)		37.60		
	C17n.2n	37.67	37.92	0.25
	C17n.3n	37.99	38.18	0.20
C18	C18n.1n	38.50	39.64	1.14
	C18n.2n	39.72	40.22	0.50
C19	C19n	41.35	41.62	0.26
C20	C20n	42.63	43.87	1.24
C21	C21n	46.28	47.86	1.58
C22	C22n	48.95	49.60	0.66

Table 2. (continued)

Polarity Chrons within Geological Stages	Subchron	Age (in Ma)		
		Top	Bottom	Duration
Eocene (Early)		48.98		
C23	C23n.1n	50.65	50.81	0.17
	C23n.2n	50.91	51.61	0.70
C24	C24n.1n	52.24	52.54	0.31
	C24n.2n	52.64	52.69	0.04
	C24n.3n	52.79	53.25	0.46
Paleocene (Late)		55.00		
C25	C25n	55.89	56.38	0.49
C26	C26n	57.55	57.91	0.36
Paleocene (Early)		60.20		
C27	C27n	60.96	61.32	0.36
C28	C28n	62.55	63.68	1.13
C29	C29n	64.01	64.76	0.75
Maestrichtian (Cretaceous)		65.00		
C30	C30n	65.67	67.93	2.26
C31	C31n	68.07	69.12	1.05
Campanian (macrofossil-defined)		71.30		
C32	C32n.1n	71.39	71.64	0.25
	C32n.2n	71.87	73.15	1.28
	C32r.1n	73.40	73.48	0.07
C33	C33n	73.70	79.29	5.59
Campanian (foraminifer-defined)		74.50		
C34[g]	C34n	83.50	118.00	34.50
Santonian		83.50		
Coniacian		86.30		
Turonian		88.70		
Cenomanian		93.30		
Albian		98.50		
Early Cretaceous-Late Jurassic "M-sequence"[h]				
	M"-3"r set	99.90	102.70	
	M"-2"r set	105.50	108.30	
Aptian		113.00		
	M"-1"r	114.00	114.10	
M1	M1n	118.70	121.81	3.11
Barremian		119.00		
M3[i]	M3n	122.25	123.03	0.78
M5	M5n	125.36	126.46	1.10
M6	M6n	127.05	127.21	0.16
Hauterivian		127.34		
M7	M7n	127.34	127.52	0.18
M8	M8n	127.97	128.33	0.36
M9	M9n	128.60	128.91	0.31
M10	M10n	129.43	129.82	0.39
M10N[j]	M10Nn.1n	130.19	130.57	0.38

Table 2.(continued)

Polarity Chrons within Geological Stages	Subchron	Age (in Ma)		
		Top	Bottom	Duration
	M10Nn.2n	130.63	131.00	0.37
	M10Nn.3n	131.02	131.36	0.34
Valanginian		131.55		
M11	M11n	131.65	132.53	0.88
	M11r.1n	133.03	133.08	0.05
M11A[k]	M11An.1n	133.50	133.90	0.40
	M11An.2n	133.92	134.31	0.39
M12	M12n	134.42	134.75	0.33
	M12r.1n	135.56	135.66	0.10
M12A	M12An	135.88	136.24	0.36
M13	M13n	136.37	136.64	0.27
M14	M14n	137.10	137.39	0.29
M15	M15n	138.30	139.09	0.79
Berriasian (Cretaceous)		138.77		
M16	M16n	139.58	141.20	1.62
M17	M17n	141.85	142.27	0.42
M18	M18n	143.76	144.33	0.57
Tithonian (Jurassic)[l]		144.75		
M19	M19n.1n	144.75	144.88	0.13
	M19n.2n	144.96	145.98	1.02
M20	M20n.1n	146.44	146.75	0.31
	M20n.2n	146.81	147.47	0.66
M21	M21n	148.33	149.42	1.09
M22	M22n.1n	149.89	151.46	1.57
	M22n.2n	151.51	151.56	0.05
	M22n.3n	151.61	151.69	0.08
M22A	M22An	152.53	152.66	0.13
Kimmeridgian		152.84		
M23	M23n	152.84	153.21	0.37
	M23r.1n	153.49	153.52	0.03
M24	M24n	154.15	154.48	0.33
	M24r.1n	154.85	154.88	0.03
M24A	M24An	155.08	155.21	0.13
M24B	M24Bn	155.48	155.84	0.36
Oxfordian		156.00		
M25	M25n	156.00	156.29	0.29
Pre-M25 Magnetic Anomaly Series[m]				
M25A	M25An.1n	156.55	156.72	0.17
	M25An.2n	156.81	156.92	0.12
	M25An.3n	157.00	157.16	0.16
M26	M26n.1n	157.28	157.39	0.12
	M26n.2n	157.47	157.56	0.08
	M26n.3n	157.64	157.72	0.08

Table 2. (continued)

Polarity Chrons within Geological Stages	Subchron	Age (in Ma)		
		Top	Bottom	Duration
	M26n.4n	157.78	157.99	0.21
M27	M27n	158.23	158.44	0.21
M28	M28n	158.67	158.88	0.21
M29	M29n.1n	159.08	159.28	0.20
	M29n.2n	159.35	159.58	0.23
	M29n.3n	159.61	159.76	0.15
M30	M30n	159.87	160.33	0.46
	M30r.1n	160.61	160.65	0.04
M31	M31n	160.73	160.87	0.15
M32	M32n	161.02	161.39	0.37
	M32r.1n	161.57	161.62	0.05
M33	M33n	161.68	161.91	0.23
M34	M34n	162.10	162.37	0.27
	M34r.1n	162.52	162.59	0.07
	M34r.2n	162.69	162.74	0.05
M35	M35n.1n	162.86	163.17	0.31
Callovian		163.00		
	M35n.2n	163.28	163.45	0.17
	M35r.1n	163.61	163.66	0.06
M36	M36n.1n	163.74	163.99	0.25
	M36n.2n	164.04	164.18	0.15
M37	M37n	164.37	164.65	0.28
	M37r.1n	164.75	164.80	0.05
	M37r.2n	164.91	164.98	0.07
M38	M38n.1n	165.07	165.27	0.21
	M38n.2n	165.29	165.48	0.19
M39	M39n	166.07		

[a] Normal-polarity chrons and subchrons within the main polarity chron. Subchrons within a main polarity chron are decimal-numbered from youngest to oldest (e.g. "C3n.1n"); sub-subchrons are denoted by another decimal qualifier (e.g. "C3n.2r.1n").

[b] Age span of normal-polarity chrons and subchrons, and boundary ages of geological stages.

[c] Pleistocene-Pliocene ages are from "astronomically calibrated" sections [34, 35, 87]. Subdivision and ages of Miocene through Eocene "C-sequence" are from Cande and Kent [9], except polarity chrons C3A through C5Bn have been scaled to be consistent with the astronomically calibrated Miocene/Pliocene boundary at 5.32 Ma. Miocene through Eocene age calibration points for the magnetic polarty time scale of Cande and Kent [9] are: (1) top of polarity chron C5Bn = 14.8 Ma; (2) base of C6Cn.2n = Oligocene/Miocene boundary = 23.8 Ma; (3) C13r.86 = Eocene/Oligocene boundary = 33.7 Ma; (4) Upper part of polarity chron C21n (C21n.67) = 46.8 Ma; (5) C24r.34 = Paleocene/Eocene boundary = 55.0 Ma. Paleocene through Campanian age calibration points are: (1) C29r.7 = Maestrichtian/Paleocene boundary = 65.0 Ma; (2) C33n.85 = 74.5 Ma (foraminifer-defined Campanian/Maestrichtian boundary); and (3) top of C34n = Santonian/Campanian boundary = 83.5 Ma.

[d] Polarity chrons within C1 and C2 have a parallel nomenclature: C1n = Brunhes Normal polarity chron, with Matuyama Reversed spanning C1r through C2r; Brunhes Normal contains brief excursions (Lascamp, Blake, Biwa I & II, and Emperor); C1r.1n = Jaramillo Normal; C1r.2n = Cobb Mountain event (duration uncertain); C2n = Olduvai Normal; C2r.1n and C2r.2n = Réunion-1 and -2 (existence uncertain). See Figure 1.

Table 2. (continued)

[e] Polarity chrons within C2A and C3 have a parallel nomenclature: C2An = Gauss Normal (subdivided by brief reversed-polarity subchrons of Kaena (2An.1r) and Mammoth (2An.2r)), with Gilbert Reversed spanning polarity chron C2Ar through C3r; C3n.1n = Cochiti Normal; C3n.2n = Nunivak Normal; C3n.3n = Sidufjall Normal; C3n.4n = Thvera Normal. See Figure 1.

[f] Polarity chron "C14" does not exist.

[g] Polarity chron C34n is the Cretaceous Long Normal-Polarity Chron (Cretaceous "Quiet Zone" in ocean magnetic anomaly pattern). Within the Aptian-Albian portion are possible brief reversed-polarity subchrons, denoted in this scale as M"-3"r set, M"-2"r set, and M"-1"r (nomenclature after Ryan et al. [86]), but the younger sets are not verified (see text).

[h] Main "M-sequence" pattern is from Larson and Hilde [50], with nomenclature revised from Cox [29]. Ages are from Kent and Gradstein [44, 45] using calibration points of (1) top of M0r = 118 Ma (which they had considered to be the base of the Aptian stage); and (2) top of M25n = Oxfordian/Kimmeridgian boundary = 156 Ma.

[i] Polarity chron M3n was originally called "M2", and chron M5n was originally "M4" [50].

[j] Polarity chron M10"N" was named after Fred Naugle [50], therefore the "N" does not imply normal polarity.

[k] Polarity chron M11An is subdivided following the magnetic anomaly model of Tamaki and Larson [95].

[l] Tithonian/Berriasian (Jurassic/Cretaceous) boundary has not been internationally defined and may eventually be placed within the interval of polarity chrons M18 or M19. See text for discussion of other stage boundary placements within M-sequence.

[m] Relative durations of pre-M25 magnetic chrons from Handschumacher et al. [28]; ages rescaled to DNAG time scale [44] (see text); nomenclature revised following system of Cox [29]. This pre-M25 sequence has not been verified by magnetostratigraphy. Callovian/Oxfordian boundary (163 Ma in DNAG time scale) is projected placement only.

stratigraphic-radiometric age calibration points to the boundaries of marine magnetic anomalies in the composite block model [9]. The spline fit procedure allows derived South Atlantic seafloor spreading rates to vary smoothly between these these chron-age controls. In this paper, the interval of polarity chrons C3r through C5ACr in the time scale of Cande and Kent [9] has been revised to be consistent with astronomically tuned ages derived for lower Pliocene polarity chrons (e.g., the beginning of the Thvera normal-polarity chron C3n.4n occurs at 5.23 Ma [35], instead at 5.046 Ma [9]).

3.3. Miocene-Campanian Geological Boundaries

The ages of the majority of stage and epoch boundaries within the Miocene through Paleocene (Table 1) are derived from the magnetic polarity time scale according to the occurrence of biostratigraphic markers within magnetostratigraphic sections [3, 4, 9].

3.3.1. Miocene/Pliocene boundary. Astronomical tuning of Pliocene magnetostratigraphic sections in southern Italy assigns an age of 5.32 Ma to the Miocene-Pliocene boundary (base of Trubi Formation) and placement in the older portion of polarity chron C3r [35], or at C3r.85 in this scale.

3.3.2. Middle/Late Miocene boundary. The beginning of Tortonian stage, as defined as first appearance datum of foraminifer *Neogloboquadrina acostaensis*, correlates to nannofossil zone NN8 and the earliest part of polarity chron C5n [58]. Therefore this boundary was arbitarily placed just after the beginning of polarity subchron C5n.2n; although it may be as old as the latest portion of polarity chron C5r [9].

3.3.3. Early/Middle Miocene boundary. The beginning of the Langhian stage is at the end of polarity chron C5Cn [9] or slightly older [3].

3.3.4. Oligocene/Miocene boundary. The radiometric age and magnetostratigraphic correlation of the Oligocene/Miocene boundary appears to vary among different biostratigraphic markers [3, 4, 58, 60]. The first appearance of foraminifer *Globorotalia kugleri* is observed near the top of the lower normal-polarity subzone in polarity zone C6Cn [58], whereas the first appearance datum of foraminifer *Globoquadrina dehiscens* [60] occurs at the top of polarity zone C6Cn [58], or about 1 m.y. younger. Cande and Kent [9] place the Oligocene/Miocene boundary at the beginning of polarity chron C5Cn.2n with an assigned age of 23.7 Ma [30].

3.3.5. Early/Late Oligocene boundary. The Rupelian/Chattian stage boundary, recognized by the last appearance datum of foraminifer *Chiloguembelina* or the NP23/NP24 nannoplankton zone boundary "is closely linked with Chron C10n" [4]. Therefore this boundary is placed at the beginning of polarity subchron C10n.1n.

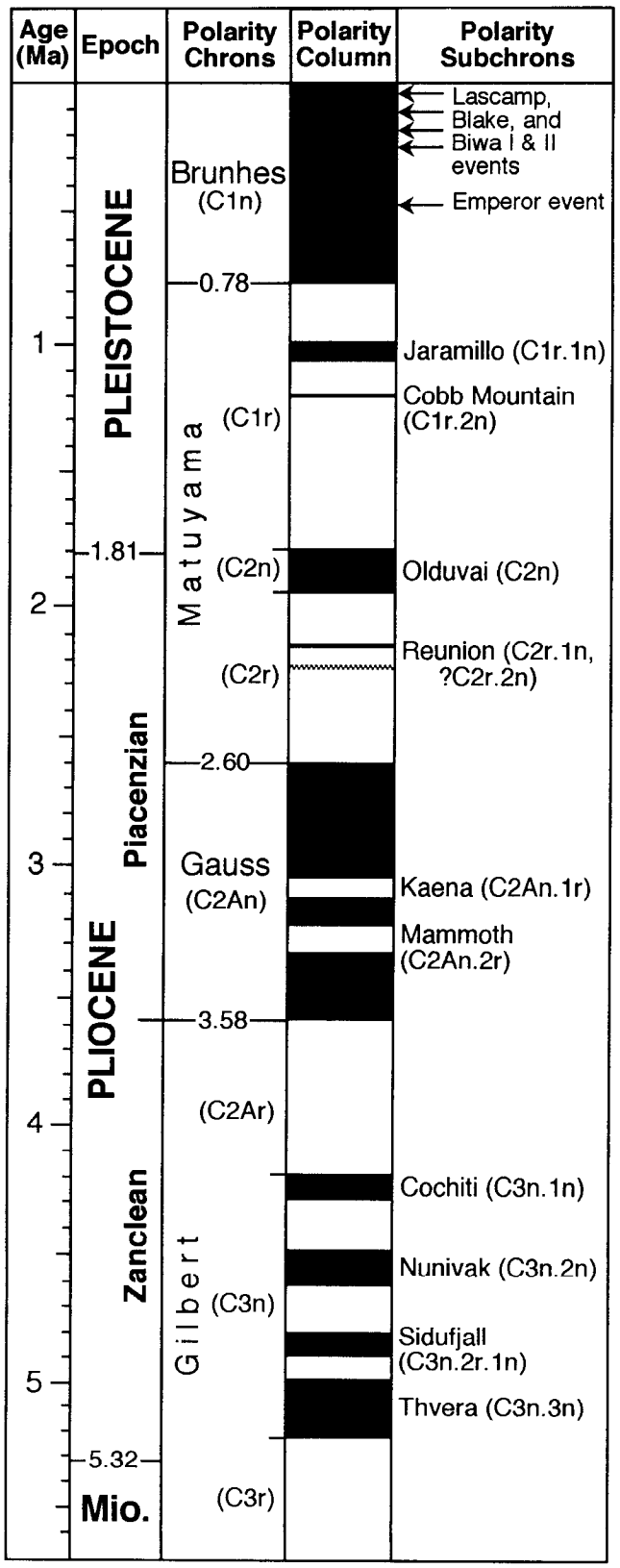

Figure 1. Pleistocene-Pliocene polarity chrons and subchrons. Time scale is calibrated by astronomical cycles (Table 2). Normal-polarity chrons are shown in black, reversed-polarity chrons are white.

3.3.6. Oligocene/Eocene boundary. The Oligocene/Eocene epoch boundary, as recognized by last appearances of different foraminifer and discoaster species, falls approximately "midway in Chron C13r" [4, 53]. Within the proposed boundary stratotype, the boundary occurs in the upper part of polarity zone C13r [64]. In this scale, the boundary is placed at polarity chron C13r.86 [9] with an age of 33.7 ±0.4 Ma [67], although a slightly younger age is possible [57].

Brief normal-polarity subchrons or events during polarity chron C13r [9, 57, 80, 100] may aid in global precision recognition of the Oligocene/Eocene boundary.

3.3.7. Middle/Late Eocene boundary. The Bartonian-Priabonian stage boundary has conflicting recognition with foraminifer and calcareous nannofossil definitions [4]. The last appearance datum of *Truncorotaloides rohri* marker occurs "within the later part of Chron C17n" [4, 61]; therefore, this boundary is arbitrarily placed in the middle of subchron C17n.1n.

3.3.8. Early/Middle Eocene boundary. The Ypresian-Lutian stage boundary, as recognized by the first appearance datum of *Hantkenina aragonensis*, occurs just prior to the end of polarity chron C22n [61], and is placed at C22n.95 in this scale.

3.3.9. Paleocene/Eocene boundary. A Paleocene/Eocene boundary age of 55 Ma [5, 94] and placement at polarity chron C24r.34 [4] was used as a calibration point in the time scale of Cande and Kent [9]; however the definition and recognition of the boundary remains unresolved.

3.3.10. Early/Late Paleocene boundary. The top of the Danian stage also has conflicting biostratigraphic definitions. An expanded Danian stage ("Danian s.l.") has its end defined by first appearance datum of *Morozovella angulata* occurring in the "lower part of Chron C26r" [4]. Accordingly, this boundary is arbitrarily placed at polarity chron C26r.25.

3.3.11. Maestrichtian/Paleocene (Cretaceous/ Tertiary) boundary. The mass extinctions at the Cretaceous/ Tertiary boundary occurred during the latter portion of polarity chron C29r. The exact placement is complicated by changes in relative sedimentation rates across the boundary, but appears to be approximately at polarity chron C29r.7 [4].

3.3.12. Campanian/Maestrichtian boundary. The

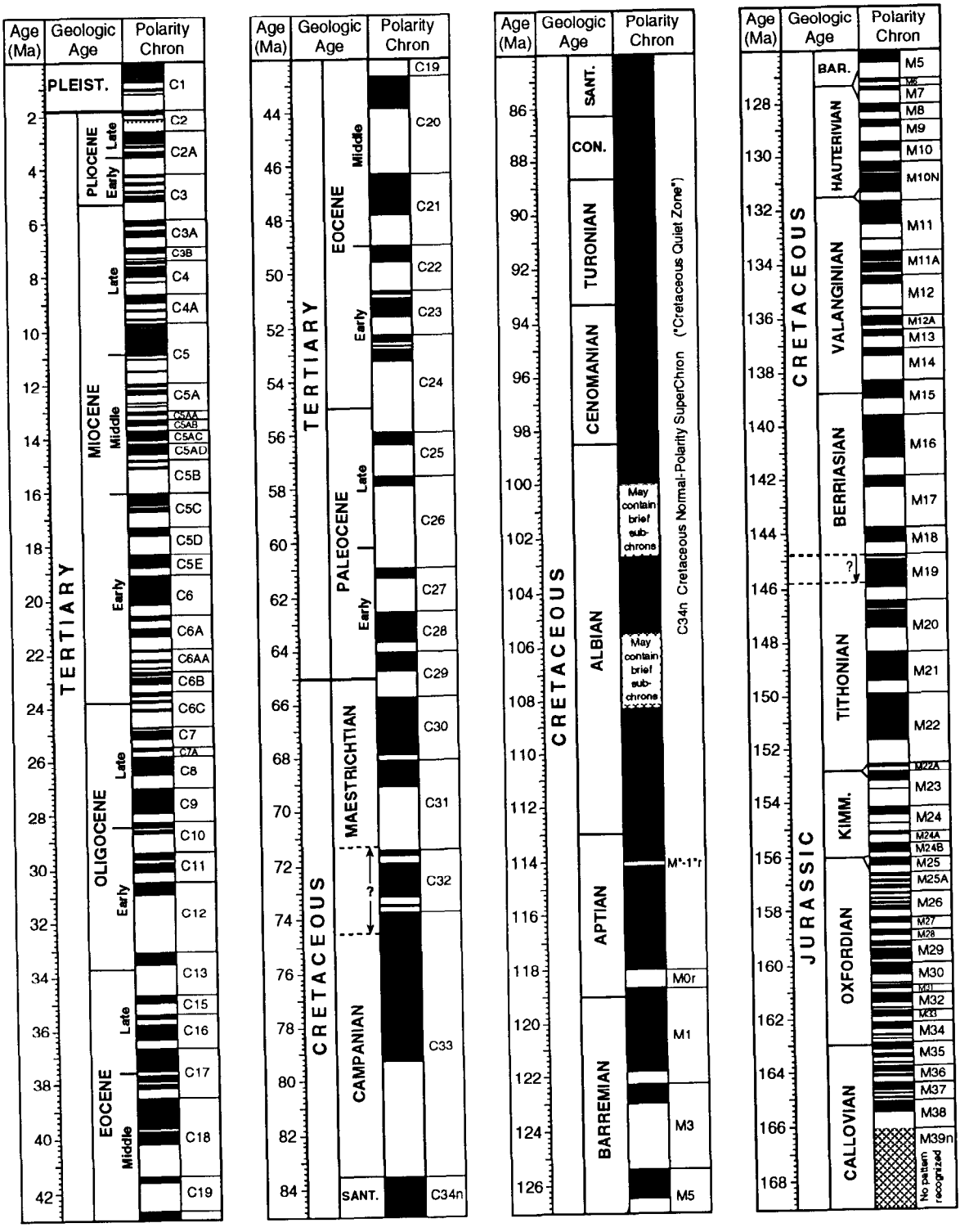

Figure 2. Cenozoic-Late Mesozoic magnetic polarity time scale. Normal-polarity chrons (Table 2) are shown in black, reversed-polarity chrons are white; intervals lacking magnetostratigraphy studies or having uncertain validity are cross-hatchured.

age of the Campanian/Maestrichtian stage boundary and corresponding correlation to the magnetic polarity time scale depends upon the biostratigraphic definition of this boundary. In the magnetostratigraphic section of Gubbio in Italy, the *Globotruncana calcarata/G. tricarinata* foraminifer zone boundary occurs in the upper part of polarity zone C33n [1]. This placement has been verified in sections in Northern Italy and in the S. Atlantic [4]. The estimated age of this microfossil-defined Campanian/ Maestrichtian boundary is 74 to 75 Ma [4]. Therefore Cande and Kent [9] assign this boundary to polarity chron C33n.85 with an age of 74.5 Ma (lower dashed line in chart).

However, other biostratigraphic markers for the Campanian/Maestrichtian boundary (e.g., last appearance datum of nannofossil *E. eximius*) occur as early as the beginning of polarity chron C31r [e.g., 19]. The macrofossil-defined Campanian/Maestrichtian boundary in northwest Europe occurs significantly later than the last occurrence of *G. calcarata* [7], and strontium-isotope stratigraphy indicates that this boundary in the English Chalk corresponds to an age of approximately 71.3 Ma in the bentonite-bearing sections of the U.S. Western Interior [55, 65, 66]. This macrofossil boundary definition, radiometric age, and corresponding placement near the beginning of polarity chron C31r is shown as the higher dashed line on the chart.

3.3.13. Santonian/Campanian boundary. The top of the Cretaceous Long Normal-Polarity Zone (polarity zone C34n) occurs near the Santonian/Campanian boundary in the magnetostratigraphy of the Gubbio section of Italy [1] and in other sections [4]. An age of 83 Ma was preferred by Cande and Kent [9] as a calibration point for assigning ages to Campanian-Maestrichtian polarity chrons, but later Ar-Ar dating indicates that 83.5 Ma is a better estimate [65].

3.3.14. Santonian through Aptian boundaries. Ages of Late and Middle Cretaceous stages in the DNAG time scale (Table 1) [44, 45, 78] are based on a composite of radiometric dates [29]. These ages have been revised to include higher precisiion Ar-Ar dates [65].

3.4. Aptian-Albian Reversed-Polarity Subchrons

An extended interval of normal polarity, the "Cretaceous Long Normal-Polarity Chron" or polarity chron C34n, extends from the early Aptian to the Santonian/Campanian boundary (Figure 2). Within the Cretaceous Long Normal-Polarity Chron, brief subchrons of reversed polarity have been observed in Aptian-Albian pelagic sediments, although there are no well-defined marine magnetic anomalies recognized in ocean crust during this interval.

A brief late Aptian or earliest Albian event has been noted in magnetostratigraphic studies in Europe [52, 79, 102, 103], and in DSDP sites in the Atlantic [24, 41, 42, 43], Indian [40, 74], and Pacific Oceans [96]. In magneto-biostratigraphic sections, the age of this brief reversed-polarity chron is late Aptian, within the *Globigerinelliodes algerianus* foraminifer zone [96, 103]. There may also be a narrow magnetic anomaly corresponding to this reversed-polarity zone [e.g., 105]. A suggested nomenclature for this subchron is M"-1"r, implying the next younger polarity chron after polarity chron M0r [e.g., 86, 89], although "Gatan zone" [79] and "ISEA reversal" [e.g., 52, 96] have also been used. The duration of this subchron is estimated as less than 100,000 years [97].

Middle Albian reversed-polarity subchrons have been reported [41, 96, 105]. However, these events, the M"-2" set [86], near the boundary of the *Biticinella breggiensis* and *Ticinella primula* foraminifer zones have not yet been verified [98].

Late Albian reversed-polarity subchrons, the M"-3" set [86], have been reported in some magnetostratigraphic studies of deep sea sediments [e.g., 22, 24, 40], and may occur at the end of the *Praediscosphaera cretacea* and within the *Eiffellithus turriseiffeli* nannoplankton zones [99]. These reported events require additional verification and improved biostratigraphic control.

3.5. Early Cretaceous and Late Jurassic Magnetic Anomaly M-Sequence:

3.5.1. Polarity chrons M0 through M25. The M-sequence polarity scale for polarity chrons M0r through M25r (Table 2, Figure 2) is derived from a block model of the Hawaiian lineations by Larson and Hilde [50]. These polarity chrons are assigned absolute ages by assuming a constant rate of spreading of the Hawaiian lineations for the Kimmeridgian through Barremian stages, and correlations of biostratigraphic markers to magnetostratigraphy enables assignment of absolute ages to intervening stage boundaries (Table 1) [44, 45]. The age calibration points for this DNAG time scale are assignment of the Barremian/Aptian boundary at 118 Ma to just below polarity chron M0r and of the Oxfordian/Kimmeridgian boundary at 156 Ma to the top of polarity chron M25n.

The following modifications were made to the M0 through M25 scale: (1) The M-sequence nomenclature and separation of additional major polarity chrons (e.g., polarity chron "M11A") follows the system of Cox [29]; (2) Normal-polarity chron M11An was extended in duration using the original Larson and Hilde [50]

pattern, and a brief reversed-polarity subchron was inserted [95].

A reversed-polarity magnetic anomaly "CL1" may occur between anomalies M1 and M0 in the Pacific [88], but there has not been verification of this event in magnetostratigraphic sections.

3.5.2. Pre-M25 magnetic anomaly series. A series of Jurassic magnetic anomalies identified in the western Pacific were named M26 through M29 by Cande et al. [8]. Later, Handschumacher et al. [28] used more detailed surveys to propose a revised M26 through M38 pattern, which retained in modified form the previous M26-M28 portion [8] and extended the series by approximately 5 m.y. They assigned ages to their M26-M38 pattern by assuming a constant spreading rate from M21-M38 in the Japanese lineations and by using the M21-M25 ages from the Larson and Hilde [50] scale.

The ages of Handschumacher et al.'s M26 through M38 have been rescaled in this paper (Table 2, Figure 2) using the DNAG time scale [44] with the following conversions: (1) the base of M25r is changed from 153.05 Ma [28] to 157.61 Ma [44]; (2) the beginning of their M30n, which they indicate corresponds to the beginning of "M29r" in the previous Cande et al. scale [8], is changed from 156.55 Ma [28] to 160.33 Ma [44]. The projected Late Callovian age of magnetic anomaly M39 is consistent with the basement age of earliest Callovian or latest Bathonian at ODP Site 801 on pre-M39 oceanic crust [51].

The anomaly numbering of Handschumacher et al. [28] is retained in this new scale, but their polarity chron and subchron nomenclature was revised to be consistent with the younger portion of the M-sequence. For example, their normal-polarity chron "35a" is renamed as subchron "M35r.1n" because it occurs within their reversed-polarity chron M35r. There may be a duplication of one chron within their marine magnetic anomaly pattern due to a spreading ridge jump (R. Larson, pers. commun., 1991), but until this possibility is verified, the published interpretation and numbering by Handschumacher et al. [28] will be used.

3.6. Early Cretaceous Boundaries

The M-sequence polarity chrons have been correlated to ammonite, calcareous nannofossil, dinoflagellate, and calpionellid zones and datums [e.g., reviews in 6, 70, 72]. Additional magnetostratigraphy studies within Lower Cretaceous strata [e.g., 13] have indicated that further refinement of the assignment of stage boundaries to polarity chrons (Table 1) is constrained by the common use of micropaleontological markers rather than ammonite zones to recognize these stage boundaries and by the variable preservation and reworking of those micropaleontological markers.

3.6.1. Barremian/Aptian boundary. The Barremian/Aptian boundary occurs just prior to reversed-polarity chron M0r [13, 70], and is placed at M1n.9. The base of polarity chron M0r could serve as a working definition of this boundary.

3.6.2. Hauterivian/Barremian boundary. This stage boundary occurs within the interval of polarity chrons M5r through M7r. A precise assignment is currently inhibited by a discrepancy between dinoflagellate and nannofossil markers [70] and by the variable relative position of the last appearance datum of nannofossil *Lithraphidites bollii* [13]. The boundary is tentatively assigned to the beginning of polarity chron M6r.

3.6.3. Valanginian/Hauterivian boundary. There are no nannofossil markers for this boundary, and the observed variability in the dinoflagellate marker (last appearance datum of *Scriniodinium dictyotum*) brackets polarity zone M10Nr [70]. The boundary was assigned to the middle of polarity chron M10Nr.

3.6.4. Berriasian/Valanginian boundary. The base of the *Thurmanniceras otopeta* ammonite zone in southern Spain occurs just below the middle of polarity zone M15n [71], and the corresponding stage boundary is placed at polarity chron M15n.4.

3.7. Late Jurassic Boundaries

3.7.1. Jurassic/Cretaceous (=Tithonian/Berriasian) boundary. This epoch boundary does not have an internationally accepted definition, although several possible biostratigraphic markers have been correlated to magnetostratigraphy [72]. The base of polarity chron M18r has been proposed as a working definition for the Jurassic/ Cretaceous boundary [69].

The regional Purbeck stage of southern England has yielded a magnetostratigraphy wich suggests correlation to polarity chrons M19r through M14r of latest Tithonian through earliest Valanginian age. The underlying Portland appears to span only polarity zones M21r through M19n, implying a middle and late Tithonian age correlation [76].

3.7.2. Kimmeridgian/Tithonian boundary. The beginning of the *Hybonoticeras hybonotum* ammonite zone in southern Spain occurs within polarity chrons M23n to M22An [68].

3.7.3. Oxfordian/Kimmeridgian boundary. The beginning of the *Sutneria platynota* ammonite zone occurs within the interval of polarity chrons M25r to M24Br within southern Spain [68]. Pending further mag-

netostratigraphic studies, this boundary is assigned as the end of polarity chron M25n.

4. MIDDLE JURASSIC THROUGH LATE PERMIAN

4.1. Early and Middle Jurassic

The Early and Middle Jurassic magnetic polarity patterns are primarily known from ammonite-bearing magnetostratigraphic sections in Europe. In order to partially compensate for variable sedimentation rates, the results of individual studies have been rescaled in the chart to make the component ammonite subzones of the Tethyan faunal realm approximately equal in duration within each stage (Table 3, Figure 3). The absolute ages of the Jurassic stages estimated by the DNAG time scale vary by much as 10 m.y. with respect to later time scales [e.g., 30; Gradstein et al., in prep.], so these projected polarity chron ages provide only relative duration estimates within each stage.

The Middle to Late Oxfordian polarity sequence is derived from northern Spain [91]. Lower Oxfordian through Callovian sequences in southern Poland have yielded a partial polarity pattern [73]. The condensed nature of these Polish sediments coupled with the observed close-spaced magnetic anomalies from Pacific crust of presumed Early Callovian-Oxfordian age [28] suggest that the actual polarity pattern in this time interval is more complex. Condensed Callovian sediments from northern Italy suggest that this interval may have a reversed-polarity bias [12], in contrast to the normal-polarity bias in the data from Poland [73]. There have been no magnetostratigraphic studies from earliest Callovian and Late Bathonian. The corresponding "pre-M39" oceanic crust in the Pacific is called the "Jurassic Quiet Zone", and the indistinct nature of the oceanic crust magnetization of this region may indicate the blurring effect caused by a high frequency of magnetic reversals.

Bajocian through Middle Bathonian ammonite-zoned sediments of southern Spain have yielded a very high frequency of magnetic reversals [92]. The polarity pattern in the chart is a correlation of the main magnetostratigraphic features within the component ammonite zones; there may be additional short-duration polarity zones.

The Aalenian and Toarcian polarity pattern is from a pelagic sediment section in southern Switzerland, and the Pliensbachian polarity sequence is from a nearby section in northern Italy [36]. Frequent magnetic reversals are indicated in other Aalenian through Pliensbachian sections [reviewed in 11], which hinders detailed correlation of individual magnetic polarity chrons. In contrast to the Aalenian section in Switzerland, the Aalenian on the Isle of Skye, Scotland, is mainly of normal polarity, with predominantly reversed-polarity zones within the uppermost Toarcian and across the proposed Aalenian/Bajocian boundary stratotype [26]. The Toarcian stratotype in the Paris Basin [18] has yielded a polarity pattern having a similar frequency of reversals to the Toarcian of Switzerland. However, the sedimentation rates of this shallow-marine Toarcian stratotype are probably more variable and distorted by sea-level fluctuations than in the Switzerland section, and correlation of polarity zones are hindered by differences in ammonite zonations among the two regions (B. Galbrun, pers. commun., 1989).

Sinemurian and latest Hettangian sections in Italy [11] and in Austria (M. Steiner and J. Ogg, unpublished; shown in the chart) have yielded tentative polarity patterns, but these sections lack biostratigraphic zonation. Magnetostratigraphic results from eastern United States [56] and from southern Germany suggest that the Hettangian may be dominated by normal polarity.

4.2. Middle and Late Triassic

Nearly all Middle and Late Triassic magnetostratigraphic studies are from North American continental sediments; therefore the ammonites and conodonts used to define the boundaries of Triassic stages are absent, and the correlations of individual polarity zones are uncertain. The Rhaetian-Norian magnetic polarity pattern (Table 3, Figure 3) is from a composite of Newark Basin sections [77, 106]. Brief normal polarity zones are observed within lower Rhaetian marine sediments on the northwestern Australian margin [19], and may correlate to features in the Chinle Formation of New Mexico [59, 81]. Magnetostratigraphy of marine sediments of Carnian through middle Norian age on the northwest Australian margin [19] and in Turkey [21] indicate that the Carnian-Norian boundary is within or near the base of a normal-polarity zone, similar to the placement of this boundary in the Newark Basin, but that there are probably many more brief polarity zones than have been published from the Newark Basin formations.

The composite Carnian and Middle Triassic magnetic polarity pattern compiled by Molina-Garza et al. [59] from numerous sources has been rescaled to the DNAG time scale [78]. The Carnian portion of their scale agrees in broad outline with the magnetostratigraphy of pelagic limestones in Turkey [21], but may omit some brief reversed-polarity events.

TABLE 3. Jurassic through Late Permian Magnetostratigraphy

Geologic Age Magnetostratigraphic sections	Polarity Chron (if named)	Age (in Ma)[a] Top	 Bottom	 Duration
Jurassic (pre-Kimmeridgian)				
Oxfordian				
N. Spain series [66]	AG-N8	157.39	157.45	0.06
	AG-N7	157.68	157.74	0.06
	AG-N6	158.08	158.14	0.06
	AG-N5	158.49	158.80	0.31
	AG-N4	158.89	158.96	0.07
	AG-N3	159.04	159.17	0.13
	AG-N2	159.28	159.30	0.02
	AG-N1	159.38	159.39	0.01
	No Data	159.70	159.96	0.26
S. Poland series [67]	par.-N	159.96	160.09	0.14
	No Data	160.09	160.22	0.13
	ant.-N	160.28	160.63	0.35
	No Data	160.63	160.87	0.24
	cord-N	161.14	161.63	0.49
	mar.-N	162.50	162.61	0.11
Callovian		163.00		
	lamb.-N	163.27	163.40	0.13
	No Data	163.53	163.87	0.33
	cor.-N	165.07	165.33	0.27
	jas.-N	165.60	165.80	0.20
	No Data	165.80	166.13	0.33
	call.-N	166.27	166.37	0.10
	No Data	166.53	170.27	3.74
Bathonian		169.00		
S. Spain series [69]	asp.-N	170.40	170.79	0.39
	No Data	170.79	171.36	0.57
	cost.-N	171.71	172.94	1.22
	sof.-N	173.24	173.64	0.39
	zig.-N1	174.86	175.12	0.26
	zig.-N2	175.39	175.48	0.09
	zig.-N3	175.82	176.00	0.18
Bajocian		176.00		
	park.-N1	176.09	176.19	0.10
	park.-N2	176.28	176.33	0.06
	park.-N3	176.53	176.62	0.10
	park.-N4	176.81	176.90	0.09
	gar.-N1	176.97	177.14	0.17
	gar.-N2	177.24	177.29	0.05
	gar.-N3	177.43	177.53	0.10
	gar.-N4	177.58	177.91	0.33
	subf.-N	178.80	178.93	0.13
	humph.-N1	179.29	179.50	0.21
	humph.-N2	179.98	180.46	0.48
	sauz.-N1	180.62	180.82	0.20

Table 3. (continued)

Geologic Age Magnetostratigraphic sections	Polarity Chron (if named)	Age (in Ma) Top	 Bottom	 Duration
	sauz.-N2	180.87	180.92	0.05
	sauz.-N3	180.99	181.07	0.08
	sauz.-N4	181.09	181.15	0.06
	sauz.-N5	181.25	181.31	0.06
	sow.-N1	181.38	181.73	0.35
	sow.-N2	181.97	182.21	0.24
	sow.-N3	182.97	182.36	0.11
	sow.-N4	182.25	182.75	0.27
S. Switzerland series [70]	sow.-N5	182.87	183.00	0.13
Aalenian		183.00		
	con.-N	183.44	184.44	1.00
	murch.-N1	184.56	185.00	0.44
	murch.-N2	186.00	186.16	0.16
	opal.-N	186.24	186.56	0.31
	men.-N1	186.69	188.10	1.41
Toarcian		187.00		
	men.-N2	188.37	188.74	0.37
	erb.-N	189.45	189.76	0.31
	bif.-N1	190.70	190.99	0.29
	bif.-N2	191.19	191.77	0.59
	fal.-N1	191.85	191.96	0.11
	fal.-N2	192.03	192.11	0.08
	fal.-N3	192.15	192.22	0.07
Pliensbachian		193.00		
	spin.-N1	193.39	193.45	0.06
	spin.-N2	193.51	193.79	0.28
	spin.-N3	193.84	193.88	0.05
	spin.-N4	193.98	194.50	0.52
	marg.-N1	194.74	195.21	0.47
	marg.-N2	195.23	195.30	0.08
	marg.-N3	195.32	195.40	0.08
	marg.-N4	195.48	195.51	0.03
	marg.-N5	195.60	195.65	0.05
	dav.-N	196.36	196.60	0.24
	ibex-N1	196.82	196.87	0.05
	ibex-N2	196.87	196.94	0.07
	ibex-N3	196.96	197.17	0.21
	ibex-N4	197.31	197.33	0.02
	ibex-N5	197.45	197.47	0.02
	ibex-N6	197.51	197.54	0.03
	ibex-N7	197.55	197.59	0.04
	ibex-N8	197.64	197.72	0.08
	jam.-N1	197.76	197.82	0.06
	jam.-N2	197.91	198.37	0.45
	No Data	198.37	199.50	1.13

Table 3. (continued)

Geologic Age Magnetostratigraphic sections	Polarity Chron (if named)	Age (in Ma) Top	 Bottom	 Duration
Sinemurian		199.00		
Austrian series		199.50	199.75	0.25
		200.00	200.10	0.10
		200.20	200.30	0.10
		202.00	202.10	0.10
		202.40	203.70	0.30
		202.80	203.15	0.35
Hettangian		204.00		
		204.40	204.60	0.20
		206.40	206.60	0.20
	No Data	206.80	208.00	1.20
Triassic Epoch		208.00		
Norian	l+	206.37	209.09	2.83
Newark Basin series[b]		210.42	210.47	0.05
		210.68	210.72	0.04
		211.50		
		212.65	212.77	0.12
		213.28	213.41	0.12
	j+	215.89	216.84	0.47
	h+	219.51	222.33	1.53
	f+	223.83	225.14	0.83
		225.00		
Carnian[c]	d+	225.56	226.14	0.58
	b+	226.37	226.61	0.23
		227.36	227.38	0.02
Western U.S. series [79]		227.98	228.41	0.43
		228.41	229.06	0.65
		229.06	230.28	1.22
		230.00		
Ladinian		232.15	232.21	0.06
		233.46	234.66	1.20
		234.81	236.84	2.03
		235.00		
Anisian		238.45	240.09	1.64
		240.00		
Spathian		240.13	240.16	0.02
Canadian Arctic series [85][d]	SpN1	240.35	240.75	0.40
		240.85	240.87	0.02
		240.98	241.01	0.02
		241.26		
Smithian	SmN3?	241.26	241.35	0.09
	SmN2	241.50	241.98	0.48
	SmN1	242.08	242.34	0.26
		242.34		

Table 3. (continued)

Geologic Age Magnetostratigraphic sections	Polarity Chron (if named)	Age (in Ma) Top	Bottom	Duration
Dienerian	DN2	242.57	242.71	0.14
	DN1	243.06	243.29	0.24
		243.45		
Griesbachian	GN2	243.58	243.82	0.24
	GN1	244.41	244.89	0.48
Late Permian[e]		245.00		
Tatarian		246.86		
Pakistan series [81]		247.78	247.11	0.26
		251.94	251.84	4.05
		253.00	252.87	0.93
Ufimian-Kasanian		255.05		
		256.88	255.15	0.10
		258.00	258.00	1.12
Kungurian		258.45		
		263.00	260.98	2.53
Artinskian				

[a] Ages and durations of polarity chrons reflect the observed pattern for each ammonite zone or each stage. The Jurassic polarity zones are labled with the associated ammonite zone and have been scaled to give equal duration to the Tethyan ammonite subzones within each stage.

[b] Lettered polarity chrons in Rhaetian-Norian-Carnian from [106], with additional unnamed chrons from other regions [19, 59]. See text.

[c] DNAG time scale arbitrarily give equal durations to Carnian, Ladinian, Anisian, and a combined Early Triassic [7].

[d] Polarity chron nomenclature from Early Triassic stratotype sections in Canadian Arctic indicates geologic stage and polarity. Smithian stage arbitrarily defined to extend from base of polarity chron SmN1 to top of chron SmN3? Griesbachian/Dienerian boundary in middle of reversed-polarity chron GR2 (polarity chron above GN2).

[e] Nomenclature for Permian stages differs among regions. Late Permian polarity zones of Pakistan [86] are rescaled to DNAG stages [7]. Early Permian-Late Carboniferous comprises the Kiaman Long Reversed-Polarity Chron.

4.3. Early Triassic

The Early Triassic has been subdivided into two stages, Olenekian and Induan, by the Subcommission on Triassic Stratigraphy [104]. There have been several magnetostratigraphic studies on Lower Triassic continental and marine sediments [e.g., 32, 33, 90, 93], but biostratigraphy on most of these sections does not allow recognition of individual geological stages. The polarity pattern from the ammonite-bearing stratotypes of the Griesbachian through Smithian substages in the Canadian Arctic (Table 3, Figure 3) has also been correlated to sequence stratigraphy [75], but these sections probably encompass intervals of non-deposition during sea-level variations which distort the magnetic polarity time scale.

4.4. Late Permian

The late Permian has different stage names in different regions due to endemic fauna, which hinders correlation of various magnetostratigraphic sections. A section in the Salt Ranges of Pakistan has yielded a magnetostratigraphy considered to span the equivalent of the upper Kungurian, Ufimian, Kazanian, and lower Tatarian stages [23]. These results were scaled linearly according

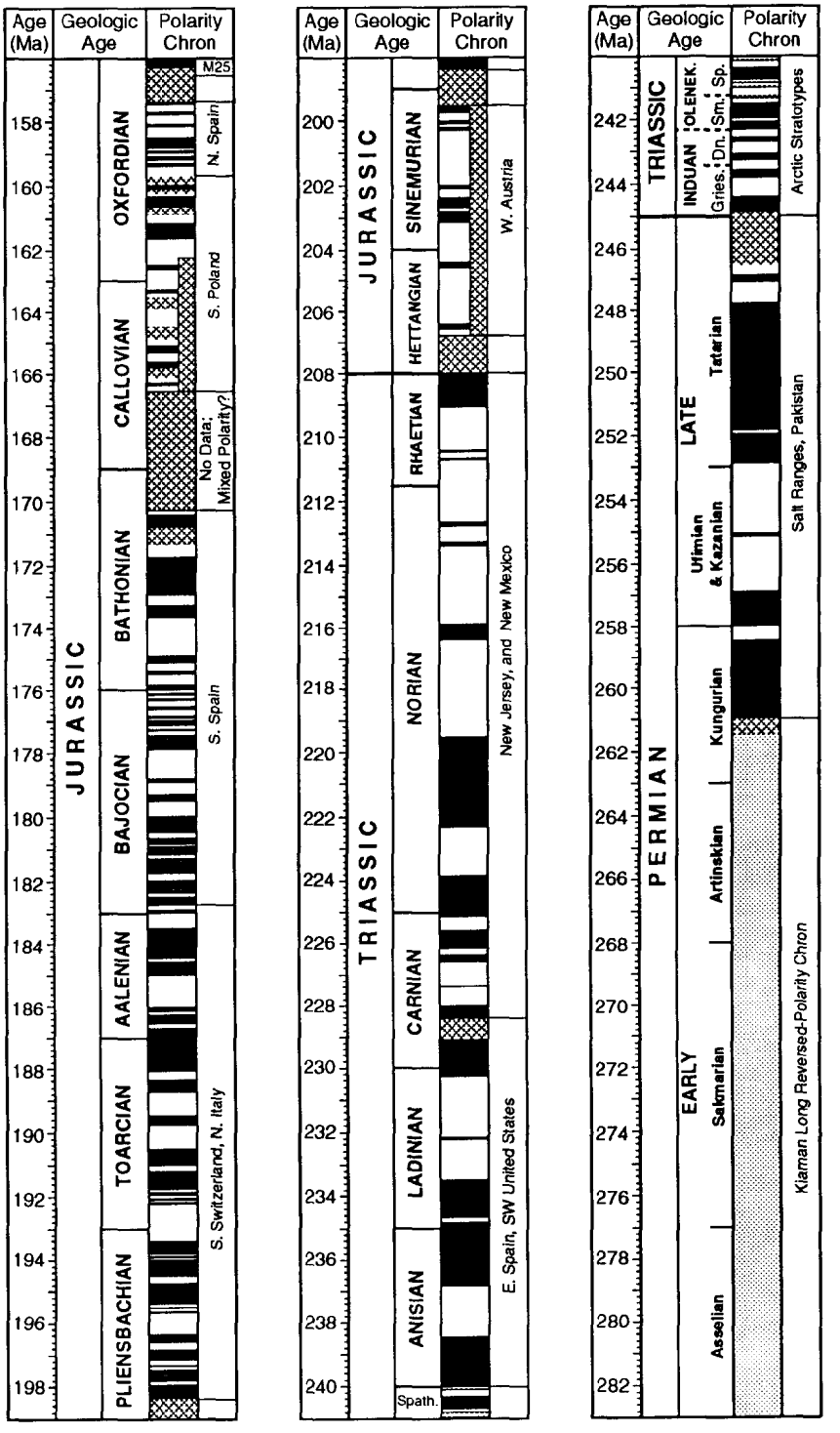

Figure 3. Jurassic to Permian magnetic polarity time scale (from magnetostratigraphy). Normal-polarity chrons (Table 3) are shown in black, reversed-polarity chrons are white; intervals lacking magnetostratigraphy studies or having uncertain validity are cross-hatchured.

to the estimated placement of the Kungurian/Ufimian boundary within the section (Figure 3). The upper Tatarian (approximately equivalent to the Dorashamian or Changxingian stage of latest Permian) has been sampled in southern China, but did not yield reliable results [32, 93].

5. PALEOZOIC

5.1. Time Scale

The various magnetostratigraphic studies of Permian through Cambrian strata are compiled using the DNAG time scale [78] with the inclusion of additional stage names as appropriate (Tables 1 and 4, Figure 4). For example, the Early Cambrian, which is undivided on the DNAG time scale, has been subdivided into three equal stages (Lenian, Atdabanian, and Tommotian) according to the time scale in Harland et al. [30]. The DNAG ages estimated for the Ordovician and Cambrian periods and internal stages vary by as much as 20 m.y. from later age dating [e.g., 14, 101].

5.2. Paleomagnetic Studies

Magnetostratigraphic studies on Paleozoic sections have mainly concentrated on compiling polarity patterns associated with major geological time boundaries.

A complete Paleozoic scale, primarily based upon Soviet outcrops, has been compiled by Khramov and Rodionov [46], but the majority of the component magnetostratigraphic sections with associated biostratigraphy have not been published in Western literature. This generalized Soviet scale agrees in its broad aspects with other magnetostratigraphic studies, but the details are commonly in disagreement with high-resolution studies and the predominance of reversed polarity suggests possible partial remagnetization of Paleozoic strata during the Carboniferous-Permian. Therefore this Soviet compilation is shown in Figure 4 in shades of gray and only for those intervals which lack other published magnetostratigraphic correlations.

5.2.1. Carboniferous-Permian. The Kiaman Long Reversed-Polarity Chron dominates the early Permian and late Carboniferous (Pennsylvanian). This extended interval of reversed polarity may contain brief normal-polarity subchrons at the beginning of the Permian and in the early Late Carboniferous [46, 63]. The predominantly reversed-polarity "Donetzk (Rn) hyperzone" of the Soviet scale [46] incorporates the majority of the Carboniferous and latest Devonian, but this magnetostratigraphy has not yet been confirmed.

A composite polarity scale has been derived from the middle Carboniferous (early Pennsylvanian and late Mississippian, or the approximately equivalent Namurian and early Westphalian-A stages) of Nova Scotia, New Brunswick, and Pennsylvania [15, 16, 17].

5.2.2. Devonian. Magnetostratigraphy of Upper Devonian strata in western Australia indicates mixed polarity across the Frasnian/Famennian boundary interval bounded by normal polarity sites [37]. Detailed sampling of the uppermost Frasnian indicated five reversals within a minimum of 0.25 m.y. [38]. These results are consistent with the mixed polarity interval reported in the Soviet time scale [46].

In the Soviet magnetic polarity time scale, the Middle Devonian through Late Silurian consists of a predominantly reversed-polarity "Sayan (Rn) hyperzone" [46]. This scale uses different stage names than the DNAG time scale and the magnetostratigraphy has not yet been verified.

5.2.3. Silurian. In the Soviet scale, the Late Silurian is entirely of reversed polarity, whereas the Llandoverian stage is entirely normal polarity (upper portion of the "Baikal (Nr) hyperzone") [46]. The magnetostratigraphy sections are not available.

5.2.4. Ordovician. According to Soviet results, the Late Ordovician is predominantly normal polarity, the Middle Ordovician has a normal-polarity chron spanning the Llanvirnian/Llandeilan boundary, and the Early Ordovician is primarily of reversed polarity [46]. The "Siberia (Rn) hyperzone" spans the mid-Cambrian to upper Early Ordovician. The relative lengths of Ordovician stages in the Soviet time scale is considerably different than in the DNAG time scale, which assigns all stages except the Tremadocian an equal 10 m.y. duration (Table 1).

5.2.5. Cambrian. The Cambrian/Ordovician boundary interval has yielded magnetostratigraphy in many locations [82; Ripperdan et al., in prep.], but a partially correlatable polarity pattern has only been obtained from northeastern Australia and northeastern China [83, 84, 85]. The Australian polarity pattern (shown on the chart) is correlated to Australian conodont zones of the Warendian stage (earliest Ordovician) and of the Datsonian and Payntonian stages (Late Cambrian). Magnetostratigraphic correlations to northeastern China enable an extension downward to the upper "pre-Payntonian" stage. The correlation of these Australian stages to European-North American stages is uncertain, and an arbitrary equivalency of the Datsonian-Payntonian stages to the Trempeleauan stage of Late Cambrian is used in the diagram.

In the Soviet scale, the upper half of the Cambrian has

TABLE 4. Paleozoic Magnetostratigraphy

Geologic Age Magnetostratigraphic sections	Polarity Chron (if named)	Age (in Ma) Top	 Bottom	 Duration
Early Permian				
Kungurian[a]		258.00		
Pakistan series [23]		258.45	260.98	2.53
Artinskian		263.00		
Sakmarian		268.00		
Asselian		277.00		
Soviet series [46][b]		*285.40*	*286.00*	*0.60*
Carboniferous Epoch				
Late Carboniferous (=Pennsylvanian)				
Kasimovian-Gzelian		286.00		
Moscovian		295.00		
"Debaltsevo superzone"[c]		*297.20*	*297.80*	*0.60*
		301.20	*301.60*	*0.40*
Bashkirian		305.00		
		305.70	*306.10*	*0.40*
		309.10	*311.80*	*2.70*
E. Canada/Penn. series[d]	N8	313.01	313.06	0.05
	N7	313.57	314.51	0.94
	N6	314.66	314.91	0.24
"Namurian/Westphalian"		315.00		
	N5	315.56	317.17	1.62
	N4	318.06	318.34	0.28
	N3	318.67	318.86	0.19
Early Carboniferous (=Mississippian)				
Serpukhovian		320.00		
	MMn1	320.00	320.49	0.49
	MMn2	320.65	321.13	0.48
	MMn3	322.14	323.10	0.97
		329.00	*329.90*	*0.90*
Visean		333.00		
"Tikhvin superzone"		*344.10*	*345.70*	*1.60*
Tournaisian		352.00		
Devonian Epoch[e]				
Famennian		360.00		
Australian series [37]	Mixed polarity			
Frasnian		367.00		
"Tashtyp superzone"				
Givetian		374.00		
		374.90	*375.20*	*0.30*
		375.60	*375.80*	*0.20*
Eifelian		380.00		
		381.00	*387.00*	*6.00*
Emsian		387.00		
		388.60	*389.00*	*0.40*

Table 4. (continued)

Geologic Age Magnetostratigraphic sections	Polarity Chron (if named)	Age (in Ma) Top	 Bottom	 Duration
		389.40	*389.80*	*0.40*
Siegenian		394.00		
Gedinnian		401.00		
"Yenisei superzone"		*405.50*	*407.00*	*1.50*
Silurian Epoch				
Pridolian		408.00		
Ludlovian		414.00		
Wenlockian		421.00		
Llandoverian		428.00		
"Nepa superzone"[f]		*428.00*	*444.90*	*16.90*
Ordovician Epoch				
Ashgillian		438.00		
		445.80	*455.10*	*9.30*
Caradocian		448.00		
"North-Baikal superzone"		*456.70*	*458.00*	*1.30*
Llandeilan		458.00		
		463.00	*471.00*	*8.00*
Llanvirnian		468.00		
Arenigian		478.00		
		481.00	*483.00*	*2.00*
Tremadocian		488.00		
Camb./Ord. boundary series[g]	H+	504.10	504.76	0.66
Cambrian Epoch				
Trempealeauan		505.00		
	G4+	505.27	505.39	0.12
	G2+	505.99	506.11	0.12
	F3+	506.68	506.77	0.09
	F1+	507.04	507.22	0.18
	D+	508.24	508.66	0.42
	B3+	509.62	510.34	0.72
	B1+	510.88	511.00	0.12
Franconian		511.00		
"Irkutsk superzone"		*512.60*	*513.40*	*0.80*
		514.80	*515.10*	*0.30*
		516.10	*517.00*	*0.90*
Dresbachian		517.00		
"Bursk superzone"		*522.10*	*522.40*	*0.30*
Middle Cambrian		523.00		
		523.10	*523.30*	*0.20*
		524.90	*525.20*	*0.30*
"Ulakhan superzone"		*526.10*	*526.40*	*0.30*
		527.30	*527.60*	*0.30*
		528.90	*529.60*	*0.70*

Table 4. (continued)

Geologic Age Magnetostratigraphic sections	Polarity Chron (if named)	Age (in Ma) Top	 Bottom	 Duration
		530.10	*530.30*	*0.20*
		530.50	*530.80*	*0.30*
		531.00	*532.00*	*1.00*
"Arga (R) hyperzone"		*536.70*	*537.30*	*0.60*
Lenaian[h]		540.00		
		542.00	*542.50*	*0.50*
Atdabanian		550.00		
Siberian composite [14, 47, 54]		552.47	552.56	0.09
		553.36	553.56	0.20
		554.36	554.55	0.19
		554.75	554.85	0.09
		555.48	556.52	1.04
		556.73	558.70	1.97
		558.73	558.88	0.15
		559.14	560.00	0.86
Tommotian		560.00		
		560.07	560.70	0.63
		562.16	562.59	0.43
		563.13	563.46	0.33
		563.99	564.32	0.33
		564.52	564.72	0.20
		565.26	565.42	0.17
		566.39	566.52	0.13
		567.02	567.09	0.07
		567.83	568.72	0.89
		568.90	569.05	0.15
		569.77	570.05	0.28
Precambrian: Vedian[i]		570.00		

Ages and durations of polarity chrons reflect the observed pattern; the pattern for each stage (or each ammonite zone) has been recomputed to be consistent with the DNAG time scale [7].

[a] End of Kungurian stage may be approximately coeval with top of lowest normal-polarity zone in Salt Range section [23; see Table 3] but regional Permian stages are different. Kiaman Long Reversed-Polarity Chron dominates the early Permian and Late Carboniferous.

[b] Polarity chrons and nomenclature of "superzones" of Soviet Paleozoic magnetic polarity time scale [46] are shown in italics, because documentation of and verification tests has not been published.

[c] Upper series of the "Donetzk (Rn) hyperzone", which extends to the middle Frasnian (late Devonian) in the Soviet scale [64].

[d] Composite scale of DiVenere and Opydke [15, 16, 17]. Boundary between Namurian and Westphalian stages (regional stages of Europe that are not part of DNAG time scale [78]) is approximately 90% above base of polarity zone "R5" below "N5". Polarity zones "MMn2" and "MMn3" of Pennsylvania are equivalent to "N2" and "N1" of Canada.

[e] DNAG time scale [78] assigns equal durations to the Famennian through Wenlockian stages (10 stages in 68 m.y.) and to the Llandoverian through Arenigian stages (6 stages in 10 m.y.).

[f] Upper series of the "Baikal (Nr) hyperzone" of the Soviet scale [46].

[g] Composite of Australia and China series across Cambrian/Ordovician boundary [82, 83, 85]. Reversed-polarity zone "A-" extends to 512 Ma or older relative to this time scale.

[h] Early Cambrian stages [30] are assigned equal durations.

[i] Upper Vedian stage consists of reversed-polarity [54]. Nomenclature of uppermost Precambrian epoch and stage has not been standardized.

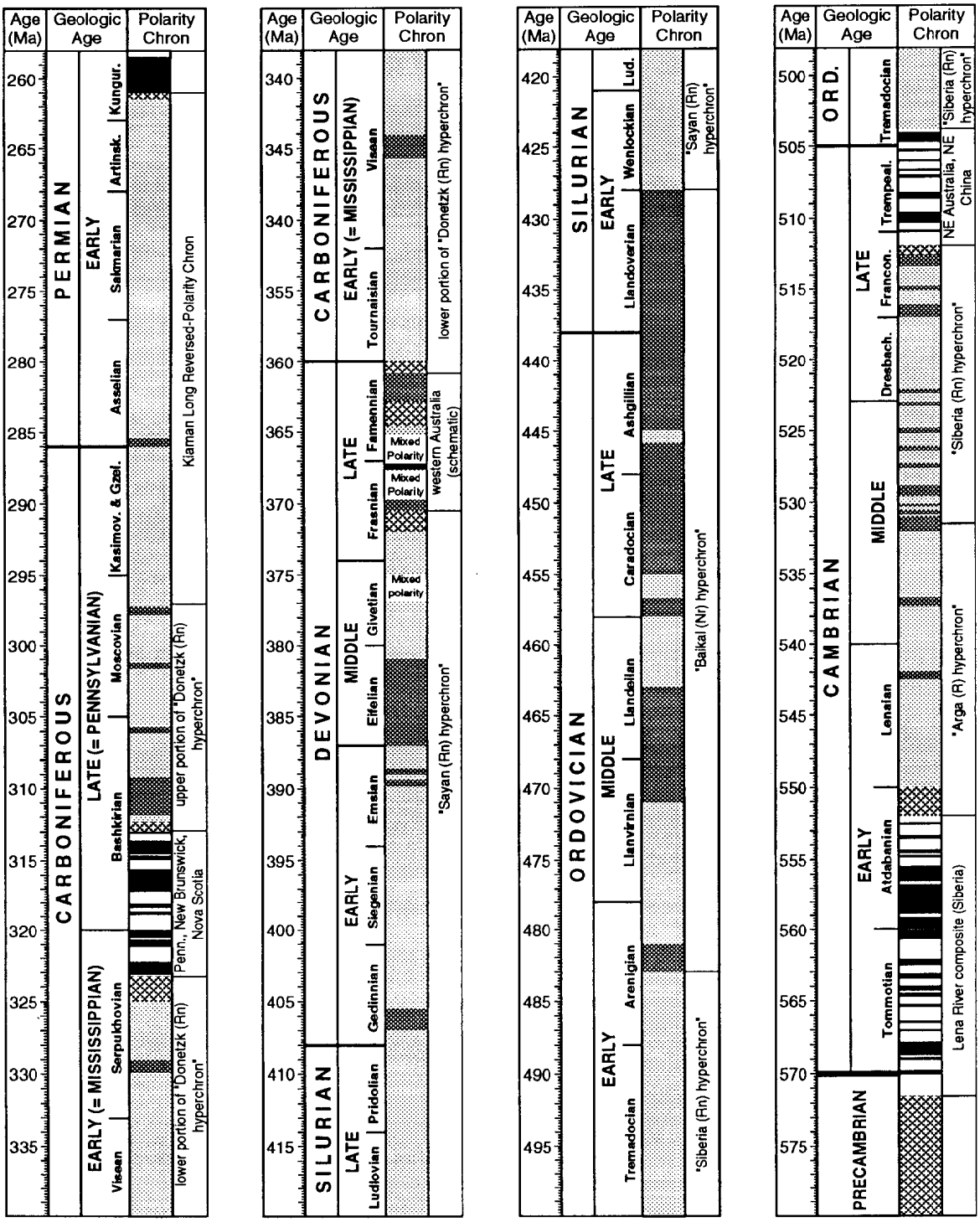

Figure 4. Paleozoic magnetic polarity time scale (from magnetostratigraphy). Normal-polarity chrons (Table 4) are shown in black, reversed-polarity chrons are white; intervals lacking magnetostratigraphy studies or having uncertain validity are cross-hatchured; unverified Paleozoic polarity chrons from the Soviet scale [46] are shown as shades of gray.

mixed polarity (early portion of the "Siberia (Rn) hyperzone"), and the lower half consists of a reversed-polarity "Arga (R) hyperzone" with two brief normal-polarity chrons [46]. This magnetic polarity scale has not yet been verified.

The Early Cambrian (Tommotian and lower Atdabanian stages) and a portion of the Vendian stage of uppermost Precambrian of Siberia, Morocco, south China, and Mongolia have been correlated with a combination of magnetostratigraphy, carbon isotopes, and trilobite zones [14, 47, 48, 54]. The composite Siberian sections along the Lena River appear to have the most complete polarity pattern.

Acknowledgments. I thank Thomas Ahrens for inviting this compilation. Partial financial support was received from the Exxon Production Research Company. Reviews and additional data were received from Robert Butler, Felix Gradstein, Jan Hardenbol, Joseph Kirschvink, and Steven Cande.

REFERENCES

1. Alvarez, W., M. A. Arthur, A. G. Fischer, W. Lowrie, G. Napoleone, I. Premoli-Silva, and W. M. Roggenthen, Upper Cretaceous-Paleocene magnetic stratigraphy at Gubbio, Italy. V. Type section for the Late Cretaceous-Paleocene geomagnetic reversal time-scale, *Geol. Soc. Am. Bull., 88*, 383-389, 1977.
2. Baksi, A. K., V. Hsu, M. O. Williams, and E. Farrar, $^{40}Ar/^{39}Ar$ dating of the Brunhes-Matuyama geomagnetic field reversal, *Science, 256*, 356-357, 1992.
3. Berggren, W. A., D. V. Kent, and J. A. van Couvering, The Neogene: Part 2, Neogene geochronology and chronostratigraphy, in *The Chronology of the Geological Record, Geol. Soc. London Mem., 10*, edited by N. J. Snelling, pp. 211-258, 1985.
4. Berggren, W. A., D. V. Kent, and J. J. Flynn, The Jurassic to Paleogene: Part 2, Paleogene geochronology and chronostratigraphy, in *The Chronology of the Geological Record, Geol. Soc. London Mem., 10*, edited by N. J. Snelling, pp. 141-195, 1985.
5. Berggren, W. A., D. V. Kent, J. D. Obradovich, and C. C. Swisher III, Toward a revised Paleogene geochronology, in *Eocene-Oligocene Climatic and Biotic Evolution*, edited by D. R. Prothero and W. A. Berggren, pp. 29-45, Princeton Univ. Press, Princeton, N.J., 1992.
6. Bralower, T. J., H. R. Thierstein, and S. Monechi, Calcareous nannofossil zonation of the Jurassic-Cretaceous boundary interval and correlation with the geomagnetic polarity timescale, *Mar. Micropaleontol., 14*, 153-235, 1989.
7. Burnett, J. A., J. M. Hancock, W. J. Kennedy, and A. R. Lord, Macrofossil, planktonic foraminiferal and nannofossil zonation at the Campanian/Maastrichtian boundary, *Newsl. Stratigr., 27*, 157-172, 1992.
8. Cande, S. C., R. L. Larson, and J. L. LaBrecque, Magnetic lineations in the Pacific Jurassic Quiet Zone, *Earth Planet. Sci. Lett., 41*, 434-440, 1978.
9. Cande, S. C., and D. V. Kent, A new geomagnetic polarity time scale for the Late Cretaceous and Cenozoic, *J. Geophys. Res., 97*, 13917-13951, 1992.
10. Cande, S. C., and D. V. Kent, Ultrahigh resolution of marine magnetic anomaly profiles: A record of continuous paleointensity variations?, *J. Geophys. Res., 97*, 15075-15083, 1992.
11. Channell, J. E. T., J. G. Ogg, and W. Lowrie, Geomagnetic polarity in the Early Cretaceous and Jurassic, *Phil. Trans. R. Soc. London, A., 306*, 137-146, 1982.
12. Channell, J. E. T., F. Massari, A. Benetti, and N. Pezzoni, Magnetostratigraphy and biostratigraphy of Callovian-Oxfordian limestones from the Trento Plateau (Monti Lessini, northern Italy), *Palaeogeogr., Palaeoclimat., Palaeoecol., 79*, 289-303, 1990.
13. Channell, J. E. T., and E. Erba, Early Cretaceous polarity chrons CM0 to CM11 recorded in northern Italian land sections near Brescia, *Earth Planet. Sci. Lett., 108*, 161-179, 1992.
14. Compston, W., I. S. Williams, J. L. Kirschvink, Z. Zhang, and G. Ma, Zircon U-Pb ages for the Early Cambrian time-scale, *J. Geol. Soc. London, 149*, 171-184, 1992.
15. DiVenere, V. J., and N. D. Opdyke, Paleomagnetism of the Maringouin and Shipody Formations, New Brunswick: A Namurian magnetic stratigraphy, *Can. J. Earth Sci., 27*, 803-810, 1990.
16. DiVenere, V. J., and N. D. Opdyke, Magnetic polarity stratigraphy and Carboniferous paleopole positions from the Joggins section, Cumberland structural basin, Nova Scotia, *J. Geophys. Res., 96*, 4051-4064, 1991.
17. DiVenere, V. J., and N. D. Opdyke, Magnetic polarity

stratigraphy in the uppermost Mississippian Mauch Chunk Formation, Pottsville, Pennsylvania, *Geology, 19*, 127-130, 1991.

18. Galbrun, B., J. Gabilly, and L. Rasplus, Magnetostratigraphy of the Toarcian stratotype sections at Thouars and Airvault (Deux-Sevres, France). *Earth Planet. Sci. Lett., 87*, 453-462, 1988.
19. Galbrun, B., Triassic (upper Carnian-lower Rhaetian) magnetostratigraphy of Leg 122 sediments, Wombat Plateau, Northest Australia, in *Proc. Ocean Drilling Program, Sci. Results, 122*, edited by U. von Rad, B. U. Haq, et al., pp. 685-698, 1992.
20. Galbrun, B., Magnetostratigraphy of Upper Cretaceous and Lower Tertiary sediments, Sites 761 and 762, Exmouth Plateau, northwest Australia, in *Proc. Ocean Drilling Program, Sci. Results, 122*, edited by U. von Rad, B.U. Haq, et al., pp. 699-706, 1992.
21. Gallet, Y., J. Besse, L. Krystyn, J. Marcoux, and H. Théveniaut, Magnetostratigraphy of the Late Triassic Bolücektasi Tepe section (southwestern Turkey): implications for changes in magnetic reversal frequency. *Phys. Earth. Planet. Interiors, 73*, 85-108, 1992.
22. Green, K. A., and A. Brecher, Preliminary paleomagnetic results for sediments from Site 263, Leg 27, in *Init. Repts. Deep Sea Drilling Project, 27*, edited by J. J. Veevers, J. R. Heirtzler, et al., pp. 405-413, 1974.
23. Haag, M., and F. Heller, Late Permian to Early Triassic magnetostratigraphy, *Earth Planet. Sci. Lett., 107*, 42-54, 1991.
24. Hailwood, E. A., Paleomagnetism of Late Mesozoic to Holocene sediments from the Bay of Biscay and Rockall Plateau, drilled on IPOD Leg 48, in *Init. Repts. Deep Sea Drilling Project, 48*, edited by L. Montadert, et al., pp. 305-339, 1979.
25. Hailwood, E. A., The role of magnetostratigraphy in the development of geological time scales, *Paleoceanography, 4*, 1-18, 1989.
26. Hailwood, E. A., D. Morgan, and N. Morton, Preliminary magnetostratigraphy of the Aalenian/ Bajocian boundary section at Bearreraig, Isle of Skye, Scotland, in *Conference on Aalenian and Bajocian Stratigraphy, Isle of Skye*, edited by N. Morton, April 1991, Univ. London, p. 98-100, 1991.
27. Hallam, A., J. M. Hancock, J. L. LaBrecque, W. Lowrie, and J. E. T. Channell, Jurassic to Paleogene: Part I. Jurassic and Cretaceous geochronology and Jurassic to Paleogene magnetostratigraphy, in *The Chronology of the Geological Record, Geol. Soc. London Mem., 10*, edited by N. J. Snelling, pp. 118-140, 1985.
28. Handschumacher, D. W., W. W. Sager, T. W. C. Hilde, and D. R. Bracey, Pre-Cretaceous evolution of the Pacific plate and extension of the geomagnetic polarity reversal time scale with implications for the origin of the Jurassic "Quiet Zone", *Tectonophysics, 155*, 365-380, 1988.
29. Harland, W. B., A. V. Cox, P. G. Llewellyn, C. A. G. Pickton, A. G. Smith, and R. Walters, *A Geologic Time Scale*, 128 pp., Cambridge University Press, Cambridge, 1982.
30. Harland, W. B., R. L. Armstrong, A. V. Cox, L. E. Craig, A. G. Smith, and D. G. Smith, *A Geologic Time Scale 1989*, 263 pp., Cambridge University Press, Cambridge, 1990.
31. Heirtzler, J. R., G. O. Dickson, E. M. Herron, W. C. Pitman III, and X. LePichon, Marine magnetic anomalies, geomagnetic field reversals and motions of the ocean floor and continents, *J. Geophys. Res., 73*, 2119-2136, 1968.
32. Heller, F., W. Lowrie, H. Li, and J. Wang, Magnetostratigraphy of the Permo-Triassic boundary section at Shangsi (Guangyuan, Sichuan Province, China), *Earth Planet. Sci. Lett., 88*, 348-356, 1988.
33. Helsley, C. E., and M. B. Steiner, Paleomagnetism of the Lower Triassic Moenkopi Formation, *Geol. Soc. Am. Bull., 85*, 457-464, 1974.
34. Hilgen, F. J., Astronomical calibration of Gauss to Matuyama sapropels in the Mediterranean and implication for the Geomagnetic Polarity Time Scale, *Earth Planet. Sci. Lett., 104*, 226-244, 1991.
35. Hilgen, F. J., Extension of the astronomically calibrated (polarity) time scale to the Miocene/Pliocene boundary, *Earth Planet. Sci. Lett., 107*, 349-368, 1991.
36. Horner, F., and F. Heller, Lower Jurassic magnetostratigraphy at the Breggia Gorge (Ticino, Switzerland) and Alpi Turati (Como, Italy), *Geophys. J., Roy. Astron. Soc., 73*, 705-718, 1983.
37. Hurley, N. F., and R. Van der Voo, Paleomagnetism of Upper Devonian reefal limestones, Canning basin, Western Australia, *Geol. Soc. Am. Bull., 98*, 138-146, 1987.
38. Hurley, N. F., and R. Van der Voo, Magnetostratigraphy, Late Devonian iridium anomaly, and impact hypotheses, *Geology, 18*, 291-294, 1990.
39. International Subcommission on Stratigraphic Classification, Magnetic polarity units, a supplemental chapter of the International Subcommission on Stratigraphic Classification, International Stratigraphic Guide, *Geology, 7*, 578-583, 1979.
40. Jarrard, R. D., Paleomagnetism of some Leg 27 sediment cores, in *Init. Repts. Deep Sea Drilling Project, 27*, edited by J. J. Veevers, J. R. Heirtzler, et al., pp. 415-423,

1974.

41. Keating, B. H., and C. E. Helsley, Magnetostratigraphic studies of Cretaceous age sediments from Sites 361, 363, and 364, in *Init. Repts. Deep Sea Drilling Project, 40,* edited by H.M. Bolli, W.B.F. Ryan, et al., pp. 459-467, 1978.
42. Keating, B. H., and C. E. Helsley, Magnetostratigraphic studies of Cretaceous sediments from DSDP Site 369, in *Init. Repts. Deep Sea Drilling Project, 41* (Supplement to Vol. 41), edited by Y. Lancelot,, E. Seibold, et al., pp. 983-986, 1978.
43. Keating, B. H., and C. E. Helsley, Paleomagnetic results from DSDP Hole 391C and the magnetostratigraphy of Cretaceous sediments from the Atlantic Ocean floor, in *Init. Repts. Deep Sea Drilling Project, 44,* edited by W. E. Benson, R. E. Sheridan, et al., pp. 523-528, 1978.
44. Kent, D. V., and F. M. Gradstein, A Cretaceous and Jurassic chronology, *Geol. Soc. Am. Bull., 96,* 1419-1427, 1985.
45. Kent, D. V., and F. M. Gradstein, A Jurassic to recent chronology, in *The Geology of North America,* vol. M, *The Western North Atlantic Region,* edited by P. R.Vogt and B. E. Tucholke, Geological Society of America, Boulder, Colo., 1986.
46. Khramov, A. N. and V. P. Rodionov, The geomagnetic field during Palaeozoic time, in *Global Reconstruction and the Geomagnetic Field during the Palaeozoic, Adv. Earth Planet. Sci., 10,* edited by M. W. McElhinny, A. N. Khramov, M. Ozima, and D. A. Valencio, pp. 99-115, 1981.
47. Kirschvink, J. L., M. Magaritz, R. L. Ripperdan, A. Yu. Zhuravlev, and A. Yu. Rozanov, The Precambrian/Cambrian boundary: Magnetostratigraphy and carbon isotopes resolve correlation problems between Siberia, Morocco, and south China, *GSA Today, 1,* 69-91, 1991.
48. Kirschvink, J. L., A paleogeographic model for Vendian and Cambrian time, in *The Proterozoic Biosphere: A Multidisciplinary Study,* edited by J. W.Schopf, C. Klein, and D. Des Maris, Oxford University Press, Oxford, England, in press.
49. LaBrecque, J. L., D. V. Kent, and S. C. Cande, Revised magnetic polarity time scale for Late Cretaceous and Cenozoic time, *Geology, 5,* 330-335, 1977.
50. Larson, R. L., and T. W. C. Hilde, A revised time scale of magnetic reversals for the Early Cretaceous and Late Jurassic, *J. Geophys. Res., 80,* 2586-2594, 1975.
51. Larson, R. L., Lancelot, Y., et al., *Proc. ODP, Sci. Results, 129,* 745 pp., Ocean Drilling Program, College Station, Texas, 1992.
52. Lowrie, W., W. Alvarez, I Premoli-Silva, and S. Monechi, 1980, Lower Cretaceous magnetic stratigraphy in Umbrian pelagic carbonate rocks, *R. Astron. Soc. Geophys. J., 60,* 263-281, 1980.
53. Lowrie, W., W. Alvarez, G. Napoleone, K. Perch-Nielsen, I. Premoli-Silva, and M. Toumarkine, Paleogene magnetic stratigraphy in Umbrian pelagic carbonate rocks: The Contessa sections, Gubbio, *Geol. Soc. Am. Bull., 93,* 414-432, 1982.
54. Magaritz, M., J. L. Kirschvink, A.J. Latham, A.Yu. Zhuravlev, and A.Yu. Rozanov, Precambrian/ Cambrian boundary problem: Carbon isotope correlations for Vendian and Tommotian time between Siberia and Morocco, *Geology, 19,* 847-850, 1991.
55. McArthur, J. M., W. J. Kennedy, A. S. Gale, M. F. Thirwall, M. Chen, J. Burnett, and J. M. Hancock, Strontium isotope stratigraphy in the Late Cretaceous: Intercontinental correlation of the Campanian/ Maastrichtian boundary. *Terra Nova, 4,* in press.
56. McIntosh, W. C., R. B. Hargraves, and C. L. West, Paleomagnetism and oxide mineralogy of the Upper Triassic to Lower Jurassic red beds and basalts in the Newark Basin. *Geol. Soc. Am. Bull., 96,* 463-480, 1985.
57. McIntosh, W. C., J. W. Geissman, C.E. Chapin, J. J. Kunk, and C. D. Henry, Calibration of the latest Eocene-Oligocene geomagnetic polarity time scale using $^{40}Ar/^{39}Ar$ dated ignimbrites, *Geology, 20,* 459-463, 1992.
58. Miller, K. G., M.-P. Aubry, M. J. Khan, A. J. Melillo, D. V. Kent, and W. A. Berggren, Oligocene-Miocene biostratigraphy, magnetostratigraphy, and isotopic stratigraphy of the western North Atlantic, *Geology, 13,* 257-261, 1985.
59. Molina-Garza, R. S., J. W. Geissman, R. Van der Voo, S. G. Lucas, and S. N. Hayden, Paleomagnetism of the Moenkopi and Chinle Formations in central New Mexico: Implications for the North American apparent polar wander path and Triassic magnetostratigraphy, *J. Geophys. Res., 96,* 14239-14262, 1991.
60. Montanari, A., A. Deino, R. Coccioni, V. E. Langenheim, R. Capo, and S. Monechi, Geochronology, Sr isotope analysis, magnetostratigraphy, and plankton stratigraphy across the Oligocene-Miocene boundary in the Contessa section (Gubbio, Italy), *Newsl. Stratigr., 23,* 151-180, 1991.
61. Napoleone, G., I. Premoli-Silva, F. Heller, P. Cheli, S. Corezzi, and A. G. Fischer, Eocene magnetic stratigraphy at Gubbio, Italy, and its implications for Paleogene geochronology, *Geol. Soc. Am. Bull., 94,* 181-191, 1983.
62. Ness, G., S. Levi, and R. Crouch,

Marine magnetic anomaly timescales for the Cenozoic and Late Cretaceous: a precise, critique and synthesis, *Rev. Geophys. Space Phys., 18*, 753-770, 1980.

63. Nick, K., K. Xia, and R. D. Elmore, Paleomagnetic and petrographic evidence for early magnetizations in successive terra rosa paleosols, Lower Pennsylvanian Black Prince Limestone, Arizona, *J. Geophys. Res., 96*, 9873-9885, 1991.
64. Nocchi, M., G. Parisi, P. Monaco, S. Monechi, M. Mandile, G. Napoleone, M. Ripepe, M. Orlando, I. Premoli-Silva, and D. M. Brice, The Eocene-Oligocene boundary in the Umbrian pelagic regression, in *Terminal Eocene Events, Dev. in Palaeontol. and Stratigr.*, vol. 9, edited by C. Pomerol and I. Premoli-Silva, pp. 25-40, Elsevier, New York, 1986.
65. Obradovich, J. D., A Cretaceous time scale, in *Evolution of the Western Interior Foreland Basin, Geol. Assoc. Canada Spec. Paper*, edited by W. G. E. Caldwell, in press.
66. Obradovich, J. D., J. F. Sutter, and M. J. Kunk, Magnetic polarity chron tie points for the Cretaceous and early Tertiary. *Terra cognita, 6*, 140, 1986
67. Odin, G.S., A. Montanari, A. Deino, R. Drake, P.G. Guise, H. Kreuzer, and D.C. Rex, Reliability of volcano-sedimentary biotite ages across the Eocene-Oligocene boundary (Apennines, Italy), *Chem. Geol., Isotope Geosci. Sect., 86*, 203-224, 1991.
68. Ogg, J. G., M. B. Steiner, F. Oloriz, and J. M. Tavera, Jurassic magnetostratigraphy, 1. Kimmeridgian-Tithonian of Sierra Gorda and Carcabuey, southern Spain. *Earth Planet. Sci. Lett., 71*, 147-162, 1984.
69. Ogg, J. G., and W. Lowrie, Magnetostratigraphy of the Jurassic/Cretaceous boundary, *Geology, 14*, 547-550, 1986.
70. Ogg, J. G., Early Cretaceous and Tithonian magnetostratigraphy of the Galicia margin (Ocean Drilling Program Leg 103), edited by G. Boillot, E. L. Winterer, et al., *Proc. Ocean Drilling Program, Sci. Results, 103*, 659-681, 1988.
71. Ogg, J. G., M. Company, M. B. Steiner, and J. M. Tavera, Magnetostratigraphy across the Berriasian-Valanginian stage boundary (Early Cretaceous) at Cehegin (Murcia Province, southern Spain). *Earth Planet. Sci. Lett., 87*, 205-215, 1988.
72. Ogg, J. G., R. W. Hasenyager, W. A. Wimbledon, J. E. T. Channell, and T. J. Bralower, Magnetostratigraphy of the Jurassic-Cretaceous boundary interval -- Tethyan and English faunal realms, *Cretaceous Research, 12*, 455-482, 1991.
73. Ogg, J. G., J. Wieczorek, M. Hoffmann, and M. B. Steiner, Jurassic magnetostratigraphy: 4. Early Callovian through Middle Oxfordian of Krakow Uplands (Poland). *Earth Planet. Sci. Lett., 104*, 289-303, 1991.
74. Ogg, J. G., K. Kodama and B. P. Wallick, Lower Cretaceous magnetostratigraphy and paleolatitudes off northwest Australia, ODP Site 765 and DSDP Site 261, Argo Abyssal Plain, and ODP Site 766, Gascoyne Abyssal Plain, in *Proc. Ocean Drilling Program, Sci. Results, 123*, edited by F. M. Gradstein, J. N. Ludden, et al., pp. 523-548, 1992.
75. Ogg, J. G., and M. B. Steiner, Early Triassic magnetic polarity time scale -- Integration of magnetostratigraphy, ammonite zonation and sequence stratigraphy from stratotype sections Canadian Arctic Archipelago). *Earth Planet. Sci. Lett., 107*, 69-89, 1991.
76. Ogg, J. G., R. W. Hasenyager, and W. A. Wimbledon, Jurassic-Cretaceous boundary: Portland-Purbeck magnetostratigraphy and possible correlation to the Tethyan faunal realm, *Géobios* in press.
77. Olsen, P. E., and D. V. Kent, Continental coring of the Newark Rift, *Eos Trans. AGU, 71*, 385 & 394, 1990.
78. Palmer, A. R. (compiler), Decade of North American Geology (DNAG) geologic time scale, *Geology, 11*, 503-504, 1983.
79. Pechersky, D. M., and A. N. Khramov, Mesozoic paleomagnetic scale of the U.S.S.R., *Nature, 244*, 499-501, 1973.
80. Premoli-Silva, I., M. Orlando, S. Moneci, M. Madile, G. Napoleone, and M. Ripepe, Calcareous plankton biostratigraphy and magnetostratigraphy at the Eocene-Oligocene transition in the Gubbio area, in *Eocene-Oligocene boundary in the Marche-Umbria Basin (Italy)*, edited by I. Premoli-Silva, et al., pp. 137-161, International Union of Geological Sciences, Ancona, Italy, 1988.
81. Reeve, S. C., D. Leythaeuser, C. E. Helsley, and K. W. Bay, Paleomagnetic results from the Upper Triassic of East Greenland, *J. Geophys. Res., 79*, 3302-3307, 1974.
82. Ripperdan, R. L., Magnetostratigraphic investigations of the Lower Paleozoic system boundaries, and associated paleogeographic implications, Ph.D. thesis, California Inst. Technology, Pasadena, Calif., 1990.
83. Ripperdan, R. L., and J. L. Kirschvink, Paleomagnetic results from the Cambrian-Ordovician boundary section at Black Mountain, Georgina Basin, western Queensland, Australia, in *Global Perspectives on Ordovician Geology*, edited by B. D.Webby, and J.

R. Laurie, pp. 93-103, Balkema, Rotterdam, 1992.

84. Ripperdan, R. L., M. Magaritz, R. S. Nicoll, and J. H. Shergold, Simultaneous changes in carbon isotopes, sea level, and conodont biozones within the Cambrian-Ordovician boundary interval at Black Mountain, Australia. *Geology, 20*, 1039-1042, 1992.
85. Ripperdan, R. L., J. L. Kirschvink, Z. C. Zhang, G. G. Ma, M. K. Apollonov, and R. Shih-Bin Chang, Magnetostratigraphy of the Cambrian-Ordovician boundary, in press.
86. Ryan, W. B. F., H. M. Bolli, G. N. Foss, J. H. Natland, W. E. Hottman, and J. B. Foresman, Objectives, principal results, operations, and explanatory notes of Leg 40, South Atlantic, in *Init. Repts. Deep Sea Drilling Project, 40*, edited by H. M. Bolli, W. B. F. Ryan, et al., pp. 5-20, 1978.
87. Shackleton, N. J., A. Berger, and W. R. Peltier, An alternative astronomical calibration of the Lower Pleistocene time scale based on ODP Site 677, *Trans. R. Soc. Edinburgh, 81*, 251-261, 1990.
88. Sharman, G. F., and D. L. Risch, Northwest Pacific tectonic evolution in the Middle Mesozoic, *Tectonophysics, 155*, 331-344, 1988
89. Shipboard Scientific Party, Site 585, in *Init. Repts. Deep Sea Drilling Project, 89*, edited by R. Moberly, S. O. Schlanger, et al., pp. 29-155, 1986.
90. Shive, P. N., M. B. Steiner, and D. T. Huycke, Magnetostratigraphy, paleomagnetism, and remanence acquisition in the Triassic Chugwater Formation of Wyoming, *J. Geophys. Res., 89*, 1801-1815, 1984.
91. Steiner, M. B., J. G. Ogg, G. Melendez, and L. Sequieros, Jurassic magnetostratigraphy, 2. Middle-Late Oxfordian of Aguilon, Iberian Cordillera, northern Spain. *Earth Planet. Sci. Lett. 76*, 151-166, 1986.
92. Steiner, M. B., J. G. Ogg, and J. Sandoval, Jurassic magnetostratigraphy, 3. Bajocian-Bathonian of Carcabuey, Sierra Harana and Campillo de Arenas, (Subbetic Cordillera, southern Spain). *Earth Planet. Sci. Lett., 82*, 357-372, 1987.
93. Steiner, M. B., J. G. Ogg, Z.-K. Zhang, and S.-W. Sun, The Late Permian/Early Triassic magnetic polarity time scale and plate motions of South China. *J. Geophys. Res., 94*, 7343-7363, 1989.
94. Swisher, C. C., and R. W. O'B. Knox, The age of the Paleocene/Eocene boundary: $^{40}Ar/^{39}Ar$ dating of the lower part of NP10, North Sea Basin and Denmark, paper presented at the International Geological Correlation Project 308: Paleocene/Eocene Boundary, Brussels meeting, Dec. 2-6, 1991.
95. Tamaki, K., and R. L. Larson, The Mesozoic tectonic history of the Magellan Microplate in the western Central Pacific, *J. Geophys. Res., 93*, 2857-2874, 1989.
96. Tarduno, J. A., W. V. Sliter, T. J. Bralower, M. McWilliams, I. Premoli-Silva, and J. G. Ogg, M-sequence reversals recorded in DSDP sediment cores from the western Mid-Pacific Mountains and Magellan Rise, *Geol. Soc. Am. Bull., 101*, 1306-1316, 1989.
97. Tarduno, J. A., A brief reversed polarity interval during the Cretaceous Normal Polarity Superchron, *Geology, 18*, 638-686, 1990.
98. Tarduno, J. A., Magnetic susceptibility cyclicity and magnetic dissolution in Cretaceous limestones of the Southern Alps (Italy), *Geophys. Res. Lett., 19*, 1515-1518, 1992.
99. Tarduno, J. A., W. Lowrie, W. V. Sliter, T. J. Bralower, and F. Heller, Reversed-polarity characteristic magnetizations in the Albian Contessa section, Umbrian Apennines, Italy: Implications for the existence of a Mid-Cretaceous mixed polarity interval, *J. Geophys. Res., 97*, 241-271, 1992.
100. Tauxe, L., P. Tucker, N. P. Petersen, and J. L. LaBrecque, Magnetostratigraphy of Leg 73 sediments, in *Init. Repts. Deep Sea Drilling Project, 73*, edited by K. J. Hsü, J. L. LaBrecque, et al., pp. 609-621, 1984.
101. Tucker, R. D., T. E. Krogh, R. J. Ross, Jr., and S. H. Williams, Time-scale calibration by high-precision U-Ph zircon dating of interstratified volcanic ashes in the Ordovician and Lower Silurian stratotypes of Britian, *Earth Planet. Sci. Lett., 100*, 51-58, 1990.
102. VandenBerg, J., C. T. Klootwijk, and A. A. H. Wonders, Late Mesozoic and Cenozoic movements of the Italian peninsula: Further paleomagnetic data from the Umbrian sequence, *Geol. Soc. Am. Bull., 89*, 133-150, 1978.
103. VandenBerg, J., and A. A. H. Wonders, Paleomagnetism of Late Mesozoic pelagic limestones from the Southern Alps, *J. Geophys. Res., 85*, 3623-3627, 1980.
104. Visscher, H., The new STS Triassic stage nomenclature, *Albertiana, 10*, 1, 1992.
105. Vogt, P. R., and A. M. Einwich, Magnetic anomalies and seafloor spreading in the western North Atlantic, and a revised calibration of the Keathley (M) geomagnetic reversal chronology, in *Init. Repts. Deep Sea Drilling Project, 43*, edited by B. E. Tucholke, P. R. Vogt, et al., pp. 857-876, 1979.
106. Witte, W. K., P. E. Kent, and P. E Olsen, Magnetostratigraphy and paleomagnetic poles from Late Triassic-earliest Jurassic strata of the Newark basin. *Geol. Soc. Am. Bull., 103*, 1648-1662, 1991.

Isotopic Decay Data

Joel D. Blum

1. INTRODUCTION

This chapter is a compilation of physical constants that pertain to the application of long-lived radioactive isotope systematics in the earth sciences. Literature reviews are included for determinations of radioactive decay constants and stable isotope ratios for eleven parent-daughter decay pairs including K-Ar, K-Ca, Rb-Sr, La-Ce, La-Ba, Sm-Nd, Lu-Hf, Re-Os, ^{235}U-Pb, ^{238}U-Pb, and Th-Pb. Decay constant data for subsets of these eleven isotopic systems have previously been reviewed by Aldrich and Wetherill [2], Wetherill [84], and Gale [22]. In 1976 the International Union of Geological Sciences - Subcommision on Geochronology (hereafter IUGS-SOG) met in Sydney, Australia and agreed to adopt a standard set of decay constants and isotopic abundances for the five isotopic systems in common use at that time (K-Ar, Rb-Sr, ^{235}U-Pb, ^{238}U-Pb, and Th-Pb). These recommendations were published by Steiger and Jäger [76] and have been included in the following chapter. Six additional isotopic systems have come into more common use since that time largely due to advances in the analytical techniques used for isotopic analysis. Data for these six isotopic systems are reviewed in detail and recommendations are made for the adoption of a common set of decay constants and isotope ratios for all eleven systems. Recent reviews of the applications of long-lived radioactive isotope systematics in the earth sciences are provided by Faure [19], Bowen [5] and Geyh and Schleicher [24].

J. E. Blum, Dartmouth College, Department of Earth Sciences, Hanover, NH 03755

Global Earth Physics
A Handbook of Physical Constants
AGU Reference Shelf 1

1.1. Decay Equations

The rate of decay of a radioactive nuclide is proportional to the number of parent atoms (N_P) present at any given time. Thus we can write the relationship

$$dN_P / dt = -\lambda N_P \quad (1)$$

where λ is a decay constant specific to a given parent-daughter pair. For a closed system the expression can be written with respect to the number of daughter isotopes (N_D) as

$$dN_D / dt = \lambda N_P. \quad (2)$$

In the case of branching decay, where a parent nuclide (P) decays to two daughter nuclides (D' and D" with decay constants λ' and $\lambda"$) the expression becomes

$$dN_P / dt = -\lambda' N_P - \lambda" N_P = -\lambda N_P \quad (3)$$

where $\lambda = \lambda' + \lambda"$.

Integration of equations (1) and (2) from some time zero (0) (when the isotopic decay clock is started) to the present time (t) yields

$$N_P(t) = N_P(0)\, e^{-\lambda t} \quad (4)$$

and

$$N_D(t) = N_D(0) + N_P(0)[1-e^{-\lambda t}] \quad (5)$$

which can be combined to give

$$N_D(t) = N_D(0) + N_P(t)[e^{\lambda t}-1]. \quad (6)$$

Similarly, for branched decay we obtain

$$N_{D'}(t) = N_{D'}(0) + (\lambda'/\lambda)N_P(t)[e^{\lambda t}-1] \quad (7)$$

Equation 6 can be solved for t yielding the so-called "age equation"

$$t = 1/\lambda \ln [(N_D(t) - N_D(0)) / N_P(t) + 1] \quad (8)$$

Thus, the age of a geological event can be determined for a closed system by measuring $N_D(t)$ and $N_P(t)$ in a sample in the laboratory if the value for $N_D(0)$ can be either assumed to be zero or determined using an isochron. Isochron determination of $N_D(0)$ can be accomplished if the element corresponding to D also has an isotope I (index isotope) that is not affected by radioactive decay (i.e., no radioactive precursor). In this case

$$N_I(t) = N_I(0) \quad (9)$$

and by substitution, equation 6 may be written in the following form which is known as the "isochron equation"

$$N_D(t) / N_I(t) = N_D(0) / N_I(0) + N_P(t) / N_I(t) [e^{\lambda t}-1]. \quad (10)$$

If we have two or more mineral or rock "systems" which had the same $N_D(0)/N_I(0)$ we may solve for the age of the initial state.

In addition to isochron ages, model ages are also frequently utilized in the earth sciences. A model age is a measure of the time at which a closed system last had the isotopic composition of a given model reservoir. They are calculated by setting the right hand side of equation 10 equal to an expression describing the change of $N_D(t)/N_I(t)$ in a model reservoir with time, and solving for t. Thus, model ages may be referenced to any reservoir for which $N_D(t)/N_I(t)$ can be estimated as a function of time. Model ages are frequently referenced to models for the isotopic evolution of the earth's mantle to estimate the time at which crustal materials separated from a mantle reservoir.

1.2. Experimental Methods and Background

In order to apply radiometric clocks to problems in the earth sciences several physical constants must be known with a high degree of certainty. The most important parameters are the radioactive decay constant and the relative abundances of the nonradiogenic parent and daughter isotopes. Decay constants are usually reported in the literature as half-lives ($T_{1/2}$) which are related to the decay constants (λ) by the following equation

$$T_{1/2} = \ln (2) / \lambda \quad (11)$$

Half-lives can be measured using three general approaches.

1. Laboratory counting experiments in which γ, β or α particles emitted during radioactive decay are measured directly by scintillation counting, by proportional counting, in ionization chambers, or by other similar methods.

2. Measurement of the amount of accumulation of a daughter nuclide in the laboratory during a fixed time period in samples enriched in the parent nuclide.

3. Isotopic measurement of parent and daughter isotope ratios in geological samples and comparison of the isotopic evolution of an isotopic system with an unknown (or poorly known) half-life to another isotopic system for which laboratory measurements of the half-life are available.

Direct laboratory determinations are preferred over geological comparisons with other isotopic systems because they are independent of the ambiguities of geological interpretation and the necessary assumptions that rocks and/or minerals act as perfectly closed systems. High precision laboratory determinations have recently become available for all of the isotopic systems of interest and, therefore, geological comparisons of half-lives will be reviewed only for historical context.

Precise measurements of the isotopic composition of parent elements and the nonradiogenic isotopes of daughter elements are critical in the determination of half-lives, the determination of geochronologic ages, and the correction of mass spectrometer isotope ratio measurements for the isotopic fractionation that occurs during analysis. For those elements that have more than two naturally occurring nonradiogenic stable isotopes, mass spectrometry data for each mass can be normalized to a known isotope ratio using an isotope fractionation law [e.g., 69, 84]. The choice of the isotopic ratio used for normalization is, therefore, an important factor that must be considered for interlaboratory comparison of the results of isotopic studies. For those elements that do not have more than two naturally occurring nonradiogenic stable isotopes, standard reference materials of known isotopic composition must be analyzed under controlled conditions to determine the level of isotope fractionation. Unknown samples are then run under identical conditions, and a mass fractionation correction is applied to the data. Thus, the choice of isotope ratios for interlaboratory standards for some isotopic systems (in particular U-Pb) are also

constants that must be agreed upon for interlaboratory comparison of the results of isotopic studies.

2. K-Ar AND K-Ca SYSTEMS

^{40}K undergoes branching decay by both beta decay (β) and electron capture (EC) in the following proportions by the four following paths

(89.5%) $^{40}K \rightarrow {}^{40}Ca + \beta^-$ (1.32 MeV)
(10.3%) $^{40}K \rightarrow {}^{40}Ar$ (EC, 0.05 MeV) + γ (1.46 MeV)
(0.16%) $^{40}K \rightarrow {}^{40}Ar$ (EC, 1.51 MeV)
(0.001%) $^{40}K \rightarrow {}^{40}Ar + \beta^+$(0.49 MeV) + 2γ(1.02 MeV)

As is the case with most of the isotopic systems discussed in this review, the ^{40}K decay constants have undergone numerous revisions as both counting methods and measurements of stable isotope ratios have undergone refinement. The usual experimental method has been to measure the gamma and beta activities of natural K by scintillation counting. The ^{40}K partial half-lives ($T_{1/2}^{\beta}$ and $T_{1/2}^{EC}$) are then calculated from the measured isotopic composition of natural K. Aldrich and Wetherill [2] reviewed the somewhat inconsistent literature on the partial half-lives of ^{40}K and suggested values (Table 1), which were widely used in geochronology until about 1977. Following a more recent compilation of counting experiments by Beckinsale and Gale [4] and more precise determinations of the isotopic composition of K by Garner et al. [23] the IUGS-SOG [76] recommended revisions of the values (Table 1), which have been universally adopted.

K has three natural isotopes with masses 39 (93.26%), 40 (0.01%) and 41 (6.73%). Nier [59] measured a value for the abundance of ^{40}K = 0.0119%, which was used in geochronology until it was superseded by the higher precision measurement of ^{40}K = 0.01167% by Garner et al. [23]. Ar has three natural isotopes with masses 36 (0.34%), 38 (0.06%) and 40 (99.60%). The isotopic composition of Ar in the atmosphere is an important reference value because it is used to correct Ar isotopic data for atmospheric Ar contamination and because atmospheric Ar is commonly used as a standard to determine mass spectrometer fractionation. This ratio was determined by Nier [59] to be $^{40}Ar/^{36}Ar$ = 295.5 and this value was adopted by the IUGS-SOG [76]. Ca has six natural isotopes with masses 40 (96.94%), 42 (0.65%), 43 (0.13%), 44 (2.09%), 46 (0.004%) and 48 (0.19%). Ca isotope ratios are normalized for mass spectrometer fractionation using a ratio of two non-radiogenic isotopes. Russell et al. [69] reviewed earlier work on Ca isotopic abundances and presented a new determination of $^{42}Ca/^{44}Ca$ = 0.31221 using a double-spike technique, which was used for normalization in the K-Ca geochronologic study of Marshall and DePaolo [47]. In a subsequent study, Jungck et al. [30] measured a non-fractionation corrected value for the isotopic composition of Ca which corresponds to $^{42}Ca/^{44}Ca$ = 0.30870. The choice between these two normalization values for Ca is at this time arbitrary, but the discrepancy points out the need for the re-determination of the absolute isotopic composition of Ca through the use of a precisely calibrated gravimetric double-spike.

3. Rb-Sr SYSTEM

^{87}Rb decays to ^{87}Sr by emission of beta particles with energies ranging from 0.275 to <0.015 MeV. Determination of the half-life by counting has proven to be experimentally difficult because of the large number of low energy beta particles in the decay spectrum. Early counting experiments yielded highly varying results (see compilation by Hamilton [27]). For many years one group of geochronologists used a value of $T_{1/2}$ derived

TABLE 1. Summary of determinations of the partial half-lives of ^{40}K.

Reference	Year	Method	$T_{1/2}^{EC}(10^{10}yr)$	$T_{1/2}^{\beta}$ (10^9 yr)
Aldrich and Wetherill [2]	1958	Review of counting exps.	1.185	1.469
Leutz et al. [37]	1965	γ and β-counting on KI, NaI, and CsI	1.209 ±0.026	1.414 ±0.003
Beckinsale and Gale [4]	1969	Review of counting exps.	1.206 ±0.010	1.413 ±0.002
Steiger and Jäger [76]	1977	By convention	1.193†	1.397†

† Recommended value.

from the counting experiments by Flynn and Glendenin [21], while another group used a significantly higher value of $T_{1/2}$ estimated by Aldrich et al. [1] based on a geological comparison of Rb-Sr ages with U-Pb ages (Table 2). A more precise counting determination of $T_{1/2}$ was made by Neumann and Huster [55] which agreed more closely with the value of Aldrich et al. [1]. Tera et al. [80] compared lunar K-Ar ages with Rb-Sr ages and found excellent agreement using the ^{87}Rb half-life of Aldrich et al. [1]. Davis et al. [13] reported a value nearly identical to that of Neumann and Huster [55] based on an entirely different experimental method in which accumulation of radiogenic ^{87}Sr was measured in a sample of a pure Rb salt. In 1977 the IUGS-SOG [76] recommended adoption of the value of Neumann and Huster [55] that has been universally adopted (Table 2), although it was subsequently suggested by Minster et al. [51] that this value may be too low based on a comparison of Rb-Sr and U-Th-Pb ages of chondrites (Table 2).

Rb has two natural isotopes with masses 85 (72.16%) and 87 (27.84%). The value of $^{85}Rb/^{87}Rb = 2.59265$ measured by Catanzaro et al. [9] was recommended by the IUGS-SOG for use in geochronology. Sr has four natural isotopes with masses 84 (0.56%), 86 (9.86%), 87 (7.00%) and 88 (82.58%). The $^{86}Sr/^{88}Sr$ ratio of 0.1194 measured by Nier [57] is universally used for Sr isotope fractionation corrections and was recommended by IUGS-SOG [76] for use in geochronology. The value of Nier [57] is very close to the slightly higher precision value of $^{86}Sr/^{88}Sr = 0.11935$ (±0.00005) measured by Moore et al. [52].

4. La-Ba AND La-Ce SYSTEMS

^{138}La undergoes branching decay by both beta decay (β^-) and electron capture (EC) in the following proportions by the two following paths

(66%) $^{138}La \rightarrow {}^{138}Ba$ (EC, 1.436 MeV)
(34%) $^{138}La \rightarrow {}^{138}Ce + \beta^-$ (0.789 MeV)

Seven counting determinations of the electron capture and beta decay half-lives were made between 1951 and 1979 yielding highly variable results. Sato and Hirose [71] determined the decay constants in 1981 with considerably higher precision than previous counting experiments (Table 3). Tanaka and Masuda [78] reviewed the highly contradictory literature on counting determinations of the partial half-lives and suggested the use of weighted average values of all previous determinations after applying a correction for adsorption of volatiles to all previous studies except that of Sato and Hirose [71], who had already accounted for this factor (Table 3). Norman and Nelson [61] measured values for the partial half-lives that were consistent with those of Sato and Hirose [71] and since these two determinations were of higher precision than previous counting experiments, they suggested that the values determined in the two studies should simply be averaged [62] (Table 3). Nakai et al. [53] made a geological comparison of the La-Ba and Sm-Nd geochronometers and suggested that the value for $T_{1/2}^{EC}$ of Sato and Hirose [71] was accurate. Dickin [15] made a geological comparison between the La-Ce and Sm-Nd geochronometers and suggested that the value for $T_{1/2}^{\beta}$ of Sato and Hirose [71] was accurate. However, Tanaka et al. [79] argued on geological grounds that one sample should be excluded from the data of Dickin [15] and recalculated a new and significantly lower value of $T_{1/2}^{\beta}$ from the partial data set of Dickin [15] (Table 3). Masuda et al. [48] carried out another geological comparison between the La-

TABLE 2. Summary of determinations of the half-life of ^{87}Rb.

Reference	Year	Method	$T_{1/2}$ (10^{10}yr)
Aldrich et al. [1]	1956	Comparison with U-Pb	5.0 ±0.2
Flynn and Glendenin [21]	1959	Liquid scintillation counting	4.70 ±0.10
Neumann and Huster [55]	1974	4π proportional counting	4.88 ±0.10
Davis et al. [13]	1977	Accumulation	4.89 ±0.04
Steiger and Jäger [76]	1977	By convention	4.88†
Minster et al. [51]	1982	Comparison with U-Pb	4.94 ±0.03

† Recommended value.

TABLE 3. Summary of determinations of the partial half-lives of ^{138}La.

Reference	Year	Method	$T_{1/2}^{EC}(10^{11}yr)$	$T_{1/2}^{\beta}$ (10^{11} yr)
Sato and Hirose [71]	1981	γ-counting on Ge(Li) and Ge	1.56 ±0.05	3.02 ±0.04
Tanaka and Masuda [78]	1982	Review of counting exps.	1.74 ±0.13	2.95 ±0.15
Norman and Nelson [61]	1983a	γ-counting on Ge(Li)	1.58 ±0.02	3.19 ±0.22
Norman and Nelson [62]	1983b	Average of counting exps.	1.57 ±0.05†	3.10 ±0.15†
Tanaka et al. [79]	1988	Comparison with Sm-Nd		2.59
Masuda et al. [48]	1988	Comparison with Sm-Nd		2.50
Makishima et al. [46]	1993	Comparison with Sm-Nd and Rb-Sr		2.98 ±0.29

† Recommended value.

Ce and Sm-Nd geochronometers and recommended the use of another value for $T_{1/2}^{\beta}$, which is much closer to the value of Tanaka et al. [79] than the value of Sato and Hirose [71] (Table 3). Finally, Makishima et al. [46] carried out a geological comparison between the La-Ce and both the Sm-Nd and Rb-Sr systems and estimated a value for $T_{1/2}^{\beta}$ that is entirely consistent with the recent counting experiments [61,71] (Table 3). Given the high precision and good agreement between the two recent determinations by counting experiments, it is recommended that the average of the experimentally determined values of Sato and Hirose [71] and Norman and Nelson [61] be adopted, following the suggestion of Norman and Nelson [62].

La has two natural isotopes with masses of 138 (0.09%) and 139 (99.91%). The most precise measurement of the $^{138}La/^{139}La$ ratio was determined by Makishima et al. [45] to be 9.025×10^{-4}. Ce has four natural stable isotopes with masses 136 (0.19%), 138 (0.25%), 140 (88.43%) and 142 (11.13%). Fractionation of Ce was corrected to a value of $^{136}Ce/^{142}Ce = 0.01720$ by most workers until Makishima et al. [45] determined the isotopic composition of Ce with higher precision and recommended a new normalization value of $^{136}Ce/^{142}Ce = 0.01688$. Ba has seven natural isotopes with masses of 130 (0.11%), 132 (0.10%), 134 (2.42%), 135 (6.59%), 136 (7.85%), 137 (11.23%) and 138 (71.70%). In the geochronologic application of the La-Ba system by Nakai et al. [53] a normalization value of $^{136}Ba/^{137}Ba = 0.6996$ was used, which is indistinguishable from the $^{136}Ba/^{137}Ba$ value determined by Eugster et al. [18].

5. Sm-Nd SYSTEM

^{147}Sm decays to ^{143}Nd by emission of an alpha particle with an energy of 2.314 MeV. Four high precision measurements of the half-life have been made by counting experiments and all are in close agreement within analytical uncertainty (Table 4). Lugmair and Marti [43] reviewed the literature on the half-life of ^{147}Sm and suggested that the weighted mean of the four determinations be adopted for use in geochronology (Table 4).

Sm has seven natural isotopes with masses of 144 (3.07%), 147 (15.00%), 148 (11.24%), 149 (13.82%), 150 (7.38%), 152 (26.74%), and 154 (22.75%). The choice of normalization isotopes for Sm varies between laboratories with the most common values being those given by Wasserburg et al. [83] ($^{148}Sm/^{154}Sm$ = 0.49419) and Lugmair and Marti [43] ($^{147}Sm/^{152}Sm$ = 0.56081). Nd has seven natural isotopes with masses 142 (27.13%), 143 (12.18%), 144 (23.80%), 145 (8.30%), 146 (17.19%), 148 (5.76%), and 150 (5.64%). The choice of normalization isotopes for Nd also varies between laboratories and must be carefully considered when comparing Nd isotope data acquired in different laboratories because of the high precision necessary in many Nd isotopic studies. The most common normalization ratios are those of Lugmair et al. [42] and O'Nions et al. [63] ($^{146}Nd/^{144}Nd = 0.72190$), Lugmair and Marti [43] ($^{148}Nd/^{144}Nd = 0.241572$), and Wasserburg et al. [83] ($^{146}Nd/^{142}Nd = 0.636151$). The first two normalizations are essentially equivalent, but the third is not and corresponds to a significantly different $^{146}Nd/^{144}Nd$ ratio of 0.724134 [83]. Gale [22] recommended the universal adoption of the value of Lugmair and Marti [43], but in the ensuing ten years all three values have remained in common use. Data reported using different normalization ratios can be compared by applying a correction that can be adequately calculated

TABLE 4. Summary of determinations of the half-life of ^{147}Sm.

Reference	Year	Method	$T_{1/2}$ (10^{11}yr)
Wright et al. [86]	1961	Liquid scintillation counting	1.05 ±0.02
Donhoffer [17]	1964	Liquid scintillation counting	1.04 ±0.03
Valli et al. [82]	1965	Liquid scintillation counting	1.08 ±0.02
Gupta and MacFarlane[26]	1970	Ionization chamber	1.06 ±0.02
Lugmair and Marti [43]	1978	Review of counting exps.	1.060 ±0.008†

† Recommended value.

from a simple linear fractionation law [e.g., 69, 83]. To compare a $^{143}Nd/^{144}Nd$ ratio corrected to a value of $^{146}Nd/^{144}Nd = 0.72190$ with a $^{143}Nd/^{144}Nd$ ratio corrected to a value of $^{146}Nd/^{142}Nd = 0.636151$, the latter value must be multiplied by a factor of 1.001550.

6. Lu-Hf SYSTEM

^{176}Lu decays to ^{176}Hf by emission of a 0.425 MeV beta particle followed by a cascade of gamma rays of 0.401, 0.307, 0.202, and 0.088 MeV. Dixon et al. [16] reported that ^{176}Lu also decays by electron capture to ^{176}Yb with a branching ratio of 3±1%. This finding has not been confirmed or disproved by subsequent studies and has largely been ignored because of the long half-life of ^{176}Lu and the small portion (<3%) that decays to ^{176}Yb. Thus, the branching decay is generally neglected and it is assumed that the total half-life of ^{176}Lu is equal to the beta decay partial half-life. Determinations of the half-life by counting experiments in the 1960's varied widely (Table 5), which led Patchett and Tatsumoto [64] and Patchett [65] to make a geological determination of the half-life by comparing a Lu-Hf whole-rock isochron for eucrite meteorites with a well-known age based on Rb-Sr, U-Pb and Sm-Nd isotope determinations (Table 5). An experimental study in 1982 by Sguigna et al. [75] utilized γ–γ coincidence counting methods and yielded a half-life that is nearly identical to the geologically derived value of Patchett [65] (Table 5). Due to the technical superiority of the experimental method of Sguigna et al. [75] and the close agreement with the value determined by Patchett [65], this value is recommended for use in geochronology.

Lu has two natural isotopes with masses of 175 (97.41%) and 176 (2.59%). A $^{175}Lu/^{176}Lu$ ratio of 37.36 was measured by McCulloch et al. [49], but this ratio was superseded by the higher precision measurement

TABLE 5. Summary of determinations of the half-life of ^{176}Lu.

Reference	Year	Method	$T_{1/2}$ (10^{10}yr)
McNair [50]	1961	γ-counting on NaI	3.6 ±0.1
Donhoffer [17]	1964	Liquid scintillation counting	2.18 ±0.06
Brinkman et al. [6]	1965	γ-counting on NaI, β on NaI, γ-coincidence	3.58 ±0.08*
Sakamoto [70]	1967	γ-counting on NaI	5.0 ±0.3
Prodi et al. [68]	1969	β–γ coincidence counting on NaI	3.27 ±0.05
Komura et al. [33]	1972	γ-counting on NaI and Ge	3.79 ±0.03
Norman [60]	1980	γ-counting on Ge	4.08 ±0.24
Patchett and Tatsumoto [64]	1980	Comparison with Rb-Sr, Sm-Nd, and U-Pb	3.53 ±0.14
Sguigna et al. [75]	1982	γ–γ coincidence counting on Ge	3.59 ±0.05†
Patchett [65]	1983	Comparison with Rb-Sr, Sm-Nd, and U-Pb	3.57 ±0.14

* Mean of three determinations.

† Recommended value.

by Patchett and Tatsumoto [64] of $^{175}Lu/^{176}Lu$ = 37.701, which has been adopted for use in Lu-Hf geochronology. Hf has six natural isotopes with masses 174 (0.16%), 176 (5.21%), 177 (18.60%), 178 (27.30%), 179 (13.63%) and 180 (35.10%). Patchett and Tatsumoto [64] measured an average $^{179}Hf/^{177}Hf$ ratio of 0.7325, and this value has been adopted for isotope ratio normalization in geochronology.

7. Re-Os SYSTEM

^{187}Re decays to ^{187}Os by emission of beta particles with a maximum energy of 0.0026 MeV. As in the case of ^{87}Rb decay the determination of the half-life by counting has proven to be experimentally difficult because of the large number of low energy beta particles in the decay spectrum. The results of counting experiments prior to 1963 were reviewed by Wetherill [84] and gave highly variable results. Thus, the half-life determined by Hirt et al. [28] from comparison with other isotopic systems was preferred for use in geochronology for many years (Table 6). Later determinations of the half-life by counting experiments [66, 6, 54] also varied considerably (Table 6) and did not result in a consensus as to the correct value for the half-life. Luck et al. [40] analyzed iron and chondritic meteorites and found that they all fell on a Re-Os isochron. By assuming a formation age of 4.55 AE based on Rb-Sr and U-Pb ages, they estimated a value for the ^{187}Re half-life (Table 6). This value was later revised by Luck and Allegre [41] after recalibration of their isotope dilution spike (Table 6). Lindner et al. [38, 39] used a method similar to that used for ^{87}Rb by Davis et al. [13] to directly measure the half-life by measuring the accumulation of radiogenic ^{187}Os daughter product from a concentrated perrhenic acid ($HReO_4$) solution. A preliminary report of the results of this experiment utilized a laser microprobe mass analyzer for Os isotope analyses [38] (Table 6). However, the half-life determined in this study was subsequently revised after refinement of the experimental techniques and utilization of inductively coupled plasma mass spectrometry for Os isotope analyses [39] (Table 6). Although this revised value is presently the best estimate of the ^{187}Re half-life, the recent development of the negative thermal ionization technique for Os isotope measurement should allow future determination of the ^{187}Re half-life with much higher precision [11].

Re has two natural isotopes with masses of 185 (37.40%), and 187 (62.60%). A $^{185}Re/^{187}Re$ ratio of 0.5974 was measured by Gramlich et al. [25], and has been adopted for Re-Os geochronology. Os has seven natural isotopes with masses 184 (0.02%), 186 (1.59%), 187 (1.61%), 188 (13.30%), 189 (16.10%), 190 (26.40%) and 192 (41.00%). Nier [56] measured an average $^{188}Os/^{192}Os$ ratio of 0.3244, which has been the basis for isotope ratio normalization in geochronology. Luck and Allegre [41] measured $^{186}Os/^{188}Os$ ratio of 0.12035 using the $^{188}Os/^{192}Os$ ratio of Nier [56] as an internal standard, and this ratio is also used by some laboratories for normalization.

8. Th-Pb AND U-Pb SYSTEMS

^{232}Th is the only long-lived nuclide of Th and decays through a series of intermediate daughter products to stable ^{208}Pb by the emission of six alpha and four beta particles. The agreement between previous determinations of the half-life are extremely good (Table 7). The most

TABLE 6. Summary of determinations of the half-life of ^{187}Re.

Reference	Year	Method	$T_{1/2}$ (10^{10}yr)
Hirt et al. [28]	1963	Comparison to U-Pb, Rb-Sr and K-Ar	4.3 ±0.5
Payne and Drever [66]	1965	Proportional counting	4.7 ±0.5
Brodzinski and Conway [7]	1965	Proportional counting	6.6 ±1.3
Luck et al. [40]	1980	Comparison to Rb-Sr and U-Pb	4.28 ±0.12
Luck and Allegre [41]	1983	Comparison to Rb-Sr and U-Pb	4.56 ±0.12
Naldrett [54]	1984	Liquid scintillation counting	3.5 ±0.4
Lindner et al. [38]	1986	Accumulation	4.35 ±0.13
Lindner et al. [39]	1989	Accumulation	4.23 ±0.13†

† Recommended value.

TABLE 7. Summary of determinations of the half-life of ^{232}Th.

Reference	Year	Method	$T_{1/2}$ (10^{10}yr)
Kovarik and Adams [34]	1955	α-counting	1.39 ±0.03
Senftle et al. [74]	1956	γ-counting on NaI	1.42 ±0.07
Picciotto and Wilgain [67]	1956	Nuclear emulsion	1.39 ±0.03
LeRoux and Glendenin [36]	1963	Liquid scintillation counting	1.401 ±0.008†

† Recommended value.

recent and highest precision determination by LeRoux and Glendenin [36] was adopted by the IUGS-SOG [76] (Table 7).

^{235}U decays through a series of intermediate daughter products to stable ^{207}Pb by the emission of seven alpha and four beta particles. Measurements of the half-life have varied considerably (Table 8) because of difficulties with interferences from alpha particles of ^{234}U and ^{238}U. Aldrich and Wetherill [2] reviewed the literature and recommended use of the value of Fleming et al. [20] which was widely used until the 1970's (Table 8). The inconsistency of previous studies prompted Jaffey et al. [29] to carry-out higher precision measurements of the half-lives of both ^{235}U and ^{238}U (Table 8). These authors reviewed the technical problems with previous studies and carried out a technically superior measurement of the half-life, which was adopted by the IUGS-SOG [76].

^{238}U decays through a series of intermediate daughter products to stable ^{206}Pb by the emission of eight alpha and six beta particles. Various measurements of the half-life prior to the 1970's were quite consistent (Table 9). Aldrich and Wetherill [2] reviewed the literature and recommended use of the value of Kovarik and Adams [34] which was widely used until the 1970's (Table 9). The consistency of these early determinations suggested that the value was known with an uncertainty of less than 1% (Table 9). However, the high-precision measurement (±0.05%) of the half-life of ^{238}U by Jaffey et al. [29] showed that the agreement had been fortuitous, and that the correct value was lower by nearly 1%. Jaffey et al. [29] reviewed the technical problems with previous studies and carried out a technically superior measurement of the half-life, which was adopted by the IUGS-SOG [76].

U has three natural isotopes (all of which are radioactive) with masses 238 (99.27%), 235 (0.72%) and

TABLE 8. Summary of determinations of the half-life of ^{235}U.

Reference	Year	Method	$T_{1/2}$ (10^{8}yr)
Nier [58]	1939	U-Pb geochronology	7.04 ±0.15
Knight [32]	1950	Ionization chamber	7.10 ±0.16
Sayag [72]	1951	Ionization chamber	6.94 ±0.25
Fleming et al. [20]	1952	Ionization chamber	7.12 ±0.16
Würger et al. [87]	1957	Ionization chamber	6.92 ±0.11
Deruytter et al. [14]	1965	Si detector	6.97 ±0.07
White et al. [85]	1965	α-counting	7.12 ±0.09
Banks and Silver [3]	1966	U-Pb geochronology	7.02 ±0.07*
Jaffey et al. [29]	1971	Proportional counter	7.0381 ±0.0048†

* Corrected using $T_{1/2}$ for ^{238}U by *Jaffey et al.* [29].

† Recommended value.

TABLE 9. Summary of determinations of the half-life of ^{238}U.

Reference	Year	Method	$T_{1/2}$ (10^9yr)
Schiedt [73]	1935	Ionization chamber	4.46 ±0.05
Curtiss et al. [12]	1941	Ionization chamber	4.514 ±0.009
Kienberger [31]	1949	Ionization chamber	4.511 ±0.005
Kienberger [31]	1949	Ionization chamber	4.489 ±0.010
Kovarik and Adams [34]	1955	Ionization chamber	4.508 ±0.018
Leachman and Schmitt [35]	1957	Ionization chamber	4.57 ±0.03
Steyn and Strelow [77]	1959	Liquid scintillation counting	4.457 ±0.007
Jaffey et al. [29]	1971	Proportional counter	4.4683 ±0.0024†

† Recommended value.

234 (0.006%). The $^{238}U/^{235}U$ ratio was determined with high precision by Cowan and Adler [10] to be 137.88 and this value was adopted by the IUGS-SOG [76]. Th occurs primarily as one radioactive isotope ^{232}Th, although five additional radioactive isotopes of Th exist in nature as short-lived intermediate daughters of ^{235}U, ^{238}U, and ^{232}Th. In addition to the radiogenic isotopes of Pb (206, 207 and 208), Pb has only one nonradiogenic isotope (204), thus Pb isotope measurements cannot be internally normalized and mass fractionation must be estimated from measurements of standards or by special double-spiking techniques using artificially produced ^{202}Pb and ^{205}Pb. The most commonly used Pb isotope standards are NBS 981, NBS 982 and NBS 983, the isotopic compositions of which are given in Table 10.

9. SUMMARY

It is important that radiogenic isotope studies carried out in various laboratories use a common set of decay constants and stable isotope ratios for mass spectrometer fractionation corrections. This practice helps to achieve consistency in isotope ratio measurement and facilitates inter-laboratory comparison of isotope ratios and geochronologic ages. Five of the eleven isotope decay schemes reviewed here were standardized by IUGS-SOG convention in 1977 [76] and there is no new data since that time that would require any changes of these values. Six additional isotopic systems have been reviewed here and standardized values are recommended. Recommendations for stable isotope ratios are found in

TABLE 10. Values for the isotopic composition of Pb standards from the literature.

Reference	$^{204}Pb/^{206}Pb$	$^{207}Pb/^{206}Pb$	$^{208}Pb/^{206}Pb$
NBS 981 - common Pb isotopic standard			
Catanzaro et al. [8]	0.059042 ±37	0.91464 ±33	2.1681 ±8
Todt et al. [81]	0.059041 ±05	0.91470 ±28	2.1672 ±1
NBS 982 - equal atom Pb isotopic standard			
Catanzaro et al. [8]	0.027219 ±27	0.46707 ±20	1.00016 ±36
NBS 983 - radiogenic Pb isotopic standard			
Catanzaro et al. [8]	0.000371 ±20	0.071201 ±40	0.013619 ±24

TABLE 11. Summary of the recommended values of the decay constants for each of the systems reviewed.

System	Decay type	$T_{1/2}$ (10^{10} yr)	λ (10^{-10} yr^{-1})	Reference
^{40}K-^{40}Ar	EC	0.1193	5.810	Steiger and Jäger [76]†
^{40}K-^{40}Ca	β^-	0.1397	4.962	Steiger and Jäger [76]†
^{87}Rb-^{87}Sr	β^-	4.88	0.142	Neumann and Huster [55]†
^{138}La-^{138}Ba	EC	15.7	0.0441	Norman and Nelson [62]
^{138}La-^{138}Ce	β^-	31.0	0.0224	Norman and Nelson [62]
^{147}Sm-^{143}Nd	α	10.60	0.06539	Lugmair and Marti [44]
^{176}Lu-^{176}Hf	β^-	3.59	0.193	Sguigna et al. [75]
^{187}Re-^{187}Os	β^-	4.23	0.164	Lindner et al. [39]
^{232}Th-^{208}Pb	$6\alpha+4\beta$	1.401	0.4948	LeRoux and Glendenin [36]†
^{235}U-^{205}Pb	$7\alpha+4\beta$	0.0070381	98.485	Jaffey et al. [29]†
^{238}U-^{206}Pb	$8\alpha+6\beta$	0.44683	1.5513	Jaffey et al. [29]†

† Standardized by IUGS-SOG convention in 1977 [76].

the text at the end of each section. A summary of the recommended half-lives and corresponding decay constants are given in Table 11.

Acknowledgements. G.W. Lugmair, D.A. Papanastassiou and J.D. Romick provided helpful reviews. This work was partially supported by NSF grant EAR 9104553 and a Sloan Foundation Fellowship.

REFERENCES

1. Aldrich, L.T., G.W. Wetherill, G.R. Tilton and G.L. Davis, Half-life of Rb^{87}, *Phys. Rev.* 103, 1045-1047, 1956.
2. Aldrich, L.T. and G.W. Wetherill, Geochronology by radioactive decay, *Ann. Rev. Nucl. Sci.*, 8, 257-295, 1958.
3. Banks, P.O. and L.T. Silver, Evaluation of the decay constant of uranium 235 from Pb isotope ratios, *J. Geophys. Res.*, 71, 4037-4046, 1966.
4. Beckinsale, R.D. and N.H. Gale, A reappraisal of the decay constants and branching ratio of ^{40}K, *Earth Planet, Sci. Lett.*, 6, 289-294, 1969.
5. Bowen, R., *Isotopes in the Earth Sciences*, Elsevier Applied Sciences, 647pp., 1988.
6. Brinkman, G.A., A.H.W. Arten Jr., and J.Th. Veenboer, *Physica A (Amsterdam)*, 31, 1305-1319, 1965.
7. Brodzinski, R.L. and D.C. Conway, Decay of Rhenium-187, *Phys. Rev.*, 138, 1368-1371, 1965.
8. Catanzaro, E.J. and T.J. Murphy, W.R. Shields, and E.L. Garner, Absolute isotopic abundance ratios of common, equal atom, and radiogenic lead isotope standards, *J. Res. U.S. Natl. Bur. Stand.* Sect. A, 72, 261-267, 1968.
9. Catanzaro, E.J. and T.J. Murphy, E.L. Garner and W.R. Shields, Absolute isotopic abundance ratio and atomic weight of terrestrial rubidium, *J. Res. U.S. Natl. Bur. Stand.* Sect. A, 73, 511-516, 1969.
10. Cowan, G.A. and H.H. Adler, The variability of the natural abundance of ^{235}U, *Geochim. Cosmochim. Acta* 40, 1487-1490, 1976.
11. Creaser, R.A., D.A. Papanastassiou and G.J. Wasserburg, Negative thermal ion mass spectrometry of osmium, rhenium, and iridium, *Geochim. Cosmochim. Acta*, 55, 397-401, 1991.
12. Curtiss, L.F., L.L. Stockman and B.W. Brown, Intercomparison of mass spectrometer and alpha-particle methods for isotopic analysis, *U.S. National Bureau of Standards Report No. A-80* (U.S. GPO, Washington, D.C., 1941).
13. Davis, D.W., J. Gray, G.L. Cumming and H. Baadsgaard, Determination of the ^{87}Rb decay constant, *Geochim. Cosmochim. Acta*, 41, 1745-1749, 1977.
14. Deruytter, A.J., I.G. Schroder, and J.A. Moore, Measurement of the half-live of U^{235} from alpha emission, *Nucl. Sci. Eng.*, 21, 325-327, 1965.
15. Dickin, A.P, La-Ce dating of Lewisian granulites to constrain the La-138 β-decay half-life, *Nature*, 325, 337-338, 1987.
16. Dixon, D. A., McNair and S.C. Curran, The Natural Radioactivity of Lutetium, *Phil. Mag.*, 45, 683-694, 1954.
17. Donhoffer, D., Bestimmung der Halbwertszeiten der in der Natur vorkommenden radioaktiven Nuklide ^{147}Sm und ^{176}Lu mittels flüssiger Szintillatoren, *Nucl. Phys.*, 50, 489-496, 1964.
18. Eugster, O., F. Tera and G.J. Wasserburg, Isotopic Analyses of Barium in Meteorites and in Terrestrial Samples, *J. Geophys. Res.*, 74, 3897-3908, 1969.

19. Faure, G., *Principles of Isotope Geology*, John Wiley and Sons, 589pp., 1986.
20. Fleming, E.H. Jr., A. Ghiorso, and B.B. Cunningham, The specific alpha-activities and half-lives of U^{234}, U^{235} and U^{238}, *Phys. Rev.*, 88, 642-652, 1952.
21. Flynn, K.F. and L.E. Glendenin, Half-life and beta spectrum of Rb^{87}, *Phys. Rev.*, 116, 744-748, 1959.
22. Gale, N. H., The physical decay constants, in: *Numerical Dating in Stratigraphy*, edited by G.S. Odin, John Wiley & Sons, Ltd., 1982.
23. Garner, E.L., T.J. Murphy, J.W. Gramlich, P.J. Paulsen and I.L. Barnes, Absolute isotopic abundance ratios and the atomic weight of a reference sample of potassium, *J. Res., U.S. Natl. Bur. Stand.* Sect. A, 79, 713-725, 1976.
24. Geyh, M.A. and H. Schleicher, *Absolute Age Determination*, Springer-Verlag, 503 pp., 1990.
25. Gramlich, J.W., T.J. Murphy, E.L. Garner and W.R. Shields, Absolute isotopic abundance ratio and atomic weight of a reference sample of rhenium, *J. Res. Nat. Bur. Stand., Sect. A*, 77, 691-698, 1973.
26. Gupta, M.C. and R.D. McFarlane, The natural alpha radioactivity of samarium, *Inorg. Nucl. Chem.*, 32, 3425-3432, 1970.
27. Hamilton, E.I., *Applied Geochronology*, Academic Press, New York, 267pp., 1965.
28. Hirt, B., G.R. Tilton, W. Herr, and W. Hoffmeister, The half-life of ^{187}Re, In *Earth Sciences and Meteoritics* (eds. J. Geiss and E.D. Goldberg), North Holland Publishing Company, 273-280, 1963.
29. Jaffey, A.H., K.F. Flynn, L.F. Glendenin, W.C. Bentley and A.M. Essling, Precision measurements of half-lives and specific activities of ^{235}U and ^{238}U, *Phys. Rev. C.*, 4, 1889-1906, 1971.
30. Jungck, M.H.A., T. Shimamura and G.W. Lugmair, Ca isotope variations in Allende, *Geochim. Cosmochim. Acta*, 48, 2651-2658, 1984.
31. Kienberger, C.A., The uranium 234 content of natural uranium and the specific alpha-activities of the isotopes, *Phys. Rev.*, 76, 1561-1563, 1949.
32. Knight, G.B., Specific alpha activity of U-235, *Oak Ridge National Laboratory Report No. K-663*, 1950.
33. Komura, K., K. Sakamoto and S. Tanaka, Half-life of long-lived ^{176}Lu, *Nucl. Phys. A*, 198, 73-80,1972.
34. Kovarik, A.F. and N.I. Adams, Redetermination of the disintegration rate of U^{238}, *Phys. Rev.*, 98, 46, 1955.
35. Leachman, R.B. and H.W. Schmitt, The cross-section for U^{238} fission by fission neutrons, *J. Nucl. Energy*, 4, 38-43, 1957.
36. LeRoux, L.J. and L.F. Glendenin, Half-life of ^{232}Th, *Proc. Natl. Meet. on Nuclear Energy*, Pretoria, South Africa, 83-94, April, 1963.
37. Leutz, H., G. Schulz and H. Wenninger, The decay of potassium-40, *Z. Physik.* 187, 151-164, 1965.
38. Lindner, M., D.A. Leich, R.J. Borg, G.P. Russ, J.M. Bazan, D.S. Simons and A.R. Date, Direct laboratory determination of the ^{187}Re half-life, *Nature*, 320, 246-248, 1986.
39. Lindner, M., D.A. Leich, G.P. Russ, J.M. Bazan and R.J. Borg, Direct determination of the half-life of ^{187}Re, *Geochim. Cosmochim. Acta*, 53, 1597-1606, 1989.
40. Luck, J.M., J.L. Birck and C.J. Allegre, ^{187}Re-^{187}Os systematics in meteorites: early chronology of the Solar System and age of the Galaxy, *Nature*, 283, 256-258, 1980.
41. Luck, J.M. and C.J. Allegre, ^{187}Re-^{187}Os systematics in meteorites and cosmochemical consequences, *Nature*, 302, 130-132, 1983.
42. Lugmair, G.W., N.B. Scheinin and K. Marti, Sm-Nd age of Apollo 17 basalt 75075: evidence for early differentiation of the lunar exterior, *Proc. Lunar. Planet. Sci. Conf. 6th*, 1419-1429, 1975.
43. Lugmair, G.W. and K. Marti, Sm-Nd-Pu timepieces in the Angra Dos Reis meteorite, *Earth Planet Sci. Lett.*, 35, 273-284, 1977.
44. Lugmair, G.W. and K. Marti, Lunar initial $^{143}Nd/^{144}Nd$: differential evolution of the lunar crust and mantle, *Earth Planet. Sci. Lett.*, 39, 349-357, 1978.
45. Makishima, A., H. Shimizu and A. Masuda, Precise measurement of cerium and lanthanum isotope ratios. *Mass Spectrosc.* 35, 64-72, 1987.
46. Makishima, A., E. Nakamura, S. Akimoto, I.H. Campbell and R.I. Hill, New constraints on the ^{138}La β-decay constant based on a geochronologic study of granites from the Yilgarn Block, Western Australia, *Chem. Geol.* 104, 293-300, 1993.
47. Marshall, B.D. and D.J. DePaolo, Precise age determinations and petrogenetic studies using the K-Ca method, *Geochim. Cosmochim. Acta*, 46, 2537-2545, 1982.
48. Masuda, A., H. Shimizu, S. Nakai, A. Makishima and S. Lahti, La-138 β-decay constant estimated from geochronological studies, *Earth Planet. Sci. Lett.* 89, 316-322, 1988.
49. McCulloch, M.T., J.R. DeLaeter and K.J.R. Rosman, The isotopic composition and elemental abundance of lutetium in meteorites and terrestrial samples and the Lu-176 cosmochrometer, *Earth Planet. Sci. Lett.* 28, 308-322, 1976.
50. McNair, A., The half-life of long-lived lutetium-176, *Philos. Mag.*, 6, 851-856, 1961.
51. Minster, J.F., J.L. Birck and C.J. Allegre, Absolute age of formation of chondrites studied by the ^{87}Rb-^{87}Sr method, *Nature*. 300, 414-419, 1982.
52. Moore, L.J., I.L. Barnes and T.J. Murphy, The absolute abundance ratios and the atomic weight of a reference sample of strontium, *J. Res. U.S. Natl. Bur. Stand. Sect. A*, 87, 1-8, 1982.
53. Nakai, S., H. Shimizu and A. Masuda, A new geochronometer using lanthanum-138, *Nature*, 320, 433-435, 1986.
54. Naldrett, S.M., Half-life of rhenium: geologic and cosmologic ages, *Can. J. Phys.*, 62, 15-20, 1984.
55. Neumann, W. and E. Huster, The half-life of ^{87}Rb measured as difference between the isotopes ^{87}Rb and ^{85}Rb, *Z. Physik*, 270, 121-127, 1974.
56. Nier, A.O., The isotopic constitution of osmium, *Phys. Rev.*, 52, 885, 1937.

57. Nier, A.O., Isotopic constitution of Sr, Ba, Bi, Tl, and Hg, *Phys. Rev.* 54, 275-278, 1938.
58. Nier, A.O., The isotopic composition of uranium and the half-lives of uranium isotopes, *Phys. Rev.*, 55, 150-153, 1939.
59. Nier, A.O., A redetermination of the relative abundances of carbon, nitrogen, oxygen, argon, and potassium, *Phys. Rev.* 77, 789-793, 1950.
60. Norman, E.B., Half-life of ^{176}Lu, *Phys. Rev. C.*, 21, 1109-1110, 1980.
61. Norman, E. and M. Nelson, Half-life and decay scheme of La-138, *Phys. Rev.* C, 27, 1321-1324, 1983a.
62. Norman, E. and M. Nelson, On the half-life of ^{138}La, *Nature*, 306, 503-504, 1983b.
63 O'Nions, R.K., P.J. Hamilton and N.M. Evensen, Variations in ^{143}Nd/^{144}Nd and ^{87}Sr/^{86}Sr ratios in oceanic basalts, *Earth Planet. Sci. Lett.*, 34, 13-22, 1977.
64. Patchett, P.J. and M. Tatsumoto, A routine high-precision method for Lu-Hf isotope geochemistry and chronology, *Contrib. Mineral Petrol.*, 75, 263-267, 1980.
65. Patchett, P.J., Importance of the Lu-Hf isotopic system in studies of planetary chronology and chemical evolution, *Geochim. Cosmochim. Acta*, 47, 81-91, 1983.
66. Payne, J.A. and R. Drever, An investigation of the beta decay of rhenium to osmium with high-temperature proportional counters, Ph.D. Thesis, University of Glascow, 1965.
67. Picciotto, E., and S. Wilgain, Confirmation of the half-life of thorium 232, *Nuovo Cimento (Italy)*, 4, 1525-1528, 1956.
68. Prodi, V., K.F. Flynn, and L.E. Glendenin, Half-life and β spectrum of ^{176}Lu, *Phys. Rev.*, 188, 1930-1933, 1969.
69. Russell, W.A., D.A. Papanastassiou and T.A. Tombrello, Ca isotope fractionation on the Earth and other solar system materials, *Geochim. Cosmochim. Acta*, 42, 1075-1090, 1978.
70. Sakamoto, K., The half-lives of natural ^{176}Lu and ^{180}Ta, *Nucl. Phys. A*, 103, 134-144, 1967.
71. Sato, J. and T. Hirose, Half-life of ^{138}La, *Radiochem. Radioanal. Lett.*, 145-152, 1981.
72. Sayag, G-J., Mesure du rapport des activités de U^{235} et U^{234} dans l'uranium naturel à l'aide d'une chambre d'ionisation à grille, *Compt. Rend.*, 232, 2091-2093, 1951.
73. Schiedt, R., A method of counting the alpha-particles emitted by uranium, *Sitz. Akad. Wiss. Wien (Math.-naturw. Klasse)*, Abt. IIa, 144, 191-211, 1935.
74. Senftle, F.E., T.A. Farley and N. Lazar, Half-life of Th^{232} and the branching ratio of Bi^{212}, *Phys. Rev.*, 104, 1629-1632, 1956.
75. Sguigna, A.P., A.J. Larabee and J.C. Waddington, The half-life of ^{176}Lu by $\gamma-\gamma$ coincidence measurement, *Can. J. Phys.*, 60, 361-364, 1982.
76. Steiger, R.H. and E. Jäger, Subcommission on geochronology: convention of the use of decay constants in geo- and cosmochronology, *Earth Planet. Sci. Lett.*, 36, 359-362, 1977.
77. Steyn, J. and F.W.E. Strelow, The determination of the half-life of U^{238} by absolute counting of alpha particles in a 4π liquid scintillation counter, In: *Metrology of Radionuclides*, ed. A. Sanielevici, IAEA, Vienna, 155-161, 1959.
78. Tanaka, T. and A. Masuda, The La-Ce geochronometer: a new dating method, *Nature*, 300, 515-518, 1982.
79. Tanaka, T., H. Shimizu, Y. Kawata, and A. Masuda, Mantle and crustal Ce/Nd isotope systematics, *Nature*, 333, 403-404, 1988.
80. Tera, F., D.A. Papanastassiou and G.J. Wasserburg, Isotopic Evidence for a Terminal Lunar Cataclysm, *Earth Planet. Sci. Lett.*, 22, 1-21, 1974.
81. Todt, W., R.A. Cliff, A. Hanser and A.W. Hofmann, ^{202}Pb + ^{205}Pb double spike for Pb isotopic analyses, *Terra Cognita*, 4, 209, 1984.
82. Valli, K., J. Aaltonen, G. Graeffe, M. Nurmia and R. Poyhonen, Half-life of ^{147}Sm: comparison of ionization chamber and liquid scintillation results, *Ann. Acad. Sci. Fenn.*, A6, 1-20, 1965.
83. Wasserburg, G.J., S.B. Jacobsen, D.J. DePaolo, M.T. McCulloch and T. Wen, Precise determination of Sm/Nd ratios, Sm and Nd isotopic abundances in standard solutions, *Geochim. et Cosochim. Acta*, 45, 2311-2323, 1981.
84. Wetherill, G.W., Radioactive decay constants and energies, In: Handbook of Physical Constants (S. Clare, ed.), *Geol. Soc. Am. Mem.*, 97, 513-519, 1966.
85. White, P.H., G.J. Wall, and F.R. Pontet, A remeasurement of the half-life of ^{235}U, *J. Nucl. Energy Pt. A and B*, 19, 33-35, 1965.
86. Wright, P.M., E.P. Steinberg and L.E. Glendenin, Half-life of samarium-147, *Phys. Rev.*, 123, 205-208, 1961.
87. Würger, E., K.P. Meyer, and P. Huber, Lebensdaver und Zerfallsschema von U^{235}, *Helv. Phys. Acta.*, 30, 157-182, 1957.

Natural Radioactivity of the Crust and Mantle

W. R. Van Schmus

1. INTRODUCTION

Radioactive elements found in the crust and mantle form the basis for several major applications in geophysics and geochemistry. Direct use of natural radionuclides and their decay products can be grouped into three main categories: (1) geochronology and cosmochronology, (2) understanding radiogenic heat production and the thermal history of the Earth, and (3) as tracers in various geologic processes, including differentiation of the Earth. The information summarized here focuses primarily on the four major, naturally occurring, radioactive nuclides ^{40}K, ^{235}U, ^{238}U, and ^{232}Th (Table 1), selected intermediate daughter products, and their applications in category 2. Geochronologic applications are covered in a separate chapter, and both geochronologic and geochemical tracer applications are well covered by Faure [6].

2. ABUNDANCE OF NATURAL RADIONUCLIDES

Compilations of K, U, and Th abundances in rocks and minerals are common, and that of Clark et al. [3] is an excellent summary of knowledge to that time. The major improvements in our understanding of these abundances since 1966 have come about through development of better analytical techniques for samples with low abundances of these elements, better understanding of the processes governing the distribution of these elements in terrestrial and extraterrestial materials, and better definition of bounding conditions (e.g., mean annual heat flow) that set limits on the abundances of these elements in the Earth. Thus, in some respects this summary will not differ significantly from earlier compilations, whereas in other respects it will present our current best estimates of the abundances involved.

Potassium is an important consitituent of the Earth. As one of the alkali metals (Li, Na, K, Rb, and Cs), with an ionic radius of ca. 1.6 angstroms, it is one of the so-called large ion lithophile (LIL) elements and tends to be concentrated in evolved crustal rocks such as granites and shales, where it is an essential constituent of several common rock-forming minerals (Table 2). Uranium, with an ionic radius of ca. 1.0 angstroms, and thorium, with an ionic radius of ca. 1.05 angstroms, are also LIL elements, but their lower overall abundances (Table 3) mean that minerals containing U or Th as essential constituents are found only as trace minerals in common rocks or as minerals in primary or secondary mineral deposits (Table 2).

In the broader context, it is not individual minerals that are important, but their host rocks. Table 3 lists K, U, and Th abundances for a variety of common crustal rock types or rock suites. Rb and Sm are two other radioactive nuclides used for geochronology, and representative abundances for these two elements are also included in Table 3, even though their contributions to general radioactivity of the crust are negligible and are not discussed further in this chapter. As is the case for minerals, the abundances of a given trace element in rocks can vary over a several orders of magnitude. The abundances given in Table 3 should therefore be considered as representative of crustal rocks and rock types in general, but caution must be used in attaching too much significance to a single example. For example, the high Th contents for G-1 and GSP-1 represent the higher end of the abundance spectrum, and the mode is probably about 10 to 20 ppm Th for felsic rocks (Table 3). Results for average crustal rock types are probably more

W. R. Van Schmus, University of Kansas, Department of Geology, Lawrence, KS 66045

Global Earth Physics
A Handbook of Physical Constants
AGU Reference Shelf 1

TABLE 1. Isotopic Abundances of K, U, and Th

Potassium			Thorium			Uranium		
Mass #	At. %	Wt. %	Mass #	At. %	Wt. %	Mass #	At. %	Wt. %
39	93.2581	92.9371	232	100	100	234	0.0057	0.0056
40	0.01167	0.01193				235	0.7200	0.7110
41	6.7302	7.0510				238	99.2743	99.2834

Isotopic abundances: ref. [18] for ^{39}K, ^{40}K, ^{41}K; ref. [6] for ^{234}U, ^{235}U, and ^{238}U.

TABLE 2. Some Typical K, U, Th - Bearing Minerals

Mineral	Nominal Composition	Abundances[a] K	U	Th
Adularia	$KAlSi_3O_8$	14.0		
Allanite	$(Ca,Ce,Y,Th)_2(Al,Fe,Mg)_3Si_3O_{12}(OH)$		*	***
Alunite	$KAl_3(SO_4)_2(OH)_6$	9.4	–	–
Apatite	$Ca_5(PO_4)_3(F,Cl,OH)$	–	*	*
Apophyllite	$KCa_4(Si_8O_{20})(OH,F)\cdot 8H_2O$	4.1	–	–
Autunite	$Ca(UO_2)_2(PO_4)_2\cdot 10\text{-}12H_2O$	–	48-50	–
Baddeleyite	ZrO_2	–	**	**
Biotite	$K(Mg,Fe)_3(AlSi_3O_{10})(OH)_2$	8-9	–	–
Carnallite	$KMgCl_3\cdot 6H_2O$	14.1	–	–
Carnotite	$K_2(UO_2)_2(VO_4)_2\cdot 3H_2O$	7.2	53	–
Glauconite	$K(Fe,Mg,Al)_2(Si_4O_{10})(OH)_2$	4.6-6.2	–	–
Hornblende	$NaCa_2(Mg,Fe,Al,)_5(Si,Al)_8O_{22}(OH)_2$	***	–	–
Jarosite	$KFe_3(SO_4)_2(OH)_6$	7.8	–	–
Lepidolite	$KLi_2Al(Si_4O_{10})(OH)_2$	7.1-8.3	–	–
Leucite	$KAlSi_2O_6$	17.9	–	–
Microcline	$KAlSi_3O_8$	14.0	–	–
Monazite	$(Ce,La,Y,Th,)PO_4$	–	**	2-20
Muscovite	$K(Al)_2(AlSi_3O_{10})(OH)_2$	9.8	–	–
Nepheline	$(Na,K)AlSiO_4$	3-10	–	–
Orthoclase	$KAlSi_3O_8$	14.0	–	–
Phlogopite	$KMg_3(AlSi_3O_{10})(OH)_2$	9.4	–	–
Pitchblende	Massive UO_2	–	88	–
Polyhalite	$K_2Ca_2Mg(SO_4)_4\cdot 2H_2O$	13.0	–	–
Sanidine	$KAlSi_3O_8$	14.0	–	–
Sphene (Titanite)	$CaTiSiO_5$	–	*	*
Sylvite	KCl	52.4	–	–
Thorianite	ThO_2	–	–	88
Thorite	$ThSiO_4$	–	***	72
Torbernite	$Cu(UO_2)_2(PO_4)_2\cdot 8\text{-}12\ H_2O$	–	32-36	–
Tyuyamunite	$Ca(UO_2)_2(VO_4)_2\cdot 5\text{-}8.5\ H_2O$	–	45-48	–
Uraninite	UO_2	–	88	–
Xenotime	YPO_4	–	***	**
Zircon	$ZrSiO_4$	–	**	**

a: Percents except as noted: *** = 0.5-3%; ** = 0.1-0.5%; * = 0.001-0.1%. See also [4, Appendix].

TABLE 3. K, U, and Th Abundances in the Earth

Rock or System	K (%)	U (ppm)	Th (ppm)	Rb (ppm)	Sm (ppm)	Ref.
USGS G-1 granite	4.45	3.4	50	220	8	7
USGS G-2 granite	3.67	3.0	24	168	7	7
USGS RGM-1 rhyolite	3.49	5.8	13	154		5,15
USGS STM-1 nepheline syenite	3.54	9.1	27	113		5,15
USGS GSP-1 granodiorite	4.50	2.0	104	254	27	7
USGS QLO-1 quartz latite	2.90	5.8	13	68		5,15
USGS AGV-1 andesite	2.35	1.9	6.4	67	6	7
USGS BCR-1 basalt	1.38	1.7	6.0	47	6.7	7
USGS W-1 diabase	0.52	0.6	2.4	21	4	7
USGS BHVO-1 basalt	0.43	0.5	0.9	9		5,15
USGS PCC-1 peridotite	0.001	0.005	0.01	0.063	0.008	7
USGS DTS-1 dunite	0.001	0.004	0.01	0.053	0.004	7
USGS MAG-1 marine mud	2.96	2.8	12.2	186		5,15
USGS SCo-1 shale	2.20	3.1	9.5	122		5,15
USGS SDC-1 mica schist	2.71	3.1	11.4	129		5,15
Avg Low-Ca granite	4.20	4.7	20	170	7.1	21
Avg. basalt	0.83	0.9	2.7	30	6.9	21
Avg. ultramafic rocks	0.003	0.001	0.004	0.13	1.1	21
Avg. shale	2.66	3.7	12	140	7.0	21
Avg. sandstone	1.07	1.7	5.5	60	1.9	21
Avg. carbonate	0.27	2.2	1.7	3	0.6	21
Avg. upper continental crust	2.7	2.5	10.5	110	5.6	19
" " " "	2.8	2.80	10.7	112	4.5	20, Table 2.15
Lower continental crust	0.28	0.28	1.06	5.3	3.17	20, Table 4.4
Avg. continental crust	1.27	1.25	4.8	42	3.7	20, Table 3.3
" " "	0.91	0.91	3.5	32	3.5	20, Table 3.5
Oceanic crust (basaltic layer)	0.1250	0.10	0.22	2.2	3.3	20, Table 11.6
Bulk Silicate Earth (BSE)	0.0240	0.021	0.084	0.635	0.444	14, Table 1
(= primitive mantle)	0.0231	0.021		0.742	0.52	23, Table 2
	0.0258	0.0203	0.0813	0.535	0.387	10, Table 1
	0.0180	0.018	0.064	0.55	0.347	20, Table 11.3
	0.0266	0.0208			0.380	9
Average BSE	*0.0235*	*0.0202*	*0.0764*	*0.616*	*0.416*	
Bulk Earth	0.0200	0.020	0.074			22, Table 7
	0.0159	0.014	0.052			BSE x 0.675
C1 Chondrites (volatile free)	0.0854	0.0122	0.0425	3.45	0.231	1, recal. in 20

representative, but even in some of these cases uncertainties of a factor of 2 or more are possible for trace constituents.

Even though K, U, and Th are chemically dissimilar from each other, their LIL character means that all three elements tend to follow one another on average when bulk components of the Earth are considered. These relationships have been used extensively in estimating the bulk composition of the Earth and its major sub-units (Table 3). Thus, the K/U ratio for the bulk Earth, primitive mantle, and continental crust is estimated at ca. 1.0 to 1.3 x 10^4 [24, 11], and the Th/U ratio is about 3.7 to 4.0. These relationships can, in turn, be used with other geochemical or geophysical constraints to put realistic limits on the abundances of these elements in the bulk Earth. The three main ways of doing so are (a) cosmochemical arguments [e.g., 23, 16], (b) assuming that most (ca. 75 ± 25%) of the Earth's radiogenic ^{40}Ar is now

in the atmosphere and was produced by the decay of ^{40}K, and (c) comparison with mean annual terrestrial heat flow [e.g., 9]. All of these have significant uncertainties associated with them, but they nontheless yield comparable and consistent results, giving substantial confidence in the values for bulk Earth given in Table 3.

3. DECAY MODES

3.1. ^{40}K Decay.

^{40}K undergoes branching decay to ^{40}Ca (via β^-) and ^{40}Ar (via electron capture), both of which are stable; the decay scheme for ^{40}K is shown in Figure 1. The total decay constant, λ, is 5.543×10^{-10} yr^{-1} [18], with a 10.5 percent probability of decaying primarily by electron capture to ^{40}Ar ($\lambda_{EC} = 0.581 \times 10^{-10}$ yr^{-1}) and an 89.5 percent probability of decaying to ^{40}Ca via β^- emission ($\lambda\beta = 4.962 \times 10^{-10}$ yr^{-1}). All of the decay to ^{40}Ca is directly to the ground state, but most of the decay to ^{40}Ar is to an excited state, followed by subsequent isomeric decay to stable ^{40}Ar with emission of 1.46 MeV γ-rays. Kelley et al. [12] determined the spectrum of β^- particles emitted in the decay to ^{40}Ca, obtaining a mean energy of 0.60 MeV (Fig. 2), or about 45% of the total (1.32 MeV); the remainder, 0.72 MeV (55%), is carried away by neutrinos. This spectrum is significantly different from the average for β^- decay, in which about 2/3 of the energy is carried away by neutrinos [8].

3.2. U and Th Decay Series

The isotopes ^{232}Th, ^{235}U, and ^{238}U do not decay directly to a stable product, but achieve ultimate stability through a succession of α and β^- decays, including several minor closed branches (e.g., branches that converge a step later to the same subsequent product). Figure 3 and Tables 4-6 summarize the principal steps in the uranium and thorium decay series; full details on each series can be derived from more detailed references [e.g., 13]. The exact (geochronologic) decay constants for the parent isotopes are: $\lambda_{238} = 1.55125 \times 10^{-10}$ yr^{-1}; $\lambda_{235} = 9.8485 \times 10^{-10}$ yr^{-1}; and $\lambda_{232} = 4.9475 \times 10^{-11}$ yr^{-1} [18].

Within the ^{238}U decay series there are significant intermediate decay products that exist naturally in secular equilibrium. The more notable are ^{234}U, ^{230}Th, and ^{231}Pa, which are useful in geochronology [6], ^{226}Ra, which has a variety of uses, and ^{222}Rn, which has potentially serious environmental consequences [4, ch. 12].

3.3. Gamma Radiation

The major penetrative natural radioactivity is γ-radiation that accompanies many α and β^- transitions.

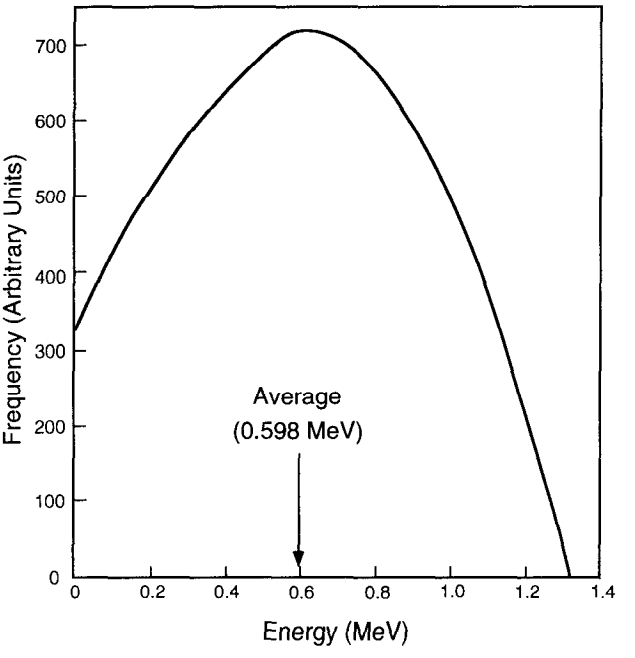

Fig. 1: Simplified decay scheme for ^{40}K based on decay constants used for geochronology [18] and energy (mass) differences between ^{40}K and ^{40}Ca, ^{40}Ar.

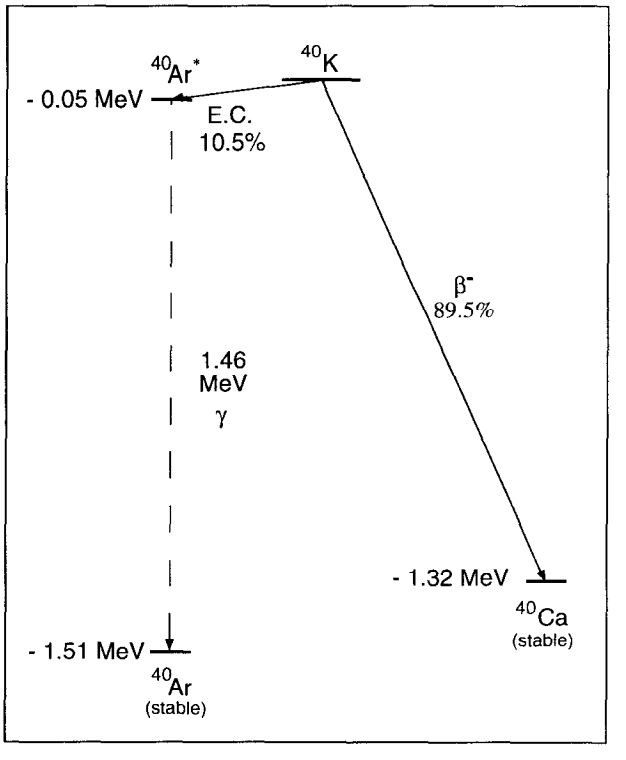

Fig. 2: Spectrum of beta-particle energies for the decay of ^{40}K to ^{40}Ca [12].

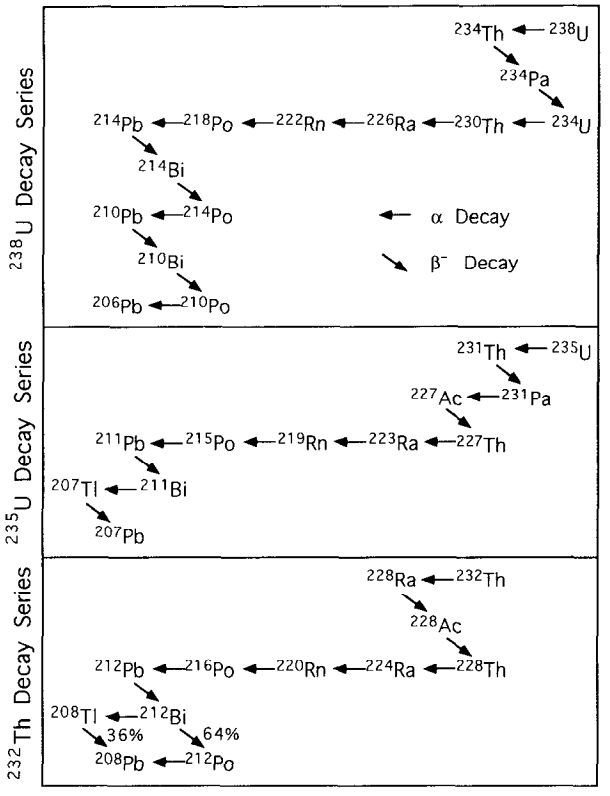

Fig. 3: Chart showing the principal steps in the decay series for ^{238}U, ^{235}U, and ^{232}Th (Tables 4 through 6). Minor branching steps have been omitted.

TABLE 4. Principal Steps in the ^{238}U Decay Series

Step	Parent	Half-life	Decay	Daughter
1	^{238}U	4.47 x 10^9 y	Alpha	^{234}Th
2	^{234}Th	24.1 d	Beta	^{234}Pa
3	^{234}Pa	1.17 m	Beta	^{234}U
4	^{234}U	2.44 x 10^5 y	Alpha	^{230}Th
5	^{230}Th	7.7 x 10^4 y	Alpha	^{226}Ra
6	^{226}Ra	1.60 x 10^3 y	Alpha	^{222}Rn
7	^{222}Rn	3.82 d	Alpha	^{218}Po
8	^{218}Po	3.05 m	Alpha	^{214}Pb
9	^{214}Pb	26.8 m	Beta	^{214}Bi
10	^{214}Bi	19.8 m	Beta	^{214}Po
11	^{214}Po	1.64 x 10^{-4} s	Alpha	^{210}Pb
12	^{210}Pb	22.3 y	Beta	^{210}Bi
13	^{210}Bi	5.01 d	Beta	^{210}Po
14	^{210}Po	138.4 d	Alpha	^{206}Pb (stable)

TABLE 5. Principal Steps in the ^{235}U Decay Series

Step	Parent	Half-life	Decay	Daughter
1	^{235}U	7.04 x 10^8 y	Alpha	^{231}Th
2	^{231}Th	25.52 h	Beta	^{231}Pa
3	^{231}Pa	3.28 x 10^4 y	Alpha	^{227}Ac
4	^{227}Ac	21.77 y	Beta	^{227}Th
5	^{227}Th	18.72 d	Alpha	^{223}Ra
6	^{223}Ra	11.43 d	Alpha	^{219}Rn
7	^{219}Rn	3.96 s	Alpha	^{215}Po
8	^{215}Po	1.78 x 10^{-3} s	Alpha	^{211}Pb
9	^{211}Pb	36.1 m	Beta	^{211}Bi
10	^{211}Bi	2.14 m	Alpha	^{207}Tl
11	^{207}Tl	4.77 m	Beta	^{207}Pb (stable)

Table 6. Principal Steps in the ^{232}Th Decay Series

Step	Parent	Half-life	Decay	Daughter
1	^{232}Th	1.40 x 10^{10} y	Alpha	^{228}Ra
2	^{228}Ra	5.75 y	Beta	^{228}Ac
3	^{228}Ac	6.13 h	Beta	^{228}Th
4	^{228}Th	1.913 y	Alpha	^{224}Ra
5	^{224}Ra	3.66 d	Alpha	^{220}Rn
6	^{220}Rn	55.6 s	Alpha	^{216}Po
7	^{216}Po	0.15 s	Alpha	^{212}Pb
8	^{212}Pb	10.64 h	Beta	^{212}Bi
9a	^{212}Bi	60.6 m	Beta	^{212}Po (64%)
9b	^{212}Bi	60.6 m	Alpha	^{208}Tl (36%)
10a	^{212}Po	2.98 x 10^{-7} s	Alpha	^{208}Pb (stable)
10b	^{208}Tl	3.053 m	Beta	^{208}Pb (stable)

This radiation is widely used in geophysical and geochemical prospecting, including well logging. The major γ-radiations from K, U and Th are summarized in Table 7 and Figure 4. No γ-rays for ^{235}U are given because its low natural abundance ($^{238}U/^{235}U$ = 137.88 [18]) means that the intensity of its major γ-rays would still be minor compared to those from ^{238}U, and hence are not detectable for all practical purposes. Of the γ-rays shown in Table 7, the main ones used as diagnostic radiations are 1.461 MeV (^{40}K), 1.765 MeV (^{238}U), and 2.615 MeV (^{232}Th); most of the others are either too low in abundance for easy measurement by routine methods or

TABLE 7. Gamma Rays from Major Natural Nuclides[a]

Parent	Nuclides	Energy (MeV)	Freq.[b]
^{40}K	^{40}K	1.461	11
^{232}Th	^{228}Ac	0.210	4
	^{212}Pb	0.239	43
	^{224}Ra	0.241	5
	^{208}Tl	0.277	3
	^{212}Pb	0.300	3
	^{228}Ac	0.339	12
	^{228}Ac	0.463	5
	^{208}Tl	0.511	8
	^{208}Tl	0.583	31
	^{212}Bi	0.727	6
	^{208}Tl	0.860	4
	^{228}Ac	0.911	27
	^{228}Ac	0.964	5
	^{228}Ac	0.969	16
	^{228}Ac	1.588	3
	^{208}Tl	2.615	36
^{238}U	^{226}Ra	0.186	3
	^{214}Pb	0.242	6
	^{214}Pb	0.295	19
	^{214}Pb	0.352	37
	^{214}Bi	0.609	46
	^{214}Bi	0.768	5
	^{214}Bi	0.934	3
	^{214}Bi	1.120	15
	^{214}Bi	1.238	6
	^{214}Bi	1.378	4
	^{214}Bi	1.408	3
	^{214}Bi	1.730	3
	^{214}Bi	1.765	16
	^{214}Bi	2.204	5

[a]Compiled from [13]; only energies > 0.100 MeV tabulated.

[b]Events per 100 decays of primary parent; secular equilibrium assumed.

overlap radiations from another element (e.g., 0.58 and 0.61 MeV), although in certain applications they can be used. Durrance [4, ch. 9] gives a detailed review of geochemical applications for γ-ray spectra.

4. RADIOGENIC HEAT PRODUCTION

In terms of the geophysical behavior of the earth, one of the most important applications of radionuclides is in modeling the thermal state and thermal history of the earth and planets. In this context it is necessary to know the specific heat production of the major heat-producing radionuclides: ^{40}K, ^{232}Th, ^{235}U, and ^{238}U.

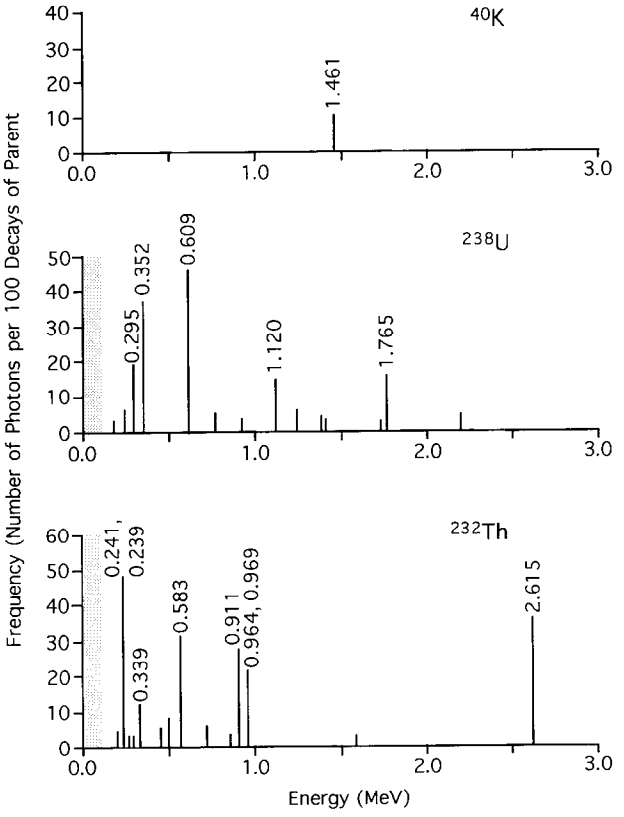

Fig. 4: Principal gamma-rays emitted during the decay of ^{40}K, ^{238}U, and ^{232}Th (Table 7). Spectra include gamma-rays from intermediate daughter products in secular equilibrium with parent for ^{238}U and ^{232}Th.

In the radioactive decay process, a portion of the mass of each decaying nuclide is converted to energy. Most of this is the kinetic energy of emitted alpha or beta particles or of electromagnetic radiation (γ-rays), which is fully absorbed by rocks within the Earth and converted quantitatively to heat. For β^- decays, however, part of the energy is carried by emitted neutrinos. Because neutrinos are not easily captured, they pass completely out of the earth, and that portion of the decay energy is lost to space. In determining the radiogenic heat production of a particular radionuclide, it is therefore necessary to correct for the loss of neutrino energy by β^- emitters.

All four of the major heat producing isotopes involve β^- decay. For ^{40}K there is the β^- decay branch to ^{40}Ca. Evaluation of the mean β^- energy for this decay branch was based on the β^- spectrum measured by Kelly et al.

TABLE 8. Specific Heat Production for Major Natural Radionuclides

Element:	Potassium	Thorium	Uranium	
Isotope:	^{40}K	^{232}Th	^{235}U	^{238}U
Isotopic abundance (weight percent)	0.0119	100.00	0.71	99.28
Decay constant, λ (year^{-1})	5.54×10^{-10}	4.95×10^{-11}	9.85×10^{-10}	1.551×10^{-10}
Total decay energy (MeV/decay)	1.340 [a]	42.66 [b]	46.40 [b]	51.70 [b]
Beta decay energy (MeV/decay)	1.181 [a]	3.5 [b]	3.0 [b]	6.3 [b]
Beta energy lost as neutrinos (MeV/decay)	0.650 [c]	2.3 [d]	2.0 [d]	4.2 [d]
Total energy retained in Earth (MeV/decay)	0.690	40.4	44.4	47.5
Specific isotopic heat production (cal/g-year)	0.220	0.199	4.29	0.714
" " " " (μW/kg)	29.17	26.38	568.7	94.65
Specific elemental heat production (cal/g-year)	2.6×10^{-5}	0.199	0.740	
" " " " (μW/kg)	3.45×10^{-3}	26.38	98.10	

[a]Averaged for branching decay: 89.5% β^- @ 1.32 MeV + 10.5% E.C. @ 1.51 MeV.
[b]Summed for entire decay series.
[c]Based on mean decay energy for β^- of 0.60 MeV; 55% of total β^- energy lost as neutrinos [12].
[d]Assumed average neutrino loss = 2/3 of total β^- energy [8, p. 52].

TABLE 9. Present Radiogenic Heat Production in Selected Rock Units

	Annual heat production[a]			
Rock unit[b]	Due to K	Due to Th	Due to U	Total
GSP-1 "granodiorite"	1.17	20.70	1.48	23.35[c]
G-1 "granite"	1.16	9.95	2.52	13.63
Av upper continental crust	0.7	2.09	1.85	4.64
AGV-1 "andesite"	0.61	1.27	1.41	3.29
Av continental crust	0.33	0.50	0.74	1.56
BHVO-1 "oceanic basalt"	0.11	0.18	0.37	0.66
PCC-1 "peridotite"	0.0003	0.0020	0.0037	0.0060
Bulk Earth	0.0052	0.0147	0.0148	0.0347

[a]In μcal/g-year; multiply x 0.004184 for J/kg-year.
[b]Elemental abundances from Table 7.
[c]Not a typical granodiorite, but it illustrates natural range due to granitic rocks high in Th or U.

[12]. The β^- emitters in the ^{232}Th, ^{235}U, and ^{238}U decay series (Tables 4 to 6) constitute only a small fraction of their total decay energy, so individual determinations of β^- spectra were not used to determine neutrino energy loss. Instead, the general relationship that, on average, neutrinos represent 2/3 of the decay energy for β^- decay [8 p. 52] was used. Table 8 [after 22] summarizes the information needed to determine specific heat production and the resulting values; this compilation was based on the data of Lederer and Shirley [13] for individual nuclides except that the ratio of electron capture to beta decay for ^{40}K is based on the recommended geochronological decay constants for that isotope [18]. Total decay energies were based on the mass differences between the starting radionuclides and their stable end products ($\Delta E = \Delta mc^2$). Perhaps one of the most interesting results of this determination of specific heat production is that the refined values listed in Table 8 do not differ significantly from those reported nearly 40 years ago [2; see also 17, ch. 7] and Stein [this volume]. The results are given in both the traditional c.g.s. units (μcal/g-yr) as well as in SI units (μW/kg).

Table 9 represents some typical ranges of specific heat production for various rock types, ranging from U,

TABLE 10. Past Heat Production in the Bulk Earth[a]

Time[b] (Ga)	Due to K		Due to Th		Due to U		Total	
	Abs.[c]	Rel.[d]	Abs.	Rel.	Abs.	Rel.	Abs.	Rel.
0.0	5.2	0.15	14.7	0.42	14.8	0.43	34.7	1.00
0.5	6.9	0.20	15.1	0.44	16.3	0.47	38.3	1.10
1.0	9.1	0.26	15.5	0.45	18.2	0.52	42.8	1.23
1.5	12.0	0.35	15.9	0.46	20.6	0.59	48.5	1.40
2.0	15.9	0.46	16.3	0.47	23.7	0.68	55.9	1.61
2.5	20.9	0.60	16.7	0.48	28.0	0.81	65.6	1.89
3.0	27.6	0.80	17.1	0.49	34.3	0.99	79.0	2.28
3.5	36.4	1.05	17.5	0.50	43.5	1.25	97.4	2.81
4.0	48.1	1.39	17.9	0.52	57.7	1.66	123.7	3.56
4.5	63.4	1.83	18.4	0.53	79.7	2.30	161.5	4.65

[a]Assumed present abundances: K = 200 ppm, Th = 74 ppb, U = 20 ppb (K: U : Th = 10,000 : 1 : 3.7).

[b]Billions of years ago.

[c]Abs. = absolute in 10^{-9} cal/g-year; multiply x 0.004184 for J/kg-year.

[d]Rel. = relative to present total.

Th-rich granite (atypical) through intermediate to mafic and ultramafic rock types. One should keep in mind, with regard to Tables 3 and 9, that attempts to model the thermal history of terrestrial components are only approximations; the abundances of K, U, and Th for any specific case (e.g., "continental crust") are not known well enough to permit precise interpretations.

Table 10 and Figure 5 summarize past heat production in the whole earth for *one* assumed bulk composition [22]. For the model used, the Th/U ratio is probably accurate to better than 10%, but the K/U ratio may be somewhat low (cf. Table 3), and the absolute concentrations for some elements could also be uncertain to a factor of 50% or more. Thus, the data in Table 10 and Figure 5 should only be considered as representative of possible past histories and not accepted as the best model. However, they do give a good indication of the relative contributions of K, U, Th to heat production in the earth now and in the past.

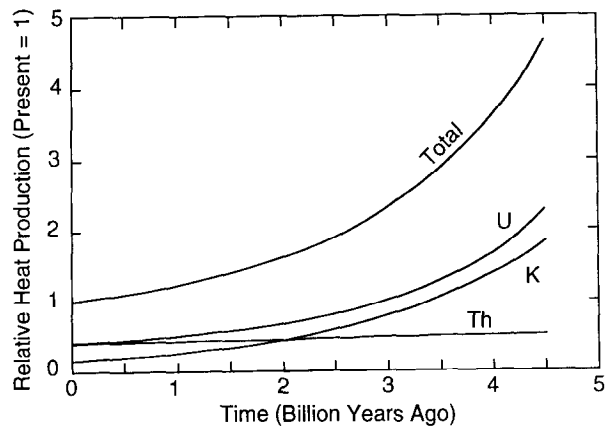

Fig. 5. Relative heat production within the Earth during the past. Projected back in time using data from Tables 9 and 10.

REFERENCES

1. Anders, E., and M. Ebihara, Solar-system abundances of the elements, *Geochim. Cosmochim. Acta, 46,* pp. 2363-2380, 1982.
2. Birch, F., Heat from radioactivity, in *Nuclear Geology*, edited by H. Faul, pp. 148-174, John Wiley & Sons, New York, 1954.
3. Clark, S. P., Jr., Z.E. Peterman, and K. S. Heier, Abundances of uranium, thorium, and potassium, in *Handbook of Physical Constants,* Revised Edition, Geological Society of America, Memoir 97, edited by S. P. Clark, Jr., pp. 521-541, GSA, Boulder, CO, 1966.
4. Durrance, E. M., *Radioactivity in Geology: Principles and applications*, 441 pp., Ellis Horwood Ltd., Chichester (U.K.), 1986.
5. Fabbi, B. B. and L. F. Espos, X-ray fluorescence analysis of 21 selected major, minor and trace elements in eight new USGS standard rocks, in *Descriptions and Analyses of Eight New USGS Rock Standards, U. S. Geological Survey Prof. Paper 840,*

edited by F. J. Flanagan, pp. 89-93, USGS, Washington, D.C., 1976.
6. Faure, G., *Principles of Isotope Geology*, 2nd ed., 589 pp., John Wiley & Sons, New York, 1986
7. Flanagan, F. J., 1972 compilation of data on USGS standards, in *Descriptions and Analyses of Eight New USGS Rock Standards, U. S. Geological Survey Prof. Paper 840,* edited by F. J. Flanagan, pp. 131-183, USGS, Washington, D.C., 1976.
8. Friedlander, G., J. W. Kennedy, and J. M. Miller, *Nuclear and Radiochemistry*, 585 pp., John Wiley & Sons, New York, 1964.
9. Hart, S. R., and A. Zindler, In search of a bulk-Earth composition. *Earth Plan. Sci. Lett., 57*, pp. 247-267, 1986.
10. Hofmann, A. W., Chemical differentiation of the Earth: the relationship between mantle, continental crust, and oceanic crust, *Earth Plan. Sci. Lett., 90,* pp. 297-314, 1988.
11. Jochum, K. P., N. T. Arndt, and A. W. Hofmann, Nb/Th in komatiites: implications for komatiite genesis and crust-mantle evolution, *Earth Plan. Sci. Lett., 107*, pp. 272-289, 1983.
12. Kelly, W. H., G. B. Beard, and R. A. Peters, The beta decay of K40, *Nucl. Phys., 11*, pp. 492-498, 1959.
13. Lederer, C. M. and V. S. Shirley (Ed.), *Table of Isotopes*, 7th ed., John Wiley & Sons, New York, 1523 pp., 1978.
14. McDonough, W.F., S.-S. Sun, A. E. Ringwood, E. Jagoutz, and A. Hofmann, Potassium, rubidium, and cesium in the Earth and Moon and the evolution of the mantle of the Earth, *Geochim. Cosmochim. Acta, 56,* pp. 1001-1012, 1992.
15. Millard, H. T., Jr., Determination of uranium and thorium in USGS standard rocks by the delayed neutron technique, in *Descriptions and Analyses of Eight New USGS Rock Standards, U. S. Geological Survey, Prof. Pap. 840,* edited by F. J. Flanagan, pp. 61-65, USGS, Washington, D.C., 1976.
16. Morgan, J. W., and E. Anders, Chemical composition of the Earth, Venus, and Mercury, *Proc. Natl. Acad. Sci. U.S., 77*, pp. 6973-6977, 1980.
17. Stacey, F. D., *Physics of the Earth,* 2nd ed., 414 pp., John Wiley and Sons, 1977.
18. Steiger, R. H. and E. Jäger, Subcommission on Geochronology: convention on the use of decay constants in geo- and cosmochronology, *Earth Planet. Sci. Lett., 36*, pp. 359-362, 1977.
19. Taylor, S. R., Island arc models and the composition of the continental crust, in *Island Arcs, Deep Sea Trenches, and Back-Arc Basins*, edited by M. Talwani and W. C. Pitman, pp. 325-335, American Geophysical Union, Washington, D. C., 1977.
20. Taylor, S. R., and S. M. McClennan, *The Continental Crust: Its Composition and Evolution*, 312 pp., Blackwell Scientific Publications, Oxford, 1985.
21. Turekian, K. K., *Chemistry of the Earth*, Holt, 131 pp., Rinehart & Winston, New York, 1972.
22. Van Schmus, W. R., Radioactivity properties of minerals and rocks, in *Handbook of Physical Properties of Rocks*, vol. III, edited by R. S. Carmichael, pp. 281-293, CRC Press, Boca Raton, Florida, 1984.
23. Wänke, H., G. Dreibus, and E. Jagoutz, Mantle chemistry and accretion history of the Earth, in *Archean Geochemistry*, edited by A. Kröner, G.N. Hanson, and A.M. Goodwin, pp. 1-24, Springer-Verlag, New York, 1984.
24. Wasserburg, J. G., G. J. F. MacDonald, F. Hoyle, and W. A., Fowler, Relative contributions of uranium, thorium, and potassium to heat production in the Earth, *Science, 143*, pp. 465-467, 1964.

Stable Isotope Distribution: Variations from Temperature, Organic and Water-Rock Interactions

Robert E. Criss

1. INTRODUCTION

Several million measurements of the stable isotope ratios of oxygen, hydrogen, and carbon in natural substances have been made. The intent of this section is to encapsulate as much information as possible about the nature and distribution of these isotopes, and to direct the reader to the most useful sources of additional information.

2. BASIC PRINCIPLES

2.1. Elementary Definitions

Every element consists of an assemblage of different types of atoms, termed nuclides, each constituted of protons, neutrons and electrons. Even though the atomic number Z, representing the nuclear charge and the number of protons, is the same for all nuclides of a given element, the number (N) of neutrons may vary. Thus the mass number A, an integer represented by the sum of Z + N, will also vary among the nuclides comprising that element. Nuclides of an element that have different values of A are termed *isotopes*, and are represented by the appropriate chemical symbol preceded by a superscript indicating the mass number. For example, a rare stable isotope of oxygen, called oxygen-18, has 8 protons and 10 neutrons, and is denoted by the symbol ^{18}O.

R. E. Criss, Washington University, St. Louis, Department of Earth and Planetary Sciences, Box 1169, One Brookings Drive, St. Louis, MO 63130-4899

Global Earth Physics
A Handbook of Physical Constants
AGU Reference Shelf 1

Properties of the approximately 2500 known nuclides, most of which are artificial radionuclides with short half lives, have been tabulated (e.g., Walker et al., 1989). Only about 270 nuclides are stable, and these are classified as being either radiogenic or nonradiogenic, depending on whether they are, or are not, the daughter products of radioactive atoms that underwent nuclear decay, respectively. Nonradiogenic stable nuclides, a group including all atoms discussed below, have been present since nucleosynthesis.

2.2. Natural Abundance

The masses and natural abundances of stable isotopes are generally determined by sensitive mass spectrometers. Table 1 reports the atomic weights for H, C and O isotopes in atomic mass units (amu, where 1 amu is defined as 1/12 the mass of an atom of ^{12}C), and their abundances in atom %.

The atomic weight of the element (bold #'s in Table 1), which is the quantity one finds in an ordinary Periodic Table, is not a fundamental physical quantity but rather the sum of the masses of the constituent isotopes weighted by their abundances. In contrast, the atomic weights of the individual nuclides are intrinsic. Isotopes with an odd mass number tend to have lower abundances than those with an even mass number, although ^{1}H is an exception.

If the abundances of the stable isotopes were truly invariant, their measurement would have very limited application. In fact, the abundances given above are averages, and in detail the values vary from sample to sample. This implies, of course, that the atomic weight of these elements will also vary slightly from sample to sample.

TABLE 1. Atomic Weights and Abundances of the Stable H, C and O Isotopes (ref. 79)

ELEMENT	ISOTOPE	ATOMIC WEIGHT (amu)	ABUNDANCE (atom %)
HYDROGEN (Z=1)		**1.0079**	
	^{1}H (Protium)	1.007825	99.985
	^{2}H (D, for Deuterium)	2.014102	0.015
CARBON (Z=6)		**12.011**	
	^{12}C	12.00000	98.90
	^{13}C	13.00335	1.10
OXYGEN (Z=8)		**15.9994**	
	^{16}O	15.994915	99.76
	^{17}O	16.999131	0.04
	^{18}O	17.999160	0.20

2.3. Notation and Standards

Natural variations in the abundance of the stable nonradiogenic isotopes are normally rather small, and sensitive electronic devices, called isotope ratio mass spectrometers, have been devised to make precise determinations. For routine measurements of H, C, and O isotopes, such instruments singly ionize, accelerate and collimate a beam of either CO_2 or H_2 gas, which is then passed through a magnetic field to resolve the beam into distinct molecular beams that contain the different isotopes. The intensities of the resolved beams are then electronically counted and compared. A switching mechanism is employed that allows rapid comparison of the intensities of the sample beams with those of a known gas standard. This method permits the isotopic constitution of the unknown to be determined by the *difference* in intensities from those of the standard, and circumvents the necessity of making measurements of absolute intensities for each sample, which are more difficult.

Given the above, it is natural to represent the difference in isotopic composition of the sample (x) and standard (std) by dimensionless δ-values (termed "delta-values"), defined by the formula:

$$\delta \equiv 1000 \frac{R_x - R_{std}}{R_{std}} \qquad (1)$$

where the R's refer to the isotope ratios, either D/H, $^{13}C/^{12}C$, or $^{18}O/^{16}O$, as appropriate. Depending on the element of interest, this formula defines the δD (or δ^2H), $\delta^{13}C$, or $\delta^{18}O$ values. The factor of 1000 converts the δ-values to per mil (‰). However, some workers use a factor of 100 when reporting hydrogen isotope data, in which case the δD values are given in percent (%). Thus equation 1 specifically becomes one of the following:

$$\delta^{18}O \equiv 1000\left[\frac{\left(\frac{^{18}O}{^{16}O}\right)_x}{\left(\frac{^{18}O}{^{16}O}\right)_{SMOW}} - 1\right] \qquad (2a)$$

$$\delta D \equiv 1000\left[\frac{\left(\frac{^{2}H}{^{1}H}\right)_x}{\left(\frac{^{2}H}{^{1}H}\right)_{SMOW}} - 1\right] \qquad (2b)$$

$$\delta^{13}C \equiv 1000\left[\frac{\left(\frac{^{13}C}{^{12}C}\right)_x}{\left(\frac{^{13}C}{^{12}C}\right)_{PDB}} - 1\right] \qquad (2c)$$

The isotopic standards used in equation 2 are those most widely used, and have been chosen for convenience. The most useful standard for oxygen and hydrogen is Standard Mean Ocean Water (SMOW), defined by Craig (1961a). That for carbon is a Cretaceous belemnite from the Peedee Formation of North Carolina (PDB; Craig, 1957; Friedman and O'Neil, 1977).

It is commonly necessary to convert the δ-value of a sample ("X") measured relative to one isotopic standard ("S1") to that which would be measured relative to another ("S2"). This conversion is approximately made by adding the per mil difference, $\delta_{S2}S1$ between the two standards, but is exactly accomplished with the standard conversion identity (Craig, 1957):

$$\delta_{S2}X \equiv \delta_{S1}X + \delta_{S2}S1 + \frac{1}{1000}\left(\delta_{S1}X\right)\left(\delta_{S2}S1\right) \qquad (3)$$

For example, the Peedee belemnite is commonly used as an alternative $^{18}O/^{16}O$ standard for carbonates. This oxygen standard is also called PDB, but will not be utilized in this paper. Thus, a $\delta^{18}O$ measurement of calcite reported on the PDB scale may be readily converted to the SMOW scale, or vice versa, with the relationship (Friedman and O'Neil, 1977):

$$\left(\delta^{18}O_x\right)_{SMOW} = 1.03086\left(\delta^{18}O_x\right)_{PDB} + 30.86 \qquad (4)$$

2.4. Conservation of Mass

Conservation of mass in an n-component isotopic system may be readily taken into account with the relation:

$$\delta_{system} \equiv \sum_{i=1}^{n} X_i \delta_i, \quad \text{where} \quad \sum_{i=1}^{n} X_i \equiv 1 \qquad (5)$$

Here the X_i and δ_i respectively represent the mole fractions and δ-values for the element of interest in each constituent phase. This simple approximation, which for the H, C and O isotopes is very accurate, has numerous applications (Gregory et al., 1989). For example, if two or more different samples are mixed in a bulk ratio defined by the X_i, then δsystem simply becomes the δ-value of the resultant mixture. In other cases, such as for a redistribution of isotopes among the different phases that constitute a closed isotopic system, the value of δsystem will be invariant even though the individual δ_i values may all vary.

2.5. Isotopic Fractionation

2.5.1. Fractionation factors. A number of processes can cause the isotopes of a given element to vary in relative abundance, or fractionate, among different chemical phases or even among the separated parts of an original homogeneous phase. The magnitudes of these variations are observed to be largest for the light elements, for which the relative difference in atomic mass between the common (m) and rare (m*) isotopes, (m*-m)/(mm*), are largest (Bigeleisen, 1965). Isotopic fractionation effects also tend to be largest for elements that form covalent bonds, with the heavy isotope preferentially concentrating in the compound that bonds the element most strongly (Bigeleisen, 1965; O'Neil, 1986).

The quantitative description of this isotopic partitioning between two phases, A and B, is generally made in terms of the isotopic fractionation factor, α, defined as:

$$\alpha_{A\text{-}B} \equiv R_A/R_B \qquad (6)$$

These factors can refer to partitioning produced by equilibrium or kinetic processes, or to some combination. This fundamental definition may be recast in terms of the δ-values of phase A and phase B provided that these are reported relative to the same isotopic standard:

$$\alpha_{A\text{-}B} \equiv \frac{1000 + \delta_A}{1000 + \delta_B} \qquad (7)$$

This important and exact relation allows one to calculate the apparent (i.e., measured) fractionation factor from the δ-values of two associated phases, or to predict the δ-value of one phase from that of another if equilibrium has been attained and if the appropriate fractionation factor is known.

Values of α tend to be close to unity for processes that fractionate the carbon and oxygen isotopes, with most values being in the range of 1.001 to 1.040. Values for hydrogen may also be similar to unity but in some cases are considerably larger, owing to the great relative mass difference between protium and deuterium. For the usual circumstance where $\alpha \sim 1$, equation 7 becomes:

$$\Delta_{A\text{-}B} \equiv \delta_A - \delta_B \cong 1000\,(\alpha_{A\text{-}B} - 1) \cong 1000 \ln \alpha_{A\text{-}B} \qquad (8)$$

The quantity $\delta_A - \delta_B$ is defined as $\Delta_{A\text{-}B}$ ("big delta") and provides a convenient but rough estimate of the "fractionation" between the two phases. Thus, if δ_A were

+15.0 and δ_B were -5.0 per mil relative to some standard, a geochemist would state that "there is a 20 per mil fractionation between phases A and B" (eq. 8), but the actual value of α_{A-B} would be close to 1.0201 (eq. 7). An alternate definition of Δ_{A-B} is $1000\ln\alpha_{A-B}$, which is also approximately equal to $\delta_A - \delta_B$ if α_{A-B} is close to unity.

2.5.2. Equilibrium fractionation. If two substances containing a light element comprising different stable isotopes are in isotopic equilibrium, they normally will not have identical isotope ratios. These fractionation effects are in most cases too small to be accurately calculated from ordinary thermodynamic data. However, Urey (1947) was able to use statistical thermodynamics and the known vibrational frequencies of ordinary and isotopically-substituted molecules to accurately predict the isotopic fractionation factor, α^{eq}, for many pairs of different gases in equilibrium. This work established that α^{eq} varies with absolute temperature (T). This discovery allowed Urey to suggest the paleotempèrature method, which has now become a standard tool for research on past climates and on the formation of rocks and ore deposits.

In the most straightforward cases, Urey's theory indicates that $\ln\alpha^{eq}$ is a linear function of 1/T at low temperatures and of $1/T^2$ at high temperatures, ultimately approaching zero fractionation ($\Delta = 0$; i.e., $\alpha=1$) at infinite temperature (Urey, 1947; see Criss, 1991). In many real cases, however, the variations of α^{eq} with temperature are more complicated (Stern et al., 1968). No dependence of α^{eq} with pressure has been found, probably because the nucleus constitutes only about one-trillionth of the atomic volume, so that addition of neutrons will negligibly affect the atomic volume and the electron shell configuration.

Some fractionation factors of geologic interest are given in Table 2 and shown in Figure 1. The coefficients refer to experimentally-determined equations of the form, where T is in Kelvins:

$$1000 \ln \alpha^{eq} = C_1 + C_2/T + C_3/T^2 \qquad (9)$$

Such empirical equations generally apply only over restricted ranges in temperature. Typically, C_1 and C_2 are zero for most solid-solid reactions, probably because the vibrational frequencies of solids are low so that the high

TABLE 2: Some Isotopic Fractionation Factors of Geologic Interest (see eq. 9)

Type	Phase A	Phase B	C_1	$C_2 \times 10^3$	$C_3 \times 10^6$	T°C range	Ref.
D/H	Water	Water Vapor	52.612	-76.248	24.844	-20° to +50°	50
$^{13}C/^{12}C$	HCO_3^-	CO_2(g)	-24.10	9.552	0	5° to 125°	51, 31
$^{18}O/^{16}O$	Water	Water Vapor	-2.0667	-0.4156	1.137	0° to 100°	50
$^{18}O/^{16}O$	CO_2(g)	Water	-15.19	16.60	0	0° to 100°	31
$^{18}O/^{16}O$	Calcite	Water	-2.89	0	2.78	0° to 500°	56, 31
$^{18}O/^{16}O$	Quartz	Water	-2.90	0	3.38	200° to 500°	12, 31
$^{18}O/^{16}O$	Albite	Water	-3.41	0	2.91	350° to 800°	55
$^{18}O/^{16}O$	Quartz	Magnetite	0	0	6.29	600° to 1300°	7
$^{18}O/^{16}O$	Quartz	Albite	0	0	0.94	600° to 1300°	7
$^{18}O/^{16}O$	Anorthite	Diopside	0	0	0.76	600° to 1300°	7
$^{18}O/^{16}O$	Diopside	Forsterite	0	0	0.92	600° to 1300°	7

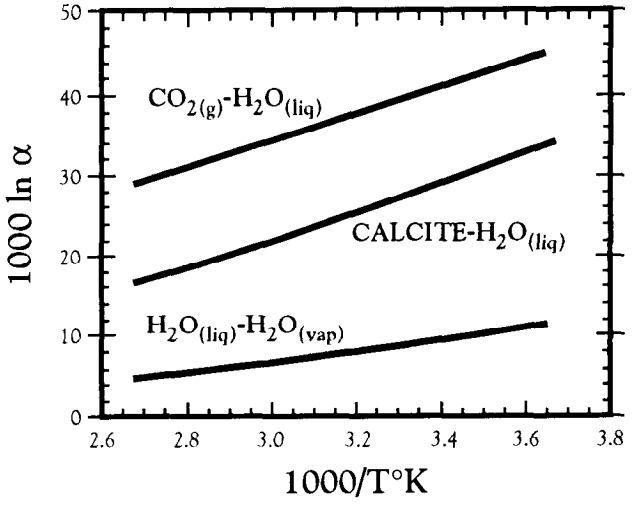

Fig. 1. Graph of oxygen isotopic fractionation factors between liquid water and either water vapor, carbon dioxide gas, or calcite as a function of inverse temperature, from Table 2. If all phases were in equilibrium at 25°C (i.e., at 1000/T = 3.354) with seawater having $\delta^{18}O = 0$, then the respective $\delta^{18}O$ values calculated from equation 7 would be -9.3 for the water vapor, +41.3 for the CO_2 gas, and +28.8 for the calcite. The latter values are rather close to those observed in water vapor and CO_2 in the marine atmosphere, and in recent shell materials; however, kinetic fractionation effects may also be involved in actual cases.

temperature condition, where $\ln\alpha = C_3/T^2$, is effectively attained (see Bottinga and Javoy, 1973). Many additional fractionation factors are compiled by Friedman and O'Neil (1977) and Richet et al. (1977); O'Neil (1986) tabulates data sources.

If two independent fractionation equations contain one phase in common, it is commonly useful to combine these equations into a new equation that directly relates the other two phases. This is possible because, according to eq. 6, $\alpha_{A\text{-}B}$ divided by $\alpha_{C\text{-}B}$ gives $\alpha_{A\text{-}C}$. For equations of the form of eq. 9, this computation is effected by simply subtracting the analogous numerical coefficients. However, fractionation equations thus derived will have greater uncertainty than the original determinations; moreover, their range of validity may be very restricted, making extrapolations dangerous. For example, combination of the quartz-water and albite-water fractionations in Table 2 gives a geologically unreasonable quartz-albite fractionation equation that disagrees with the new determination by Chiba et al. (1989).

2.5.3. Kinetic fractionation and exchange effects. A number of unidirectional processes can fractionate isotopes because the transport and/or reaction rates are not equal for molecules containing the different isotopes of an element. A simple case is the different diffusion rates for the various isotopic species of a gas. According to the kinetic theory of gases, all gas molecules at a given temperature have the same average kinetic energy. A direct consequence is "Graham's law of diffusion", which states that the translational velocity ratio v*/v of two gaseous molecules with masses of m* and m is:

$$\frac{v^*}{v} = \sqrt{\frac{m}{m^*}} \qquad (10)$$

This relation is applicable to a gas that diffuses through a porous plug or an opening that is smaller than the mean free path. Owing to their faster translational velocities the molecules with the lowest mass will preferentially escape, and the original mixture will separate into a light fraction and a residue that is enriched in the heavy isotope.

Kinetic isotope effects can also arise from differences in reaction rates, as could occur if the chemical bonds containing the light isotope were easier to break, perhaps because of a higher vibrational frequency. Evaporation of water involves a combination of surface effects and diffusion that together produce a significant kinetic isotope effect (e.g., Craig and Gordon, 1965).

One common type of kinetic effect arises during isotopic exchange between substances out of equilibrium. In such a case and regardless of the reaction order or the exchange mechanism, as time (t) increases the δ-value of a substance will vary from the initial value δ_i to the equilibrium value δ_{eq}, according to the exponential relation, where k is a constant (Criss et. al., 1987):

$$\frac{\delta - \delta_{eq}}{\delta_i - \delta_{eq}} = e^{-kt} \qquad (11)$$

3. NATURAL ISOTOPIC VARIATIONS OF OXYGEN AND HYDROGEN

3.1. Natural Waters

Hydrogen and oxygen isotope ratios are conservative, uniquely intrinsic tracers for elucidation of the origin and transport of H_2O in the hydrologic cycle. In addition, the physical processes that govern H_2O transport are amenable to theoretical modelling using isotope data. The characteristics of the principal reservoirs of natural waters are as follows:

3.1.1. Ocean water. The oceans have a mean depth

of 3.8 km, a volume of 1.37×10^9 km^3, and constitute 97.25% of the hydrosphere. This large reservoir is strikingly uniform, with almost all samples having $\delta^{18}O = 0 \pm 1$ and $\delta D = 0 \pm 5$ per mil relative to SMOW (Craig and Gordon, 1965). Most variations occur in surface waters, are coupled with variations in salinity, and are attributable to evaporation, formation of sea ice, or addition of meteoric precipitation.

Although some workers have argued that a large secular change in the $\delta^{18}O$ values of ocean water has occurred over geologic time, it is likely a value near zero is buffered by fluid-rock interactions at spreading centers (Muehlenbachs and Clayton, 1976, Gregory and Taylor, 1981). In contrast, preferential loss of protium from the upper atmosphere to space may have resulted in a significant change in the δD value of the Earth over geologic time. Fluctuations of approximately $\pm$ 1 and $\pm$ 8 per mil for the $\delta^{18}O$ and δD values of ocean water, respectively, occurred during the Quaternary because of the cycles of growth and melting of icecaps.

3.1.2. Meteoric Waters. The physical processes responsible for the transport and precipitation of atmospheric water impart a very characteristic signature to meteoric precipitation, so that modern meteoric waters conform closely to the "Meteoric Water Line", or MWL, of Craig (1961b); Fig. 2:

$$\delta D = 8\,\delta^{18}O + 10 \qquad (12)$$

Note that SMOW does not lie on the MWL; the δD difference of +10 is defined as the "deuterium excess", and to first order is a kinetic effect produced during evaporation of seawater (Craig and Gordon, 1965). In detail, the precise value of the deuterium excess varies geographically, and different equations have been proposed for different regions (e.g., Sheppard et al., 1986).

The δD and $\delta^{18}O$ values of meteoric waters are strongly correlated with temperature, and vary with latitude, altitude, proximity to the ocean, and other effects (Dansgaard, 1964). In general, precipitation processes progressively and preferentially deplete an atmospheric mass of its D and ^{18}O, so that the δD and $\delta^{18}O$ values of rain in the tropics is similar to ocean water, whereas very low δD (to ~ -500) and $\delta^{18}O$ (to ~ -60) values occur in winter ice at the South Pole. The variations can to first-order be simulated with the Rayleigh fractionation equation that describes the progressive condensation of a cloud during cooling:

$$\frac{1000+\delta}{1000+\delta_i} = f^{\alpha-1} \qquad (13)$$

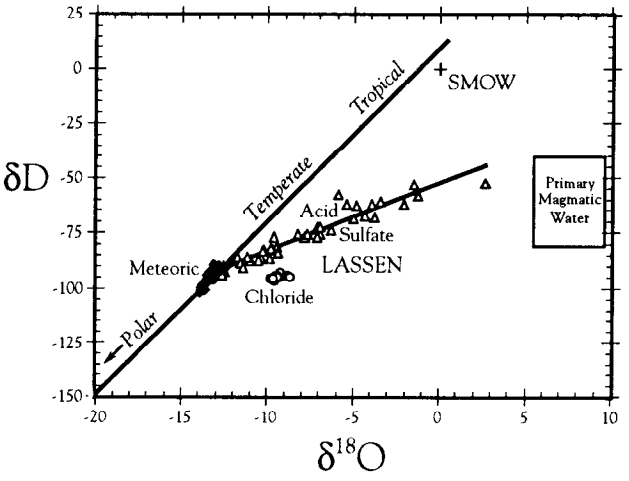

Fig. 2. Graph of δD vs $\delta^{18}O$ values of some natural waters, relative to SMOW. Meteoric waters generally lie along or near the meteoric water line of slope 8 (Craig, 1961b), and become more depleted in D and ^{18}O as one progresses from the tropics to temperate zones to higher latitude regions. A similar diagram was used by Craig (1963) to show that geothermal fluids from numerous areas in the world are predominantly derived from ordinary meteoric waters. As an example, chloride type (circles) and acid-sulfate (open triangles) geothermal fluids from Lassen Volcanic National Park are distinct from magmatic waters, defining trends that clearly originate on the MWL at a point identical to the local meteoric waters (solid diamonds) in that vicinity (see Janik et al., 1983). However, the chloride waters exhibit a significant, zero slope " ^{18}O-shift" due to water-rock interactions, whereas the acid sulfate trend (slope ~ 3) is characteristic of evaporation at near-boiling temperatures.

where δ_i and δ are the δ-values of the water at the beginning and at any time of the condensation process; α refers to the liquid-vapor (or ice-vapor) fractionation factor which is for simplicity here assumed to be constant; and f refers to the fraction of vapor that remains. Although no simple model can explain all the complexities of global precipitation, the Rayleigh equation approximately accounts for the slope of the MWL, for the variation of $\delta^{18}O$ and δD values with temperature, and for the existence of small amounts of precipitation in cold regions that is highly depleted in ^{18}O and D relative to temperate and tropical meteoric waters.

3.1.3. Glaciers and icecaps. Ice comprises more than 2% of the hydrosphere and provides a direct and sequential record of "fossil" meteoric precipitation. Ice cores from the several-km-thick Greenland and Antarctic

ice sheets contain "fossil" precipitation over the last ~170,000 years that conforms to a "sawtooth-shaped" climatic cycle (Fig. 3). Specifically, ice representing the last glacial maximum (10,000-20,000 years ago) is more strongly depleted in D and ^{18}O than modern precipitation at these localities, and conforms to a MWL with a lower deuterium excess than today (Johnson et al., 1972; Lorius et al., 1985; Barnola et al., 1987). This "sawtooth" cycle corresponds to the last of many rather similar, 100 ka Quaternary cycles known from the $\delta^{18}O$ record of carbonate from deep sea cores, and thought to represent a combination of climatic change and changes in the $\delta^{18}O$ value of seawater caused by the growth or retreat of icecaps (Fig. 3; e.g., Shackleton and Pisias, 1985).

3.1.4. Formation waters. Formation waters are low- to moderate-temperature aqueous fluids of various origins that occur in sediments. Most shallow, dilute groundwaters lie along the MWL at values similar to those of the modern local precipitation from which they originated. However, some groundwaters such as those in artesian basins have lower δD and $\delta^{18}O$ values and clearly migrated tens or hundreds of kilometers from higher-elevation points of recharge, whereas other groundwaters represent recharge of ancient pluvial periods. Other formation waters have a complex origin.

Formation waters commonly contain small to substantial concentrations of dissolved constituents that commonly originate from fluid-rock interactions but in some cases clearly have a connate (seawater) origin. These water-rock interactions are temperature dependent and also affect the δD and $\delta^{18}O$ values. If fluids at low temperature are in contact with reactive materials, for example in shallow marine sediments (Lawrence and Geiskes, 1981), the $\delta^{18}O$ values may decrease by several per mil and the fluid may plot to the *left* of the MWL. In contrast, in hotter, deeper zones, formation waters range into hot (>150°C) concentrated (>10 wt %) brines. On a graph of δD vs. $\delta^{18}O$, oil-field waters plot along positive-sloped trends that originate on the MWL, at a point appropriate for local precipitation, with the hottest, most saline samples having anomalously high $\delta^{18}O$ values (Clayton et al., 1966). These trends indicate that the fluids contain a significant meteoric component (Clayton et al., 1966). In other cases, particularly where the fluid is overpressured, meteoric infiltration is impossible and the fluids are probably modified connate waters (Kharaka and Carothers, 1986).

3.1.5. Hydrothermal Fluids. The two most important types of hot (mostly 100°-350°C) fluid observed in geothermal areas are chloride-type waters and acid-sulfate waters. Craig (1963) unequivocally proved that both types are dominantly derived from the local meteoric waters of each area of occurrence.

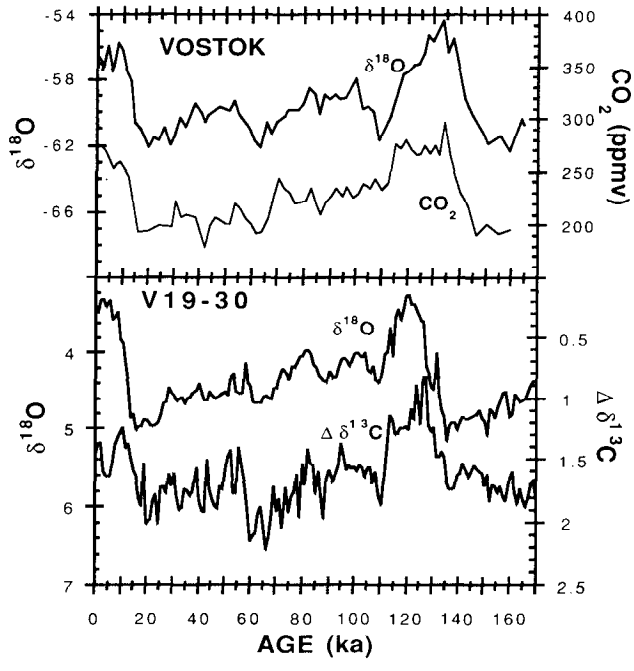

Fig. 3. Temporal variation of the $\delta^{18}O$ values (upper curve, left scale; Lorius et al.,1985) of glacial ice in the 2 km-deep Vostock, Antarctica, ice core, and of the mean CO_2 contents (lower curve, right scale; Barnola et al., 1987) of trapped air bubbles released by crushing the ice. For comparison, interpolated $\delta^{18}O$ values for the benthic foram *Uvigerina senticosta* (upper curve, left scale) in equatorial deep sea core V19-30, and the difference in $\delta^{13}C$ values between plantonic species *Neogloboquadrina dutertrei* and this benthic foram are shown (lower curve, right scale; Shackleton and Pisias, 1985). The sawtooth curves record global climatic changes influencing both ocean and continental temperatures, carbon cycle changes, and changes in the $\delta^{18}O$ value of seawater caused by removal of low ^{18}O water and storage in ice, over the last ~170,000 years, all of which correlate to first order with the concentration of atmospheric CO_2 .

Chloride-type geothermal waters are volumetrically dominant, have salinities up to many thousands of g/kg dominated by Na^+, K^+, Ca^{++}, and Cl^-, have near-neutral pH, are close to saturation with silica, and are associated with free-flowing hot springs and in spectacular cases with silica terraces and geyser systems (White et al., 1971). These fluids inherit the D/H ratio of the local meteoric waters from which they are derived, but are higher in ^{18}O.

The latter effect, known as the "^{18}O-shift", reflects interaction and exchange with rocks (Fig. 2).

Acid-sulfate waters have very low pH (commonly < 2.5), high $SO_4^=$ but low Cl^- contents, and are typically associated with steaming ground, mud pots and fumaroles. The δD and $\delta^{18}O$ trend lines characteristic of these waters also originate on the MWL at points appropriate for the local meteoric precipitation, and their low (2 to 3) positive slopes suggest evaporative (kinetic) effects at near-boiling temperatures (Fig. 2). Acid-sulfate waters commonly occur in proximity to chloride-type waters, and probably represent condensed steam derived from them (White et al., 1971).

The hot (to 350°C) chloride-rich fluids that discharge from mid-ocean ridge spreading centers are clearly derived from seawater, but have undergone changes in chemistry including complete Mg loss, along with increases of about 2 per mil in the δD and $\delta^{18}O$ values (e.g., Bowers and Taylor, 1985).

3.1.6. Magmatic and Metamorphic Waters. Significant volumes of magmatic and metamorphic waters have not been observed to discharge at the Earth's surface. However, the δD (-40 to -80) and $\delta^{18}O$ (+5.5 to +9.5) values of magmatic waters, and the δD (0 to -70) and $\delta^{18}O$ (+3 to +20) values of metamorphic waters, may be determined from fluid inclusion data and from calculations that assume equilibrium with crystalline rocks at appropriate temperatures (e.g., Sheppard, 1986). A fluid of any origin that undergoes extensive fluid-rock interaction at elevated temperatures would develop similar characteristics, so many magmatic and metamorphic waters may be derived from subducted or deep-circulating surface waters. B. E. Taylor (1986) provides a very complete discussion of magmatic volatiles.

3.2. Oxygen Isotope Systematics of Rocks

3.2.1. Earth-moon system. Oxygen isotope data have confirmed many of the petrographic assignments of meteorites to various families and inferred parent bodies, and have dramatically proved that the Earth and Moon have a very close mutual affinity (Fig. 4; Clayton et al., 1976). In particular, combined studies of the $\delta^{18}O$ *and* $\delta^{17}O$ values show that lunar and terrestrial materials lie along a common "Earth-Moon Line" that is distinct from virtually all other samples of extraterrestrial materials (Fig. 4); hence, the bulk $\delta^{18}O$ composition of these bodies is the appropriate reference point for discussion of terrestrial rocks.

The $\delta^{18}O$ values of lunar materials, including diverse lithologies such as Mare basalts, breccias, and highland crystalline rocks, are remarkably uniform at +5.4 to +6.8,

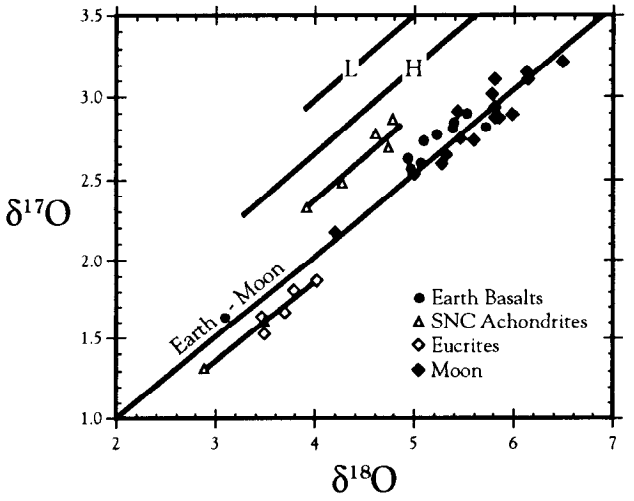

Fig. 4. Graph of $\delta^{17}O$ vs $\delta^{18}O$ values of terrestrial and extraterrestrial materials. Analyses of $\delta^{17}O$ are difficult and not normally made, particularly because normal processes that cause isotopic fractionation produce variations restricted to lie along lines with slopes very close to 1/2, so no additional information is normally gained. Thus, all terrestrial and lunar samples lie along the "Earth-Moon" line. However, in a series of important papers R. N. Clayton and his coworkers have shown that different types of meteorites define distinct trends on a $\delta^{17}O$ vs. $\delta^{18}O$ plot that must be the result of compositional heterogeneities that relate back to the earliest history of the Solar System. Thus, the SNC achondrites (from Mars?) and the eucrites define distinct trend lines close to but not on the Earth-Moon line; the H and L chondrites are further removed, and the very primitive carbonaceous chondrites (not shown) are highly distinct and for the most part are offscale. In general, the greater the petrographic similarity to terrestrial materials, the closer the $\delta^{17}O$ - $\delta^{18}O$ trend lines to the Earth-Moon line. Data from Clayton and Mayeda (1975, 1983) and Clayton et al. (1976), who provide detailed discussions.

with the subset of lunar igneous rocks showing an even smaller range of +5.7 ± 0.2 (e.g., Taylor and Epstein, 1973). These values reflect the simple geologic history of the Moon, its lack of water, and the fact that simple fractional crystallization processes can produce only small (< 2 per mil; see Taylor and Sheppard, 1986) variations in the $\delta^{18}O$ values of significant volumes of melts during igneous differentiation, owing to the small values of the fractionation factors between silicates at high temperatures.

3.2.2. Igneous rocks. The Earth's upper mantle and rocks directly derived from it represent the largest

reservoir of oxygen for which we have samples. The $\delta^{18}O$ values of MORB basalts, which are the most abundant igneous rock type on Earth, are highly uniform at +5.7 ± 0.5 (Kyser, 1986). In fact, the $\delta^{18}O$ values of virtually all mafic lavas on Earth are between +5.0 and +8.0 per mil, with alkalic basalts and samples from continental areas tending to be ^{18}O rich (Kyser, 1986). The whole-rock $\delta^{18}O$ values of most mantle materials are also in the latter range, including peridotite and pyroxenite xenoliths, and peridotite massifs. The values for ophiolite sequences and eclogites vary more widely and their ranges overlap (Fig. 5; Kyser, 1986). These large, rather uniform reservoirs provide the best estimate for the $\delta^{18}O$ value of the "bulk" Earth, and their similarity to the value for lunar material is not coincidental.

In contrast to the Moon, however, the total range of $\delta^{18}O$ values in terrestrial magmas is wide- at least +2 to +16 per mil (Taylor and Sheppard, 1986). The ^{18}O contents tend to increase with increasing SiO_2 contents, generally in the order basalts to andesites to rhyolites for volcanic rocks, and from ultramafic rocks to gabbroes and anorthosites to tonalites and granodiorites to granites for plutonic rocks (Fig. 5). These $\delta^{18}O$ variations are much too large to be the result of simple fractional crystallization, and must indicate that the more siliceous magmas have incorporated high-^{18}O sedimentary or metamorphic materials. Similarly, magmas with anomalously low $\delta^{18}O$ values must have assimilated low-^{18}O materials, most likely hydrothermally-altered roof rocks (Taylor and Sheppard, 1986). It is likely that any rock with a $\delta^{18}O$ value outside the range of +5 to +8 has, or includes a component that has, resided near the Earth's surface at some time in its history.

The ^{18}O fractionations between igneous minerals are small and reflect their high crystallization temperatures (e.g., Chiba et al., 1989). The observed $\delta^{18}O$ values of igneous minerals generally decrease in the order : quartz-feldspars-pyroxene-mafic minerals-magnetite, consistent with a tendency to approach equilibrium fractionation (e.g., Epstein and Taylor, 1967). The patterns of ^{18}O fractionation may be disturbed by subsolidus alteration effects, most importantly those related to fluid infiltration (Gregory et al., 1989) or to slow cooling of deeply-emplaced plutons (Giletti, 1986; Taylor and Sheppard, 1986).

3.2.3. Sedimentary and metamorphic rocks. The $\delta^{18}O$ values of sedimentary and metamorphic rocks are mostly higher than those of igneous rocks. The high values indicate formation of the constituent materials at rather low temperatures where fractionation factors are large, and in particular are attributable to interactions with the hydrosphere.

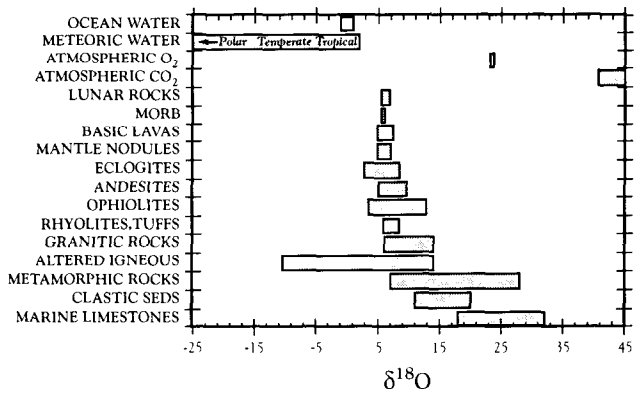

Fig. 5. Typical ranges of the $\delta^{18}O$ values of rocks and other natural substances, from numerous sources. The $\delta^{18}O$ value of the bulk Earth is probably very similar to that of the Moon, as suggested by values for MORB, basic lavas and mantle xenoltihs. Interactions with the hydrosphere buffer the $\delta^{18}O$ value of seawater at a value near zero, and similar water-rock interacticns produce most of the dispersion of $\delta^{18}O$ values observed in ophiolites and crustal crystalline rocks. For example, the range for "altered igneous" rocks represents their hydrothermal interactions with surface waters; such low values can also occur in altered sedimentary and metamorphic rocks. Because isotopic fractionation factors are large at low temperatures, the $\delta^{18}O$ values of meteoric waters, carbonates, and atmospheric CO_2 are comparatively extreme.

The highest $\delta^{18}O$ values occur in the chemical precipitates of seawater. For example, recent limestones are approximately 30 per mil richer in ^{18}O, and cherts are as much as 36 per mil richer (Knauth and Epstein, 1976), than the seawater from which they precipitate, as a consequence of the large calcite-water and quartz-water fractionations at low temperatures (see Table 2). The $\delta^{18}O$ values of older chemical precipitates such as ancient limestones, cherts or banded iron formations are also high (mostly > +18) but generally decrease with increasing age, in part because secondary alteration processes tend to reduce their values (e.g., Keith and Weber, 1964; Anderson and Arthur, 1983).

The $\delta^{18}O$ values of clastic sediments are greater than or equal to those of their protoliths. Sandstones typically have values of +13 ± 2.5, principally reflecting inherited igneous and metamorphic quartz, although the presence of authigenic quartz or calcite cement commonly has increased the whole-rock $\delta^{18}O$ value above the values for

beach sands (+9 to +12.5; Savin and Epstein, 1970a). Typical $\delta^{18}O$ values of shales are +14 to +19, reflecting the inheritance of high ^{18}O protolith materials as well as the presence of high ^{18}O authigenic clay minerals (Savin and Epstein, 1970b). The $\delta^{18}O$ values of greywackes ($+13 \pm 1.5$) are similar to sandstones and are substantially higher than those of volcanic rocks, probably because of the formation of authigenic minerals including clays.

The $\delta^{18}O$ values of metamorphic rocks are variable but tend to be intermediate between those of igneous rocks and recent sediments. Orthoquartzites, granitic gneisses and carbonate granofels may inherit the $\delta^{18}O$ values of their protolith materials without substantial change. More commonly, the $\delta^{18}O$ values of rocks become progressively reduced with increasing grades of metamorphism. For example, the $\delta^{18}O$ values of carbonates are progressively lowered, by as much as 20 per mil, with increasing grade or decreasing distance to igneous contacts (Valley, 1986).

In addition, in numerous regional metamorphic terranes, the $\delta^{18}O$ values of pelitic metasediments are reduced with increasing grades from their original sedimentary values (e.g., Garlick and Epstein, 1967). In the highest-grade (e.g., amphibolite) zones, the $\delta^{18}O$ values of diverse rock types may be effectively "homogenized", by pervasive, large-scale exchange processes, to a common value appropriate for igneous rocks (Shieh and Schwarcz, 1974). In other areas, the $\delta^{18}O$ values of different rock types remain heterogeneous, with localized isotopic exchange producing diffusion-like ^{18}O gradients between contrasting rock units, particularly between rather impermeable carbonates and interbedded pelites (e.g., Rye et al., 1976; Nabelek et al., 1984).

3.3. Hydrogen Isotope Systematics of Rocks.

The δD values of meteorites and lunar rocks vary enormously, in part because of intense bombardment by the deuterium-free solar wind. In contrast, except for certain hydrothermally-altered samples discussed below, the δD values of virtually all igneous, metamorphic and sedimentary rocks on Earth are in the remarkably narrow range of -40 to -95 (Taylor and Sheppard, 1986). Magmatic and deep-seated waters on Earth also fall in this range (Sheppard and Epstein, 1970). The δD values of hydrous phases are typically 30 ± 20 per mil lower than those of the water in isotopic equilibrium at temperatures where they are stable (e.g., Suzuoki and Epstein, 1970). Thus, the δD values observed for terrestrial rocks are similar to those of clay and alteration minerals formed in contact with seawater or with the abundant meteoric waters of tropical and temperate zones. In fact, on a plot of δD vs $\delta^{18}O$, many clays fall along lines that parallel the MWL, being offset by the ^{18}O and D fractionation factors between the particular clay mineral and water (Savin and Epstein, 1970c).

The similarity of the δD values for magmatic and deep-seated waters, rocks and clay minerals on Earth probably indicates that the H_2O is mostly derived from dehydration of surface material subducted at trenches (Taylor and Sheppard, 1986). Over geologic time, subducted water would completely dominate the δD value of the upper mantle, so that a "steady state" relationship has been attained.

3.4. Water-Rock Interactions

Because of its extensive hydrosphere and dynamic interior, the Earth has a uniquely large potential for fluid-rock interactions. Isotopic evidence for interaction and exchange between fluid and rocks is in fact practically ubiquitous in the rocks of the crust and upper mantle.

The response of a rock to isotopic exchange with fluid depends on the temperature (e.g., on the rock-fluid fractionation factor Δ), on the rates of infiltration and exchange, on the event duration, and on the relative proportions (W/R) and initial δ-values ($\delta_i W$ and $\delta_i R$) of the water and rock. In the simplest case, where isotopic equilibrium is attained in a closed system, equation 5 may be used to derive the conservation relation (Taylor, 1977):

$$\frac{W}{R} = -\frac{\delta_i R - \delta_{eq} R}{\delta_i W - (\delta_{eq} R - \Delta)} \qquad (14)$$

where $\delta_{eq}R$ and $\delta_{eq}R-\Delta$ respectively represent the final equilibrium value of the rock and water. Here the W/R ratio, defined as the relative molar amounts of the element in question (oxygen or hydrogen), is equal to the ratio of the isotopic shifts that would be observed in the rock and water, analogous to the "lever rule". Note that the W/R ratio is a dimensionless quantity, unlike the fluid flux or the time integrated flux which have different physical meanings. Additional exchange models are discussed and compared to natural data by Taylor (1977) and Gregory et al. (1989).

Given these variables, the $\delta^{18}O$ and δD values of rocks that interact with significant amounts of low ^{18}O, low D meteoric waters at typical hydrothermal temperatures (150-350°C) can become as low as -10 and -200, respectively, (see compilation in Criss and Taylor, 1986). The reduction of the rocks in ^{18}O is the material-balance

counterpart of the "^{18}O-shift" in geothermal waters discussed above. However, a significant "D-shift" in the water is generally absent because the hydrogen content of rocks is so low that the W/R ratio for hydrogen is, for any given case, much larger than that for oxygen (eq. 14). At very low temperatures (< 100°C), interaction with meteoric waters will again reduce the δD values, but in this case the $\delta^{18}O$ value of rocks may actually increase because the rock-fluid ^{18}O fractionation (Δ) is large at low T.

Significant changes in the $\delta^{18}O$ values of rocks also occur during interactions with heated seawater. Owing to the variation of Δ with temperature, interactions below 350°C increase the $\delta^{18}O$ value of the rock, but at higher temperatures such interactions cause a reduction in the $\delta^{18}O$ value. The overall $\delta^{18}O$ value of seawater is effectively unchanged by this process, so that its interactions with mantle-derived rocks at mid-ocean spreading centers effectively buffer its composition (Muehlenbachs and Clayton, 1976; Gregory and Taylor, 1981).

On δ–δ plots, the $\delta^{18}O$ values of coexisting minerals from hydrothermally-altered rocks define linear, positive-sloped trends that are clearly diagnostic of isotopic disequilibrium and open-system (infiltration) histories (Fig. 6; Gregory et al., 1989). Graphs of δD vs. $\delta^{18}O$ values for altered minerals commonly define characteristic "inverted L" patterns (Taylor, 1977). Detailed discussions and examples of these alteration trends are given in Taylor (1977), Criss and Taylor (1986) and Gregory et al. (1989).

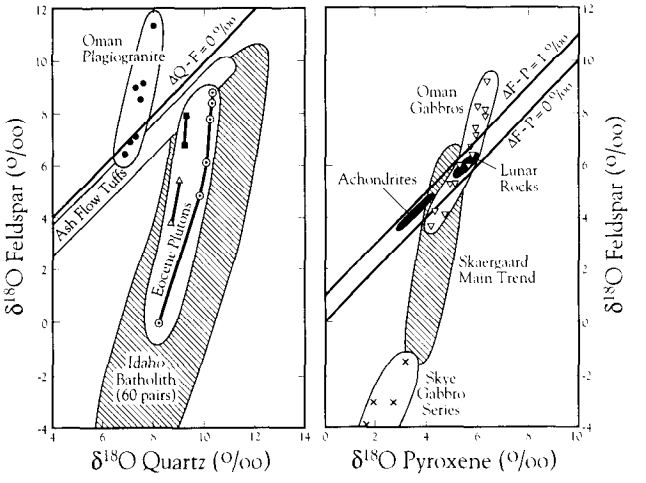

Fig. 6. Graph of $\delta^{18}O$ values of feldspar vs the $\delta^{18}O$ value of coexisting quartz or pyroxene in igneous rocks. Isotopic equilibrium at magmatic temperatures is indicated by the small fractionations and unit-sloped trends typical of ash-flow tuffs (stipple), achondritic meteorites (solid black; Clayton et al., 1976), and lunar rocks (solid black; e.g., Taylor and Epstein, 1973). In contrast, marked isotopic disequilibrium produced by interactions with infiltrating hydrothermal fluids occurs in 1) plagiogranite and gabbros from the Oman ophiolite, which interacted with heated seawater, and in 2) granitic rocks of the Idaho batholith, as well as in gabbros from Skaergaard and Skye, which exchanged with hot fluids derived from high latitude, low ^{18}O meteoric waters. These steep disequilibrium trends are diagnostic of hydrothermal alteration in open systems. Modified after Gregory et al. (1989), who provide discussion and models for these effects.

4. NATURAL VARIATIONS OF CARBON ISOTOPES

4.1. Ocean and Atmosphere

Bicarbonate ion (HCO_3^-) dominates the carbon inventory of the ocean-atmosphere system. The $\delta^{13}C$ value of deep ocean water is typically 0 ± 0.5, but metabolic effects in surface water typically increase this value to about +2.0 (Kroopnick, 1985). The average $\delta^{13}C$ (-8) and $\delta^{18}O$ (+41) values of atmospheric CO_2 are to first order in isotopic equilibrium with the bicarbonate and water of the oceanic reservoir (e.g., Bottinga and Craig, 1969; see Table 2). However, the $\delta^{13}C$ value of CO_2 is lower in urban areas because of fuel combustion, and is affected by the diurnal and annual cycles of plant respiration, growth and decay. Fossil fuel burning, which has since the Industrial Revolution increased the atmospheric CO_2 content from 280 to 350 ppm (Wahlen et al., 1991), has progressively decreased the $\delta^{13}C$ value of atmospheric CO_2 by a surprisingly low 1.5 per mil, probably because the anthropogenic effect is moderated by rather rapid exchange with the vast reservoir of oceanic bicarbonate (Fig. 7; Keeling et al., 1989). Quaternary climatic variations, as inferred from the δD and $\delta^{18}O$ record of ice cores, correlate closely with the CO_2 content of air trapped in the ice (Fig. 3; Barnola et al., 1987).

4.2. Organic Matter and its Derivatives

Relative to primordial carbon ($\delta^{13}C \sim -6$; see below), virtually all carbon in the biosphere is depleted in ^{13}C because of kinetic and metabolic effects associated with photosynthesis (Fig. 8). Thus, most terrestrial plants have $\delta^{13}C$ values of -20 to -32, but grasses have a different pathway of carbon fixation and are heavier (mostly -10 to -20; Deines, 1980a). In contrast, marine

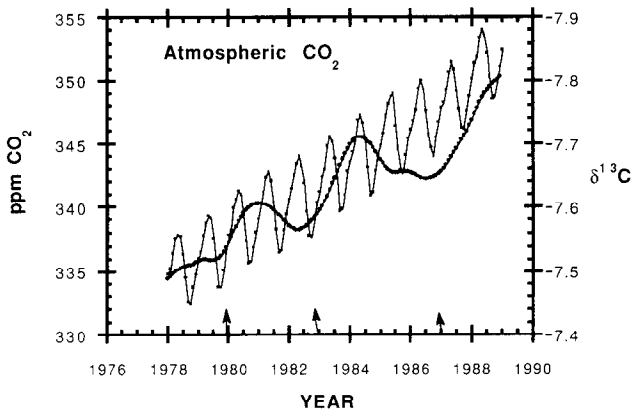

Fig. 7. Graph of concentrations (light line; Mauna Loa data set) and smoothed, globally-averaged $\delta^{13}C$ values of atmospheric CO_2 (heavy line; note inverted scale), tabulated by Keeling et al. (1989). The secular change in both curves is primarily due to the addition of isotopically light (~ - 27 ‰) CO_2 from fossil fuel combustion, of which approximately 56.6% remains in the atmosphere. The distinct periodicity in the concentration curve at Mauna Loa represents biomass seasonality, particularly cycles of growth and decay of northern hemisphere vegetation. This annual periodicity is also present in the $\delta^{13}C$ curve at Mauna Loa, but is out of phase with southern hemisphere cycles, and tends to cancel out in the globally-averaged curve shown here. Arrows denote possible (Dec., 1979), strong (Dec., 1983) and unranked (Dec., 1986) El Nino events that appear to correspond to the global ^{13}C patterns. See Keeling et al. (1989).

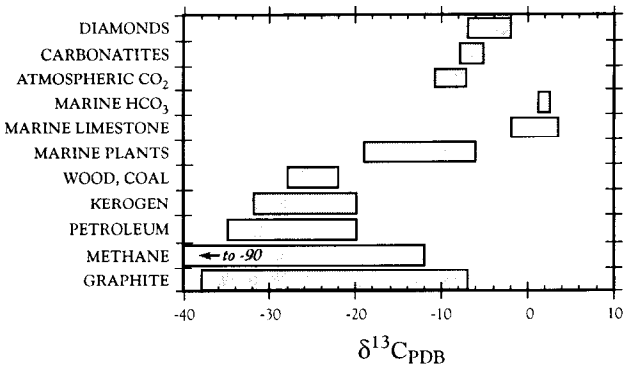

Fig. 8. Typical ranges of the $\delta^{13}C$ values of natural substances, from numerous sources. A primordial $\delta^{13}C$ value of about -6 is suggested by measurements of deep-seated materials such as diamonds and carbonatites. However, the large ^{13}C depletions that are typical of the biosphere (e.g., wood, marine plants) originate from preferential ^{12}C fixation during photosynthesis, and are passed along in the food chain, ultimately to be inherited by derivative materials such as coal, kerogen and petroleum. See text.

plants (excluding plankton) are mostly -7 to -19 (Deines, 1980a); these higher values occur in part because the $\delta^{13}C$ value of total dissolved CO_2 is generally higher than that of CO_2 gas, and because aquatic photosynthesis does not involve diffusion in air. Animals obtain their carbon either directly or indirectly from plants, and to within a few per mil, the low $\delta^{13}C$ values of plants are passed along in the food chain (DeNiro and Epstein, 1978). Beyond these generalities, the ^{13}C fractionations in biological systems are extremely complex.

The degradation of organic matter is also very complex. In shallow sedimentary environments, the aerobic decomposition and anaerobic processes associated with sulfate reduction are associated with the release of CO_2 having low $\delta^{13}C$ values (e.g., Irwin et al., 1977). In contrast, deeper anaerobic decomposition of organic matter releases ^{13}C-rich CO_2 (Irwin et al., 1977), along with methane that has extremely low $\delta^{13}C$ values of -25 to -90 (e.g., Claypool and Kaplan, 1974). The consistent, ~ 70 per mil ^{13}C fractionation between methane and CO_2 commonly observed in shallow sediments is probably not related to isotopic equilibrium (Sackett and Chung, 1979), but rather to the derivation of methane from the anaerobic reduction of CO_2 (Claypool and Kaplan, 1974).

In spite of these complex chemical transformations that occur during maturation, the low $\delta^{13}C$ values of organisms are conferred to organic carbon in sediments (Fig. 8). For example, the $\delta^{13}C$ value of coal (-21 to -27) is virtually identical to that of modern woody plants. The low $\delta^{13}C$ values of petroleum (mostly -21 to -32) are also indicative of an organic origin, but during petroleum formation minor (1 to 2 ‰) ^{13}C depletion may occur (Deines, 1980a). However, the principal end product of organic maturation is marine kerogen, which constitutes about 95% of the organic matter on Earth. Most kerogens have $\delta^{13}C$ values of -20 to -32 (Deines, 1980a), although kerogens in Tertiary and Recent marine sediments tend to be heavier (-18 to -23), and Precambrian kerogens tend to be lighter (-29 to -37; Degens, 1969). Numerous mechanisms, including differential preservation of various types of organic matter, diagenesis, and secular environmental changes, have been invoked to explain these variations.

4.3. Rocks

The primordial $\delta^{13}C$ value of about -6 can be inferred

for the Earth from the $\delta^{13}C$ values of diamonds (Deines, 1980b), of CO_2 in basalt vesicles (Kyser, 1986), and of carbonatites (Deines and Gold, 1973). Almost all samples of these materials are in the range of 0 to -10, with distinct abundance peaks at -5 or -6 (Fig. 8), although diamonds rarely have values as low as -30. Furthermore, a value of about -6 can be calculated (eq. 5) from the gross partitioning of terrestrial carbon into a carbonate reservoir, representing about 75% of total carbon and with $\delta^{13}C$ ~0, and into a reservoir representing sedimentary organic matter, representing about 25% of total carbon and having $\delta^{13}C$ ~ -25 (Epstein, 1969).

The $\delta^{13}C$ value of most marine limestones, shells and fossils (mostly 0 ± 2) are very close to the PDB standard (Keith and Weber, 1964). This restricted value has remained essentially unchanged at least since the early Proterozoic (Keith and Weber, 1964; Veizer et al., 1992). Freshwater limestones tend to have lower values, in part because of the influx of terrigenous organic matter (Keith and Weber, 1964). However, brief but sharp (to 4 ‰) excursions in the $\delta^{13}C$ values of marine carbonates have occurred (Kennett and Stott, 1991), as have cyclical ^{13}C variations on regional or global scales (Magaritz et al., 1991). Such features may facilitate stratigraphic correlation and provide information about paleoceanographic conditions and the carbon cycle.

The $\delta^{13}C$ value of diagenetic carbonates, such as cements and concretions, vary widely. Most common are rather low values (-10 to -20) that reflect dissolved CO_2 derived from the decay of organic matter (e.g., Hodgson, 1966). Extremely low (to -50) values have been reported where the dissolved CO_2 is produced by methane oxidation. However, bacterial fermentation reactions can form carbonates with high $\delta^{13}C$ values (> +15; Irwin et al., 1977).

The $\delta^{13}C$ values of graphites vary widely (most are -7 to -38; Schwarcz, 1969), probably reflecting derivation from diverse source materials such as kerogens (Fig. 8).

4.4. Organic-Rock Interactions

Donovan et al. (1974) demonstrated that carbonate cements with very unusual $\delta^{13}C$ and $\delta^{18}O$ values are spatially associated with two shallow, seeping petroleum reservoirs in Oklahoma. They found that the cap rock cements in one had extremely low $\delta^{13}C$ values (to -39) and elevated $\delta^{18}O$ values. In the other case, gas seepage produced $\delta^{18}O$ values as high as +48.8. Donovan et al. (1974) attributed the low $\delta^{13}C$ values to near-surface oxidation of the hydrocarbon, and suggested that the extremely high $\delta^{18}O$ values were the result of evaporation of groundwater due to natural gas expansion near the surface.

Acknowledgments. I have greatly benefitted from lectures by S. Epstein and S. M. Savin, longstanding collaborations with R. T. Gregory and H. P. Taylor, and colleagial associations with J. R. O'Neil and many others. This work was supported by NSF grant EAR-9204993.

REFERENCES

1. Anderson, T.F., and M.A. Arthur, Stable isotopes of oxygen and carbon and their application to sedimentologic and paleoenvironmental problems, in *Stable Isotopes in Sedimentary Geology*, Society of Economic Paleontologists and Mineralogists, SEPM Short Course *10*, 1-1 to 1-151, 1983.
2. Barnola, J.M., Raynaud, D., Korotkevich, Y.S., and Lorius, C., Vostok ice core provides 160,000-year record of atmospheric CO_2, *Nature, 329*, 408-414, 1987.
3. Bigeleisen, J., Chemistry of isotopes, *Science, 147*, no. 3657, 463-471, 1965.
4. Bottinga, Y., and M. Javoy, Comments on oxygen isotope geothermometry, *Earth Planet. Sci. Lett., 20*, 250-265, 1973.
5. Bottinga, Y., and H. Craig, Oxygen isotope fractionation between CO_2 and water, and the isotopic composition of marine atmospheric CO_2, *Earth Planet. Sci. Lett., 5*, 285-295, 1969.
6. Bowers, T.S. and H.P. Taylor, Jr., An integrated chemical and stable-isotope model of the origin of midocean ridge hot spring systems, *J. Geophys. Res., 90*, 12,583-12,606, 1985.
7. Chiba, H., T. Chacko, R.N. Clayton, and J.R. Goldsmith, Oxygen isotope fractionation involving diopside, forsterite, magnetite, and calcite: Application to geochemistry, *Geochim. Cosmochim. Acta, 53*, 2985-2995, 1989.
8. Claypool, G.E., and I.R. Kaplan, The origin and distribution of methane in marine sediments, in *Natural Gases in Marine Sediments*, I.R. Kaplan, ed., Plenum Pub. Co., 99-139, 1974.
9. Clayton, R.N., I. Friedman, D.L. Graf, T.K.Mayeda, W.F. Meents, and N.F. Shimp, The origin of saline formation waters. I. Isotopic composition, *J. Geophys Res., 71*, 3869-3882, 1966.
10. Clayton, R.N. and T.K. Mayeda, Oxygen isotopes in eucrites, shergottotes, nakhlites, and chassignites, *Earth Planet. Sci. Lett., 62*, 1-6, 1983.
11. Clayton, R.N., and T.K. Mayeda, Genetic relations between the moon and meteorites, *Proc. Lunar Sci. Conf. 6th*, 1761-1769, 1975.
12. Clayton, R.N., J.R. O'Neil, and T.K. Mayeda, Oxygen isotope

fractionation between quartz and water, *J. Geophys. Res., 77*, 3057-3067, 1972.
13. Clayton, R.N., N. Onuma, and T.K. Mayeda, A classification of meteorites based on oxygen isotopes, *Earth Planet. Sci. Lett., 30*, 10-18, 1976.
14. Craig, H., Isotopic standards for carbon and oxygen and correction factors for mass-spectrometric analysis of carbon dioxide, *Geochim. Cosmochim. Acta, 12*, 133-149, 1957.
15. Craig, H., Standard for reporting concentrations of deuterium and oxygen-18 in natural waters, *Science, 133*, 1833-1834, 1961a.
16. Craig, H., Isotopic variations in meteoric waters. *Science, 133*, 1702-1703, 1961b.
17. Craig, H., The isotope geochemistry of water and carbon in geothermal areas: in Tongiorgi, E., ed., *Nuclear Geology on Geothermal Areas*, Spoleto, 1963. CNR, Lab Geol. Nucl. Pisa, p. 17-53, 1963.
18. Craig, H. and Gordon, L.I., Deuterium and oxygen 18 variations in the ocean and the marine atmosphere. Symp. Marine Geochem., Narra-ganset Marine Lab., Univ. of Rhode Island Publ. *3*, p. 277-374, 1965.
19. Criss, R. E., and H.P. Taylor, Jr., Meteoric-hydrothermal systems, *Rev. Mineral.,16*, 373-424,1986.
20. Criss, R. E., R.T. Gregory, R. T., and H.P. Taylor, Jr., 1987, Kinetic theory of oxygen isotopic exchange between minerals and water: *Geochim. Cosmochim. Acta, 51*, 1099-1108, 1987.
21. Criss, R. E., Temperature dependence of isotopic fractionation factors. *Geochem. Soc. Spec. Pub., 3*, 11-16, 1991.
22. Dansgaard, W., Stable isotopes in precipitation, *Tellus, 16*, 436-468, 1964.
23. Degens, E.T., Biogeochemistry of stable carbon isotopes, in Eglinton and Murphy, *Organic Geochemistry*, Springer-Verlag, 304-329, 1969.
24. Deines, P., The isotopic composition of reduced organic carbon, in *Handbook of Environmental Isotope Geochemistry*, P. Fritz, P. and J. Ch. Fontes, eds., *1*, 329-406, 1980a.
25. Deines, P., The carbon isotopic composition of diamonds: relationship to diamond shape, color, occurrence and vapor composition, *Geochim. Cosmochim. Acta, 44*, 943-961, 1980b.
26. Deines, P. and D.P. Gold, The isotopic composition of carbonatite and kimberlite carbonates and their bearing on the isotopic composition of deep-seated carbon, *Geochim. Cosmochim. Acta, 37*, 1709-1733, 1973.
27. DeNiro, M.J. and S. Epstein, Influence of diet on the distribution of carbon isotopes in animals, *Geochim. Cosmochim. Acta, 42*, 495-506, 1978.
28. Donovan, T.J., I. Friedman, and J. D. Gleason, Recognition of petroleum-bearing traps by unusual isotopic compositions of carbonate-cemented surface rocks, *Geology, 2*, 351-354, 1974.
29. Epstein, S., Distribution of carbon isotopes and their biochemical and geochemical significance, *NASA, SP-188*, 5-14, 1969.
30. Epstein, S. and H.P. Taylor, Jr., Variations of O^{18}/O^{16} in minerals and rocks, in *Researches in Geochemistry*, P.H. Abelson, ed., 2, John Wiley & Sons, 29-62, 1967.
31. Friedman, I. and J.R. O'Neil, Compilation of Stable Isotope Fractionation Factors of Geochemical Interest, *U. S. Geol. Survey Prof. Paper 440-KK*, 1977.
32. Garlick, G.D., and S. Epstein, Oxygen isotope ratios in coexisting minerals or regionally metamorphosed rocks, *Geochim. Cosmochim. Acta, 31*, 181-214, 1967.
33. Giletti, B., Diffusion effects on oxygen isotope temperatures of slowly cooled igneous and metamorphic rocks, *Earth Planet. Sci. Lett., 77*, 218-228, 1986.
34. Gregory, R. T., R.E. Criss, and H.P. Taylor , Jr., Oxygen isotope exchange kinetics of mineral pairs in closed and open systems: Applications to problems of hydrothermal alteration of igneous rocks and Precambrian iron formations: *Chem. Geol., 75*, no. 1-2, 1-42, 1989.
35. Gregory, R.T., and H.P. Taylor, Jr., An oxygen isotope profile in a section of Cretaceous oceanic crust, Samail ophiolite, Oman: Evidence for $\delta^{18}O$-buffering of the oceans by deep (>5 km) seawater-hydrothermal circulation at mid-ocean ridges. *J. Geophys. Res., 86*, 2737-2755, 1981.
36. Hodgson, W.A., Carbon and oxygen isotope ratios in diagenetic carbonates from marine sediments, *Geochim. Cosmochim. Acta, 30*, 1223-1233, 1966.
37. Irwin, H., C. Curtis and M. Coleman, Isotopic evidence for source of diagenetic carbonates formed during burial of organic-rich sediments, *Nature, 269*, 209-213, 1977.
38. Janik, C.J., Nehring, N.L., and Truesdell, A.H. (1983) Stable isotope geochemistry of thermal fluids from Lassen Volcanic National Park, California, *Geothermal Resources Council, Transactions, 7*, 295-300.
39. Johnson, S.J., Dansgaard, W., Clausen, H.B., and Langway, C.C. (1972) Oxygen isotope profiles through the Antarctic and Greenland ice sheets. *Nature, 235*, p. 429-434.
40. Kyser, T.K., Stable isotope variations in the mantle, *Rev. Mineral., 16*, 141-164, 1986.
41. Keeling, C.D., R.B. Bacastow, A.F. Carter, S.C. Piper, T.P. Whorf, M. Heimann, W.G. Mook, and H. Roeloffzen, A three-dimensional model of atmospheric CO_2 transport based on observed winds: I. Analysis of observational data; Amer. Geophys Union, *Geophys. Mon., 55*, 165-236, 1989.
42. Keith, M.L., and J.N. Weber, Carbon and oxygen isotopic composition of selected limestones and fossils, *Geochim. Cosmochim. Acta, 28*, 1787-1816, 1964.
43. Kennett, J.P. and L.D. Stott, Abrupt deep-sea warming, palaeoceanographic changes and benthic extinctions at the end of the Palaeocene, *Nature, 353*, 225-229, 1991.
44. Kharaka, Y.K. and W.W. Carothers, Oxygen and hydrogen

isotope geochemistry of deep basin brines, in *Handbook of Environmental Isotope Geochemistry*, P. Fritz, P. and J. Ch. Fontes, eds., *2*, 305-360, 1986.
45. Knauth, L.P. and S. Epstein, Hydrogen and oxygen isotope ratios in nodular and bedded cherts, *Geochim. Cosmochim. Acta, 40*, 1095-1108, 1976.
46. Kroopnick, P., The distribution of ^{13}C of ΣCO_2 in the world oceans, *Deep Sea Res., 32*, 57-84, 1985.
47. Lawrence, J. R. and J. M. Gieskes, Constraints on water transport and alteration in the oceanic crust from the isotopic composition of pore water, *J. Geophys. Res., 86*, 7924-7934, 1981.
48. Lorius, C., Jouzel, J., Ritz, C., Merlivat, L, Barkov, N.I., Korotkevich, Y.S., and Kotlyakov, V.M., A 150,000-year climatic record from Antarctic ice, *Nature, 316*, 591-596, 1985.
49. Magaritz, M., J.L. Kirschvink, A.J. Latham, A. Yu. Zhuravlev, and A. Yu. Rozanov, Precambrian/Cambrian boundary problem: Carbon isotope correlations for Vendian and Tommotian time between Siberia and Morocco, *Geology, 19*, 847-850, 1991.
50. Majoube, M., Fractionnement en oxygene 18 et en deuterium entre l'eau et sa vapeur. *J. Chim. Phys., 68*, 1425-1436, 1971.
51. Mook, W.G., J.C. Bommerson, and W.H. Staverman, Carbon isotope fractionation between dissolved bicarbonate and gaseous carbon dioxide, *Earth Planet. Sci. Lett., 22*, 169-176, 1974.
52. Muehlenbachs, K., and R.N. Clayton, Oxygen isotope composition of the oceanic crust and its bearing on seawater, *J. Geophys. Res., 81*, 4365-4369, 1976.
53. Nabelek, P.I., T.C. Labotka, J.R. O'Neil, and J.J. Papike, Contrasting fluid/rock interaction between the Notch Peak granitic intrusion and argillites and limestones in western Utah: Evidence from stable isotopes and phase assemblages, *Contrib. Mineral. Petrol., 86*, 25-34, 1984.
54. O'Neil, J. R., Theoretical and experimental aspects of isotopic fractionation, *Rev. Mineral., 16*, 1-40, 1986.
55. O'Neil, J. R., and H.P. Taylor, Jr., The oxygen isotope and cation exchange chemistry of feldspars, *Am. Mineral., 52*, 1414-1437, 1967.
56. O'Neil, J.R., R.N. Clayton, and T.K. Mayeda, Oxygen isotope fractionation in divalent metal carbonates, *J. Chem. Phys., 51*, 5547-5558, 1969.
57. Richet, P., Bottinga, Y., and Javoy, M., A review of hydrogen, carbon, nitrogen, oxygen, sulphur, and chlorine stable isotope fractionation among gaseous molecules, *Ann. Rev. Earth Planet. Sci., 1977.5*, 65-110, 1977.
58. Rye, R.O., R.D. Schuiling, D.M. Rye, and J.B.H. Janssen, Carbon, hydrogen, and oxygen isotope studies of the regional metamorphic complex at Naxos, Greece, *Geochim. Cosmochim. Acta, 40*, 1031-1049, 1976.
59. Sackett, W.M. and H.M. Chung, Experimental confirmation of the lack of carbon isotope exchange between methane and carbon oxides at high temperatures, *Geochim. Cosmochim. Acta, 43*, 273-276, 1979.
60. Savin, S.M. and S. Epstein, The oxygen isotope compositions of coarse grained sedimentary rocks and minerals, *Geochim. Cosmochim. Acta, 34*, 323-329, 1970a.
61. Savin, S.M. and S. Epstein, The oxygen and hydrogen isotope geochemistry of ocean sediments and shales, *Geochim. Cosmochim. Acta, 34*, 43-63, 1970b.
62. Savin, S.M. and S. Epstein, The oxygen and hydrogen isotope geochem-istry of clay minerals, *Geochim. Cosmochim. Acta, 34*, 25-42, 1970c.
63. Schwarcz, H. P., The stable isotopes of carbon, in *Handbook of Geochemistry*, ed. K.H. Wedepohl, Springer-Verlag, *II-1*, 6-B-1 to 6-B-16, 1969.
64. Shackleton, N.J. snd N.G. Pisias, Atmospheric carbon dioxide, orbital forcing, and climate, Amer. Geophys Union, *Geophys. Mon., 32*, 303-317, 1985.
65. Sheppard, S.M.F., Characterization and isotopic variations in natural waters, *Rev. Mineral., 16*, 165-183, 1986.
66. Sheppard, S.M.F., and S. Epstein, D/H and $^{18}O/^{16}O$ ratios of minerals of possible mantle or lower crustal origin, *Earth Planet. Sci. Lett., 9*, 232-239, 1970.
67. Shieh, Y.N., and H.P. Schwarcz, Oxygen isotope studies of granite and migmatite, Grenville province of Ontario, Canada, *Geochim. Cosmochim. Acta, 38*, 21-45, 1974.
68. Stern, M. J., Spindel, W., and Monse, E. U. (1968) Temperature dependence of isotope effects. *J. Chem. Phys., 48*, 2908-2919.
69. Suzuoki, T. and S. Epstein, Hydrogen isotope fractionation between OH-bearing minerals and water, *Geochim. Cosmochim. Acta, 40*, 1229-1240, 1970.
70. Taylor, B.E., Magmatic volatiles: Isotopic variations of C, H and S, *Rev. Mineral.,16*, 185-219,1986.
71. Taylor, H. P., Jr., Water/rock interactions and the origin of H_2O in granitic batholiths. *J. Geol. Soc. London, 133*, 509-558, 1977.
72. Taylor, H.P., Jr., Igneous rocks: II. Isotopic case studies of circumpacific magmatism, *Rev. Mineral., 16*, 273-317, 1986.
73. Taylor, H.P., Jr., and S. Epstein, O^{18}/O^{16} and Si^{30}/Si^{28} studies of some Apollo 15, 16, and 17 samples, *Proc. 4th Lunar Sci. Conf., 2*, 1657-1679, 1973.
74. Taylor, H.P., Jr. and S.M.F. Sheppard, Igneous rocks: I. Processes of isotopic fractionation and isotope systematics, *Rev. Mineral., 16*, 227-271, 1986.
75. Urey, H. C., The thermodynamic properties of isotopic substances. *J. Chem. Soc.* (London), 562-581, 1947.
76. Valley, J.W., Stable isotope geochemistry of metamorphic rocks, *Rev. Mineral., 16*, 445-489, 1986.
77. Veizer, J., R.N. Clayton, and R.W. Hinton, Geochemistry of Precambrian carbonates: IV Early paleoproterozoic (2.25±0.25 Ga) seawater, *Geochim. Cosmochim. Acta, 56*, 875-885, 1992.
78. Walen, M., D. Allen, B. Deck, and

A. Herchenroder, Initial measurements of CO_2 concentrations (1530 to 1940 AD) in air occluded in the GISP 2 ice core from central Greenland, *Geophys. Res. Lett., 18*, 1457-1460, 1991.

79. Walker, F.W., J.R. Parrington, and F. Feiner, *Chart of the Nuclides*, 14th ed., General Electric Co, San Jose, 1989.

80. White, D.E., L.J.P. Muffler, and A.H. Truesdell, Vapor dominated hydrothermal systems compared with hot water systems, *Econ. Geol., 66*, 75-97, 1971.

Volcanic Gases From Subaerial Volcanoes on Earth

Richard E. Stoiber

1. INTRODUCTION

There are approximately 1300 volcanoes which have been active on earth in the last 10,000 years, 627 with dated eruptions [111]. Volcanoes on other planets are not considered in this summary. Volcanoes of the World [111] is the standard reference responsible for the summarized knowledge of volcanic activity. Volcanoes are dormant or at times quiescent without gas emission. At times they degas strongly and sometimes they erupt: gas is emitted together with the solid products. Active volcanoes are those which are emitting solid products such as lava, pyroclastic flows and comminuted rock called volcanic ash. It has been estimated that 60 volcanoes erupt each year [110]. More than this number were degassing, approximately 100 each year [117]. Of the erupting volcanoes 72% were in the northern hemisphere, 20% were located 5°N.-20°N. and another 20% located 35°N.-50°N. [11]. An estimate of the total flux of any gas may be proportioned in this way to suggest its geographical distribution if one assumes that in the region the number of active volcanoes is proportional to the flux.

Volcanic emanations consist of solid and liquid particulates and true gases. These, often collectively called volcanic gases or more correctly volcanic emanations, usually consist primarily of water, carbon dioxide, sulfur dioxide and hydrochloric acid as well as other gases in smaller amounts including many different metals. Most metals are believed to be carried as chlorides though vanadium [56] and iridium [140] are probably carried as fluorides and molybdenum and tungsten are thought to be carried as molybdic acid and tungstic acid respectively [14]. Thermodynamic modeling predicts most trace elements are transported from Augustine Volcano as simple chlorides, arsenic as a sulfide and Mo, in contrast to Bernard just cited, as Mo_2Cl_2 [122].

Gas from a volcano is emitted in large part from magma underlying the volcano or volcanic rift. The process is complex. Gases may come direct from the magma or be stored in a summit reservoir [136,43]. It has been suggested [45] that at White Island, New Zealand there is a magmatic component and also, surroundintg the magmatic system, a secondary hydrothermal comoponent rising from an envelope of saline brine and vapor, a suggestion that may have wider geographical application.

Standard textbooks on volcanology [20, 23, 36, 133] summarize the many aspects of volcanic activity.

2. TECTONIC SETTING OF VOLCANOES

Volcanoes occur in several tectonic settings. Most volcanoes occur at converging plate margins, most commonly around the Pacific. Plate margin volcanoes often erupt at the crater with pyroclastic material thrown in the air or cascaded down the slopes as hot pyroclastic flows. Lavas are commonly among the eruptive products. There are volcanoes along rifts both in the ocean and on the continents. Prominent examples are volcanoes of the Atlantic ocean and those along the East African Rift. Etna, the largest volcano in Europe, is on a fracture where there is subduction within a continental plate. A few volcanoes occur at hot spots, for example, those that are active on Reunion Island in the Indian Ocean and those of the Hawaiian Islands in the Pacific. Lava flows are the chief products of hot spot eruptions. Volcanic activity on the

R. E. Stoiber, Department of Earth Sciences, Dartmouth College, Hanover, NH 03755-3571

Global Earth Physics
A Handbook of Physical Constants
AGU Reference Shelf 1

sea floor is prominent at rifts and undersea fracture zone. Only gases from subaerial eruptions are considered in this summary. There are, however, significant amounts of volcanic gases dissolved in the submarine hydrothermal systems. Hydrothermal plumes of volcanic affiliations on the sea floor or ridges in the sea contain sulfides contributed by underwater volcanism but probably not in the form of gas.

3. LIMITS WITH RESPECT TO OBTAINING DATA

Gases are collected from lava lakes and fumaroles [107, 108, 109] but usually are not available for collection at active volcanoes. Much gas is emitted from very active vents where emission of solid products creates dangerous or impossible conditions for collection of gases. In rare instances has gas been collected from active vents by airplanes entering eruption clouds [17]. The advent of remote sensing spectrographic methods for detection of some gases, using a correlation spectrometer, has made gas measurements possible well away from dangerous sites. Because these measurements must be made in daylight and where the light through the volcanic plume is not obscured by volcanic ash in the plume, gas at very few active eruptions have been studied even using remote sensing equipment.

4. METHODS OF COLLECTION AND ANALYSIS OF VOLCANIC GAS

4.1. Collection and Evaluation of Analytical Data

There are several means in common used for finding the composition of volcanic gas. They include collection of gas in evacuated vessels, collecting condensates, allowing gas to pass through filters, as well as the use of spectroscopic detectors and sensors designed for analysis of a specific gas. Evaluation of the quality of the analytical data from St. Helens indicates that highest quality data are obtained by field chromatographic measurements and caustic soda bottle samples as compared with those collected in evacuated bottles or pumped through double stopcock tubes [44]. Errors inherent in the use of the correlation spectrometer for determining SO_2 flux have been evaluated [114]. Evaluation of the techniques and the errors in results of volcanic gas analysis has been the purpose of several field workshops [47]. Some investigators dispute the basic assumption that all species were in equilibrium under one set of conditions [45].

4.2. Collection of Volcanic Gas in Evacuated Vessels

Samples of gas may be collected in evacuated containers. They are analysed by the usual laboratory methods or in some instances by a gas chromatograph designed for use in the field [69]. Air content is accounted for by the nitrogen and argon content in the sample. Because of the change in species after collection, resort has been made to recalculation of analyses based on thermodynamic considerations. The result is the probable composition of the gas before emission when it was in thermodynamic equilibrium. Disequilibrium modification results from atmospheric oxidation of H_2 and to a lesser extent of CO. The resulting analyses are characterized as "improved compositions" or "restored analyses" [40].

Lava lakes are the safest sites for such collections. A variant on collecting gas from fumaroles is the collection of gases from pyroclastic flows [82]. Beneath the fine compact crust on the ash deposit on the surface of the flows two weeks after the eruption the pyroclastic material was saturated with gases which were collected in an evacuated vessel. The gases were very largely juvenile as indicated by isotopic analysis.

4.3. Condensates

The major constituent of volcanic gases, water vapor, is condensed, often in an alkaline solution. Condensates are usually collected safely from volcanic fumaroles. Analysis of condensate includes the gases which dissolve in it. Gas collected in an evacuated tube at the fumarole may be used to supplement the analyses of condensates so as to include insoluble gases in the total analysis [81].

A modified collection technique is to allow volcanic gas to pass for periods of many days over an alkaline solution and subsequently analyze the solution thus integrating the amount and kind of soluble constituents in the gas over the time of collection [89]. The amount of gas is dependent on the part of the gas cloud sampled as well as wind conditions during sampling. This technique does, however, provide data as to the ratio of these gases in the plume.

4.4. Filters

Allowing volcanic gas to pass through treated filters and subsequent analysis of the filters is used to analyze the acid gases, aerosols and particulates in the gas stream [35, 67, 97, 124].

4.5. Sensors Designed for Analysis of Specific Gases

Sensors through which volcanic gas is pumped have been devised and used in the field to analyze for H [103], He [93], Hg [129], Rn [38], Oxygen [104], HCl, SO_2 [116] and reduced gases [78].

4.6. Spectral Analysis

Flames at volcanic vents as the source of emission spectra and absorption spectra using glowing lava as the light source [86] have indicated the presence of several constituents in volcanic gas, most often Na, Cu, H_2 and water, but have not provided much significant quantitative information. A spectrometer, Miran, in which a sample of gas is analysed in the field [51] has enlarged our data base providing the direct measurements of CO_2 [51, 77].

A spectroscopic method produces quantitative data is the portable correlation spectrometer known as a COSPEC. The blue sky is used as a light source for the SO_2 spectrum to be analysed. This has allowed SO_2 in volcanic clouds to be measured remotely [114]. The concentration-pathlength product multiplied by the wind speed at which the SO_2 is moving is the flux.

An important quantitative application of spectroscopy to gas analysis is the use of TOMS, the total ozone mapping spectrometer, [27, 60, 61, 62, 131]. Sulfur dioxide is detectable from space, if the emission is large enough or if the plume rises high enough, using the near ultraviolet absorption bands of this compound. TOMS produces global images of the atmospheric ozone distribution and can also observe volcanic clouds. From the spectral data the SO_2 content of the cloud can be calculated. Although the TOMS data are not cited directly in Table 1 with respect to the annual SO_2 flux, they are of great significance in this regard.

5. SOURCES WHICH PROVIDE LIMITED QUANTITATIVE INFORMATION

5.1. Leachates

Volcanic ash is a product of many eruptions. If collected before it has been rained on, the water soluble components can be washed from the ash and are known as leachates [8]. Condensed water soluble volatile compounds and aerosols in the cloud of gas are adsorbed on the ash surface. It has been suggested that some of the soluble chemicals in the leachates are the result of adsorbed acid gases reacting with the glass or minerals of the ash fragments [100]. The several hypotheses have been summarized [53]. Many elements have been detected in leachates but all are found in volcanic gas by some other more direct method [85, 112].

5.2. Melt Inclusions

Analysis of gas content of melt inclusions and volcanic glass in rocks is an indirect method by which one may

TABLE 1. Volcanic Gases: Estimates of Annual Subaerial Flux

Gas	Class of volcanoes	Annual Flux Tg.yr $^{-1}$	Reference
CO_2	All subaerial	65	[135]
	Erupting	31	[135]
	Passive degassing	34	[135]
SO_2	All subaerial	18.7	[117]
	Erupting	11.9	[117]
	Not erupting	6.8	[117]
HCl	All subaerial	0.4-11	[120]
	Small explosions and degassing	0.3-10	[120]
HF	All subaerial	0.06-6	[120]
	Small explosions and degassing	0.05-5	[120]

learn the quantity of the analysed gases which may have escaped from a body of rock [5, 26]. The quantitative estimates when applied to gas discharge depend on the amount of magma degassed which is not easily estimated. To the extent that a greater volume of magma has been degassed than has been erupted the estimates of the volume of gas erupted calculated from melt inclusion data are minimal [7].

5.3. Vapor phase minerals

Minerals entrapped in vesicles or in miarolitic cavities indicate the presence of some elements (Cu, Mn, Ti, Fe, Sn) in volcanic gas but do not provide quantitative estimates of the amount [28, 29, 55, 71, 72].

5.4. Wallrock Alteration

The composition of altered wallrock around volcanic gas vents is a clue to the chemical composition of the gas. [70, 94].

5.5. Sublimates

Elements derived from volcanic gas are major elements, or less often trace elements in minerals deposited as sublimates at fumaroles. Artificially formed sublimates are deposited in silica glass tubes inserted into fumaroles. These sublimates form without the intervention of the air [68, 13, 119], resulting in the deposition of many elements before they escape into the atmosphere. Elements in sublimates are not present in amounts related to the quantitative amount in the gas [87]. A compilation of sublimate minerals [118] refers to the earlier classical studies [84, 139, 137, 138]. Additional elements found in sublimates are recorded in more recent papers [9, 14, 32, 59, 95, 98, 105, 128]. All elements in sublimates have been detected in volcanic gas by other more direct methods.

6. NON-VOLCANIC MATERIAL WHICH ARE INDICATORS OF VOLCANIC GAS COMPOSITION

Analysis of non-volcanic natural products may be indicative of volcanic gas composition but frequently leads only to qualitative information as to the gas species or elemental composition of volcanic gas and chemical fallout. These inferential sources of information include composition of lakes [1], seawater, (an unusual amount of some elements such as B, Fe, Mn, Si, P are in the sea water near Santorin [99]), rainwater downwind from a degassing volcano [57], ice, in antarctica [25] and the Greenland Ice Sheet [50, 52], snow [2] and vegetation growing in a volcanic environment, Mt. Etna [90]. The volcanic constituents have been found to occur in volcanic gases by other more direct procedures.

7. VARIATIONS IN THE COMPOSITION OF VOLCANIC GAS

7.1. Overview

Variations in volcanic gas in time and place emphasize the uncertainties in quantitative estimates of gas flux. Emission, even from one volcano, is episodic, making it extremely difficult to calibrate the accuracy of estimates. The variability in the total amount of gas emitted, the kinds of gases and the relative amounts of constituents in emissions require a large data base if the overall composition of volcanic gas is to be properly evaluated. Data are getting better each year as more volcanic emissions are being monitored, new instruments are being used to measure gas and better analytical methods are employed.

Many things contribute to the variability in volcanic gas data including the original abundance of each volatile component in the magma, the specific magmatic product from which the gas is evolving, the temperature of collection, the temperature at which it is evolved from the magma, the length of time gas has been evolving which is a function of the stage of the volcanic eruptive activity, the possible reactions within the gas after evolution but before collection, the degree to which the gases are derived from a non-magmatic source such as ground water, the reaction of gas with wallrock as it exits from the magma. There are also variations due to conditions of collection. The distance down-wind from the volcano or below the gas plume at which gas is sampled determines the amount of fallout by dry deposition. Inappropriate collection methods such as those which allow the possibility of reaction of gas with the collection apparatus may result in variations in the data.

Some volcanoes have emitted gas unusually rich in one or another component and the reason is unexplained. The eruption at the Valley of Ten Thousand Smokes emitted large amounts of fluorine. Etna erupts unusually large amounts of CO_2. Observers of Etna and Vesuvius have considered that Cu is the characteristic element of Etna and Pb of Vesuvius [33]. St. Augustine and Sakurajima are Cl rich relative to SO_2 [58]. Differences in the SO_2 flux are highlighted by the contrast of the very large flux at Bagana and that at Arenal. The later is very much smaller though many other volcanic features of the two volcanoes are very similar [134].

7.2. Variation related to the type of volcanic deposit from which the gases are derived

A noteworthy variation depends on the type of volcanic

setting from which the gases are derived, whether the gases are from the main vent or from associated lava flows or pyroclastic deposits. Long ago it was noted [25] that HCl was preferentially emitted from flows and SO_2 from main vents. Ratios of two gases are most often shown to vary rather than absolute amounts of one.

7.3 Variation related to magma type

Gases differ because of the composition of the magma from which gases are generated. The type of magma is related to the tectonic setting and to the stage of differentiation or assimilation the magma has undergone. The kind and amount of volcanic gases are related to the magmatic products from which they are derived. The composition of glass inclusions in phenocrysts in tephra indicates strikingly different yields of S, Cl and F are to be expected from basaltic, intermediate and silicic eruptions: S, 600; Cl, 65 and F,100 ppm from eruptions of basaltic magma; S, 560; Cl,900 and F,520 ppm from eruptions of intermediate magma; S, 70; Cl,135; F,160 ppm from eruptions of silicic magma [108]. More alkaline magmas are distinctly richer in CO_2. Those from less alkaline or tholeiitic lava are richer in water.

There is an increase in CO_2/SO_2 ratio with increasing magmatic alkalinity and tholeiitic magmas are richer in water [41]. Icelandic rift zone tholeiitic volcanism is distinguished [92] by low halogen contents and very low F/Cl ratios. Off-rift volcanism (alkaline) is associated with high halogen content and high F/Cl ratios. In incrustations in Cl rich system alkali metals dominate, and trace metals are Fe, Cu and Zn. In F rich systems major cations are Ca, Al, Na and Si and trace metals Ti, Mg, Mo and Sr are abundant. Mo is more prominent in the fumarolic incrustations at dacitic domes than in fumaroles in other locations and Cu more prevalent at fumaroles of volcanoes with lavas of andesitic or basaltic composition [Stoiber, unpublished data, 1983].

7.4. Variation related to tectonic setting

Variability in gas composition depending upon tectonic type has been noted in a few instances. The Hawaiian hot spot volcanoes have less HCl relative to sulfur gases when compared to volcanoes in other tectonic settings [73]. Ir is found at hot spot volcanoes in the particulates and in deposits in silica tubes inserted in fumaroles. It is not limited to hot spot volcanoes for it has been reported from a Russian converging plate margin volcano [31].

7.5. Variations related to the stage of activity

The most prominent variations in gases or gas ratios are related to the stage of activity of the volcano [88]. The stage in the eruptive cycle influences the composition of the gas, the least soluble being evolved from the magma earliest. SO_2 variations have been studied more than any others. The flux of SO_2 has been shown to vary between quiet times and times of active eruptions [74, 79], and over periods of years or days [7, 22, 116]. Hg is said to increase at times of greater activity. Radon increased more than four times before the commencement of a new eruption during the 1970 activity of Karensky volcano [21].

7.6. Variation in gas composition indicated by variations in ratios of component gases

Changes in ratios such as S/Cl, Cl/F, $^3He/^{20}Ne$ and CO_2/CO_2+H_2 have been examined because they may be useful precursors of change in eruptive activity of a volcano [54, 79, 89, 101, 123]. Large As/Se ratios [97] may be associated with volcanoes that have recently had large eruptions. Concentrations of SO_4, Ti Al, K, Na, Sn, Zn and Cr tend to decrease in Central American fumarolic condensates as the mean temperatures of the fumaroles decreases [39]. At White Island gas composition has been related to cyclic variations in outlet temperature [45]. There were variations in trace metal and halogen ratios in magmatic gases through an eruptive cycle of the Pu'u O'o vent, Kilauea, Hawaii, July-August 1985 [34].

8. COMPOSITION OF VOLCANIC EMANATIONS

8.1. Overview

Almost all the elements have been detected in volcanic gas, condensates or aerosols and many are found in ash leachates and in fumarolic incrustations. Estimates of gas flux or the percent of each of the gas constituents made in more recent years are an improvement on estimates in classical accounts of volcanic gas [4, 6, 132].

The concentration of an element in a volcanic plume is of little significance relative to the volcanic flux of the element. Measured concentrations depend on where in the plume the sample was taken and how much air had been admixed [30]. Estimates of volcanic gas flux have many shortcomings. Many are based on a published estimate of total SO_2 flux, but all are not from the same estimate. In many instances the flux for degassing volcanoes is estimated separately from that for active volcanoes and the definition of these may differ from author to author. There may be specific caveats in the estimates made for each gas. For CO_2, for example [135], diffusive gas through flanks of volcanoes [3, 19] is not included. The amount of CO_2 gas from such localities as Lake Nyos and other similar localities [46] is unknown.

8.2. Water

Water, believed by most investigators to be the most abundant constituent of volcanic gas, is estimated to vary from 87-98% by volume [6]. most often 95% or more. Menyailov [personal communication 1992] believes that the average water in the gas from circumpacific volcanoes is 95-97 volume per cent. There has been some disagreement. Not over 50% has been suggested as the appropriate value 126]. A recent compilation of 18 analyses [48, 125] contains none from the main vent eruptions of subduction zone volcanoes but does include much of the best data available. The median for H_2O is 78.5 mole per cent. An equal number of data are between 69-79% and 81-98%. A few estimates have been made for water flux at individual volcanoes: 1300 tons per day at Parícutin and 39,000 tons during its period of activity [37], 3.2 million tons from St. Helens [33] and 8500 tons per day (equivalent to 3 $Tg \cdot y^{-1}$) at White Island [101] where it was estimated that the SO_2 discharge was about 1% of the total world discharge of 18.7 $Tg \cdot y^{-1}$ [76]. Information relative to the abundance of water has never been completely assembled. Indirect methods of estimation of the water flux as a percent of solid products erupted give estimates of the annual flux of water of the same order of magnitude despite the uncertainty in the figures on which such estimates are based [5, 16].

The amount of water in volcanic plumes that is magmatic is the subject of debate. In some fumaroles it seems to be very large, based on isotopic evidence [125]. Ground water may supply the gas for eruptions which are then called phreatic. Large volcanic plumes erupted by St. Helens a month before the May 1980 eruption, were largely meteoric, the eruptions phreatic.. The ash was not new magmatic material. Only very small amounts of SO_2 were detected by COSPEC [113]. Lava which enters the sea may heat and react with the sea water to create acid-bearing aerosols [102]

8.3. Major Constituents CO_2, SO_2, HCl, HF

The annual subaerial flux of several of the major constituents of volcanic gas, CO_2, SO_2, HCl and HF has been estimated (Table 1).

8.5. Less Common Constituents: CO, COS, HBr, H_2, He, H_2S

Both the concentration of CO, COS, HBr, He, H_2S and H_2 and their volcanic gas flux are poorly known. Estimates are in Table 2. In a compendium of basaltic volcanism [10] it has been concluded that H_2, H_2S and the noble gases are all present in minor concentrations, less than 0.1 mole per cent in gases from basaltic magmas. In a table of basaltic gas analyses by Taran and others [125, the median values for CO and H_2S are respectively 0.57, and 1.72 mole per cent. Oxygen fugacity ranges from Ni-NiO to a half order of magnitude below quartz-magnetite-fayalite. Concentrations of minor species in volcanic gas are extremely sensitive to temperature and oxygen fugacity within the NNO-QMF bounded region. Calculations of limiting compositions of volcanic gas indicates that SO_2 is favored by temperature above 800°, O_2 fugacities above QMF and relatively anhydrous conditions. H_2S is favored by low temperature, low oxygen fugacities and higher water concentrations [41].

The use of sulfur dioxide COSPEC measurements are the key to the estimates of the annual flux of Cl, CO2, HCl and HF. The COSPEC allows the flux of SO_2 to be measured but without measurement of any other constituent simultaneously. If however the ratio of a constituent with sulfur can be measured by some other method in a plume for which COSPEC information is available, the output of the ratioed element in the plume may be ascertained. The more common procedure is to estimate the ratio of an element with sulfur in as many volcanic plumes or hot fumaroles at sites of volcano degassing as possible. The average ratio is then applied to the latest COSPEC estimate of the annual flux of sulfur from all volcanoes to arrive at an annual flux from all volcanoes for the ratioed element.

8.6. Metallic elements

Annual flux data available for some metallic elements in volcanic gas (Table 3) are estimates usually derived from ratios with SO_2 the flux of which has been measured. All estimates except for Hg are from few data. Patterson and Settle have data from two sites and four volcanoes. Phelan's data in Table 3 is from six non-erupting volcanoes. Nriagu writes that his values are a good order of magnitude [91]. These annual fluxes of the metals for which estimates have been made (excluding Mn and Al) are all small, 7 to 15000 Megagrams (Tonnes) per year. The flux estimates in Mg per year of the 26 elements in Table 3 vary from less than 100 to 250,000. For two of the elements the flux is less than 100, for seven the flux is 100-1000 for nine elements the flux is 1000-10,000 and for eight elements the flux is over 10,000.

The world Pb flux and Po/element ratios have also been used to estimate gas flux in a few instances [66]. The C/3He ratio, a best estimate being 2×10^9 is believed to be unfractionated during degassing. It has been used with the ^3He flux of the solid earth to estimate carbon flux per year [75], (but see discussion [42]).

TABLE 2. Flux Estimates of Gases Exclusive of Major Constituents in Table 1 and Metals and Rock-Forming Elements in Table 3

Gas	Annual Flux	Comments	Reference
CO	0.02 $Tg \cdot y^{-1}$	(approximate)	[18]
COS (all volcanoes)	0.006-0.09 $Tg \cdot y^{-1}$		[12]
COS (erupting volcanoes)	3500-40,000 $Mg \cdot y^{-1}$		[12]
H_2	0.24$Tg \cdot y^{-1}$	(said to be a poor estimate)	[18]
H_2S	<1% of S gas	(exceptions cited)	[117]
HBr	0.0033 $Tg \cdot y^{-1}$		[115]
CH_4	0.34 $Tg \cdot y^{-1}$	(most common organic)	[18]
^{210}Po	50,000 $Ci \cdot y^{-1}$		[64]

TABLE 3. Mineral and Rock-forming Elements: Subaerial Flux

Element	$Mg \cdot y^{-1}$	Reference	Element	$Mg \cdot y^{-1}$	Reference	Element	$Mg \cdot y^{-1}$	Reference
As	3800	[91]	Cu	9400	[91]	Ni	14000	[91]
Al	88000	[66]	Cu	15000	[66]	Pb	400	[91]
Au	8	[97]	Hg	880	[130]	Pb	2500	[66]
Bi	1200	[96]	K	250000	[66]	Sb	710	[91]
Bi	1500	[66]	Mg	1000	[91]	Se	240	[97]
Cd	820	[91]	Mg	45000	[66]	Tl	200	[96]
Cd	1000	[66]	Mn	42000	[91]	W	53	[97]
Cr	15000	[91]	Mo	400	[91]	Zn	9600	[91]
Na	194000	[66]	Zn	5000	[66]			

The daily flux for many elements for which annual flux estimates are not available have been estimated at each of four volcanoes: Erebus [63], White Island [127], Etna [15] and Merapi [119]. Symonds [121] has used Augustine data and equilibrium calculations to estimate the emission rates of many species. There is wide variation in flux at the different localities.

There are analyses of elements in volcanic gas from diverse locations without estimation of any flux values. Many elements, for which there are no estimates of flux, were detected at Tolbachik [80]: Ce, Eu, Ga, Hf, La, Lu, Pt, Sm, Sn, Ti, Ba. In Hawaii Os and Re and Ir [140] have been detected. Information regarding the radioactive elements ^{210}Pb, ^{210}Bi and ^{210}Po, daughter products of ^{222}Rn is derived from the work of Lambert, Andouin and Polisan [65].

9. ESTIMATE OF SUBAERIAL VOLCANIC GAS COMPOSITION AND FLUX

Variation in volcanic gas data emphasizes the difficulty in arriving at estimates of annual subaerial volcanic gas flux. Quantitative information in Table 1 suggests that the annual flux of the major constituents excluding water, CO_2, SO_2, HCl, HF, is 84-100 $Tg \cdot y^{-1}$. The constituents, weight percent, calculated water free, are 65-77% CO_2, 19-22% SO_2, 0.5-11% HCl, 0.01%-6% HF. If we assume that H_2O is 95% volume percent in volcanic gas, an assumption open to question, the weight percent of water is approximately 88%. If 88% by weight of the annual gas flux from subaerial volcanoes is H_2O, the weight of volcanic gas emitted annually is approximately 800 $Tg \cdot y^{-1}$. This gas, calculated from the annual flux esti-

mates, is composed, by weight, of CO_2, 8%; SO_2, 3%; HCl, 1%; HF, less than 0.1%; and H_2O, 88%. together with at most a very few percent of gases for which there is inadequate quantitative information. These include H_2, CO, H_2S, COS, CH_4 and HBr. There is also very small amounts of the metals.

REFERENCES

1. Alcaraz, A., and M. Cardozo, Lake Taal, *Comvol. Lett.*, 3, (4), 1-4, 1969.
2. Alekseev, V., and N. Alexseeva, Avacha fumarolic trace elements: distribution in snow and surface waters, *Volc. Seis., 11,* 325-336, 1990.
3. Allard, P., J. Le Bronec, R. Faivre-Pierret, P. Morel, M. C. Robe, C. Roussel, C. Vavasseur, and P. Zettwoog, Geochemistry of soil emanations from Etna, Sicily., *Terra Cognita, 7,* (2), 407, 1987.
4. Allen, E. T., Chemical aspects of volcanism with a collection of the analyses of volcanic gases, *Franklin Inst. J., 193,* 29-80, 1922.
5. Anderson, A. T. Chlorine, sulfur and water in magmas and oceans. *Bull. Geol. Soc. Am., 85,* 1485-1492, 1974.
6. Anderson, A. T., Some basaltic and andesitic gases, *Rev. Geophys Space Phys., 13,* 37-56, 1975.
7. Andres, R., W. Rose, P. Kyle, F. DeSilva, P. Francis, M. Gardeweg, and H. Morena Roa, Excessive sulfur dioxide emission from Chilean volcanoes, *J. Volcan. Geotherm. Res., 46,* 323-329, 1991.
8. Ashina, T., and Y. Miyake, A geochemical study of the water soluble sublimates of volcanoes; I, water soluble sublimates of volcanic ashes, *Meteor. Soc. Japan, 13,* (Series II), 549-554, 1935.
9. Barnard, W., J. Halbig, and J. Fountain, Geochemical study of fumarolic condensates, *Pacific Science, 44,* (3), 197-206, 1990.
10. Basaltic volcanism study project, *Basalt volcanism on terreestrial planets,* pp. 1286, Pergamon Press, New York, 1981.
11. Bates, T., B. Lamb, A. Guenther, J. Dignon, and R. Stoiber, Sulfur emissions to the atmosphere from natural sources, *J. Atmos. Chem., 14,* 315-337, 1992.
12. Belviso, S., B. C. Nguygen, and P. Allard, Estimate of carbonyl sulfide (OCS) volcanic source strength deduced from OCS/CO2 ratios in volcanic gases, *Geophys. Res. Lett., 13,* (2), 133-136, 1986.
13. Bernard, A. and F. LeGuern, Condensation of volatile elements in high temperature gases at Mt. St. Helens, *J. Volc. Geotherm. Res., 25,* 91-105, 1986.
14. Bernard, A., R. Symonds, and W. I. Rose, Volatile transport and deposition of Mo, W and Re in high temperature magmatic fluids, *Appl. Geochem., 5,* 317-326, 1990.
15. Buat-Menard, P., and M. Arnold, The heavy metal chemistry of particulate matter emitted by Mt. Etna volcano, *Geophys Res. Lett., 5,* 245-248, 1978.
16. Cadle, R. D. Volcanic emissions of halides and sulfur compounds to the troposphere and stratosphere *J. Geophys. Res., 80,* 1650-1652,1975.
17. Cadle, R. D., A. L. Lazrus, B. J. Huebert, L. E. Heidt, R. W.I.Jr., D. C. Woods, R. L. Chuan, R. E. Stoiber, D.B. Smith, and R. A. Zielinski, Atmospheric implications of studies of Central American eruption clouds, *J. Geophys. Res., 84,* (C11), 6961-6968, 1979.
18. Cadle, R. D., A comparison of volcanic with other fluxes of atmospheric trace gas constituents, *Rev. Geophys. Space Phys., 18,* (4), 746-752, 1980.
19. Carbonelle, J., D. Dajlevic, J. Le Bronec, P. Morel, J. C. Obert, and P. Zettwoog, Comesantes sommitales et parietales, des emissions de gas carbonique. Resulta obtenu sur la periode de 1981-1985, *Bull. Pirpsev., 108,* 1-62, 1985.
20. Cas, R. A. F. and J. V. Wright, *Volcanic successions, modern and ancient,* Allen and Unwin, London, pp. 528, 1986.
21. Chirkov, A. M., Radon as possible criterion for predicting eruptions as observed at Karymsky volcano, *Bull. Volcan., 38,* 126-131 1976.
22. Connor, C., R. Stoiber, and L. Malinconico, Variations in sulfur dioxide emissions related to earth tides, Halemaumau crater, Kilauea Volcano, Hawaii, *J. Geophys. Res., 93,* 14,867-14,871, 1988.
23. Decker, R., and B. Decker, Volcanoes, Revised ed. W. H. Freeman and Co., 285pp., New York, 1989.
24. Delmas, R., M. LeGrand, A. Aristarain, and F. Zanolini, Volcanic deposits in antarctic snow and ice, *J. Geophys. Res., 90,* 912-920, 1985.
25. Deville, C. S.-C., Mémoire sur les émanations volcanologique, *Bull. Geol. Soc. France. ser.* 2, *13,* 606, 1855-56.
26. Devine, J., H. Sigurdsson, A. Davis, and S. Self, Estimates of sulfur yield to the atmosphere from volcanic eruptions and potential climatic effects, *J. Geophys. Res., 89,* (B7), 6309-6325, 1984.
27. Doiron, S., G. Bluth, C. Schnetzler, A. Krueger, and W. L., Transport of Cerro Hudson SO_2 clouds, *Eos, 72,* 489 and 498, 1991.
28. Duffield, W. A., Fire fountains of high silica rhyolite magma, a tin rich aerosol?, *Abstr. with Programs Geol.Soc. Am., 19,* (7), 648, 1987.
29. Eggleston, T., and D. Norman, Vapor phase crystallization related to the origin of tin deposits, Black Range NM, *Geol. Soc Am. Abst. with programs, 18,* (6), 593, 1986
30. Faivre-Pierret, R., and F. LeGuern, Health risks linked with inhalation of volcanic gases and aerosols in *Forecasting volcanic events,* H. Tazieff and J. C. Sabroux, Editors, 69-81, New York, 1983.
31. Felitsyn, S. B., P. A. Vaganov, Iridium in the ash of Kamchatkan volcanoes, *Internat. Geol. Rev.,*

30, (12), 1288-1291, 1988.

32. Felitsyn, S. B., P. A. Vaganov, and V. Y. Kir'yanov, Trace element distribution in Kamchatkan ashes from instrumental neutron activation analysis, *Volcan. Seis.*, 12, 195-213, 1991.
33. Fenner, C. N., Pneumatolytic processes in the formation of minerals and ores, in *Ore Deposits of the Western States*, Edited by A. I. M. E. Committee on the Lindgren Volume, 58-106, Am. Inst. Mining and Metallurgical Engineers, New York, 1933.
34. Finnegan, D. L., Variations in trace metal and halogen ratios in magmatic gases through an eruptive cycle of the Pu'u O'o vent, Kilauea, Hawaii, *J. Geophys. Res., 95*, (8), 12,607-12,615, 1990
35. Finnegan, D. L., J. P.Kotra, D. M. Hermann, and W. H. Zoller, Use of ^{7}LiOH impregnated filters for the for the collection of acidic gases and analysis by neutron activation analysis, *Bull. Volcan., 51*, 83-87, 1989.
36. Francis, P., *Volcanoes*, 368 pp., ed. Pelican Books, New York, 1976, pp.368.
37. Fries, C., Volumes and weights of pyroclastic material, lava and water erupted by Parícutin volcano, Michoacan, Mexico, *Trans. Am. Geophys. Union. 34*, (4), 1953.
38. Fruchter, Mt. St. Helens ash from 18 May 1980 eruption, chemical, physical and biological properties, *Science, 209*, 1116, 1980.
39. Gemmell, B., Geochemistry of metallic trace elements in fumarolic condensates from Nicaraguan and Costa Rican volcanoes, *J. Volc. Geotherm. Res., 43*, 161-182, 1987
40. Gerlach, T. M. Evaluation and restoration of the 1970 volcanic gas analyses from Mt. Etna, Sicily, *J. Volc. Geotherm. Res., 6*, 165-178, 1979.
41. Gerlach, T. M., Interpretation of volcanic gas data from tholeiitic and alkaline mafic lavas, *Bull. Volc., 45*, (3), 235-243, 1982.
42. Gerlach, T. M., Present day CO_2 gas emissions from volcanoes. *Eos Trans. AGU, 72*, (23), 249 and 254-255, 1991.
43. Gerlach, T. M., and E. J. Graeber, Volatile budget of Kilauea volcano, *Nature, 313*, 273, 1985.
44. Gerlach, T., and T. Casadevall, Evaluation of gas data from high temperature fumaroles at Mt. St. Helens, 1980-1982, *J. Volcan. Geotherm. Res., 28*, 107-140, 1986.
45. Giggenbach, W. F., Redox processes governing the chemistry of fumarolic gas discharges from White Island, New Zealand, *App. Geochem., 2*, 141-161, 1987.
46. Giggenbach, W., Y. Cabno, and H. Schminke, CO_2-rich gases from L. Nyos, and Mondun, Cameroon, Lacher See, Germany, Dieng, Indonesia and Mt. Gambier, Australia., *J. Volcan. Geotherm. Res., 46*, 331-334, 1991.
47. Giggenbach, W. F., and S. Matsuo, Evaluation of results from second and third IAVCEI field workshops on volcanic gases, Mt. Usu, Japan and White Island, New Zealand, *J. Volcan. Geotherm. Res., 6*, (2), 125-141, 1991.
48. Graeber E. J., T. M. Gerlach, P. Hlava, and A. Bernard, Metal transport and deposition by high temperature gases of the 1983 East Rift eruption, Kilauea volcano, *Eos, Trans. AGU., 64*, (45), 904, 1983.
49. Greenland, P., W. I. Rose, and J.B. Stokes, An estimation of gas emission and magmatic gas content from Kilauea volcano, *Geochim. Cosmochim. Acta, 49*, 125-129, 1985.
50. Hammer, C., Past volcanism revealed by Greenland ice sheet impurities, *Nature , 270*, 482-486, 1977.
51. Harris, D. M., M. Sato, T. Casadevall, W. Rose, and T. Bornhurst, Emission rates of CO_2 from plume measurements in *The 1980 eruption of Mt. St. Helens, Washington*, P. W. Lipman and D. L. Mullineaux, editors, U. S. G. S. Prof. Paper 1250, 201-207, 1981.
52. Herron, M. M., and C. Langway, Impact of volcanic eruptions on atmospheric composition as revealed in Greenland ice sheet strata, *Geol.Soc.Am. Abstr. Programs, 10*, (7), 420, 1978.
53. Hinkley, T. K., and K. S. Smith, Leachate chemistry of ash from the May 18, 1980 eruption of Mt. St. Helens, in *Chemistry of ash and leachates from the May 18, 1980 eruption of Mount St. Helens*, U. S. G. S. Prof. Paper 1375 7-65, 1987.
54. Hirabayashi, J., and M. Kusakabe, A review of the chemical precursors of volcanic eruptions, *Bull. Volc. Soc. Japan, 30*, (3), 171-183, 1985.
55. Hollabaugh, C., B. Robertson, and V. Purcell, The petrology and vapor phase mineralogy of rhyolite and tuffs from Garnet Hill White Pine County, NV, *Northwest Science, 63*, (5), 201-210, 1989.
56. Hughes, J., and R. Stoiber, Vanadium sublimates from the fumaroles of Izalco volcano, El Salvador, *Jour. Volcan. and Geotherm. Res., 24*, 1985.
57. Johnson, N., and R. A. Parnell, Composition, distribution and neutralization of "acid rain" derived from Masaya Volcano, Nicaragua, *Tellus, 38B*, 106-117, 1986.
58. Johnston, D., Contribution of volcanic gas to the atmosphere during explosive eruptions; estimate based on magmatic gas composition, *Eos Trans Am Geophys Union, 61*, (6), 67-68, 1980.
59. Kirsanova, T. P., L. P. Vergasova, L. M. Yurova, and Y. A. Taran, Fumarolic activity of Shivluch and Kizimen Volcanoes in 1979-1980, *Volcan. Seis., 5*, 275-286, 1984.
60. Krueger, A., *Detection of volcanic eruptions from space by their sulfur dioxide clouds*, Am. Inst. Aero. Astron. 23rd Aerospace Sci. Meeting, Reno, NV, 1985.
61. Krueger, A., W. L., C. Schnetzler, G. Bluth, and S. Doiron, The sulfur dioxide content of the June 1991 eruptions of Mt. Pinatubo, *Eos Trans. Am. Geophys. Union 72*, (44), 94, 1991.
62. Krueger, A., L. Walter, and C. Schnetzler, TOMS measurement of the sulfur dioxide emitted during the 1985 Nevado del Ruiz eruptions, *J. Volcan. Geotherm. Res., 41*, 7-16, 1990.
63. Kyle, P., K. Meeker, and D. Finnegan, Emission rates of sulfur

dioxide trace gases and metals from Mt. Erebus, Antarctica, *Geophys. Res. Lett., 17,* (12), 2125-2148, 1990.
64. Lambert, G., A. Buisson, J. Sanak, and B. Ardoin, Modification of atmospheric polonium 210 to lead 210 ratio by volcanic emissions, *J. Geophys. Res., 84,* 6980-6986, 1979.
65. Lambert, G., B. Andouin, and G. Polian, *J. Geophys. Res., 87,* 11, 103-108, 1982.
66. Lambert, G., M. Le Cloerac, and M. Pennisi, Volcanic output of SO_2 and trace metals; a new approach, *Geochim. Cosmochim. Acta, 52,* (1), 29-42, 1988.
67. Lazrus, R. L., R. Cadle, B. Gangrud, J. P. Greenberg, B. J. Huebert, and W. J. Rose, Sulfur and halogen chemistry of the atmosphere and volcanic eruption plumes, *J. Geophys. Res., 84,* 869-875, 1979.
68. LeGuern, F., and A. Bernard, A new method for analyzing volcanic sublimates- application to Merapi volcano, Java., *J. Volcanol. Geotherm. Res., 12,* 133-146, 1982.
69. LeGuern, F., T. Gerlach, and A. Nohl, Field gas chromatograph analyses of gases from a glowing dome at Merapi Volcano, Indonesia, 1977, 1978, 1979, *J. Volcan. Geotherm. Res., 14,* (3-4), 223-245, 1982.
70. Lovering, T., Halogen-acid alteration of ash at Fumarole #1, Valley of Ten Thousand Smokes, Alaska, *Geol. Soc. Am. Bull., 68,* 1585-1604, 1957.
71. Lowenstern, J., G. Mahood, M. Rivers, and S. R. Sutton, Evidence for extreme partitioning of copper into a magmatic vapor phase, *Science, 252,* 1405-1409, 1991.
72. Lufkin, J., Oxide minerals in miarolitic rhyolite, Black Range, New Mexico, *Am. Miner., 61,* 425-430, 1975.
73. Macdonald, G., *Volcanoes,* 510 pp., Prentice-Hall, 1972.
74. Malinconico, L., Fluctuations in SO_2 emissions during recent eruptions of Etna, *Nature, 778,* 43-45, 1979.
75. Marty, B. and A. Jambon, $C/^3He$ in volatile fluxes from the solid earth: implictions for carbon geodynamics, *Earth Planet. Sci Lett., 83,* 16-26, 1987.
76. Marty, B. and W. Giggenbach, Major and rare gases at White Island volcano, New Zealand: origin and flux of volatiles, *Geophys. Res. Lett., 17,* (3) 247-250, 1990
77. McGee, K. Structural dynamics and chemical composition of noneruptive plumes of Mt. St. Helens 1980- 1988, J. Volcan. *Geotherm. Res., 51,* 269-282, 1991.
78. McGee and A. Sutton, A detailed study of the USGS reducing gas sensor with field tests at Long Valley CA, *U.S.Geol. Survey Open File Rept.,* 90-0061, 1990.
79. Menyailov, I., Predictions of eruptions using changes of composition of volcanic gas, *Bull. Volcan., 39,* 112-125, 1975.
80. Menyailov, I., L. Nikitina, V. Shapar, R. V. Guseva, A. Z. Miklishanskiy, V. P. Koloytov, and B. V. Savel'yev, Chemical composition and metal content of magmatic gases of the New Tolbachik volcanoes in 1976, *Dokl. Akad. Nauk, SSSR, 236,* 188-191, 1977.
81. Menyailov, I., L. Nikitina, and V. Shapar, Methode de prelevemnt des gaz et des condensats magmatiques lors de l'eruption du volcan Tobachik (Kamchatka) 1975-77, *Bull. Volcan., 45,* (3), 223-227, 1982.
82. Menyailov, I., L. Nikitina, and V. Shapar, Chemical composition and isotopic ratios of gases from pyroclastic flows in the July 1985 eruption of Bezymyanni volcano, *Volc. Seis., 9,* (4), 557-572, 1990.
83. Murcray, D., F. Murcray, and D. Barker, Changes in stratospheric water vapor associated with the Mt. St. Helens eruption, *Science, 211,* 823-824, 1981.
84. Naboko, S. I., Volcanic exhalations and products of their reactions as exemplified by the Kurile-Kamchatka volcanoes, *Bull. Volcan. , 20,* (Series 2) 129, 1959.
85. Naboko, S., and S. Glavatskikh, The behavior of Cu, Zn, and Pb in modern volcanic processes: implications for the genesis of sulfide deposits, *Volc. Seis., 12,* 214-240, 1991.
86. Naughton, J. J., Volcanic flame: source of fuel and relation to volcanic gas-lava equilibrium, *Geochim. Cosmochim. Acta, 37,* 1163-1169, 1973.
87. Naughton, J., V. Greenburg, and R. Gofuel, Incrustations and fumarolic condensates at Kilauea Volcano, Hawaii: field, drill hole and laboratory observations, *J. Volcan. Geotherm. Res., 1,* 149-165, 1976
88. Naughton, J. J., V. Lewis, D. Thomas, and J. B. Finlayson, Fume compositions found in various stages of activity at Kilauea Volcano, Hawaii, *J. Geophys. Res., 80,* 2963-2966, 1975.
89. Noguchi, K., and H. Kamiya, Prediction of volcanic eruptions by measuring the chemical composition of the amounts of gases, *Bull. Volcan., 26,* 367-378, 1963.
90. Nottcut, G., and F. Davies, Accumulation of volcanogenic fluoride by vegetation; Mt. Etna, Sicily, *J. Volcan. Geotherm. Res., 39,* (4), 329-333, 1989.
91. Nriagu, J., A global assessment of natural sources of trace metals, *Nature, 338,* 47, 1989
92. Oskarsson, N., The chemistry of Icelandic lava incrustations and the latest stages of degassing, *J. Volcanol. Geotherm. Res., 10,* 93-110, 1981.
93. Oskarsson, N., The interaction between volcanic gases and tephra, *J. Volcan. Geotherm. Res., 8,* 251-266, 1980.
94. Papike, J., T. Keith, M. Spilde, K. Galbraith, C. Shearter, and J. Laul, Geochemistry and mineralogy of fumarolic deposits, Valley of Ten Thousand Smokes, Alaska: bulk chemical and mineralogical evolution of dacite-rich protolith, *Am. Miner., 76,* 1662-1673, 1991.
95. Patterson, J. A., 1983, The systematics of fumarolic incrustations, B.S., Dartmouth College, Hanover, NH.
96. Patterson, and Settle, Magnitude of lead flux to the atmosphere from volcanoes, *Geochim. Cosmochim. Acta, 52,* 245, 1988.
97. Phelan, J. M., 1983, Volcanoes as a source of volatile trace elements in the atmosphere, Ph.D., Univ. of Maryland, Baltimore, MD.
98. Popova, V. I., N. S. Popov, N. S.

Rudashevskiy, S. F. Glavatskikh, V. O. Polyakov, and A. F. Bushmakin, Nabokoite $Cu_7TeO_4(SO_4)_5KCl$ and atlasovite $Cu_6Fe_3Bi_3O_4(SO_4)_5 \cdot KCl$, new minerals from volcanic gases, *Zapiski Vsesoyuznogo Mineralogicheskogo Obshchestva, 116*, (3), 358-369, 1987.

99. Pushkina, Z. V., Iron, manganese, silicon, phosphorus, boron, and aluminum in sea water in the area of Santorin volcano, *Litol. Polez. Iskop., 2*, 87-96, 1967.
100. Rose, W. I., Scavenging of volcanic aerosol by ash: atmospheric and volcanologic implications, *Geol., 5*, 621-624, 1977.
101. Rose, W. I., R. I. Chuan, W. F. Giggenbach, P. R. Kyle, and R. B. Symonds, Rates of sulfur dioxide and particle emissions from White Island volcano, New Zealand, and an estimate of total flux of the major gaseous species, *J. Volcanol., 48*, 181, 1986.
102. Sansone, F. J., J. Resing, G. W. Tribble, P. N. Sedwick, K. M. Kelly, and K. Hon, Lava-sea water interactions at shallow-water submarine lava flows, *Geophys. Res. Lett., 18*, (9), 1731-1734, 1991.
103. Sato, M., K. A. McGee, and I. Furukawa, Continuous hydrogen monitoring at Mt. St. Helens, *Eos Trans. AGU, 80*, 1139, 1980.
104. Sato, M., and T. L. Wright, Oxygen fugacities directly measured in volcanic gases, *Science, 153*, (3740), 1103-1105, 1966.
105. Serafimova, V., L. Verghasova, and T. Ziborova, Carbonate formations in fumaroles of the great fissure eruption of Tolbachik, *Volc i Seis., 2*, 46-59, 1986.
106. Shephard, E. S., The composition of the gases from Kilauea, *Hawaiian Volc. Obs. Bull., 7*, (7), 94-97, 1919.
107. Shephard, E. S., Two gas collections from Mauna Loa, *Hawaiian Volc. Obs. Monthly Bull.*, 8, (5), 65-67, 1920.
108. Sigurdsson, H., and N. Metrich, Volcanic volatile mass yield estimates to the atmosphere and climatic effects, *NM Sch. of Mines and Mineral Res., 131*, 242, 1990.
109. Sigvaldason, G., and G. Elisson, Collection and analyses of volcanic gas at Surtsey, *Geochim. cosmochim. Acta, 32*, 797-805, 1968.
110. Simkin, T., and L. Siebert, Explosive eruptions in space and time: Duration, intervals and a comparison of the world's active volcanic belts, in *Explosive Volcanism: Inception, Evolution and Hazards*, 110-121, Natl. Acad. Press, Washington, D.C., 1984.
111. Simkin, T. L., L. Siebert, L. McClelland, D. Bridge, C. Newhall, and J. H. Latter, editors, *Volcanoes of the World*, 232 pp., Hutchinson Ross, Stroudsburg, PA, 1981.
112. Smith, D. B., R. A. Zielinski, and W. I. Rose, Leachability of U and other elements from from freshly erupted volcanic ash, *U.S.G.S. Open file report.* (81-118), 1981.
113. Stoiber, R., S. Williams, and L. Malinconico, Mt. St. Helens, Washngton, 1980 volcanic eruption: magmatic gas component during the first 18 days, *Science, 208*, 1258-1259, 1980.
114. Stoiber, R., S. Williams and L. Malinconico, Use of the correlation spectrometer at volcanoes, in *Forecasting Volcanic Events*, H. Tazieff and J. C. Sabroux, editors, 421-444, Elsevier, New York, 1983.
115. Stoiber, R., S. Williams, and B. Huebert, Sulfur dioxide, hydrochloric acid, hydrofluoric acid, hydrobromic acid from volcanoes; annual atmospheric contribution, *Geol Soc. Am. Abstracts with programs, 15*, (6), 698-699, 1983.
116. Stoiber, R., S. Williams, and B. Huebert, Sulfur and halogen gases at Masaya Caldera Complex, Nicaragua: total flux and variations with time, *J. Geophys. Res., 91*, (B12), 12,215-12,231, 1986.
117. Stoiber, R., S. N. Williams, and B. Huebert, Annual contribution of sulfur dioxide to the atmosphere by volcanoes, *J. Volc. Geotherm. Res., 33*, 1-8, 1987.
118. Stoiber, R., and W. I. Rose, Fumarolic incrustations at active Central American volcanoes, *Geochim. Cosmochim. Acta, 38*, 495-516, 1974.
119. Symonds, R. B., W. I. Rose, M. H. Reed, F. E. Lichte, and D. L. Finnegan, Volatilization, transport and sublimation of metallic and non-metallic elements in high temperature gases at Merapi volcano, Indonesia, *Geochim. Cosmochim. Acta, 51*, 2083-2101, 1987.
120. Symonds, R., Rose, W.I., and Reed M., Contribution of Cl^- and F^- bearing gases to the atmosphere, *Nature, 344*, 415-418, 1988.
121. Symonds, R. Evaluation of gases condensates and SO_2 emission from Augustine volcano, Alaska: the degassing of a Cl-rich volcanic system, *Bull. Volcan.*, 355-374, 1990.
122. Symonds, R., Reed, M. and Rose,W.I., Origin, speciation and fluxes of trace element gases at Augustine volcano, Alaska: Insights into magma degassing and fumarolic processes, *Geochim. Cosmochim. Acta, 56*, 633-657, 1992.
123. Takaona, N., Study of volcanic gas by isotopic analysis of noble gas for eruption prediction by geochemical techniques, *Bull. Volcan. Soc. Japan, 30*, (3), 185-196, 1985.
124. Tanaka, S., Y. Hashimoto, M. Darzi, and J. Winchester, Sampling methods and PIXE analysis for atmospheric sulfur dioxide with alkali coated filters, *Nuclear Instruments and Methods, 181*, 509-515, 1981.
125. Taran, Y. A., A. M. Rozhkov, E. K. Serafinova, and A. D. Esikov, Chemical and isotopic composition of magmatic gases from the 1988 eruption of Klyuchevskoy volcano, Kamchatka, *J. Volcan. Geotherm. Res., 46*, 255-263, 1991.
126. Tazieff, H., New investigations on eruptive gas, *Bull. Volcanol., 31*, 424-438, 1971.
127. Tedesco, D., and J.-P. Toutain, Chemistry and emission rate of volatiles from White Island Volcano, *Applied Geochem., 18*, (1), 113-116, 1991.
128. Toutain, J. P., and G. Meyer, Iridium bearing sublimates at a hot spot volcano (Piton de la Fournaise, Indian Ocean), *Geophys. Res. Lett., 16*, (12), 1391-1394, 1989.

129. Varekamp, J., and P. Buseck, Mercury emissions from Mt. St. Helens during Sept. 1980, *Nature, 293,* 555-556, 1981.
130. Varekamp, J. C., and P. R. Buseck, Global mercury flux from volcanic and geothermal sources, *Applied Geochem., 1,* (1), 65-73, 1986.
131. Walter, L., A. Krueger, C. Schnetzler, S. Doiron, and D. Sullivan, Satellite survey of sulfur dioxide emissions during explosive eruptions, *NM Bur. Mines and Mineral. Res. Bull., 131,* 286, 1989.
132. White, D. A., and Waring G.A., Volcanic Emanations, in *Data of Geochemistry,* K1-K29, U. S. G. S. Prof. Paper 440, 1963.
133. Williams, H., and A. MacBirney, *Volcanology,* pp. 397, Freeman Cooper and Co., San Fransisco, CA, 1979.
134. Williams, S., and R. E. Stoiber, 1992, Arenal (Costa Rica) and Bagana (PNG); similar volcanoes yet different SO2 emission patterns in *Chapman Conference-Climate, volcanism and global change, 22,* 1992.
135. Williams, S. N., S. J. Schaefer, V. Calvache M., and D. Lopez, Global carbon dioxide emission to the atmosphere by volcanoes, *Geochim. Cosmochim. Acta, 36,* 1765-1770, 1992.
136. Wilson, L., Volcanic gas release rates, *Nature, 313,* 266, 1985.
137. Zambonini, F. Mineralogia Vesuviana, *Atti della R. Accad. della sci. fis. e mat.,* Napoli, ser. 2 (6), 1-359, 1910.
138. Zambonini, F. Mineralogia Vesuviana, 2nd edition, *Atti della R. Accad. della sci. fis. e mat.,* Napoli, ser. 2 (supp. a cure di Emaueler Quercigh), 1936.
139. Zeis, E. G. The valley of ten thousand smokes, the fumarolic incrustations and their bearing on ore deposition, *Nat. Geog. Soc. Tech. Papers, 1,* (4), 1-81, 1929.
140. Zoller, W. H., J. R. Parrington, and J. M. P. Kotra, Iridium enrichment in airborne particles from Kilauea volcano, *Science, 222,* 1883, 1983.

Properties and Composition of the Terrestrial Oceans and of the Atmospheres of the Earth and Other Planets

Bruce Fegley, Jr.

1. PHYSICAL PROPERTIES AND COMPOSITION OF THE TERRESTRIAL OCEANS

Geographical data on the areas, volumes, and depths of the major ocean basins are summarized by Turekian [209]. Many physical properties of seawater are summarized by Cox [49] and Riley [182]. The major element composition of seawater is reviewed by Wilson [216]. A comprehensive discussion of the chemistry of the atmosphere-ocean system, of continental weathering, riverine inputs to the oceans, and the composition of sea water over geologic time is given in two books by Holland [105,106]. Many in depth reviews of different aspects of the chemistry of seawater are given in the multivolume series *Chemical Oceanography,* most recently edited by Riley and Chester.

The temperature of ocean surface waters depends on the geographic location and season of the year. It is also affected by the presence of oceanic currents which transport waters from northern or southern latitudes. Thus, surface waters in the Gulf Stream still have relatively high temperatures at northern latitudes. The deeper regions of the oceans, below about 1 km depth, have a nearly constant temperature of 275-277 K due to their origins in high latitudes around Greenland and the Antarctic continent. Between about 100 meters depth, the bottom of the well mixed layer, and 1 km depth, the temperature of sea water decreases nearly monotonically to the low values typical for the deeper regions of the oceans. This transition region is known as the thermocline.

The salinity of ocean water is about 35 parts per thousand by mass (35 ‰); variations from about 33 ‰ to 38 ‰ are observed in the open oceans. As illustrated in Table 1, the composition of sea water is dominated by the six elements Cl, Na, S, Mg, Ca, and K. Despite the observed variations in salinity, their concentrations relative to one another are essentially constant. These elements and the other elements in sea water which behave similarly are conservative elements. Variations in their concentrations can be explained solely by either the addition or subtraction of pure water to the oceans. Because of this conservative behavior the salinity of sea water can be determined by measuring the content of chloride, the most abundant anion in sea water. The salinity (S) is related to the chlorinity (Cl) by the approximate equation S(‰) ~ 1.805 Cl(‰) + 0.030, where both S and Cl are in g/kg of sea water. Cox [49] describes several methods, including conductivity measurements, for more accurate and precise measurements of the salinity of sea water.

Other elements display variable concentrations relative to local salinity and are nonconservative. Several of these elements such as C, N (as nitrate), Si, and P are nutrients, and are generally depleted in surface waters and are enriched in deeper regions. Many other elements (e.g., Cr, Mn, Fe, Co, Ni, Cu, Zn, Sr, Cd) have vertical concentration profiles similar to those of the nutrient elements. However, it is not always clear if this similarity is due to passive processes (e.g., coprecipitation, adsorption on dead sinking organisms) or to active biochemical processes. For example, growth of phytoplankton is apparently limited by the availability of Fe. On the other hand, Al also displays nutrient-like profiles but this is probably due to surface inputs by

B. Fegley Jr., Department of Geology and Planetary Sciences, Washington University, St. Louis, MO 63130

Global Earth Physics
A Handbook of Physical Constants
AGU Reference Shelf 1

TABLE 1. Chemical Composition of Seawater[a,b]

At. No.	Element	Dissolved Form	Mean Concentration	Notes & References
1	H	H_2		biogenic or hydrothermal origin
2	He	Dissolved He	1.9 nmole/kg	non-nutrient dissolved gas
3	Li		178 µg/kg	conservative
4	Be		0.2 ng/kg	increases with depth
5	B	Inorganic boron	4.4 mg/kg	conservative
6	C	Total CO_2	2200 µmole/kg	nutrient
7	N	N_2	590 µmole/kg	non-nutrient dissolved gas
		NO_3	30 µmole/kg	nutrient
8	O	Dissolved O_2	150 µmole/kg	biologically controlled profile
9	F	Fluoride	1.3 mg/kg	conservative
10	Ne	Dissolved Ne	8 nmole/kg	non-nutrient dissolved gas
11	Na		10.781 g/kg	conservative
12	Mg		1.28 g/kg	conservative
13	Al		1 µg/kg	nutrient-like profile
14	Si	Silicate	110 µmole/kg	nutrient
15	P	Reactive phosphate	2 µmole/kg	nutrient
16	S	Sulfate	2.712 g/kg	conservative
17	Cl	Chloride	19.353 g/kg	conservative
18	Ar	Dissolved Ar	15.6 µmole/kg	non-nutrient dissolved gas
19	K		399 mg/kg	conservative
20	Ca		415 mg/kg	conservative (1st. approx.)
21	Sc		<1 ng/kg	
22	Ti		<1 ng/kg	
23	V		<1 µg/kg	conservative
24	Cr		330 ng/kg	nutrient-like profile
25	Mn		10 ng/kg	nutrient-like profile
26	Fe		40 ng/kg	nutrient-like profile
27	Co		2 ng/kg	nutrient-like profile
28	Ni		480 ng/kg	nutrient-like profile
29	Cu		120 ng/kg	nutrient-like profile
30	Zn		390 ng/kg	nutrient-like profile
31	Ga		7-60 ng/kg	[164]
32	Ge		5 ng/kg	correlated with silicate
33	As	As(V)	2 µg/kg	nutrient-like profile
34	Se	Total Se	170 ng/kg	correlated with phosphate

TABLE 1. (continued).

At. No.	Ele-ment	Dissolved Form	Mean Concentration	Notes & References
35	Br	Bromide	67 mg/kg	conservative
36	Kr	Dissolved Kr	3.7 nmole/kg	non-nutrient dissolved gas
37	Rb		124 μg/kg	conservative
38	Sr		7.8 mg/kg	correlated with phosphate
39	Y		13 ng/kg	conservative (1st approx.)
40	Zr		<1 μg/kg	
41	Nb		1 ng/kg	
42	Mo		11 μg/kg	conservative
44	Ru		~1 ng/kg	[14]
45	Rh			
46	Pd		0.2-0.7 pmole/kg	[132]
47	Ag		3 ng/kg	
48	Cd		70 ng/kg	correlated with phosphate
49	In		0.2 ng/kg	
50	Sn		0.5 ng/kg	anthropogenic
51	Sb		0.2 μg/kg	conservative
52	Te	Total Te	0.6-1.3 pmole/kg	[133]
53	I		59 μg/kg	correlated with phosphate
54	Xe		0.5 nmole/kg	non-nutrient dissolved gas
55	Cs		0.3 ng/kg	conservative
56	Ba		11.7 μg/kg	nutrient-like profile
57	La		4 ng/kg	nutrient-like profile
58	Ce		4 ng/kg	nutrient-like profile
59	Pr		0.6 ng/kg	nutrient-like profile
60	Nd		4 ng/kg	nutrient-like profile
62	Sm		0.6 ng/kg	nutrient-like profile
63	Eu		0.1 ng/kg	nutrient-like profile
64	Gd		0.8 ng/kg	nutrient-like profile
65	Tb		0.1 ng/kg	nutrient-like profile
66	Dy		1 ng/kg	nutrient-like profile
67	Ho		0.2 ng/kg	nutrient-like profile
68	Er		0.9 ng/kg	nutrient-like profile
69	Tm		0.2 ng/kg	nutrient-like profile
70	Yb		0.9 ng/kg	nutrient-like profile
71	Lu		0.2 ng/kg	nutrient-like profile

TABLE 1. (continued).

At. No.	Element	Dissolved Form	Mean Concentration	Notes & References
72	Hf		<8 ng/kg	
73	Ta		<2.5 ng/kg	
74	W		<1 ng/kg	
75	Re		7.2-7.4 ng/kg	conservative, [1]
76	Os			
77	Ir			
78	Pt			
79	Au		50-150 fmole/liter	[75]
80	Hg		6 ng/kg	correlated with silicate
81	Tl		12 ng/kg	conservative
82	Pb		1 ng/kg	anthropogenic
83	Bi		10 ng/kg	
90	Th		<0.7 ng/kg	
92	U		3.2 μg/kg	conservative

[a]Modified from [179]

[b]Abbreviations: mg/kg = 10^{-3}g/kg, μg/kg = 10^{-6}g/kg, ng/kg = 10^{-9}g/kg, pmole/kg = 10^{-12}mole/kg, fmole/l = 10^{-15}mole/liter

dust and decreases at depth as a result of scavenging by organic particulates and by sedimentation of mineral grains.

Dissolved gases generally have abundance patterns that are initially controlled by their solubility in surface waters at the ambient temperature and gas partial pressure. The mixing produced by waves can also lead to trapping of air bubbles, which will introduce a deviation from the solubility controlled abundance. The exceptions to this behavior are gases such as O_2, CO_2, CO, H_2S, H_2, N_2O, and N_2 which are involved in biological processes. For example, the O_2 concentration is higher in surface waters where it is produced by photosynthesis and is lower in deeper regions where it is consumed by respiring organisms.

Quinby-Hunt and Turekian [179] discuss several other factors which also affect the vertical profiles of some elements in sea water. Radionuclides produced from fission and fusion bombs (e.g., tritium (T), the bomb component of ^{14}C, ^{90}Sr, ^{137}Cs, Pu) are supplied to the ocean from the atmosphere and coastal sources. As a consequence their concentrations decrease with increasing depth in the oceans. Likewise, the concentration of Pb, which is an anthropogenic input to the oceans, displays similar behavior. On the other hand, the major source for ^3He is at oceanic spreading centers; infalling cosmic dust and meteorites are estimated to contribute <25% of the ^3He in the oceans [140]. Removal processes at the sea floor also influence the distribution of some trace elements and nuclides.

To a first approximation, chemical equilibria between atmospheric CO_2, dissolved carbonate and bicarbonate, and $CaCO_3$(s) are responsible for controlling the pH of the oceans. The relevant equilibria and equilibrium constants at 298 K are

$$CO_2(g) = CO_2(aq)$$
$$K_{eq} = 10^{-1.43}$$
$$CO_2(aq) + H_2O = H^+(aq) + HCO_3^-(aq)$$
$$K_{eq} = 10^{-6.35}$$
$$HCO_3^-(aq) = H^+(aq) + CO_3^{2-}(aq)$$
$$K_{eq} = 10^{-10.33}$$
$$CaCO_3(s) = Ca^{2+}(aq) + CO_3^{2-}(aq)$$
$$K_{eq} = 10^{-8.34}$$

If this system of equations is solved using the constraints of mass balance, chemical equilibrium, and charge balance, the derived pH for the observed CO_2 partial pressure

TABLE 2. Physical Properties of Planetary Atmospheres[k]

Planet/Satellite	Surface Temperature (K)	Surface Pressure (Bars)	Surface Gravity (cm s^{-2})	Mean Mol. Wt. (g $mole^{-1}$)	Pressure Scale Height (km)[h]
Mercury[a]	590-725[i]	$<10^{-12}$	372	species dependent	species dependent
Venus[b]	737	95	887	43.45	15.9
Earth[c]	288	1.01	978	28.97	8.5
Mars[d]	215	~6.36 mbars	372	43.34	11.1
Jupiter[e]	165±5(1 bar)	adiabat P>1 bar	2312	2.22	27
Saturn[e]	134±4 (1 bar)	adiabat P>1 bar	896	2.07	59.5
Uranus[e]	76±2 (1 bar)	adiabat P>1 bar	869	2.64	27.7
Neptune[e]	71.5±2 (1 bar)	adiabat P>1 bar	1100	2.53-2.69	19.1-20.3
Pluto[f]	~50(?)	~3 μbars(?)	40(?)	~16-25(?)	~60
Titan[g]	94	1.5	135	~28.6	~20.2
Triton[j]	38±4	16±3μbars	78	~28(?)	~14.4(?)

[a]Values from [212].

[b]Values from [186].

[c]Values from [214].

[d]Values from [7]. The CO_2 pressure varies by about 37% due to the annual condensation into & sublimation out of the polar caps.

[e]Values for the temperatures at 1 bar and the equatorial surface gravity for the Jovian planets are from [135]. The Jovian planets do not have a solid surface. The observed P,T profiles are adiabatic below the tropopauses and the necessity to transport the observed heat fluxes out of the planets (except Uranus) requires adiabatic P,T profiles at lower levels below those directly probed by spacecraft. An adiabatic profile is also assumed in theoretical models of Uranus [175].

[f]Values from [108]. The lower value for the mean mol. wt. corresponds to a pure CH_4 atmosphere, the upper value is that chosen by [108].

[g]Values from [109].

[h]The pressure scale height values are either at the planetary surface or at the 1 bar level.

[i]Temperature of the sunward side of Mercury.

[j]Data from [29,95,211].

[k](?) indicates that the value is uncertain

(~ 0.34 mbars) is about 8.4. This is close to the value of ~ 8 observed in sea water.

The concentrations of the major conservative elements in sea water are controlled by a balance between riverine inputs and various loss processes For example, most Na and Cl are removed from the oceans in porc waters in ocean sediments, as sea spray, and as evaporites. Magnesium is mainly removed by hydrothermal exchange. Sulfur is depleted by the deposition of biogenic sediments (which also depletes Ca) and by hydrothermal exchange. Potassium is apparently removed by ion exchange with clay minerals to form illite and by some reactions with basalt, but its mass balance is not well understood.

2. COMPOSITION OF THE ATMOSPHERES OF THE EARTH AND OTHER PLANETS

This section presents physical and chemical data on the at-

mospheres of the Earth, the other planets, Titan, the largest satellite of Saturn, and Triton, the largest satellite of Neptune. The physical properties of the different planetary atmospheres are summarized in Table 2; their chemical and isotopic compositions are summarized in Tables 3-13. The data in these tables come from various sources. Compositional data on the terrestrial atmosphere are obtained from direct measurements at ground level, from balloons and high flying aircraft, ground-based spectroscopy, and satellite measurements. Earth-based remote sensing and *in situ* spacecraft measurements provide the data for the other planets, Titan, and Triton (e.g., see Hanel et al [98] for a review of infrared remote sensing techniques). Schematic P,T profiles for Venus, Earth, Mars, and Titan are illustrated in Figure 1 and those for the four Jovian planets are displayed in Figure 2. The properties of the different planetary atmospheres are discussed below in order of increasing radial distance from the Sun.

2.1 Mercury

The planet Mercury has a very tenuous atmosphere composed of atomic H, He, O, Na and K. Dayside number densities are 100 to 40,000 atoms cm^{-3} , about two orders of magnitude lower than the Mariner 10 radio occultation upper limit of $P < 10^{-12}$ bars. The atoms in the Mercurian atmosphere come from the solar wind (H, He) and from evaporation of meteoritic material (O, Na, K) impacting the surface. Recent descriptions of the properties of the Mercurian atmosphere are given in Vilas et al [212] and Sprague [192].

2.2 Venus

The chemical composition of the Venusian atmosphere and the probable sources and sinks for the gases in it are listed in Table 3. The isotopic composition of the Venusian atmosphere is summarized in Table 4. A comprehensive review of the chemistry and spectroscopy of the atmosphere of Venus is given by Von Zahn et al [213]. This has recently been updated by Fegley and Treiman [77].

The abundance of SO_2 (Table 3) decreases with increasing altitude above 48 km (the main cloud base) due to its photochemical conversion to H_2SO_4 droplets which make up the global cloud layer. At cloud top levels (~70 km) the SO_2 abundance is 100 ppb or less, and has been decreasing with time during the 1978-1992 period [154]. The water vapor abundance also decreases above the cloud base to typical values of a few ppm at cloud top levels [213]. As indicated in Table 3, the H_2O abundance is also altitude dependent in the sub-cloud atmosphere. It decreases from values of about 150 ppm at 42 km to values of about 20 ppm at the surface [60,153]. The cause(s) for this profile is/are controversial; formation of another hydrogen bearing gas or atmosphere-surface reactions may be involved. The ongoing controversy about the abundance and vertical profile of water vapor on Venus is discussed by Fegley and Treiman [77]. Data from the Pioneer Venus (PV) and Venera 11/12 spacecraft [87,149,172] also show an apparent decrease in the CO abundance with decreasing altitude. The Kr abundance given in Table 3 is also a subject of debate. Inconsistent Kr abundances were obtained by the PV Large Probe neutral mass spectrometer and the Venera

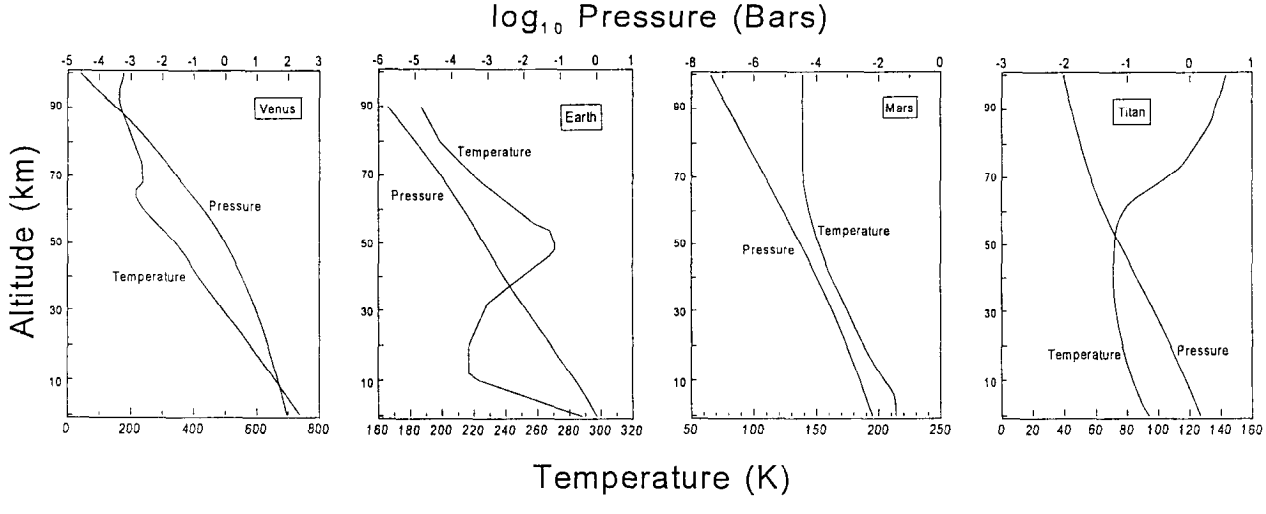

Fig. 1. Schematic P,T profiles for the atmospheres of Venus, Earth, Mars, and Titan. Data from Seiff (1983), Warneck (1988), Barth (1985), and Lindal et al (1983).

11/12 mass spectrometers [213]. The values given in Table 3 reflect Donahue's analysis of the PV data [59].

The isotopic ratios in Table 4 for C, N, O, Cl, and $^{36}Ar/^{38}Ar$ are identical to the terrestrial values within the uncertainties of the measurements. However, the isotopic ratios for D/H, $^{20}Ne/^{22}Ne$, and $^{40}Ar/^{36}Ar$ are not identical. The D/H ratio on Venus is about 100-120 times larger than the D/H ratio of the Earth as defined by standard mean ocean water (SMOW, see Table 6). The $^{20}Ne/^{22}Ne$ ratio is also larger and is closer to the assumed solar value [174]. The $^{40}Ar/^{36}Ar$ ratio is about 300 times smaller than the terrestrial value. No information is available on the $^{3}He/^{4}He$ ratio. The implications of the isotopic data for the origin and evolution of the atmosphere of Venus have been extensively discussed [134,174].

2.3 Earth

Table 5 summarizes the chemical composition of important constituents in the non-urban terrestrial troposphere, Figure 3 displays vertical abundance profiles for important minor and trace gases in the terrestrial stratosphere, and Table 6 summarizes the isotopic composition of the noble gases in the terrestrial atmosphere and of terrestrial standards for isotopic analysis of H, C, N, O, and Cl for comparison with data for other planetary atmospheres. Chamberlain and Hunten [33] summarize atmospheric chemistry, dynamics, and spectroscopy. Terrestrial atmospheric chemistry is summarized by Warneck [214]. The different chemical compounds found in the terrestrial atmosphere are tabulated by Graedel [90].

The terrestrial atmosphere is divided into several regions, primarily on the basis of temperature. The troposphere is the region closest to the surface where temperature decreases with altitude. The gradient (lapse rate) is about 6.5 K/km up to the tropopause, at about 12 km, where the mean temperature is about 216 K (see Figure 1). The region immediately above the tropopause is the stratosphere. In contrast to the troposphere which contains about 1-4 % water vapor by volume, the stratosphere is extremely dry due to the cold trap at the tropopause. The stratosphere is also characterized by a temperature increase with increasing altitude up to the stratopause (at about 50 km) where the temperature peaks. The temperature rise is due to absorption of solar ultraviolet radiation by O_3. The mesosphere, where temperature again decreases with altitude, lies between 50-80 km. The thermosphere where strong heating occurs due to absorption of solar UV radiation, leading to extensive photodissociation and photoionization of N_2 and O_2, is at about 80-100 km.

Important aspects of tropospheric chemistry include biogeochemical cycles such as those involving carbon, water,

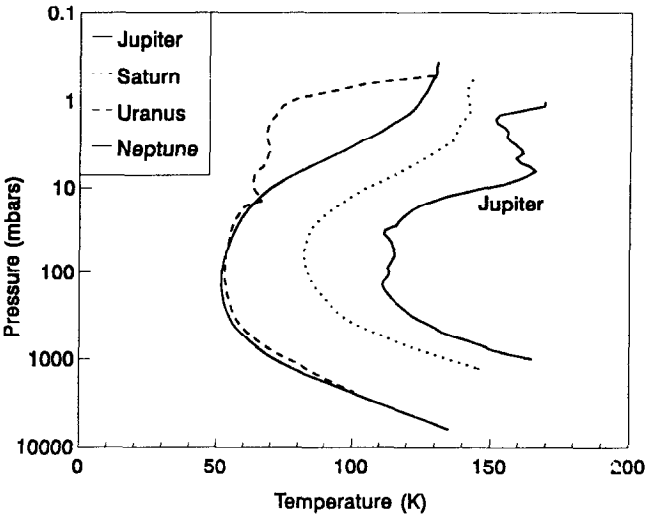

Fig. 2. Schematic P,T profiles based on Voyager radio occultation data for the atmospheres of the Jovian planets (Lindal 1992).

nitrogen, and sulfur and the production and destruction of various trace gases (e.g., CH_4, other hydrocarbons, SO_2, reduced sulfur gases, NO_x, O_3). Important greenhouse gases produced naturally or via human activity in the troposphere are CO_2, CH_4, N_2O, and the halocarbons. The OH radical plays an important role in the production and destruction of many trace gases as the major oxidizer in tropospheric chemistry. Hydroxyl radicals in the troposphere are produced from the photolysis of O_3 to produce electronically excited O atoms which subsequently react with H_2O to produce two OH radicals from each water molecule. The globally averaged mean OH concentration in the troposphere is about $10^{5.7}$ OH per cm^3.

Stratospheric chemistry is closely connected to the O_3 layer at 15-35 km, which both shields the Earth from biologically harmful solar UV radiation shorter than about 300 nm and also dissipates the absorbed radiation as heat. The O_3 distribution in the stratosphere is controlled by a balance between production and destruction and by the transport of O_3 from regions of net production to regions of net destruction. In the absence of other perturbing influences, the production and destruction of O_3 involves the four reactions of the Chapman cycle:

$$O_2 + h\nu(\lambda = 180 - 240nm\ ) \rightarrow O +$$
$$O + O_2 + M \rightarrow O_3 + M$$
$$O_3 + h\nu(\lambda = 200 - 300nm\ ) \rightarrow O_2 +$$
$$O + O_3 \rightarrow O_2 + O_2$$

This cycle is perturbed by the presence of other trace

TABLE 3. Chemical Composition of the Atmosphere of Venus

Gas	Abundance	Source(s)	Sink(s)	Notes & References
CO_2	96.5±0.8%	Outgassing	Carbonate formation	[213]
N_2	3.5±0.8%	Outgassing	---	[213]
SO_2[a]	185±43 ppm	Photochemistry &	H_2SO_4 formation &	22km, [172]
	130±35 ppm	Outgassing	$CaSO_4$ formation	<42 km, [87]
H_2O[a]	150 ppm	Outgassing	H escape &	42 km, [153]
	60 ppm		Fe^{2+} oxidation	22 km, [153]
	20 ppm			0 km, [153]
	40 ppm			35-45 km, [19]
Ar	70±25 ppm	Outgassing, primordial	---	[213]
CO[a]	45±10 ppm	CO_2 photolysis	Photooxidation	cloud top, [40]
	30±18 ppm			42 km, [172]
	20±3 ppm			22 km, [172]
	28±7 ppm			36-42 km, [87]
	17±1 ppm			12 km, [149]
	45 ppm			35-45 km, [19]
He	12^{+24}_{-8} ppm	Outgassing (U, Th)	---	[213]
Ne	7±3 ppm	Outgassing, primordial	---	[213]
H_2S[a]	3±2 ppm	Outgassing (FeS_2)	Conversion to SO_2	<20 km, [102]
HDO[a]	1.3±0.2 ppm	Outgassing	H escape	sub-cloud, [51]
HCl	0.6±0.12 ppm	Outgassing	Cl mineral formation	cloud top, [39]
	0.4 ppm			cloud top, [56]
	0.5 ppm			35-45 km, [19]
COS[a]	0.3 ppm	Outgassing (FeS_2)	Conversion to SO_2	35-45 km, [19]
Kr	~25 ppb	Outgassing, primordial	---	[61]
SO[a]	20±10 ppb	Photochemistry	Photochemistry	cloud top, [154]
$S_{1\text{-}8}$[a]	20 ppb	Outgassing	Conversion to SO_2	<50 km, [152]
HF	$5^{+5}_{-2.5}$ ppb	Outgassing	F mineral formation	cloud top, [39]
	4.5 ppb			35-45 km, [19]
Xe	~1.9 ppb	Outgassing, primordial	---	[59,174]

[a]Abundances of these species are altitude dependent. See [213] and [77] for detailed information.

TABLE 4. Isotopic Composition of the Atmosphere of Venus[a]

Isotopic Ratio	Observed Value	Notes & References
D/H	1.6±0.2 %	Pioneer Venus MS[b] [62]
	1.9±0.6 %	IR spectroscopy [51]
$^{12}C/^{13}C$	86±12	IR spectroscopy [18]
	88.3±1.6	Venera 11/12 MS [110]
$^{14}N/^{15}N$	273±56	Pioneer Venus MS [101]
$^{16}O/^{18}O$	500±25	Pioneer Venus MS [102]
	500±80	IR spectroscopy [18]
$^{20}Ne/^{22}Ne$	11.8±0.7	Pioneer Venus MS [59]
$^{35}Cl/^{37}Cl$	2.9±0.3	IR spectroscopy [39,219]
$^{36}Ar/^{38}Ar$	5.56±0.62	Pioneer Venus MS [59]
	5.08±0.05	Venera 11/12 MS [110]
$^{40}Ar/^{36}Ar$	1.03±0.04	Pioneer Venus MS [102]
	1.19±0.07	Venera 11/12 MS [110]

[a]No isotopic compositions are available for Kr and Xe on Venus.

[b]MS = Mass Spectrometer

gases, notably the oxides of Br, Cl, H, and N, which are involved in the gas phase catalytic destruction of O_3 in the stratosphere. These cycles are more rapid than the O_3 loss in the Chapman cycle and are the dominant O_3 loss processes. The gas phase catalytic cycles involving oxides of halogens are exemplified by the following reaction sequence:

$$Cl + O_3 \rightarrow ClO + O_2$$
$$\underline{ClO + O \rightarrow Cl + O_2}$$
$$O + O_3 \rightarrow 2O_2$$

The reactive halogens involved in these cycles come from photochemical destruction of halocarbon gases, such as CF_2Cl_2 and $CFCl_3$, which are anthropogenic emissions transported upward into the stratosphere. As shown in Table 5, the atmospheric concentrations of many halocarbon gases are increasing at the rate of several percent a year.

The HO_x and NO_x catalytic cycles for O_3 destruction are exemplified by the reaction sequences below:

$$OH + O_3 \rightarrow HO_2 + O_2$$
$$\underline{HO_2 + O_3 \rightarrow OH + 2O_2}$$
$$O_3 + O_3 \rightarrow 3O_2$$

$$O_3 + h\nu \rightarrow O + O_2$$
$$O + NO_2 \rightarrow O_2 + NO$$
$$\underline{NO + O_3 \rightarrow NO_2 + O_2}$$
$$O_3 + O_3 \rightarrow 3O_2$$

The major source of stratospheric OH is the reaction of $O(^1D)$ atoms with H_2O, which is either transported from the troposphere or produced via CH_4 oxidation in the stratosphere. At present, the major source of stratospheric NO_x is N_2O transported upward from the troposphere.

Recently (1985-1992) ozone depletions have been observed to occur in the Antarctic stratosphere during southern spring. These depletions are due to heterogeneous reactions on the surfaces of polar stratospheric clouds which convert relatively inert chlorine reservoir molecules such as $ClONO_2$ and HCl into highly reactive species such as HOCl, Cl_2, and $ClNO_2$, which release Cl-bearing radicals upon photolysis. These radicals then deplete ozone via gas phase catalytic cycles such as those illustrated above. The current status of ozone monitoring and of the apparent decreases at different geographic locations is reviewed by Stolarski et al [193].

The isotopic composition of the noble gases in the terrestrial atmosphere and of terrestrial standards for isotopic

TABLE 5. Chemical Composition of the Terrestrial Troposphere[a,b]

Gas	Abundance*	Source(s)	Sink(s)	Notes & References
N_2	78.084%	Denitrifying bacteria	Nitrogen fixing bacteria	[214]
O_2	20.946%	Photosynthesis	Respiration & decay	[214]
H_2O	<4%	Evaporation	Condensation	variable
Ar	9340 ppm	Outgassing (^{40}K)	---	[173]
CO_2	350 ppm	Combustion, biology	Biology	Keeling et al 1984
Ne	18.18 ppm	Outgassing	---	[173]
^4He	5.24 ppm	Outgassing (U, Th)	Escape	[173]
CH_4	1.7 ppm	Biology & agriculture	Reaction with OH	+1%/yr, [70]
Kr	1.14 ppm	Outgassing	---	[173]
H_2	0.55 ppm	H_2O Photolysis	H atom escape	[214]
N_2O	~320 ppb	Biology	Photolysis (stratosphere)	[214]
CO	125 ppb	Photochemistry	Photochemistry	[214]
Xe	87 ppb	Outgassing	---	[173]
O_3	~10-100 ppb	Photochemistry	Photochemistry	[214]
HCl	~1 ppb	Derived from sea salt	Rainout	[214]
Isoprene, etc.	~1-3 ppb	Foliar emissions	Photooxidation	[214]
C_2H_6, etc	~3-80 ppb	Combustion, biomass burning, grasslands	Photooxidation	[214]
H_2O_2	~0.3-3 ppb	Photochemistry	Photochemistry	[187]
C_2H_2, etc	~0.2-3 ppb	Combustion, biomass burning, oceans	Photooxidation	[214]
C_2H_4, etc	~0.1-6 ppb	Combustion, biomass burning, oceans	Photooxidation	[214]
C_6H_6 etc	~0.1-1 ppb	Anthropogenic	Photooxidation	[214]
NH_3	0.1-3 ppb	Biology	Wet & dry deposition	[214]
HNO_3	~0.04-4 ppb	Photochemistry (NO_x)	Rainout	[214]
CH_3Cl	612 ppt	Ocean, biomass burning	Reaction with OH	[176]
COS	500 ppt	Biology	Photodissociation	[214]
NO_x	~30-300 ppt	Combustion, biology	Photooxidation	[214]
CF_2Cl_2 (F12)	300 ppt	Anthropogenic	Photolysis (stratosphere)	+5.1%/yr, [176]
$CFCl_3$ (F11)	178 ppt	Anthropogenic	Photolysis (stratosphere)	+5.1%/yr, [176]
CH_3CCl_3	157 ppt	Anthropogenic	Reaction with OH	+4.4%/yr, [177]
CCl_4	121 ppt	Anthropogenic	Photolysis (stratosphere)	+1.3%/yr, [176]
CF_4 (F14)	69 ppt	Anthropogenic	Photolysis (upper atm.)	+2.0%/yr, [176]
$CHClF_2$ (F22)	59 ppt	Anthropogenic	Reaction with OH	+10.9%/yr, [176]
H_2S	30-100 ppt	Biology	Photooxidation	[214]
$C_2Cl_3F_3$ (F113)	30-40 ppt	Anthropogenic	Photolysis (stratosphere)	+11.5%/yr, [176]

TABLE 5. (continued).

Gas	Abundance*	Source(s)	Sink(s)	Notes & References
CH_2Cl_2	30 ppt	Anthropogenic	Reaction with OH	[214]
CH_2ClCH_2Cl	26 ppt	Anthropogenic	Reaction with OH	[214]
CH_3Br	22 ppt	Ocean, marine biota	Reaction with OH	[214]
SO_2	20-90 ppt	Combustion	Photooxidation	marine air, [214]
$CHCl_3$	16 ppt	Anthropogenic	Reaction with OH	[214]
CS_2	~15 ppt	Anthropogenic	Photooxidation	[214]
$C_2Cl_2F_4$ (F114)	14 ppt	Anthropogenic	Photolysis (stratosphere)	[214]
C_2H_5Cl	12 ppt	Anthropogenic	Reaction with OH	[214]
$CHClCCl_2$	7.5 ppt	Anthropogenic	Reaction with OH	[214]
$(CH_3)_2S$	5-60 ppt	Biology	Photooxidation	marine air, [214]
C_2ClF_5 (F115)	4 ppt	Anthropogenic	Photolysis (stratosphere)	[214]
C_2F_6 (F116)	4 ppt	Anthropogenic	Photolysis (upper atm)	[214]
$CClF_3$ (F13)	3.3 ppt	Anthropogenic	Photolysis (stratosphere)	[214]
CH_3I	~2 ppt	Ocean, marine biota	Photolysis (troposphere)	[214]
$CHCl_2F$ (F21)	1.6 ppt	Anthropogenic	Reaction with OH	[214]
$CClF_2Br$	1.2 ppt	Anthropogenic	Photolysis (stratosphere)	+20%/yr, [176]

[a]Abundances by volume in dry air

[b]Abbreviations: ppm = parts per million, ppb = parts per billion, ppt = parts per trillion

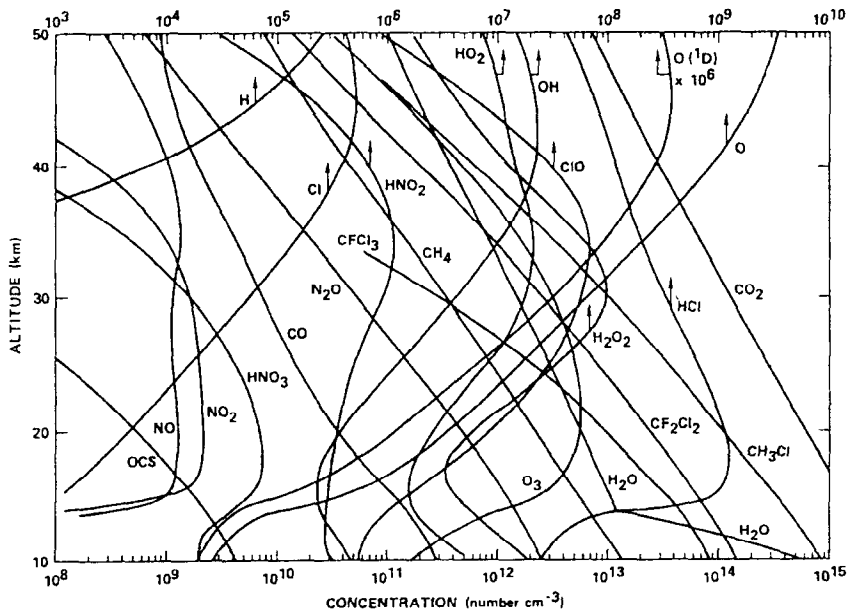

Fig. 3. Vertical concentration profiles for important minor and trace gases in the terrestrial stratosphere. Note the two different concentration scales. The total number density at 10 km altitude is $10^{18.9}$ and the total number density at 50 km altitude is $10^{16.3}$. From Turco (1985).

TABLE 6. Isotopic Composition of the Noble Gases in the Terrestrial Atmosphere and of Terrestrial Standards for Isotopic Analyses

Isotopic Ratio	Observed Value	Notes & References
D/H	$(1.5576\pm0.0005) \times 10^{-4}$	SMOW [96]
$^{3}He/^{4}He$	$(1.399\pm0.013) \times 10^{-6}$	[148]
$^{12}C/^{13}C$	89.01±0.38	[104]
$^{14}N/^{15}N$	272.0±0.3	air [113]
$^{16}O/^{17}O$	2681.80±1.72	SMOW [104]
$^{16}O/^{18}O$	498.71±0.25	SMOW [104]
$^{20}Ne/^{22}Ne$	9.800±0.080	[69]
$^{21}Ne/^{22}Ne$	$(2.899\pm0.025) \times 10^{-2}$	[69]
$^{35}Cl/^{37}Cl$	3.1273±0.1990	[104]
$^{36}Ar/^{38}Ar$	5.320±0.002	[155]
$^{40}Ar/^{36}Ar$	296.0±0.5	[155]
$^{78}Kr/^{84}Kr$	$(6.087\pm0.002) \times 10^{-3}$	[9]
$^{80}Kr/^{84}Kr$	3.960±0.002 %	[9]
$^{82}Kr/^{84}Kr$	20.217±0.021 %	[9]
$^{83}Kr/^{84}Kr$	20.136±0.021 %	[9]
$^{86}Kr/^{84}Kr$	30.524±0.025 %	[9]
$^{124}Xe/^{132}Xe$	$(3.537\pm0.0011) \times 10^{-3}$	[173]
$^{126}Xe/^{132}Xe$	$(3.300\pm0.017) \times 10^{-3}$	[173]
$^{128}Xe/^{132}Xe$	7.136±0.009 %	[173]
$^{129}Xe/^{132}Xe$	98.32±0.12 %	[173]
$^{130}Xe/^{132}Xe$	15.136±0.012 %	[173]
$^{131}Xe/^{132}Xe$	78.90±0.11 %	[173]
$^{134}Xe/^{132}Xe$	38.79±0.06 %	[173]
$^{136}Xe/^{132}Xe$	32.94±0.04 %	[173]

analysis are listed in Table 6. Atmospheric N_2 is the standard for nitrogen isotopes, but H, C, and O gases in the terrestrial atmosphere are isotopically fractionated relative to the standard isotopic ratios. Atmospheric O_2 is enriched in ^{18}O relative to SMOW, an effect which is believed to be due to biological activity. This is a mass fractionation effect. However, stratospheric O_3 is more enriched in $^{50}O_3$ than expected for mass fractionation. The exact nature of the enrichment (e.g., the symmetric or asymmetric form of $^{18}O^{16}O_2$) and its cause are currently debated [89,117]. The isotopic composition of the terrestrial atmosphere and possible mechanisms for explaining the observed fractionations are reviewed by Kaye [117]. The systematics of stable isotopes in precipitation are reviewed by Dansgaard [50].

2.4 Mars

Table 7 summarizes the chemical composition of the Martian atmosphere and the probable sources and sinks of the gases in it. Carbon dioxide, the dominant atmospheric constituent, annually condenses into and resublimes from the Martian polar caps. This process produces a global pressure change of about 37% relative to the global mean pressure of 6.36 mbars. As a consequence the mixing ratios, but not the column densities of the non-condensible gases are seasonally variable. The abundances of two other con-

TABLE 7. Chemical Composition of the Atmosphere of Mars[a]

Gas	Abundance	Source(s)	Sink(s)	Notes & References
CO_2	95.32%	Outgassing & evaporation	Condensation	[124,168]
N_2	2.7%	Outgassing	Escape as N	[168]
Ar	1.6%	Outgassing (^{40}K)	---	[168]
O_2	0.13%	CO_2 Photolysis	Photoreduction	[6,32,205]
CO	0.08%	CO_2 Photolysis	Photooxidation	[35,114,115]
H_2O[b]	~210 ppm	Evaporation & desorption	Condensation & adsorption	[112,116]
NO	~100 ppm	Photochemistry (N_2, CO_2)	Photochemistry	120 km, [156]
Ne	2.5 ppm	Outgassing, primordial	---	[168]
HDO	0.85±0.02 ppm	Evaporation & desorption	Condensation & adsorption	[27,170]
Kr	0.3 ppm	Outgassing, primordial	---	[168]
Xe	0.08 ppm	Outgassing, primordial	---	[168]
O_3[b]	~(0.04-0.2) ppm	Photochemistry (CO_2)	Photochemistry	[7,8]

[a]The mixing ratios, but not the column densities of non-condensible gases are seasonally variable due to the annual condensation and sublimation of CO_2.

[b]Spatially & temporally variable.

stituents, water vapor and O_3 are also observed to be variable. The average water vapor abundance observed by the Viking Mars Atmospheric Water Vapor Detector (MAWD) experiment is about 15 precipitable (ppt) μm (~210 ppm). The maximum observed value was about 90 ppt μm, and the lowest observed value was below the detection limit of 1 ppt μm [112]. Recent Earth-based microwave observations of the 1.35 cm water line gave a global average water vapor abundance of only 3±1 ppt μm during the 1990 northern winter [34]. This is about a factor of two lower that the Viking MAWD data during the 1977-78 northern winter. The O_3 abundance is highly variable. Ozone is present in cold and dry atmospheric regions, such as those found over the winter polar caps. It is absent in warmer, wetter regions, such as those over the polar caps in the summer [7]. The implications of the observed CO, O_2, and O_3 abundances for models of Martian atmospheric photochemistry are reviewed by Barth [7] and Lewis and Prinn [134].

Table 8 summarizes the isotopic composition of the Martian atmosphere. Only the $^{12}C/^{13}C$ ratio is terrestrial within measurement uncertainties. The observed D/H ratio is about 5 times higher than the terrestrial value as defined by SMOW. Mechanisms for producing the enhanced D/H ratio are discussed by Yung et al [221] and Jakosky [111]). The $^{14}N/^{15}N$ ratio is about 62% of the terrestrial value. Nonthermal escape processes which may have enriched ^{15}N on Mars have been discussed in several papers by Fox and Dalgarno (e.g., [82,83]). Earth-based IR spectroscopic measurements of the oxygen isotopic composition of Martian water vapor [27] show that the $^{16}O/^{17}O$ ratio is Earth-like but that the $^{16}O/^{18}O$ ratio is about 9% larger. A prior measurement of the $^{16}O/^{18}O$ ratio in Martian CO_2 gave a value identical, within the uncertainties, to that in SMOW [156]. In contrast to Venus where ^{40}Ar is depleted relative to the Earth, the $^{40}Ar/^{36}Ar$ ratio on Mars is about 10 times larger than the terrestrial value. The Martian $^{129}Xe/^{132}Xe$ ratio has also been measured and is about 2.5 times larger than the terrestrial value. Again, the reader is referred to Pepin [174] and Lewis and Prinn [134] for the implications of the noble gas isotopic data for the origin and evolution of the Martian atmosphere.

2.5 The Jovian Planets: Jupiter, Saturn, Uranus and Neptune

Compositional data for these four planets are summarized in Tables 9-11. Observed isotopic ratios are presented in Table 12. Their atmospheres are predominantly H_2 + He with minor amounts of all other gases. Schematic P,T profiles for the upper atmospheres of the Jovian planets are il-

TABLE 8. Isotopic Composition of the Atmosphere of Mars[a]

Isotopic Ratio	Observed Value	Notes & References
D/H	$(9\pm4) \times 10^{-4}$	IR spectroscopy, [170]
	$(7.8\pm0.3) \times 10^{-4}$	IR spectroscopy, [27]
$^{12}C/^{13}C$	90±5	Viking MS, [156]
$^{14}N/^{15}N$	170±15	Viking MS, [156]
$^{16}O/^{17}O$	2655±25	IR spectroscopy, [27]
$^{16}O/^{18}O$	490±25	Viking MS, [156]
	545±20	IR spectroscopy, [27]
$^{36}Ar/^{38}Ar$	5.5±1.5	Viking MS, [22]
$^{40}Ar/^{36}Ar$	3000±500	Viking MS, [168]
$^{129}Xe/^{132}Xe$	2.5^{+2}_{-1}	Viking MS, [168]

[a]Isotopic compositions inferred from measurements on different SNC meteorites are tabulated by [174]. However, only direct observations of the isotopic composition of the Martian atmosphere are listed here.

lustrated in Figure 2. These profiles are derived from radio wavelength observations by the Voyager spacecraft [135,136,138,139], which extend down to a few bars pressure. Observational data and theoretical models of the planetary interiors indicate that the atmospheric P,T profiles are adiabatic below the tropopause levels, which typically occur at 100 mb pressure.

The data in Tables 9-11 illustrate several important points. The observed He/H_2 ratios vary from planet to planet. The solar He/H_2 ratio (~13.6% atomic or ~27% by mass) is difficult to determine by direct observations of the Sun. Despite this uncertainty, He is clearly depleted in the atmosphere of Saturn, and may also be slightly depleted in the Jovian atmosphere. In contrast, Uranus apparently has a solar He/H_2 ratio and Neptune may have a He enrichment relative to the solar ratio. The compositional data also show that the elemental compositions of the atmospheres of Jupiter and Saturn are close to solar composition. However, both planets are slightly enriched in elements heavier than He. The apparent depletion of water vapor on Jupiter may be an exception to this trend or more plausibly, may be due to meteorological effects. The observations of the CH_4/H_2 ratio on Uranus and Neptune, and the higher mean densities of these two planets indicate that they have substantial heavy element enrichments.

The Earth-based and spacecraft spectroscopic observations show a wealth of species in the atmospheres of Jupiter and Saturn. Some of these, such as hydrocarbons, are produced by the photochemical destruction of CH_4 while others, such as CO, PH_3, GeH_4, and AsH_3, are mixed upward from the hot, deep atmospheres of these two planets. Isotopically substituted species such as HD, CH_3D, $^{13}CH_4$, and $^{15}NH_3$ are also observed. The D/H ratio on Jupiter and Saturn is about 2×10^{-5} and is similar to the primordial D/H ratio estimated from noble gases in meteorites [2]. The $^{12}C/^{13}C$ ratio obtained by Earth-based and spacecraft observations of CH_4, C_2H_2, and C_2H_6 ranges from 20-160. The reasons for this large range are unclear. However, an emerging consensus is that Jupiter has an Earth-like carbon isotope ratio. The $^{14}N/^{15}N$ ratio determined from observations of NH_3 is poorly constrained; the most recent observations apparently indicate a value only about half the terrestrial ratio. Less compositional diversity is observed on Uranus and Neptune, presumably because the observable regions of their atmospheres are substantially colder than the observable regions of the Jovian and Saturnian atmospheres.

2.6 Titan

Titan is the largest satellite of Saturn and possesses the most massive atmosphere of any satellite in the solar system. The chemical composition of its atmosphere is summarized in Table 13. The abundances of the major atmospheric constituents N_2, CH_4, and Ar are indirectly inferred from Voyager IRIS and radio occultation data that constrain the mean molecular weight of the atmosphere. The direct spectroscopic detection of N_2 at high altitudes by the Voyager UVS and of CH_4 by the Voyager IRIS do

TABLE 9. Chemical Composition of the Atmosphere of Jupiter

Gas	Abundance	Comments	References
H_2	89.8±2.0 %	Voyager IRIS & radio occultation result, many studies of the H_2 pressure-induced dipole and quadrupole lines and the ortho-para ratio	[36,41,52,53,72,86, 181,202]
He	10.2±2.0 %	Voyager IRIS & radio occultation	[41,86]
CH_4	$(3.0\pm1.0) \times 10^{-3}$	abundance ~4 × solar C/H_2 ratio [92], CH_4 photolyzed to hydrocarbons in stratosphere	[25,72,84,181,185]
NH_3	$(2.6\pm0.4) \times 10^{-4}$	abundance ~ solar N/H_2 ratio [91], NH_3 undergoes condensation & photolysis in the upper troposphere & stratosphere	[25,57,126,181,185, 218]
HD	28^{+30}_{-8} ppm	reevaluation for HD by [190]	[72,151,190,206,207]
$^{13}CH_4$	33 ppm	for $^{12}C/^{13}C \sim 90$, Voyager data give ~ 160, but all other values are ~ 90	[38,45]
H_2O	30±20 ppm	refers to 6 bar level, drops to 4±1 ppm at 2-4 bar range, apparently depleted below solar O/H_2 ratio, see text	[25,26,126,131]
C_2H_6	5.8±1.5 ppm	abundance from [162], C_2H_6 is due to CH_4 photolysis in stratosphere, abundance varies with altitude and latitude	[37,119,120,123,162, 180,181,197-199]
$^{15}NH_3$	~2 ppm	$^{14}N/^{15}N \sim 125$ from [64]	[64,73,198]
PH_3	0.7±0.1 ppm	due to vertical mixing from deep atmosphere, photolyzed in stratosphere	[25,65,67,126,130, 181]
C_2H_2	0.11±0.03 ppm	abundance of [162], C_2H_2 is due to CH_4 photolysis in stratosphere, abundance varies with altitude and latitude	[37,63,119,162,165, 180,181,197,199]
CH_3D	0.20±0.04 ppm	formed by D/H exchange of CH_4 + HD in the deep atmosphere	[11,12,25,65,126]
$^{13}CCH_6$	~ 58 ppb	for $^{12}C/^{13}C \sim 94$ as reported	[215]
$^{13}CCH_2$	~10 ppb	for $C_2H_2/^{13}CCH_2 \sim 10$ as reported	[66]
C_2H_4	7±3 ppb	in N. polar auroral zone, 0.4 ppb in equatorial region	[119,121]
CH_3C_2H	2.5^{+2}_{-1} ppb	in N. polar auroral zone	[119]
HCN	2^{+2}_{-1} ppb	due to vertical mixing from deep atmosphere or photochemistry	[195]
C_6H_6	2^{+2}_{-1} ppb	in N. polar auroral zone	[119]
CO	1.6±0.3 ppb	due to vertical mixing from deep atmosphere	[10,13,25,129, 161]
GeH_4	$0.7^{+0.4}_{-0.2}$ ppb	due to vertical mixing from deep atmosphere, destroyed in stratosphere	[25, 65,81,126]
C_4H_2	0.3±0.2 ppb	midlatitude region	[88]

TABLE 9. (continued).

Gas	Abundance	Comments	References
AsH_3	0.22±0.11 ppb	due to vertical mixing from deep atmosphere, destroyed in stratosphere	[158,163]
H_3^+	---	in auroral regions	[23,68]
C_3H_8	<0.6 ppm	in N. polar auroral zone	[119]
H_2S	<40 ppb	upper limit from IR spectroscopy	[127]

TABLE 10. Chemical Composition of the Atmosphere of Saturn[a]

Gas	Abundance	Comments	References
H_2	96.3±2.4 %	abundance from Voyager IRIS & radio occultation results, many spectroscopic studies of the pressure-induced dipole and quadrupole lines of H_2, and the ortho-para ratio	[30,36,41,52,53, 202]
He	3.25±2.4 %	Voyager IRIS & radio occultation	[41]
CH_4	$4.5^{+2.4}_{-1.9} \times 10^{-3}$	abundance from Voyager IRIS is ~6 × solar C/H_2 ratio [92], CH_4 is photolyzed to hydrocarbons in stratosphere	[38,44,79,178]
NH_3	(0.5-2.0) × 10^{-4}	abundance from Voyager IRIS is ~(0.2-1.0) × solar N/H_2 ratio[91], NH_3 undergoes condensation & photolysis in the upper troposphere & stratosphere	[44,57,80,178, 189,218]
HD	110±58 ppm	discovered on Saturn by[207]	[144]
$^{13}CH_4$	~51 ppm	$^{12}C/^{13}C$ ~ 89	[38]
C_2H_6	7.0±1.5 ppm	abundance of [162], C_2H_6 is due to CH_4 photolysis in stratosphere, abundance varies with altitude and latitude	[24,44,162,196, 217]
PH_3	1.4±0.8 ppm	due to vertical mixing from deep atmosphere, photolyzed in stratosphere	[44,128,157,178]
CH_3D	0.39±0.25 ppm	formed by D/H exchange of CH_4 + HD in the deep atmosphere	[44,78,157]
C_2H_2	0.30±0.10 ppm	due to CH_4 photolysis in stratosphere	[44,162]
AsH_3	3±1 ppb	due to vertical mixing from deep atmosphere, destroyed in stratosphere	[20,157,163]
CO	1.0±0.3 ppb	due to vertical mixing from deep atmosphere, destroyed in upper atmosphere	[157,159]
GeH_4	0.4±0.4 ppb	due to vertical mixing from deep atmosphere, destroyed in stratosphere	[20,157,160]
C_3H_4	---	tentative detection, no abundance given	[97]
C_3H_8	---	tentative detection, no abundance given	[97]
H_2S[b]	<0.2 ppm	upper limit of 1 cm amagat	[171]

TABLE 10. (continued).

Gas	Abundance	Comments	References
H_2O[b]	<0.02 ppm	upper limit of 15 ppt μm	[128]
HCN[b]	<4 ppb	upper limit of 0.025 cm amagat	[195]
SiH_4[b]	<4 ppb	upper limit of 0.025 cm amagat	[128]

[a]Definitions: 1 ppt μm = 10^{-4} g cm^{-2} = 0.124 cm amagat. 1 amagat = 2.69×10^{19} molecules cm^{-3}.

[b]Converted to a mixing ratio using a H_2 column abundance of 70 km amagat from [201].

TABLE 11. Chemical Composition of the Atmospheres of Uranus and Neptune

Gas	Uranus	Neptune	Comments	References
H_2	~82.5±3.3%	~80±3.2 %	Voyager IRIS & radio occultation, by difference from sum of He + CH_4, many studies of the pressure-induced dipole & quadrupole lines and the ortho-para ratio	[5,16,36,42,43, 79,188,203]
He	15.2±3.3 %	19.0±3.2 %	Voyager IRIS & radio occultation	[42, 43]
CH_4	~2.3 %	~1-2 %	Uranus & Neptune CH_4 ~32 & ~14-28 × solar C/H_2 ratio [92], respectively, abundances from Voyager radio occultation data on lapse rate, abundance from vis/IR spectroscopy is 1-10 %	[4,5,7,15,138, 139,142,145]
HD	~148 ppm	~192 ppm	based on D/H ~ 9×10^{-5} for Uranus and D/H ~ 1.2×10^{-4} for Neptune, no reliable observations of HD lines on these planets according to[191]	[36,144,191,204]
CH_3D	~8.3 ppm	~12 ppm	based on $CH_3D/CH_4 = 3.6^{+3.6}_{-2.8} \times 10^{-4}$ [54] and 2.3 % CH_4 for Uranus and $CH_3D/CH_4 = 6^{+6}_{-4} \times 10^{-4}$ [54], and 2 % CH_4 for Neptune	[17,54]
C_2H_6	~1-20 ppb	$1.5^{+2.5}_{-0.5}$ ppm	due to CH_4 photolysis, abundance varies with height & latitude, Uranus abundance from Voyager is a few times 10^{-8}	[3,21,100,122, 166,167]
C_2H_2	~10 ppb	60^{+140}_{-40} ppb	due to CH_4 photolysis, abundance varies with height & latitude	[3,21,31,100,143, 166,167]
H_2S[a]	<0.8 ppm	<3 ppm	upper limits of 30 and 100 cm amagat on Uranus & Neptune	[79]
NH_3[a]	<100 ppb	<600 ppb	upper limit of 5 cm amagat on Uranus from IR spectroscopy, abundance varies with height and latitude and is larger at lower lev-	[58,79,93,94,103, 139]

TABLE 11. (continued).

Gas	Uranus	Neptune	Comments	References
			els, extensive microwave studies, Voyager radio occultation upper limit at 6 bar level on Neptune	
CO	<40 ppb	0.65±0.35 ppm	Uranus upper limit for stratosphere, present in troposphere & stratosphere of Neptune, abundances of Rosenqvist et al 1992	[150,183]
CH_3CN	---	<5 ppb	in stratosphere	[183]
HCN	<15 ppb	0.3±0.15 ppb	in stratosphere, abundances of Rosenqvist et al 1992	[150,183]
HC_3N	<0.8 ppb	<0.4 ppb	in stratosphere	[183]

[a]Converted to a mixing ratio using a H_2 column abundance of 400 km amagat from [79].

TABLE 12. Isotopic Ratios in the Atmospheres of the Outer Planets

Isotopic Ratio	Jupiter	Saturn	Uranus	Neptune	Notes
D/H	$(2.6\pm1.0) \times 10^{-5}$	$(1.7\pm1.0) \times 10^{-5}$	$9.0^{+9.0}_{-4.5} \times 10^{-5}$	$1.2^{+1.2}_{-0.8} \times 10^{-4}$	a
$^{12}C/^{13}C$	94±12	89^{+25}_{-18}			b
$^{14}N/^{15}N$	125^{+145}_{-75}				c

[a]D/H for Jupiter & Saturn from [76]; D/H for Uranus and Neptune from [17,54].

[b]The $^{12}C/^{13}C$ for Jupiter is from ^{13}C-ethane [215], other reported values for methane are 110±35 , 70^{+35}_{-15}, 89^{+12}_{-11}, and 160^{+40}_{-55}, [38,45] and 20^{+20}_{-10} [66] for C_2H_2. No data are available for Uranus & Neptune as of the time of writing (6/92).

[c]The $^{14}N/^{15}N$ for Jupiter is from [64], earlier work by [73,198] gave $^{14}N/^{15}N$ ~ terrestrial, within about a factor of 2. No data are available for Saturn, Uranus & Neptune as of the time of writing (6/92).

TABLE 13. Chemical Composition of the Atmosphere of Titan

Gas	Abundance	Comments	References
N_2	65-98 %	Abundance indirectly inferred from Voyager IRIS & radio occultation data that constrain mean mol. wt. of atmosphere, directly detected by Voyager UVS in upper atmosphere	[74,109,137]
Ar	≤25 %	Upper limit from deduced mean mol. wt. of atmosphere, UVS data show $Ar/N_2 < 6$ % at 3900 km	[28,109]
CH_4	2-10 %	Indirectly inferred from Voyager IRIS & radio occultation data, about 2% at tropopause	[74,97,137]
H_2	0.2%	Directly measured by Voyager IRIS, detected by Trafton 1972	[109,200]

TABLE 13. (continued).

Gas	Abundance	Comments	References
CO	60-150 ppm	From Earth-based IR spectroscopy	[109,141]
CH_3D	110^{+70}_{-60} ppm	Voyager IRIS measurements, gives D/H = $1.5^{+1.4}_{-0.5} \times 10^{-4}$	[47,55,118,169]
C_2H_6	13-20 ppm	Voyager IRIS measurements, uniformly mixed over disk	[46,48,97,125]
C_3H_8	0.5-4 ppm	Voyager IRIS measurements, uniformly mixed over disk	[46,48,109]
C_2H_2	2-5 ppm	Voyager IRIS measurements, uniformly mixed over disk	[46,48,97,125]
C_2H_4	0.09-3 ppm	Voyager IRIS measurements, polar/equatorial ratio ~30	[46,48,97,125]
HCN	0.2-2 ppm	Voyager IRIS measurements & Earth-based mm wavelength observations, polar/equatorial ratio ≤ 2 from Coustenis et al 1991	[46,48,125,194]
HC_3N	80-250 ppb	Voyager IRIS measurements, abundances in N. polar region, no detection in equatorial region	[46,48]
CH_3C_2H	4-60 ppb	Voyager IRIS measurements, polar/equatorial ratio ~2-5	[46,48,125,147]
C_4H_2	1-40 ppb	Voyager IRIS measurements, polar/equatorial ratio ~16	[46,48,125]
C_2N_2	5-16 ppb	Voyager IRIS measurements, abundances in N. polar region, no detection in equatorial region	[46,48]
CO_2	1.5-14 ppb	Voyager IRIS measurements, polar/equatorial ratio ~0.5	[46,48,109]

not provide constraints on their abundances in the lower atmosphere. Implications of the observed abundances for origin and evolution of Titan's atmosphere and for atmospheric photochemistry are reviewed by Hunten et al [109] and Yung et al [220].

2.7 Triton

Voyager observations of Triton during the August 1989 Neptune encounter showed that it has a thin atmosphere predominantly composed of N_2 containing about 100 ppm of CH_4 at the surface [29,211]. Voyager UVS data give an upper limit of about 1% for the CO/N_2 ratio in Triton's atmosphere. The observed surface temperature and pressure are 38±4 K and 16±3 μbars. Its low surface temperature makes Triton the coldest natural body in the solar system.

2.8 Pluto

The discovery of CH_4 absorption features in spectra of Pluto provided the first inconclusive evidence for an atmosphere. This was finally confirmed by stellar occultation observations made by several groups in 1988 [71,107]. The occultation data constrain the ratio of the temperature to the mean molecular weight, and thus derived atmospheric compositions are model dependent. In addition to CH_4, other plausible constituents are CO and/or N_2. Atmospheric models based on the occultation data are discussed in the papers cited above.

Acknowledgments. This work was supported by grants from the NASA Planetary Atmospheres and Origins of Solar Systems Programs.

REFERENCES

1. Anbar, A.D., R.A. Creaser, D.A. Papanastassiou, and G.J. Wasserburg, Rhenium in seawater: Confirmation of generally conservative behavior, *Geochim. Cosmochim. Acta* 56, 4099-4103, 1992.
2. Anders, E. and N. Grevesse, Abundances of the elements: Meteoritic and solar, *Geochim. Cosmochim. Acta* 53, 197-214, 1989.
3. Atreya, S.K., B.R. Sandel, and P.N. Romani, Photochemistry and vertical mixing, in *Uranus*, edited by J. Bergstralh, E. Miner, and M.S. Matthews, pp. 110-146, University of Arizona Press, Tucson, AZ, 1991.
4. Baines, K.H., Interpretation of the 6818.9-Å methane feature observed on Jupiter, Saturn, and Uranus, *Icarus* 56, 543-559, 1983.
5. Baines, K.H., and J.T. Bergstralh, The structure of the Uranian atmosphere: Constraints from the geometric albedo spectrum and H_2 and CH_4 line profiles, *Icarus* 65, 406-441, 1986.
6. Barker, E.S., Detection of molecular oxygen in the Martian atmosphere, *Nature* 238, 447-448, 1972.
7. Barth, C.A., The photochemistry of the atmosphere of Mars, in *The Photochemistry of Atmospheres*, edited by J.S. Levine, pp. 337-392, Academic Press, NY, 1985.
8. Barth, C.A. and C.W. Hord, Mariner ultraviolet spectrometer: topography and polar cap, *Science* 173, 197-201, 1971.
9. Basford, J.R., J.C. Dragon, R.O. Pepin, M.R. Coscio Jr., and V.R. Murthy, Krypton and xenon in lunar fines, *Proc. 4th Lunar Sci. Conf.* 2, 1915-1955, 1973.
10. Beer, R., Detection of carbon monoxide in Jupiter, *Astrophys. J.* 200, L167-L169, 1975.
11. Beer, R., and F.W. Taylor, The abundance of CH_3D and the D/H ratio in Jupiter, *Astrophys. J.* 179, 309-327, 1973.
12. Beer, R., and F.W. Taylor, The D/H and C/H ratios in Jupiter from the CH_3D phase, *Astrophys. J.* 219, 763-767, 1978a.
13. Beer, R., and F.W. Taylor, The abundance of carbon monoxide in Jupiter, *Astrophys. J.* 221, 1100-1109, 1978b.
14. Bekov, G.I., V.S. Letokhov, V.N. Radaev, G.N. Baturin, A.S. Egorov, A.N. Kursky, and V.A. Narseyev, Ruthenium in the ocean, *Nature* 312, 748-750, 1984.
15. Benner, D.C. and U. Fink, Application of methane band-model parameters to the visible and near-infrared spectrum of Uranus, *Icarus* 42, 343-353, 1980.
16. Bergstralh, J.T. and K.H. Baines, Properties of the upper tropospheres of Uranus and Neptune derived from observations at "visible" and near-infrared wavelengths, in *Uranus and Neptune*, ed. J.T. Bergstralh, NASA CP-2330, pp. 179-206, 1984.
17. Bergstralh, J.T., E. Miner, and M.S. Matthews (eds.), *Uranus*, University of Arizona Press, Tucson, AZ, 1991.
18. Bézard, B., J.P. Baluteau, A. Marten, and N. Coron, The $^{12}C/^{13}C$ and $^{16}O/^{18}O$ ratios in the atmosphere of Venus from high-resolution 10-μm spectroscopy, *Icarus* 72, 623-634, 1987.
19. Bézard, B., C. DeBergh, D. Crisp, and J.P. Maillard, The deep atmosphere of Venus revealed by high-resolution nightside spectra, *Nature* 345, 508-511, 1990.
20. Bézard, B., P. Drossart, E. Lellouch, G. Tarrgo, and J.P. Maillard, Detection of arsine in Saturn, *Astrophys. J.* 346, 509-513, 1989.
21. Bézard, B., P.N. Romani, B.J. Conrath, and W.C. Maguire, Hydrocarbons in Neptune's stratosphere from Voyager infrared observations, *J. Geophys. Res.* 96, 18961-18975, 1991.
22. Biemann, K., T. Owen, D.R. Rushneck, A.L. La Fleur, and D.W. Howarth, The atmosphere of Mars near the surface: Isotope ratios and upper limits on noble gases, *Science* 194, 76-78, 1976.
23. Billebaud, F., P. Drossart, J.P. Maillard, J. Caldwell, and S. Kim, Spatial variation of 2 μm H_3^+ emission in the southern auroral region of Jupiter, *Icarus* 96, 281-283, 1992.
24. Bjoraker, G.L., H.P. Larson, U. Fink, and H.A. Smith, A study of ethane on Saturn in the 3 micron region, *Astrophys. J.* 248, 856-862, 1981.
25. Bjoraker, G.L., H.P. Larson, and V.G. Kunde, The gas composition of Jupiter derived from 5-μm airborne spectroscopic observations, *Icarus* 66, 579-609, 1986a.
26. Bjoraker, G.L., H.P. Larson, and V.G. Kunde, The abundance and distribution of water vapor in Jupiter's atmosphere, *Astrophys. J.* 311, 1058-1072, 1986b.
27. Bjoraker, G.L., M.J. Mumma, and H.P. Larson, The value of D/H in the Martian atmosphere: Measurements of HDO and H_2O using the Kuiper Airborne Observatory, *Abstracts of the Fourth International Conference on Mars*, pp. 69-70, 1989.
28. Broadfoot, A.L., B.R. Sandel, D.E. Shemansky, J.B. Holberg, G.R. Smith, D.F. Strobel, S. Kumar, J.C. McConnell, D.M. Hunten, S.K. Atreya, T.M. Donahue, H.W. Moos, J.L. Bertaux, J.E. Blamont, R.B. Pomphray, S. Linick, Extreme ultraviolet observations from Voyager 1 encounter with Saturn, *Science* 212, 206-211, 1981.
29. Broadfoot, A.L., S.K. Atreya, J.L. Bertaux, J.E. Blamont, A.J. Dessler, T.M. Donahue, W.T. Forrester, D.T. Hall, F. Herbert, J.B. Holberg, D.M. Hunten, V.A. Krasnopolsky, S. Linick, J.I. Lunine, J.C. McConnell, H.W. Moos, B.R. Sandel, N.M. Schneider, D.E. Shemansky, G.R. Smith, D.F. Strobel, R.V. Yelle, Ultraviolet spectrometer observations of Neptune and Triton, *Science* 246, 1459-1466, 1989.
30. Buriez, J.C. and C. DeBergh, A study of the atmosphere of Saturn based on methane line profiles near 1.1 μm, *Astron. Astrophys.* 94, 382-390, 1981.
31. Caldwell, J.T., R. Wagener, and K.H. Fricke, Observations of Neptune and Uranus below 2000A with the IUE, *Icarus* 74, 133-140, 1988.
32. Carleton, N.P. and W.A. Traub, Detection of molecular oxygen on

Mars, *Science* 177, 988-992, 1972.

33. Chamberlain, J.W. and D.M. Hunten, *Theory of Planetary Atmospheres*, Academic Press, NY, 1987.
34. Clancy, R.T., A.W. Grossman, and D.O. Muhleman, Vertical, latitudinal and diurnal distributions of water in the Mars atmosphere from VLA 1.35 cm spectral line mapping, *Bull. Amer. Astron. Soc.* 23, 1213, 1991.
35. Clancy, R.T., D.O. Muhleman, and G.L. Berge, Global changes in the 0-70 km thermal structure of the Mars atmosphere derived from 1975-1989 microwave CO spectra, *J. Geophys. Res.* 95, 14543-14554, 1990.
36. Cochran, W.D. and W.H. Smith, Desaturation of H_2 quadrupole lines in the atmospheres of the outer planets, *Astrophys. J.* 219, 756-762, 1983.
37. Combes, M., T. Encrenaz, L. Vapillon, Y. Zeau, and C. Lesqueren, Confirmation of the identification of C_2H_2 and C_2H_6 in the Jovian atmosphere, *Astron. Astrophys. 34*, 33-35, 1974.
38. Combes, M., J.P. Maillard, and C. DeBergh, Evidence for a telluric value of $^{12}C/^{13}C$ ratio in the atmospheres of Jupiter and Saturn, *Astron. Astrophys.* 61, 531-537, 1977.
39. Connes, P., J. Connes, W.S. Benedict, and L.D. Kaplan, Traces of HCl and HF in the atmosphere of Venus, *Astrophys. J.* 147, 1230-1237, 1967.
40. Connes, P., J. Connes, L.D. Kaplan, and W.S. Benedict, Carbon monoxide in the Venus atmosphere, *Astrophys. J.* 152, 731-743, 1968.
41. Conrath, B.J., D. Gautier, R.A. Hanel, and J.S. Hornstein, The helium abundance of Saturn from Voyager measurements, *Astrophys. J.* 282, 807-815, 1984.
42. Conrath, B.J., D. Gautier, R.A. Hanel, G. Lindal, and A. Marten, The helium abundance of Uranus from Voyager measurements, *J. Geophys. Res.* 92, 15003-15010, 1987.
43. Conrath, B.J., D. Gautier, G.F. Lindal, R.E. Samuelson, and W.A. Shaffer, The helium abundance of Neptune from Voyager measurements, *J. Geophys. Res.* 96, 18907-18919, 1991.
44. Courtin, R., D. Gautier, A. Marten, B. Bézard, and R. Hanel, The composition of Saturn's atmosphere at northern temperate latitudes from Voyager IRIS spectra: NH_3, PH_3, C_2H_2, C_2H_6, CH_3D, CH_4, and the Saturnian D/H isotopic ratio, *Astrophys. J.* 287, 899-916, 1984.
45. Courtin, R., D. Gautier, A. Marten, and V. Kunde, The $^{12}C/^{13}C$ ratio in Jupiter from the Voyager infrared investigation, *Icarus* 53, 121-132, 1983.
46. Coustenis, A., B. Bézard, and D. Gautier, Titan's atmosphere from Voyager infrared observations I. The gas composition of Titan's equatorial region, *Icarus* 80, 54-76, 1989a.
47. Coustenis, A., B. Bézard, and D. Gautier, Titan's atmosphere from Voyager infrared observations II. The CH_3D abundance and D/H ratio from the 900-1200 cm^{-1} spectral region, *Icarus* 82, 67-80, 1989b.
48. Coustenis, A., B. Bézard, D. Gautier, A. Marten, and R. Samuelson, Titan's atmosphere from Voyager infrared observations III. Vertical distributions of hydrocarbons and nitriles near Titan's north pole, *Icarus* 89, 152-167, 1991.
49. Cox, R.A., The physical properties of seawater, in *Chemical Oceanography*, edited by J.P. Riley and G. Skirrow, vol. 1, pp. 73-120, Academic Press, NY, 1965.
50. Dansgaard, W., Stable isotopes in precipitation, *Tellus* XVI, 436-468, 1964.
51. DeBergh, C., B. Bézard, T. Owen, D. Crisp, J.P. Maillard, and B.L. Lutz, Deuterium on Venus: Observations from Earth, *Science* 251, 547-549, 1991.
52. DeBergh, C., J. Lecacheux, M. Combes, and J.P. Maillard, New infrared spectra of the Jovian planets from 1200 to 4000 cm^{-1} by Fourier transform spectroscopy. III. First-overtone pressure-induced H_2 absorption in the atmospheres of Jupiter and Saturn, *Astron. Astrophys.* 35, 333-337, 1974.
53. DeBergh, C., J. Lecacheux, and J.P. Maillard, The 2-0 quadrupole spectrum of H_2 in the atmospheres of Jupiter and Saturn, *Astron. Astrophys. 56*, 227-233, 1977.
54. DeBergh, C., B.L. Lutz, T. Owen, J. Brault, and J. Chauville, Monodeuterated methane in the outer solar system. II. Its detection on Uranus at 1.6 microns, *Astrophys. J.* 311, 501-510, 1986.
55. DeBergh, C., B.L. Lutz, T. Owen, and J. Chauville, Monodeuterated methane in the outer solar system. III. Its abundance on Titan, *Astrophys. J.* 329, 951-955, 1988.
56. DeBergh, C., J.P. Maillard, B. Bézard, T. Owen, and B.L. Lutz, Ground-based high resolution spectroscopy of Venus near 3.6 microns, *Bull. Amer. Astron. Soc.* 21, 926, 1989.
57. DePater, I. and S.T. Massie, Models of the millimeter-centimeter spectra of the giant planets, *Icarus* 62, 143-171, 1985.
58. DePater, I. and M. Richmond, Neptune's microwave spectrum from 1 mm to 20 cm, *Icarus* 80, 1-13, 1989.
59. Donahue, T.M., Fractionation of noble gases by thermal escape from accreting planetesimals, *Icarus* 66, 195-210, 1986.
60. Donahue, T.M. and R.R. Hodges, Jr., Past and present water budget of Venus, *J. Geophys. Res.* 97, 6083-6091, 1992.
61. Donahue, T.M., J.H. Hoffman, and R.R. Hodges, Jr., Krypton and xenon in the atmosphere of Venus, *Geophys. Res. Lett.* 8, 513-516.
62. Donahue, T.M., J.H. Hoffman, R.R. Hodges, Jr., and A.J. Watson, Venus was wet: A measurement of the ratio of D to H, *Science* 216, 630-633, 1982.
63. Drossart, P., B. Bézard, S. Atreya, J. Lacy, E. Serabyn, A. Tokunaga, and T. Encrenaz, Enhanced acetylene emission near the north pole of Jupiter, *Icarus* 66, 610-618, 1986.
64. Drossart, P., T. Encrenaz, and M. Combes, The $^{14}N/^{15}N$ ratio in the Jovian atmosphere, *Astron. Astrophys.* 146, 181-184, 1985a.
65. Drossart, P., T. Encrenaz, V. Kunde, R. Hanel, and M. Combes, An estimate of the PH_3, CH_3D, and GeH_4 abundances on Jupiter from the

Voyager IRIS data at 4.5 μm, *Icarus* 49, 416-426, 1982.

66. Drossart, P., J. Lacy, E. Serabyn, A. Tokunaga, B. Bézard, and T. Encrenaz, Detection of $^{13}C^{12}CH_2$ on Jupiter at 13 μm, *Astron. Astrophys.* 149, L10-L12, 1985b.
67. Drossart, P., E. Lellouch, B. Bézard, J.P. Maillard, and G. Tarrago, Jupiter: Evidence for a phosphine enhancement at high northern latitudes, *Icarus* 83, 248-253, 1990.
68. Drossart, P., J.P. Maillard, J. Caldwell, S.J. Kim, J.K.G. Watson, W.A. Majewski, J. Tennyson, S. Miller, S.K. Atreya, J.T. Clarke, J.H. Waite, Jr., and R. Wagener, Detection of H_3^+ on Jupiter, *Nature* 340, 539-541, 1989.
69. Eberhardt, P., O. Eugster, and K. Marti, A redetermination of the isotopic composition of atmospheric neon, *Z. Naturfor.* 20a, 623-624, 1965.
70. Ehhalt, D.H., How has the atmospheric concentration of CH_4 changed?, in *The Changing Atmosphere*, edited by F.S. Rowland and I.S.A. Isaksen, J. Wiley & Sons, pp. 25-32, 1988.
71. Elliot, J.L., E.W. Dunham, A.S. Bosh, S.M. Slivan, L.A. Young, L.H. Wasserman, and R.L. Millis, Pluto's atmosphere, *Icarus* 77, 148-170, 1989.
72. Encrenaz, T. and M. Combes, On the C/H and D/H ratios in the atmospheres of Jupiter and Saturn, *Icarus* 52, 54-61, 1982.
73. Encrenaz, T., M. Combes, and Y. Zeau, The spectrum of Jupiter between 10 and 13 microns: An estimate of the Jovian $^{14}N/^{15}N$ ratio, *Astron. Astrophys.* 70, 29-36, 1978.
74. Eshelman, V.R., G.F. Lindal, and G.L. Tyler, Is Titan wet or dry? *Science* 221, 53-55, 1983.
75. Falkner, K.K. and J.M. Edmond, Gold in seawater, *Earth Planet. Sci. Lett.* 98, 208-221, 1990.
76. Fegley, B., Jr. and R.G. Prinn, The predicted abundances of deuterium-bearing gases in the atmospheres of Jupiter and Saturn, *Astrophys. J.* 326, 490-508, 1988.
77. Fegley, B., Jr. and A.H. Treiman, Chemistry of atmosphere-surface interactions on Venus and Mars, in Venus and Mars: Atmospheres, Ionospheres, and Solar Wind Interactions, edited by J.G. Luhmann, M. Tatrallyay, and R.O. Pepin, AGU Geophysical Monograph 66, pp. 7-71, 1992.
78. Fink, U. and H.P. Larson, Deuterated methane observed on Saturn, *Science* 201, 343-345, 1978.
79. Fink, U. and H.P. Larson, The infrared spectra of Uranus, Neptune, and Titan from 0.8-2.5 microns, *Astrophys. J.* 233, 1021-1040, 1979.
80. Fink, U., H.P. Larson, G.L. Bjoraker, and J.R. Johnson, The NH_3 spectrum in Saturn's 5 μm window, *Astrophys. J.* 268, 880-888, 1983.
81. Fink, U., H.P. Larson, and R.R. Treffers, Germane in the atmosphere of Jupiter, *Icarus* 34, 344-354, 1978.
82. Fox, J.L., Dissociative recombination in aeronomy, in *Dissociative Recombination: Theory, Experiment and Applications*, edited by J.B.A. Mitchell and S.L. Guberman, pp. 264-285, World Scientific, Singapore, 1989.
83. Fox, J.L. and A. Dalgarno, Nitrogen escape from Mars, *J. Geophys. Res.* 88, 9027-9032, 1983.
84. Gautier, D. and T. Owen, Cosmogonical implications of elemental and isotopic abundances in atmospheres of the giant planets, *Nature* 304, 691-694, 1983.
85. Gautier, D., B. Bézard, A. Marten, J.P. Baluteau, N. Scott, A. Chedin, V. Kunde, and R. Hanel, The C/H ratio in Jupiter from the *Voyager* infrared investigations, *Astrophys. J.* 257, 901-912, 1982.
86. Gautier, D., B. Conrath, M. Flasar, R. Hanel, V. Kunde, A. Chedin, and N. Scott, The helium abundance of Jupiter from Voyager, *J. Geophys. Res.* 86, 8713-8720, 1981.
87. Gel'man, B.G., V.G. Zolotukhin, N.I. Lamonov, B.V. Levchuk, A.N. Lipatov, L.M. Mukhin, D.F. Nenarokov, V.A. Rotin, and B.P. Okhotnikov, Analysis of chemical composition of Venus atmosphere by gas chromatography on Venera 12, *Cosmic Res.* 17, 585-589, 1979.
88. Gladstone, G.R. and Y.L. Yung, An analysis of the reflection spectrum of Jupiter from 1500 Å to 1740 Å, *Astrophys. J.* 266, 415-424, 1983.
89. Goldman, A., F.J. Murcray, D.G. Murcray, J.J. Kosters, C.P. Rinsland, J.M. Flaud, C. Camy-Peyret, and A. Barbe, Isotopic abundances of stratospheric ozone from balloon-borne high-resolution infrared solar spectra, *J. Geophys. Res.* 94, 8467-8473, 1989.
90. Graedel, T., *Chemical Compounds in the Atmosphere*, Academic Press, NY, 1978.
91. Grevesse, N., D.L. Lambert, A.J. Sauval, E.F. van Dishoeck, C.B. Farmer, and R.H. Norton, Identification of solar vibration-rotation lines of NH and the solar nitrogen abundance, *Astron. Astrophys.* 232, 225-230, 1990.
92. Grevesse, N., D.L. Lambert, A.J. Sauval, E.F. van Dishoeck, C.B. Farmer, and R.H. Norton, Vibration-rotation bands of CH in the solar infrared spectrum and the solar carbon abundance. *Astron. Astrophys.* 242, 488-495, 1991.
93. Gulkis, S. and I. DePater, A review of the millimeter and centimeter observations of Uranus, in *Uranus and Neptune*, ed. J.T. Bergstralh, NASA CP-2330, pp. 225-262, 1984.
94. Gulkis, S., M.A. Janssen, and E.T. Olsen, Evidence for the depletion of ammonia in the Uranus atmosphere, *Icarus* 34, 10-19, 1978.
95. Gurrola, E.M., E.A. Marouf, V.R. Eshleman, and G.L. Tyler, Voyager radio occultation observations of Triton's neutral atmosphere Bull. Amer. Astron. Soc. 23, 1207, 1991.
96. Hagemann, R., G. Nief, and E. Roth, Absolute isotopic scale for deuterium analysis of natural waters. Absolute D/H ratio for SMOW, *Tellus* 22, 712-715, 1970.
97. Hanel, R.A., B.J. Conrath, F.M. Flasar, V.G. Kunde, W. Maguire, J. Pearl, J. Pirraglia, R. Samuelson, L. Herath, M. Allison, D. Cruikshank, D. Gautier, P. Gautier, L. Horn, R. Koppany, and C. Ponnamperuma, Infrared observations of the Saturnian system from Voyager 1, *Science* 212, 192-200, 1981.
98. Hanel, R.A., B.J. Conrath, D.E. Jen-

nings, and R.E. Samuelson, *Exploration of the Solar System by Infrared Remote Sensing*, Cambridge University Press, 1992.

99. Hanel, R., V. Kunde, W. Maguire, J. Pearl, J. Pirraglia, R. Samuelson, P. Gierasch, A. Weir, B. Bézard, D. Gautier, D. Cruikshank, L. Horn, R. Springer, and W. Shaffer, Infrared observations of the Neptunian system, *Science* 246, 1454-1459, 1989.
100. Herbert, F.L., B.R. Sandel, A.L. Broadfoot, D.E. Shemansky, J.B. Holberg, R.V. Yelle, S.K. Atreya, and P.N. Romani, The upper atmosphere of Uranus: EUV occultations observed by Voyager 2, *J. Geophys. Res.* 92, 15093-15109, 1987.
101. Hoffman, J.H., R.R. Hodges, T.M. Donahue, M.B. McElroy, and M. Kolpin, Composition and structure of the Venus atmosphere: Results from Pioneer Venus, *Science* 205, 49-52, 1979.
102. Hoffman, J.H., R.R. Hodges, T.M. Donahue, and M.B. McElroy, Composition of the Venus lower atmosphere from the Pioneer Venus mass spectrometer, *J. Geophys. Res.* 85, 7882-7890, 1980.
103. Hofstadter, M.D. and D.O. Muhleman, Latitudinal variations of ammonia in the atmosphere of Uranus: An analysis of microwave observations, *Icarus* 81, 396-412, 1988.
104. Holden, N.E., R.L. Martin, and I.L. Barnes, Isotopic compositions of the elements 1981, *Pure Appl. Chem.* 55, 1119-1136, 1983.
105. Holland, H.D., *The Chemistry of the Atmosphere and Oceans*, John Wiley, NY, 1978.
106. Holland, H.D., *The Chemical Evolution of the Atmosphere and Oceans*, Princeton University Press, Princeton, NJ, 1984.
107. Hubbard, W.B., D.M. Hunten, S.W. Dieters, K.M. Hill, and R.D. Watson, Occultation evidence for an atmosphere on Pluto, *Nature* 336, 452-454, 1988.
108. Hubbard, W.B., R.V. Yelle, and J.I. Lunine, Nonisothermal Pluto atmosphere models, *Icarus* 84, 1-11, 1990.
109. Hunten, D.M, M.G. Tomasko, F.M. Flasar, R.E. Samuelson, D.F. Strobel, and D.J. Stevenson, Titan, in *Saturn*, edited by T. Gehrels and M.S. Matthews, pp. 671-759, University of Arizona Press, Tucson, AZ, 1984.
110. Istomin, V.G., K.V. Grechnev, and V.A. Kochnev, Mass spectrometry of the lower atmosphere of Venus: Krypton isotopes and other recent results of the Venera-11 and -12 data processing, 23rd COSPAR meeting, Budapest, Hungary, 1980.
111. Jakosky, B.M., Mars volatile evolution: Evidence from stable isotopes, *Icarus* 94, 14-31, 1991.
112. Jakosky, B.M. and R.M. Haberle, The seasonal behavior of water on Mars, in *Mars*, edited by H. Kieffer, B. Jakosky, C. Snyder, and M. Matthews, pp. 969-1016, University of Arizona Press, Tucson, AZ, 1992.
113. Junk, G. and H.J. Svec, The absolute abundance of the nitrogen isotopes in the atmosphere and compressed gas from various sources, *Geochim. Cosmochim. Acta* 14, 234-243, 1958.
114. Kakar, R.K., J.W. Walters, and W.J. Wilson, Mars: Microwave detection of carbon monoxide, *Science* 196, 1090-1091, 1977.
115. Kaplan, L.D., J. Connes, and P. Connes, Carbon monoxide in the Martian atmosphere, *Astrophys. J.* 157, L187-L192, 1969.
116. Kaplan, L.D., G. Münch, and H. Spinrad, An analysis of the spectrum of Mars, *Astrophys. J.* 139, 1-15, 1964.
117. Kaye, J.A, Mechanisms and observations for isotope fractionation of molecular species in planetary atmospheres, *Rev. Geophys.* 25, 1609-1658, 1987.
118. Kim, S.J. and J. Caldwell, The abundance of CH_3D in the atmosphere of Titan, derived from 8- to 14-μm thermal emission, *Icarus* 52, 473-482, 1982.
119. Kim, S.J., J. Caldwell, A.R. Rivolo, R. Wagener, and G.S. Orton, Infrared polar brightening on Jupiter III. Spectrometry from the Voyager 1 IRIS experiment, *Icarus* 64, 233-248, 1985.
120. Kostiuk, T., F. Espenak, M.J. Mumma, D. Deming, and D. Zipoy, Variability of ethane on Jupiter, *Icarus* 72, 394-410, 1987.
121. Kostiuk, T., F. Espenak, M.J. Mumma, P. Romani, Infrared studies of hydrocarbons on Jupiter, *Infrared Physics* 29, 199-204, 1989.
122. Kostiuk, T., F. Espenak, P. Romani, D. Zipoy, and J. Goldstein, Ethane abundance on Neptune, *Icarus* 88, 87-96, 1990.
123. Kostiuk, T., M.J. Mumma, F. Espenak, D. Deming, D.E. Jennings, and W. Maguire, Measurements of the stratospheric ethane in the Jovian south polar region from infrared heterodyne spectroscopy of the ν_9 band near 12 μm, *Astrophys. J.* 265, 564-569, 1983.
124. Kuiper, G.P., Planetary atmospheres and their origin, in *Atmospheres of the Earth and Planets*, edited by G.P. Kuiper, pp. 306-405, University of Chicago Press, Chicago, IL, 1952.
125. Kunde, V.G., A.C. Aikin, R.A. Hanel, D.E. Jennings, W.C. Maguire, and R.E. Samuelson, C_4H_2, HC_3N and C_2N_2 in Titan's atmosphere, *Nature* 292, 686-688, 1981.
126. Kunde, V., R. Hanel, W. Maguire, D. Gautier, J.P. Baluteau, A. Marten, A. Chedin, N. Husson, and N. Scott, The tropospheric gas composition of Jupiter's north equatorial belt (NH_3, PH_3, CH_3D, GeH_4, H_2O) and the Jovian D/H isotopic ratio, *Astrophys. J.* 263, 443-467, 1982.
127. Larson, H.P., D.S. Davis, R. Hofmann, and G.L. Bjoraker, The Jovian atmospheric window at 2.7 μm: A search for H_2S, *Icarus* 60, 621-639, 1984.
128. Larson, H.P., U. Fink, H.A. Smith, and D.S. Davis, The middle-infrared spectrum of Saturn: Evidence for phosphine and upper limits to other trace atmospheric constituents, *Astrophys. J.* 240, 327-337, 1980.
129. Larson, H.P., U. Fink, and R.R. Treffers, Evidence for CO in Jupiter's atmosphere from airborne spectroscopic observations at 5 microns, *Astrophys. J.* 219, 1084-1092, 1978.
130. Larson, H.P., R.R. Treffers, and U. Fink, Phosphine in Jupiter's atmosphere: The evidence from high-altitude observations at 5 micrometers, *Astrophys. J.* 211, 972-979,

1977.
131. Larson, H.P., U. Fink, R. Treffers, and T.N. Gautier III, Detection of water vapor on Jupiter, *Astrophys. J* 197, L137-L140, 1975.
132. Lee, D.S., Palladium and nickel in north-east Pacific waters, *Nature* 305, 47-48, 1983.
133. Lee, D.S. and J.M. Edmond, Tellurium species in seawater, *Nature* 313, 782-785, 1985.
134. Lewis, J.S. and R.G. Prinn, *Planets and Their Atmospheres: Origin and Evolution*, Academic Press, NY, 1984.
135. Lindal, G.F., The atmosphere of Neptune: an analysis of radio occultation data acquired with Voyager 2, *Astron. J.* 103, 967-982, 1992.
136. Lindal, G.F., G.E. Wood, G.S. Levy, J.D. Anderson, D.N. Sweetnam, H.B. Hotz, B.J. Buckles, D.P. Holmes, P.E. Doms, V.R. Eshelman, G.L. Tyler, and T.A. Croft, The atmosphere of Jupiter: An analysis of the Voyager radio occultation measurements, *J. Geophys. Res.* 86, 8721-8727, 1981.
137. Lindal, G.F., G.E. Wood, H.B. Hotz, D.N. Sweetnam, V.R. Eshelman, and G.L. Tyler, The atmosphere of Titan: an analysis of the Voyager 1 radio occultation measurements, *Icarus* 53, 348-363, 1983.
138. Lindal, G.F., J.R. Lyons, D.N. Sweetnam, V.R. Eshleman, D.P. Hinson, and G.L. Tyler, The atmosphere of Uranus: Results of radio occultation measurements with Voyager 2, *J. Geophys. Res.* 92, 14987-15001, 1987.
139. Lindal, G.F., J.R. Lyons, D.N. Sweetnam, V.R. Eshleman, D.P. Hinson, and G.L. Tyler, The atmosphere of Neptune: Results of radio occultation measurements with the Voyager 2 spacecraft, *Geophys. Res. Lett.* 17, 1733-1736, 1990.
140. Lupton, J.E., Terrestrial inert gases: Isotope tracer studies and clues to primordial components in the mantle, *Ann. Rev. Earth Planet. Sci.* 11, 371-414, 19783.
141. Lutz, B.L., C. DeBergh, and T. Owen, Titan: Discovery of carbon monoxide in its atmosphere, *Science* 220, 1374-1375, 1983.
142. Lutz, B.L., T. Owen, and R.D. Cess, Laboratory band strengths of methane and their application to the atmospheres of Jupiter, Saturn, Uranus, Neptune, and Titan, *Astrophys. J.* 203, 541-551, 1976.
143. Macy, W., Mixing ratios of methane, ethane, and acetylene in Neptune's stratosphere, *Icarus* 41, 153-158, 1980.
144. Macy, W., Jr. and W.H. Smith, Detection of HD on Saturn and Uranus, and the D/H ratio, *Astrophys. J.* 222, L73-L75, 1978.
145. Macy, W., Jr., J. Gelfand, and W.H. Smith, Interpretation of the 6818.9 Å methane line in terms of inhomogeneous scattering models for Uranus and Neptune, *Icarus* 26, 428-436, 1978.
146. Maguire, W.C., R.A. Hanel, D.E. Jennings, V.G. Kunde, and R.E. Samuelson, Propane and methyl acetylene in Titan's atmosphere, *Nature* 292, 683-686, 1981.
147. Maguire, W.C., R.E. Samuelson, R.A. Hanel, and V.G. Kunde, Latitudinal variation of acetylene and ethane in the Jovian atmosphere from Voyager IRIS observations, *Bull. Amer. Astron. Soc.* 17, 708, 1985.
148. Mamyrin, B.A., G.S. Anufriyev, I.L. Kamenskii, and I.N. Tolstikhin, Determination of the isotopic composition of atmospheric helium, *Geochem. Intl.* 7, 498-505, 1970.
149. Marov, M.Ya., V.P. Volkov, Yu.A. Surkov, and M.L. Ryvkin, Lower atmosphere, in *The Planet Venus: Atmosphere, Surface, Interior Structure*, edited by V.L. Barsukov and V.P. Volkov, pp. 25-67, Nauka, Moscow, USSR, 1989.
150. Marten, A., D. Gautier, T. Owen, D. Sanders, R.T. Tilanus, J. Deane, and H. Matthews, First observations of CO and HCN on Neptune and Uranus at millimeter wavelengths and their implications for atmospheric chemistry, *Astrophys. J.*, in press, 1993.
151. McKellar, A.R.W., W. Goetz, and D.A. Ramsay, The rotation-vibration spectrum of HD: Wavelength and intensity measurements of the 3-0, 4-0, 5-0, and 6-0 electric dipole bands, *Astrophys. J.* 207, 663-670, 1976.
152. Moroz, V.I., Yu.M. Golovin, A.P. Ekonomov, B.E. Moshkin, N.A. Parfent'ev, and N.F. San'ko, Spectrum of the Venus day sky, *Nature* 284, 243-244, 1980.
153. Moroz, V.I., N.A. Parfent'ev, and N.F. San'ko, Spectrophotometric experiment on the Venera 11 and 12 descent modules. 2. Analysis of Venera 11 spectra by layer-addition method, *Cosmic Res.* 17, 601-614, 1979.
154. Na, C.Y., L.W. Esposito, and T.E. Skinner, International ultraviolet explorer observations of Venus SO_2 and SO, *J. Geophys. Res.* 95, 7485-7491, 1990.
155. Nier, A.O., A redetermination of the relative abundances of the isotopes of carbon, nitrogen, oxygen, argon and potassium, *Phys. Rev.* 77, 789-793, 1950.
156. Nier, A.O. and M.B. McElroy, Composition and structure of Mars' upper atmosphere: Results from the neutral mass spectrometer on Viking 1 and 2, *J. Geophys. Res.* 82, 4341-4349, 1977.
157. Noll, K.S. and H.P. Larson, The spectrum of Saturn from 1990 to 2230 cm^{-1}: Abundances of AsH_3, CH_3D, CO, GeH_4, NH_3, and PH_3, *Icarus* 89, 168-189, 1990.
158. Noll, K.S., T.R. Geballe, and R.F. Knacke, Arsine in Saturn and Jupiter, *Astrophys. J.* 338, L71-L74, 1989.
159. Noll, K.S., R.F. Knacke, T.R. Geballe, and A.T. Tokunaga, Detection of carbon monoxide in Saturn, *Astrophys. J.* 309, L91-L94, 1986.
160. Noll, K.S., R.F. Knacke, T.R. Geballe, and A.T. Tokunaga, Evidence for germane in Saturn, *Icarus* 75, 409-422, 1988a.
161. Noll, K.S., R.F. Knacke, T.R. Geballe, and A.T. Tokunaga, The origin and vertical distribution of carbon monoxide in Jupiter, *Astrophys. J.* 324, 1210-1218, 1988b.
162. Noll, K.S., R.F. Knacke, A.T. Tokunaga, J.H. Lacy, S. Beck, and E. Serabyn, The abundances of ethane and acetylene in the atmospheres of Jupiter and Saturn, *Icarus* 65,

257-263, 1986.

163. Noll, K.S., H.P. Larson, and T.R. Geballe, The abundance of AsH_3 in Jupiter, *Icarus* 83, 494-499, 1990.
164. Orians, K.J. and K.W. Bruland, Dissolved gallium in the open ocean, *Nature* 332, 717-719, 1988.
165. Orton, G.S. and G. Aumman, The abundance of acetylene in the atmosphere of Jupiter, *Icarus* 32, 431-436, 1977.
166. Orton, G.S., D.K. Aitken, C. Smith, P.F. Roche, J. Caldwell, and R. Snyder, The spectra of Uranus and Neptune at 8-14 and 17-23 μm, *Icarus* 70, 1-12, 1987.
167. Orton, G.S., K.H. Baines, J. Caldwell, P. Romani, A.T. Tokunaga, and R.A. West, Calibration of the 7- to 14-μm brightness spectra of Uranus and Neptune, *Icarus* 85, 257-265, 1990.
168. Owen, T., K. Biemann, D.R. Rushneck, J.E. Biller, D.W. Howarth, and A.L. Lafleur, The composition of the atmosphere at the surface of Mars, *J. Geophys. Res.* 82, 4635-4639, 1977.
169. Owen, T., B.L. Lutz, and C. DeBergh, Deuterium in the outer solar system: Evidence for two distinct reservoirs, *Nature* 320, 244-246, 1986.
170. Owen, T., J.P. Maillard, C. DeBergh, and B.L. Lutz, Deuterium on Mars: The abundance of HDO and the value of D/H, *Science* 240, 1767-1770, 1988.
171. Owen, T., A.R.W. McKellar, T. Encrenaz, J. Lecacheux, C. DeBergh, and J.P. Maillard, A study of the 1.56 μm NH_3 band on Jupiter and Saturn, *Astron. Astrophys.* 54, 291-295, 1977.
172. Oyama, V.I., G.C. Carle, F. Woeller, J.B. Pollack, R.T. Reynolds, and R.A. Craig, Pioneer Venus gas chromatography of the lower atmosphere of Venus, *J. Geophys. Res.* 85, 7891-7902, 1980.
173. Ozima, M. and F.A. Podosek, *Noble Gas Geochemistry*, Cambridge University Press, 1983.
174. Pepin, R.O., On the origin and early evolution of terrestrial planet atmospheres and meteoritic volatiles, *Icarus* 92, 2-79, 1991.
175. Podolak, M., W.B. Hubbard, and D.J. Stevenson, Models of Uranus' interior and magnetic field, in *Uranus*, edited by J. Bergstralh, E. Miner, and M.S. Matthews, pp. 29-61, University of Arizona Press, Tucson, AZ, 1991.
176. Prinn, R.G., How have the atmospheric concentrations of the halocarbons changed?, in *The Changing Atmosphere*, edited by F.S. Rowland and I.S.A. Isaksen, J. Wiley & Sons, pp. 33-48, 1988.
177. Prinn, R.G., D. Cunnold, P. Simmonds, F. Alyea, R. Boldi, A. Crawford, P. Fraser, D. Gutzler, D. Hartley, R. Rosen, and R. Rasmussen, Global average concentration and trend for hydroxyl radicals deduced from ALE/GAGE trichloroethane (methyl chloroform) data for 1978-1990, *J. Geophys. Res.* 97, 2445-2461, 1992.
178. Prinn, R.G., H.P. Larson, J.J. Caldwell, and D. Gautier, Composition and chemistry of Saturn's atmosphere, in *Saturn*, edited by T. Gehrels and M.S. Matthews, University of Arizona Press, Tucson, AZ, pp. 88-149, 1984.
179. Quinby-Hunt, M.S. and K.K. Turekian, Distribution of elements in sea water, *EOS Trans. AGU* 64, 130-132, 1983.
180. Ridgway, S.T., Jupiter: Identification of ethane and acetylene, *Astrophys J.* 187, L41-L43; erratum 192, L51, 1974
181. Ridgway, S.T., H.P. Larson, and U. Fink, The infrared spectrum of Jupiter, in *Jupiter*, edited by T. Gehrels, pp. 384-417, University of Arizona Press, Tucson, AZ, 1976.
182. Riley, J.P., Table of physical and chemical constants relevant to marine chemistry, in *Chemical Oceanography*, edited by J.P. Riley and G. Skirrow, vol. 3, 2nd. ed., pp. 515-547, Academic Press, NY, 1975.
183. Rosenqvist, J., E. Lellouch, P.N. Romani, G. Paubert, and T. Encrenaz, Millimeter-wave observations of Saturn, Uranus and Neptune: CO and HCN on Neptune, *Astrophys. J.* 392, L99-L102, 1992.
184. Samuelson, R.E., W.C. Maguire, R.A. Hanel, V.G. Kunde, D.E. Jennings, Y.L. Yung, and A.C. Aikin, CO_2 on Titan, *J. Geophys. Res.* 88, 8709-8715, 1983.
185. Sato, M. and J.E. Hansen, Jupiter's atmospheric composition and cloud structure deduced from absorption bands in reflected sunlight, *J. Atmos. Sci.* 36, 1133-1167, 1979.
186. Schubert, G., General circulation and the dynamical state of the Venus atmosphere, in *Venus*, edited by D.M. Hunten, L. Colin, T.M. Donahue, and V.I. Moroz, pp. 681-765, University of Arizona Press, Tucson, AZ, 1983.
187. Sigg, A., T. Staffelbach, and A. Neftel, Gas phase measurements of hydrogen peroxide in Greenland and their meaning for the interpretation of H_2O_2 records in ice cores, *J. Atmos. Chem.* 14, 223-232, 1992.
188. Smith, W.H., On the ortho-para equilibrium of H_2 in the atmospheres of the Jovian planets, *Icarus* 33, 210-216, 1978.
189. Smith, W.H., W. Macy, and W. Cochran, Ammonia in the atmospheres of Saturn and Titan, *Icarus* 42, 93-101, 1980.
190. Smith, W.H., W.V. Schempp, and K.H. Baines, The D/H ratio for Jupiter, *Astrophys. J.* 336, 967-970, 1989.
191. Smith, W.H., W.V. Schempp, J. Simon, and K.H. Baines, D/H for Uranus and Neptune, *Astrophys. J.* 336, 962-966, 1989.
192. Sprague, A.L., A diffusion source for sodium and potassium in the atmospheres of Mercury and the Moon, *Icarus* 84, 93-105, 1990.
193. Stolarski, R., R. Bojkov, L. Bishop, C. Zerefos, J. Staeheln, and J. Zawodny, Measured trends in stratospheric ozone, *Science* 256, 342-349, 1992.
194. Tanguy, L., B. Bézard, A. Marten, D. Gautier, E. Gérard, G. Paubert, and A. Lecacheux, Stratospheric profile of HCN on Titan from millimeter observations, *Icarus* 85, 43-57, 1990.
195. Tokunaga, A.T., S.C. Beck, T.R. Geballe, J.H. Lacy, and E. Serabyn, The detection of HCN on Jupiter, *Icarus* 48, 283-289, 1981.
196. Tokunaga, A.T., R.F. Knacke, and T. Owen, The detection of ethane on Saturn, *Astrophys. J.* 197, L77-L78, 1975.
197. Tokunaga, A.T., R.F. Knacke, and T. Owen, Ethane and acetylene abun-

dances in the Jovian atmosphere, *Astrophys. J.* 209, 294-301, 1976.
198. Tokunaga, A.T., R.F. Knacke, and S.T. Ridgway, High spatial and spectral resolution 10-μm observations of Jupiter, *Icarus* 44, 93-101, 1980.
199. Tokunaga, A.T., R.F. Knacke, S.T. Ridgway, and L. Wallace, High-resolution spectra of Jupiter in the 744-980 inverse centimeter spectral range, *Astrophys. J.* 232, 603-615, 1979.
200. Trafton, L.M., On the possible detection of H_2 in Titan's atmosphere, *Astrophys. J.* 175, 285-293, 1972.
201. Trafton, L.M., Saturn: Long term variation of H_2 and CH_4 absorptions, *Icarus* 31, 369-384, 1977.
202. Trafton, L.M., The atmospheres of the outer planets and satellites, *Rev. Geophys. Space Phys.* 19, 43-89, 1981.
203. Trafton, L.M., Uranus' (3-0) quadrupole line profiles, *Icarus* 70, 13-30, 1987.
204. Trafton, L.M. and D.A. Ramsay, The D/H ratio in the atmosphere of Uranus: Detection of the $R_5(1)$ line of HD, *Icarus* 41, 423-429, 1980.
205. Trauger, J.T. and J.I. Lunine, Spectroscopy of molecular oxygen in the atmospheres of Venus and Mars, *Icarus* 55, 272-281, 1983.
206. Trauger, J.T., F.L. Roesler, N.P. Carleton, and W.A. Traub, Observation of HD on Jupiter and the D/H ratio, *Astrophys. J.* 184, L137-L141, 1973.
207. Trauger, J.T., F.L. Roesler, and M.E. Mickelson, The D/H ratios on Jupiter, Saturn and Uranus based on new HD and H_2 data, *Bull. Amer. Astron. Soc.* 9, 516, 1977.
208. Turco, R.P., The photochemistry of the stratosphere, in *The Photochemistry of Atmospheres,* edited by J.S. Levine, pp. 77-128, Academic Press, NY, 1985.
209. Turekian, K.K., The oceans, streams, and atmosphere, in *Handbook of Geochemistry,* edited by K.H. Wedepohl, vol. 1, pp. 297-323, 1969.
210. Tyler, G.L., V.R. Eshelman, J.D. Anderson, G.S. Levy, G.F. Lindal, G.E. Wood, and T.A. Croft, Radio science with Voyager 2 at Saturn: Atmosphere and ionosphere and the masses of Mimas, Tethys, and Iapetus, *Science* 315, 553-558, 1982.
211. Tyler, G.L., D.N. Sweetnam, J.D. Anderson, S.E. Borutzki, J.K. Campbell, V.R. Eshleman, D.L. Gresh, E.M. Gurrola, D.P. Hinson, N. Kawashima, E.R. Kursinski, G.S. Levy, G.F. Lindal, J.R. Lyons, E.A. Marouf, P.A. Rosen, R.A. Simpson, and G.E. Wood, Voyager radio science observations of Neptune and Triton, *Science* 246, 1466-1473, 1989.
212. Vilas, F., C.R. Chapman, and M.S. Matthews, eds., *Mercury,* University of Arizona Press, Tucson, AZ, 1988.
213. Von Zahn, U., S. Kumar, H. Niemann, and R. Prinn, Composition of the Venus atmosphere, in *Venus,* edited by D.M. Hunten, L. Colin, T.M. Donahue, and V.I. Moroz, pp. 299-430, University of Arizona Press, Tucson, AZ, 1983.
214. Warneck, P., *Chemistry of the Natural Atmosphere,* Academic Press, New York, NY, 1988.
215. Wiedemann, G., G.L. Bjoraker, and D.E. Jennings, Detection of ^{13}C-Ethane in Jupiter's atmosphere, *Astrophys. J.* 383, L29-L32, 1991.
216. Wilson, T.R.S., Salinity and the major elements of sea water, in *Chemical Oceanography,* vol. 1, 2nd. ed., edited by J.P. Riley and G. Skirrow, pp. 365-413, Academic Press, NY, 1975.
217. Witteborn, F.C., J.B. Pollack, J.D. Bregman, H.J. Goebel, B.T. Soifer, R.C. Puetter, R.J. Rudy, and S.P. Willner, Observations of Saturn in the 5 to 8 μm spectral region, *Icarus* 45, 653-660, 1981.
218. Woodman, J.H., L.M. Trafton, and T. Owen, The abundances of ammonia in the atmosphere of Jupiter, Saturn, and Titan, *Icarus* 32, 314-320, 1977.
219. Young, L.D.G., High resolution spectra of Venus: A review, *Icarus* 17, 632-658, 1972.
220. Yung, Y.L., M. Allen, and J.P. Pinto, Photochemistry of the atmosphere of Titan: Comparison between model and observations, *Astrophys. J. Suppl.* 55, 465-506, 1984.
221. Yung, Y.L., J.S. Wen, J.P. Pinto, M. Allen, K.K. Pierce, and S. Paulson, HDO in the Martian atmosphere: Implications for the abundance of crustal water, *Icarus* 76, 146-159, 1988.

Fundamental Physical Constants and Conversion Factors

Bruce M. Moskowitz

1. INTRODUCTION

SI is the servant of man, not his master
P. Vigoureux [1971]

This section provides a summary of important units for geomagnetism and geoelectricty. In addition, a summary of conversion factors and fundamental units of relevance to earth and planetary science are presented for reference.

Despite the sentiment expressed above by Vigoureux, it still seems that plenty of us slave over SI units in geomagnetism. There is probably no other scientific discipline in which the topic of units generates so much endless discussion and confusion than in magnetism. Before the late 1970's, practically all the geophysical literature in geomagnetism and paleomagnetism used the Gaussian CGS system of units. The CGS system is a perfectly sound, internally consistent, system of units, but, like all systems of units and dimensions, is totally arbitrary. As the name implies, the cgs system is based on three base units: centimeter, gram, and second. All other units are derived from these three. The Gaussian cgs system is based on two earlier systems, the electrostatic units (esu) and electromagnetic units (emu). Electrostatic units were defined by Coulomb's law describing the force between two electrical charges. Similarly, electromagnetic units were defined by the force between two magnetic charges or two current-carrying wires. One consequence of this dichotomy is that the dimensions of electric charge and other related quantities are different in the esu and emu systems. The Gaussian system is a mixture of these two subsets and uses the emu system to describe magnetic quantities and the esu system to describe electrical quantities. As a result of combining the emu and esu system into the Gaussian system, the velocity of light in vacuum appears explicitly in some equations dealing with magnetic and electric effects. This resulted in a cumbersome set of units with "inconvenient" magnitudes for practical electrical units such as the volt, ohm, and ampere.

The Système International, or SI system of units, are now the recommended (and required!) units for scientific and commercial use, as decided by international committees and journal editors. The SI system, or MKSA, is also totally arbitrary and is based on four base units: meter, kilogram, second, and ampere. The introduction of the ampere as a base unit instead of a derived unit has some great advantages. Besides doing away with the emu and esu systems, the SI system incorporating ampere as a base unit also eliminates all those weird "ab" and "stat" emu and esu units, such as abampere and statcoulomb. The price we pay for this "unit-fication", however, becomes apparent for workers in magnetism. Suddenly factors of 4π disappear from, or reappear elsewhere in, formulae. Further, the permeability of free space (μ_0) and the permittivity of free space (ε_0), which were dimensionless, equal to unity, and often ignored in the cgs world, now take on dimensions and numerical values much different from unity. Likewise, the magnitudes of various magnetic parameters that we deal with every day in the laboratory have changed, some becoming much larger, others smaller, and all somewhat unfamiliar. This short section provides a brief review of the cgs and SI system of units in magnetism (also see 2,5-8).

B. M. Moskowitz, University of Minnesota, Institute for Rock Magnetism, 100 Union Street, SE, Minneapolis, MN 55455

Global Earth Physics
A Handbook of Physical Constants
AGU Reference Shelf 1

2. THE REALLY IMPORTANT MAGNETIC TERMS

Following Shive [7] and Payne [5], there are four fundamental magnetic quantities:

B= magnetic induction, or flux density
H= magnetic field strength, or magnetizing force
M= magnetization per unit volume
J= magnetic polarization, or magnetization

In the SI system, the relationship between B, H, M, and J is given by

$$B = \mu_0 H + J \tag{1}$$

$$B = \mu_0 (H + M) \tag{2}$$

$$J = \mu_0 M \tag{3}$$

where μ_0 is $4\pi x10^{-7}$ Newton/Ampere^2 and is called the permeability of free space. In free space a magnetic field produces a magnetic induction given by $B=\mu_0 H$. If the space is filled by any magnetic material the magnetization will produce an additional magnetic induction given by $\mu_0 M$. The total induction is the sum of these two contributions and is given by equation (2). Equations (1) and (2) are usually associated respectively with the names of Kennelly and Sommerfeld and represent two alternative definitions of the magnetic moment of a current loop. By equation (1), the dimensions of B and J are the same and the appropriate unit is the Weber/m^2 or tesla. Similarly, by equation (2), the dimensions of H and M are the same and the appropriate unit is the ampere m^{-1}, or Am^{-1}. Equation (2) is the officially recognized SI convention. Another related quantity is the volume magnetic susceptibility (κ) and is defined as

$$\kappa = \frac{M}{H} = \frac{J}{\mu_0 H} \tag{4}$$

The volume magnetic susceptibility is dimensionless.

In the cgs system, the relationship between B, H, M, and J is given by

$$B = H + 4\pi J \tag{5}$$

$$J = M \tag{6}$$

The constant μ_0 is arbitrarily set to unity and is dimensionless. Therefore, the dimensions for B, H, J, and M are the same. The volume susceptibility is given by equation (4) and is also dimensionless. However, just because the dimensions of these quantities are the same, there is no reason to have the same names for the units. The name for B is gauss (G), for H is oersted (Oe), and for M and J is emu/cm^3. Often H and M are both given in gauss and no distinction is made between J and M. Since in free space B=H (in cgs), gauss is frequently used to express the magnitude of H. Yet this conceals a subtle difference between M (and H) and the induction J (and B), or flux density, it produces. By equation (5), one emu/cm^3 unit of magnetization will produce a magnetic induction B of 4πJ gauss. The "correct" procedure would be to assign M or J units of emu/cm^3, and the quantity 4πJ units of gauss. This is rarely done in the geophysical literature, but is common in engineering and physics.

3. CONVERSION ADVENTURES

The conversion factors between B, H, M and J in SI and cgs are as follows:

B: 1 T = 10^4 G
H: 1 Am^{-1} = $4\pi x10^{-3}$ Oe
M: 1 Am^{-1} = 10^{-3} emu cm^{-3}
J: 1 T = $10^4/4\pi$ emu cm^{-3}

Right away we see a problem with converting emu cm^{-3} to the appropriate SI unit. Do we use the conversion for M or J? Although B and H, and, J and M, are used interchangeably in CGS system, we need to be more precise when converting to SI. For example, the earth's magnetic field is approximately 0.5 G, or 0.5 Oe. However, in SI

0.5 G = $5x10^{-4}$ T or 50 μT
0.5 Oe = 39.8 Am^{-1}

It is much easier to convert gauss to tesla (move the decimal point 4 places) than to convert oersted to Am^{-1}. So it is not too surprising that the current practice used by geophysicists is to report both B and H in free space (ie., in the absence of magnetized material, M=0) in tesla. We have not decided suddenly that the B field is more fundamental than the H field just that it is more convenient to use the units of B. When we now talk about an alternating "magnetic field" or some other H field of say 10 millitesla (mT), we really mean an induction of $\mu_0 H$=10 mT. However, this is rarely noted. The corresponding procedure for J (and M) in cgs is to convert emu cm^{-3} to Am^{-1} by moving the decimal three places and call the result the magnetization per unit volume, magnetization, or the intensity of magnetization.

To summarize briefly, when using cgs units, we usually deal with the magnetization J and the magnetic field H. When we convert to SI units, we use the magnetic moment

TABLE 1. Conversion factors for Magnetic Quantities

Magnetic Term	Symbol	SI Unit	CGS Unit	Conversion Factor
Magnetic induction	B	tesla (T)	gauss (G)	1 T = 10^4 G
Magnetic field	H	A m^{-1}	oersted (Oe)	1 A m^{-1} = 4π x 10^{-3} Oe
Magnetization	M	A m^{-1}	emu cm^{-3}	1 A m^{-1} = 10^{-3} emu cm^{-3}
Magnetic polarization	J	T	G	1 T = $10^4/4\pi$ emu cm^{-3}
Magnetic moment	m	A m^2	emu = G cm^3	1 A m^2 = 10^3 emu
Magnetic moment per unit mass	σ	A m^2 kg^{-1}	emu g^{-1}	1 A m^2 kg^{-1} = 1 emu g^{-1}
Volume magnetic susceptibility (κ=M/H)	κ	dimensionless	dimensionless	1(SI) = $1/4\pi$ (cgs)
Mass magnetic susceptibility ($\chi=\kappa/\rho$)	χ	m^3 kg^{-1}	emu Oe^{-1} g^{-1}	1 m^3 kg^{-1} = $10^3/4\pi$ emu Oe^{-1} g^{-1}
Molar magnetic susceptibility ($\chi_m=\chi M^*$)	χ_m	m^3 mol^{-1}	emu Oe^{-1} g^{-1} mol^{-1}	1 m^3 mol^{-1} = $10^6/4\pi$ emu $Oe^{-1}g^{-1}$ mol^{-1}
Magnetic permeability (μ=B/H)	μ	H m^{-1}	G Oe^{-1}	1 H m^{-1} = $10^7/4\pi$ G Oe^{-1}
Magnetic flux	Φ	Weber (Wb)	maxwell (Mx)	1 Wb = 10^8 Mx
Magnetic scalar potential; Magnetomotive force	ϕ	A	gilbert	1 A = $4\pi/10$ gilbert
Magnetic vector potential	A	Wb m^{-1}	emu = G cm	1 Wb m^{-1} = 10^6 emu
Magnetic pole strength	p	A m	emu = G cm^2	1 A m = 10 emu
Demagnetizing factor	N	dimensionless	dimensionless	1(SI) = 4π (cgs)
Magnetostriction constant	λ	dimensionless	dimensionless	1(SI) = 1(cgs)
Anisotropy constant Magnetostatic energy Energy product	K, K_1, K_u E_m $(BH)_{max}$	J m^{-3}	erg cm^{-3}	1 J m^{-3} = 10 erg cm^{-3}

A=ampere; H=Henry=Newton/Ampere; M^*=molecular weight; Tesla=Weber/m^2; ρ=density (1 kg/m^3=10^3 g/cm^3). Volume magnetic susceptibility in cgs units is sometimes given as emu cm^{-3} Oe^{-1} or G/Oe, both are dimensionless. Mass magnetic susceptibility in cgs units is sometimes given as emu g^{-1}, emu g^{-1} oe^{-1}, emu $g^{-1}G^{-1}$, G cm^3 g^{-1}, or cm^3 g^{-1}. The csg unit gamma $\gamma = 10^{-5}$ G = 10^{-9} T = 1 nanotesla (nT). The SI units are based on the Sommerfeld convention which gives the unit of magnetic moment as A m^2. The Kennelly convention gives the unit of magnetic moment as Wb m.

per unit volume, or simply the magnetization M and the magnetic induction B. As shown by Shive [7], when we convert to SI, J (gauss) and H (Oe) are first converted to M (emu/cm^3) and B (gauss) in cgs. Then we use the SI conversion scheme to convert M and B in cgs to their corresponding SI units of A/m and tesla. For example, to convert a magnetization of 10^{-3}G and a magnetic field of 100 oe from cgs to SI, we do the following:

TABLE 2. Conversion Factors for Electrical Quantities

Quantity	Symbol	SI Unit	CGS emu unit	CGS esu unit
Electric Charge	q	1 Coulomb (C)	0.1 abcoulomb	$0.1c$ statcoulomb
Current	I	1 Ampere (A)	0.1 abampere	$0.1c$ statampere
Electric Potential(emf)	V	1 volt (V)	10^8 abvolt	10^8c^{-1} statvolt
Resistance	R	1 ohm (Ω)	10^9 cm s^{-1}	10^9c^{-2} s cm^{-1}
Capacitance	C	1 farad (F)	10^{-9} s^2 cm^{-1}	$10^{-9}c^2$ cm
Inductance	L	1 Henry (H)	10^9 cm	10^9c^{-2} s^2 cm^{-1}
Conductance	G	1 siemen (S)	10^{-9} cm^{-1} s	$10^{-9}c^{-2}$ cm s^{-1}
Charge density	ρ_e	1 C m^{-3}	10^{-7} abcoul cm^{-3}	$10^{-7}c$ statcoul cm^{-3}
Current density	J_e	1 A m^{-2}	10^{-5} abamp cm^{-2}	$10^{-5}c$ statamp cm^{-2}
Electric Field	E	1 V m^{-1}	10^6 abvolt cm^{-1}	10^6c^{-1} statvolt cm^{-1}
Displacement vector	D	1 C m^{-2}	$4\pi x10^{-5}$ abcoul cm^{-2}	$4\pi x10^{-5}c$ statcoul cm^{-2}
Electric Polarization	P	1 C m^{-2}	10^{-5} abcoul cm^{-2}	$10^{-5}c$ statcoul cm^{-2}
Electrical conductivity	σ	1 S m^{-1}	10^{-11} cm^{-2} s	$10^{-11}c^2$ s^{-1}
Electrical Resistivity	ρ	1 Ω m	10^{11} cm^2 s^{-1}	$10^{11}c^{-2}$ s
Electric permittivity	ε	1 F m^{-1}	10^{-11} cm^{-2} s^2	$10^{-11}c^2$ esu

The table is arranged so that one SI unit equals the corresponding number of units in emu and esu. Quantities in each row, therefore, stands for the identical amount expressed in different units. The symbol c stands for the magnitude of the speed of light in vacuo expressed in cm/sec (=$2.99792458x10^{10}$). For example, 1 coulomb = $0.1c$ statcoulomb ≈ $3x10^9$ statcoulomb. The Gaussian units for electrical quantities consist mostly of the es units in the last column.

$$J(cgs) = 10^{-3}\ G = M(cgs) = 10^{-3}\ emu\ cm^{-3} = M(SI) = 1\ Am^{-1}$$

$$H(cgs) = 100\ Oe = B(cgs) = 100\ G = B(SI) = 10\ mT$$

This is the official conversion scheme recommended by the International Association of Geomagnetism and Aeronomy (IAGA) in 1973; unfortunately, the world outside geomagnetism uses a different convention. In most physics and engineering research papers that use SI units, a direct conversion using the Sommerfeld convention [equation (2)] is employed. In this case, the magnetizing field and magnetization are given in Am^{-1}. For example, a magnetic field of 100 Oe (CGS) would be given as 8000 Am^{-1} (SI) in a physics journal, but as 10 mT (SI) in a geophysics journal.

Various parameters and conversion factors are presented in the following tables. Tables 1 and 2 summarizes conversion factors for magnetic and electrical units, respectively. An extensive list of fundamental equations in electromagnetism in both SI and CGS is given by Payne [6] and the errata published later [7]. In Tables 3 to 6, conversion factors dealing with pressure, energy, spectroscopy units and fundamental physical constants are summarized.

TABLE 3. Conversion Factors for Pressure Units

	atm	bar	dyne cm^{-2}	kg m^{-2}	lb in^{-2} psi	Pascal Pa
1 atm=	1	1.01325	1.01325 $x10^{6}$	1.033227 $x10^{4}$	14.695595	1.01325 $x10^{5}$
1 bar=	9.86923 $x10^{-1}$	1	10^{6}	1.0197 $x10^{4}$	14.504	10^{5}
1 dyne cm^{-2}=	9.86923 $x10^{-7}$	10^{-6}	1	1.0197 $x10^{-2}$	1.4504 $x10^{-5}$	10^{-1}
1 kg m^{-2}=	9.678 $x10^{-5}$	9.8067 $x10^{-5}$	98.067	1	1.423 $x10^{-3}$	9.8067
1 lb in^{-2}=	0.068046	6.8948 $x10^{-2}$	6.8948 $x10^{4}$	7.0306 $x10^{2}$	1	6.8948 $x10^{3}$
1 Pascal=	9.869 $x10^{-6}$	10^{-5}	10	1.019 $x10^{-1}$	1.450 $x10^{-4}$	1

The SI pressure unit is the Pascal (Pa) = 1 Newton m^{-2}.
1 Torr = 1 mm Hg = $1.33322x10^{-3}$ bar =133.3 Pa.
1 Kilobar = 100 MPa.

TABLE 4. Conversion Factors for Energy Units

	erg	joule	calorie (g)	watt-hr	BTU	ev
1 erg=	1	10^{-7}	2.39006 $x10^{-8}$	2.778 $x10^{-11}$	9.4845 $x10^{-11}$	6.242 $x10^{11}$
1 joule=	10^{7}	1	2.39006 $x10^{-1}$	2.778 $x10^{-4}$	9.4845 $x10^{-4}$	6.242 $x10^{18}$
1 calorie (g)=	4.184 $x10^{7}$	4.184	1	1.1622 $x10^{-3}$	3.9683 $x10^{-3}$	2.612 $x10^{19}$
1 watt-hr=	3.60 $x10^{10}$	3600	860.421	1	3.4144	2.247 $x10^{22}$
1 BTU=	1.05435 $x10^{10}$	1054.35	251.99576	2.92875 $x10^{-1}$	1	6.581 $x10^{21}$
1 eV=	1.602 $x10^{-12}$	1.602 $x10^{-19}$	3.829 $x10^{-20}$	4.450 $x10^{-23}$	1.519 $x10^{-22}$	1

The calorie (g) is the thermochemical calorie as defined by the U.S. National Bureau of Standards.
1 joule = 1 watt-sec.
1 atomic mass unit = $1.492x10^{-10}$ joule.

TABLE 5. Conversion Factors for Frequency and Energy Units used in Spectroscopy[a]

	Hz	cm^{-1}	J mol^{-1}	eV
1 Hz=	1	3.3356×10^{-11}	3.9915×10^{-10}	4.1353×10^{-15}
1 cm^{-1}=	2.9979×10^{10}	1	11.9660	1.2397×10^{-4}
1 J mol^{-1}=	2.5053×10^{9}	8.3567×10^{-2}	1	1.0360×10^{-5}
1 eV=	2.4182×10^{14}	8.0663×10^{3}	9.6522×10^{4}	1

[a]Conversion factors taken from [3]. 1 Kayser = 1 cm^{-1}

TABLE 6. Fundamental Physical Constants[a]

Quantity	Symbol	Value	SI Units
Universal Constants			
Speed of light in vacuum	c	299 792 458	m sec^{-1}
Permeability of vacuum	μ_0	$4\pi \times 10^{-7}$	N A^{-2}
Permittivity of vacuum	ε_0	$1/\mu_0 c^2$ = 8.854 187 817	10^{-12} F m^{-1}
Newtonian constant of gravitation	G	6.672 59(85)	10^{-11} $m^3 kg^{-1} sec^{-2}$
Planck constant	h	6.626 075 5(40)	10^{-34} J sec
in electron volts, $h/\{e\}$		4.135 669 2(12)	10^{-15} eV sec
$h/2\pi$	$\hbar$	1.054 572 66(63)	10^{-34} J sec
in electron volts, $\hbar/\{e\}$		6.582 122 0(20)	10^{-16} eV sec
Planck mass, $(\hbar c/G)^{1/2}$	m_p	2.176 71(14)	10^{-8} kg
Planck length, $\hbar/m_p c = (\hbar G/c^3)^{1/2}$	l_p	1.616 05(10)	10^{-35} m
Planck time, $l_p/c = (\hbar G/c^5)^{1/2}$	t_p	5.390 56(34)	10^{-44} sec
Physicochemical constants			
Avogadro constant	N_A	6.022 136 7(36)	10^{23} mol^{-1}
Atomic mass constant, $m(C^{12})/12$	m_u	1.660 540 2(10)	10^{-27} kg
in electron volts, $m_u c^2/\{e\}$		931.494 32(28)	MeV
Faraday constant	F	96 485.309(29)	C mol^{-1}
Molar Planck constant	$N_A h$	3.990 313 23(36)	10^{-10}J sec mol^{-1}
	$N_A hc$	0.119 626 58(11)	J m mol^{-1}
Molar gas constant	R	8.314 510(70)	J mol^{-1} K^{-1}
Boltzmann constant, R/N_A	k	1.380 658(12)	10^{-23} J K^{-1}
in electron volts, $k/\{e\}$		8.617 385(73)	10^{-5} eV K^{-1}
in hertz, k/h		2.083 674(18)	10^{10} Hz K^{-1}
in wavenumbers, k/hc		69.503 87(59)	m^{-1} K^{-1}
Molar volume (ideal gas), RT/p (at 273.15 K, 101 325 Pa)	V_m	22 414.10(19)	cm^3 mol^{-1}
Loschmidt constant, N_A/V_m	n_0	2.686 763(23)	10^{25} m^{-3}

TABLE 6. (continued)

Quantity	Symbol	Value	SI Units
Stefan-Boltzmann constant, $(\pi^2/60)k^4/\hbar^3c^2$	σ	5.670 51(19)	10^{-8} W m^{-2}K^{-4}
First radiation constant, $2\pi hc^2$	c_1	3.741 774 9(22)	10^{-16} W m^2
Second radiation constant, hc/k	c_2	0.014 387 69(12)	m K
Wien displacement law constant, $\lambda_{max}T=c_2/4.965\ 114\ 23...$	b	2.897 756(24)	10^{-3} m K
Electromagnetic constants			
Elementary charge	e	1.602 177 33(49)	10^{-19} C
	$e/\hbar$	2.417 988 36(72)	10^{14} A J^{-1}
Magnetic flux quantum, $h/2e$	Φ_0	2.067 834 61(61)	10^{-15} Wb
Josephson frequency-voltage quotient	$2e/h$	4.835 976 7(14)	10^{14} Hz V^{-1}
Quantized Hall conductance	e^2/h	3.874 046 14(7)	10^{-5} S
Quantized Hall resistance, $h/e^2=\mu_0c/2\alpha$	R_H	25 812.805 6(12)	Ω
Bohr magneton, $e\hbar/2m_e$	μ_B	9.274 015 4(31)	10^{-24} J T^{-1}
in electron volts, $\mu_B/\{e\}$		5.788 382 63(52)	10^{-5} eV T^{-1}
in hertz, μ_B/h		1.399 624 18(42)	10^{10} Hz T^{-1}
in wavenumbers, μ_B/hc		46.686 437(14)	m^{-1} T^{-1}
in kelvins, μ_B/k		0.671 709 9(57)	K T^{-1}
Nuclear magneton, $e\hbar/2m_p$	μ_N	5.050 786 6(17)	10^{-27} J T^{-1}
in electron volts, $\mu_N/\{e\}$		3.152 451 66(28)	10^{-8} eV T^{-1}
in hertz, μ_N/h		7.622 591 4(23)	MHz T^{-1}
in wavenumbers, μ_N/hc		2.542 622 81(77)	10^{-2} m^{-1} T^{-1}
in kelvins, μ_N/k		3.658 246(31)	10^{-4} K T^{-1}
Atomic constants			
Fine-structure constant, $\mu_0ce^2/2h$	α	7.297 353 08(33)	10^{-3}
inverse fine-structure constant	α^{-1}	137.035 989 5(61)	
Rydberg constant, $m_ec\alpha^2/2h$	R_∞	10 973 731.534(13)	m^{-1}
in hertz, $R_\infty c$		3.289 841 949 9(39)	10^{15} Hz
in joules, $R_\infty hc$		2.179 874 1(13)	10^{-18} J
in eV, $R_\infty hc/\{e\}$		13.605 698 1(40)	eV
Bohr radius, $\alpha/4\pi R_\infty$	a_0	0.529 177 249(24)	10^{-10} m
Hartree energy, $e^2/4\pi\varepsilon_0a_0=2R_\infty hc$	E_h	4.359 748 2(26)	10^{-18} J
in eV, $E_h/\{e\}$		27.211 396 1(81)	eV
Quantum of circulation	$h/2m_e$	3.636 948 07(33)	10^{-4} m^2 sec^{-1}
Electron Constants			
Mass	m_e	9.109 389 7(54)	10^{-31} kg
in atomic mass units		5.485 799 03(13)	10^{-4} u
in electron volts, $m_ec^2/\{e\}$		0.510 999 06(15)	MeV
Electron-muon mass ratio	m_e/m_μ	4.836 332 18(71)	10^{-3}

TABLE 6. (continued)

Quantity	Symbol	Value	SI Units
Electron-proton mass ratio	m_e/m_p	5.446 170 13(11)	10^{-4}
Electron-deuteron mass ratio	m_e/m_d	2.724 437 07(6)	10^{-4}
Electron-α-particle mass ratio	m_e/m_α	1.370 933 54(3)	10^{-4}
Specific charge	$-e/m_e$	-1.758 819 62(53)	10^{11} C kg^{-1}
Molar mass	M(e)	5.485 799 03(13)	10^{-7} kg mol^{-1}
Compton wavelength, $h/m_e c$	λ_c	2.426 310 58(22)	10^{-12} m
Classical radius, $\alpha^2 a_0$	r_e	2.817 940 92(38)	10^{-15} m
Thomson cross section, $(8\pi/3)r_e^2$	σ_e	0.665 246 16(18)	10^{-28} m^2
Magnetic moment	μ_e	928.477 01(31)	10^{-26} J T^{-1}
in Bohr magnetons	μ_e/μ_B	1.001 159 652 193(10)	
in nuclear magnetons	μ_e/μ_N	1838.282 000(37)	
Magnetic moment anomaly, μ_e/μ_B-1	a_e	1.159 652 193(10)	10^{-3}
g-factor, $2(1+a_e)$	g_e	2.002 319 304 386(20)	
Electron-muon magnetic moment ratio	μ_e/μ_μ	206.766 967(30)	
Electron-proton magnetic moment ratio	μ_e/μ_p	658.210 688 1(66)	
Muon Constants			
Mass	m_μ	1.883 532 7(11)	10^{-28} kg
in atomic mass units		0.113 428 913(17)	u
in electron volts, $m_\mu c^2$/{e}		105.658 389(34)	MeV
Muon-electron mass ratio	m_μ/m_e	206.768 262(30)	
Molar mass	$M(\mu)$	1.134 289 13(17)	10^{-4} kg mol^{-1}
Magnetic moment	μ_μ	4.490 451 4(15)	10^{-26} J T^{-1}
in Bohr magnetons	μ_μ/μ_B	4.841 970 97(71)	10^{-3}
in nuclear magnetons	μ_μ/μ_N	8.890 598 1(13)	
Magnetic moment anomaly, $[\mu_\mu/(e\hbar/2m_\mu)]$-1	a_μ	1.165 923 0(84)	10^{-3}
g-factor, $2(1+a_\mu)$	g_μ	2.002 331 846(17)	
Muon-proton magnetic moment ratio	μ_μ/μ_p	3.183 345 47(47)	
Proton Constants			
Mass	m_p	1.672 623 1(10)	10^{-27} kg
in atomic mass units		1.007 276 470(12)	u
in electron volts, $m_p c^2$/{e}		938.272 31(28)	MeV
Proton-electron mass ratio	m_p/m_e	1836.152 701(37)	
Proton-muon mass ratio	m_p/m_μ	8.880 244 4(13)	
Specific charge	e/m_p	9.578 830 9(29)	10^7 C kg^{-1}
Molar mass	M(p)	1.007 276 470(12)	10^{-3} kg mol^{-1}
Compton wavelength, $h/m_p c$	$\lambda_{c,p}$	1.321 410 02(12)	10^{-15} m
Magnetic moment	μ_p	1.410 607 61(47)	10^{-26} J T^{-1}
in Bohr magnetons	μ_p/μ_B	1.521 032 202(15)	10^{-3}
in nuclear magnetons	μ_p/μ_N	2.792 847 386(63)	
Shielded proton moment (H_2O,	μ_p'	1.410 571 38(47)	10^{-26} J T^{-1}

TABLE 6. (continued)

Quantity	Symbol	Value	SI Units
spherical sample, 25°C)			
Diamagnetic shielding correction for protons (H_2O, spherical sample, 25°C), $1-\mu_p'/\mu_p$	σ_{H2O}	25.689(15)	10^{-6}
Gyromagnetic ratio	γ_p	26 752.212 8(81)	10^4 sec^{-1} T^{-1}
uncorrected (H_2O, spherical sample, 25°C)	γ_p'	26 751.525 5(81)	10^4 sec^{-1} T^{-1}
Neutron Constants			
mass	m_n	1.674 928 6(10)	10^{-27} kg
in atomic mass units		1.008 664 904(14)	u
in electron volts, $m_nc^2/\{e\}$		939.565 63(28)	MeV
Neutron-electron mass ratio	m_n/m_e	1838.683 662(40)	
Neutron-proton mass ratio	m_n/m_p	1.001 378 404(9)	
Molar mass	M(n)	1.008 664 904(14)	10^{-3} kg mol^{-1}
Compton wavelength, h/m_nc	$\lambda_{C,n}$	1.319 591 10(12)	10^{-15} m
Magnetic moment	μ_n	0.966 237 07(40)	10^{-26} J T^{-1}
in Bohr magnetons	μ_n/μ_B	1.041 875 63(25)	10^{-3}
in nuclear magnetons	$\mu_n\mu_N$	1.913 042 75(45)	
Neutron-electron magnetic moment ratio	μ_n/μ_e	1.040 668 82(25)	10^{-3}
Neutron-proton magnetic moment ratio	μ_n/μ_p	0.684 979 34(16)	
Deuteron Constants			
mass	m_d	3.343 586 0(20)	10^{-27} kg
in atomic mass units		2.013 553 214(24)	u
in electron volts, $m_dc^2/\{e\}$		1875.613 39(57)	MeV
Deuteron-electron mass ratio	m_d/m_e	3670.483 014(75)	
Deuteron-proton mass ratio	m_d/m_p	1.999 007 496(6)	
Molar mass	M(d)	2.013 553 214(24)	10^{-3} kg mol^{-1}
Magnetic moment	μ_d	0.433 073 75(15)	10^{-26} J T^{-1}
in Bohr magnetons	μ_d/μ_B	0.466 975 447 9(91)	10^{-3}
in nuclear magnetons	μ_d/μ_N	0.857 438 230(24)	
Deuteron-electron magnetic moment ratio	μ_d/μ_e	0.466 434 546 0(91)	
Deuteron-proton magnetic moment ratio	μ_d/μ_p	0.307 012 203 5(51)	
Conversion Factors and Units			
Electron volt, (e/C)J=\{e\}J	eV	1.602 177 33(49)	10^{-19}J
Atomic mass unit (unified), $m_u=m(C^{12})/12$	u	1.660 540 2(10)	10^{-27} kg
Standard atmosphere	atm	101 325	Pa

TABLE 6. (continued)

Quantity	Symbol	Value	SI Units
Standard acceleration of gravity	g_n	9.806 65	m sec^{-2}
X-ray standards			
Cu x-unit: $\lambda(CuK\alpha_1)\equiv 1537.400$ xu	xu($CuK\alpha_1$)	1.002 077 89(70)	10^{-13} m
Mo x-unit: $\lambda(MoK\alpha_1) \equiv 707.831$ xu	xu($MoK\alpha_1$)	1.002 099 38(45)	10^{-13} m
Å*: $\lambda(WK\alpha_1) \equiv 0.209\ 100$ Å	Å*	1.000 014 81(92)	10^{-10} m
Lattice spacing of Si (in vacuum, 22.5°C)	a	0.543 101 96(11)	nm
$d_{220}=a/\sqrt{8}$	d_{220}	0.192 015 540(40)	nm
Molar volume of Si, $M(Si)/\rho(Si)=N_A a^3/8$	$V_m(Si)$	12.058 817 9(89)	cm^3 mol^{-1}

*Values are the set of recommended values of fundamental physical constants resulting from the 1986 least-squares adjustment [4] and recommended by CODATA, the Committee for Science and Technology of the International Council of Scientific Union. Digits in parentheses indicate the standard deviation uncertainty in the last digits of the given value. {e} refers to the numerical value only. The abbreviations for the units are: A=ampere; Å=angstrom; C=coulomb; eV=electron-volt; F=farad; Hz=hertz; J=joule; K=kelvin; kg= kilogram; m=meter; nm= nanometer; mol= mole; N=newton; Pa=pascal; S=siemen; T=tesla; u=unified mass unit; V=volt; W=watt; Wb=weber; Ω=ohm.

Acknowledgments. This is contribution no. 9208 of the Institute for Rock Magnetism. Support for the IRM is provided by grants from the Keck Foundation and the National Science Foundation.

REFERENCES

1. Anonymous, *The Pressure, Strain, and Force Handbook*, vol. 27, Omega Engineering Inc.,1991.
2. Brown, W.F., Jr., Tutorial paper on dimensions and units, *IEEE Transactions on Magnetics, 20*, 112-117, 1984.
3. Calas, G., and F.C. Hawthorne, Introduction to spectroscopic methods, *Reviews in Mineralogy, 18*, 1-10, 1988.
4. Cohen, E. R., and B.N. Taylor, The fundamental physical constants, *Physics Today, 44*, part 2, 9-13, 1991.
5. Payne, M.A., SI and Gaussian CGS units, conversions and equations for use in geomagnetism, *Phys. Earth Planet. Int., 26*, 10-16, 1981a.
6. Payne, M.A., Errata, *Phys. Earth Planet. Int.*, 27, 233, 1981b.
7. Shive, P.N., Suggestions for the use of SI in magnetism, *EOS Trans. AGU, 67*, 25, 1986.
8. Smith, D.H., Electrical and Magnetic Units in the Système International, *Contemp. Phys., 11*, 287-300, 1970.
9. Vigoureux, P., *Units and Standards of Electromagnetism*, 81 pp., Wykeham Publications LTD, London, 1971.
10. Weast, R., *CRC Handbook of Chemistry and Physics*, 54th edition, CRC Press, Cleveland, Ohio, 1974.

Earth Rotation

Jean O. Dickey

1. INTRODUCTION

The study of the Earth's rotation in space (encompassing Universal Time (UT1), length of day, polar motion, and the phenomena of precession and nutation) addresses the complex nature of Earth orientation changes, the mechanisms of excitation of these changes and their geophysical implications in a broad variety of areas. In the absence of internal sources of energy or interactions with astronomical objects, the Earth would move as a rigid body with its various parts (the crust, mantle, inner and outer cores, atmosphere and oceans) rotating together at a constant fixed rate. In reality, the world is considerably more complicated, as is schematically illustrated (Figure 1). The rotation rate of the Earth's crust is not constant, but exhibits complicated fluctuations in speed amounting to several parts in 10^8 [corresponding to a variation of several milliseconds (ms) in the length of the day (LOD) (Figure 2a) and about one part in 10^6 in the orientation of the rotation axis relative to the solid Earth's axis of figure (polar motion) (Figure 3). These changes occur over a broad spectrum of time scales, ranging from hours to centuries and longer, reflecting the fact that they are produced by a wide variety of geophysical and astronomical processes. Geodetic observations of Earth rotation changes thus provide insights into the geophysical processes illustrated (Figure 1), which are often difficult to obtain by other means. In addition, these measurements are required for engineering purposes; for example, the tracking and navigation of interplanetary spacecraft place strong constraints on measurement accuracies.

The principle of conservation of angular momentum requires that changes in the Earth's rotation must be manifestations of (a) torques acting on the solid Earth and (b) changes in the mass distribution within the solid Earth, which alters its inertia tensor. Angular momentum transfer occurs between the solid Earth and the fluid regions (the underlying liquid metallic core and the overlying hydrosphere and atmosphere) with which it is in contact; concomitant torques are due to hydrodynamic or magnetohydrodynamic stresses acting at the fluid/solid Earth interfaces. Changes in the inertia tensor of the solid Earth are caused not only by interfacial stresses and the gravitational attraction associated with astronomical objects and mass redistributions in the fluid regions of the Earth but also by processes that redistribute the material of the solid Earth, such as earthquakes, postglacial rebound, mantle convection, and movement of tectonic plates. Earth rotation provides a unique and truly global measure of natural and man-made changes in the atmosphere, oceans, and interior of the Earth.

Theoretical studies of Earth rotation variations are based on the application of Euler's dynamical equations to the problem of finding the response of a slightly deformable solid Earth to a variety of surface and internal stresses [51, 53]. Let $\mathbf{H}$ be the angular momentum of the Earth and $\mathbf{L}$ be the external torque exerted on the Earth. The fundamental equations of a rotating body, Euler's dynamical equations, require that

$$\dot{\mathbf{H}} = \mathbf{L} . \qquad (1)$$

In an arbitrary rotating terrestrial frame with a rotation vector $\boldsymbol{\omega}$, the appropriate form of Euler's dynamical

J. O. Dickey, JPL 238-332, 4800 Oak Grove Drive, Pasadena, CA 91109

Global Earth Physics
A Handbook of Physical Constants
AGU Reference Shelf 1

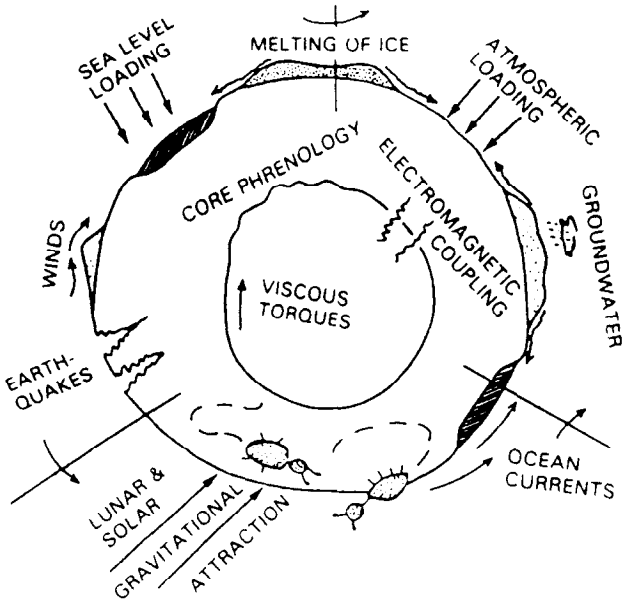

Fig. 1. Schematic illustration of the forces that perturb Earth rotation. Topographic coupling of the mantle to the core has been referred to as "Core Phrenology" by R. Hide, while the beetles, following T. Gold, represent the effect of continental drift. After [52].

equations is given by:

$$\dot{\mathbf{H}} + \boldsymbol{\omega} \times \mathbf{H} = \mathbf{L} \tag{2}$$

which is exact in any rotating reference frame. In both cases, the angular momentum is given by

$$\mathbf{H}(t) = \mathbf{I}(t)\boldsymbol{\omega}(t) + \int \mathbf{x}(t) \times \dot{\mathbf{x}}(t)dm, \tag{3}$$

where $\mathbf{I}(t)$ is the inertia tensor of the mass over which (1) or (2) will be applied. The formulation of equation (2) is usually used when the torques change slowly in an Earth-fixed frame; examples include atmospheric excitation and Chandler wobble problems. On the other hand, equation (1) is usually utilized when torques change slowly in inertial space; precession/nutation problems are prime applications. One must be able to transform from an Earth-fixed system (i.e., a Terrestrial Reference System, TRS, where equation (2) applies) to one attached to an inertial system (that is, the Celestial Reference System, CRS, where equation (1) applies). This transformation requires a minimum of three angles; however, the traditional formulation includes the conventional representations of nutations and polar motions and hence five angles are utilized, four of which change slowly with the remaining angle (representing the solid Earth's sidereal rotation) changing at an almost uniform rate. Table 1 provides estimates of the moments of inertia for the Earth's various sub-systems, giving the reader the relative important of each.

Space geodetic techniques, including laser ranging to the moon and artificial satellites (LLR and SLR) and very long baseline interferometry (VLBI) using radio telescopes, have brought about a new age in Earth rotation and related studies. The length of day and polar motion are now routinely measured at the ~0.5 milliarcsecond level (~1.5 cm) [44], while periodic corrections to the standard nutation model have been determined to the 0.1 milliarcsecond level for many terms [38].

This paper provides an overview of Earth rotation, defining terms, describing the measurements and their availability, the models and constants used in their reduction, and the application and analyses of these data. The second section provides definitions and describes the measurement techniques, while the third section highlights applications and advances in the analysis of Earth rotation. Section 4 discusses the constants and models used in the analysis and interpretation of Earth rotation data. The final section addresses the availability of data and outlines the activities of the International Earth Rotation Service (IERS).

The reader is referred to several more detailed accounts of the excitation of Earth orientation changes. References to early work can be found in [64] and recent work is reported in [6, 14, 40-44, 51, 53, 62, 77].

2. DEFINITIONS AND MEASUREMENTS

Earth rotation refers collectively to variations in the orientation of the solid Earth, encompassing Universal Time (UT1), length of day, polar motion, and the phenomena of precession and nutation. Universal time (UT1) is the rotation angle of the Earth: the direction of the Greenwich meridian in an equinox-based inertial frame. The UT1 measurements are usually given in units of time (1 msec is 46 cm at the equator). The actual observable is UT1-T, where T is some independent time series such as ET (ephemeris time) or IAT (international interatomic time). The LOD can be estimated from the time rate of change of UT1-T. The motion of the pole can be divided into two classes, nutational motion (which includes precession) and the polar motion (PM). Nutations are motions of the spin axis of the Earth with respect to an inertial reference frame, while polar motion or wobble is the motion of the solid Earth with respect to the spin axis of the Earth. The precession is the gravest nutation with a period of about 26,000 years, caused by the gravitational

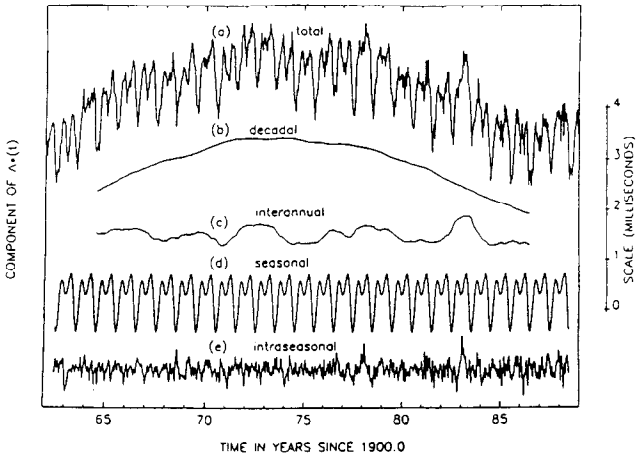

Fig. 2. Time series of irregular fluctuations in the length of the day from 1963 to 1988 (curve a) and its decadal, interannual, seasonal, and intraseasonal components (curves b, c, d and e, respectively). The decadal (curve b) component largely reflects angular momentum exchange between the solid Earth and the underlying liquid metallic outer core produced by torques acting at the core-mantle boundary. The other components (curves c, d and e) largely reflect angular momentum exchange between the atmosphere and the solid Earth, produced by torques acting directly on the solid Earth over continental regions of the Earth's surface and indirectly over oceanic regions. (b) Time series of the equivalent axial torques. Adapted from [44].

torque on the Earth's equatorial bulge from the Sun, Moon and planets.

Earth orientation measurements in current use can be classified as arising from two sources: classical techniques (optical astrometry and lunar occultation) and modern space geodetic techniques. Optical astrometry is based on measurements of the apparent angular positions of selected bright stars [24, 35]. Both the latitude and the longitude of the observatory can be determined from observations of the time and elevation of the star at meridian passage. A network of stations with a proper geometry can be used to determine all components of the Earth's rotation. Polar motion has been routinely observed since 1900; from 1900 through 1980, the International Latitude Service [81] produced measurements based on a network of five stations located at the same latitude. Nutation values have been determined through the analysis of optical data sets beginning in 1955 (see for example, 4); the classical determination of the precession constant is based on the analysis of stellar proper motions [27, 28]. Prior to the advent of modern atomic clocks (1955), records of the solar time of ancient solar and lunar eclipses and of occultation of stars by the Moon form the basis for historical time series of UT1 and LOD [74].

The classical techniques were superseded by the new space geodetic techniques in the 1970s and 1980s. The new techniques are all based on measurements of electromagnetic signal delay or its time derivative. Delay and delay rate measurements are both more precise and somewhat less sensitive to systematic error than angular measurements. These measurement types include Very Long Baseline Interferometry (VLBI), satellite and lunar laser ranging (SLR and LLR), and utilization of the Global Positioning System (GPS) technology. VLBI is based on positional observations of distant quasars using the techniques of radio astronomy; SLR and LLR use range measurements to corner reflectors on artificial satellites and the Moon, respectively. GPS utilizes a large constellation of satellites transmitting at microwave frequencies together with a globally distributed network of receivers to determine universal time and polar motion variations. In each technique, changes in Earth orientation are monitored by observations of extraterrestrial objects from the surface of the Earth. The observed objects or signals are used to approximate a reference frame, either directly, for example, in the case of slow-moving objects such as quasars, or from dynamical theories of their motion in the case of planetary and satellite observations. In each case, Earth orientation is estimated from the apparent motion of the Earth with respect to this frame as defined by each technique. The accuracy of each technique is thus limited by unmodeled reference frame rotations, intrinsic measurement error, and any unmodeled motions of the observatories. In addition, measurements are most often referenced to some standard frame (see later discussion on reference frames); hence, error is also introduced by the frame tie determinations.

Improvements in the observing systems (hardware, software and the development of well-distributed global networks) have lead to dramatic improvements in the determination of Earth orientation parameters. For example, estimates from a combined Kalman-filtered series utilizing the modern space techniques of LLR, SLR and VLBI have uncertainties in polar motion and universal time (UT1) at the ~2 mas (6 cm) and the 0.5 ms (~23 cm) level, respectively, for the late 1970s, whereas current uncertainties have improved to 0.3 mas for polar motion and 0.03 ms for UT1 [32]. There has also been an impressive increase in time resolution. The classical optical technique, utilizing a global network of more than 50 observatories, obtained UT1 at the millisecond level at 5-day intervals [24]; in contrast, the VLBI Extended Research and Development Experiment (ERDE) obtained sub-hourly measurements of both UT1 and polar motion [12, 37].

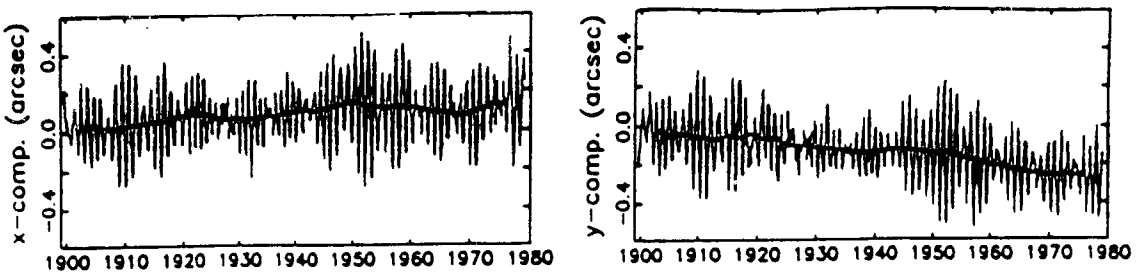

Fig. 3. Polar motion, 1900-1980, after [31].

3. APPLICATION AND ANALYSIS OF EARTH ROTATION

3.1. Universal Time (UT1) and Variations in the Length-of-Day

Observed variations in the Earth's rate of rotation—or changes in the length-of-day (LOD)—are attributed to a variety of sources (Figure 1) and can be roughly divided into three categories: an overall linear increase from tidal dissipation, irregular large variations on a time scale of decades, and the smaller higher frequency changes—interannual, seasonal and intraseasonal. The linear increase in the LOD, determined from ancient eclipse records [e.g., 74] is estimated to be about 1 to 2 msec per century. The LOD has large, irregular variations over time scales of 10 years to centuries (Figures 2a, curve B) with amplitudes of many milliseconds; these changes are too large to be of atmospheric origin and are thought to arise from fluid motions in the liquid outer core [40, 47, 51]. Variations with periods of five years or less are driven primarily by exchanges of angular momentum with the atmosphere (Figures 2a, curves C, D and E). Estimates of the equivalent torques associated with each component, formed by taking centered differences in the time domain, are shown (Figure 2b). Although the amplitude of the decadal LOD time series is larger than that of the faster components (Figure 2a), the corresponding equivalent axial torque time series has the smallest amplitude (Figure 2b—these are a consequence of the time derivatives in equations 1 and 2). At the other extreme, the most rapid intraseasonal contributions have the smallest amplitude, typically less than 0.2 ms, but are associated with the largest torques. The decadal fluctuations integrate coherently over many years resulting in large variations, in contrast, the intraseasonal atmospheric excitations are quite sizable but cancel out to a large extent. The apparent increase in the magnitude of the extraneous torques during the period studied reflects improvements in both quality and quantity of Earth rotation data as well as better sampling methods, leading to a decreasing uncertainty in the LOD estimates with time. The Kalman filter used to produce this LOD series automatically adjusts the effective smoothing to the formal errors in the data, leading to increasing high-frequency variability in the latter part of the series allowing more precise estimation of the magnitude of the shorter-period torques. These pronounced and rapid torque variations probably reflect changes in the orographic contribution to the total torque exerted by the atmosphere on the underlying planet, associated with the passage of synoptic weather systems over mountain ranges. Determinations incorporating space-geodetic data, in fact, show that the intraseasonal torque can change by as much as 50 Hadleys (1 Hadley = 10^{18}Nm) in 10 days. Synoptic variations in the atmosphere occur on these time scales, associated with surface pressure gradients which, if applied across a mountain range with the dimensions of the Rockies or Andes, would produce transient torques of this magnitude. The seasonal torque, which, by definition, fluctuates with constant amplitude over the 30-year span of data used, reflects annual and semi-annual variations of the position and strength of the major atmospheric jet streams.

The exchange of angular momentum between the atmosphere and solid Earth is evident in fluctuations in the length-of-day at periods of a year and less (Figure 4). Recent improvements in Earth rotation measurements have been accompanied by improvements in numerical models and measurements of Earth's global atmosphere which can be used to calculate the atmospheric angular momentum (AAM) [for a review, see 44]. Both U.S. and foreign meteorological services maintain global atmospheric models for weather forecasting; surface and upper-air wind data and other meteorological measurements are assimilated into these models on a regular basis. Certain atmospheric variables, including pressure and horizontal wind velocity, are estimated at each model grid point at twelve-hour intervals by combining measurements of these variables with their forecasted values in a statistically optimal fashion. Calculation of an effective atmospheric excitation function, χ, a three-dimensional pseudo-vector

including Love number corrections for rotational and surface loading deformation of the Earth, can be made directly from the meteorological data [1]. From intercomparisons between fluctuations in χ_3 (the axial component of χ) and length-of-day (LOD), it has been established that non-tidal rotation rate variations over time scales less than several years are largely due to atmospheric effects [44]. Also evident is a dominant seasonal cycle (Figure 2d) and additional variability on the intraseasonal (30 to 60 day—Figure 2e) and interannual time scales [Figure 2c; see also, 5, 16, 18, 22, 54, 61, 66]. The correlation between short-period variations in length-of-day and AAM is so well established that numerical forecasts of atmospheric angular momentum are now being used for the purpose of predicting Earth rotation variations [26]. There are also short-period fluctuations in the LOD due to solid Earth and ocean tides which arise because of tidal perturbations in the Earth's inertia tensor. The largest tidally induced LOD fluctuations occur for the fortnightly, monthly, semi-annual, and annual tides [80]. The amplitudes of these oscillations are sensitive to mantle anelasticity, which is not well constrained in this frequency range.

On interannual time scales (Figure 2c), length-of-day changes are related to atmospheric and climatic phenomena such as the Quasi-Biennial Oscillation and the El Niño/Southern Oscillation [7-9, 15, 17, 18, 21, 67]. However, at periods of more than several years (Figure 2b), the "decade" fluctuations are most likely caused by torques exerted by the core on the overlying mantle [40, 47]. In addition, the effects of long-period variability in the global ice and water budget may affect the rotation rate over periods of several decades or more [51, 53].

Because we have no direct access to the core, Earth rotation observations are of prime importance in the study of the structure and dynamics of the Earth's deep interior. In general, torques can be produced at the core-mantle boundary by viscous, electromagnetic, topographic and gravitational coupling. Two candidate mechanisms under investigation for these decade variations are (1) topographic torques due to dynamic pressure forces associated with core motions acting on undulations of the core-mantle boundary and, (2) torques of electromagnetic origin arising through Lorentz forces in the weakly-conducting lower mantle, which could be significant if the unknown electrical conductivity of the lower mantle, were sufficiently high. Estimates of topographic torques can be made from core motion deduced from geomagnetic secular variation, in combination with core-mantle boundary topography deduced either directly from seismic tomography or from dynamic models of the lower mantle based on tomographic and long-wavelength gravity anomaly data [43, 45]. Geodetic torque estimates inferred from the LOD provide a means of checking results from seismology and geomagnetism and imposing constraints on the models used.

3.2. Polar Motion

Polar motion is dominated by nearly circular oscillations at periods of one year (the annual wobble) and about 434

TABLE 1. Moments of Inertia of the Earth's Subsystems

A (mantle)	7.0999×10^{37} kg m^2;
A (fluid core)	0.90583×10^{37} kg m^2;
A (solid inner core)	0.0058531×10^{37} kg m^2;
A (atmosphere)	0.0000138×10^{37} kg m^2 [71];
(C-A) mantle	0.02377×10^{37} kg m^2;
(C-A) fluid core	0.002328×10^{37} kg m^2 [57 for the PREM model].

*A, B and C are the principle moments of inertia. In many applications the two smallest moments of inertia are assumed equal and the minimum of inertia is taken to be the average of A and B. In the separation of Equation 2, the changes in the orientation of the rotation axis depends on (C-A) and therefore the orientation changes (polar motion and nutations) are generally two orders of magnitude larger than the rotation rate changes. The effects of each of subsystems in the Earth (i.e., fluid core, oceans and atmosphere) depends not only on its moment of inertia (relative to the mantle) but also the velocity changes of the subsystem. Therefore, although the atmosphere has a very small moment of inertia, its rapid velocity variations produce large rotation variations.

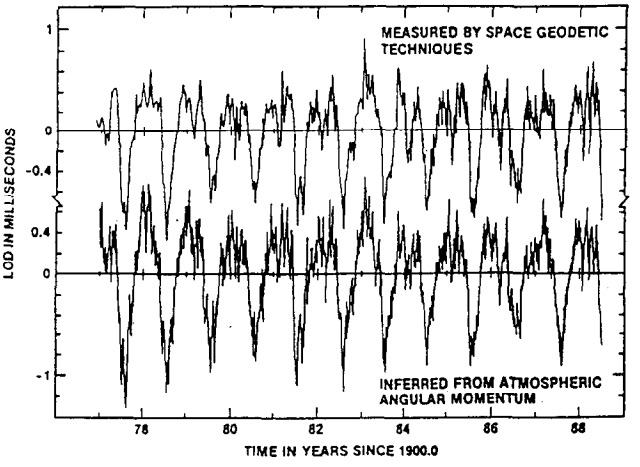

Fig. 4. Time series of the sum of the seasonal and intraseasonal LOD components, with the upper curve measured by space geodetic techniques (see Fig. 2d and e) and the lower curve inferred from routine daily determinations of changes in the axial component of the atmospheric angular momentum made by the U. S. National Meteorological Center.

days (the Chandler wobble), with amplitudes of about 100 and 200 milliarcseconds (mas), respectively, together with a long-term drift of a few milliarcseconds per year (1 and Figure 3]. In addition, astrometric data sets exhibit decade time-scale polar motion of amplitude less than 50 mas, while analysis of geodetic data reveals rapid polar motion with peak-to-peak variations of approximately 2 to 20 mas, fluctuating on time scales between two weeks and several months. Comparisons with meteorological data (Figure 5) suggest that these latter motions are at least partially driven by surface air pressure changes, as modified by the response of sea level to atmospheric loading and by wind variations [23, 34].

The atmosphere and oceans, together with the effect of variable ground water storage, are clearly responsible for exciting a large portion of the annual wobble [10, 50, 60, 76]. However, the entire annual wobble excitation is not fully accounted for. The Chandler wobble is a free oscillation of the Earth [70, 79] whose source of excitation is uncertain. Since polar motion is assumed to be a linear response to geophysical excitation, the problem is to find an excitation source with enough power near the Chandler period of about 434 days. The major candidates are the atmosphere and the redistribution of ground water. Other proposed sources, such as earthquakes, are probably too small in magnitude although great earthquakes may contribute [30]. A complication in determining the amount of excitation needed is that we do not know what the dissipation of the mode (or Q) is. The current estimates of Q assume a white noise excitation which may not be valid. If the Q is increased sufficiently, the current excitation mechanisms may be enough to explain its amplitude. Continual and improved monitoring of polar motion combined with improved models of atmospheric wind and pressure and ground water variations may resolve the degree to which the atmosphere drives polar motion.

The changing distribution of water in the ground and oceans is likely to be important at periods of a year and longer. On time scales of hundreds to thousands of years, water storage variations in the polar ice caps and the associated loading deformation of the solid Earth is a dominant influence on polar motion. Although one must account for other secular variations in these calculations, much of the observed secular drift of the pole in this century can be explained by redistributions of water and ice together with the post-glacial rebound following the last deglaciation around 20,000 years ago [51]. Contributions from plate motions, seismic deformation and present day melting of glaciers are also present; the study of these long-period polar motions is hampered by systematic errors in the optical astrometric data which must be relied on prior to 1976.

3.3. Nutations and Precession

Torques on the oblate Earth from the Sun, Moon and other bodies in the solar system cause a change in the direction of the Earth's rotation and figure axes, resulting in the precession of the Earth's equator along the ecliptic with superimposed oscillations. These motions are defined as the nutations. The response of the Earth to these externally applied torques is largely that of a rigid body. However, there are observable effects that arise because the Earth is deformable, with a solid-inner core, fluid-outer core, anelastic mantle, fluid oceans, and an atmosphere. It is these effects of the Earth's deformability that make nutations geophysically interesting [for a review, see 56].

From an inertial coordinate system, the Earth's nutations have periods much longer than a day. The largest such motion is the long-period precession, a nutation of the spin axis with a period of about 26,000 years. The precession is caused by the gravitational torque on the Earth's equatorial bulge from the Sun, Moon and the planets and thus has an angular amplitude of 23.5°, the angle between the equator and the plane of the Earth's orbit (the ecliptic). The inclination of the Moon's orbit with respect to the Earth's equator induces a lunar nutation on the Earth. The Sun perturbs the lunar orbit and causes it to precess (rotate in the plane of the ecliptic) with a period of 18.6 years, with

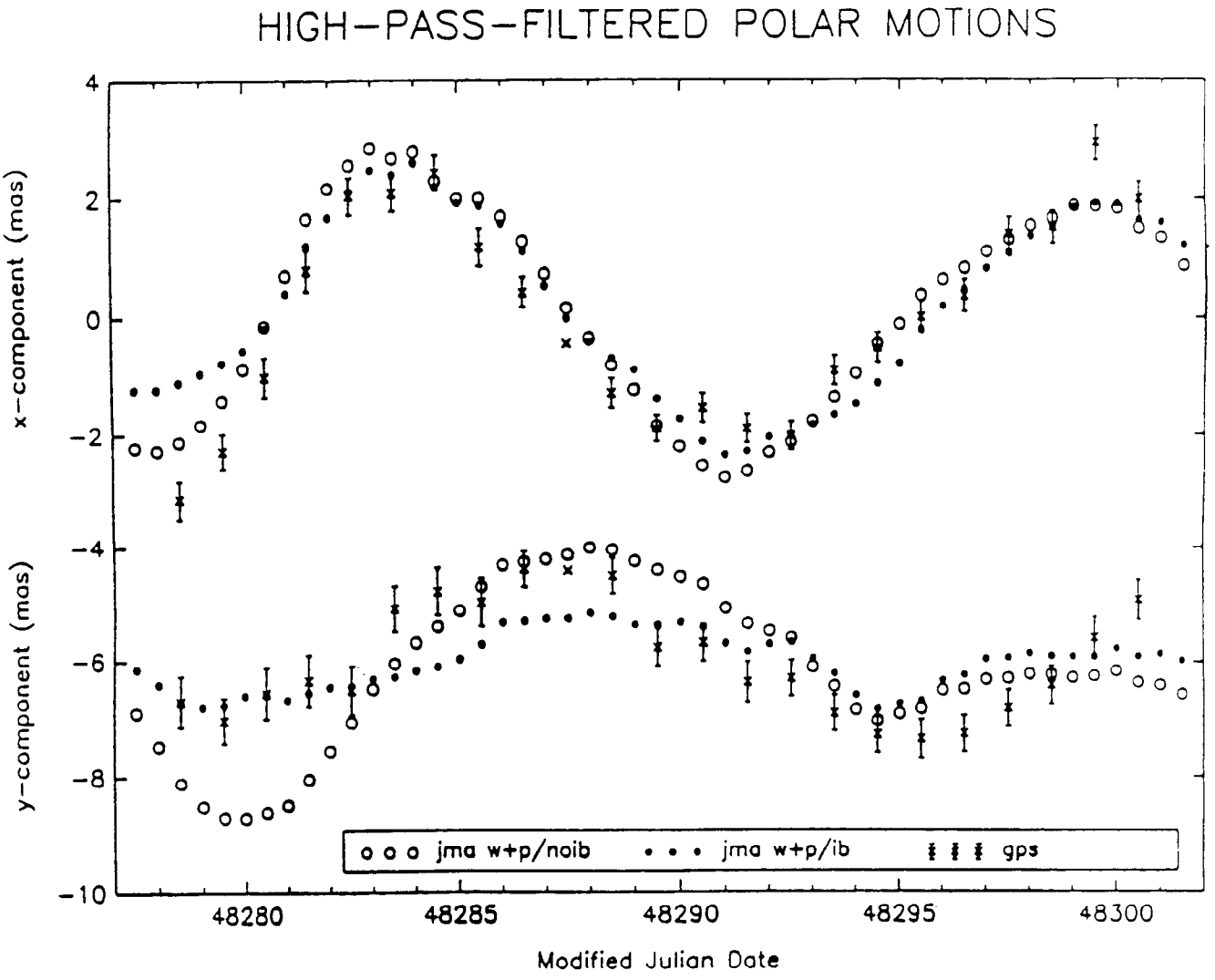

Fig. 5. The x-component (top) and y-component (bottom) of the observed and Japanese Meteorological Agency (JMA) AAM-induced polar motion series (both series have been high-pass-filtered using a cutoff period of 23 days). The crosses with error bars represent the observed series (one data point is plotted without error bars indicating that it is an interpolated point). The open circles represent the polar motion series induced by the JMA AAM χ-functions formed by summing the wind term with the pressure term computed under the rigid ocean approximation. The filled circles represent the polar motion series induced by the JMA AAM χ-functions formed by summing the wind term with the pressure term computed under the inverted barometer approximation, after [34].

the induced nutation having the same period and an amplitude of about 9 s of arc. There are also nutations with periods of one solar year, one lunar month and at the harmonics of the dominant frequencies with smaller nutations occurring at periods of half a solar year and a half-month and the harmonics of these. The half period is caused by the torque being symmetric about the equatorial plane. Nutation series are calculated assuming that the individual periodic components can be linearly summed and that the motion of the body axis with respect to inertial space can be obtained from the addition of the periodic nutations, precession, and the motions due to polar motion. The currently recommended nutation model, the IAU 1980 Theory of Nutation [69] is based on the work of Kinoshita

[48] for the rigid Earth series and of Wahr [75] for the perturbing effects of elasticity on a rigid Earth model. Analyses of the data from the space techniques have indicated that sizable corrections are required to the standard nutations models, which are a consequence of the incompleteness of the geophysical models (see Figure 6). The largest of these (~ 2 mas) is the correction to the retrograde annual nutation, caused by the closeness to the free core nutation (FCN) response frequency [37], which has been interpreted as being due to the flattening of the core-mantle boundary which deviates from its hydrostatic equilibrium by about 5% [36]. A similar discrepancy between theory and observations has also been observed in tidal gravity data [65], with results which are consistent with this increased flattening of 5%. Although the real parts of the FCN frequency agree well in both analyses, the tidal results have a significantly larger imaginary part (that is, smaller Q than the geodetic results), the reason for which is under current investigation.

3.4. Reference Frames

In general, each space geodetic system defines a reference frame based on technique-dependent considerations. Furthermore, each technique makes some unique contribution to reference frame considerations. For example, the VLBI technique provides a direct link to the already adopted inertial reference frame, but it has no sensitivity to the Earth's center of mass. Conversely, SLR and GPS are sensitive to the center of mass but are nearly independent of the adopted reference frame. Thus, SLR and GPS, for example, are not inertial sources of UT1 and must be tied periodically to an inertial system. LLR is sensitive to the center of mass, defines its own reference frame, the lunar ephemeris, which is a component of the planetary ephemeris, and is of great importance in spacecraft navigation and in the unification of reference systems. The interested reader is referred to the text [49] which is entirely devoted to reference frames.

Commonly used frames are the IERS (International Earth Rotation Service) Celestial and Terrestrial Reference Frames (ICRF and ITRF, respectively). The ICRF is derived from the VLBI measured positions of ~400 quasars as reported by various analysis centers, while the ITRF is based on ~120 IERS observing sites [25].

4. CONSTANTS AND MODELS UTILIZED IN EARTH ROTATION REDUCTION AND ANALYSIS

A variety of models and constants are used in the reduction and analysis of Earth rotation. The International

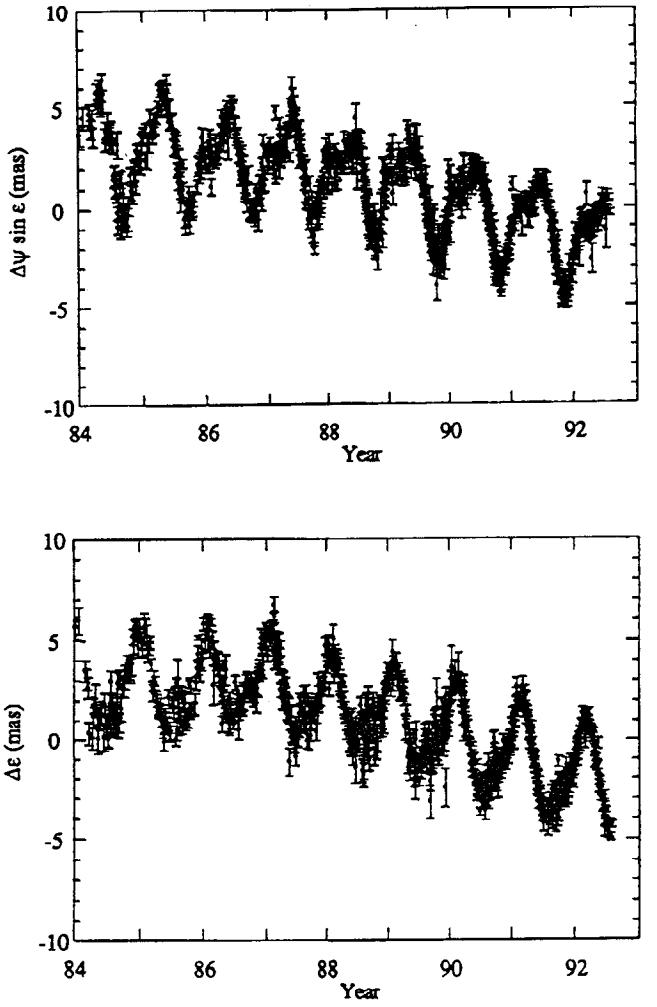

Fig. 6. Estimates of corrections, (a) $\delta\Delta\psi \sin \varepsilon_o$ and (b) $\delta\Delta\varepsilon$ to the IAU 1980 values for the nutation in longitude, $\Delta\psi \sin \varepsilon_o$ and the nutation in obliquity, $\Delta\varepsilon$ (T. Herring, Priv. Comm., 1993).

Earth Rotation Services (IERS—see Section 5) has published the *IERS Standards* as an IERS Technical Note [58, 59], which provides guidance to the international community on the use of constants and models. Numerical standards [adapted from 61] are given in Table 2; a short description and relevant references for the main model being utilized are listed below:

4.1. Nutation Model

The currently recommended nutation model, IAU 1980 Theory of Nutation [69], is based on the work of Kinoshita [48] for the rigid Earth series and of Wahr [75] for the

TABLE 2. Numerical Standards [adapted from 59]

Astronomical Constants	Recommended Value
Defining Constants	
• Gaussian Gravitational Constant	$k = 0.01720209895$
• Velocity of Light	$c = 2.99792458 \times 10^{8} ms^{-1}$
Primary Constants	
• Astronomical Unit in Light-Seconds	$\tau_A = 499.00478353$ s
• Equatorial Radius of the Earth	$a_e = 6378136.3$m
• Dynamical Form Factor for Earth	$J_2 = 0.0010826362$
• Geocentric Constant of Gravitation	$GM\oplus = 3.986004415 \times 10^{14} m^3 s^{-2}$
• Constant of Gravitation	$G = 6.67259 \times 10^{-11} m^3 kg^{-1} s^{-2}$
• Earth-Moon Mass Ratio	$\mu = 0.012300034$
• General Precession* in Longitude Per Century for J2000.0	$p = 5029.''0966$
• Obliquity of the Ecliptic for J2000.0	$\varepsilon_0 = 23°26'21.''4119$
• Mean Angular Velocity of the Earth	$\omega = 7.292115 \times 10^{-5}$ rad s^{-1}
Derived Constants	
• Astronomical Unit	$c\tau_A = 1.4959787061 \times 10^{11}$m
• Solar Parallax	$\pi = \sin^{-1}(a_e / A) = 8.''794142$
• Earth Flattening	$f^{-1} = 298.257$
• Heliocentric Constant for Gravitation	$GM_\odot = 1.32712440 \times 10^{20} m^3 s^{-2}$
• Ratio of the Solar Mass to the Mass of the Earth	$GM_\odot / GM\oplus = 332{,}946.045$
• Ratio of the Solar Mass to the Mass of the Earth-Moon System	$GM_\odot / GM\oplus\ (1 + \mu) = 328{,}900.56$
• Solar Mass	$M_\odot = 1.9889 \times 10^{30}$kg

*General precession includes planetary and geodetic precession.

perturbing effects of elasticity on a rigid Earth model. VLBI and LLR observations have shown that there are deficiencies in both the currently accepted IAU 1976 Precession and the IAU 1980 Theory of Nutation [11, 38, 39]. For users requiring accuracies of 2 mas (the error in the annual term, the dominant correction term) at best, the current model may be employed. It should be noted that the resulting error due to the adaptation of this series will grow as the time span increases, reaching, for example, 10 mas in a decade. However, for those with more stringent requirements, the series regularly reported by the IERS (see Section 5) is recommended. Another alternative is to utilize empirically derived correction series [see for example 38, 82].

4.2. Tidal Variations in Earth Rotation

Tidal variations in Earth rotation are caused by the periodic changes in the inertia tensor produced by the gravitational attraction of the Moon, Sun and other astronomical bodies. These variations (with amplitude up to 0.5 ms in UT1) must be substracted from the series before further geophysical analysis is performed. The Yoder *et al.* model [80] is in current use to calculate the periodic variations in UT1 due to modification of the polar moment of inertia by tidal deformation of the Earth with a decoupled core. Oceanic tides also cause variations in UT1 and are an active area of research [2, 3, 19, 33]. They make a significant contribution at the fortnightly period and dominate sub-daily variations.

4.3. Geopotential Model

An accurate geopotential model is required, particularly in the analysis of satellite laser ranging data; the recommended model is the GEM-T3 Model [55].

4.4. Solid Earth Tide Model

A solid Earth tide model is required in the reduction of all geodetic data types. Observatories and sites are displaced by the solid Earth tides, and if not properly accounted for, the resulting systematic error would corrupt Earth rotation measurements. The current generally used model [59, Ch. 7] is an abbreviated form of the Wahr model [75] using the Earth model 1066A of Gilbert and Dziewonski [29].

4.5. Ocean Tide Model

An ocean tidal model is required, particularly in analysis of satellite laser ranging data [20]. The currently recommended model is that of Schwiderski [68].

4.6. Plate Motion Model

Observatories are located on plates and thus Earth rotation series are corrupted if plate motion is improperly modeled. The NUVEL NNR-1 Model [13] is now commonly used.

4.7. Lunar and Planetary Ephemeris

The planetary and lunar ephemerides recommended by the IERS Standards are the JPL Development Ephemeris DE200 and the Lunar Ephemeris LE200 [72, 73].

5. The International Earth Rotation Service and Data Availability

An important development has been the introduction in 1988 of the International Earth Rotation Service (IERS) centered in Paris, to consolidate the earlier activities of the BIH (Bureau Internationale de l'Heure, based in Paris) for determining UT1 and of the International Polar Motion Service (IPMS), based in Japan, for determining polar motion. The IERS is charged with defining and maintaining both conventional terrestrial and celestial reference systems, determining the Earth orientation parameters connecting these systems (the terrestrial and celestial coordinates of the pole and the universal time), organizing operational activities for observation and data analyses, collecting and archiving data and results, and the dissemination of the results [63].

The IERS results are based primarily on the space geodetic techniques of laser ranging to the moon and artificial satellites, and Very Long Baseline Interferometry [63] with the recent addition of GPS as a fourth technique [46]. It is composed of a Coordinating Center and other technical centers for each of the four observing techniques, and a Central Bureau with associated Sub-Bureaus. The Central Bureau combines the various types of data and disseminates to the international community the relevant information on Earth rotation and the terrestrial and celestial reference systems. Two sub-bureaus are associated with the Central Bureau: a Sub-Bureau for Rapid Service and Predictions and a Sub-Bureau for Atmospheric Angular Momentum.

Earth rotation results of the IPMS are archived at the National Astronomical Observatory, Misuzawa, Japan; a copy is also archived at the IERS Central Bureau. The BIH results are archived at the Paris Observatory. The results on Earth rotation and reference frames from the modern techniques (VLBI, LLR, SLR and GPS) are archived at the Central Bureau. In addition, complementary geophysical data sets such as atmospheric angular momentum are also stored there.

Information and data are distributed through a variety of mechanisms, both electronic and hard copy [46]. Typical information disseminated on a regular basis includes polar motion, UT1, and celestial pole offsets (i.e., the combined effect of precession and notation); both combined and individual-technique series are distributed. The weekly *Bulletin A* includes a rapid service and prediction; whereas the monthly *Bulletin B* presents the results of a more comprehensive analysis, taking into consideration more data sets. The Annual Report of the IERS includes further-refined, state-of-the-art solutions with information on Terrestrial and Celestial Reference systems. The nominal precision of the published results depends on the delay of their availability. For the operational solutions of Earth rotation (weekly and monthly bulletins), it is a few mas. The prediction accuracy is in the range of 3 to 20 mas for polar motion and 2 to 15 ms for UT for lead times of 10 to 90 days. For the IERS combined solution of Earth rotation, the nominal uncertainties of polar motion and UT1 are normally better than 0.3 mas (1 cm); those of the celestial pole offsets ($d\Psi \sin \varepsilon$ and $d\varepsilon$) are about 0.3 mas. The individual coefficients from the nutation series are determined (see previous section) with accuracies of about 0.04 mas, and should yield more accurate celestial pole offsets than the daily estimates. The IERS, in addition, publishes Technical Notes, which provide information of relevance to the IERS work on Earth rotation and the reference system. The IERS Standards, published as an IERS Technical Note, provide guidance to the international community on the use of constants and models (see Section 4).

Requests for IERS publications and further information may be addressed to: Central Bureau of IERS, Observatoire de Paris, 61 avenue de l'Observatoire, 75014 Paris, France. Telephone: 33 (1) 4051-24226; Telex: OBS270776P; Fax: 33 (1) 4051-2232; GE Mark III: IERS-CB; EARN/BITNET/SPAN: IERS@FRIAP51.

Acknowledgments. The author gratefully acknowledges R. S. Gross, S. L. Marcus, and an anonymous reviewer for helpful comments on this manuscript, and T. A. Herring for Figure 6. The work of the author presents the results of one phase of research carried out at the Jet Propulsion Laboratory, California Institute of Technology, sponsored by the National Aeronautics and Space Administration.

REFERENCES

1. Barnes, R. T. H., R. Hide, A. A. White, and C. A. Wilson, Atmospheric Angular Momentum Fluctuations, Length of Day Changes and Polar Motion, *Proc. R. Soc. Lon.*, **387**, 31-73, 1983.
2. Brosche, P. U. Seiler, J. Sündermann and J. Wünsch, Periodic Changes in Earth's Rotation due to Oceanic Tides, *Astron. Astrophys.*, **220**, 318-320, 1989.
3. Brosche, P., J. Wünsch, J. Campbell and H. Schuh, Ocean Tide Effects in Universal Time detected by VLBI, *Astron., Astrophys.*, **245**, 676-682, 1991.
4. Capitaine, N., "Corrections to Some Terms of Nutation Deduced from the Paris Astrolabe Observations," in Nutation and the Earth's Rotation, eds. E. P. Federov, M. L. Smith and P. L. Bender, 87-94, 1980.
5. Carter, W. E. D. S. Robertson, J. E. Pettey, B. D. Tapley, B. E. Schutz, R. J. Eanes, and M. Lufeng, Variations in the Rotation of the Earth, *Science*, **224**, 957-961, 1984.
6. Cazenave, A. (ed.), *Earth Rotation: Solved and Unsolved Problems, NATO Advanced Institute Series C: Mathematical and Physical Sciences Vol. 187*, ed. A. Cazenave, D. Reidel, Boston, 1986.
7. Chao, B. F., Interannual Length of Day Variations with Relation to the Southern Oscillation/El Niño, *Geophys. Res. Letts.*, **11**, 541-544, 1984.
8. Chao, B. F., Correlation of Interannual Lengths-of-Day Variation with El Niño/Southern Oscillation, 1972-1986, *J. Geophys. Res.*, **93**, B7, 7709-7715, 1988.
9. Chao, B. F., Length-of-Day Variations Caused by El Niño/Southern Oscillation and the Quasi-Biennial Oscillation, *Science*, **243**, 923-925, 1989.
10. Chao, B. F., and A. Y. Au, Atmospheric Excitation of the Earth's Annual Wobble, 1980-1988, *J. Geophys. Res.*, **96**, 6577-6582, 1991.
11. Charlot, P., O. J. Sovers, J. G. Williams and X X Newhall, A Global VLBI/LLR Analysis for the Determination of Precession and Nutation Constants, *Proceedings of the International Astronomical Union 1227th Colloquium, Reference Systems*, J. A. Hughes, C. A. Smith and G. H. Kaplan, Eds., U. S. Naval Observatory, Washington D. C., 228-233, 1991.
12. Clark, T. A., J. W. Ryan, and K. D. Baver, ERDE: High Resolution Observations of Earth Orientation Parameters by Very Long Baseline Interferometry, *EOS, Trans. Amer. Geophys. Union*, **71**, 1271, 1990.
13. DeMets, C., R. G. Gordon, D. F. Argus and S. Stein, Current Plate Motions, *Geophys. J. Int.*, **101**, 425-478, 1990.
14. Dickey, J. O., and T. M. Eubanks, The Application of Space Geodesy to Earth Orientation Studies, *Space Geodesy and Geodynamics* (eds.) by A. J. Anderson and A. Cazenave, Academic Press, New York, 221-269, 1986.
15. Dickey, J. O., T. M. Eubanks, and R. Hide, Interannual and Decade Fluctuations in the Earth's Rotation, *Variations in the Earth's Rotation, Geophysical Monograph Series of the American Geophysical Union*, Washington, D. C., D. McCarthy (ed.), 157-162, 1990.
16. Dickey, J. O., M. Ghil, and S. L. Marcus, Extratropical Aspects of the 40-50 Day Oscillation in Length-of-Day and Atmospheric Angular Momentum, *J. Geophys. Res.*, **96**, 22, 643-22, 658, 1991.
17. Dickey, J. O., S. L. Marcus and R. Hide, Global Propagation of Interannual Fluctuations in Atmospheric Angular Momentum, *Nature*, 357, 484-408, 1992b.
18. Dickey, J. O., S. L. Marcus, R. Hide, and T. M. Eubanks, Climate Studies via Space Geodesy: Relationships Between ENSO and Interannual Length-of-Day Variations, *American Geophysical Union Monograph, IUGG Symposium Volume, Hans Symposium: Fluxes of Matter Between Global Climate Subsystems*, in press, 1993.
19. Dickman, S. R., Ocean Tides for Satellite Geodesy, *Mar. Geod.*, **14**, 21-56, 1991.
20. Eanes, R. J., B. Schutz and B. Tapley, Earth and Ocean Tide Effects on Lageos and Starlette, *Proceedings of the Ninth International Symposium on Earth Tides*, E. Sckweizerbart'sche Verlagabuchhandlung, Stuttgart, 1983.
21. Eubanks, T. M., J. A. Steppe, and J. O. Dickey, The El Niño, the Southern Oscillation and the Earth's Rotation, in *Earth Rotation; Solved and Unsolved Problems, NATO Advanced Institute Series C: Mathematical and Physical Sciences*, **187**, ed. A. Cazenave, 163-186, D. Reidel, Hingham, Mass., 1986.
22. Eubanks, T. M., J. A. Steppe, J. O. Dickey, and P. S. Callahan, A Spectral Analysis of the Earth's Angular Momentum Budget, *J.*

Geophys. Res., **90**, B7, 5385-5404, 1985.

23. Eubanks, T. M., J. A. Steppe, J. O. Dickey, R. D. Rosen and D. A. Salstein, 1988: Causes of rapid motions of the Earth's pole. *Nature*, **334**, 115-119, 1988.
24. Feissel, M., Determination of the Earth Rotation Parameters by the BIH 1962-1979, *Bull. Geod.*, **54**, 81-102, 1980.
25. Feissel, M., D. Bourquard, P. Charlot, E. Eisop, N. Essaifi, D. Gambis, J.-F. Lestrade, E. F. Arias, C. Boucher, Z. Altamimi, Earth Orientation and Related Reference Frames, *Space Geodesy and Geodynamics*, Geophysical Monograph Series of the American Geophysical Union, Washington, D. C., D. L. Turcotte (ed.), in press, 1993.
26. Freedman, A. P., and J. O. Dickey, Intercomparison of AAM analysis and forecast data in UT1 estimation and prediction. *Proceedings of the AGU Chapman Conference on Geodetic VLBI: Monitoring Global Change*, U. S. Department of Commerce/ NOAA/NOS, NOAA Technical Report NOS 137 NGS 49, Washington, D. C. 279-293, 1991.
27. Fricke, W., Arguments in Favor of a Change in Precession, *Astron. Astrophys.*, **54**, 363-366, 1977.
28. Fricke, W., Definition and Practical Realization of the Reference Frame in the FK5—the Role of Planetary Dynamics and Stellar Kinematics in the Definition, in *Reference Coordinate Systems for Earth Dynamics*, F, M. Gaposchkin and B. Kolaczek (eds.), D. Reidel, 331-340, 1981.
29. Gilbert, F. and A. M. Dziewonski, An Application of Normal Mode Theory to the Retrieval of Structural Parameters and Space Mechanisms from Seismic Spectra, *Phil. Trans. R. Soc. of Lond.*, **A278**, 187-269, 1975.
30. Gross, R. S., The Influence of Earthquakes on the Chandler Wobble during 1973-1983, *Geophys. J. R. Astr. Soc.*, **85**, 161-177, 1986.
31. Gross, R. S., The Secular Drift of the Rotation Pole, *Earth Rotation and Coordinate Reference Frames*, C. Boucher and G. A. Wilkins (eds.), Springer-Verlag, New York, 146-153, 1990.
32. Gross, R. S., A Combination of Earth Orientation Data: SPACE91, in *IERS Technical Note 11: Earth Orientation, Reference Frame and Atmospheric Excitation Functions*, P. Charlot (ed), Observatoire de Paris, Paris, France, 113-118, 1992.
33. Gross, R. S., The Effect of Ocean Tides on the Earth's Rotation as Predicted by the Results of an Ocean Tide Model, *Geophys. Res. Lett.*, in press, 1993.
34. Gross, R. S., and U. J. Lindqwister, Atmospheric Excitation of Polar Motion during the GIG'91 Measurement Campaign, *Geophys. Res. Lett.*, **19**, 849-852, 1992.
35. Guinot, B., Rotation of the Earth and Polar Motion Services In *Proc. GEOP Conf. Int. Symp. Appl. Geod. Geodyn. 9th*, pp. 13-18, Dept. of Geodetic Science, Rep. No. 280, Ohio State Univ., 1978.
36. Gwinn, C. R., T. A. Herring, and I. I. Shapiro, Geodesy by Radio Interferometry: Studies of the Forced Nutations of the Earth 2 Interpretation, *J. Geophys. Res.*, **91**, 4755-4765, 1986.
37. Herring, T. A., and D. Dong, Current and Future Accuracy of Earth Orientation Measurements, *Proceedings of the AGU Chapman Conference on Geodetic VLBI: Monitoring Global Change* (NOAA Technical Report **NOS 137 NGS 49**), 306-324, 1991.
38. Herring, T. A., B. A. Buffett, P. M. Mathews, and I. I. Shapiro, Forced Motions of the Earth: Influence of Inner Core Dynamics: 3. Very Long Baseline Interferometry Data Analysis, *J. Geophys. Res.*, **96**, 8259-8273, 1991.
39. Herring, T. A., C. R. Gwinn, and I. I. Shapiro, Geodesy by Radio Interferometry: Studies of the Forced Nutations of the Earth 1. Data Analysis, *J. Geophys. Res.*, **91**, 4745-4754, 1986.
40. Hide, R., Towards a Theory of Irregular Variations in the Length of the Day and Core-Mantle Coupling, *Phil. Trans. Roy. Soc.*, **A284**, 547-554, 1977.
41. Hide, R., Rotation of the Atmospheres of the Earth and Planets, *Phil. Trans. R. Soc. Lond.* **A313**, 107-121, 1984.
42. Hide, R., Presidential Address: The Earth's Differential Rotation, *Quart. J. Roy. Astron. Soc.*, **278**, 3-14, 1986.
43. Hide, R. Fluctuations in the Earth's Rotation and the Topography of the Core-Mantle Interface, *Phil. Trans. Roy. Soc.*, **A328**, 351-363, 1989.
44. Hide, R., and J. O. Dickey, Earth's Variable Rotation, *Science*, **253**, 629, 1991.
45. Hide, R., R. W. Clayton, B. H. Hager, M. A. Spieth, and C. V. Voorhies, Topographic Core-Mantle Coupling and Fluctuations in the Earth's Rotation, *Geophysical Monograph Series of the American Geophysical Union*, Washington D. C., K.-I. Aki (ed), in press, 1993.
46. International Earth Rotation Service (IERS), 1992, Activities of the IERS, Geodesist's Handbook, *Bulletin Géodésique*, **66**, 2, 1992.
47. Jault, D., and J-L. Le Mouël, "Exchange of Angular Momentum Between the Core and Mantle, *J. Geomag. Geoelect.*, **43**, 111-129, 1991.
48. Kinoshita, H., Theory of the Rotation of the Rigid Earth, *Celest. Mech.*, **15**, 277-326, 1977.
49. Kovalesky, J., I. I. Mueller and B. Kolaczek, eds., *Reference Frames in Astronomy and Geophysics*, Kluwer Academic Publishers, Boston, 1989.
50. Kuehne, J. W., and C. R. Wilson, Terrestrial Water Storage and Polar

Motion, *J. Geophys. Res.*, **96**, B3, 4337-4345, 1991.

51. Lambeck, K., *The Earth's Variable Rotation,* Cambridge Univ. Press, London and New York, 1980.
52. Lambeck, K., Changes in Length of Day and Atmospheric Circulation, *Nature*, **26**, 104, 1980.
53. Lambeck, K., *Geophysical Geodesy, The Slow Deformation of the Earth,* Clarendon Press, Oxford, 1988.
54. Langley, R. B., R. W. King, I. I. Shapiro, R. D. Rosen, and D. A. Salstein, Atmospheric Angular Momentum and the Length of the Day: A Common Fluctuation with a Period Near 50 Days, *Nature*, **294**, 730-733, 1981.
55. Lerch, F., R. Nerem, B. Putney, T. Felstentreger, B. Sanchez, S. Klosko, G. Patel, R. Williamson, D. Chinn, J. Chan, K. Rachlin, N. Chandler, J. McCarthy, J. Marshall, S. Luthcke, D. Pavlis, J. Robbins, S. Kappor, E. Pavlis, *NASA Technical Memorandum 104555*, NASA Goddard Space Flight Center, Greenbelt, MD.
56. Mathews, P. M., and I. I. Shapiro, Nutations of the Earth, *Annu. Rev. Earth Planet. Sci.*, **20**, 469-500, 1992.
57. Mathews, P. M., B. A. Buffet, T. A. Herring, and I. I. Shapiro, Forced Nutations of the Earth: Influence of Inner Core Dynamics 2. Numerical Results and Comparisons, *J. Geophys. Res.*, 96, 8243-57, 1991.
58. McCarthy, D. D., ed., International Earth Rotation Series Standards (1989), *IERS Technical Note B,* Observatoire de Paris, 1989.
59. McCarthy, D. D., ed., International Earth Rotation Series Standards (1992), *IERS Technical Note 13,* 1992.
60. Merriam, J. B., Meteorological Excitation of the Annual Polar Motion, *Geophys. J. R. Astron. Soc.*, **70**, 41-56, 1982.
61. Morgan, P. J., R. W. King, and I. I. Shapiro, Length of Day and Atmospheric Angular Momentum: A Comparison for 1981-1983, *J. Geophys. Res.*, **90**, 12645-12652, 1985.
62. Moritz, H., and I. I. Mueller, *Earth Rotation: Theory and Observation,* The Ungar Publishing Co., New York, 1987.
63. Mueller, I. I., and G. A. Wilkins, Rotation of the Earth and the Terrestrial Reference Systems, *EOS*, **67**, 31, 601-605, 1986 and *Bulletin Geodesique*, **60**, 85-100, 1986.
64. Munk, W. H., and G. J. F. MacDonald, *The Rotation of the Earth*, Cambridge University Press, 1960.
65. Neuberg, J., J. Hinderer, and W. Zurn, Stacking Gravity-Tied Observations in Central Europe for the Retrieval of the Complex Eigenfrequency of the Nearly Diurnal Free-Wobble, *Geophys. J. R. Ast. Soc.*, **91**, 853-868, 1987.
66. Rosen, R. D., and D. A. Salstein, Variations in Atmospheric Angular Momentum on Global and Regional Scales and the Length of Day, *J. Geophys. Res.*, **88**, C9, 5451-5470, 1983.
67. Salstein, D. A., and R. D. Rosen, Earth Rotation as a Proxy for Interannual Variability in Atmospheric Circulation, 1860-Present, *J. Clim. and Appl. Meteorol.*, **25**, 1870-1877, 1986.
68. Schwiderski, E., Atlas of Ocean Tidal Charts and Maps, Part I: The Semidiurnal Principal Lunar Tide M2, *Mar. Geod.*, **6**, 219-256, 1983.
69. Seidelmann, P. K., 1980 IAU Nutation: The Final Report of the IAU Working Group on Nutation, *Celest. Mech.*, **27**, 79-106, 1982.
70. Smith, M. L., and F. A. Dahlen, The Period and Q of the Chandler Wobble, *Geophys. J. R. Astron. Soc.*, **64**, 223-281, 1981.
71. Stacy, F. D., Physics of the Earth, John Wiley & Sons, New York, 1977.
72. Standish, E. M., The JPL Planetary Ephemerides, *Cel. Mech. J.*, **26**, 181-186, 1982.
73. Standish, E. M., The Observational Basis for JPL's DE200, the Planetary Ephemerides of the Astronomical Almanac, *Astron. Astrophys.*, **233**, 252-271, 1990.
74. Stephenson, F. R., and L. V. Morrison, Long-Term Changes in the Rotation of the Earth: 700 B.C. to A.D. 1980, *Phil. Trans. R. Soc. London*, **A313**, 47-70, 1984.
75. Wahr, J. M., The Forced Nutations of an Elliptical, Rotating, Elastic, and Oceanless Earth, *Geophys. J. Roy. Astron. Soc.*, 64, 705-727, 1981.
76. Wahr, J. M., The Effects of the Atmosphere and Oceans on the Earth's Wobble and on the Seasonal Variations in the Length of Day—II, Results, *Geophys. J. R. Astron. Soc.*, **74**, 451-487, 1983.
77. Wahr, J. M., The Earth's Rotation, *Ann. Rev. Earth Planet Sci.*, **16**, 231-249, 1988.
78. Williams, J. G., X X Newhall, J. O. Dickey, Luni-solar Precession: Determination from Lunar Laser Ranging, *Astron. Astrophys. Lett.*, **241**, L9-L12, 1991.
79. Wilson, C. R., and R. O. Vincente, An Analysis of the Homogeneous ILS Polar Motion Series, *Geophys. J. R. Astron. Soc.*, **62**, 605-616, 1980.
80. Yoder, C. F., M. W. Parke, and J. G. Williams, Tidal Variations of the Earth's Rotation, *J. Geophys. Res.*, **86**, B2, 881-891, 1981.
81. Yumi, S. and K. Yokoyama, Results of the International Latitude Service in a Homogeneous System 1899.9-1979.0, Publications, *Central Bureau of the International Polar Motion Service,* Mizusawa, 1980.
82. Zhu, S. Y., E. Groten and C. Reigber, Various Aspects of the Numerical Determination of Nutation Constants, II, An Improved Nutation Series for the Deformable Earth, *Astron. J.*, **99**, 1024-1044, 1990.

Subject Index